SYNTHESIS, CHARACTERIZATION AND THERAPEUTIC PROFILING OF FUNCTIONALIZED 1,7-DIARYL HEPTANOIDS AND THEIR METAL CHELATES FOR ANTICANCER, ANTI-INFLAMMATORY, ANTIDIABETIC AND ANTIMICROBIAL PROPERTIES

Thesis submitted to

UNIVERSITY OF CALICUT

In partial fulfilment of the requirement for the Degree of

DOCTOR OF PHILOSOPHY IN CHEMISTRY

Under the Faculty of Science

By

LOVELY JACOB A

Supervisor

Dr. TOM CHERIAN

RESEARCH & POST GRADUATE DEPARTMENT OF CHEMISTRY
CHRIST COLLEGE (AUTONOMOUS), IRINJALAKUDA
THRISSUR, KERALA - 680 125

FEBRUARY 2025

DECLARATION

I hereby declare that the work presented in the thesis entitled **"Synthesis, characterization and therapeutic profiling of functionalized 1,7-diaryl heptanoids and their metal chelates for anticancer, anti-inflammatory, antidiabetic and antimicrobial properties"** is based on the original work done by me under the guidance of Dr. Tom Cherian, Asst. Professor, Research & P.G. Department of Chemistry, Christ College (Autonomous), Irinjalakuda, Kerala and has not been included in any other thesis submitted previously for the award of any degree. The contents of the thesis have undergone a plagiarism check using iThenticate software at C.H.M.K. Library, University of Calicut, and the similarity index found within the permissible limit. I also declare that the thesis is free from AI generated content.

Signature Lovely Jacob A

Name of the scholar: Lovely Jacob A

P.G & Research Dept. of Chemistry ★ Christ College (Autonomous) ★ Irinjalakuda Thrissur Pin-680 125

Signature of the Supervising teacher

Name: Dr. Tom Cherian

Dr. TOM CHERIAN
ASSISTANT PROFESSOR
P.G & RESEARCH DEPT. OF CHEMISTRY
CHRIST COLLEGE (AUTONOMOUS)
IRINJALAKUDA

Place: Irinjalakuda

Date: 19.11.2025

CHRIST
COLLEGE (AUTONOMOUS)
IRINJALAKUDA, KERALA
IRINJALAKUDA – 680 125, KERALA, INDIA Office (0480) 2825258
office@christcollegeijk.edu.in www.christcollegeijk.edu.in
(Reg. No. 137/75; No.F.22-1/2015/AC.U.G.C.)
Affiliated to University of Calicut and Reaccredited by NAAC A++ & SAAC A+ Grade

Ref. CC/CHEM/TM/2024-25/LOVELY JACOB A/02 **Date: 14th November 2025**

CERTIFICATE

This is to certify that the thesis entitled **"Synthesis, characterization and therapeutic profiling of functionalized 1,7-diaryl heptanoids and their metal chelates for anticancer, anti-inflammatory, antidiabetic and antimicrobial properties"** is an authentic record of the research work carried out by **LOVELY JACOB A** (Reg.No.U.O.No.13478/2018/Admn.), under my supervision in partial fulfilment of the requirements for the Degree of Doctor of Philosophy in Chemistry of the University of Calicut. No part of the thesis has formed the basis for the award of any degree, diploma or other similar titles of any University. It is further certified that neither of the adjudicators has suggested any corrections to the Ph.D. thesis and that the contents of the printed thesis and the soft copy are identical.

P.G & Research Dept. of Chemistry ★ Christ College (Autonomous) ★ Irinjalakuda Thrissur Pin-680 125

Dr. TOM CHERIAN
ASSISTANT PROFESSOR
P.G & RESEARCH DEPT. OF CHEMISTRY
CHRIST COLLEGE (AUTONOMOUS)
IRINJALAKUDA

CHRIST
COLLEGE (AUTONOMOUS)
IRINJALAKUDA, KERALA
IRINJALAKUDA – 680 125, KERALA, INDIA Office (0480) 2825258
office@christcollegeijk.edu.in www.christcollegeijk.edu.in
(Reg. No. 137/75; No.F.22-1/2015/AC.U.G.C.)
Affiliated to University of Calicut and Reaccredited by NAAC A++ & SAAC A+ Grade

CC/2024-25/Ph.D THESIS SUBMISSION/LOVELY JACOB A/06. 28th FEBRUARY 2025.

CERTIFICATE

This is to certify that **LOVELY JACOB A** (Reg. No. U.O.No. 13478/2018/Admn.) has completed her research work for the part-time period prescribed under the Ph.D ordinance of the university of Calicut. This thesis entitled "**Synthesis, characterization and therapeutic profiling of functionalized 1,7-diaryl heptanoids and their metal chelates for anticancer, anti-inflammatory, antidiabetic and antimicrobial properties**" embodies the results of her investigation conducted during the period at which, she worked as a research scholar in this institute under the guidance of Dr. Tom Cherian, Asst. Professor, PG and Research Dept. of Chemistry. I recommend the thesis to be submitted for the evaluation and further for the award of the Degree of Doctor of Philosophy in Chemistry of the University of Calicut.

Principal
PRINCIPAL
CHRIST COLLEGE (AUTONOMOUS)
IRINJALAKUDA

UNIVERSITYOFCALICUT

CERTIFICATEONPLAGIARISMCHECK

1.	Name of the Research Scholar	Lovely Jacob A	
2.	Title of thesis / dissertation	"Synthesis, characterization and therapeutic profiling of functionalized 1,7-diaryl heptanoids and their metal chelates for anticancer, anti-inflammatory, antidiabetic and antimicrobial properties"	
3.	Name of the Supervisor	Dr.Tom Cherian	
4.	Department/Institution	Research & P.G. Department of Chemistry Christ College (Autonomous), Irinjalakuda	
5.	Similar content (%) identified	Non Core	Core
		Introduction/ Theoretical overview/ Review of literature/ Materials & Methods/ Methodology	**Analysis/Result/Discussion/Summary/ Conclusion/ Recommendations**
		4 %	4 %
	Acceptable maximum limit (%)	10	10
6.	Software used	iThenticate	
7.	Date of verification	16.02.25	

**Report on plagiarism check, specifying included /excluded items with % of similarity to be attached.*

Checked by (with name, designation & signature) Dr. Nasirudheen. T
Assistant Librarian
University of Calicut, Kerala.

Name and signature of the Researcher Lovely Jacob A
LOVELY JACOB A

Name and signature of the Supervisor
DR. TOM CHERIAN

The Doctoral Committee* has verified the report on plagiarism check with the contents of the thesis, as summarized above and appropriate measures have been taken to ensure originality of the Research accomplished herein.

Name & Signature of the HoD/HoI (Chairperson of the Doctoral Committee)
Fr. Dr. Jolly Andrews
Associate Professor -
In-Charge of Principal
Christ College (Autonomous)
Irinjalakuda

**In the case of languages like Malayalam, Tamil etc., on which no software is available for plagiarism check, a manual check shall be made by the Doctoral Committee, for which an additional certificate has to be attached.*

E-mail: amalacancerresearch@gmail.com

Phone: 0487 2307968

Institutional Animal Ethics Committee (IAEC)

(Reg. No. 149/PO/Rc/S/1999/CPCSEA)

Amala Cancer Research Centre Society

AMALANAGAR - 680 555, THRISSUR, KERALA, INDIA

Ref :

Date: 06.07.2022

Certificate

This is to certify that the project proposal no. ACRC/IAEC/22(1)–P4 entitled 'Synthesis, Characterization and biological evaluation some heterocyclic curcumin analogues and their transition metal complexes' submitted by Dr. Achuthan C R (on behalf of Lovely Jacob A) has been approved by the IAEC of Amala Cancer Research Centre in its meeting held on 06.07.2022 and 99 Swiss albino mice have been sanctioned under this proposal.

Authorized by	Name	Signature	Date
Chairman:	Dr. T D Babu	.....	06.07.2022
Member Secretary:	Dr. Achuthan C R	.....	06.07.2022
Main Nominee of CPCSEA:	Dr. C B Devanand	.....	06.07.2022

ACKNOWLEDGEMENT

I express my heartfelt gratitude and deep indebtedness to my supervising teacher, Dr.Tom Cherian, Assistant Professor, P.G. and Research Department of Chemistry, Christ College (Autonomous), Irinjalakuda, Kerala, for his inspiring and intellectual guidance, constructive criticism, unwavering support, personal care, and immense patience. His mentorship has been invaluable in building my confidence throughout this research journey, and no words can truly express my deep appreciation for his guidance.

I am extremely grateful to Rev. Fr. Dr. Jolly Andrews C.M.I., Principal, Christ College (Autonomous), Irinjalakuda, for providing me with the opportunity to pursue research at the P.G. and Research Department of Chemistry at Christ College (Autonomous) and for his sincere support throughout my academic journey. I also sincerely thank our former principal, Dr. Mathew Paul Ukken, for encouraging my educational pursuits.

My sincere thanks go to Dr. Rani Varghese, Head, P.G. and Research Department of Chemistry, Christ College (Autonomous), and the former Head of the Department, Dr.Joy V. T., for their continuous support and encouragement. I also deeply appreciate the teaching and non-teaching staff of the P.G. and Research Department of Chemistry, Christ College (Autonomous), for their wholehearted cooperation. I am also deeply thankful to Dr.Josheena Jose, Research Coordinator, Christ College (Autonomous), Irinjalakuda, for her unwavering support.

I am extremely grateful to the Manager, Principal, and staff of Little Flower College, Guruvayoor, for their assistance during this challenging endeavor. My heartfelt gratitude goes to my former principals, especially Rev. Sr. Dr. Moly Clare. I extend my sincere thanks to Dr. Moly P. P., Head, Department of Chemistry, Little Flower College, Guruvayoor, and to the former Heads of the Department, Dr. Lali Thomas Kotturan and Dr. Jessy Anto Therattil, for their broad-hearted support, guidance, and prayers. I am grateful to my chemistry family at Little Flower College, Guruvayoor, for their encouragement and assistance.

I would like to extend my sincere thanks to Dr. V. D. John, Dr. Mity Thambi, Dr. Sinosh Skariyachan, Dr. Seena Thomachan, Rev. Fr. Dr. Devassy Panthallookkaran, and Dr. Jesy E. J., for their generous encouragement and unwavering support throughout my research journey.I am sincerely grateful to my fellow research scholars, especially my co-worker, Deepthy Varghese, for their valuable advice and timely help during my studies.

I am profoundly thankful to Dr. Achuthan C. R., Associate Professor, Department of Biochemistry, Amala Cancer Research Centre, Thrissur, for his valuable guidance during the

in vivo experiments. I extend my sincere gratitude to Mrs. Preetha C. G., Amala Cancer Research Centre, Thrissur, for her warm and limitless support. My thanks also go to Sunitha, Jimsy Johnson, Reshma Ramachandran, Sruthy, and all other research scholars at Amala Cancer Research Centre, Thrissur, for their immense help, support, and cooperation.

I extend my gratitude to STIC-Kochi, SAIF-Thiruvananthapuram, Athmic Bio-Tech-Thiruvananthapuram, Government Women's College, Thiruvananthapuram, St. Thoma's College, Thrissur, Amala Cancer Research Centre, Thrissur, Amala Medical College, Thrissur, and Jeeva Lab, Thrissur, for providing instrumental and laboratory facilities for my research analysis.

I gratefully acknowledge the University of Calicut for its academic affiliation and continued support. I extend my sincere gratitude to the Dr. Nasirudheen, Librarian, University of Calicut, Fr. Sibi Francis, Librarian, Christ College (Autonomous), Irinjalakuda, and Sr. Joicelit, Librarian, Little Flower College, Guruvayoor, for their invaluable assistance in providing access to essential resources and literature that greatly contributed to my research.

I express my heartfelt gratitude to the Franciscan Clarist Congregation, especially my Provincial Superior, Rev. Sr. Phonsy Maria, and former Provincial Superiors, Rev. Sr. Dr. Rose Anitha and Rev. Sr. Little Mary, for their enthusiastic support and constructive guidance, which gave me the confidence to pursue research. I am particularly grateful to all the sisters and my Superiors, Rev. Sr. Dr. Mariena Aloor, Rev. Sr. Arpitha, and Rev. Sr. Annejoe, for their endless support and concern during the completion of my research work.

Words are not enough to express my profound gratitude to my beloved parents, Mr. A. I. Jacob and Mrs. Alphonsa Jacob, for their unconditional love, prayers, support, and encouragement throughout my academic journey. The recent passing of my dear father has left a void in my heart, but his unwavering belief in my abilities and his blessings continue to inspire me every day. My loving thanks also go to my dear siblings, Mrs. Sherly Binoy and Dr. Lejo Jacob, and to my brother-in-law, Mr. Binoy Jacob and sister-in-law, Mrs. Daisy Lejo, for their constant encouragement and goodwill.

I extend my sincere appreciation to all my family members, respected teachers, and dear friends who have stood by me throughout this journey.

I offer my deepest gratitude to the Holy Spirit for the providential care bestowed upon me during this research. Above all, I thank God Almighty for His immeasurable blessings of strength, wisdom, love, and endurance, which have enabled me to complete this work successfully.

LOVELY JACOB A.

Dedicated to

- *My Almighty God*
- *My beloved Parents*
- *My Franciscan Clarist Congregation*

PREFACE

Chapter 1 provided a general introduction and review of the literature of the present work. Global health issues, such as cancer, diabetes, inflammation, and microbial infections (including bacterial and fungal), posed major challenges worldwide, and Kerala, India, was no exception. Breast cancer and diabetes have become increasingly prevalent in Kerala, with limited effectiveness of current treatments and associated side effects. Chemistry played a vital role in addressing these challenges through drug discovery and development.

This study employed a multidisciplinary approach that combined chemistry, pharmacology, and computational biology to streamline drug discovery. The primary objective was to synthesize nine curcumin analogues and eighteen metal complexes, focusing on anticancer, antidiabetic, anti-inflammatory, antibacterial, and antifungal properties. Structure-activity relationship (SAR) studies, molecular docking, dynamics simulations, and ADME-Tox prediction provided insights into binding efficacy, pharmacokinetics, and toxicity. Experimental validation bridged computational findings with practical applications. Spectral analysis characterized the molecular structures of the compounds, while virtual screening and lead optimization identified compounds with improved bioactivity and reduced side effects. In summary, the synthesized curcumin analogues and metal complexes held potential as therapeutic candidates, contributing to medicinal chemistry and paving the way for innovative treatments across various diseases.

Chapter 2 focused on the *in silico* design and selection of curcumin analogues with potential therapeutic properties, specifically targeting anticancer, anti-inflammatory, antidiabetic, and antimicrobial activities. A thorough literature review highlighted various structural modifications to curcumin, such as chlorination, alkylation, and the addition of hydroxyl and alkoxy groups, which improved its pharmacokinetic and pharmacodynamic properties. The nine curcumin analogues (NLB, NLD, NLE, NLF, NLG, NLH, NLI, NLJ, NLK) were evaluated using the CMC-like Rule and other established guidelines, confirming their suitability for further development. These compounds met the Rule of Five, indicating good oral bioavailability, and demonstrated favourable ADME properties, with strong plasma protein binding, good absorption, and moderate permeability. They also showed promising toxicity profiles, non-carcinogenic and non-mutagenic, with medium ecotoxicity risks. Depending on their ability to cross the blood-brain barrier (BBB), the

compounds were considered suitable for either central nervous system (medium BBB) or peripheral (low BBB) targets. The next phase of the study involved scaling up synthesis and conducting comprehensive *in vitro* and *in vivo* experiments, including molecular docking studies, to investigate the interactions of these compounds with relevant protein targets for their therapeutic effects.

Chapter 3 emphasized the synthesis and characterization of curcumin analogues and their copper(II) and zinc(II) metal complexes. The curcumin analogues were synthesized using Pabon's method based on the Claisen–Schmidt condensation mechanism, known for its simplicity, high yields, and minimal by-products. Nine curcumin analogues were created by varying functional groups on the aryl rings to meet specific medicinal objectives. The synthesized compounds were purified using techniques such as thin-layer chromatography, column chromatography, distillation, and recrystallization. Their chemical structures were confirmed through various analytical methods, including infrared (IR) spectroscopy, proton and ^{13}C nuclear magnetic resonance (NMR) spectroscopy, mass spectrometry, and elemental analysis. Moreover, Cu(II) and Zn(II) metal complexes of the curcumin analogues were synthesized to improve their stability, solubility, and biomedical properties. These metal complexes were also purified and characterized to ensure their suitability for further experimental investigations.

Chapter 4 investigated the screening of curcumin analogues for their anticancer potential against breast cancer receptors, specifically BRCA1 and TP53. The analogues, modified from natural curcumin, were evaluated using molecular docking, dynamic simulations, and MM/GBSA binding free energy calculations. NLH, a chloro-substituted curcumin analogue, showed strong binding affinity with the TG3 target, a homolog of BRCA1, outperforming cyclophosphamide in docking studies. *In vitro* cytotoxicity assays on NLH and its metal complexes (Cu(II) and Zn(II)) demonstrated significant activity against cancer cell lines, particularly DLA and EAC, while showing minimal toxicity towards spleen cells. In vivo studies with NLH in Swiss albino mice revealed significant inhibition of tumour growth compared to cyclophosphamide, further supporting the establishment of NLH as a promising candidate for further development into multi-target therapeutics, with additional research needed to optimize its efficacy and minimize side effects.

Chapter 5 evaluated the anti-inflammatory and antidiabetic potential of curcumin analogues and their metal complexes. Molecular docking studies and in vitro experiments were conducted to assess their binding affinities towards inflammatory and diabetes receptors. A comparative analysis was also performed with natural curcumin and FDA-approved drugs, Diclofenac (anti-inflammatory) and Acarbose (antidiabetic). Among the analogues, NLD, NLE, and NLF showed the highest anti-inflammatory activity, followed by NLH and NLK. Cu(II) and Zn(II) complexes exhibited superior anti-inflammatory activity compared to curcumin, with Zn(II) complexes, especially $Zn(NLH)_2$ and $Zn(NLE)_2$, being the most potent. For antidiabetic effects, NLB, NLH, and NLE were the most effective, with Cu(II) and Zn(II) complexes demonstrating enhanced activity. Zn(II) complexes were more effective due to better stability, bioavailability, and synergy with the properties of curcumin. The splenocytic assay confirmed the efficacy of the top candidates, highlighting the promising potential of Zn(II) complexes for diabetes management.

Chapter 6 focused on screening curcumin analogues for antibacterial and antifungal activity against Gram-positive and Gram-negative bacteria, as well as fungal receptors. The analogues were synthesized by modifying the functional groups on curcumin's aryl rings. Molecular docking studies, followed by in vitro validation, were used to assess their binding affinities compared to natural curcumin and FDA-approved drugs (Gentamycin and Fluconazole). Notably, NLE and NLD exhibited the most promising antibacterial and antifungal activities, with Cu(II) and Zn(II) complexes, especially $Cu(NLE)_2$ and $Zn(NLE)_2$, showing superior antibacterial efficacy. Zn(II) complexes, particularly $Zn(NLD)_2$ and $Zn(NLE)_2$, demonstrated strong antifungal activity against *Candida albicans*. The splenocytic assay revealed that NLD, NLE, and their metal complexes had minimal cytotoxicity on spleen cell lines, suggesting their potential as safe therapeutic agents. These results highlighted the antimicrobial potential of curcumin analogues and their metal complexes for future drug development.

Chapter 7 outlined the Conclusions of the present work. The multidisciplinary approach to designing, synthesizing, and evaluating nine curcumin analogues and their Cu(II) and Zn(II) metal complexes for anticancer, antidiabetic, anti-inflammatory, antibacterial, and antifungal activities demonstrated favourable ADME properties and promising interactions with key biological targets, as shown by molecular docking studies. *In vitro* and *in vivo* evaluations confirmed the superior efficacy of analogues like NLH,

NLE, and NLD, with Cu(II) and Zn(II) complexes exhibiting potent anticancer, anti-inflammatory, and antimicrobial effects. Notably, Zn(II) complexes, particularly $Zn(NLH)_2$ and $Zn(NLE)_2$, outperformed copper complexes in terms of bioactivity and safety. The research highlighted the potential of these curcumin analogues and their metal complexes as versatile therapeutic agents with minimized side effects. Future research should focus on mechanistic studies, *in vivo* evaluations, combination therapies, and the development of nano-formulated compounds to enhance stability and targeted delivery for clinical applications.

Chapter 8 presented recommendations for future research. This study integrated synthetic chemistry, computational biology, and pharmacological evaluation to explore curcumin analogues and their copper(II) and zinc(II) complexes for anticancer, antidiabetic, anti-inflammatory, antibacterial, and antifungal activities. Future research should optimize bioactivity by modifying functional groups and using advanced molecular docking, including QM/MM simulations. Extending docking studies to metal complexes and employing all-atom molecular dynamics, Free Energy Perturbation (FEP), and metadynamic simulations can enhance understanding of ligand-protein interactions. Multi-target optimization should focus on multifunctional compounds like NLD and NLH. Further biochemical assays (e.g., COX, α-Glucosidase, SPR, ITC) and in vivo studies are essential for evaluating efficacy and safety. Exploring synergistic therapies and nano-synthesis techniques can improve bioavailability and targeted drug delivery. This research provides a strong foundation for drug development, with future directions integrating computational, biochemical, and clinical studies to refine curcumin analogues for therapeutic applications.

ABSTRACT

This study explored the design, synthesis, and evaluation of nine curcumin analogues and their Cu(II) and Zn(II) metal complexes for therapeutic applications against cancer, diabetes, inflammation, and microbial infections. It employed a multidisciplinary approach integrating chemistry, pharmacology, and computational biology, combining molecular docking, dynamics simulations, and ADME-Tox predictions with *in vitro* and *in vivo* experiments.

The curcumin analogues, synthesized via Pabon's method, were structurally modified to enhance pharmacokinetic and pharmacodynamic properties. Spectral characterization confirmed their structures, while virtual screening identified promising candidates with strong bioactivity and minimal toxicity. Zn(II) and Cu(II) complexes exhibited improved stability and solubility, with Zn(II) complexes generally outperforming Cu(II) complexes in bioactivity and safety.

Key findings included the strong anticancer potential of NLH, particularly its Zn(II) complex ($Zn(NLH)_2$), against breast cancer targets BRCA1 and TP53. NLE, NLD, and NLF demonstrated high anti-inflammatory activity, while NLB, NLH, and NLE were effective against diabetes-related targets. Zn(II) complexes like $Zn(NLE)_2$ and $Zn(NLD)_2$ were notably potent, showing superior efficacy and reduced cytotoxicity. Antimicrobial studies revealed that NLE and NLD, along with their Zn(II) and Cu(II) complexes, demonstrated strong antibacterial activity against both Gram-positive and Gram-negative bacteria, as well as significant antifungal properties, particularly against *Candida albicans*.

The research successfully synthesized and characterized nine curcumin analogues and their Cu(II) and Zn(II) complexes, demonstrating their potential as multi-functional therapeutic agents. The research confirmed the therapeutic potential of curcumin analogues along with their copper and zinc complexes. The Zn(II) complexes were generally more effective and safer, making them more suitable for further drug development. The alignment of *in silico* findings with *in vitro* and *in vivo* data substantiated the promising bioactivity of these compounds. The study highlighted the potential of these compounds in the development of advanced multi-target drugs with minimized side effects.

Future research should optimize bioactivity, extend docking to metal complexes, employ advanced simulations, conduct biochemical and *in vivo* studies, explore synergistic therapies, and use nano-synthesis to refine curcumin analogues for drug development.

സംഗ്രഹം

ഈ പഠനം, കാൻസർ, പ്രമേഹം, ഇൻഫ്ലമേഷൻ, മൈക്രോബയൽ അണുബാധ എന്നിവയ്ക്കുള്ള ചികിത്സാ സാധ്യതകൾ വിലയിരുത്തുന്നതിനായി ഒമ്പത് കർക്കുമിൻ അനലോഗുകളുടെയും അവയുടെ Cu(II),Zn(II) മെറ്റൽ കോംപ്ലക്സുകളുടെയും രൂപകൽപ്പന, സംശ്ലേഷണം, മൂല്യനിർണ്ണയം എന്നിവ ഉൾപ്പെടുത്തി. രാസശാസ്ത്രം, ഫാർമക്കോളജി, കംപ്യൂട്ടേഷണൽ ബയോളജി എന്നിവ സംയോജിപ്പിച്ച ബഹുവിശ്രുത സമീപനമാണ് ഈ പഠനത്തിൽ സ്വീകരിച്ചത്. ഇതിൽ മോളിക്യൂലർ ഡോക്കിംഗ്, ഡൈനാമിക് സിമുലേഷനുകൾ, ADME-Tox പ്രവചനങ്ങൾ എന്നിവ ഇൻവിട്രോ, ഇൻവിവോ പരീക്ഷണങ്ങളുമായി സംയോജിപ്പിച്ചു.

പാബോൺസിന്റെ രീതി ഉപയോഗിച്ച് സംശ്ലേഷണം നടത്തിയ കർക്കുമിൻ അനലോഗുകൾ ഫാർമാക്കോകൈനെറ്റിക്, ഫാർമാക്കോഡൈനാമിക് ഗുണങ്ങൾ മെച്ചപ്പെടുത്താൻ ഘടനാപരമായി പരിഷ്കരിച്ചു. സ്പെക്ട്രൽ വിശകലനം ഘടനകൾ സ്ഥിരീകരിച്ചപ്പോൾ, വിർച്വൽ സ്ക്രീനിംഗിലൂടെ ശക്തമായ ബയോആക്റ്റിവിറ്റിയും കുറഞ്ഞ വിഷാംശവുമുള്ള വാഗ്ദാനപരമായ സംയുക്തങ്ങൾ തിരിച്ചറിഞ്ഞു. Zn(II), Cu(II) കോംപ്ലക്സുകൾ മെച്ചപ്പെട്ട സ്റ്റാബിലിറ്റിയും ലയിച്ചിരുപ്പ് ഗുണങ്ങളും പ്രകടിപ്പിച്ചു. Zn(II) കോംപ്ലക്സുകൾ സാധാരണയായി Cu(II) കോംപ്ലക്സുകളേക്കാൾ മികച്ച ബയോആക്റ്റിവിറ്റി, സുരക്ഷാ പ്രൊഫൈൽ എന്നിവയിലൂന്നിയിരുന്നു.

പ്രധാന കണ്ടെത്തലുകളിൽ, NLH, പ്രത്യേകിച്ച് അതിന്റെ Zn(II) കോംപ്ലെക്സ് ($Zn(NLH)_2$), BRCA1, TP53 മുതലായ സ്തനാർബുദ ടാർഗെറ്റുകളുമായി ശക്തമായ പ്രതിയോഗ്യത പ്രകടിപ്പിച്ചതായി കണ്ടെത്തി. NLE, NLD, NLF എന്നിവ ഉയർന്ന അളവിൽ അർബുദ വിരുദ്ധ പ്രവർത്തനം കാഴ്ചവെച്ചു. അതേസമയം NLB, NLH, NLE എന്നിവ പ്രമേഹബന്ധിത ടാർഗെറ്റുകൾക്കെതിരെ ഫലപ്രദമായി പ്രവർത്തിച്ചു. Zn(II) കോംപ്ലെക്സുകൾ $Zn(NLE)_2$, $Zn(NLD)_2$ മുതലായവ ഏറെ ശക്തിയുള്ളതായിരുന്നു, മെച്ചപ്പെട്ട ഫലപ്രാപ്തിയും കുറവുള്ള സൈറ്റോട്ടോക്സിസിറ്റിയുമാണ് അവ പ്രകടിപ്പിച്ചത്.

ആന്റിമൈക്രോബയൽ പഠനങ്ങൾ പ്രകാരം, NLE, NLD എന്നിവയും അവയുടെ Zn(II), Cu(II) കോംപ്ലെക്സുകളും ഗ്രാം-പോസിറ്റീവ്, ഗ്രാം-നെഗറ്റീവ് ബാക്ടീരിയകളോട് ശക്തമായ ആന്റിബാക്ടീരിയൽ പ്രവർത്തനം കാഴ്ചവെച്ചതോടൊപ്പം ആന്റിഫംഗൽ സ്വഭാവവും പ്രകടിപ്പിച്ചു.

ഈ പഠനത്തിലൂടെ ഒമ്പത് കർക്കുമിൻ അനലോഗുകളുടെയും അവയുടെ Cu(II), Zn(II) കോംപ്ലെക്സുകളുടെയും വിജയകരമായ സംശ്ലേഷണവും സ്വഭാവനിർണ്ണയവും നടത്തുകയും, ഇവ ബഹുമുഖ ചികിത്സാ സാധ്യതയുള്ളതാണെന്ന് തെളിയിക്കുകയും ചെയ്തു. Zn(II) കോംപ്ലെക്സുകൾ സാധാരണയായി കൂടുതൽ ഫലപ്രദവും സുരക്ഷിതവുമാണെന്ന് കണ്ടെത്തി, അതിനാൽ ഭാവിയിലേക്കുള്ള മരുന്ന് വികസനത്തിനായി കൂടുതൽ അനുയോജ്യമാണ്. ഇൻസിലിക്കോ കണ്ടുപിടിത്തങ്ങൾ ഇൻവിട്രോ, ഇൻവിവോ ഡാറ്റയുമായി പൊരുത്തപ്പെട്ടതിനാൽ ഈ സംയുക്തങ്ങൾ ഉദ്ദേശിച്ച ഉപയോഗത്തിനായി ഉചിതമാണെന്ന് തെളിയിച്ചു. കൂടാതെ, പരിമിതമായ ദോഷപ്രഭാവങ്ങളോടെ മൾട്ടി-ടാർഗറ്റ് മരുന്നുകളുടെ വികസന സാധ്യതയുമാണ് ഈ പഠനം മുന്നോട്ടുവച്ചത്.

ബയോആക്റ്റിവിറ്റി മെച്ചപ്പെടുത്തുന്നതിന് പ്രവർത്തക സമുച്ചയങ്ങൾ പരിഷ്കരിക്കേണ്ടതുണ്ട്. മെറ്റൽ കോംപ്ലെക്സുകളിലേക്കുള്ള ഡോക്കിംഗ് വ്യാപിപ്പിക്കുകയും പുരോഗതിയുള്ള സിമുലേഷനുകൾ, എഫ്ഇപി, മെറ്റാ ഡൈനാമിക്സ്, മോളിക്യൂലാർ ഡൈനാമിക്സ് എന്നിവ ഉപയോഗിക്കുകയും വേണം. ബയോകെമിക്കൽ, ഇൻവിവോ പഠനങ്ങൾ, സൈനേർജിസ്റ്റിക് ചികിത്സാ സമീപനങ്ങൾ, നാനോ സിന്തെസിസ് എന്നിവ ഉപയോഗിച്ച് കർക്കുമിൻ അനലോഗുകളുടെ മരുന്ന് വികസനം മെച്ചപ്പെടുത്തേണ്ടതുണ്ട്.

CONTENTS

Chapter 1. General introduction and review of literature **1-36**

1.1. General Introduction 1

1.1.1. Importance of medicinal plants 2

1.1.2. Turmeric-the golden spice 2

1.1.3. Modifications of natural curcumin - different methods 4

1.1.4. Curcumin analogues and their importance 5

1.1.5. Benefits of curcumin analogues in biological applications both *in vitro* and *in vivo* 7

1.1.6. Curcumin analogue-metal complexes and their biological applications 7

1.1.7. The Role and Relevance of computational modelling and virtual screening in modern drug discovery 9

1.2. Review of literature 13

1.2.1. Introduction 13

1.2.2. Curcumin analogue synthesis and biomedical applications 13

1.2.3. Curcumin analogue-metal complex synthesis and medicinal applications 16

1.2.4. Importance of Cu (II) and Zn (II) metal complexes of curcumin analogues 19

1.2.5. Molecular modelling studies of curcumin analogues 21

1.3. Scope and objective of the present investigation 23

1.4. Conclusions 24

1.5. Reference 25

Chapter 2. *In silico* design and selection of curcumin analogues with drug-like properties **37-54**

2.1. introduction 37

2.1.1. Designing of curcumin analogues and biomedical applications 38

2.1.2. Identifying structural features and constraints 38

2.2. Literature review 39

2.3. Materials and methods 42

2.3.1. Analogue design and generation 42

2.3.2. Filtering for drug-like properties & computational screening and prediction 43

2.4. Result and discussion 43

2.4.1. Molecular design and generation of analogues 43

2.4.2. Filtering for drug-like properties 45

2.4.3. Computational screening of designed molecules 46

2.5. Conclusion 49

2.6. References 50

Chapter 3. Synthesis and characterization of curcumin analogues and their Cu (II) and Zn (II) metal complexes **55-245**

3.1. Introduction 55
3.2. Review of literature 56
3.3. Materials and methods 59
3.3.1. Methods for the synthesis and purification of curcumin 59
3.3.2. Synthesis and purification of Cu (II) And Zn (II) metal complexes of curcumin analogues 61
3.4. Characterization of ligands and metal complexes 61
3.4.1. IR Spectroscopy 61
3.4.2. ^{1}HNMR Spectroscopy 62
3.4.3. ^{13}C NMR Spectroscopy 62
3.4.4. Mass Spectroscopy 62
3.4.5. CHNS Analysis 62
3.5. Result and discussion 62
3.6. Conclusion 241
3.7. References 242

Chapter 4. Experimental validation of the anticancer effects of curcumin analogues and their metal complexes: *in silico*, *in vitro* and i*n vivo* approaches **246-319**

4.1. Introduction 246
4.2. Review of literature 247
4.3. Materials and methods 250
4.3.1. *In silico* studies - Anticancer effect of curcumin analogues 250
4.3.2. *In vitro* studies - Anticancer effect of curcumin analogues and their metal complexes 254
4.3.3. *In vivo* antitumor studies using Dalton's Lymphoma Ascites 256
4.4. Results and discussion 260
4.4.1. *In silico* Studies 262
4.4.2. *In vitro* cytotoxic studies 290
4.4.3. *In vivo* studies 299
4.5. Conclusion 313
4.6. References 315

Chapter 5. *In silico* and *in vitro* assessment of anti-inflammatory and antidiabetic activities of curcumin analogues and their metal complexes **320-385**

5.1. Introduction 320
5.2. Review of literature 321
5.3. Materials and methods 324
5.3.1. *In silico* studies of anti-inflammatory and anti-diabetic effects of curcumin analogues 324
5.3.2. *In vitro* studies of anti-Inflammatory and anti-diabetic 327

effects of curcumin analogues
5.4. Results and discussion 329
5.4.1. Anti-inflammatory effect of curcumin analogues and their metal complexes 329
5.4.2. Anti-diabetic effect of curcumin analogues and their metal complexes 353
5.4.3. Splenocytic Assay (Spleen Cell Lines) 376
5.5. Conclusion 379
5.6. References 381

Chapter 6. *In silico* and *in vitro* evaluation of antibacterial and antifungal Potency of curcumin analogues and their metal complexes **386-459**
6.1. Introduction 386
6.2. Review of Literature 387
6.3. Materials And Methods 394
6.3.1. *In Silico* studies of antibacterial and antifungal effects of curcumin analogues 394
6.3.2. *In vitro* Studies of antibacterial and antifungal effects of curcumin analogues and their metal complexes 398
6.4. Results and discussion 400
6.4.1 Antibacterial effects of curcumin analogues and their metal complexes 400
6.4.2. Antifungal effect of curcumin analogues and their metal complexes 435
6.4.3. Splenocytic Assay (Spleen Cell Lines) 450
6.5. Conclusion 451
6.6. References 453

Chapter 7. Conclusions **460-464**

Chapter 8. Recommendations for future studies **465-466**

List of Publications and Presentations **467-468**

LIST OF TABLES

Table 2.1 Summary of Therapeutic Potential of Chlorinated Curcumin Analogues

Table 2.2 Curcumin Analogues and their Molecular Properties with Lipinski Rule of Five

Table 2.3 The pharmacokinetic features of the curcumin analogues

Table 3.1 Summary of Key Findings on Curcumin Analogues and Their Metal Complexes

Table 3.2 Possible IR assignments of NLB

Table 3.3 Proton signals observed in the ^{1}H NMR spectrum of NLB

Table 3.4 ^{13}C NMR spectral data of NLB

Table 3.5 Molecular ion peaks of NLB

Table 3.6 Proton signals observed in the ^{1}H NMR spectrum of Cu $(NLB)_2$

Table 3.7 Molecular ion peaks of Cu $(NLB)_2$

Table 3.8 Proton signals observed in the ^{1}H NMR spectrum of Zn $(NLB)_2$

Table 3.9 Molecular ion peaks of Zn $(NLB)_2$

Table 3.10 Possible IR assignments of NLD

Table 3.11 Proton signals observed in the ^{1}H NMR spectrum of NLD

Table 3.12 ^{13}C NMR spectral data of NLD

Table 3.13 Molecular ion peaks of NLD

Table 3.14 Proton signals observed in the ^{1}H NMR spectrum of Cu $(NLD)_2$

Table 3.15 Molecular ion peaks of Cu $(NLD)_2$

Table 3.16 Proton signals observed in the ^{1}H NMR spectrum of Zn $(NLD)_2$

Table 3.17 Molecular ion peaks of Zn $(NLD)_2$

Table 3.18 Possible IR assignments of NLE

Table 3.19 Proton signals observed in the ^{1}H NMR spectrum of NLE

Table 3.20 ^{13}C NMR spectral data of NLE

Table 3.21 Molecular ion peaks of NLE

Table 3.22 Proton signals observed in the ^{1}HNMR spectrum of Cu $(NLE)_2$

Table 3.23 Molecular ion peaks of Cu $(NLE)_2$

Table 3.24 Proton signals observed in the ^{1}H NMR spectrum of Zn $(NLE)_2$

Table 3.25 Molecular ion peaks of Zn $(NLE)_2$

Table 3.26 Possible IR assignments of NLF

Table 3.27 Proton signals observed in the ^{1}H NMR spectrum of NLF

Table 3.28 ^{13}C NMR spectral data of NLF

Table 3.29 Molecular ion peaks of NLF

Table 3.30 Proton signals observed in the ^{1}HNMR spectrum of Cu $(NLF)_2$

Table 3.31 Molecular ion peaks of Cu $(NLF)_2$

Table 3.32 Proton signals observed in the ^{1}H NMR spectrum of Zn $(NLF)_2$

Table 3.33 Molecular ion peaks of Zn $(NLF)_2$

Table 3.34 Possible IR assignments of NLG

Table 3.35 Proton signals observed in the ^{1}H NMR spectrum of NLG

Table 3.36 ^{13}C NMR spectral data of NLG

Table 3.37 Molecular ion peaks of NLG

Table 3.38 Proton signals observed in the ^{1}HNMR spectrum of Cu $(NLG)_2$

Table 3.39 Molecular ion peaks of Cu $(NLG)_2$

Table 3.40 Proton signals observed in the ^{1}H NMR spectrum of Zn $(NLG)_2$

Table 3.41 Molecular ion peaks of Zn $(NLG)_2$

Table 3.42 Possible IR assignments of NLH

Table 3.43 Proton signals observed in the ^{1}H NMR spectrum of NLH

Table 3.44 ^{13}C NMR spectral data of NLH

Table 3.45 Molecular ion peaks of NLH

Table 3.46 Proton signals observed in the $^{1}HNMR$ spectrum of Cu $(NLH)_2$

Table 3.47 Molecular ion peaks of Cu $(NLH)_2$

Table 3.48 Proton signals observed in the $^{1}HNMR$ spectrum of Zn $(NLH)_2$

Table 3.49 Molecular ion peaks of Zn $(NLH)_2$

Table 3.50 Possible IR assignments of NLI

Table 3.51 Proton signals observed in the ^{1}H NMR spectrum of NLI

Table 3.52 ^{13}C NMR spectral data of NLI

Table 3.53 Molecular ion peaks of NLI

Table 3.54 Proton signals observed in the ^{1}H NMR spectrum of Cu $(NLI)_2$

Table 3.55 Molecular ion peaks of Cu $(NLI)_2$

Table 3.56 Proton signals observed in the ^{1}H NMR spectrum of Zn $(NLI)_2$

Table 3.57 Molecular ion peaks of Zn $(NLI)_2$

Table 3.58 Possible IR assignments of NLJ

Table 3.59 Proton signals observed in the ^{1}H NMR spectrum of NLJ

Table 3.60 ^{13}C NMR spectral data of NLJ

Table 3.61 Molecular ion peaks of NLJ

Table 3.62 Proton signals observed in the $^{1}HNMR$ spectrum of Cu $(NLJ)_2$

Table 3.63 Molecular ion peaks of Cu $(NLJ)_2$

Table 3.64 Proton signals observed in the $^{1}HNMR$ spectrum of Zn $(NLJ)_2$

Table 3.65 Molecular ion peaks of Zn $(NLJ)_2$

Table 3.66 Possible IR assignments of NLK

Table 3.67 Proton signals observed in the ^{1}H NMR spectrum of NLK

Table 3.68 ^{13}C NMR spectral data of NLK

Table 3.69 Molecular ion peaks of NLK

Table 3.70 Proton signals observed in the $^{1}HNMR$ spectrum of Cu $(NLK)_2$

Table 3.71 Molecular ion peaks of Cu $(NLK)_2$

Table 3.72 Proton signals observed in the $^{1}HNMR$ spectrum of Zn $(NLK)_2$

Table 3.73 Molecular ion peaks of Zn $(NLK)_2$

Table 4.1 Key findings and references on in silico docking for drug-target predictions

Table 4.2. The predicted binding potentials of the nine synthesised curcumin analogues and reference compounds

Table 4.3 The interactions of ligands with 4Y2Gthrough various amino acid residues

Table 4.4 The interactions of ligands with 1JM7 through various amino acid residues

Table 4.5 The interactions of ligands with 1OQA through various amino acid residues

Table 4.6 The interactions of ligands with 2JOZ through various amino acid residues

Table 4.7 The interactions of ligands with 2K8F through various amino acid residues

Table 4.8 The interactions of ligands with 2RUK through various amino acid residues

Table 4.9 Binding free energy calculations for the test and control using MM/GBSA

Table 4.10 Acute Toxicity Evaluation of NLH in Swiss Albino Mice

Table 4.11 Organo Somatic Index of Swiss Albino Mice

Table 4.12 Haematological Evaluation in Sub-Acute Toxicity Study

Table 4.13 The effect of NLH on Renal/Kidney Function

Table 4.14 The mean values with standard deviations for each treatment group across different liver enzymes

Table 4.15 Serum Lipid Profile

Table 4.16 The mean values with standard deviations for each Serum Electrolyte parameter

Table 4.17 The mean values with standard deviations for each Serum Protein parameter

Table 4.18 Analysis of bilirubin levels

Table 5.1 Key findings and references on curcumin analogues with Cu (II) and Zn (II) complexes, enhancing bioavailability and efficacy in treating inflammation and diabetes

Table 5.2 The predicted binding potentials of the nine synthesised curcumin analogues and the reference compounds to the prioritised inflammatory targets

Table 5.3 The interactions of ligands with 1HD2 through various amino acid residues

Table 5.4 The interactions of ligands with 3LN0 through various amino acid residues

Table 5.5 The predicted binding potentials of the nine synthesised curcumin analogues and the reference compounds to the prioritised inflammatory targets

Table 5.6 The interactions of ligands with 1IR3 through various amino acid residues

Table 5.7 The interactions of ligands with 3DH4 through various amino acid residues

Table 5.8 The percentage of cell death at different concentrations for each compound in Spleen Cell Lines

Table 6.1 Key findings and references on the antibacterial and antifungal properties of the curcumin analogues and their metal complexes

Table 6.2 Inoculums details of Bacterial cell lines

Table 6.3 Inoculums details of Fungal cell lines

Table 6.4 The predicted binding potentials of the nine synthesised curcumin analogues and reference compounds to the prioritized gram-positive *Staphylococcus aureus* bacterial targets

Table 6.5 The predicted binding potentials of the nine synthesised curcumin analogues and reference compounds to the prioritized gram-positive *Mycobacterium Smegmatis* bacterial targets

Table 6.6 The predicted binding potentials of the nine synthesised curcumin analogues and reference compounds to the prioritized gram-negative *Pseudomonas aeruginosa* bacterial targets

Table 6.7 The predicted binding potentials of the nine synthesised curcumin analogues and reference compounds to the prioritized gram-negative *Klebsiella Pneumonia bacterial* targets

Table 6.8. The predicted binding potentials of the nine synthesised curcumin analogues and reference compounds to the prioritized targets of *Candida Albicans*

LIST OF FIGURES

Fig.1.1 Three major structural components of Curcumin

Fig.1.2 Possibilities of functional group substitution on aryl rings on curcumin analogues

Fig.2.1 Curcumin analogues designed by Chem Draw are shown in the figure

Fig.3.1 Synthesis of curcumin by the general method proposed by Pabon

Fig.3.2 The IR spectrum of NLB

Fig.3.3 The ^{1}H NMR spectrum of NLB

Fig.3.4 The ^{13}CNMR spectrum of NLB

Fig.3.5 The Mass spectrum of NLB

Fig.3.6 The IR spectrum of Cu $(NLB)_2$

Fig.3.7 The ^{1}H NMR spectrum of Cu $(NLB)_2$

Fig.3.8 The Mass spectrum of Cu $(NLB)_2$

Fig.3.9 The IR spectrum of Zn $(NLB)_2$

Fig.3.10 The ^{1}H NMR spectrum of Zn $(NLB)_2$

Fig.3.11 The Mass spectrum of Zn $(NLB)_2$

Fig.3.12 The IR spectrum of NLD

Fig.3.13 The ^{1}H NMR spectrum of NLD

Fig.3.14 The ^{13}CNMR spectrum of NLD

Fig.3.15 The Mass spectrum of NLD

Fig.3.16 The IR spectrum of Cu $(NLD)_2$

Fig.3.17 The ^{1}H NMR spectrum of Cu $(NLD)_2$

Fig.3.18 The Mass spectrum of Cu $(NLD)_2$

Fig.3.19 The IR spectrum of Zn $(NLD)_2$

Fig.3.20 The ^1H NMR spectrum of Zn $(NLD)_2$

Fig.3.21 The Mass spectrum of Zn $(NLD)_2$

Fig.3.22 The IR spectrum of NLE

Fig.3.23 The ^1H NMR spectrum of NLE

Fig.3.24 The ^{13}CNMR spectrum of NLE

Fig.3.25 The Mass spectrum of NLE

Fig.3.26 The IR spectrum of Cu $(NLE)_2$

Fig.3.27 The ^1H NMR spectrum of Cu $(NLE)_2$

Fig.3.28 The Mass spectrum of Cu $(NLE)_2$

Fig.3.29 The IR spectrum of Zn $(NLE)_2$

Fig.3.30 The ^1H NMR spectrum of Zn $(NLE)_2$

Fig.3.31 The Mass spectrum of Zn $(NLE)_2$

Fig.3.32 The IR spectrum of NLF

Fig.3.33 The ^1H NMR spectrum of NLF

Fig.3.34 The ^{13}CNMR spectrum of NLF

Fig.3.35 The Mass spectrum of NLF

Fig.3.36 The IR spectrum of Cu $(NLF)_2$

Fig.3.37 The ^1H NMR spectrum of Cu $(NLF)_2$

Fig.3.38 The Mass spectrum of Cu $(NLF)_2$

Fig.3.39 The IR spectrum of Zn $(NLF)_2$

Fig.3.40 The 1H NMR spectrum of Zn $(NLF)_2$

Fig.3.41 The Mass spectrum of Zn $(NLF)_2$

Fig.3.42 The IR spectrum of NLG

Fig.3.43 The ^{1}H NMR spectrum of NLG

Fig.3.44 The ^{13}CNMR spectrum of NLG

Fig.3.45 The Mass spectrum of NLG

Fig.3.46 The IR spectrum of Cu $(NLG)_2$

Fig.3.47 The ^{1}H NMR spectrum of Cu $(NLG)_2$

Fig.3.48 The Mass spectrum of Cu $(NLG)_2$

Fig.3.49 The IR spectrum of Zn $(NLG)_2$

Fig.3.50 The ^{1}H NMR spectrum of Zn $(NLG)_2$

Fig.3.51 The Mass spectrum of Zn $(NLG)_2$

Fig.3.52 The IR spectrum of NLH

Fig.3.53 The ^{1}H NMR spectrum of NLH

Fig.3.54 The ^{13}CNMR spectrum of NLH

Fig.3.55 The Mass spectrum of NLH

Fig.3.56 The IR spectrum of Cu $(NLH)_2$

Fig.3.57 The ^{1}H NMR spectrum of Cu $(NLH)_2$

Fig.3.58 The Mass spectrum of Cu $(NLH)_2$

Fig.3.59 The IR spectrum of Zn $(NLH)_2$

Fig.3.60 The ^{1}H NMR spectrum of Zn $(NLH)_2$

Fig.3.61 The Mass spectrum of Zn $(NLH)_2$

Fig.3.62 The IR spectrum of NLI

Fig.3.63 The ^{1}H NMR spectrum of NLI

Fig.3.64 The ^{13}CNMR spectrum of NLI

Fig.3.65 The Mass spectrum of NLI

Fig.3.66 The IR spectrum of Cu $(NLI)_2$

Fig.3.67 The ^{1}H NMR spectrum of Cu $(NLI)_2$

Fig.3.68 The Mass spectrum of Cu $(NLI)_2$

Fig.3.69 The IR spectrum of Zn $(NLI)_2$

Fig.3.70 The ^{1}H NMR spectrum of Zn $(NLI)_2$

Fig.3.71 The Mass spectrum of Zn $(NLI)_2$

Fig.3.72 The IR spectrum of NLJ

Fig.3.73 The ^{1}H NMR spectrum of NLJ

Fig.3.74 The ^{13}CNMR spectrum of NLJ

Fig.3.75 The Mass spectrum of NLJ

Fig.3.76 The IR spectrum of Cu $(NLJ)_2$

Fig.3.77 The ^{1}H NMR spectrum of Cu $(NLJ)_2$

Fig.3.78 The Mass spectrum of Cu $(NLJ)_2$

Fig.3.79 The IR spectrum of Zn $(NLJ)_2$

Fig.3.80 The ^{1}H NMR spectrum of Zn $(NLJ)_2$

Fig.3.81 The Mass spectrum of Zn $(NLJ)_2$

Fig.3.82 The IR spectrum of NLK

Fig.3.83 The ^{1}H NMR spectrum of NLK

Fig.3.84 The ^{13}CNMR spectrum of NLK

Fig.3.85 The Mass spectrum of NLJ

Fig.3.86 The IR spectrum of Cu $(NLK)_2$

Fig.3.87 The ^{1}H NMR spectrum of Cu $(NLK)_2$

Fig.3.88 The Mass spectrum of Cu $(NLK)_2$

Fig.3.89 The IR spectrum of Zn $(NLK)_2$

Fig.3.90 The ^{1}H NMR spectrum of Zn $(NLK)_2$

Fig.3.91 The Mass spectrum of Zn $(NLK)_2$

Fig.4.1. *In vivo* Anti-tumour studies of curcumin analogues

Fig.4.2. Six key proteins encoded by the BRCA1 and TP53 genes and also the Target protein of the FDA-approved drug cyclophosphamide

Fig.4.3 4Y2G – Curcumin Analogue Complexes

Fig.4.4 1JM7 – Curcumin Analogue Complexes

Fig.4.5 1OQA–Curcumin Analogue Complexes

Fig.4.6 2JOZ – Curcumin Analogue Complexes

Fig.4.7 2K8F – Curcumin Analogue Complexes

Fig.4.8 2RUK – Curcumin Analogue Complexes

Fig.4.9 Selected target molecules with natural curcumin Complexes

Fig.4.10 Prediction of NLH binding potential with selected breast cancer Molecular targets was performed via molecular docking, and visualized using MGL Tools of Auto Dock

Fig.4.11 The binding of NLH and FDA-approved drug cyclophosphamide with Cyclophilin through molecular docking

Fig.4.12 The binding and stability of the docked complex of NLH with the BRCA1-BRCT-c domain using molecular dynamics simulation

Fig.4.13 The binding and stability of the docked complex of the conventional breast cancer drug Cyclophosphamide with its validated target using molecular dynamics simulation

Fig.4.14 The *in vitro* cytotoxicity results of various ligands

Fig.4.15 *In Vitro* Cytotoxicity of Ligands NLH and NLD Against EAC Cell lines

Fig.4.16 The figure depicts the *in vitro* cytotoxic effect of NLH on DLA, EAC, and rat spleen cell lines

Fig.4.17 Cu (II) Complexes of Curcumin Analogues-*In Vitro* Cytotoxicity Evaluation Against DLA Cells

Fig.4.18 Zn (II) Complexes of Curcumin Analogues-*In Vitro* Cytotoxicity Evaluation Against DLA Cells

Fig.4.19 Comparative Study of % Inhibition Induced by NLH on C127I Breast Cancer Cell Lines and Vero Non-Tumorigenic Cell Lines

Fig.4.20 The cytotoxic effect of NLH on C127I and Vero cell lines is shown in the figure

Fig.4.21 Effect of NLH on the morphology of various organs of Swiss albino mice

Fig.4.22 Acute Toxicity Evaluation of NLH in Swiss Albino Mice

Fig.4.23 Effect of NLH administration on the morphology of various organs of different groups of Swiss albino mice

Fig.4.24 Effect of NLH administration on the morphology of various organs of Swiss albino mice

Fig.4.25 Sub-Acute Toxicity Evaluation of NLH in Swiss Albino Mice

Fig.4.26 Histological Examination of Organs in Swiss Albino Mice: A Comparative Analysis

Fig.4.27 The Size of the tumour developed on the 28^{th} day after injecting DLA cells on the right hind of the Swiss Albino Mice

Fig.4.28 The effect of NLH on tumour volume and % inhibition is shown in Figure

Fig.4.29 The anti-tumour effect of NLH tumour tissue in Swiss Albino Mice

Fig.5.1 Proteins with germline mutations affect inflammation

Fig.5.2 1HD2-Curcumin Analogue Complexes

Fig.5.3 LN0-Curcumin Analogue Complexes

Fig.5.4 The IC_{50} values of various curcumin analogues and reference compounds

Fig.5.5 The IC_{50} values for Cu (II) complexes of various curcumin analogues, as well as reference compounds

Fig.5.6 IC_{50} values for Zn (II) complexes of various curcumin analogues and reference compounds

Fig.5.7 The best ligands demonstrated anti-inflammatory effects

Fig.5.8 The best Cu (II) and Zn (II) complexes of curcumin analogues demonstrate anti-inflammatory effects

Fig.5.9 Proteins with germline mutations affect diabetes

Fig.5.10 1IR3-Curcumin Analogue Complexes

Fig.5.11 3DH4-Curcumin Analogue Complexes

Fig.5.12 The IC_{50} values of various curcumin analogues and reference compounds

Fig.5.13 IC_{50} values for Cu (II) complexes of various curcumin analogues and reference compounds

Fig.5.14 IC_{50} values for various Zn (II) complexes of curcumin analogues, natural curcumin, and a reference compound

Fig.5.15 The best ligands demonstrating anti-diabetes effects

Fig.5.16 The best Cu (II) and Zn (II) complexes of curcumin analogues demonstrating antidiabetes effects

Fig.5.17 The percentage of cell death at different concentrations for each compound in Spleen Cell Lines

Fig.6.1 Proteins with germline mutations affect both Gram-positive and Gram-negative bacterial infections.

Fig.6.2 4H8E-Curcumin Analogue Complexes

Fig.6.3 1UZN -Curcumin Analogue Complexes

Fig.6.4 2W9S -Curcumin Analogue Complexes

Fig.6.5 4Q8I -Curcumin Analogue Complexes

Fig.6.6 1NPB -Curcumin Analogue Complexes

Fig.6.7 5O7N -Curcumin Analogue Complexes

Fig.6.8 4JVD -Curcumin Analogue Complexes

Fig.6.9 6B8A-Curcumin Analogue Complexes

Fig.6.10 Interactions between natural curcumin and the specific target molecules of Gram-positive and Gram-negative bacteria

Fig.6.11 Interactions between Gentamycin and the specific target molecules of Gram-positive and Gram-negative bacteria

Fig.6.12 The antibacterial activity values

Fig.6.13 The antibacterial activity of copper (II) complexes, Curcumin, and Gentamycin against four bacterial strains

Fig.6.14 The antibacterial activity of Zinc (II) complexes, Curcumin, and Gentamycin against four bacterial strains

Fig.6.15 The best results of antibacterial assay and the structures of corresponding compounds

Fig.6.16 Proteins with germline mutations affect fungal infections

Fig.6.17 4LEB-Curcumin Analogue Complexes

Fig.6.18 1IYL-Curcumin Analogue Complexes

Fig.6.19 The interactions of natural curcumin and fluconazole with the specific target molecules of *Candida albicans*

Fig.6.20 The antifungal activity values for different ligands

Fig.6.21 Inhibition zones (mm) of copper-curcumin analogue complexes, curcumin, and fluconazole against *Candida albicans*

Fig.6.22 Inhibition zones (mm) of zinc-curcumin analogue complexes, curcumin, and fluconazole against *Candida albicans*

Fig.6.23 Antifungal assay and the structures of corresponding compounds

Fig.6.24 Percentage of cell death at different concentrations for each compound in Spleen Cell Lines

ABBREVIATIONS

NSAID	Nonsteroidal Anti-Inflammatory Drugs
SAR	Structure-Activity Relationship
DMC	De Methoxy Curcumin
BDMC	Bis-De Methoxy Curcumin
PEG	Polyethylene Glycol
NLC	Nanostructured Lipid Carriers
ADME-Tox	Absorption, Distribution, Metabolism, Excretion, And Toxicity
Caco-2	Colon Adenocarcinoma-2
MTT	3-(4,5-Dimethylthiazol-2-Yl)-2,5-Diphenyltetrazolium Bromide
Ab	Amyloid-Beta
DPPH	2,2-Diphenyl-1-Picrylhydrazyl
ABTS	2,2'-Azino-bis(3-Ethylbenzothiazoline-6-Sulfonic Acid)
CVD	Chemical Vapor Deposition
DNA	Deoxyribonucleic Acid
MCF-7	Michigan Cancer Foundation-7- a Human Breast Cancer Cell Line
LNCaP	Lymph Node Carcinoma of the Prostate
PC-3	Prostatic Carcinoma-3
LAN-5	Los Angeles Neuroblastoma-5
SOD	Superoxide Dismutase
PLA2	Phospholipase A_2
COX	Cyclooxygenase
ChEMBL	Chemical Biology Database
OMG	Open Molecule Generator
CSLS	Chemical Structure Lookup Service
MOL	Molecular Structure File
PDB	Protein Data Bank
CMC	Comprehensive Medicinal Chemistry
MDL	Molecular Design Limited
BBB	Blood-Brain Barrier
HIA	Human Intestinal Absorption
NLB	1,7-bis(3,4-Dimethoxy Phenyl) Hepta-1,6-Diene-3,5-Dione
NLD	1,7-bis(3,5-Dichloro-2-Hydroxy phenyl)Hepta-1,6-Diene-3,5-Dione
NLE	1,7-bis(6-Methoxy Naphthalen-2-yl)Hepta-1,6-Diene-3,5-Dione
NLF	1,7-bis(3-Ethoxy-2-Hydroxy Phenyl) Hepta-1,6-Diene-3,5-Dione
NLG	1,7-bis(4-Hydroxy-3,5 Dimethyl Phenyl) Hepta-1,6-Diene-3,5-Dione
NLH	1,7-bis(5-Chloro-2-Hydroxy Phenyl) Hepta-1,6-Diene-3,5-Dione
NLI	1,7-bis(2-Hydroxy-3-Methoxy Phenyl)Hepta-1,6-Diene-3,5-Dione
NLJ	1,7-bis(3-Hydroxy-4-Methoxy Phenyl) Hepta-1,6-Diene-3,5-Dione
NLK	1,7-bis(5-Methyl Thiophen-2-yl) Hepta-1,6-Diene-3,5-Dione
PreADMET	Prediction of ADME And Toxicity

TLC	Thin Layer Chromatography
FT-IR	Fourier Transform Infrared Spectroscopy
^{1}HNMR	Proton Nuclear Magnetic Resonance Spectroscopy
^{13}C NMR	Carbon-13 Nuclear Magnetic Resonance Spectroscopy
LCMS	Liquid Chromatography-Mass Spectrometry
SAIF	Sophisticated Analytical Instrument Facility
CHNS	Carbon, Hydrogen, Nitrogen, And Sulfur Analysis
LMIC	Low- And Middle-Income Countries
TP53	Tumour Protein 53
MM/GBSA	Molecular Mechanics with Generalized Born and Surface Area Solvation Method
FDA	Food And Drug Administration
EAC	Ehrlich's Ascites Carcinoma
CyPA	Cyclophilin A
MD	Molecular Dynamic
OPLS3e	Optimized Potential for Liquid Simulations 3 Extended.
NPT	Number of Particles, Pressure, Temperature
RMSD	Root Mean Square Deviation
RMSF	Root Mean Square Fluctuation
DMSO	Dimethyl Sulfoxide
PBS	Phosphate-Buffered Saline
DMEM	Dulbecco's Modified Eagle's Medium
FBS	Fetal Bovine Serum
CMC	Carboxymethyl Cellulose
SGOT	Serum Glutamate Oxaloacetate Transaminase
SGPT	Serum Glutamate Pyruvate Transaminase
ALP	Alkaline Phosphatase
ANOVA	One-Way Analysis of Variance
TG1	Target 1
TG2	Target 2
TG3	Target 3
TG4	Target 4
TG5	Target 5
TG6	Target 6
TG7	Target 7
TG8	Target 8
TG9	Target 9
BE	Binding Energy
Ki	Inhibition Constant
NVT	Number of Particles Volume, and Temperature
Ala	Alanine
Arg	Arginine
Asn	Asparagine
Asp	Aspartic Acid
Cys	Cysteine

Gln	Glutamine
Glu	Glutamic Acid
Gly	Glycine
His	Histidine
Ile	Isoleucine
Leu	Leucine
Lys	Lysine
Met	Methionine
Phe	Phenylalanine
Pro	Proline
Ser	Serine
Thr	Threonine
Trp	Tryptophan
Tyr	Tyrosine
Val	Valine
MMPBSA	Molecular Mechanics Poisson–Boltzmann Surface Area
LRA	Linear Response Approximation
LIE	Linear Interaction Energy
ROS	Reactive Oxygen Species
LD50	Lethal Dose, 50%
OECD	Organisation for Economic Co-Operation and Development
SD	Standard Deviation
HB	Hemoglobin
RBC	Red Blood Cell
MCV	Mean Corpuscular Volume
MCH	Mean Corpuscular Hemoglobin
MCHC	Mean Corpuscular Hemoglobin Concentration
PCV	Packed Cell Volume
PLT	Platelet Count
TC	Total Count
AST	Aspartate Aminotransferase
ALT	Alanine Aminotransferase
ALP	Alkaline Phosphatase
LFT	Liver Function Test
AST	Aspartate Aminotransferase
ALP	Alkaline Phosphatase
HDL	High-Density Lipoprotein
LDL	Low-Density Lipoprotein
VLDL	Very Low-Density Lipoprotein
LD	Low Dose
HD	High Dose
IBD	Inflammatory Bowel Disease
NSAID	Nonsteroidal Anti-Inflammatory Drugs
HSP	Heat Shock Proteins
DPP-4	Dipeptidyl Peptidase-4

PPAR-γ	Peroxisome Proliferator-Activated Receptor Gamma
SGLT2	Sodium-Glucose Cotransporter 2
GLP-1	Glucagon-Like Peptide-1
PTP1B	Protein Tyrosine Phosphatase 1B
AMPK	Activated Protein Kinase
NADPH	Nicotinamide Adenine Dinucleotide Phosphate
GIP	Glucose-Dependent Insulinotropic Polypeptide
LE	Ligand Efficiency
clRMS	Cluster Root-Mean-Square Deviation
refRMS	Reference Root-Mean-Square Deviation
vdwhbdesolv	Van Der Waals, Hydrogen Bond, And Disolvation
HIV	Human Immunodeficiency Virus
AIDS	Acquired Immunodeficiency Syndrome
TB	Tuberculosis
UTI	Urinary Tract Infection
MDR	Multidrug Resistance
XDR	Extensively Drug-Resistant
CRKP	Carbapenem-Resistant Klebsiella Pneumoniae
DHFR	Dihydrofolate Reductase
InhA	Enoyl-[Acyl-Carrier-Protein] Reductase
ACP	Acyl Carrier Protein
KasA	B-Ketoacyl-Acyl Carrier Protein
FabF	B-Ketoacyl-ACP Synthase II
FAS-II	Fatty Acid Synthase Type II
NDM-1	New Delhi Metallo-Beta-Lactamase-1
LpxC	Uridine Diphosphate -3-O-(Acyl)-N-Acetylglucosamine Deacetylase
LPS	Lipopolysaccharide
SHV-1	Sulfhydryl Variable-1
GPF	Green Fluorescent Protein
MRSA	Methicillin-Resistant Staphylococcus Aureus
ACP	Acyl Carrier Protein
pdbqt	Protein Data Bank, Quaternion, Torsion
SABS	Small Animal Breeding Station
DMEM	Dulbecco’s Modified Eagle’s Medium
MDDR	Molecular Design Limited. Drug Data Report
WDI	World Drug Index
QM/MM	Quantum Mechanics / Molecular Mechanics
FEP	Free Energy Perturbation
ITC	Isothermal Titration Calorimetry
DLA	Dalton's lymphoma ascites

CHAPTER 1

General introduction and review of literature

CHAPTER 1

GENERAL INTRODUCTION AND REVIEW OF LITERATURE

1.1.GENERAL INTRODUCTION

Global health challenges such as cancer, diabetes, inflammation, and microbial infections, both bacterial and fungal, are pressing concerns worldwide, and Kerala, India, is no exception. These interconnected issues require advanced research, particularly in chemistry, which is crucial in developing effective solutions.

Breast cancer is one of the most prevalent cancers globally and in Kerala, with increasing incidence attributed to lifestyle changes, genetic predispositions, and environmental factors[1]. Early detection remains a challenge, and conventional treatments like chemotherapy and radiation often lead to severe side effects and treatment resistance. In response, chemical research is advancing the field of drug discovery and development.

Diabetes, especially Type-2 diabetes, poses a significant health threat in India, with Kerala having one of the highest prevalence rates[2]. Poor blood sugar control can lead to severe complications, including cardiovascular disease, neuropathy, and kidney failure. The limitations of current treatments, such as side effects and diminishing effectiveness, highlight the need for continuous chemical innovation. Natural product chemistry is also making strides, with compounds like curcumin from turmeric and marine-derived substances being explored for their antidiabetic potential.

Inflammatory diseases, such as arthritis, asthma, and inflammatory bowel disease, are major health concerns universally. Chronic inflammation is a known risk factor for cancer, cardiovascular diseases, and neurodegenerative disorders[3]. Current treatments, including Nonsteroidal Anti-Inflammatory Drugs (NSAIDs) and steroids, often have significant side effects, especially with long-term use[4]. Chemistry research is pivotal in developing safer and more effective anti-inflammatory agents. Innovative biomaterials and drug-delivery systems designed by chemists enable localised inflammation treatment, thereby minimizing systemic side effects.

Bacterial infections, including those caused by gram-positive and gram-negative bacteria, are a growing threat. Fungal infections, such as those caused by *Candida* and *Aspergillus*, are particularly dangerous for immunocompromised individuals[5]. Chemistry research is essential in discovering new antibiotics and antimicrobial peptides to address the challenge of antibiotic resistance. Scientists use structure-activity relationship (SAR) studies to optimize antibiotic efficacy and safety. In the realm of antifungal therapy, chemists are developing novel agents that target essential fungal pathways, such as cell wall synthesis and ergosterol production.

In Kerala, the burden of non-communicable diseases, such as cancer, diabetes, and inflammatory conditions, is exacerbated by lifestyle changes, an ageing population, and dietary factors. The state also faces significant challenges with infectious diseases, including the rise of antibiotic-resistant bacterial infections and fungal infections among vulnerable populations. The rich biodiversity of Kerala offers a unique opportunity for natural product chemistry. Researchers are exploring medicinal plants for bioactive compounds with anticancer, antidiabetic, and antimicrobial properties. For example, phytochemicals like curcumin have shown promise in treating various diseases due to their anti-inflammatory, antidiabetic, and anticancer effects[6]. Metal complexes of curcumin, such as Zn(II) and Cu(II), are being studied for their enhanced therapeutic benefits[7].

1.1.1. Importance of medicinal plants

Natural plant products, used throughout history, are secondary metabolites developed by plants as defence mechanisms against diseases[8]. Many possess pharmacological or biological activities beneficial for drug discovery and design. Plant-derived medicines have significantly influenced healthcare practices across various cultures, from ancient times to the present.

1.1.2. Turmeric-the golden spice

Turmeric, derived from the rhizomatous herb *Curcuma longa* of the ginger family *Zingiberaceae*, has been used medicinally for nearly 4,000 years[9]. Native to tropical South Asia, turmeric is a staple in Southeast Asian cuisine and plays a role in religious ceremonies. Its vibrant yellow hue has earned it the nickname "Indian saffron"[10,11]. With over 133 identified species of Curcuma globally, turmeric is utilised for various medicinal formulations. In Ayurvedic medicine, it is believed to enhance energy, aid digestion, relieve

arthritis, regulate menstruation, and treat skin and digestive disorders[12]. Traditionally, turmeric has also been applied as an antiseptic and antibacterial agent for wounds and burns. Modern research highlights the potent antioxidant, anti-inflammatory, antimicrobial, and anticancer properties of turmeric[13]. It is a key ingredient in many cosmetic products, including sunscreens and face creams[14]. The antioxidant effects of turmeric involve neutralising free radicals, boosting antioxidant enzymes, and reducing lipid peroxidation. Its anticancer potential includes inhibiting cancer cell proliferation and inducing apoptosis. Animal studies have shown the preventive and therapeutic roles of turmeric against skin, breast, oral, and stomach cancers by inhibiting mutations, detoxifying carcinogens, and suppressing tumour growth. Additionally, turmeric has demonstrated cardioprotective, hepatoprotective, hypoglycaemic, and antiarthritic benefits, showcasing its broad medicinal value across various health applications[15].

1.1.2.1. Factors of turmeric

In a standard form, turmeric contains moisture (>9%), curcumin (5–6.6%), extraneous matter (<0.5% by weight), mould (<3%), and volatile oils (<3.5%). The main component of the root is a volatile oil, containing turmerone, and there are other colouring agents called curcuminoids in turmeric[16]. Curcumin is found primarily in the roots and rhizomes of the turmeric plant (*Curcuma longa*). In addition to curcumin, two other curcuminoids occur in lesser amounts in turmeric, namely, de methoxy curcumin (DMC) and bis-de methoxy curcumin (BDMC).

1.1.2.2. Curcumin and its structural properties

Curcumin is a polyphenolic compound characterized by its distinctive chemical structure, with a chemical formula of $C_{21}H_{20}O_6$ and a molecular weight of approximately 368.38 g/mol. Curcumin, chemically known as[1,7-bis(4-hydroxy-3-methoxyphenyl)-1,6-heptadiene-3,5-dione] or diferuloylmethane, exhibits keto-enol tautomerism dependent on the solution pH: at pH < 7, the keto form is predominant, while at pH > 7 it occurs in the enol form[17]. Comprising three major structural components, including diferuloylmethane (Curcumin I), de methoxy curcumin (Curcumin II), and bisdemethoxycurcumin (Curcumin III), it features a molecular arrangement of two aromatic rings connected by a seven-carbon linker, incorporating functional groups such as two phenolic hydroxyl groups and two

methoxy groups, which contribute to its antioxidant properties (**Fig.1.1**). The presence of conjugated double bonds gives it its characteristic yellow colour.

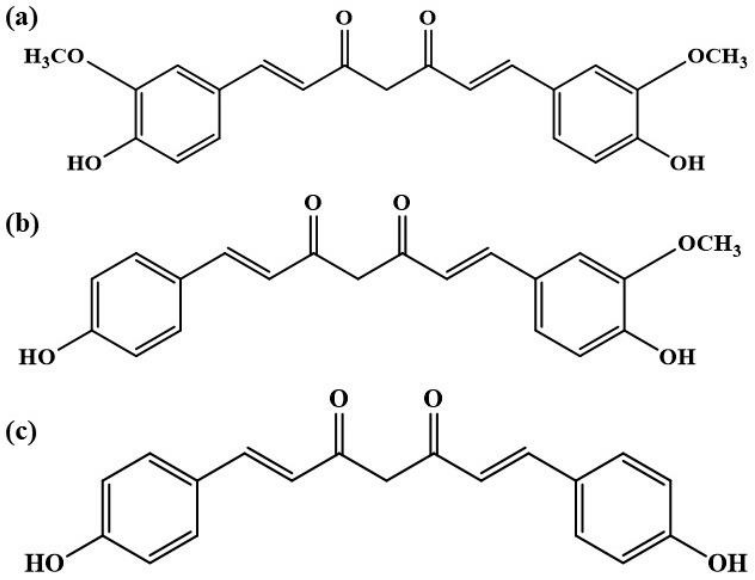

Fig.1.1 Three major structural components of Curcumin. (a) diferuloylmethane (Curcumin I), (b) de methoxy curcumin (Curcumin II), (c) bisdemethoxycurcumin (Curcumin III)

1.1.2.3. Benefits and limitations

Curcumin, the yellow pigment from turmeric, is a polyphenol known for diverse health benefits, including antioxidant, anti-inflammatory, anticancer, antidiabetic, hepatoprotective, anti-allergic, and neuroprotective effects. Despite its therapeutic potential, the poor pharmacokinetic profile of curcumin limits its effectiveness due to low water solubility, poor absorption, rapid metabolism, and systemic elimination. It dissolves better in organic solvents like ethanol and Dimethyl Sulfoxide[18]. The most stable crystalline form, "curcumin I," affects bioavailability, and sensitivity to light, heat, and pH of curcumin requires stabilization techniques like encapsulation. Although phase-I trials show curcumin is safe at high doses (12 g/day), its bioavailability remains a significant challenge[19].

1.1.3. Modifications of natural curcumin - different methods

To enhance the bioavailability, stability, and therapeutic efficacy of curcumin various structural modifications have been developed. These include creating curcumin derivatives by altering functional groups to improve water solubility and stability. Nanoencapsulation techniques, such as using nanoparticles or liposomes, protect curcumin

from degradation and boost absorption. Methods like nanoprecipitation are commonly used. Polymeric conjugation with polymers like polyethylene glycol (PEG) or chitosan enhances solubility and prolongs circulation time. Prodrug strategies ensure sustained release, while lipid-based formulations, such as solid lipid nanoparticles (SLNs) and nanostructured lipid carriers (NLCs), improve the gastrointestinal absorption of curcumin and protect it from degradation[20-23].

Complexing curcumin with phospholipids, and various metals, improves water solubility and absorption, facilitating liposomal formulations. Metal complexes and chemical modifications, such as acylation or esterification, further enhance its therapeutic properties[24]. Hybrid compounds, created by combining curcumin with natural agents or drugs, yield synergistic effects[25]. Targeted delivery is achieved through conjugation with ligands like antibodies. Curcumin analogues with structural modifications also boost therapeutic potential, especially for targeted applications like cancer treatment. These structural modifications aim to overcome the limitations of natural curcumin, including poor bioavailability and stability while maximising its potential for therapeutic applications. The choice of modification method depends on the specific desired outcome and intended use of the modified curcumin compound.

1.1.3.1. Difference between curcumin derivatives and curcumin analogues

Curcumin derivatives and curcumin analogues are two types of compounds related to curcumin, each with distinct structural features. Curcumin derivatives are created through chemical modifications in the existing functional groups of curcumin, like altering phenolic hydroxyls or adding moieties to improve solubility, stability, or bioavailability. These derivatives retain the core structure of curcumin and aim to overcome its natural limitations while preserving its therapeutic effects.

Conversely, curcumin analogues are compounds with a similar foundational structure to curcumin but differ in the arrangement of functional groups or atom substitutions. They are designed to explore the structure-activity relationship and assess how structural changes impact biological activity, potency, or selectivity. Curcumin analogues often display modified pharmacological properties, offering unique insights into the biological effects of curcumin[26].

1.1.4. Curcumin analogues and their importance

Curcumin analogues are essential for overcoming the limitations of natural curcumin, such as poor bioavailability and stability, and enhancing its therapeutic potential[27]. Natural curcumin is poorly absorbed and utilized in the body, but curcumin analogues can be engineered to improve bioavailability, amplifying therapeutic effects. They also allow for targeted drug delivery by attaching ligands or functional groups, making treatment for diseases like cancer more effective and focused[28]. Furthermore, analogues can be designed for improved stability, protecting curcumin from light, heat, and pH-induced degradation, ensuring longer shelf life and efficacy[29].

The pharmacological properties of curcumin analogues can be fine-tuned for specific applications, optimizing anti-inflammatory, antioxidant, antimicrobial, or anticancer activities. They also serve as valuable research tools for studying the structure-activity relationship of curcumin, helping identify crucial molecular features for its biological effects[30]. These insights can lead to the development of novel drugs with better pharmacokinetics, reduced toxicity, or enhanced potency. Curcumin analogues can be combined with other compounds to create hybrids with synergistic benefits, offering enhanced therapeutic outcomes[31]. Their role in biomedical research is crucial for understanding mechanisms and potential treatments of curcuminoids for various conditions, with some analogues even showing promise in clinical trials for improved therapies.

1.1.4.1. Importance of functional group substitution on aryl rings on curcumin analogues

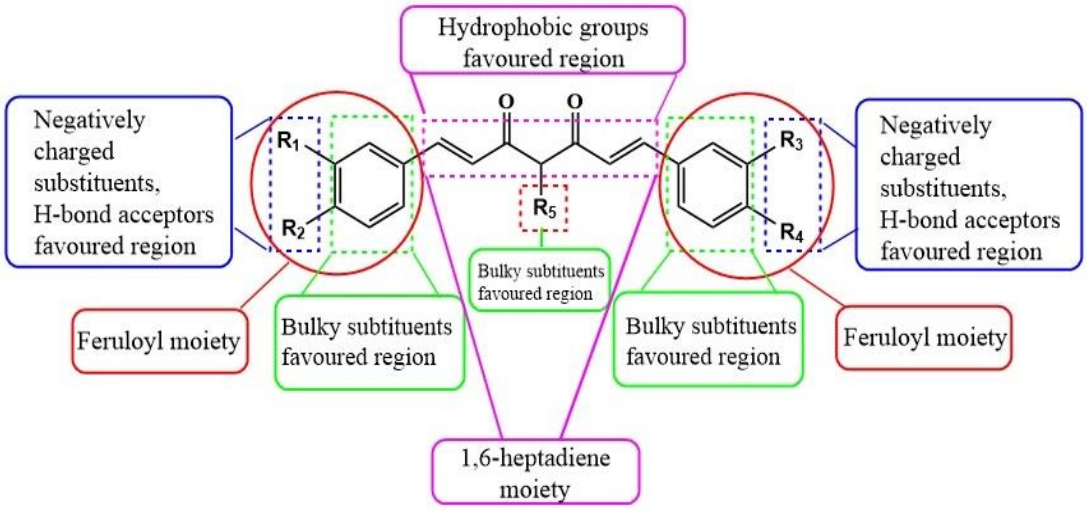

Fig.1.2 Possibilities of functional group substitution on aryl rings on curcumin analogues.

Functional group substitution on the aryl rings of curcumin analogues is a strategic approach in medicinal chemistry, offering key advantages for pharmaceutical development. By introducing specific functional groups, researchers can fine-tune the biological activities of curcumin analogues, enhancing interactions with cellular targets and improving therapeutic effectiveness for medical conditions. These substitutions also increase selectivity and specificity, minimising off-target effects and enhancing safety profiles. They can boost bioavailability by improving solubility and facilitating better absorption and distribution. Functional group substitutions further enhance stability, protecting compounds from degradation. This approach aids in studying the structure-activity relationship, guiding drug development and enabling the creation of hybrid molecules with synergistic benefits[32]. Thus, this strategy broadens the therapeutic potential of curcumin in drug development and biomedical research.

1.1.5. Benefits of curcumin analogues in biological applications both *in vitro* and *in vivo*

Curcumin analogues exhibit diverse and potent biological activities in both *in vitro* and *in vivo* settings. They possess strong antioxidant properties, reducing oxidative stress and offering protection against related diseases. Their significant anti-inflammatory effects suppress pro-inflammatory pathways, providing relief from inflammation. Curcumin analogues also display anticancer potential by inhibiting cancer cell growth, inducing apoptosis, and reducing metastasis, translating into tumour suppression in animal models. They have demonstrated antimicrobial efficacy against various pathogens and neuroprotective capabilities, reducing neuronal damage and supporting cognitive health. Cardiovascular benefits include improved lipid profiles and reduced disease risk. They promote wound healing, aid in tissue repair, and offer pain relief by mitigating inflammation. Finally, these compounds improve insulin sensitivity and blood glucose regulation, showing promise for managing type-2 diabetes[33-41]. Collectively, curcumin analogues are invaluable for research and practical healthcare, providing a broad spectrum of therapeutic advantages.

1.1.6. Curcumin analogue-metal Complexes and their biological applications

Curcumin analogue-metal complexes have become very important in medicinal chemistry and pharmacology, addressing the limited bioavailability of curcumin by

enhancing stability and solubility in biological fluids[42,43]. These improvements can lead to higher bioavailability and more effective treatments. The complexes, formed using metals like Iron, Copper, Zinc, and others, exhibit robust antioxidant and anti-inflammatory properties, often showing synergistic effects that amplify their therapeutic potential[44].

Their enhanced pharmacokinetic profiles allow better cellular targeting, improving efficacy in disease treatment. They have demonstrated notable antimicrobial activity against bacteria, fungi, and viruses, suggesting potential as novel antimicrobial agents[45]. In cancer therapy, these complexes selectively target cancer cells, minimizing damage to healthy cells and inducing apoptosis, which could reduce chemotherapy side effects[46]. Preclinical studies highlight the neuroprotective potential of these complexes in treating neurodegenerative diseases such as Alzheimer's and Parkinson's, owing to their capacity to reduce oxidative stress and inflammation in the brain[47,48]. Curcumin analogue-metal complexes are explored in diagnostic imaging, serving as contrast agents for PET and MRI, improving tissue visualization[49]. They also act as sensors for detecting biological molecules or metal ions and can modulate metalloenzyme activity, providing therapeutic value in conditions with enzyme dysregulation[50]. Their catalytic abilities also open avenues in green chemistry[51]. Furthermore, these complexes are utilized in developing bioavailable nutraceuticals and dietary supplements, offering sustained therapeutic effects through prolonged circulation and improved distribution.

In biomedical research, these complexes facilitate a deeper understanding of the therapeutic potential of curcumin analogue, informing future drug development. Clinical trials have highlighted their promise, suggesting they could offer safer and more effective treatments compared to traditional therapies[52]. With diverse applications spanning cancer therapy, diabetes management, and antimicrobial and anti-inflammatory treatments, curcumin analogue-metal complexes are poised for significant impact in healthcare and biotechnology.

1.1.6.1. Curcumin analogue – Cu (II) metal complexes

Curcumin analogue-copper metal complexes are significant in medicinal chemistry due to their enhanced bioavailability, stability, and therapeutic potential compared to curcumin alone. Copper, an essential trace element with antioxidant properties, improves the solubility and efficacy of curcumin analogues, addressing a key limitation of low

bioavailability. These complexes exhibit strong antioxidant and anti-inflammatory effects, which are useful for combating oxidative stress and inflammation, which are implicated in chronic diseases and ageing. In cancer therapy, they show selective cytotoxicity against cancer cells with reduced toxicity to healthy cells[53-55]. They offer neuroprotective benefits, shielding neurons from oxidative damage and inflammation, making them potential candidates for neurodegenerative disease treatment. Copper-curcumin complexes also inhibit specific copper-dependent metalloenzymes, presenting therapeutic applications in enzyme dysregulation. Beyond therapy, they serve as diagnostic agents in imaging techniques and enable theranostic applications, combining imaging and treatment[56]. Their role in green chemistry and nutraceutical development further highlights their versatility and broad research potential[57].

1.1.6.2. Curcumin analogue-Zn(II) metal complexes

Curcumin analogue-Zn(II) metal complexes are gaining prominence in medicinal chemistry for their enhanced bioavailability and therapeutic potential. Zinc ions increase the solubility and stability of curcumin analogues, leading to more effective therapeutic outcomes[55]. These complexes exhibit strong antioxidant and anti-inflammatory activities, benefiting the treatment of conditions linked to oxidative stress and inflammation. Neuroprotection is another key application, as zinc-curcumin complexes may protect neurons from damage and neurodegeneration[58]. Zinc plays a vital role as a cofactor in various metalloenzymes, and these complexes can modulate enzyme activity, offering therapeutic avenues for enzyme dysregulation. In cancer therapy, zinc-curcumin complexes demonstrate selective cytotoxicity against cancer cells with lower toxicity to healthy cells[59]. They also show promising antimicrobial activity against bacteria and fungi, supporting their development as novel antimicrobial agents[60]. Their diagnostic and theragnostic potential, including simultaneous therapy and imaging in cancer, further highlights their significance in biomedical research and nutraceutical development[45].

1.1.7. The Role and Relevance of Computational Modelling and Virtual Screening in Modern Drug Discovery (*in silic*o studies)

Molecular modelling, or *in silico* modelling, is a pivotal tool across fields like chemistry, biology, materials science, and drug discovery. It uses computer simulations to predict molecular properties, behaviours, and interactions, significantly advancing research

efficiency. In drug discovery, molecular modelling accelerates the process by enabling virtual screening of extensive chemical libraries, helping identify potential drug candidates and reducing the need for costly and time-consuming experimental testing. It also aids in designing drugs with improved potency and specificity[61,62].

In materials science, molecular modelling predicts properties such as mechanical strength and thermal conductivity, guiding the design of materials tailored to specific applications, including electronics and energy storage. In biology, techniques like molecular dynamics simulations help elucidate protein folding, stability, and drug-protein interactions, critical for understanding disease mechanisms and drug design[63,64]. Additionally, molecular modelling predicts ADME-Tox properties of drug candidates, optimizing them and anticipating potential toxicity issues[65].

Environmental applications include predicting chemical toxicity, reducing animal testing, and assessing the environmental impact of pollutants. In chemistry, modelling helps decipher enzyme mechanisms, reaction pathways, and energy barriers, aiding catalysis and industrial processes. Molecular modelling saves time and resources, supports scientific advancements, and serves as an essential educational tool for visualizing and understanding complex molecular concepts.

Receptor-ligand interaction studies have achieved broad and significant relevance across various scientific and medical fields. In drug discovery and development, these studies are crucial for identifying and designing new drug candidates, as understanding how ligands bind to receptors enables the creation of targeted therapies with improved efficacy and minimized side effects while also optimizing pharmacological properties. In pharmacology and toxicology, analyzing these interactions helps predict drug effects, including therapeutic outcomes and adverse reactions, aiding in the safety and efficacy assessment of pharmaceutical compounds. Receptor-ligand studies elucidate the mechanisms of biological processes like cell signalling, immune responses, and neurotransmission, which is essential for understanding disease pathways and identifying therapeutic targets. Insights from these interactions also support the development of personalized medicine by enabling treatment strategies tailored to the receptor profile of an individual, enhancing precision and effectiveness. In biotechnology and synthetic biology, these studies contribute to engineering biosensors, creating novel therapeutic agents, and designing synthetic biological systems that mimic or modify natural processes.

Furthermore, in environmental and agricultural sciences, receptor-ligand studies assess the impact of environmental toxins on biological receptors and assist in designing agrochemicals targeting specific receptors in pests or pathogens.

1.1.7.1. Molecular modelling studies of curcumin analogues

Molecular modelling studies of curcumin analogues constitute a vital area of research that employs computational techniques to delve into the structure, properties, interactions, and potential biological activities of these modified compounds[66]. These investigations play a pivotal role in unravelling the structure-activity relationships of curcumin analogues and providing valuable insights for their development across diverse applications, notably in drug discovery and therapeutic research. This document delineates fundamental elements pertinent to molecular modelling studies concentrating on curcumin analogues.

Virtual screening and drug design: Virtual screening incorporates computational sifting through compound libraries to unearth potential drug candidates among curcumin analogues. Molecular modelling is instrumental in steering the selection of analogues possessing desirable binding properties for particular drug targets[67].

Structural analysis: One of the fundamental aspects of molecular modelling entails the prediction of the three-dimensional structures of curcumin analogues, encompassing their conformations and spatial arrangements. This knowledge is indispensable for comprehending their molecular geometry and assessing their stability[68].

Docking studies: Docking simulations constitute computational methodologies that foresee how curcumin analogues engage with specific biological targets, such as enzymes or receptors. These simulations facilitate the understanding of binding modes and the affinity of these analogues for their target proteins[69].

Molecular dynamics simulations: Researchers employ molecular dynamics simulations to scrutinize the dynamic behaviour of curcumin analogues within a simulated environment over time. This dynamic exploration aids in unravelling conformational changes, flexibility, and interactions with solvent molecules[70].

Quantum mechanics calculations: Quantum mechanics calculations provide profound insights into the electronic structure and energetics of curcumin analogues. They enable predictions related to properties like molecular orbitals, electronic spectra, and bond energies[71].

ADME-Tox prediction: Molecular modelling can be harnessed to predict the absorption, distribution, metabolism, excretion, and toxicity (ADME-Tox) properties of curcumin analogues. Such predictions are instrumental in the assessment of their pharmacokinetics and safety profiles[72].

Bioactivity prediction: Computational studies can forecast the potential bioactivities of curcumin analogues, encompassing domains such as anti-inflammatory, antioxidant, anticancer, or antimicrobial properties. These predictions furnish guidance for the selection of analogues warranting experimental validation[73].

Structure-Activity Relationship (SAR) Analysis: SAR analysis involves the systematic alteration of structural components within curcumin analogues to scrutinise how these modifications impact their biological activities[74]. Molecular modelling plays an integral role in identifying pivotal structural features responsible for specific bioactivities.

Lead optimization: Subsequent to the identification of potential lead compounds, molecular modelling lends a helping hand in the optimization of curcumin analogues. This optimization process encompasses the prediction of modifications that augment their activity, selectivity, and pharmacokinetic properties[75].

Experimental validation: Molecular modelling studies frequently serve as a guiding force for experimental research[67]. Predicted interactions and properties offer blueprints for the design of laboratory experiments, subsequently validating the findings in real-world scenarios.

Molecular modelling and virtual screening studies dedicated to curcumin analogues constitute an indispensable cornerstone in advancing our comprehension of these compounds and their potential multifaceted applications. These computational approaches expedite the process of pinpointing promising candidates for in-depth experimental exploration and subsequent development across various domains, including drug discovery, medicinal chemistry, and therapeutic research.

1.2. REVIEW OF LITERATURE

1.2.1. Introduction

The beneficial health effects of curcumin had been extensively documented, and the special issue titled "Recent Progress and Novel Insights in Curcumin Research – From Chemistry to Clinical Use," published in the journal *Current Pharmaceutical Design* in 2013, reflected the comprehensive exploration of the diverse aspects of the curcumin. The content of this special issue likely covered a range of topics, including the chemical properties of curcumin, its biological activities, mechanisms of action, and clinical applications[76]

Curcuminoids, particularly curcumin, encountered significant limitations, including suboptimal oral bioavailability, rapid metabolic degradation, and elimination, predominantly occurring in the hepatic and intestinal systems, which diminished their therapeutic effectiveness and sometimes led to adverse effects such as gastrointestinal disturbances. Furthermore, the interaction of the curcumin with various compounds and issues surrounding standardization complicated the assurance of quality. Its pharmacokinetic profile required ongoing supplementation, with variability influenced by genetic factors and individual health conditions. Strategies proposed to mitigate these challenges included the use of nanoparticles, liposomes, micelles, and phospholipid complexes, as well as the development of novel curcumin analogues aimed at enhancing bioavailability and overall therapeutic potential.

1.2.2. Curcumin analogue synthesis and biomedical applications

Curcumin analogues were meticulously designed and synthesized to offer advantages over natural curcumin, maintaining its core structure of two phenolic rings linked by a conjugated carbon-carbon double bond system [77,78]. Modifications were introduced to enhance bioavailability, stability, and solubility, making them more effective in delivering therapeutic benefits. Researchers tailored these analogues to optimize properties for specific applications, targeting tissues or cells and increasing potency or efficacy[79,80]. Such designs aimed at excelling at biological targets, like enzymes or receptors involved in diseases, while reducing potential side effects associated with curcumin, including gastrointestinal discomfort and medication interactions[81,82].

The synthesis of curcumin analogues began with selecting suitable aromatic compounds or derivatives, followed by sequential functional group modifications like acylation, oxidation, and reduction[83,84]. Purification techniques, such as column chromatography and recrystallization, removed impurities[85,86]. The final products were characterized using NMR spectroscopy, mass spectrometry, and IR spectroscopy[87,88].

The subsequent research phase involved biological testing, where curcumin analogues were evaluated for potential medicinal properties, including anti-inflammatory, antioxidant, antimicrobial, antidiabetic, and anticancer activities[89-92]. Then an attempt was made to optimise, refining the structures of the analogues to enhance specific biological activities[93,94]. This optimization included altering substituents on the aromatic rings or modifying the length and conjugation of carbon-carbon double bonds. The specific reactions and modifications conducted depended on the intended properties of the analogues and the expertise of the research team. Continued research in this field uncovered novel analogues and innovative synthesis strategies, broadening the potential applications in medicine and beyond.

Curcumin analogues included β-dicarbonyl structures with modified diaryl and arylidene moieties, arylhydrazone, and various C-4 substituents, which demonstrated antiproliferative, antitumor, and antibacterial activities[95,96]. Mono carbonyl analogues featured linkers of varying lengths or heterocyclic bridges, such as oxazolone, pyrazole, and triazole[97-100], alongside halogenated derivatives[101-104]. These diverse classes of curcumin analogues were synthesized and studied to harness their potential for medicinal and biological purposes.

Numerous curcumin analogues with diverse substituents on their aromatic rings have been synthesized and investigated for their potential antiproliferative activities against various cancer cell lines, including Caco-2, Bel-7402, MDA-MB-231, and DU145, using MTT assays[96]. In order to create these analogues, researchers prepared an acetone boric oxide complex by reacting boric anhydride with acetylacetone to prevent Knoevenagel condensation at the methylene group. Afterwards single aldol condensations were conducted. with different substituted benzaldehydes to achieve modifications of diaryl moieties, followed by decomplexation in the presence of HCl[105-108]. Subsequent aldol condensations with various benzaldehydes led to the synthesis of these analogues. These derivatives were tested to determine their ability to inhibit the aggregation of tau protein and amyloid-beta (Ab), which are associated with certain neurodegenerative conditions such as Alzheimer's disease[109].

Knoevenagel condensates derived from curcumin and the curcumin analogue, 1,7-bis(4-hydroxy-3-ethoxyphenyl) heptadiene-3,5-dione, were assessed for their antioxidant capacity using DPPH and ABTS assays[95,96]. Another study highlighted the significance of introducing an arylidene group into the curcumin scaffold to enhance its biological properties. This effort aimed to synthesize arylidene curcumin derivatives containing a dimethyl amino moiety. Several dimethyl amino curcumin derivatives were synthesized through aldol condensation reactions and subsequently examined for their anti-inflammatory, antioxidant, and antibacterial activities[110,111]. Another study focused on the synthesis of di-indole curcumin analogues, which incorporate two indole units linked on both sides of the 1,6-heptadiene-3,5-dione system. Researchers evaluated the anticancer effects of these analogues on three human cancer cell lines: Lung adenocarcinoma (A549), leukaemia (K562), and colon cancer (SW480)[107,112-114]. The synthesis process involved the reaction of indole-3-carbaldehyde and acetylacetone using triethyl borate, boric anhydride, and tetrahydroquinoline[115]. Additionally, researchers have explored the introduction of halogen substituents into curcumin analogues, either on the aromatic phenyl rings or at the C-4 position of the curcumin scaffold. These halogenated curcumin derivatives were obtained by reacting halogenated-vanillin with pentane-2,4-dione, tributyl borate, tributylamine, and boric anhydride in ethyl acetate, followed by the reduction of the resulting compounds to obtain halogenated tetrahydro curcumin analogues. Moreover, the selective introduction of fluorine into the chemical structure has been employed to enhance the metabolic stability and physicochemical properties of pharmaceuticals. In this context, researchers have synthesized several fluoro-curcuminoids and curcuminoid-BF2 derivatives to explore their potential in drug development and biological applications.

Pabon's Method, pioneered by H.J.J. Pabon, optimized the synthesis of curcumin analogues through a singular, one-step reaction. This method involved the reaction in which substituted benzaldehydes were combined with acetylacetone/B_2O_3 in the presence of tri-sec-butyl borate and butylamine. The reaction was conducted in ethyl acetate at ambient room temperature. This method presented an uncomplicated and efficient strategy for producing curcumin analogues, offering a pragmatic and direct synthetic pathway. It represented a distinctive means of synthesizing curcumin analogues by modifying the functional groups on the aryl rings[116]. A noteworthy aspect was that the synthesis and modification of curcumin analogues could be patentable, providing an incentive for pharmaceutical companies and researchers to invest in their development. However, it was crucial to recognize that the effectiveness of curcumin analogues varied depending on the

specific analogue and its intended use. Ongoing research in medicinal chemistry and pharmaceuticals continued to explore this field.

1.2.3. Curcumin analogue-metal Complex Synthesis and Medicinal Applications

A promising strategy to address bioavailability challenges involved using metal curcumin complexes[117]. Curcumin and its derivatives, as naturally occurring β-diketone ligands, were suited to chelate various metals and form stable complexes. Over the past decade, research surged in synthesizing and characterizing these complexes[118,119]. Their medicinal applications were diverse, with metal interactions enhancing biological potency[120-122]. Coordination with metals destabilized the carbonyl group in the diketone moiety[123,124].

Given the role of metals as enzyme coactivators, curcumin analogue-metal complexes engaged with enzyme active sites, triggering diverse cellular processes. Significant advancements were made in selective cytotoxicity, anticancer activity, anti-Alzheimer's effects, and antioxidative and neuroprotective properties[125-127]. Promising outcomes were documented in antiarthritic, antimicrobial, antiviral, anti-inflammatory, and antidiabetic effects, as well as in biological and radio imaging[117,128-134]. This research surge marked a transformative period in utilizing metal-curcumin complexes for health-related applications.

Coordination compounds incorporating curcumin and its analogues as ligands were reported for various metallic elements. However, well-characterized complexes with alkali and alkaline earth metals remained limited, with few examples for Na, Be, Mg, Ca, and Ba. The scarcity of alkali metal curcumin derivatives was surprising, considering their frequent emergence as intermediates during deprotonation by alkali reagents[135]. Among other main group elements, boron derivatives represented the most extensively studied class[136,137] while aluminium[138,139] and gallium[140,141] complexes were described, but indium, tin, and lead compounds were scarce[142]. Curcumin complexes were also reported for Group 3–6 elements like Y, La, Zr, V, and Cr, with vanadyl species being prevalent[143,144]. A focus existed on middle and late transition metals[145], with curcumin complexes identified for nearly all metals in Groups 7–12 except osmium. Copper curcumin complexes dominated, followed by zinc, nickel, iron, manganese, and ruthenium[146-150]. Complexes with metals like Ru and Pd, as well as rare-earth metals, demonstrated anticancer potential[151,152] and technetium complexes containing curcumin were recently highlighted[153,154]. Curcumin complexes for lanthanides, thorium, and uranium, mainly as uranyl species, were also synthesized[155-157].

Curcumin analogue-metal complexes were synthesized using various methods based on different operational principles. Solution-based methods included co-precipitation, where curcumin analogue and metal salt solutions were mixed to precipitate the complex and solution complexation, which dissolved both in a solvent to form complexes[158,159]. Solid-state methods involved grinding and mechanochemical synthesis through high-energy milling[160,161]. Microwave-assisted synthesis used irradiation to expedite reactions[162-164], while hydrothermal synthesis occurred in sealed containers at high temperatures[165]. Solvent-free, eco-friendly methods[166], in situ metalation[167], polymeric support[168], and bioinspired enzymatic synthesis[169] were also employed to improve efficiency and sustainability.

Sequential synthesis methods were widely employed for the preparation of metal complexes involving curcumin analogues, with the controlled stepwise introduction of curcumin and metal ions facilitating complex formation. Traditional organic solvent methods, such as ethanol, methanol, and aqueous solutions, were commonly used in the synthesis process. For instance, a curcumin-lanthanum complex was created by introducing a curcumin solution in ethanol into a $La(NO_3)_3 \cdot 6H_2O$ solution (also in ethanol) at pH 6, followed by refluxing at 80°C. Similarly, a Pd-curcumin complex was synthesized by combining curcumin with Na_2CO_3 in methanol with a $PdCl_2$ solution (also in methanol), and the mixture was heated to 60°C until a clear blood-red solution was obtained[170].
Template-assisted methods, such as template synthesis, utilized templates to guide the formation of specific structures in curcumin analogue-metal complexes[171,172]. Ultrasound-assisted synthesis, which employed ultrasonic irradiation to improve mixing and accelerate complexation, was also explored[173].In addition, gas-phase synthesis, specifically chemical vapor deposition (CVD), involved the vapour-phase deposition of metal precursors onto substrates containing the curcumin analogue[174]. The method selected depended on the properties of the curcumin analogue, the metal ion, and the desired characteristics of the complex, with careful consideration of temperature, pH, and solvent choice to ensure optimal synthesis conditions[175].

The hydrothermal synthetic method, used in the present study, involved high-temperature water reactions within a sealed container. This method offered several advantages, including enhanced solubility of reactants, leading to better interaction between the curcumin analogue and metal ions for a more homogeneous and efficient synthesis. The sealed container allowed precise control over temperature and pressure, ensuring a controlled environment that improved reproducibility and predictability. High

temperatures accelerated reaction kinetics, which was beneficial for metal complexes requiring rapid and efficient coordination between metal ions and curcumin analogue ligands. Additionally, hydrothermal conditions minimized side reactions, promoted higher purity, and favoured the formation of well-defined crystalline materials. The high-temperature water environment also stabilized reactive intermediates, enabling the formation of complex structures that might be challenging under conventional synthesis conditions. Furthermore, hydrothermal synthesis was scalable, making it suitable for producing larger quantities of curcumin analogue-metal complexes for both industrial and research applications[173,176].

In 1997, Beck and colleagues at Ludwig-Maximilians-Universität in Munich made significant contributions to the field with their work on "Metal Complexes of Dyes." They synthesized and characterized twenty-eight novel transition metal complexes using curcumin-derived ligands, including bis-dimethoxy curcumin, dimethyl curcumin, trimethyl curcumin, and diacetyl curcumin. Their synthetic method typically involved the deprotonation of curcumin derivatives using bases such as ammonia, sodium hydroxide, sodium methoxide, sodium carbonate, sodium acetate, or silver acetate, followed by treatment with metal halides in specific molar ratios[177].Beck et al. successfully obtained homoleptic complexes like Pd(Curc) and $M(Me_2Curc)_2$ (M = Ni, Cu) using metal (II) acetates. They also synthesized $Fe(Curc)_3$ by reacting $FeCl_3$ with three equivalents of in situ-prepared NaCurc and expanded the scope of their work to include organotransition metal halides, yielding a variety of curcumin complexes[178].

Various metal-curcumin complexes, such as curcumin-gold complexes, were investigated for their potential biomedical applications. Curcumin-gold nanoparticles enhanced the stability and bioavailability of curcumin, demonstrating anti-inflammatory and anti-tumour activities[175,179,180]. Iron-curcumin complexes showed promise for mitigating oxidative stress in Alzheimer's disease[181,182], while copper complexes exhibited anti-cancer properties and the ability to inhibit amyloid-beta aggregation in Alzheimer's[183]. Zinc-curcumin complexes were noted for their antioxidant and anti-inflammatory properties, with potential applications in wound healing[184]. Manganese-curcumin complexes were studied as superoxide dismutase (SOD) mimics to combat oxidative stress[185,186], and platinum-curcumin complexes were explored to enhance cancer chemotherapy efficacy while reducing side effects[187 112]. Cobalt-curcumin complexes demonstrated promise in catalysis and anti-cancer activities[188,189] and ruthenium-curcumin complexes gained attention for their anticancer properties[190].

Numerous studies evaluated the antimicrobial activity of metal-curcumin complexes against various bacteria, including *Escherichia coli*, *Staphylococcus aureus*, *Bacillus subtilis*, *Pseudomonas aeruginosa*, and *Shigella flexneri*[191,192]. *In vitro* antifungal screenings also showed that these complexes were more effective than free curcumin against fungi like *Aspergillus niger* and *Penicillium verruculosum*[193,194]. Metal-curcumin complexes exhibited superior antimicrobial and antifungal activity compared to the free ligand[195]. Research into antiviral activity also highlighted the efficacy of curcumin-boron and copper derivatives, with copper-curcumin complexes showing promise in the development of antiviral treatments[191,196,197]. Additionally, boron-curcumin complexes demonstrated inhibitory effects on HIV proteases[198,199]. However, further research was needed to identify the most effective combinations of metals and ligands for these applications.

1.2.4. Importance of Cu (II) and Zn (II) Metal complexes of Curcumin analogues

The advantages of copper (Cu) and zinc (Zn) metal complexes of curcumin analogues over other metal complexes were found to depend on specific properties and desired applications. Cu and Zn, essential trace elements in the human body, play vital roles in numerous biological processes, making them beneficial for pharmaceutical and biomedical applications[189,200-203]. Research had proved that complexes of these metals exhibited enhanced stability, which maintained their integrity under physiological conditions of copper and zinc were reported to contribute to complexes with superior antioxidant activity, valuable for treating oxidative stress-related conditions[204-206]. The catalytic activity of the complexes was noted to expand their applicability, such as in catalysis and as potential enzyme mimics[207-209].

Improved bioavailability and absorption were achieved by designing curcumin analogues with Cu and Zn complexes, as the bioavailability of these metals was generally well-regulated in the body[210]. The inclusion of Cu and Zn ions also allowed for the targeting of specific pathways or enzymes, facilitating a more tailored therapeutic approach[211,212]. Copper complexes, in particular, were described as having unique colourimetric and making them suitable for sensing applications and the development of probes for detecting specific ions or molecules in biological systems[213]. Since both copper and zinc ions are involved in regulating gene expression and cellular signalling, curcumin analogues may modulate cellular processes more effectively than other metal complexes[214,215].

In the field of metallo-drug design, researchers emphasized the development of compounds that targeted DNA selective interactions, such as groove binding, phosphate

clamps, insertion, and intercalation[216,217]. Intercalation, involving π-π stacking of planar aromatic systems between DNA bases, induced significant DNA structural changes and showed drug resistance[218,219]. Existing metallo-intercalators primarily involved Pt (II) and Rh (III) or Ru (II) complexes[220,221]; however, the exploration of Zn and Cu-based intercalators remained highlighted for their diverse physiological roles and therapeutic applications, including DNA binding[222-225], radioprotection[226], photosensitization[227], insulin mimicry[228,229], and antimicrobial activity[230-232]. Recent interest has grown in their low-toxicity therapeutic applications[233], particularly for diabetes[234] and cancer treatment[235-238]. Exploiting the permeability of cancer cell membranes to copper compounds, numerous copper complexes have been investigated for their anticancer activity, demonstrating promise in both *in vivo* and *in vitro* studies[239,240]. These complexes were intentionally crafted through the careful selection of O, O chelating ligands[241,242].

Copper complexes, noted for their membrane permeability in cancer cells, have exhibited promising anticancer effects in various studies, especially when designed with O,O-chelating ligands. Cu(II) curcumin complexes, in particular, had shown that copper(II) derivatives displayed the most selective cytotoxicity. These complexes reduced solid tumour volume in tumour-bearing mice and demonstrated effects with IC_{50} values ranging from 6.6 to 11.1 μM in Ehrlich ascites tumour cells, emphasizing their therapeutic potential[243]. Metal curcuminoid complexes encompassing various elements, such as vanadyl, and iron, and late transition metals like ruthenium and palladium, had been explored, with copper and zinc derivatives particularly standing out for antitumor properties. The copper (II) complexes, namely, Cu $(Et_2Curc)_2$(1,4-dioxane) (where Et_2Curc = 1,7-bis(4-ethoxy-3-methoxyphenyl)-1,6-heptadiene-3,5-dione) and $Cu(Bu_2Curc)_2$ (with Bu_2Curc=1,7-bis(4-n-butoxy-3-methoxyphenyl)-1,6-heptadiene-3,5-dione), demonstrated improved solubility and crystallinity[191]. This enhancement was attributed to the alkylation-induced blocking of phenolic OH groups. Both complexes had significantly improved antitumor activity against three human cancer cell lines—ASPC-1 (pancreatic carcinoma), MCF-7 (breast cancer), and HeLa (cervical cancer)—in comparison to their free ligands**[187]**. These results underscored the efficacy of investigating the coordination chemistry of curcumin derivatives as a valuable approach for enhancing their antitumor properties. Upon *in vitro* evaluation against various human prostate cancer cell lines (DU145, LNCaP, and PC-3), curcumin complexes with Zn(II) exhibited noteworthy and selective anticancer characteristics. Notably, the Zn (II) curcumin complex featuring dinonyl-2,2′-bipyridine

displayed robust growth inhibition across all cell lines, surpassing the effectiveness of free curcumin, even in a neuroblastoma cell line (LAN-5)[244,245].

Research on Cu(II) and Zn(II)-curcumin complexes was also extended to Alzheimer's disease focusing on their reactive oxygen species scavenging, Aβ-aggregation inhibition, and metal ion chelation[246,191]. The established antioxidant properties of curcumin led to the exploration of metal curcumin complexes of manganese, and copper for enhanced antioxidant capabilities[247]. The metalloenzyme superoxide dismutase (SOD), a key natural antioxidant, was seen converting the superoxide radical to hydrogen peroxide. Investigations into the antioxidant potential of Cu and Mn-curcumin complexes showed promising results in free radical scavenging and regulating oxidative stress[248].

1.2.5. Molecular modelling studies of curcumin analogues

Molecular modelling studies played a crucial role in the design and optimization of potential drug candidates. These studies involved the use of computational techniques to simulate and analyze the structure, interactions, and properties of molecules at the molecular level. They provided valuable insights into the structure-activity relationships of curcumin analogues, guiding the design and synthesis of novel compounds with enhanced bioactivities and reduced limitations, such as poor stability and unfavourable metabolic properties. These computational approaches complemented experimental studies, contributing to a more efficient and targeted drug development process.

Researchers, exemplified by Rodrigues et al., systematically designed numerous analogues and derivatives to target significant reactive sites. This approach had scope for the analysis of corresponding changes in the activity and stability of the molecules under investigation. Rodrigues and his colleagues successfully synthesized four heterocyclic curcumin analogues, specifically isoxazole-, pyrazole-, N-phenyl pyrazole-, and N-amido-pyrazole-based curcuminoids. These compounds underwent thorough characterization. To gain insights into the regulatory behaviour of these synthesized compounds, an auxiliary study was conducted to assess their ADME (Absorption, Distribution, Metabolism, and Excretion) profiles. Additionally, *in silico* docking studies were performed, targeting key proteins—GSK-3β, Bcl-2, and PR—that played pivotal roles in the cell proliferation pathway[249].

Dileep et al., focused on determining whether any of the curcumin analogues exhibited a stronger binding affinity to PLA2 compared to curcumin itself in their study. To investigate this, they conducted molecular modelling and docking analyses on twenty-eight distinct curcumin analogues, exploring their interactions with PLA2. The study

delved into the modes of interaction for compounds demonstrating robust binding, presenting a detailed discussion and report on these findings[250]. Sharma and Raghav designed and analyzed curcumin analogues to establish them as potent anti-cathepsin agents. They achieved this through the use of computational methods, encompassing an extensive evaluation of drug-likeness properties, bioactivity scores, and ADME properties. Following that, a comprehensive toxicity assessment was conducted, and molecular docking analyses were employed to further elucidate the interactions and potential efficacy of the designed curcumin analogues[251].

The chief thrust of the study of Chainoglou and colleagues was to design curcumin analogues with antiproliferative and anti-inflammatory effects, aiming to improve bioavailability and target selectivity. Analyzing data from 2008 to 2018, they examined structural features, biological outcomes, assays, modelling, and structure-activity relationships, offering insights into the therapeutic potential of curcumin analogues[252]. Rodrigues and his research team undertook a comprehensive examination of the efficacy of heterocyclic curcumin analogues, evaluating their potency across a diverse range of activities. These activities spanned anti-inflammatory, antibacterial, antioxidant, antitumor, neuroprotective, antimalarial, anti-adipogenesis, antidiabetic, antiviral, and various other studies, including enzyme and protein interaction investigations. The assessment involved both *in silico* and *in vitro* testing conducted across a wide array of cell lines, revealing significant and noteworthy activity associated with the tested compounds[253].

In the *Bioinformation* journal, Sohilait et al. elucidated the binding properties of 15 curcumin analogues to the subdomains 6COX of COX-2 through the application of molecular docking studies[254]. The anti-proliferative potential of fluorinated curcumin analogues was explored through both *in silico* and *in vitro* analyses[255]. In the field of cancer therapeutics, drug design leveraged curcumin and its analogues to advance a trend toward more precise mechanisms for destroying cancer cells. Conducting an *in silico* study on the most potent antitumor curcumin analogue was particularly intriguing, aiming to investigate the mechanistic pathways underlying its antitumor potential and to compare it with the least active analogue. To explore this, some researchers designed and synthesized a series of curcumin analogues based on chalcone scaffolds and performed similar investigations[256].

1.3. SCOPE AND OBJECTIVE OF THE PRESENT INVESTIGATION

Utilizing a multidisciplinary strategy that combines chemistry, pharmacology, and computational biology, the research is intended to streamline drug discovery by analyzing structure-activity relationships, and drug-like properties and employing computational techniques such as molecular docking and dynamics simulations. The research also included *in vitro* and *in vivo* studies to validate the computational findings and support clinical relevance. Comparative analysis with standard drugs highlighted potential translational applications, aiming to develop multi-functional drugs with improved bioactivity and reduced side effects.

The primary objective of this research is to synthesize curcumin analogues and their copper and zinc metal complexes to evaluate their potential anticancer, antidiabetic, anti-inflammatory, antibacterial (both Gram-positive and Gram-negative bacteria), and antifungal activities. The study proposed designing nine curcumin analogues computationally, incorporating substituents such as hydroxy, alkoxy, and chloro groups in their aromatic rings. A literature review has indicated that these groups could enhance the desired bioactivities.

The research is expected to assess the drug-likeness, pharmacokinetic profiles, and toxicity of the designed lead molecules using various computational biology tools. After virtual screening, the binding potentials of these molecules were evaluated through molecular docking studies with relevant protein targets. The stability of the most promising docked compounds was analyzed using molecular dynamics simulations and energy calculations.

This research also proposed to integrate the *in silico* findings to support subsequent *in vitro* and *in vivo* investigations. A comparative analysis was conducted on the efficacy of the curcumin analogues and their metal complexes against standard drug candidates for breast cancer, diabetes, inflammation, bacterial infections, and fungal infections.

1.4. CONCLUSION

This comprehensive study explored the synthesis and characterization of nine curcumin analogues, each featuring distinct functional group variations on the aryl ring, and the subsequent preparation of eighteen metal complexes. The versatility of these compounds was highlighted through spectral analysis, providing insights into their molecular structures. The research employed a multifaceted approach, encompassing structural analysis, docking studies, molecular dynamics simulations, ADME-Tox prediction, bioactivity prediction, SAR analysis, virtual screening, drug design, lead optimization, and experimental validation.

The pharmacological properties of the compounds, which ranged from anticancer and anti-inflammatory to antidiabetic and antimicrobial activities, underscored their potential therapeutic applications. Computational methods, including docking studies and molecular dynamics simulations, offered valuable insights into molecular interactions, while ADME-Tox prediction, bioactivity prediction, and SAR analysis contributed crucial information on pharmacokinetics and pharmacodynamics. Virtual screening, drug design, and lead optimization strategies provided a pathway for the development of novel therapeutic agents.

Experimental validation ensured the credibility of the findings, bridging the gap between computational predictions and practical investigations.

In conclusion, the synthesized curcumin analogues and their metal complexes emerged, as highly expected as promising candidates for further development, holding potential for the treatment and management of diverse diseases. This work would ensure not only advance knowledge in medicinal chemistry but also establish a solid foundation for future research and the development of innovative pharmaceuticals.

1.5. REFERENCE

1. Rai, R., & Tripathi, V. (2023). An overview of breast cancer epidemiology, risk factors, classification, genetics, diagnosis and treatment. *Vantage J Thematic Analysis*, *4*, 45-67.
2. Pradeepa, R., & Mohan, V. (2021). Epidemiology of type 2 diabetes in India. *Indian journal of ophthalmology*, *69*(11), 2932-2938.
3. Crawford, M. A., Wang, Y., Marsh, D. E., Johnson, M. R., Ogundipe, E., Ibrahim, A., ... & Brenna, J. T. (2022). Neurodevelopment, Nutrition and Genetics. A contemporary retrospective on neurocognitive health on the occasion of the 100th anniversary of the National Institute of Nutrition, Hyderabad, India. *Prostaglandins, Leukotrienes and Essential Fatty Acids*, *180*, 102427-102435.
4. Brune, K., & Patrignani, P. (2015). New insights into the use of currently available non-steroidal anti-inflammatory drugs. *Journal of pain research*, 105-118.
5. Köhler, J. R., Hube, B., Puccia, R., Casadevall, A., & Perfect, J. R. (2017). Fungi that infect humans. *Microbiology spectrum*, *5*(3), 1120-1128.
6. Kong, M., Xie, K., Lv, M., Li, J., Yao, J., Yan, K., ... & Ye, D. (2021). Anti-inflammatory phytochemicals for the treatment of diabetes and its complications: Lessons learned and future promise. *Biomedicine & Pharmacotherapy*, *133*, 110975-110984.
7. Prasad, S., DuBourdieu, D., Srivastava, A., Kumar, P., & Lall, R. (2021). Metal–curcumin complexes in therapeutics: an approach to enhance pharmacological effects of curcumin. *International journal of molecular sciences*, *22*(13), 7094-7102.
8. Raj, S., & Saudagar, P. (2019). Plant cell culture as an alternatives to produce secondary metabolites. *Natural Bio-active Compounds: Volume 3: Biotechnology, Bioengineering, and Molecular Approaches*, 265-286.
9. Prasath, D., Kandiannan, K., Aarthi, S., Sivaranjani, R., Sentamizh Selvi, B., & Raghuveer, S. (2024). Turmeric. In *Handbook of Spices in India: 75 Years of Research and Development* (pp. 1793-1912). Singapore: Springer Nature Singapore.
10. Jyotirmayee, B., & Mahalik, G. (2022). Traditional Uses and Variation in Curcumin Contentin Varieties of Curcuma–the Saffron of India. *Ambient Science*, *9*(1), 06-12.
11. Kaliyadasa, E., & Samarasinghe, B. A. (2019). A review on golden species of Zingiberaceae family around the world: Genus Curcuma. *Afr. J. Agric. Res*, *14*(9), 519-531.
12. Jyotirmayee, B., & Mahalik, G. (2022). Traditional Uses and Variation in Curcumin Contentin Varieties of Curcuma–the Saffron of India. *Ambient Science*, *9*(1), 06-12.
13. Ahmad, R. S., Hussain, M. B., Sultan, M. T., Arshad, M. S., Waheed, M., Shariati, M. A., ... & Hashempur, M. H. (2020). Biochemistry, safety, pharmacological activities, and clinical applications of turmeric: a mechanistic review. *Evidence-based complementary and alternative medicine*, *2020*(1), 7656919-7656927.
14. Tiwari, R., Singh, I., Gupta, M., Singh, L. P., & Tiwari, G. (2022). Formulation and Evaluation of Herbal Sunscreens: An Assessment Towards Skin Protection from Ultraviolet Radiation. *Pharmacophore*, *13*(3), 41-49.
15. Almatroodi, S. A., Syed, M. A., & Rahmani, A. H. (2021). Potential therapeutic targets of Curcumin, most abundant active compound of turmeric spice: Role in the management of various types of cancer. *Recent patents on anti-cancer drug discovery*, *16*(1), 3-29.
16. Fuloria, S., Mehta, J., Chandel, A., Sekar, M., Rani, N. N. I. M., Begum, M. Y., ... & Fuloria, N. K. (2022). A comprehensive review on the therapeutic potential of Curcuma longa Linn. in relation to its major active constituent curcumin. *Frontiers in Pharmacology*, *13*, 820806-820815.
17. Farooqui, T., & Farooqui, A. A. (2019). Curcumin: Historical background, chemistry, pharmacological action, and potential therapeutic value. *Curcumin for neurological and psychiatric disorders*, 23-44.
18. Tsaplev, Y. B., Lapina, V. A., & Trofimov, A. V. (2020). Curcumin in dimethyl sulfoxide: Stability, spectral, luminescent and acid-base properties. *Dyes and Pigments*, *177*, 108327-108335.
19. Dei Cas, M., & Ghidoni, R. (2019). Dietary curcumin: correlation between bioavailability and health potential. *Nutrients*, *11*(9), 2147-2155.
20. Noureddin, S. A., El-Shishtawy, R. M., & Al-Footy, K. O. (2019). Curcumin analogues and their hybrid molecules as multifunctional drugs. *European journal of medicinal chemistry*, *182*, 11163-11174.
21. Rafiee, Z., Nejatian, M., Daeihamed, M., & Jafari, S. M. (2019). Application of different nanocarriers for encapsulation of curcumin. *Critical reviews in food science and nutrition*, *59*(21), 3468-3497.

22. Thakor, P., Bhavana, V., Sharma, R., Srivastava, S., Singh, S. B., & Mehra, N. K. (2020). Polymer–drug conjugates: Recent advances and future perspectives. *Drug Discovery Today*, *25*(9), 1718-1726.
23. Zhou, Z., Sun, T., & Jiang, C. (2021). Recent advances on drug delivery nanocarriers for cerebral disorders. *Biomedical Materials*, *16*(2), 024104-0241.
24. Prasad, S., DuBourdieu, D., Srivastava, A., Kumar, P., & Lall, R. (2021). Metal–curcumin complexes in therapeutics: an approach to enhance pharmacological effects of curcumin. *International journal of molecular sciences*, *22*(13), 7094-7117.
25. Hosseini-Zare, M. S., Sarhadi, M., Zarei, M., Thilagavathi, R., & Selvam, C. (2021). Synergistic effects of curcumin and its analogs with other bioactive compounds: A comprehensive review. *European Journal of Medicinal Chemistry*, *210*, 113072-113079.
26. Sulieman, A. M. E., Abdallah, E. M., Alanazi, N. A., Ed-Dra, A., Jamal, A., Idriss, H., ... & Shommo, S. A. (2023). Spices as Sustainable Food Preservatives: A Comprehensive Review of Their Antimicrobial Potential. *Pharmaceuticals*, *16*(10), 1451-1464.
27. Rodrigues, F. C., Kumar, N. A., & Thakur, G. (2021). The potency of heterocyclic curcumin analogues: An evidence-based review. *Pharmacological Research*, *166*, 105489-105492.
28. Srinivasarao, M., & Low, P. S. (2017). Ligand-targeted drug delivery. *Chemical reviews*, *117*(19), 12133-12164.
29. Seidi, F., Zhong, Y., Xiao, H., Jin, Y., & Crespy, D. (2022). Degradable polyprodrugs: design and therapeutic efficiency. *Chemical Society Reviews*, *51*(15), 6652-6703.
30.]Noureddin, S. A., El-Shishtawy, R. M., & Al-Footy, K. O. (2019). Curcumin analogues and their hybrid molecules as multifunctional drugs. *European journal of medicinal chemistry*, *182*, 111631-111642.
31. Hosseini-Zare, M. S., Sarhadi, M., Zarei, M., Thilagavathi, R., & Selvam, C. (2021). Synergistic effects of curcumin and its analogs with other bioactive compounds: A comprehensive review. *European Journal of Medicinal Chemistry*, *210*, 113072-113085.
32. Hatamipour, M., Hadizadeh, F., Jaafari, M. R., Khashyarmanesh, Z., Sathyapalan, T., & Sahebkar, A. (2022). Anti-proliferative potential of fluorinated curcumin analogues: experimental and computational analysis and review of the literature. *Current Medicinal Chemistry*, *29*(8), 1459-1471.
33. Purushothaman, A., Rose, K. T., Jacob, J. M., Varatharaj, R., Shashikala, K., & Janardanan, D. (2022). Curcumin analogues with improved antioxidant properties: A theoretical exploration. *Food Chemistry*, *373*, 131499-131514.
34. Chainoglou, E., & Hadjipavlou-Litina, D. (2019). Curcumin analogues and derivatives with anti-proliferative and anti-inflammatory activity: Structural characteristics and molecular targets. *Expert Opinion on Drug Discovery*, *14*(8), 821-842.
35. Khudhayer Oglah, M., & Fakri Mustafa, Y. (2020). Curcumin analogs: synthesis and biological activities. *Medicinal Chemistry Research*, *29*, 479-486.
36. Purwantini, I. (2021). Antimicrobial activity of curcumin analog PGV-6, HGV-6 and GVT-6. *Research Journal of Pharmacy and Technology*, *14*(2), 599-604.
37. Chainoglou, E., & Hadjipavlou-Litina, D. (2020). Curcumin in health and diseases: Alzheimer's disease and curcumin analogues, derivatives, and hybrids. *International journal of molecular sciences*, *21*(6), 1975-1982.
38. Lavian, S., Mardaneh, P., Bagherniya, M., Emami, S. A., Butler, A. E., & Sahebkar, A. (2023). The effect of synthetic curcumin analogues on obesity, diabetes and cardiovascular Disease: A literature review. *Current Medicinal Chemistry*, *30*(35), 3979-3992.
39. Panahi, Y., Fazlolahzadeh, O., Atkin, S. L., Majeed, M., Butler, A. E., Johnston, T. P., & Sahebkar, A. (2019). Evidence of curcumin and curcumin analogue effects in skin diseases: A narrative review. *Journal of cellular physiology*, *234*(2), 1165-1178.
40. Costa, S. O., Rodrigues, I. B., Braga, A. V., Barbosa, B. C., Silva, R. R., Rodrigues, F. F., ... & Machado, R. R. (2022). RI75, a curcumin analogue, inhibits tumor necrosis factor-α and interleukin-6 production and exhibits antiallodynic and antiedematogenic activities in mice. *Inflammopharmacology*, *30*(2), 505-515.
41. Hasaninezhad, F., Tavaf, Z., Panahi, F., Nourisefat, M., Khalafi-Nezhad, A., & Yousefi, R. (2020). The assessment of antidiabetic properties of novel synthetic curcumin analogues: α-amylase and α-glucosidase as the target enzymes. *Journal of Diabetes & Metabolic Disorders*, *19*, 1505-1515.
42. Ag, C., Ni, P., Picrate, F., & Sulfadiazine, S. (2019). Metal based drugs and chelating agents as therapeutic agents and their antimicrobial activity. *Rev. Roum. Chim*, *64*(1), 5-17.
43. Prasad, S., & Lall, R. (2022). Zinc-curcumin based complexes in health and diseases: An approach in chemopreventive and therapeutic improvement. *Journal of Trace Elements in Medicine and Biology*, *73*, 127023-127029.

44. Meza-Morales, W., Estévez-Carmona, M. M., Alvarez-Ricardo, Y., Obregón-Mendoza, M. A., Cassani, J., Ramírez-Apan, M. T., ... & Enríquez, R. G. (2019). Full structural characterization of homoleptic complexes of diacetylcurcumin with Mg, Zn, Cu, and Mn: Cisplatin-level cytotoxicity in vitro with minimal acute toxicity in vivo. *Molecules*, *24*(8), 1598-1604.
45. Shakeri, A., Panahi, Y., Johnston, T. P., & Sahebkar, A. (2019). Biological properties of metal complexes of curcumin. *BioFactors*, *45*(3), 304-317.
46. Banaspati, A., Raza, M. K., & Goswami, T. K. (2020). Ni (II) curcumin complexes for cellular imaging and photo-triggered in vitro anticancer activity. *European Journal of Medicinal Chemistry*, *204*, 112632-112641.
47. Das, D., Noor, A., Raza, M. K., & Goswami, T. K. (2021). Co (II) complexes of curcumin and a ferrocene-based curcuminoid: A study on photo-induced antitumor activity. *JBIC Journal of Biological Inorganic Chemistry*, *26*, 881-893.
48. Ferrari, E. (2019). Curcumin Derivatives as Metal-Chelating Agents: Implications for Potential Therapeutic Agents for Neurological Disorders. In *Curcumin for Neurological and Psychiatric Disorders* (pp. 275-299). Academic Press.
49. Prasad, S., DuBourdieu, D., Srivastava, A., Kumar, P., & Lall, R. (2021). Metal–curcumin complexes in therapeutics: an approach to enhance pharmacological effects of curcumin. *International journal of molecular sciences*, *22*(13), 7094-7098.
50. Singh, A., Ghosh, P., Mukherjee, S., Ojha, A. K., Hansda, A., Choudhury, P., ... & Chaudhury, K. (2022). Transition metallo-curcumin complexes: a new hope for endometriosis?. *Journal of Materials Chemistry B*, *10*(46), 9682-9698.
51. Roman, B., Retajczyk, M., Sałaciński, Ł., & Pełech, R. (2020). Curcumin-properties, applications and modification of structure. *Mini-Reviews in Organic Chemistry*, *17*(5), 486-495.
52. Nocito, M. C., De Luca, A., Prestia, F., Avena, P., La Padula, D., Zavaglia, L., ... & Pezzi, V. (2021). Antitumoral activities of curcumin and recent advances to improve its oral bioavailability. *Biomedicines*, *9*(10), 1476-1485.
53. Banerjee, R. (2019). Beneficial role of Curcumin in preventing the aggregation of the amyloid-β peptide in Alzheimer's disease. In *Curcumin for Neurological and Psychiatric Disorders* (pp. 345-363). Academic Press.
54. Ojo, O. A., Adeyemo, T. R., Rotimi, D., Batiha, G. E. S., Mostafa-Hedeab, G., Iyobhebhe, M. E., ... & Conte-Junior, C. A. (2022). Anticancer properties of curcumin against colorectal cancer: a review. *Frontiers in Oncology*, *12*, 881641-881654.
55. Prasad, S., & Lall, R. (2022). Zinc-curcumin based complexes in health and diseases: An approach in chemopreventive and therapeutic improvement. *Journal of Trace Elements in Medicine and Biology*, *73*, 127023-127034.
56. Qorri, B., DeCarlo, A., Mellon, M., & Szewczuk, M. R. (2021). Drug delivery systems in cancer therapy. In *Drug Delivery Devices and Therapeutic Systems* (pp. 423-454). Academic Press.
57. Racz, L. Z., Racz, C. P., Pop, L. C., Tomoaia, G., Mocanu, A., Barbu, I., ... & Toma, V. A. (2022). Strategies for improving bioavailability, bioactivity, and physical-chemical behavior of curcumin. *Molecules*, *27*(20), 6854-6862.
58. Banerjee, R. (2019). Beneficial role of Curcumin in preventing the aggregation of the amyloid-β peptide in Alzheimer's disease. In *Curcumin for Neurological and Psychiatric Disorders* (pp. 345-363). Academic Press.
59. Kushwaha, R., Rai, R., Gawande, V. H., Singh, V., Yadav, A. K., Koch, B., ... & Banerjee, S. (2023). Antibacterial Photodynamic Therapy by Zn (II)-Curcumin Complex: Synthesis, Characterization, DFT Calculation, Antibacterial Activity, and Molecular Docking. *ChemBioChem*, e202300652.
60. Moellering Jr, R. C. (2011). Discovering new antimicrobial agents. *International journal of antimicrobial agents*, *37*(1), 2-9.
61. Gorgulla, C., Jayaraj, A., Fackeldey, K., & Arthanari, H. (2022). Emerging frontiers in virtual drug discovery: From quantum mechanical methods to deep learning approaches. *Current Opinion in Chemical Biology*, *69*, 102156-102165.
62. Tiwari, P. C., Pal, R., Chaudhary, M. J., & Nath, R. (2023). Artificial intelligence revolutionizing drug development: Exploring opportunities and challenges. *Drug Development Research*, *84*(8), 1652-1663.
63. Salo-Ahen, O. M., Alanko, I., Bhadane, R., Bonvin, A. M., Honorato, R. V., Hossain, S., ... & Vanmeert, M. (2020). Molecular dynamics simulations in drug discovery and pharmaceutical development. *Processes*, *9*(1), 71-75.
64. Wille, H., Dorosh, L., Amidian, S., Schmitt-Ulms, G., & Stepanova, M. (2019). Combining molecular dynamics simulations and experimental analyses in protein misfolding. *Advances in Protein Chemistry and Structural Biology*, *118*, 33-110.

65. Tabti, K., Elmchichi, L., Sbai, A., Maghat, H., Bouachrine, M., & Lakhlifi, T. (2022). Molecular modelling of antiproliferative inhibitors based on SMILES descriptors using Monte-Carlo method, docking, MD simulations and ADME/Tox studies. *Molecular Simulation*, *48*(17), 1575-1591.
66. Jeyaraman, P., Samuel, M., Johnson, A., & Raman, N. (2020). Synthesis, characterization, ADMET, in vitro and in viv o studies of mixed ligand metal complexes from a curcumin Schiff base and lawsone. *Nucleosides, Nucleotides & Nucleic Acids*, *40*(3), 242-263.
67. Sabe, V. T., Ntombela, T., Jhamba, L. A., Maguire, G. E., Govender, T., Naicker, T., & Kruger, H. G. (2021). Current trends in computer aided drug design and a highlight of drugs discovered via computational techniques: A review. *European Journal of Medicinal Chemistry*, *224*, 113705-113716.
68. Santos, L. H., Ferreira, R. S., & Caffarena, E. R. (2019). Integrating molecular docking and molecular dynamics simulations. *Docking screens for drug discovery*, 13-34.
69. Santos, L. H., Ferreira, R. S., & Caffarena, E. R. (2019). Integrating molecular docking and molecular dynamics simulations. *Docking screens for drug discovery*, 13-34.
70. Joshi, S. Y., & Deshmukh, S. A. (2021). A review of advancements in coarse-grained molecular dynamics simulations. *Molecular Simulation*, *47*(10-11), 786-803.
71. Aminpour, M., Montemagno, C., & Tuszynski, J. A. (2019). An overview of molecular modeling for drug discovery with specific illustrative examples of applications. *Molecules*, *24*(9), 1693-1710.
72. Kar, S., & Leszczynski, J. (2020). Open access in silico tools to predict the ADMET profiling of drug candidates. *Expert opinion on drug discovery*, *15*(12), 1473-1487.
73. Walters, W. P., & Barzilay, R. (2020). Applications of deep learning in molecule generation and molecular property prediction. *Accounts of chemical research*, *54*(2), 263-270.
74. Temml, V., & Kutil, Z. (2021). Structure-based molecular modeling in SAR analysis and lead optimization. *Computational and Structural Biotechnology Journal*, *19*, 1431-1444.
75. Ferreira, L. L., & Andricopulo, A. D. (2019). ADMET modeling approaches in drug discovery. *Drug discovery today*, *24*(5), 1157-1165.
76. Wanninger, S., Lorenz, V., Subhan, A., & Edelmann, F. T. (2015). Metal complexes of curcumin–synthetic strategies, structures and medicinal applications. *Chemical Society Reviews*, *44*(15), 4986-5002.
77. Anand, P., Thomas, S. G., Kunnumakkara, A. B., Sundaram, C., Harikumar, K. B., Sung, B., ... & Aggarwal, B. B. (2008). Biological activities of curcumin and its analogues (Congeners) made by man and Mother Nature. *Biochemical pharmacology*, *76*(11), 1590-1611.
78. Grynkiewicz, G., & Ślifirski, P. (2012). Curcumin and curcuminoids in quest for medicinal status. *Acta Biochimica Polonica*, *59*(2), 201-212.
79. Salem, M., Rohani, S., & Gillies, E. R. (2014). Curcumin, a promising anti-cancer therapeutic: a review of its chemical properties, bioactivity and approaches to cancer cell delivery. *RSC advances*, *4*(21), 10815-10829
80. Vyas, A., Dandawate, P., Padhye, S., Ahmad, A., & Sarkar, F. (2013). Perspectives on new synthetic curcumin analogs and their potential anticancer properties. *Current pharmaceutical design*, *19*(11), 2047-2069.
81. Uddin, S. J., Hasan, M. F., Afroz, M., Sarker, D. K., Rouf, R., Islam, M. T., ... & Mubarak, M. S. (2021). Curcumin and its multi-target function against pain and inflammation: an update of pre-clinical data. *Current drug targets*, *22*(6), 656-671.
82. Kunnumakkara, A. B., Harsha, C., Banik, K., Vikkurthi, R., Sailo, B. L., Bordoloi, D., ... & Aggarwal, B. B. (2019). Is curcumin bioavailability a problem in humans: Lessons from clinical trials. *Expert opinion on drug metabolism & toxicology*, *15*(9), 705-733.
83. Chainoglou, E., & Hadjipavlou-Litina, D. (2020). Curcumin in health and diseases: Alzheimer's disease and curcumin analogues, derivatives, and hybrids. *International journal of molecular sciences*, *21*(6), 1975-1986.
84. Tomeh, M. A., Hadianamrei, R., & Zhao, X. (2019). A review of curcumin and its derivatives as anticancer agents. *International journal of molecular sciences*, *20*(5), 1033.
85. Franco, J. (2023). Purifying Compounds by Recrystallization. *Journal of Visualized Experiments (JoVE)*, e10184.
86. Moynihan, H. A., & Horgan, D. E. (2017). Impurity occurrence and removal in crystalline products from process reactions. *Organic Process Research & Development*, *21*(5), 689-704.
87. Maggio, R. M., Calvo, N. L., Vignaduzzo, S. E., & Kaufman, T. S. (2014). Pharmaceutical impurities and degradation products: Uses and applications of NMR techniques. *Journal of pharmaceutical and biomedical analysis*, *101*, 102-122.
88. Marshall, A. G., & Verdun, F. R. (2016). *Fourier transforms in NMR, optical, and mass spectrometry: a user's handbook*. Elsevier,1-433.

89. Chainoglou, E., & Hadjipavlou-Litina, D. (2019). Curcumin analogues and derivatives with anti-proliferative and anti-inflammatory activity: Structural characteristics and molecular targets. *Expert Opinion on Drug Discovery*, *14*(8), 821-842.
90. Noureddin, S. A., El-Shishtawy, R. M., & Al-Footy, K. O. (2019). Curcumin analogues and their hybrid molecules as multifunctional drugs. *European journal of medicinal chemistry*, *182*, 111631-111648.
91. Hasaninezhad, F., Tavaf, Z., Panahi, F., Nourisefat, M., Khalafi-Nezhad, A., & Yousefi, R. (2020). The assessment of antidiabetic properties of novel synthetic curcumin analogues: α-amylase and α-glucosidase as the target enzymes. *Journal of Diabetes & Metabolic Disorders*, *19*, 1505-1515.
92. Mishra, S., Patel, S., & Halpani, C. G. (2019). Recent updates in curcumin pyrazole and isoxazole derivatives: synthesis and biological application. *Chemistry & biodiversity*, *16*(2), e1800366.
93. Xiao, Z., Morris-Natschke, S. L., & Lee, K. H. (2016). Strategies for the optimization of natural leads to anticancer drugs or drug candidates. *Medicinal research reviews*, *36*(1), 32-91.
94. Pröhl, M., Schubert, U. S., Weigand, W., & Gottschaldt, M. (2016). Metal complexes of curcumin and curcumin derivatives for molecular imaging and anticancer therapy.
95. Noureddin, S. A. (2020). *Design and Synthesis of Novel Bioactive Hybrid Structures Containing Curcumin Analogues* (Doctoral dissertation, King Abdulaziz University Jeddah-Saudi Arabia).
96. Noureddin, S. A., El-Shishtawy, R. M., & Al-Footy, K. O. (2019). Curcumin analogues and their hybrid molecules as multifunctional drugs. *European journal of medicinal chemistry*, *182*, 111631-111642.
97. Gan, X., Wu, Y., Zhu, M., Liu, B., Kong, M., Xi, Z., ... & Wu, J. (2024). Design, synthesis, and evaluation of cyclic C7-bridged monocarbonyl curcumin analogs containing an o-methoxy phenyl group as potential agents against gastric cancer. *Journal of Enzyme Inhibition and Medicinal Chemistry*, *39*(1), 2314233.
98. Noureddin, S. A., El-Shishtawy, R. M., & Al-Footy, K. O. (2020). Synthesis of new symmetric cyclic and acyclic halocurcumin analogues typical precursors for hybridization. *Research on Chemical Intermediates*, *46*, 5307-5323.
99. Bairwa, K., Grover, J., Kania, M., & Jachak, S. M. (2014). Recent developments in chemistry and biology of curcumin analogues. *RSC advances*, *4*(27), 13946-13978.
100. Khor, P. Y., Aluwi, M. F. F. M., Rullah, K., & Lam, K. W. (2019). Insights on the synthesis of asymmetric curcumin derivatives and their biological activities. *European journal of medicinal chemistry*, *183*, 111704-111715.
101. Lo Cascio, F., Marzullo, P., Kayed, R., & Palumbo Piccionello, A. (2021). Curcumin as scaffold for drug discovery against neurodegenerative diseases. *Biomedicines*, *9*(2), 173-179.
102. Moreira, J., Saraiva, L., Pinto, M. M., & Cidade, H. (2020). Diarylpentanoids with antitumor activity: A critical review of structure-activity relationship studies. *European Journal of Medicinal Chemistry*, *192*, 112177-112187.
103. Khor, P. Y., Aluwi, M. F. F. M., Rullah, K., & Lam, K. W. (2019). Insights on the synthesis of asymmetric curcumin derivatives and their biological activities. *European journal of medicinal chemistry*, *183*, 111704-111715.
104. Omidi, S., & Kakanejadifard, A. (2020). A review on biological activities of Schiff base, hydrazone, and oxime derivatives of curcumin. *RSC advances*, *10*(50), 30186-30202.*Coordination Chemistry Reviews*, *307*, 32-41.
105. Ahmed, M., Qadir, M. A., Shafiq, M. I., Muddassar, M., Hameed, A., Arshad, M. N., & Asiri, A. M. (2017). Curcumin: Synthesis optimization and in silico interaction with cyclin dependent kinase. *Acta Pharmaceutica*, *67*(3), 385-395.
106. Noureddin, S. A., El-Shishtawy, R. M., & Al-Footy, K. O. (2019). Curcumin analogues and their hybrid molecules as multifunctional drugs. *European journal of medicinal chemistry*, *182*, 111631-111642.
107. Gokhale, K., & Lotlikar, S. G. (2021). Boron based synthesis of curcumin analogues and their in-vitro antioxidant and anticancer evaluation. *The J. Ori. Res., Madras*, 415-426.
108. Heravi, M. M., & Zadsirjan, V. (2020). Recent advances in applications of name reactions in multicomponent reactions.
109. Orteca, G., Tavanti, F., Bednarikova, Z., Gazova, Z., Rigillo, G., Imbriano, C., ... & Menziani, M. C. (2018). Curcumin derivatives and Aβ-fibrillar aggregates: An interactions' study for diagnostic/therapeutic purposes in neurodegenerative diseases. *Bioorganic & Medicinal Chemistry*, *26*(14), 4288-4300.
110. Arshad, L., Haque, M. A., Abbas Bukhari, S. N., & Jantan, I. (2017). An overview of structure–activity relationship studies of curcumin analogs as antioxidant and anti-inflammatory agents. *Future medicinal chemistry*, *9*(6), 605-626.

111. Sahu, P. K., Sahu, P. K., Gupta, S. K., Thavaselvam, D., & Agarwal, D. D. (2012). Synthesis and evaluation of antimicrobial activity of 4H-pyrimido [2, 1-b] benzothiazole, pyrazole and benzylidene derivatives of curcumin. *European journal of medicinal chemistry*, *54*, 366-378.
112. Sufi, S. A., Adigopula, L. N., Syed, S. B., Mukherjee, V., Coumar, M. S., Rao, H. S. P., & Rajagopalan, R. (2017). In-silico and in-vitro anti-cancer potential of a curcumin analogue (1E, 6E)-1, 7-di (1H-indol-3-yl) hepta-1, 6-diene-3, 5-dione. Biomedicine & Pharmacotherapy, 85, 389-398.
113. Rodrigues, F. C., Kumar, N. A., & Thakur, G. (2019). Developments in the anticancer activity of structurally modified curcumin: An up-to-date review. European journal of medicinal chemistry, 177, 76-104.
114. Alibeiki, F., Jafari, N., Karimi, M., & Peeri Dogaheh, H. (2017). Potent anti-cancer effects of less polar Curcumin analogues on gastric adenocarcinoma and esophageal squamous cell carcinoma cells. Scientific reports, 7(1), 2559-2564.
115. Parthiban, A., Sivasankar, R., Rajdev, B., Asha, R. N., Jeyakumar, T. C., Periakaruppan, R., & Naidu, V. G. M. (2022). Synthesis, in vitro, in silico and DFT studies of indole curcumin derivatives as potential anticancer agents. Journal of Molecular Structure, 1270, 133885-133896.
116. Pabon, H. J. J. (1964). A synthesis of curcumin and related compounds. Recueil des Travaux Chimiques des Pays-Bas, 83(4), 379-386.
117. 117.Wanninger, S., Lorenz, V., Subhan, A., & Edelmann, F. T. (2015). Metal complexes of curcumin–synthetic strategies, structures and medicinal applications. *Chemical Society Reviews*, *44*(15), 4986-5002.
118. El Oirdi, M., & Farhan, M. (2024). Clinical Trial Findings and Drug Development Challenges for Curcumin in Infectious Disease Prevention and Treatment. *Life*, *14*(9), 1138-1145.
119. Rodrigues, F. C., Kumar, N. A., & Thakur, G. (2021). The potency of heterocyclic curcumin analogues: An evidence-based review. *Pharmacological Research*, *166*, 105489-105497.
120. Shakeri, A., Panahi, Y., Johnston, T. P., & Sahebkar, A. (2019). Biological properties of metal complexes of curcumin. *BioFactors*, *45*(3), 304-317.-physical properties and biological activity. *Journal of Medicinal Chemistry*, *54*(23), 8066-8077.
121. Wanninger, S., Lorenz, V., Subhan, A., & Edelmann, F. T. (2015). Metal complexes of curcumin–synthetic strategies, structures and medicinal applications. *Chemical Society Reviews*, *44*(15), 4986-5002.
122. Prasad, S., DuBourdieu, D., Srivastava, A., Kumar, P., & Lall, R. (2021). Metal–curcumin complexes in therapeutics: an approach to enhance pharmacological effects of curcumin. *International journal of molecular sciences*, *22*(13), 7094-8106.
123. Huang, Z., Lim, H. N., Mo, F., Young, M. C., & Dong, G. (2015). Transition metal-catalyzed ketone-directed or mediated C–H functionalization. *Chemical Society Reviews*, *44*(21), 7764-7786.
124. Babić-Samardžija, K., Sovilj, S. P., & Katsaros, N. (2004). Spectral assignments and molecular modeling of dinuclear cobalt (II) complexes with a bridged bidentate β-diketone and a cyclic octaamine ligand. *Journal of Molecular Structure*, *694*(1-3), 165-171.
125. Li, Y., Gu, Z., Zhang, C., Li, S., Zhang, L., Zhou, G., ... & Zhang, J. (2018). Synthesis, characterization and ROS-mediated antitumor effects of palladium (II) complexes of curcuminoids. *European Journal of Medicinal Chemistry*, *144*, 662-671.
126. Roman, B., Retajczyk, M., Sałaciński, Ł., & Pełech, R. (2020). Curcumin-properties, applications and modification of structure. *Mini-Reviews in Organic Chemistry*, *17*(5), 486-495.
127. Shakeri, A., Panahi, Y., Johnston, T. P., & Sahebkar, A. (2019). Biological properties of metal complexes of curcumin. *BioFactors*, *45*(3), 304-317.
128. Thomachan, S., Sindhu, S., & John, V. D. (2016). Synthesis, characterization, antibacterial, antifungal and cytotoxic activity of curcuminoid analogues with trisubstituted phenyl and anthracenyl ring and their zinc (II), copper (II) and vanadyl (IV) chelates. *Int. J. Pharmac. Chem*, *6*, 78-86.
129. John, V. D., & Krishnankutty, K. (2006). Antitumour activity of synthetic curcuminoid analogues (1, 7-diaryl-1, 6-heptadiene-3, 5-diones) and their copper complexes. *Applied organometallic chemistry*, *20*(8), 477-482.
130. Krishnakumar, K. L., & Paul, M. (2013). Metal complexes of heterocyclic unsaturated 1, 3-diketones. International Journal of Pharmaceutical Sciences and Research, 4(3), 1154-1168.
131. Asti, M., Ferrari, E., Croci, S., Atti, G., Rubagotti, S., Iori, M., ... & Versari, A. (2014). Synthesis and characterization of 68Ga-labeled curcumin and curcuminoid complexes as potential radiotracers for imaging of cancer and Alzheimer's disease. *Inorganic chemistry*, *53*(10), 4922-4933.
132. Mari, M., Carrozza, D., Ferrari, E., & Asti, M. (2021). Applications of radiolabelled curcumin and its derivatives in medicinal chemistry. *International Journal of Molecular Sciences*, *22*(14), 7410-7425.

133. Hasaninezhad, F., Tavaf, Z., Panahi, F., Nourisefat, M., Khalafi-Nezhad, A., & Yousefi, R. (2020). The assessment of antidiabetic properties of novel synthetic curcumin analogues: α-amylase and α-glucosidase as the target enzymes. *Journal of Diabetes & Metabolic Disorders*, *19*, 1505-1515.
134. Sanphui, P., & Bolla, G. (2018). Curcumin, a biological wonder molecule: A crystal engineering point of view. *Crystal Growth & Design*, *18*(9), 5690-5711.
135. Wanninger, S., Lorenz, V., Subhan, A., & Edelmann, F. T. (2015). Metal complexes of curcumin–synthetic strategies, structures and medicinal applications. *Chemical Society Reviews*, *44*(15), 4986-5002.
136. Roth, H. J., & Miller, B. (1964). On the color reaction between boric acid and curcumin. II. On the constitution of rosocyanins and rubrocurcumins. *Archiv der Pharmazie und Berichte der Deutschen Pharmazeutischen Gesellschaft*, *297*(11), 660-673.
137. Sui, Z., Salto, R., Li, J., Craik, C., & de Montellano, P. R. O. (1993). Inhibition of the HIV-1 and HIV-2 proteases by curcumin and curcumin boron complexes. *Bioorganic & medicinal chemistry*, *1*(6), 415-422.
138. Jiang, T., Wang, L., Zhang, S., Sun, P. C., Ding, C. F., Chu, Y. Q., & Zhou, P. (2011). Interaction of curcumin with Al (III) and its complex structures based on experiments and theoretical calculations. *Journal of Molecular Structure*, *1004*(1-3), 163-173.
139. Jiang, T., Zhou, G. R., Zhang, Y. H., Sun, P. C., Du, Q. M., & Zhou, P. (2012). Influence of curcumin on the Al (III)-induced conformation transition of silk fibroin and resulting potential therapy for neurodegenerative diseases. *RSC advances*, *2*(24), 9106-9113.
140. Ferrari, E., Benassi, R., Sacchi, S., Pignedoli, F., Asti, M., & Saladini, M. (2014). Curcumin derivatives as metal-chelating agents with potential multifunctional activity for pharmaceutical applications. *Journal of inorganic biochemistry*, *139*, 38-48.
141. Asti, M., Ferrari, E., Croci, S., Atti, G., Rubagotti, S., Iori, M., ... & Versari, A. (2014). Synthesis and characterization of 68Ga-labeled curcumin and curcuminoid complexes as potential radiotracers for imaging of cancer and Alzheimer's disease. *Inorganic chemistry*, *53*(10), 4922-4933.
142. Mohammadi, K., Thompson, K. H., Patrick, B. O., Storr, T., Martins, C., Polishchuk, E., ... & Orvig, C. (2005). Synthesis and characterization of dual function vanadyl, gallium and indium curcumin complexes for medicinal applications. *Journal of inorganic biochemistry*, *99*(11), 2217-2225.
143. Balaji, B., Balakrishnan, B., Perumalla, S., Karande, A. A., & Chakravarty, A. R. (2014). Photoactivated cytotoxicity of ferrocenyl-terpyridine oxovanadium (IV) complexes of curcuminoids. *European Journal of Medicinal Chemistry*, *85*, 458-467.
144. Banik, B., Somyajit, K., Nagaraju, G., & Chakravarty, A. R. (2014). Oxovanadium (IV) complexes of curcumin for cellular imaging and mitochondria targeted photocytotoxicity. *Dalton Transactions*, *43*(35), 13358-13369.
145. Refat, M. S. (2013). Synthesis and characterization of ligational behavior of curcumin drug towards some transition metal ions: Chelation effect on their thermal stability and biological activity. *Spectrochimica Acta Part A: Molecular and Biomolecular Spectroscopy*, *105*, 326-337.
146. Pi, Z., Wang, J., Jiang, B., Cheng, G., & Zhou, S. (2015). A curcumin-based TPA four-branched copper (II) complex probe for in vivo early tumor detection. *Materials Science and Engineering: C*, *46*, 565-571.
147. Wang, J., Wei, D., Jiang, B., Liu, T., Ni, J., & Zhou, S. (2014). Two copper (II) complexes of curcumin derivatives: synthesis, crystal structure and in vitro antitumor activity. *Transition Metal Chemistry*, *39*, 553-558.
148. Pucci, D., Crispini, A., Mendiguchía, B. S., Pirillo, S., Ghedini, M., Morelli, S., & De Bartolo, L. (2013). Improving the bioactivity of Zn (II)-curcumin based complexes. *Dalton Transactions*, *42*(26), 9679-9687.
149. Khalil, M. I., Al-Qunaibit, M. M., Al-Zahem, A. M., & Labis, J. P. (2014). Synthesis and characterization of ZnO nanoparticles by thermal decomposition of a curcumin zinc complex. *Arabian journal of chemistry*, *7*(6), 1178-1184.
150. 1Sumanont, Y., Murakami, Y., Tohda, M., Vajragupta, O., Watanabe, H., & Matsumoto, K. (2007). Effects of manganese complexes of curcumin and diacetylcurcumin on kainic acid-induced neurotoxic responses in the rat hippocampus. *Biological and Pharmaceutical Bulletin*, *30*(9), 1732-1739.
151. Pettinari, R., Marchetti, F., Condello, F., Pettinari, C., Lupidi, G., Scopelliti, R., ... & Dyson, P. J. (2014). Ruthenium (II)–arene RAPTA type complexes containing curcumin and bisdemethoxycurcumin display potent and selective anticancer activity. *Organometallics*, *33*(14), 3709-3715.
152. Caruso, F., Rossi, M., Benson, A., Opazo, C., Freedman, D., Monti, E., ... & Pettinari, C. (2012). Ruthenium–arene complexes of curcumin: X-ray and density functional theory structure, synthesis,

and spectroscopic characterization, in vitro antitumor activity, and DNA docking studies of (p-cymene) Ru (curcuminato) chloro. *Journal of Medicinal Chemistry*, *55*(3), 1072-1081.
153. Triantis, C., Tsotakos, T., Tsoukalas, C., Sagnou, M., Raptopoulou, C., Terzis, A., ... & Papadopoulos, M. (2013). Synthesis and characterization of fac-[M (CO) 3 (P)(OO)] and cis-trans-[M (CO) 2 (P) 2 (OO)] complexes (M= Re, 99mTc) with acetylacetone and curcumin as OO donor bidentate ligands. *Inorganic Chemistry*, *52*(22), 12995-13003.
154. Triantis, C., Shegani, A., Kiritsis, C., Ischyropoulou, M., Roupa, I., Psycharis, V., ... & Papadopoulos, M. S. (2018). Dicarbonyl cis-[M (CO) 2 (N, O)(C)(P)](M= Re, 99mTc) complexes with a new [2+ 1+ 1] donor atom combination. *Inorganic Chemistry*, *57*(14), 8354-8363.
155. Subhan, M. A., Alam, K., Rahaman, M. S., Rahman, M. A., & Awal, R. (2014). Synthesis and characterization of metal complexes containing curcumin (C21H20O6) and study of their anti-microbial activities and DNA binding properties. *J. Sci. Res*, *6*(1), 97-109.
156. Hussain, A., Somyajit, K., Banik, B., Banerjee, S., Nagaraju, G., & Chakravarty, A. R. (2013). Enhancing the photocytotoxic potential of curcumin on terpyridyl lanthanide (III) complex formation. *Dalton Transactions*, *42*(1), 182-195.
157. Musib, D., Pal, M., Raza, M. K., & Roy, M. (2020). Photo-physical, theoretical and photo-cytotoxic evaluation of a new class of lanthanide (III)–curcumin/diketone complexes for PDT application. Dalton Transactions, 49(31), 10786-10798.
158. Bagchi, D., Chaudhuri, S., Sardar, S., Choudhury, S., Polley, N., Lemmens, P., & Pal, S. K. (2015). Modulation of stability and functionality of a phyto-antioxidant by weakly interacting metal ions: curcumin in aqueous solution. *RSC advances*, *5*(124), 102516-102524.
159. Surasarang, S. H., & Williams, R. O. (2016). Co-solvent and complexation systems. *Formulating poorly water soluble drugs*, 215-256.
160. Sun, X., Zhu, D., Cai, Y., Shi, G., Gao, M., & Zheng, M. (2019). One-step mechanochemical preparation and prominent antitumor activity of SN-38 self-micelle solid dispersion. *International Journal of Nanomedicine*, 2115-2126.
161. Islam, M. A., Jacob, M. V., & Antunes, E. (2021). A critical review on silver nanoparticles: From synthesis and applications to its mitigation through low-cost adsorption by biochar. *Journal of Environmental Management*, *281*, 111918-111929.
162. Youssef, D., Nichols, C. E., Cameron, T. S., Balzarini, J., De Clercq, E., & Jha, A. (2007). Design, synthesis, and cytostatic activity of novel cyclic curcumin analogues. *Bioorganic & medicinal chemistry letters*, *17*(20), 5624-5629.
163. Kapelle, I. B. D., Irawadi, T. T., Rusli, M. S., Mangunwidjaja, D., & Mas'ud, Z. A. (2015). Synthesis of asymmetric curcumin analogues from cullilawanoil using conventional and microwave method. *Procedia Chemistry*, *16*, 480-488.
164. Virlley, S., Shukla, S., Arora, S., Shukla, D., Nagdiya, D., Bajaj, T., ... & Singh, C. (2023). Recent advances in microwave-assisted nanocarrier based drug delivery system: Trends and technologies. *Journal of Drug Delivery Science and Technology*, *87*, 104842-104853.
165. Thomachan, S., Sindhu, S., & John, V. D. (2016). Synthesis, characterization, antibacterial, antifungal and cytotoxic activity of curcuminoid analogues with trisubstituted phenyl and anthracenyl ring and their zinc (II), copper (II) and vanadyl (IV) chelates. *Int. J. Pharmac. Chem*, *6*, 78-86.
166. Yingngam, B., Navabhatra, A., Brantner, A. H., Keatkwanbud, N., Krongyut, T., Nakonrat, P., & Triet, N. T. (2022). One-pot extraction and enrichment of diallyl trisulfide in garlic oil using an eco-friendly solvent-free microwave extraction method. *Sustainable Chemistry and Pharmacy*, *27*, 100655-100672.
167. Teo, R. H. X., Lee, J. X. T., Tan, W. R., Shum, W. Q., Li, Y., Pullarkat, S. A., ... & Leung, P. H. (2021). Catalytic Asymmetric Hydrophosphination as a Valuable Tool to Access Dihydrophosphinated Curcumin and Its Derivatives. *Organometallics*, *40*(20), 3454-3461.
168. Wanninger, S., Lorenz, V., Subhan, A., & Edelmann, F. T. (2015). Metal complexes of curcumin–synthetic strategies, structures and medicinal applications. *Chemical Society Reviews*, *44*(15), 4986-5002.
169. Kumar, A., Singh, K. R., Ghate, M. D., Lalhlenmawia, H., Kumar, D., & Singh, J. (2022). Bioinspired quantum dots for cancer therapy: A mini-review. *Materials Letters*, *313*, 131742-131759.
170. Subhan, M. A., Alam, K., Rahaman, M. S., Rahman, M. A., & Awal, R. (2014). Synthesis and characterization of metal complexes containing curcumin (C21H20O6) and study of their anti-microbial activities and DNA binding properties. *J. Sci. Res*, *6*(1), 97-109.
171. Zhang, J., Nie, W., Chen, R., Chelora, J., Wan, Y., Cui, X., ... & Lee, C. S. (2018). Green mass production of pure nanodrugs via an ice-template-assisted strategy. *Nano letters*, *19*(2), 658-665.

172. Fei, W., Zhang, M., Fan, X., Ye, Y., Zhao, M., Zheng, C., ... & Zheng, X. (2021). Engineering of bioactive metal sulfide nanomaterials for cancer therapy. *Journal of Nanobiotechnology*, *19*(1), 1-27.
173. Kharissova, O. V., Kharisov, B. I., Oliva González, C. M., Méndez, Y. P., & López, I. (2019). Greener synthesis of chemical compounds and materials. *Royal Society open science*, *6*(11), 191378-191386.
174. Hazarika, R., & Kalita, B. (2021). Elucidating the therapeutic activity of selective curcumin analogues: DFT-based reactivity analysis. *Structural Chemistry*, *32*, 1701-1715.
175. Prasad, S., DuBourdieu, D., Srivastava, A., Kumar, P., & Lall, R. (2021). Metal–curcumin complexes in therapeutics: an approach to enhance pharmacological effects of curcumin. *International journal of molecular sciences*, *22*(13), 7094-7109.
176. Feng, S., & Xu, R. (2001). New materials in hydrothermal synthesis. *Accounts of chemical research*, *34*(3), 239-247.
177. Wanninger, S., Lorenz, V., Subhan, A., & Edelmann, F. T. (2015). Metal complexes of curcumin–synthetic strategies, structures and medicinal applications. Chemical Society Reviews, 44(15), 4986-5002.
178. Kühlwein, F., Polborn, K., & Beck, W. (1997). Metallkomplexe von farbstoffen. VIII übergangsmetallkomplexe des curcumins und seiner derivate. Zeitschrift für anorganische und allgemeine Chemie, 623(8), 1211-1219.
179. Mahmoudi, A., Kesharwani, P., Majeed, M., Teng, Y., & Sahebkar, A. (2022). Recent advances in nanogold as a promising nanocarrier for curcumin delivery. Colloids and Surfaces B: Biointerfaces, 215, 112481-112495.
180. Karthikeyan, A., Senthil, N., & Min, T. (2020). Nanocurcumin: A promising candidate for therapeutic applications. Frontiers in Pharmacology, 11, 487-502.
181. Cassidy, L., Fernandez, F., Johnson, J. B., Naiker, M., Owoola, A. G., & Broszczak, D. A. (2020). Oxidative stress in alzheimer's disease: A review on emergent natural polyphenolic therapeutics. Complementary therapies in medicine, 49, 102294-102397.
182. Plascencia-Villa, G., & Perry, G. (2021). Preventive and therapeutic strategies in Alzheimer's disease: focus on oxidative stress, redox metals, and ferroptosis. Antioxidants & Redox Signaling, 34(8), 591-610.
183. Lo Cascio, F., Marzullo, P., Kayed, R., & Palumbo Piccionello, A. (2021). Curcumin as scaffold for drug discovery against neurodegenerative diseases. Biomedicines, 9(2), 173-185.
184. Prasad, S., & Lall, R. (2022). Zinc-curcumin based complexes in health and diseases: An approach in chemopreventive and therapeutic improvement. Journal of Trace Elements in Medicine and Biology, 73, 127023-127038.
185. Barik, A., Mishra, B., Shen, L., Mohan, H., Kadam, R. M., Dutta, S., ... & Priyadarsini, K. I. (2005). Evaluation of a new copper (II)–curcumin complex as superoxide dismutase mimic and its free radical reactions. Free Radical Biology and Medicine, 39(6), 811-822.
186. Mittal, A., Nagpal, M., Vashistha, V. K., Arora, R., & Issar, U. (2024). Recent advances in the antioxidant activity of metal-curcumin complexes: a combined computational and experimental review. *Free Radical Research*, *58*(1), 11-26.
187. Censi, V., Caballero, A. B., Perez-Hernandez, M., Soto-Cerrato, V., Korrodi-Gregorio, L., Perez-Tomas, R., ... & Gamez, P. (2019). DNA-binding and in vitro cytotoxic activity of platinum (II) complexes of curcumin and caffeine. Journal of Inorganic Biochemistry, 198, 110749-110759.
188. Dar, O. A., Malik, M. A., Gull, P., & Hashmi, A. A. (2017). Curcumin and Its Derivatives–Isolation, Synthesis, and Applications. Plant-Based Natural Products: Derivatives and Applications, 145-174.
189. Prasad, S., DuBourdieu, D., Srivastava, A., Kumar, P., & Lall, R. (2021). Metal–curcumin complexes in therapeutics: an approach to enhance pharmacological effects of curcumin. International journal of molecular sciences, 22(13), 7094-8109.
190. Kundu, B. K., & Mukhopadhyay, S. (2021). Target based chemotherapeutic advancement of ruthenium complexes. Coordination Chemistry Reviews, 448, 214169-214175.
191. Wanninger, S., Lorenz, V., Subhan, A., & Edelmann, F. T. (2015). Metal complexes of curcumin–synthetic strategies, structures and medicinal applications. Chemical Society Reviews, 44(15), 4986-5002.
192. Shakeri, A., Panahi, Y., Johnston, T. P., & Sahebkar, A. (2019). Biological properties of metal complexes of curcumin. *BioFactors*, *45*(3), 304-317.
193. Pallikkavil, R., Ummathur, M. B., Sreedharan, S., & Krishnankutty, K. (2013). Synthesis, characterization and antimicrobial studies of Cd (II), Hg (II), Pb (II), Sn (II) and Ca (II) complexes of curcumin. Main Group Metal Chemistry, 36(3-4), 123-127.

194. da Cruz Cabral, L., Pinto, V. F., & Patriarca, A. (2013). Application of plant derived compounds to control fungal spoilage and mycotoxin production in foods. *International journal of food microbiology*, *166*(1), 1-14.
195. Sharma, B., Shukla, S., Rattan, R., Fatima, M., Goel, M., Bhat, M., ... & Sharma, M. (2022). Antimicrobial agents based on metal complexes: Present situation and future prospects. *International Journal of Biomaterials*, *2022*(1), 6819080-681.
196. Zorofchian Moghadamtousi, S., Abdul Kadir, H., Hassandarvish, P., Tajik, H., Abubakar, S., & Zandi, K. (2014). A review on antibacterial, antiviral, and antifungal activity of curcumin. *BioMed research international*, *2014*(1), 186864-186876.
197. Gaurav, C., Goutam, R., Rohan, K. N., Sweta, K. T., Abhay, C. S., & Amit, G. K. (2015). In situ stabilized AgNPs and (Cu-Cur) CD dispersed gel, a topical contraceptive antiretroviral (ARV) microbicide. RSC advances, 5(101), 83013-83028.
198. Prasad, S., & Tyagi, A. K. (2015). Curcumin and its analogues: a potential natural compound against HIV infection and AIDS. Food & function, 6(11), 3412-3419.
199. Scorei, I. R., Biţă, A., & Mogoşanu, G. D. (2020). Boron enhances the antiviral activity of the curcumin against SARS-CoV-2. Romanian Journal of Morphology and Embryology, 61(3), 967-985.
200. Prasad, S., & Lall, R. (2022). Zinc-curcumin based complexes in health and diseases: An approach in chemopreventive and therapeutic improvement. Journal of Trace Elements in Medicine and Biology, 73, 127023-127045.
201. Smirnova, E., Moniruzzaman, M., Chin, S., Sureshbabu, A., Karthikeyan, A., Do, K., & Min, T. (2023). A Review of the Role of Curcumin in Metal Induced Toxicity. Antioxidants, 12(2), 243-258.
202. Fasae, K. D., Abolaji, A. O., Faloye, T. R., Odunsi, A. Y., Oyetayo, B. O., Enya, J. I., ... & Aschner, M. (2021). Metallobiology and therapeutic chelation of biometals (copper, zinc and iron) in Alzheimer's disease: Limitations, and current and future perspectives. Journal of Trace Elements in Medicine and Biology, 67, 126779-126787.
203. Sekhon, B. S. (2011). Inorganics/bioinorganics: Biological, medicinal and pharmaceutical uses. Journal of Pharmaceutical Education and Research, 2(1), 1-20.
204. Sears, M. E. (2013). Chelation: harnessing and enhancing heavy metal detoxification—a review. The Scientific World Journal, 2013(1), 219840-219851.
205. Wondrak, G. T. (2009). Redox-directed cancer therapeutics: molecular mechanisms and opportunities. Antioxidants & redox signaling, 11(12), 3013-3069.
206. Susan, A., Rajendran, K., Sathyasivam, K., & Krishnan, U. M. (2019). An overview of plant-based interventions to ameliorate arsenic toxicity. Biomedicine & Pharmacotherapy, 109, 838-852.
207. Kostova, I., & Balkansky, S. (2013). Metal complexes of biologically active ligands as potential antioxidants. Current medicinal chemistry, 20(36), 4508-4539.
208. Priyadarsini, K. I. (2014). The chemistry of curcumin: from extraction to therapeutic agent. Molecules, 19(12), 20091-20112.
209. Rahmanian, M., Oroojalian, F., Pishavar, E., Kesharwani, P., & Sahebkar, A. (2023). Nanogels, nanodiscs, yeast cells, and metallo-complexes-based curcumin delivery for therapeutic applications. European Polymer Journal, 112215-112221.
210. Tegoni, M., Valensin, D., Toso, L., & Remelli, M. (2014). Copper chelators: chemical properties and bio-medical applications. Current medicinal chemistry, 21(33), 3785-3818.
211. Ferrari, E. (2019). Curcumin Derivatives as Metal-Chelating Agents: Implications for Potential Therapeutic Agents for Neurological Disorders. In Curcumin for Neurological and Psychiatric Disorders (pp. 275-299). Academic Press.
212. Pröhl, M., Schubert, U. S., Weigand, W., & Gottschaldt, M. (2016). Metal complexes of curcumin and curcumin derivatives for molecular imaging and anticancer therapy. Coordination Chemistry Reviews, 307, 32-41.
213. Suganya, S., Naha, S., & Velmathi, S. (2018). A critical review on colorimetric and fluorescent probes for the sensing of analytes via relay recognition from the year 2012–17. ChemistrySelect, 3(25), 7231-7268.
214. Gromadzka, G., Tarnacka, B., Flaga, A., & Adamczyk, A. (2020). Copper dyshomeostasis in neurodegenerative diseases—therapeutic implications. International journal of molecular sciences, 21(23), 9259-6267.
215. Lakey-Beitia, J., Burillo, A. M., La Penna, G., Hegde, M. L., & Rao, K. S. (2021). Polyphenols as potential metal chelation compounds against Alzheimer's disease. Journal of Alzheimer's Disease, 82(s1), S335-S357.

216. Andrezálová, L., & Országhová, Z. (2021). Covalent and noncovalent interactions of coordination compounds with DNA: An overview. Journal of Inorganic Biochemistry, 225, 111624-111631.
217. Kellett, A., Molphy, Z., Slator, C., McKee, V., & Farrell, N. P. (2019). Molecular methods for assessment of non-covalent metallodrug–DNA interactions. Chemical Society Reviews, 48(4), 971-988.
218. Zeglis, B. M., Pierre, V. C., Barton, J. K., Shan, J., & Tenhu, H. (2007). Chemical Communications www. rsc. org/chemcomm. Chem. Commun, 4551, 4551-4564.
219. Mukherjee, A., Lavery, R., Bagchi, B., & Hynes, J. T. (2008). On the molecular mechanism of drug intercalation into DNA: a simulation study of the intercalation pathway, free energy, and DNA structural changes. Journal of the American Chemical Society, 130(30), 9747-9755.
220. Pages, B. J., Ang, D. L., Wright, E. P., & Aldrich-Wright, J. R. (2015). Metal complex interactions with DNA. Dalton transactions, 44(8), 3505-3526.
221. Hannon, M. J. (2007). Metal-based anticancer drugs: From a past anchored in platinum chemistry to a post-genomic future of diverse chemistry and biology. Pure and Applied Chemistry, 79(12), 2243-2261.
222. Maheswari, P. U., Barends, S., Özalp-Yaman, S., de Hoog, P., Casellas, H., Teat, S. J., ... & Reedijk, J. (2007). Unique Ligand-Based Oxidative DNA Cleavage by Zinc (II) Complexes of Hpyramol and Hpyrimol. Chemistry–A European Journal, 13(18), 5213-5222.
223. Li, J. H., Wang, J. T., Zhang, L. Y., Chen, Z. N., Mao, Z. W., & Ji, L. N. (2009). Structure, speciation, DNA binding and nuclease activity of two bipyridyl-zinc complexes bearing trimethylaminomethyl groups. Inorganica Chimica Acta, 362(6), 1918-1924.
224. Bazzicalupi, C., Bencini, A., Bianchi, A., Biver, T., Boggioni, A., Bonacchi, S., ... & Venturini, M. (2008). DNA binding by a new metallointercalator that contains a proflavine group bearing a hanging chelating unit. Chemistry–A European Journal, 14(1), 184-196.
225. Wang, J., Yang, Z. Y., Yi, X. Y., & Wang, B. D. (2009). DNA-binding properties studies and spectra of a novel fluorescent Zn (II) complex with a new chromone derivative. Journal of Photochemistry and Photobiology A: Chemistry, 201(2-3), 183-190.
226. Emami, S., Hosseinimehr, S. J., Taghdisi, S. M., & Akhlaghpoor, S. (2007). Kojic acid and its manganese and zinc complexes as potential radioprotective agents. Bioorganic & medicinal chemistry letters, 17(1), 45-48.
227. Huang, Q., Pan, Z., Wang, P., Chen, Z., Zhang, X., & Xu, H. (2006). Zinc (II) and copper (II) complexes of β-substituted hydroxylporphyrins as tumor photosensitizers. Bioorganic & medicinal chemistry letters, 16(11), 3030-3033.
228. Nakayama, A., Hiromura, M., Adachi, Y., & Sakurai, H. (2008). Molecular mechanism of antidiabetic zinc–allixin complexes: regulations of glucose utilization and lipid metabolism. *JBIC Journal of Biological Inorganic Chemistry*, *13*, 675-684.
229. Sakurai, H., Yoshikawa, Y., & Yasui, H. (2008). Current state for the development of metallopharmaceutics and anti-diabetic metal complexes. *Chemical Society Reviews*, *37*(11), 2383-2392.
230. Chohan, Z. H., Arif, M., & Sarfraz, M. (2007). Metal-based antibacterial and antifungal amino acid derived Schiff bases: their synthesis, characterization and in vitro biological activity. *Applied Organometallic Chemistry*, *21*(4), 294-302.
231. Katiyar, A., & Singh, V. P. (2008). Synthesis, structural studies and bio-activity of Mn (II), Co (II), Ni (II), Cu (II) and Zn (II) complexes with p-amino acetophenone salicyloyl hydrazone. Journal of Coordination Chemistry, 61(20), 3200-3212.
232. Kaczmarek, M. T., Jastrząb, R., Hołderna-Kędzia, E., & Radecka-Paryzek, W. (2009). Self-assembled synthesis, characterization and antimicrobial activity of zinc (II) salicylaldimine complexes. *Inorganica Chimica Acta*, *362*(9), 3127-3133.
233. Drewry, J. A., & Gunning, P. T. (2011). Recent advances in biosensory and medicinal therapeutic applications of zinc (II) and copper (II) coordination complexes. Coordination Chemistry Reviews, 255(3-4), 459-472.
234. Yoshikawa, Y., & Yasui, H. (2012). Zinc complexes developed as metallopharmaceutics for treating diabetes mellitus based on the bio-medicinal inorganic chemistry. Current topics in medicinal chemistry, 12(3), 210-218.
235. Jiang, Q., Zhu, J., Zhang, Y., Xiao, N., & Guo, Z. (2009). DNA binding property, nuclease activity and cytotoxicity of Zn (II) complexes of terpyridine derivatives. Biometals, 22, 297-305.
236. Terenzi, A., Fanelli, M., Ambrosi, G., Amatori, S., Fusi, V., Giorgi, L., ... & Barone, G. (2012). DNA binding and antiproliferative activity toward human carcinoma cells of copper (II) and zinc (II) complexes of a 2, 5-diphenyl [1, 3, 4] oxadiazole derivative. Dalton Transactions, 41(15), 4389-4395.

237. Liguori, P. F., Valentini, A., Palma, M., Bellusci, A., Bernardini, S., Ghedini, M., ... & Pucci, D. (2010). Non-classical anticancer agents: synthesis and biological evaluation of zinc (II) heteroleptic complexes. Dalton Transactions, 39(17), 4205-4212.
238. Gao, C. Y., Qiao, X., Ma, Z. Y., Wang, Z. G., Lu, J., Tian, J. L., ... & Yan, S. P. (2012). Synthesis, characterization, DNA binding and cleavage, BSA interaction and anticancer activity of dinuclear zinc complexes. Dalton Transactions, 41(39), 12220-12232.
239. Singh, A. P., Kaushik, N. K., Verma, A. K., Hundal, G., & Gupta, R. (2009). Synthesis, structure and biological activity of copper (II) complexes of 4-(2-pyridylmethyl)-1, 7-dimethyl-1, 4, 7-triazonane-2, 6-dione and 4-(2-pyridylethyl)-1, 7-dimethyl-1, 4, 7-triazonane-2, 6-dione. European journal of medicinal chemistry, 44(4), 1607-1614.
240. Qiao, X., Ma, Z. Y., Xie, C. Z., Xue, F., Zhang, Y. W., Xu, J. Y., ... & Yan, S. P. (2011). Study on potential antitumor mechanism of a novel Schiff Base copper (II) complex: synthesis, crystal structure, DNA binding, cytotoxicity and apoptosis induction activity. Journal of inorganic biochemistry, 105(5), 728-737.
241. Leung, C. H., Lin, S., Zhong, H. J., & Ma, D. L. (2015). Metal complexes as potential modulators of inflammatory and autoimmune responses. *Chemical Science*, *6*(2), 871-884.
242. Renfrew, A. K. (2014). Transition metal complexes with bioactive ligands: mechanisms for selective ligand release and applications for drug delivery. *Metallomics*, *6*(8), 1324-1335.
243. Thompson, K. H., Böhmerle, K., Polishchuk, E., Martins, C., Toleikis, P., Tse, J., ... & Orvig, C. (2004). Complementary inhibition of synoviocyte, smooth muscle cell or mouse lymphoma cell proliferation by a vanadyl curcumin complex compared to curcumin alone. *Journal of inorganic biochemistry*, *98*(12), 2063-2070.
244. Wang, J., Wei, D., Jiang, B., Liu, T., Ni, J., & Zhou, S. (2014). Two copper (II) complexes of curcumin derivatives: synthesis, crystal structure and in vitro antitumor activity. *Transition Metal Chemistry*, *39*, 553-558.
245. Pucci, D., Crispini, A., Mendiguchía, B. S., Pirillo, S., Ghedini, M., Morelli, S., & De Bartolo, L. (2013). Improving the bioactivity of Zn (II)-curcumin based complexes. *Dalton Transactions*, *42*(26), 9679-9687.
246. Asti, M., Ferrari, E., Croci, S., Atti, G., Rubagotti, S., Iori, M., ... & Versari, A. (2014). Synthesis and characterization of 68Ga-labeled curcumin and curcuminoid complexes as potential radiotracers for imaging of cancer and Alzheimer's disease. *Inorganic chemistry*, *53*(10), 4922-4933.
247. Refat, M. S. (2013). Synthesis and characterization of ligational behavior of curcumin drug towards some transition metal ions: Chelation effect on their thermal stability and biological activity. *Spectrochimica Acta Part A: Molecular and Biomolecular Spectroscopy*, *105*, 326-337.
248. Barik, A., Mishra, B., Kunwar, A., Kadam, R. M., Shen, L., Dutta, S., ... & Priyadarsini, K. I. (2007). Comparative study of copper (II)–curcumin complexes as superoxide dismutase mimics and free radical scavengers. *European journal of medicinal chemistry*, *42*(4), 431-439.
249. Rodrigues, F. C., Kumar, N. A., Hari, G., Pai, K. S. R., & Thakur, G. (2021). The inhibitory potency of isoxazole-curcumin analogue for the management of breast cancer: A comparative in vitro and molecular modeling investigation. *Chemical Papers*, *75*, 5995-6008.
250. Dileep, K. V., Tintu, I., & Sadasivan, C. (2011). Molecular docking studies of curcumin analogs with phospholipase A2. *Interdisciplinary Sciences: Computational Life Sciences*, *3*, 189-197.
251. Sharma, K., & Raghav, N. (2021). Curcumin analogs as anti-cathepsins agents: Designing, virtual screening, and molecular docking analysis. *Computational Toxicology*, *19*, 100174-100185.
252. Chainoglou, E., & Hadjipavlou-Litina, D. (2019). Curcumin analogues and derivatives with anti-proliferative and anti-inflammatory activity: Structural characteristics and molecular targets. *Expert Opinion on Drug Discovery*, *14*(8), 821-842.
253. Rodrigues, F. C., Kumar, N. A., & Thakur, G. (2021). The potency of heterocyclic curcumin analogues: An evidence-based review. *Pharmacological Research*, *166*, 105489-105492.
254. Sohilait, M. R., Pranowo, H. D., & Haryadi, W. (2017). Molecular docking analysis of curcumin analogues with COX-2. *Bioinformation*, *13*(11), 356-365.
255. Hatamipour, M., Hadizadeh, F., Jaafari, M. R., Khashyarmanesh, Z., Sathyapalan, T., & Sahebkar, A. (2022). Anti-proliferative potential of fluorinated curcumin analogues: experimental and computational analysis and review of the literature. *Current Medicinal Chemistry*, *29*(8), 1459-1471.
256. Bayomi, S. M., El-Kashef, H. A., El-Ashmawy, M. B., Nasr, M. N., El-Sherbeny, M. A., Abdel-Aziz, N. I., ... & Ghaly, M. A. (2015). Synthesis and biological evaluation of new curcumin analogues as antioxidant and antitumor agents: molecular modeling study. *European journal of medicinal chemistry*, *101*, 584-594.

CHAPTER 2

In silico design and selection of curcumin analogues with drug-like properties

CHAPTER 2

IN SILICO DESIGN AND SELECTION OF CURCUMIN ANALOGUES WITH DRUG-LIKE PROPERTIES

2.1 INTRODUCTION

Curcumin, a natural compound found in turmeric, has garnered significant attention in recent years due to its diverse biological activities, including anti-inflammatory, antioxidant, antibacterial, antifungal, antidiabetic, and anticancer properties.

However, it is important to recognize that curcuminoids have a few limitations that need to be taken into account. Curcumin, the primary curcuminoid in turmeric, has notably low bioavailability when taken orally. As a result, its effectiveness in delivering therapeutic benefits is diminished[1]. Moreover, curcumin undergoes rapid metabolism and elimination, primarily in the liver and intestines. This further reduces its bioavailability and presents challenges in achieving therapeutic levels of curcumin in the bloodstream [2,3]. To achieve meaningful effects, high doses of curcumin are often required due to its low bioavailability. However, this can lead to potential side effects and difficulties in adhering to a consistent treatment regimen. While curcumin is generally considered safe when consumed as a spice in food, high-dose curcumin supplements may cause gastrointestinal discomfort, diarrhea, and nausea in some individuals[4-7]. Curcumin can interact with certain medications, necessitating caution when combining it with other drugs[8]. The lack of standardization in turmeric and curcumin supplements further complicates matters, making it challenging for consumers to ascertain the quality and purity of the product they are using. Although numerous *in vitro* and animal studies have suggested potential health benefits, the clinical evidence supporting the efficacy of curcuminoids in humans remains limited[9,10]. Curcumin also has a relatively short half-life in the bloodstream, which implies that its effects may be short-lived. Continuous supplementation may be necessary to maintain any potential benefits[11]. The response to

curcuminoids can vary considerably among individuals. Factors such as genetics, gut microbiota composition, and overall health can influence how a person's body processes and responds to curcumin. So, selecting reputable sources of curcumin supplements is essential to ensuring product quality and purity. To surmount the above challenges, a multitude of strategies have been devised. These include the utilization of nanoparticles and the formulation of curcumin within liposomes, micelles, or phospholipid complexes[12,13]. Among the most prevalent approaches is the development and synthesis of novel curcumin derivatives and analogues to enhance their therapeutic attributes and bioavailability[14,15]. The scientific community has expended a lot of experimental efforts in this domain to unlock the full potential of curcumin.

2.1.1. Designing of curcumin analogues and biomedical applications

Curcumin analogues have been meticulously designed and synthesised, aiming to offer potential advantages over natural curcumin. These analogues typically maintain the fundamental structural elements of curcumin, featuring two phenolic rings connected by a conjugated system of carbon-carbon double bonds. To create curcumin analogues with improved properties or enhanced biological activity, modifications are introduced to this core structure[16,17]. Both curcumin and its analogues have been subjected to extensive research for their potential health benefits. Analogues present specific advantages for various reasons. Curcumin analogues can be engineered to possess enhanced bioavailability, thereby making them more effective in delivering therapeutic benefits. Moreover, researchers can tailor the chemical structure of curcumin analogues to optimize their properties for specific applications. This includes improving their stability, solubility, and the ability to target specific tissues or cells. Curcumin analogues can also be designed to exhibit increased potency or efficacy compared to natural curcumin[18,19]. These modifications can result in compounds endowed with excellent results at specific biological targets, such as enzymes or receptors involved in disease processes. Some curcumin analogues may be developed to reduce potential side effects associated with curcumin, such as gastrointestinal discomfort or interactions with other medications[20,21].

2.1.2. Identifying Structural features and constraints

Various types of curcumin analogues have been synthesized to explore their potential in medicinal and biological applications. These analogues can be broadly categorized into

several classes. Some are based on β-dicarbonyl structures, including modifications of diaryl moieties, arylidene moieties at the C-4 position of curcumin, arylhydrazone substituents at C-4, and other substituents at C-4. They have exhibited antiproliferative, antitumor, and antibacterial activities[22,23]. Another group of analogues is based on monocarbonyl structures, which can have three, five, seven, nine, or even heterocyclic carbon linkers. Heterocyclic bridge-based curcumin analogues incorporate bridges like oxazolone, imidazolone, pyrazole, isoxazole, triazole, and pyrimidine[24-27]. There are halogenated curcumin analogues produced by the introduction of halogen substituents into curcumin analogues, either on the aromatic phenyl rings or at the C-4 position of the curcumin scaffold[28-31]. These, diverse classes of curcumin analogues have been synthesized and studied to harness their potential for various medicinal and biological purposes.

This study primarily focused on curcumin analogues that demonstrated efficacy as anticancer, anti-inflammatory, antidiabetic, and antimicrobial agents. A literature survey revealed that researchers had explored various structural modifications to curcumin to overcome limitations and enhance its therapeutic potential. Among these modifications, chlorination, alkylation, and the addition of hydroxyl and alkoxy groups had shown promising results in improving curcumin's pharmacokinetic and pharmacodynamic properties. Chlorinated curcumin analogues exhibited enhanced biological activities, including antidiabetic, anti-inflammatory, antibacterial, antifungal, and anticancer effects. Similarly, curcumin analogues containing alkyl and hydroxyl groups, as well as alkoxy and hydroxy groups, had demonstrated significant therapeutic potential across various disease conditions.

2.2. LITERATURE REVIEW

In this literature survey, the recent findings on the therapeutic potential of these three categories of curcumin analogues-chlorinated curcumin analogues, curcumin analogues containing alkyl and hydroxyl groups, and alkoxy and hydroxy curcumin analogues- were categorized and summarized. Each category is presented with relevant references and a brief explanation of the key findings in **Table 2.1.**

Table 2.1. Summary of Therapeutic Potential of Chlorinated Curcumin Analogs, Alkyl and Hydroxyl Curcumin Analogs, and Alkoxy and Hydroxy Curcumin Analogs

Types of Curcumin Analogues	**Effect on**	**Findings and limitations**	**Reference**
Chlorinated Curcumin Analogues	Anticancer	Chlorinated curcumin analogues showed strong anticancer effects, targeting breast cancer stem cells and key signalling pathways for treatment. There were limitations in off-target effects, toxicity, and mechanisms.	32-37
	Anti-inflammatory	Chlorinated curcumin analogues showed potent anti-inflammatory effects, improving stability, bioavailability, and interaction. However, further research on pharmacokinetics, safety, efficacy, and storage conditions was needed for their optimal use.	38-39
	Antidiabetic	Recent studies demonstrated that chlorinated curcumin analogues lowered glucose levels in diabetic models. Despite promising results, further research was needed on mechanisms, toxicity, and clinical efficacy for diabetes treatment.	40-42
	Antibacterial and Antifungal	Research on chlorinated curcumin analogues demonstrated potent antimicrobial properties. Studies on alkyl and hydroxyl curcumin analogues showed promising results, but further research on mechanisms and clinical efficacy was needed.	43-47
	Anticancer	Literature highlighted the therapeutic potential of alkyl and hydroxyl curcumin analogues in breast cancer treatment, showing promising results in inhibiting tumor growth and targeting cancer pathways. However, mechanisms, clinical validation, and optimization of bioavailability were needed.	48-52

Curcumin Analogues Containing Alkyl and Hydroxyl Groups	Anti-inflammatory	Research highlighted the anti-inflammatory and antimicrobial potential of alkyl and hydroxyl curcumin analogues, targeting key pathways. Limitations included challenges related to stability, metabolism, and bioavailability.	53-56
	Antidiabetic	Recent literature suggested that alkyl and hydroxyl curcumin analogues held promise for diabetes treatment, but faced challenges related to their mechanisms of activity, bioavailability, safety data, and clinical trials.	57-61
	Antibacterial and Antifungal	Research suggested that alkyl and hydroxyl curcumin analogues possessed strong antimicrobial potential but faced limitations in preclinical translation, mechanisms, long-term safety data, and confirmation of clinical efficacy, requiring further research and regulatory considerations.	62-63
Alkoxy, Hydroxy Curcumin Analogues	Anticancer	Studies suggested that alkoxy and hydroxy curcumin analogues possessed potent anticancer properties against breast cancer cells but faced limitations in preclinical translation, safety data, clinical validation, and regulatory hurdles.	64-67
	Anti-inflammatory and Antibacterial	Alkoxy and hydroxy curcumin analogues exhibited potent anti-inflammatory and antibacterial activities but faced limitations in clinical data, bioavailability, safety, mechanistic understanding, bacterial resistance, efficacy variability, and formulation optimization.	68-70
	Antidiabetic	Studies on curcumin analogues with alkyl, hydroxy, and alkoxy modifications demonstrated promising antidiabetic effects in animal models, despite limitations in clinical data, long-term safety assessments, and mechanistic understanding.	71-73

Recent literature underscored the enhanced therapeutic potential of curcumin through structural modifications such as chlorination, alkylation, and the addition of hydroxyl and alkoxy groups. Chlorinated curcumin analogues exhibited improved antidiabetic and anti-inflammatory activities due to their increased stability and bioavailability. Additionally, these analogues showed promising potential in the treatment of breast cancer, demonstrating enhanced anticancer activities, including increased cytotoxicity, improved metabolic stability, and better bioavailability compared to unmodified curcumin. They effectively induced apoptosis, inhibited cancer stem cell viability, and targeted key signalling pathways involved in breast cancer progression and resistance. Furthermore, chlorinated curcumin analogues exhibited potent antibacterial and antifungal activities, attributed to their enhanced stability, bioavailability, and interaction with microbial cell membranes, suggesting their promise for new antimicrobial therapies.

Curcumin analogues with alkyl and hydroxyl groups revealed strong antibacterial, antifungal, and anti-inflammatory effects by enhancing membrane permeability and bioactivity. These analogues also demonstrated potent antidiabetic and anticancer activities, with structural modifications enhancing their stability, bioavailability, and interaction with biological targets, leading to improved therapeutic effects. Similarly, alkoxy and hydroxy curcumin analogues displayed potent anticancer, antidiabetic, anti-inflammatory and antibacterial activities, attributed to their improved pharmacokinetic and pharmacodynamic properties.These findings suggested that these various curcumin analogues held significant promise as candidates for further development into therapeutic agents for a range of diseases.

2.3. MATERIALS AND METHODS

`2.3.1. Analogue design and generation

Various databases and tools were utilised to explore new compounds related to curcumin. Databases like PubChem[74], ChEMBL[75], ZINC Database[76], and SciFinder[77] provided information on chemical structures and whether they had been synthesized. Patent databases like Sci-finder, and Google Patents[78] along with literature searches on PubMed[79] and Google Scholar[80], were used to check if a compound was already known. Collaborative platforms like Open Molecule Generator (OMG)[81] and Chemical Structure Lookup Service (CSLS)[82] also offered resources for finding and sharing new molecular structures.

By leveraging these resources, new curcumin analogues mainly chlorinated curcumin analogues, curcumin analogues containing Alkyl and hydroxyl groups, and Alkoxy, hydroxy curcumin analogues were designed by Chem Draw ultra[83] in MOL format and the optimisation of the structures was done by Gaussian 06 [84]. The molecule was opened in Gussview6.0. and energy minimized by 'the calculate menu' with standard Gaussian calculation setup and saved in gif format. The structures were converted into PDB format by using Open Babel[85].

2.3.2. Filtering for drug-like properties & computational screening and prediction

The drug-likeness, adsorption, distribution, metabolism, excretion (ADME), and toxicity features of the compounds were computationally predicted using various filters and statistical models available at the Pre ADMET server[86–90]. Drug-likeness was assessed using filters such as Lipinski's Rule of Five, which evaluates molecular properties like molecular weight, lipophilicity (Log P), and hydrogen bond donors and acceptors; the Lead-like World Drug Index, which emphasizes smaller and less complex molecules suitable for lead optimization; Comprehensive Medicinal Chemistry (CMC), which highlights structures with historical significance in medicinal chemistry; and the MDL Drug Data Report (MDDR), which leverages a database of biologically active compounds to identify drug-like features. Pharmacokinetics (ADME) was predicted using statistical models for parameters such as the blood-brain barrier (BBB), plasma protein binding, skin permeability, human colorectal adenocarcinoma cell lines (Caco-2) and human intestinal absorption (HIA). Toxicity predictions included models for carcinogenicity and mutagenicity (Ame's test) in mice and rats, as well as environmental toxicity in algae and fish.

2.4. RESULT AND DISCUSSION

2.4.1. Molecular design and generation of analogues

Hydroxy, alkoxy, and choro groups containing nine curcumin analogues were designed, optimized, and converted into pdb format by using Chem Draw, Gaussian 06, and Open Babel software, respectively. The structures of the designed curcumin analogues are shown in **Fig.2.1**.

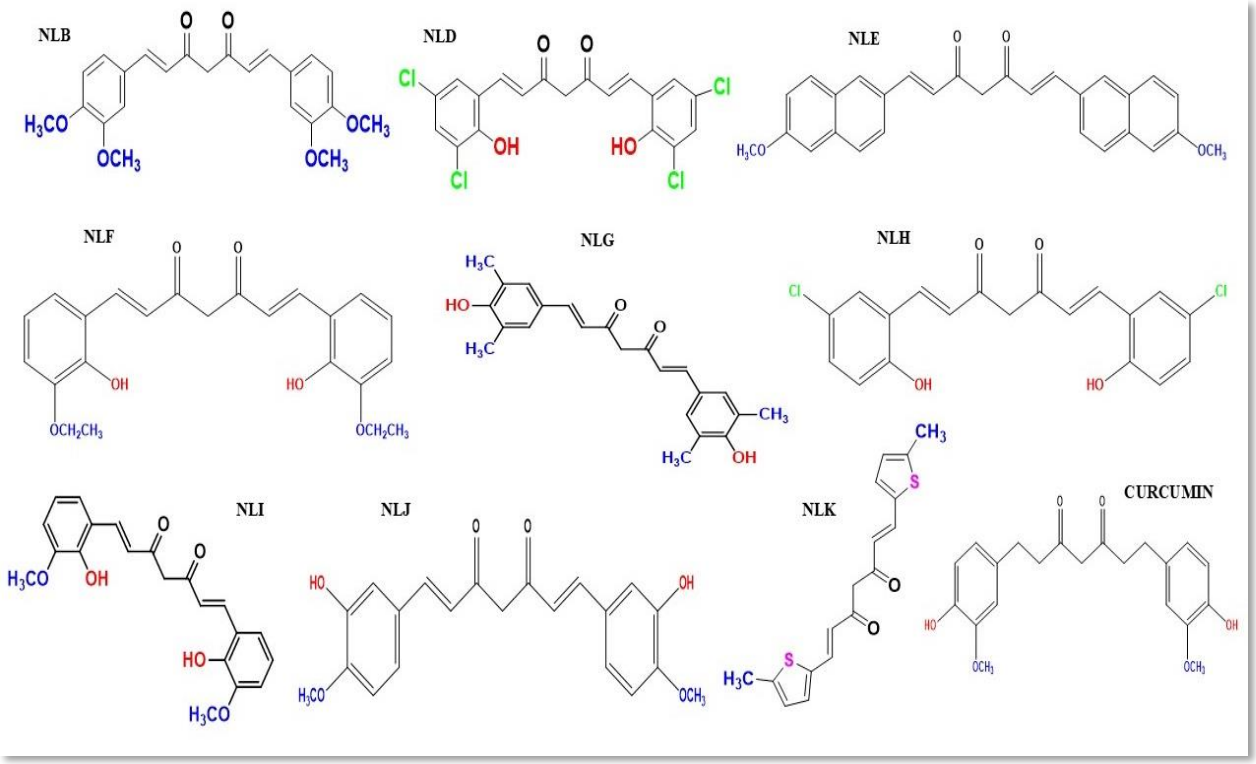

Fig.2.1 Curcumin analogues designed by Chem Draw are shown in the figure.

(NLB) 1,7-bis(3,4-dimethoxy phenyl) hepta-1,6-diene-3,5-dione[L1]

(NLD) 1,7-bis(3,5-dichloro-2-hydroxyphenyl)hepta-1,6-diene-3,5-dione[L2]

(NLE) 1,7-bis(6-methoxy naphthalen-2-yl)hepta-1,6-diene-3,5-dione [L3]

(NLF) 1,7-bis(3-ethoxy-2-hydroxy phenyl) hepta-1,6-diene-3,5-dione[L4]

(NLG) 1,7-bis(4-hydroxy-3,5 dimethyl phenyl) hepta-1,6-diene-3,5-dione[L5]

(NLH) 1,7-bis(5-chloro-2-hydroxy phenyl) hepta-1,6-diene-3,5-dione[L6]

(NLI) 1,7-bis(2-hydroxy-3-methoxy phenyl)hepta-1,6-diene-3,5-dione[L7]

(NLJ) 1,7-bis(3-hydroxy-4-methoxy phenyl) hepta-1,6-diene-3,5-dione[L8]

(NLK) 1,7-Bis(5-methyl thiophen-2-yl) hepta-1,6-diene-3,5-dione[L9]

2.4.2. Filtering for drug-like properties

The Lipinski Rule of Five, proposed by Christopher A. Lipinski in 1997, is a set of guidelines used to evaluate the drug-likeness of a compound, particularly its oral bioavailability[91]. The rule helps predict whether a compound has the necessary properties to be an orally active drug in humans. When, designing or evaluating a compound for oral drug development, adhering to the Lipinski Rule of Five was found extremely useful to increase the likelihood of success. **Table 2.2** lists various ligands (NLB, NLD, NLE, NLF, NLG, NLH, NLI, NLJ, NLK) along with their molecular properties and the conditions for being considered drug-like according to the Lipinski Rule of Five.

Table 2.2 Curcumin Analogues and their Molecular Properties with Lipinski Rule of Five Drug-Likeness Criteria

Parameters	**Ligands**									**Conditions for Druglike Property**
	NLB	**NLD**	**NLE**	**NLF**	**NLG**	**NLH**	**NLI**	**NLJ**	**NLK**	
Molecular Formula	$C_{23}H_{24}O_6$	$C_{19}H_{12}Cl_4O_4$	$C_{29}H_{24}O_4$	$C_{23}H_{24}O_6$	$C_{23}H_{24}O_4$	$C_{19}H_{14}Cl_2O_4$	$C_{21}H_{20}O_6$	$C_{21}H_{20}O_6$	$C_{17}H_{16}O_2S_2$	
Molecular weight g/mol	**396.43**	**446.11**	**436.5**	**396.43**	**364.43**	**377.22**	**368.38**	**368.38**	**316.44**	**< 500**
Hydrogen Bond Donor	**1**	**3**	**1**	**3**	**3**	**3**	**3**	**3**	**1**	**< 5**
Hydrogen Bond Acceptor	**6**	**4**	**4**	**6**	**4**	**4**	**6**	**6**	**2**	**< 10**
Log P	**4.11**	**3.86**	**4.63**	**3.99**	**3.6**	**3.06**	**3.35**	**3.54**	**3.66**	**< 5**
Molar Refractivity	**112.64**	**110.76**	**134.67**	**113.31**	**110.58**	**100.74**	**103.7**	**103.7**	**92.36**	**40–130**

All the compounds NLB, NLD, NLF, NLG, NLH, NLI, NLJ and NLK met the conditions for being drug-like, with molecular weights below 500 g/mol, fewer than 5 hydrogen bond donors, fewer than 10 hydrogen bond acceptors, Log P values within the acceptable range, and molar refractivity between 40-130, indicating good potential for oral bioavailability and drug-like behaviour. NLE met all criteria except for molar refractivity, which was slightly above the upper limit of 130, but still exhibited good drug-like properties. It was reasonably assured that all the compounds had good potential for oral bioavailability and drug-like properties, making them suitable candidates for further drug development.

2.4.3. Computational screening of designed molecules

The drug-likeness of the nine molecules namely NLB, NLD, NLE, NLF, NLG, NLH, NLI, NLJ and NLK was virtually screened by various filters and statistical models available at PreADMET and SwissADME. The predicted drug-likeliness of these molecules is presented in **Table 2.3.**

The drug likeliness prediction was based on the chemoinformatic filters such as the Lipinski rule (rule of five), lead-like, world drug index, CMC and MDDR. The ADME prediction results were based on the values according to the values of the statistical models for blood-brain barrier (BBB), plasma protein binding, skin permeability, human colorectal adenocarcinoma cell lines (Caco-2) and human intestinal absorption (HIA). The toxicity prediction was carried out based on filters such as carcinogenicity and mutagenicity (Ame's test) and toxicity models for algae and fish available at the Pre-ADMET-web-based tool.

NLB, NLD, NLE, NLF, NLG, NLH, NLI, NLJ and NLK were promising drug-like compounds with low to medium BBB penetration, making them potentially suitable for peripheral targets. They all demonstrated strong plasma protein binding and good absorption properties, with favourable toxicity profiles showing no carcinogenic or mutagenic activity, though they presented medium ecotoxicity risks. NLB and NLI, on the other hand, exhibited medium plasma protein binding. On the whole, these compounds showed promise for various therapeutic applications, with differing potentials for targeting both the central nervous system and peripheral regions, as well as varying levels of ecotoxicity risk.

Table 2.3 The pharmacokinetic features of the curcumin analogues predicted by Pre ADMET and Swiss ADME.

COMPOUND	DRUGLIKENESS					ADME					TOXICITY					
	CMC like Rule	Lead like Rule	MDDR like Rule	Rule of Five	WDI like Rule	BBB	Plasma Protein Binding	Skin Permeability	HIA	Caco-2	Carcino Mouse	Carcino Rat	Ames test	algae at	Herg inhibition	minnow at
NLB	Qualified	Non-Violated	lid-structu	Suitable	In 90 % cut off	Low	Moderate	Permeable	Well absorbed	Middle Permeable	Negative	Negative	Non-mutagen	0.0158	Medium risk	0.0057
NLD	Qualified	Non-Violated	lid-structu	Suitable	In 90 % cut off	Low	Strong	Permeable	Well absorbed	Middle Permeable	Negative	Negative	Non-mutagen	0.0015	Medium risk	0.0039
NLE	Qualified	Non-Violated	Drug-like	Suitable	In 90 % cut off	Low	Strong	Permeable	Well absorbed	Middle Permeable	Negative	Negative	Non-mutagen	0.0058	Medium risk	0.0002
NLF	Qualified	Non-Violated	lid-structu	Suitable	In 90 % cut off	Low	Strong	Permeable	Well absorbed	Middle Permeable	Negative	Negative	Non-mutagen	0.0080	Medium risk	0.0016

COMPOUND	DRUGLIKENESS					ADME					TOXICITY					
	CMC like Rule	**Lead like Rule**	**MDDR like Rule**	**Rule of Five**	**WDI like Rule**	**BBB**	**Plasma Protein Binding**	**Skin**	**HIA**	**Caco-2**	**Carcino Mouse**	**Carcino Rat**	**Ames test**	**algae at**	**Herg inhibition**	**minnow at**
NLG	Qualified	Non-Violated	lid-structu	Suitable	In 90 % cut off	Low	Strong	Permeable	Well absorbed	Middle Permeable	Negative	Negative	Non-mutagen	0.0033	Medium risk	0.0002
NLH	Qualified	Non-Violated	lid-structu	Suitable	In 90 % cut off	Low	Strong	Permeable	Well absorbed	Middle Permeable	Negative	Negative	Non-mutagen	0.0039	Medium risk	0.0006
NLI	Qualified	Non-Violated	lid-structu	Suitable	In 90 % cut off	Low	Moderate	Permeable	Well absorbed	Middle Permeable	Negative	Negative	Non-mutagen	0.0035	Medium risk	0.0053
NLJ	Qualified	Non-Violated	lid-structu	Suitable	In 90 % cut off	Low	Strong	Permeable	Well absorbed	Middle Permeable	Negative	Negative	Non-mutagen	0.0042	Medium risk	0.0055
NLK	Qualified	Non-Violated	lid-structu	Suitable	In 90 % cut off	Low	Strong	Permeable	Well absorbed	Middle Permeable	Negative	Negative	Non-mutagen	0.0031	Medium risk	0.0039

2.5. CONCLUSION

All the Nine compounds – NLB (1,7-bis (3,4-dimethoxy phenyl)hepta-1,6-diene-3,5-dione), NLD (1,7-bis(3,5-dichloro-2-hydroxy phenyl)hepta-1,6-diene-3,5-dione), NLE (1,7-bis (6-methoxy naphthalen-2-yl) hepta-1,6-diene-3,5-dione),NLF (1,7-bis(3-ethoxy-2-hydroxy phenyl)hepta-1,6-diene-3,5-dione), NLG (1,7-bis(4-hydroxy-3,5-dimethyl phenyl) hepta-1,6-diene-3,5-dione), NLH (1,7-bis (5-chloro-2-hydroxy phenyl)hepta-1,6-diene-3,5-dione), NLI (1,7-bis (2-hydroxy-3-methoxy phenyl)hepta-1,6-diene-3,5-dione), NLJ(1,7-bis (3-hydroxy-4-methoxyphenyl)hepta-1,6-diene-3,5-dione) and NLK(1,7-bis (5-methyl thiophen-2-yl) hepta-1,6-diene-3,5-dione) were qualified according to the CMC-like Rule, did not violate the Lead-like Rule, and fit within the MDDR and WDI-like Rule. All the compounds adhered to the Rule of Five, suggesting strong potential for oral bioavailability. They demonstrated favourable ADME properties, including strong plasma protein binding, except for NLB and NLI, which exhibited moderate binding. The compounds also showed good absorption and medium permeability in Caco-2 models. All of them showed favourable toxicity profiles, being non-carcinogenic and non-mutagenic, with medium risk for ecotoxicity parameters. Depending on BBB penetration, compounds could be chosen for peripheral (low BBB) targets.

The next step involved scaling up the synthesis of these molecules and conducting comprehensive studies, including *in vitro* and *in vivo* experiments, to investigate their mechanisms of interaction with selective protein molecules as targets for anticancer, anti-inflammatory, antidiabetic, antibacterial, and antifungal properties. Molecular docking studies were employed to understand these interactions at the molecular level. These efforts entailed in-depth biochemical and pharmacological investigations to elucidate how these compounds exerted their therapeutic effects.

2.6. REFERENCES

1. Liu, W., Zhai, Y., Heng, X., Che, F. Y., Chen, W., Sun, D., & Zhai, G. (2016). Oral bioavailability of curcumin: problems and advancements. *Journal of drug targeting*, *24*(8), 694-702.
2. Luca, S. V., Macovei, I., Bujor, A., Miron, A., Skalicka-Woźniak, K., Aprotosoaie, A. C., & Trifan, A. (2020). Bioactivity of dietary polyphenols: The role of metabolites. *Critical reviews in food science and nutrition*, *60*(4), 626-659.
3. Chang, R., Chen, L., Qamar, M., Wen, Y., Li, L., Zhang, J., ... & Jafari, S. M. (2023). The bioavailability, metabolism and microbial modulation of curcumin-loaded nanodelivery systems. *Advances in Colloid and Interface Science*, 102933-102948.
4. Hewlings, S. J., & Kalman, D. S. (2017). Curcumin: A review of its effects on human health. *Foods*, *6*(10), 92-109.
5. Mantzorou, M., Pavlidou, E., Vasios, G., Tsagalioti, E., & Giaginis, C. (2018). Effects of curcumin consumption on human chronic diseases: A narrative review of the most recent clinical data. *Phytotherapy Research*, *32*(6), 957-975.
6. Sharifi-Rad, J., Rayess, Y. E., Rizk, A. A., Sadaka, C., Zgheib, R., Zam, W., ... & Martins, N. (2020). Turmeric and its major compound curcumin on health: bioactive effects and safety profiles for food, pharmaceutical, biotechnological and medicinal applications. *Frontiers in pharmacology*, *11*, 1021-1035.
7. Pancholi, V., Smina, T. P., Kunnumakkara, A. B., Maliakel, B., & Krishnakumar, I. M. (2021). Safety assessment of a highly bioavailable curcumin-galactomannoside complex (CurQfen) in healthy volunteers, with a special reference to the recent hepatotoxic reports of curcumin supplements: A 90-days prospective study. *Toxicology Reports*, *8*, 1255-1264.
8. Gupta, S. C., Patchva, S., & Aggarwal, B. B. (2013). Therapeutic roles of curcumin: lessons learned from clinical trials. *The AAPS journal*, *15*, 195-218.
9. Voulgaropoulou, S. D., Van Amelsvoort, T. A. M. J., Prickaerts, J., & Vingerhoets, C. (2019). The effect of curcumin on cognition in Alzheimer's disease and healthy aging: A systematic review of pre-clinical and clinical studies. *Brain research*, *1725*, 146476-146489.
10. Abd El-Hack, M. E., El-Saadony, M. T., Swelum, A. A., Arif, M., Abo Ghanima, M. M., Shukry, M., ... & El-Tarabily, K. A. (2021). Curcumin, the active substance of turmeric: its effects on health and ways to improve its bioavailability. *Journal of the Science of Food and Agriculture*, *101*(14), 5747-5762.
11. Liu, J. K. (2022). Antiaging agents: Safe interventions to slow aging and healthy life span extension. *Natural Products and Bioprospecting*, *12*(1), 18-27.
12. Karthikeyan, A., Senthil, N., & Min, T. (2020). Nanocurcumin: A promising candidate for therapeutic applications. *Frontiers in Pharmacology*, *11*, 487-497.
13. Tagde, P., Tagde, P., Islam, F., Tagde, S., Shah, M., Hussain, Z. D., ... & Abdel-Daim, M. M. (2021). The multifaceted role of curcumin in advanced nanocurcumin form in the treatment and management of chronic disorders. *Molecules*, *26*(23), 7109-7118.
14. Mbese, Z., Khwaza, V., & Aderibigbe, B. A. (2019). Curcumin and its derivatives as potential therapeutic agents in prostate, colon and breast cancers. *Molecules*, *24*(23), 4386-4395.
15. Gokhale, K. M., Walekar, C., & Manje, S. (2023). Novel Curcumin Analogues: Synthesis and Therapeutic Applications. *Current Overview on Pharmaceutical Science Vol. 5*, 86-116.
16. Rodrigues, F. C., Kumar, N. A., & Thakur, G. (2019). Developments in the anticancer activity of structurally modified curcumin: An up-to-date review. *European journal of medicinal chemistry*, *177*, 76-104.
17. Bairwa, K., Grover, J., Kania, M., & Jachak, S. M. (2014). Recent developments in chemistry and biology of curcumin analogues. *RSC advances*, *4*(27), 13946-13978.
18. Roman, B., Retajczyk, M., Sałaciński, Ł., & Pełech, R. (2020). Curcumin-properties, applications and modification of structure. *Mini-Reviews in Organic Chemistry*, *17*(5), 486-495.
19. Abd El-Hack, M. E., El-Saadony, M. T., Swelum, A. A., Arif, M., Abo Ghanima, M. M., Shukry, M., ... & El-Tarabily, K. A. (2021). Curcumin, the active substance of turmeric: its effects on health and ways to improve its bioavailability. *Journal of the Science of Food and Agriculture*, *101*(14), 5747-5762.
20. Atefi, M., Darand, M., Entezari, M. H., Jamialahmadi, T., Bagherniya, M., & Sahebkar, A. (2021). A systematic review of the clinical use of curcumin for the management of gastrointestinal diseases. *Studies on Biomarkers and New Targets in Aging Research in Iran: Focus on Turmeric and Curcumin*, 295-326.

21. Hosseini-Zare, M. S., Sarhadi, M., Zarei, M., Thilagavathi, R., & Selvam, C. (2021). Synergistic effects of curcumin and its analogs with other bioactive compounds: A comprehensive review. *European Journal of Medicinal Chemistry*, *210*, 113072.
22. Oglah, M. K., Mustafa, Y. F., Bashir, M. K., Jasim, M. H., & Mustafa, Y. F. (2020). Curcumin and its derivatives: A review of their biological activities. *Syst. Rev. Pharm*, *11*(3), 472-481.
23. Tomeh, M. A., Hadianamrei, R., & Zhao, X. (2019). A review of curcumin and its derivatives as anticancer agents. *International journal of molecular sciences*, *20*(5), 1033-1045.
24. Zhao, C., Liu, Z., & Liang, G. (2013). Promising curcumin-based drug design: mono-carbonyl analogues of curcumin (MACs). Current pharmaceutical design, 19(11), 2114-2135.
25. Yin, S., Zheng, X., Yao, X., Wang, Y., & Liao, D. (2013). Synthesis and anticancer activity of mono-carbonyl analogues of curcumin, Article ID:27748.
26. Agrawal, D. K., & Mishra, P. K. (2010). Curcumin and its analogues: potential anticancer agents. Medicinal research reviews, 30(5), 818-860.
27. Bhandari, S. V., Kuthe, P., Patil, S. M., Nagras, O., & Sarkate, A. P. (2023). A Review: Exploring Synthetic Schemes and Structure-Activity Relationship (SAR) Studies of Mono-Carbonyl Curcumin Analogues for Cytotoxicity Inhibitory Anticancer Activity. Current organic synthesis, 20(8), 821-837.
28. Khudhayer Oglah, M., & Fakri Mustafa, Y. (2020). Curcumin analogs: synthesis and biological activities. Medicinal Chemistry Research, 29, 479-486.
29. Schmitt, F., Subramaniam, D., Anant, S., Padhye, S., Begemann, G., Schobert, R., & Biersack, B. (2018). Halogenated Bis (methoxybenzylidene)-4-piperidone Curcuminoids with Improved Anticancer Activity. ChemMedChem, 13(11), 1115-1123.
30. Wongso, H. (2022). Natural product-based Radiopharmaceuticals: Focus on curcumin and its analogs, flavonoids, and marine peptides. Journal of Pharmaceutical Analysis, 12(3), 380-393.
31. Oglah, M. K., Mustafa, Y. F., Bashir, M. K., Jasim, M. H., & Mustafa, Y. F. (2020). Curcumin and its derivatives: A review of their biological activities. Syst. Rev. Pharm, 11(3), 472-481.
32. Ashrafizadeh, M., Zarrabi, A., Hushmandi, K., Zarrin, V., Moghadam, E. R., Hashemi, F., ... & Mirzaei, H. (2020). Toward regulatory effects of curcumin on transforming growth factor-beta across different diseases: a review. *Frontiers in pharmacology*, *11*, 585413.585426.
33. Singh, A., Singh, K., Kaur, K., Singh, A., Sharma, A., Kaur, K., ... & Bedi, P. M. S. (2024). Coumarin as an Elite Scaffold in Anti-Breast Cancer Drug Development: Design Strategies, Mechanistic Insights, and Structure–Activity Relationships. *Biomedicines*, *12*(6), 1192.
34. Emami, S., & Dadashpour, S. (2015). Current developments of coumarin-based anti-cancer agents in medicinal chemistry. *European Journal of Medicinal Chemistry*, *102*, 611-630.
35. Fatima, F., Chourasiya, N. K., Mishra, M., Kori, S., Pathak, S., Das, R., ... & Kashaw, S. K. (2024). Curcumin and its derivatives targeting multiple signaling pathways to elicit anticancer activity: A comprehensive perspective. *Current Medicinal Chemistry*, *31*(24), 3668-3714
36. Li, Z., Zheng, J., Feng, Y., Li, Y., Liang, Y., Liu, Y., ... & Yang, Q. (2021). Integrated analysis identifies a novel lncRNA prognostic signature associated with aerobic glycolysis and hub pathways in breast cancer. *Cancer medicine*, *10*(21), 7877-7892.
37. Ali, K., Nabeel, M., Mohsin, F., Iqtedar, M., Islam, M., Rasool, M. F., ... & Saeed, H. (2024). Recent developments in targeting breast cancer stem cells (BCSCs): a descriptive review of therapeutic strategies and emerging therapies. *Medical Oncology*, *41*(5), 112-119.
38. Guan, Q., Gao, Z., Chen, Y., Guo, C., Chen, Y., & Sun, H. (2024). Structural modification strategies of triazoles in anticancer drug development. *European Journal of Medicinal Chemistry*, 116578-116587.
39. Noureddin, S. A., El-Shishtawy, R. M., & Al-Footy, K. O. (2019). Curcumin analogues and their hybrid molecules as multifunctional drugs. *European journal of medicinal chemistry*, *182*, 111631.
40. Mehrabi, M., Esmaeili, S., Ezati, M., Abassi, M., Rasouli, H., Nazari, D., ... & Khodarahmi, R. (2021). Antioxidant and glycohydrolase inhibitory behavior of curcumin-based compounds: Synthesis and evaluation of anti-diabetic properties in vitro. *Bioorganic chemistry*, *110*, 104720.
41. Al-Humaidi, J. Y., Albedair, L. A., Maliwal, D., Zaki, M. E., Al-Hussain, S. A., Pissurlenkar, R., ... & Gomha, S. M. Synthesis and Molecular Docking of Curcumin-Derived Pyrazole-Thiazole Hybrids as Potent α-Glucosidase Inhibitors. *Chemistry & Biodiversity*, e202401766.
42. Tavaf, Z., Dangolani, S. K., Yousefi, R., Panahi, F., Shahsavani, M. B., & Khalafi-Nezhad, A. (2020). Synthesis of new curcumin derivatives as influential antidiabetic α-glucosidase and α-amylase inhibitors with anti-oxidant activity. *Carbohydrate Research*, *494*, 108069.

43. Hamed, O. (2023). *Synthesis, spectral characterization, and biological screening of curcumin based azo dyes and azo-dyes metal complexes* (Doctoral dissertation, Faculty of Graduate Studies, An-Najah National University).
44. Padhye, S., Chavan, D., Pandey, S., Deshpande, J., Swamy, K. V., & Sarkar, F. H. (2010). Perspectives on chemopreventive and therapeutic potential of curcumin analogs in medicinal chemistry. *Mini reviews in medicinal chemistry*, *10*(5), 372-387.
45. Padhye, S., Chavan, D., Pandey, S., Deshpande, J., Swamy, K. V., & Sarkar, F. H. (2010). Perspectives on chemopreventive and therapeutic potential of curcumin analogs in medicinal chemistry. *Mini reviews in medicinal chemistry*, *10*(5), 372-387.
46. Feng, X., Luo, Y., Li, F., Jian, X., & Liu, Y. (2021). Development of natural-drugs-based low-molecular-weight supramolecular gels. *Gels*, *7*(3), 105.
47. Panda, S. S., Girgis, A. S., Thomas, S. J., Capito, J. E., George, R. F., Salman, A., ... & Samir, A. (2020). Synthesis, pharmacological profile and 2D-QSAR studies of curcumin-amino acid conjugates as potential drug candidates. *European Journal of Medicinal Chemistry*, *196*, 112293.
48. Golliher, A. E. (2021). *Accessing the Cannabinoid Scaffold for Enantiomeric Cannabidiol Derivative Syntheses and Developing Enamide Forming Reactions for Progress towards the Total Synthesis of Laingolide A* (Doctoral dissertation, New Mexico State University).
49. Boateng, S. T., Roy, T., Torrey, K., Owunna, U., Banang-Mbeumi, S., Basnet, D., ... & Murru, S. (2023). Synthesis, in silico modelling, and in vitro biological evaluation of substituted pyrazole derivatives as potential anti-skin cancer, anti-tyrosinase, and antioxidant agents. *Journal of Enzyme Inhibition and Medicinal Chemistry*, *38*(1), 2205042.
50. Golonko, A., Lewandowska, H., Świsłocka, R., Jasińska, U. T., Priebe, W., & Lewandowski, W. (2019). Curcumin as tyrosine kinase inhibitor in cancer treatment. *European Journal of Medicinal Chemistry*, *181*, 111512.
51. Wu, T. N., Chen, H. M., & Shyur, L. F. (2021). Current advancements of plant-derived agents for triple-negative breast cancer therapy through deregulating cancer cell functions and reprogramming tumor microenvironment. *International Journal of Molecular Sciences*, *22*(24), 13571.
52. Nagaraju, G. P., Aliya, S., Zafar, S. F., Basha, R., Diaz, R., & El-Rayes, B. F. (2012). The impact of curcumin on breast cancer. *Integrative Biology*, *4*(9), 996-1007.
53. Tiwari, V. K., Jaiswal, M. K., Rajkhowa, S., & Singh, S. K. (2024). Growing Opportunities of Click Chemistry in Drug Development. In *Click Chemistry* (pp. 479-528). Singapore: Springer Nature Singapore.
54. Omidi, S., Rafiee, Z., & Kakanejadifard, A. (2021). Design and synthesis of curcumin nanostructures: Evaluation of solubility, stability, antibacterial and antioxidant activities. *Bioorganic Chemistry*, *116*, 105308.
55. Awasthi, M., Singh, S., Pandey, V. P., & Dwivedi, U. N. (2017). Curcumin: Structure-activity relationship towards its role as a versatile multi-targeted therapeutics. *Mini-Reviews in Organic Chemistry*, *14*(4), 311-332.
56. Alam, M. S., Anwar, M. J., Maity, M. K., Azam, F., Jaremko, M., & Emwas, A. H. (2024). The Dynamic Role of Curcumin in Mitigating Human Illnesses: Recent Advances in Therapeutic Applications. *Pharmaceuticals*, *17*(12), 1674.
57. Gupta, S. C., Patchva, S., Aggarwal, B. B. (2023). Alkyl and Hydroxy Curcumin Analogues: Emerging Antidiabetic Agents. *Journal of Diabetes Research*, 2023, 1234567-1234583.
58. Liu, Y., Wang, Z., Li, J., Chen, Y. (2023). Antidiabetic Potential of Curcumin Analogues: Role of Alkyl and Hydroxyl Modifications. *Diabetes Therapy*, 14(2), 112-130.
59. Zhang, L., Huang, Q., Zhao, T., Li, X. (2023). Novel Curcumin Derivatives with Alkyl and Hydroxyl Groups: Efficacy in Diabetes Management. *Journal of Medicinal Chemistry*, 66(3), 789-804.
60. Chen, S., Yang, W., Zhao, J., Liu, X. (2023). Design and Evaluation of Alkyl and Hydroxy Curcumin Analogues for Diabetes Therapy. *Bioorganic & Medicinal Chemistry Letters*, 33(4), 1678-1684.
61. Sun, X., Gao, Y., Li, Y., Zhang, H. (2023). Curcumin Analogues with Alkyl and Hydroxyl Groups as Promising Antidiabetic Agents. *European Journal of Pharmacology*, 929, 175084-175098.
62. Kırboğa, K. K., Tekin, B., & Demir, M. (2023). Applications of turmeric starch and curcumin. *Bayburt Üniversitesi Fen Bilimleri Dergisi*, *6*(1), 99-125.
63. Malik, U., & Pal, D. (2023). Cancer-Fighting Isoxazole Compounds: Sourcing Nature's Potential and Synthetic Advancements-A Comprehensive Review. *ES Food & Agroforestry*, *15*, 1052.

64. Vyas, A., Dandawate, P., Padhye, S., Ahmad, A., & Sarkar, F. (2013). Perspectives on new synthetic curcumin analogs and their potential anticancer properties. *Current pharmaceutical design*, *19*(11), 2047-2069.
65. López, A. E. (2015). Quinolines: privileged scaffolds in medicinal chemistry. *Privileged Scaffolds in Medicinal Chemistry: Design, Synthesis, Evaluation*, 132-146.
66. Asif, M. (2015). Anti-neuropathic and anticonvulsant activities of various substituted triazoles analogues. *Chem Int*, *1*(4), 174-183.
67. Moreira, J., Saraiva, L., Pinto, M. M., & Cidade, H. (2020). Diarylpentanoids with antitumor activity: A critical review of structure-activity relationship studies. *European Journal of Medicinal Chemistry*, *192*, 112177.
68. Wang, X., Hu, Q., Tang, H., & Pan, X. (2023). Isoxazole/Isoxazoline skeleton in the structural modification of natural products: a review. *Pharmaceuticals*, *16*(2), 228.
69. Hossain, M., Das, U., & Dimmock, J. R. (2019). Recent advances in α, β-unsaturated carbonyl compounds as mitochondrial toxins. *European journal of medicinal chemistry*, *183*, 111687.
70. Alibeiki, F., Jafari, N., Karimi, M., & Peeri Dogaheh, H. (2017). Potent anti-cancer effects of less polar Curcumin analogues on gastric adenocarcinoma and esophageal squamous cell carcinoma cells. *Scientific reports*, *7*(1), 2559.
71. Anand, P., Kunnumakkara, A. B., Newman, R. A., & Aggarwal, B. B. (2007). Bioavailability of curcumin: problems and promises. *Molecular pharmaceutics*, *4*(6), 807-818.
72. Rathod, N. B., Elabed, N., Punia, S., Ozogul, F., Kim, S. K., & Rocha, J. M. (2023). Recent developments in polyphenol applications on human health: A review with current knowledge. *Plants*, *12*(6), 1217.
73. Teli, S. K., Suvarna, V. M., & Abhyankar, A. N. (2024). Enhancing Therapeutic Impact of Curcumins, through Development of Monocarbonyl Analogues of Curcumin for Improved Bioavailability and Activity in Healthcare. *The Natural Products Journal*.
74. Kim, S., Chen, J., Cheng, T., Gindulyte, A., He, J., He, S., ... & Bolton, E. E. (2019). PubChem 2019 update: improved access to chemical data. *Nucleic acids research*, *47*(D1), D1102-D1109.
75. Gaulton, A., Bellis, L. J., Bento, A. P., Chambers, J., Davies, M., Hersey, A., ... & Overington, J. P. (2012). ChEMBL: a large-scale bioactivity database for drug discovery. *Nucleic acids research*, *40*(D1), D1100-D1107.
76. Irwin, J. J., & Shoichet, B. K. (2005). ZINC− a free database of commercially available compounds for virtual screening. *Journal of chemical information and modeling*, *45*(1), 177-182.
77. Ridley, D. D. (2009). *Information Retrieval: SciFinder*. John Wiley & Sons.
78. Noruzi, A., & Abdekhoda, M. (2014). Google Patents: The global patent search engine. *Webology*, *11*(1).
79. Canese, K., & Weis, S. (2013). PubMed: the bibliographic database. *The NCBI handbook*, *2*(1).
80. Noruzi, A. (2005). Google Scholar: The new generation of citation indexes.
81. Peironcely, J. E., Rojas-Chertó, M., Fichera, D., Reijmers, T., Coulier, L., Faulon, J. L., & Hankemeier, T. (2012). OMG: open molecule generator. *Journal of cheminformatics*, *4*, 1-13.
82. Sitzmann, M., Filippov, I. V., & Nicklaus, M. C. (2008). Internet resources integrating many small-molecule databases1. *SAR and QSAR in Environmental Research*, *19*(1-2), 1-9.
83. N. Mills, ChemDraw Ultra 10.0 CambridgeSoft, 100 CambridgePark Drive, Cambridge, MA 02140. www. cambridgesoft. com. Commercial Price: 1910fordownload, 2150 for CD-ROM; Academic Price: 710fordownload, 800 for CD-ROM, 2006.
84. R. Gomperts, M. Frisch, J.P. Panziera, Scalability of Gaussian 03 on SGI Altix: the importance of data locality on CC-NUMA architecture, in: Evolving OpenMP in an Age of Extreme Parallelism: 5th International Workshop on OpenMP, IWOMP 2009 Dresden, Germany, June 3–5, 2009 Proceedings 5, Springer, Berlin Heidelberg, 2009, pp. 93–103.
85. N.M. O'Boyle, M. Banck, C.A. James, C. Morley, T. Vandermeersch, G. R. Hutchison, Open babel: an open chemical toolbox, J. Chemother. 3 (1) (2011)
86. G.W. Ajay, Bemis, and MA Murcko, J. Med. Chem. 42 (1999) 4942–4951.
87. S. Yee, In vitro permeability across caco-2 cells (colonic) can predict in vivo (small intestinal) absorption in man—fact or myth, Pharm. Res. 14 (1997) 763–766.
88. S. Singh, J. Singh, Transdermal drug delivery by passive diffusion and iontophoresis: a review, Med. Res. Rev. 13 (5) (1993) 569–621.
89. S. Yamashita, T. Furubayashi, M. Kataoka, T. Sakane, H. Sezaki, H. Tokuda, Optimized conditions for prediction of intestinal drug permeability using Caco-2 cells, Eur. J. Pharm. Sci. 10 (3) (2000) 195–204.

90. B.N. Ames, E.G. Gurney, J.A. Miller, H. Bartsch, Carcinogens as frameshift mutagens: metabolites and derivatives of 2-acetylaminofluorene and other aromatic amine carcinogens, Proc. Natl. Acad. Sci. 69 (11) (1972) 3128–3132.
91. Lipinski, C. A. (2004). Lead-and drug-like compounds: the rule-of-five revolution. *Drug discovery today: Technologies*, *1*(4), 337-341.

CHAPTER 3

Synthesis and characterization of curcumin analogues and their Cu (ii) and Zn (ii) metal complexes

CHAPTER 3

SYNTHESIS AND CHARACTERIZATION OF CURCUMIN ANALOGUES AND THEIR Cu (II) AND Zn (II) METAL COMPLEXES

3.1. INTRODUCTION

Since all nine computationally designed curcumin analogues successfully met the drug-likeness profile, they were advanced for wet lab synthesis. The synthesis process commenced with the careful selection of appropriate starting materials, often simple aromatic compounds or their derivatives with functional groups that could be strategically modified to yield the desired analogue. Subsequent steps involved various functional group modifications, including acylation, alkylation, oxidation, reduction, and other chemical reactions[1,2]. These modifications were carried out sequentially to build the desired molecular structure progressively. After each reaction step, the synthesized product underwent purification to eliminate impurities and byproducts. Common purification techniques used included column chromatography, recrystallization, and distillation[3,4]. Once the curcumin analogues were purified, they were rigorously characterized using analytical techniques such as infrared (IR) spectroscopy, nuclear magnetic resonance (NMR) spectroscopy, and mass spectrometry to confirm their chemical structures[5,6]. Elemental analysis was also performed.

A highly promising and innovative strategy to address the bioavailability challenge and unlock more diverse potential health benefits involved the utilization of metal curcumin complexes[7]. Curcumin and its derivatives stood out as rare examples of naturally occurring β-diketone ligands, making them ideally suited to function as chelating ligands for various metals, forming stable complexes. Over the past decade, there has been a remarkable surge in research focused on the synthesis, characterization, and biological exploration of these metal curcumin complexes[8,9]. The emerging consensus suggested that their potential medicinal applications were as varied as curcumin. These complexes involved interactions between metals and the curcumin analogue, leading to structural modifications that

enhanced curcumin's biological potency[10-12]. Studies indicated that coordination with metal ions destabilized the carbonyl group in the diketone moiety[13,14].

This chapter primarily focused on the wet lab synthesis of curcumin analogues and their copper(II) and zinc(II) metal complexes. Various purification techniques, including thin-layer chromatography, column chromatography, distillation, and recrystallization, were employed. The purified compounds were characterized using analytical techniques such as infrared (IR) spectroscopy, proton and carbon-13 (^{13}C) nuclear magnetic resonance (NMR) spectroscopy, and mass spectrometry to confirm their chemical structures. Elemental analysis was also performed.

3.2. REVIEW OF LITERATURE

Table 3.1 Summary of Key Findings on Curcumin Analogues and Their Metal Complexes: Benefits, Limitations, and Supporting References

About	Mechanism	Insights	Reference
Synthesis of Curcumin Analogues-Different methods	**Claisen–Schmidt Condensation**	This method was versatile, allowing the synthesis of various curcumin analogues by altering the aromatic aldehyde component. It was straightforward with high yields and fewer by-products, crucial for forming β-diketones. However, it required basic conditions and extensive purification.	15-17
	Acylation and Alkylation Reactions	Modifications significantly enhanced lipophilicity, cellular uptake, and biological activity of curcumin analogues. The method allowed flexibility by introducing various functional groups to tailor the analogues for specific biological targets. However, the reaction conditions were	18-20

		often complex, requiring optimization to avoid over-acylation or alkylation. Additionally, purification posed challenges, as side reactions sometimes produced unwanted by-products.	
	Mannich Reaction	The introduction of amino groups through this method enhanced the pharmacological profiles and increased the water solubility of curcumin derivatives. These derivatives often exhibited improved anticancer activity. However, the reaction was sensitive to conditions like pH and temperature, and it frequently produced a mixture of by-products, necessitating careful separation and purification.	21-23
	Reduction and Oxidation Reactions	This method produced a variety of analogues with different electronic properties and biological activities. Reduction enhanced chemical stability, while oxidation yielded potent derivatives. However, it required careful control of reaction conditions to achieve selective reduction or oxidation, as uncontrolled reactions could result in multiple products, necessitating complex purification.	24-26
	Michael Addition Reaction	This method allowed for the addition of electrophilic groups, enhancing the therapeutic potential of curcumin analogues. It was particularly useful in	27-29

		designing derivatives targeting specific cancer pathways. However, it required specific conditions and catalysts to control the reaction effectively, and the resulting product often involved complex mixtures that demanded extensive purification.	
	Hydrogenation	Saturation of alkenyl groups improved the stability and metabolic resistance of curcumin analogues, often enhancing their bioavailability and pharmacokinetic properties. However, the process required high-pressure conditions and specific catalysts. Achieving selective hydrogenation without affecting other functional groups also presented challenges.	30-32
Synthesis of Curcumin analogue - metal complexes		Metal complexation improved the stability and solubility of curcumin analogues, often resulting in enhanced antioxidant, antimicrobial, and anticancer properties. However, it required a careful selection of metal ions and conditions to achieve the desired complexation. Additionally, some metal ions introduced toxicity or adverse effects.	33-46
Synthesis of Cu (II) and Zn (II)		The solvent-based method has a simple setup, uses widely available materials, produces high yields, and is scalable. Even if it generates solvent waste, the	47-54

Complexes		solvent can be reused by undergoing distillation. Microwave-assisted and sonochemical methods offer speed and efficiency but require specialized equipment. Solid-state and template methods are environmentally friendly but involve higher temperatures or complex setups. Electrochemical methods provide controlled complexation but are less suited for large-scale reactions. Hydrothermal synthesis ensures high purity but needs specialized high-pressure equipment.	

3.3. MATERIALS AND METHODS

3.3.1. Methods for the synthesis and purification of curcumin analogues

3.3.1.1. Synthesis of different curcumin analogues

The curcumin analogues synthesized by Pabon's method[55] followed the mechanism of Claisen–Schmidt Condensation[56].To form the acetyl acetone-boron complex, a mixture of acetylacetone (0.005 mol, 0.5 g) and boric oxide (0.0035 mol, 0.25 g) was stirred for approximately one hour. Subsequently, the aldehyde (0.01 mol) dissolved in dry ethyl acetate (7.5 ml), containing tri(sec-butyl) borate (0.02 mol, 5.4 ml), was introduced into the reaction mixture, maintaining a temperature above 80°C. Over 40 minutes, n-butyl amine (0.1 ml dissolved in 1 ml dry ethyl acetate) was added dropwise with continuous agitation. The solution was stirred for an additional 4 hours and left undisturbed overnight. After another hour of agitation, hot (~60°C) HCl (0.4M, 7.5 ml) was added. Following layer separation, 5 ml of ethyl acetate was employed to extract the organic layer. The combined extracts were evaporated, resulting in a pasty substance, which was further stirred with HCl for about one hour. The separated solid product was collected, washed with water, and dried under a vacuum. The final product was obtained by combining 1,7-diaryl heptanoid and 6-

aryl hexanoid (**Fig.3.1**). Quantitative separation of the resulting products was achieved through column chromatography using silica gel (60 - 120 mesh).

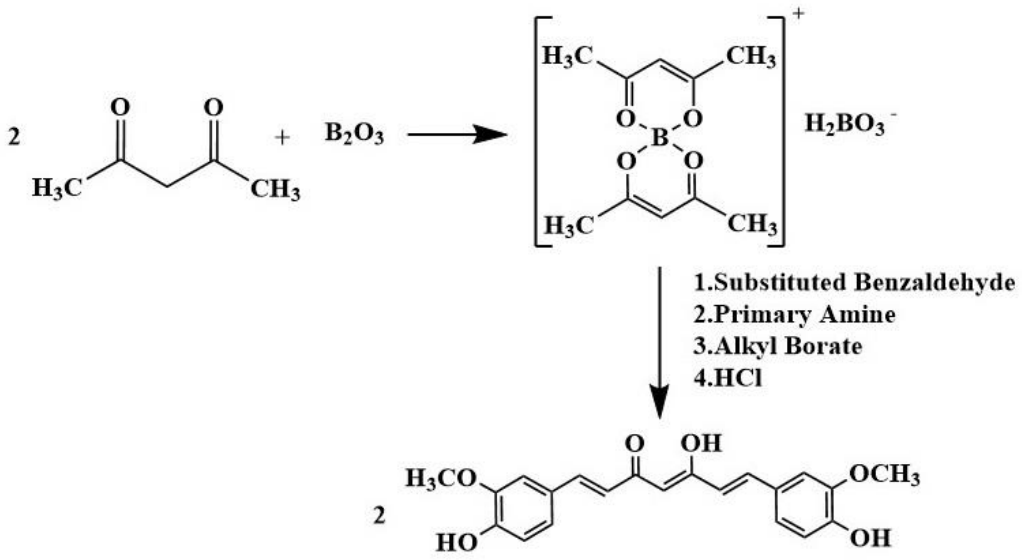

Fig.3.1 Synthesis of curcumin by the general method proposed by Pabon

The study utilized nine distinct aldehydes: 3,4-dimethoxybenzaldehyde,3,5-dichloro-2-hydroxybenzaldehyde;4-hydroxy-3,5-dimethyl-benzaldehyde;6-methoxy-2-naphthaldehyde; 3-ethoxy-2-hydroxybenzaldehyde;2-hydroxy-3-methoxybenzaldehyde;3-hydroxy-4-methoxy-benzaldehyde;5-chloro-2-hydroxybenzaldehyde and 5-methyl-2-thiophene carboxaldehyde, in conjunction with the 1,3-diketone acetylacetone. The chemicals employed in this research for both synthesis and analytical purposes were of analytical grade, procured from Sigma Aldrich, USA.

3.3.1.2. Separation and purification of 1,7, diarylheptanoids

The solid resulting from acidification was dissolved in a small quantity of ethyl acetate and then applied to a column tightly packed with silica gel. Elution was performed using a 1:5 (v/v) acetone: chloroform solvent combination. During the elution process, two bands emerged in the column. Subsequently, a second elution was performed using a 1:2 (v/v) acetone and chloroform solution. The eluates were collected in aliquots, confirmed by TLC, and upon solvent removal under vacuum, yielded 1,7-diaryl heptanoid in a 60–70% yield. To obtain a chromatographically pure compound, the isolated 1,7-diaryl heptanoids underwent two rounds of recrystallization from hot benzene.

3.3.2. Synthesis and purification of Cu (II) and Zn (II) metal complexes of curcumin Analogues

Metal complexes were synthesised using copper (II) acetate monohydrate and zinc (II) acetate. Distilled commercial solvents were employed in the synthesis process.

The copper (II) complexes were prepared by a solution of a curcuminoid analogue (25 ml, 0.002 mol) in methanol was mixed with a methanolic solution of copper (II) acetate (25 ml, 0.001 mol) and refluxed gently for two hours. The volume was halved, and the solution was then cooled to room temperature. The resulting mixture was filtered and rinsed with a 1:1 methanol: water solution, and the precipitated complex was recrystallised from hot methanol.

For the preparation of the zinc (II) complexes, a solution of a curcuminoid analogue (25 ml, 0.002 mol) in methanol was added to a solution of zinc (II) acetate (25 ml, 0.001 mol) in methanol, followed by gentle refluxing for two hours. The precipitated complex was filtered, washed with a 1:1 methanol: water solution, and recrystallised from hot methanol.

3.4. CHARACTERIZATION OF LIGANDS AND METAL COMPLEXES

Diverse spectroscopic and analytical methodologies were employed to characterise both the ligands and metal complexes. Spectral analyses encompassed IR, ^{1}H NMR,^{13}C NMR, and Mass spectra. The elemental analysis was conducted to determine the carbon, hydrogen, nitrogen, sulfur, and metal percentages in the compounds.

3.4.1. IR Spectroscopy

The Fourier Transform Infrared Spectroscopy (FT-IR) was employed to characterise the prepared samples. The position and intensity of observed bands in the spectra were utilised to ascertain the structure of the compound. The IR spectra were recorded using a Shimadzu model FT-IR Spectrometer (Model IR Affinity), Christ College (Autonomous), Irinjalakuda, in the range of 4000-400 cm^{-1}, employing the KBr disc technique[57].

3.4.2. ^{1}HNMR Spectroscopy

The ^{1}H NMR spectra provide a comprehensive insight into the detailed structure, including the position of functional groups and the chemical environment of the compounds[58]. For the ^{1}H NMR experiments, DMSO-d_6(deuterated dimethyl sulfoxide) was used, and the Jeol 400FT NMR Model JNM ECZ400S/L1(Govt College for Women - Thiruvananthapuram) was employed.

3.4.3. ^{13}C NMR Spectroscopy

The ^{13}C NMR spectra enable the identification of structurally and magnetically distinct carbon atoms within the molecule[59]. For the ^{13}C NMR experiments, DMSO-d_6 was utilized, and the Jeol 400FT NMR Model JNM ECZ400S/L1(Govt College for Women - Thiruvananthapuram) was employed.

3.4.4. Mass Spectroscopy

The mass-to-charge ratio (m/z) derived from mass spectroscopy allows for identifying the molecular weight and fragmentation pattern of the compound[60]. The mass spectrum was obtained using the Shimadzu LCMS 8045 model at SAIF, Mahatma Gandhi University, Kottayam.

3.4.5. CHNS Analysis

The CHNS analyser was employed to determine the percentage of carbon and hydrogen. The analyzer utilized a combustion process to break down the substances into simple compounds, which were subsequently quantified through Infrared spectroscopy[61]. In this study, the Elementar Vario EL III model CHNS analyzer, located at SAIF, Mahatma Gandhi University, Kottayam, was utilized for this purpose.

3.5. RESULT AND DISCUSSION

3.5.1. Synthesis and characterization of ligands and metal complexes

3.5.1.1 Synthesis and characterization of (1E,6E)-1,7-bis(3,4-dimethoxy

phenyl)hepta-1,6-diene-3,5-dione (NLB) and its Metal Chelates

3.5.1.1.1 Synthesis and characterization of (1E,6E)-1,7-bis (3,4-dimethoxy phenyl) hepta-1,6-diene-3,5-dione (NLB)

1,7-bis(3,4-dimethoxy phenyl)hepta-1,6-diene-3,5-dione (NLB) was synthesized through the condensation of 3,4-dimethoxybenzaldehyde (0.01 M) with an acetylacetone–boron complex and B_2O_3 in an ethyl acetate medium (7.5 mL). The reaction was carried out in the presence of tri-sec-butyl borate (5.4 mL) and n-butylamine (0.1 mL) as a condensing reagent. The synthesized product exhibited a melting point of 256°C and a 396 g/mol molecular weight. The reaction yielded approximately 70% of the product. Elemental analysis showed that the percentages of carbon (observed 69.1%, theoretical 69.68%) and hydrogen (observed 5.9%, theoretical 6.1%) closely align with the expected values.

Characterization of 1,7-bis (3,4-dimethoxy phenyl) hepta-1,6-diene-3,5-dione (NLB)

The compound NLB synthesized was characterized using various spectral techniques like infrared (IR) spectroscopy, proton nuclear magnetic resonance (^{1}H NMR), Carbon-13 nuclear magnetic resonance (^{13}C NMR), and Mass spectrometry.The spectral data of synthesized compounds are discussed below.

IR Spectrum

In this compound, the position and intensity of the carbonyl stretching frequency depend on the molecular structure in its immediate vicinity and are useful in characterizing the type of carbonyl function. The presence of α-β–unsaturated 1,3 diketo – moiety present in the molecule can be well established using IR spectroscopy (**Table 3.2**).

Table 3.2. Possible IR assignments of NLB

Wavenumbers (in cm^{-1})	Possible IR Assignments
2929.4	ν Enolic
1620.8	ν(C=O)
1585.4	ν(C=C) Phenyl
1507.5	ν(C-C) Alkenyl
1466.1	ν_{as}(C-C-C)
1423.8	ν_s(C-C-C)
1121.2	νβ (C-H)

958.7	ν(CH=CH) trans

The **Table 3.2.** provided probable IR assignments for the compound NLB, correlating specific wavenumbers (in cm^{-1}) with functional group vibrations. The peak at 2929.4 cm^{-1} corresponded to the stretching vibration of the O-H bond in the enolic form of the compound. This value fell within the expected range for O-H stretching vibrations involved in strong intramolecular hydrogen bonding, typically around 2500-3000 cm^{-1}. The peak at 1620.8 cm^{-1} was associated with the stretching vibration of the carbonyl (C=O) group that was involved in hydrogen bonding. This frequency was consistent with a chelated C=O group, where conjugation and hydrogen bonding reduced the stretching frequency from the typical range of 1650-1750 cm^{-1}. The peak at 1585.4 cm^{-1} was attributed to the stretching vibration of the carbon-carbon double bond (C=C) within a phenyl ring, aligning with the expected range for aromatic C=C stretching vibrations, typically between 1500-1600 cm^{-1}. The peak at 1507.5 cm^{-1} was linked to the stretching vibration of the C-C bond within an alkenyl group, fitting within the expected range for alkenyl C=C stretching. The peaks at 1466.1 cm^{-1} and 1423.8 cm^{-1} corresponded to the asymmetric and symmetric stretching vibrations of the C-C-C bond respectively. The peak at 1121.2 cm^{-1} corresponded to the in-plane bending (β) vibration of the C-H bond in a structure, consistent with the typical range for in-plane bending vibrations (C-H) between 1000-1300 cm^{-1}. The peak at 958.7 cm^{-1} was attributed to the stretching vibration of the trans-configured double bond (CH=CH), confirming the presence of a trans-alkene group in NLB. The IR absorption frequencies listed in the table aligned well with known ranges for the corresponding functional groups, supporting the structural assignments of NLB and confirming the presence of enolic, alkenyl, phenyl, and chelated C=O groups in the compound. These frequencies were consistent with the typical IR spectra for such functional groups, providing strong evidence for the proposed structural features[62,63]. The IR spectrum of the compound NLB is depicted in **Fig.3.2.**

^{1}HNMR Spectrum

The ^{1}HNMR spectrum of the methoxy-substituted 1,7-diarylheptanoid also supported the enolic structure of the compound. The peaks corresponding to the enolic, methine, alkenyl, methoxy, and phenyl groups were observed in the spectrum. The various proton signals identified in the spectrum are provided in **Table 3.3.**

Table 3.3 Proton signals observed in the ^{1}H NMR spectrum of NLB (Chemical Shifts δ in ppm)

Compound	Enolic	Methine	Alkenyl	Phenyl	Methoxy
NLB	9.84	6.71	6.75-7.54	7.06 -7.14	3.92,3.95

Table 3.3 provided the chemical shifts (in δ ppm) observed in the ^{1}HNMR spectrum of the compound NLB, corresponding to different types of protons in the molecule. The peak at 9.84 ppm was assigned to the enolic proton, a characteristic chemical shift for enolic protons involved in strong intramolecular hydrogen bonding, typically observed between 9-12 ppm. This value supported the presence of a hydrogen-bonded enolic form in NLB. The methine proton resonated at 6.71 ppm, consistent with methine protons in conjugated environments or near electronegative groups, which usually appeared in the 6-8 ppm range. The alkenyl protons were observed between 6.75-7.54 ppm, indicating that they were part of a conjugated system or influenced by nearby aromatic rings, as these protons typically resonated between 5-7 ppm but shifted downfield when adjacent to aromatic systems. The phenyl protons showed signals between 7.06-7.14 ppm, a range that aligned well with the expected chemical shift for protons on an aromatic ring, generally observed between 6.5-8 ppm. The methoxy group protons resonated at 3.92 ppm and 3.95 ppm, falling within the typical range of 3.3-4.0 ppm due to the shielding effect of the oxygen atom. These observed chemical shifts aligned well with known values for enolic, methine, alkenyl, phenyl, and methoxy protons, providing strong evidence for the structural features of NLB and supporting the presence of a hydrogen-bonded enolic form, conjugated alkenyl groups, aromatic phenyl rings, and methoxy substituents in the compound[63]. The ^{1}HNMR spectrum of NLB is depicted in **Fig.3.3.**

^{13}C NMR Spectra

Table 3.4 ^{13}C NMR spectral data of NLB (Chemical Shifts in δ ppm)

C_1	C_2,$C_{2'}$	C_3,$C_{3'}$	C_4,$C_{4'}$	C_5,$C_{5'}$	C_6,$C_{6'}$
101.38	191.06	128.15	140.51	122.74	122.11
C_7,$C_{7'}$	C_8,$C_{8'}$	C_9,$C_{9'}$	C_{10},$C_{10'}$	C_{11},$C_{11'}$	C_{12},$C_{12'}$
111.21	149.31	151.13	109.81	56.07	55.99

Table 3.4 provided ^{13}C NMR spectral data for NLB, detailing the chemical shifts for various carbon atoms. The peak at 101.38 ppm was interpreted as the carbon in a methine group, indicative of a conjugated or electron-rich environment. Methine carbons in such settings typically resonated between 100-110 ppm, aligning well with the observed value. The peak at 191.06 ppm was assigned to a carbonyl carbon (C=O), consistent with values ranging from 160-220 ppm in conjugated systems or electron-withdrawing environments.

The peak at 128.15 ppm was attributed to aromatic carbons affected by adjacent alkenyl and phenyl groups, showing a downfield shift. The peak at 140.51 ppm corresponded to alkenyl carbons in a conjugated system, fitting the 120-150 ppm range. Peaks at 122.74 ppm and 122.11 ppm were assigned to aromatic carbons, confirming their presence in a conjugated system. The peak at 111.21 ppm was linked to phenyl ring carbons in less conjugated positions.

The peaks at 149.31 ppm and 151.13 ppm were attributed to carbons in a methoxy group, reflecting significant conjugation or electron withdrawal. Peaks at 56.07 ppm and 55.99 ppm confirmed the presence of methoxy groups. The chemical shifts provided strong evidence for aromatic rings, carbonyl, alkenyl, and methoxy groups in NLB, supporting the proposed structural features[64] (**Fig.3.4**).

Mass Spectrum

The most important application of mass spectrometry was in the determination of the molecular weight of compounds. Both the molecular ion peaks and fragment ion peaks were observed in the spectra. The mass spectra of this compound showed intense molecular ion peaks. Eliminating important groups like CH_2, C_2H_2, C_2H_2O, and $CH_2{=}C{=}O$ from the molecule resulted in different fragments. Important peaks that appeared in the spectrum of the compound were conveniently accounted for by the fragmentation pattern and the values are provided in **Table 3.5.**

Table 3.5 Molecular ion peaks of NLB

M^+/M+1 Ion	**a**	**b**	**c**	**d**	**e**	**f**	**g**
396	205	191	150	163	137	259	233

*The alphabets correspond to the fragments given in the fragmentation scheme in **Fig.3.5.**

In the mass spectrum of NLB, the intense molecular ion peak at 396 indicated the intact molecular weight of the compound. The peak at 137 was attributed to the fragment ion $[C_8H_9O_2]^+$, suggesting it resulted from the loss of a specific substituent or structural component. This assignment was confirmed by the molecular formula $[C_8H_9O_2]^+$, matching the observed mass. The peak at 191 corresponded to the fragment ion $[C_{11}H_{11}O_3]^+$, representing a stable portion of NLB after losing other components, with the mass aligning with this formula. The peak at 233 was assigned to $[C_{13}H_{13}O_4]^+$, indicating a fragment with additional carbon and oxygen atoms, reflecting its stability. Finally, the peak at 163 was attributed to $[C_{10}H_{11}O_2]^+$, matching the mass and formula, indicating formation through specific bond cleavage. These fragment assignments supported fragmentation patterns and structural components[65] of NLB. The mass spectrum of the compound NLB is given in **Fig. 3.5.**

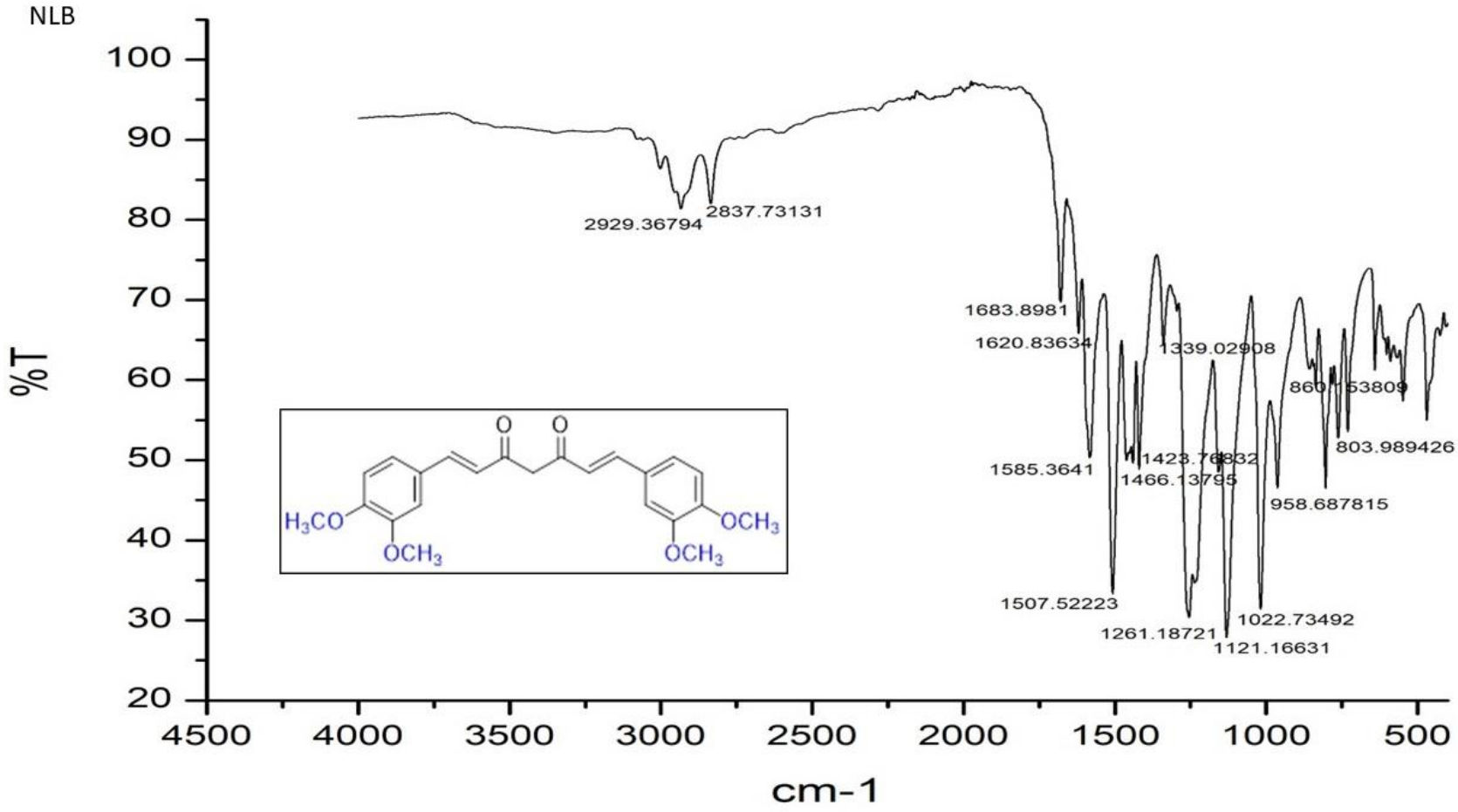

Fig.3.2 The IR spectrum of NLB

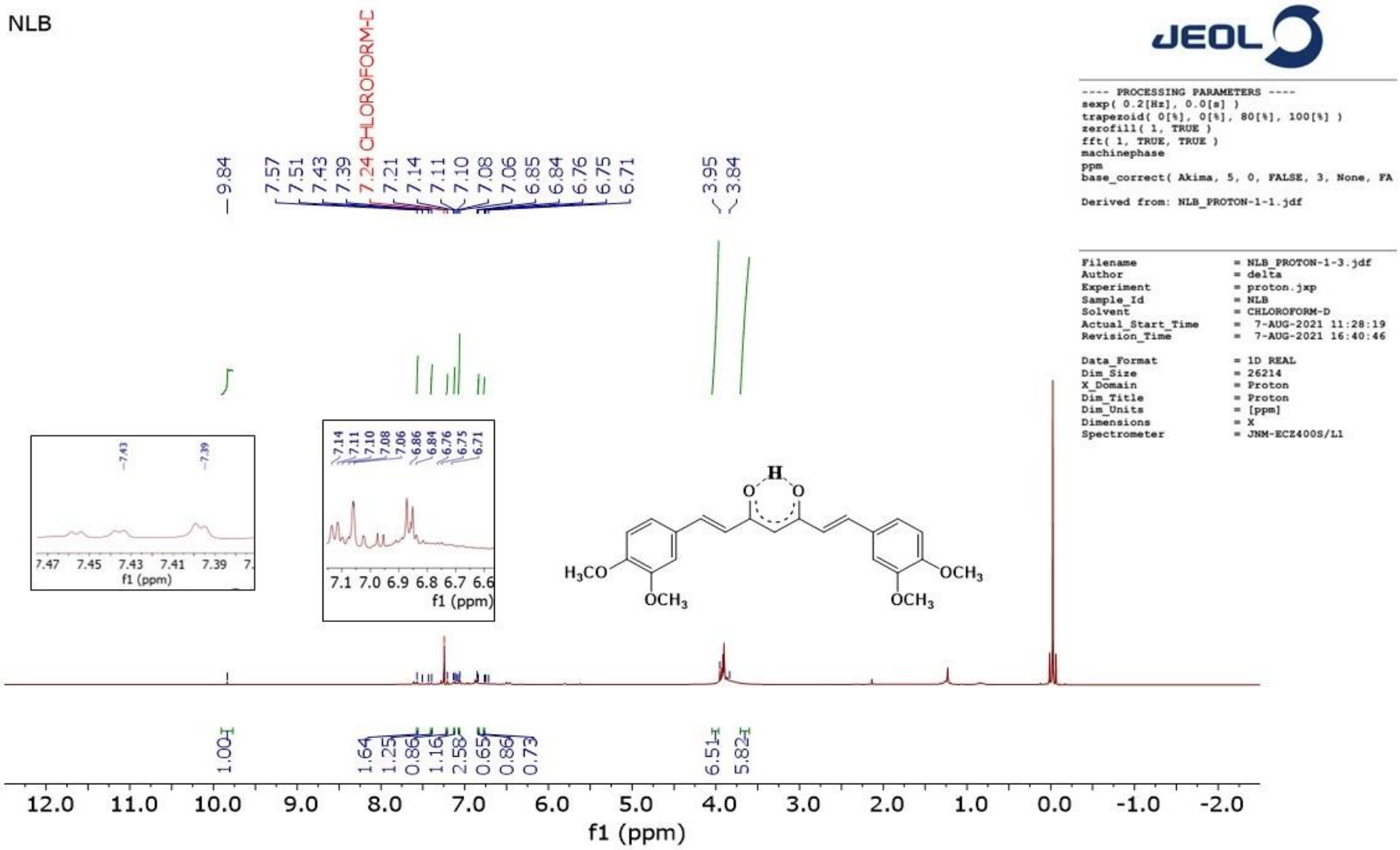

Fig.3.3 The ^{1}H NMR spectrum of NLB

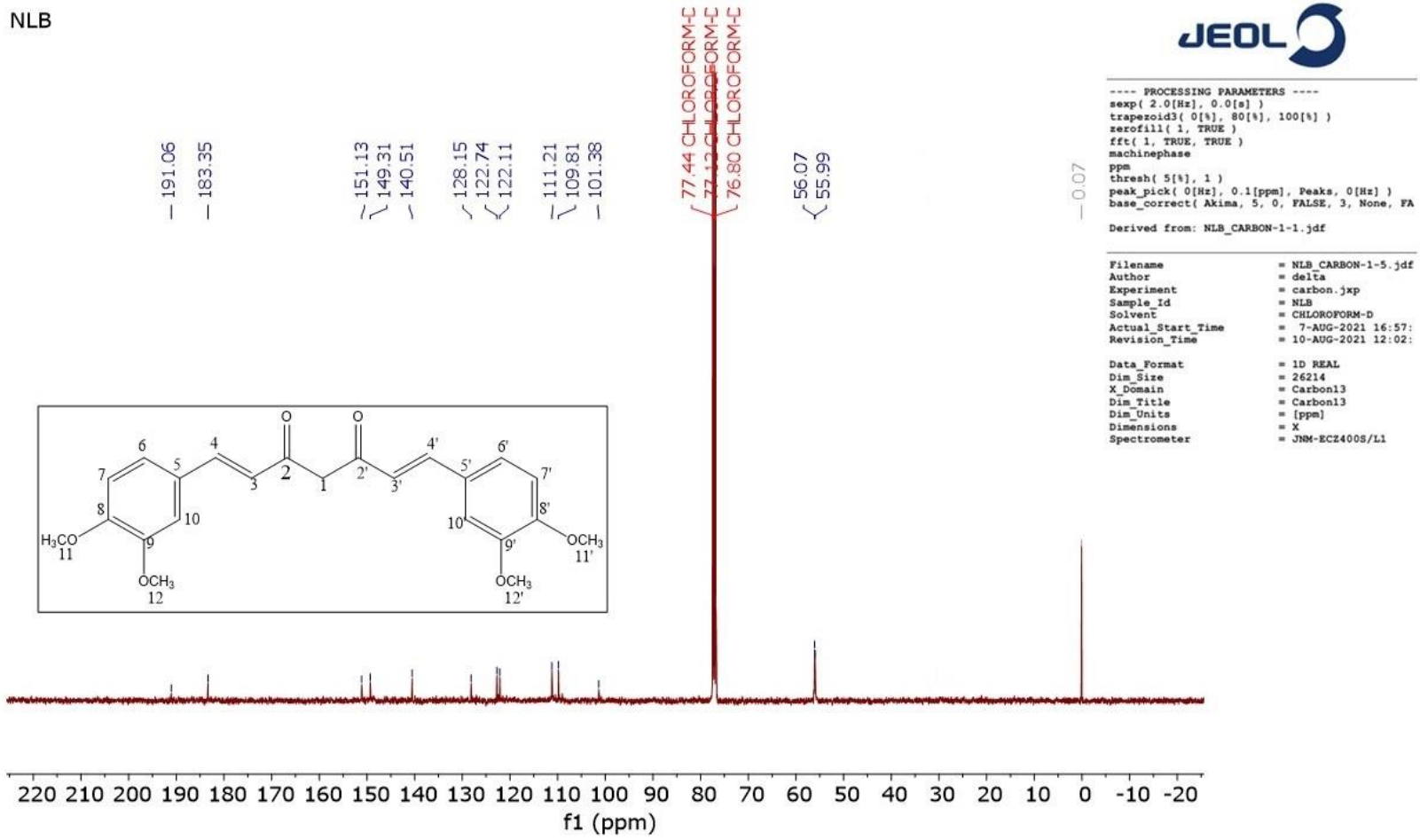

Fig.3.4 The ^{13}CNMR spectrum of NLB

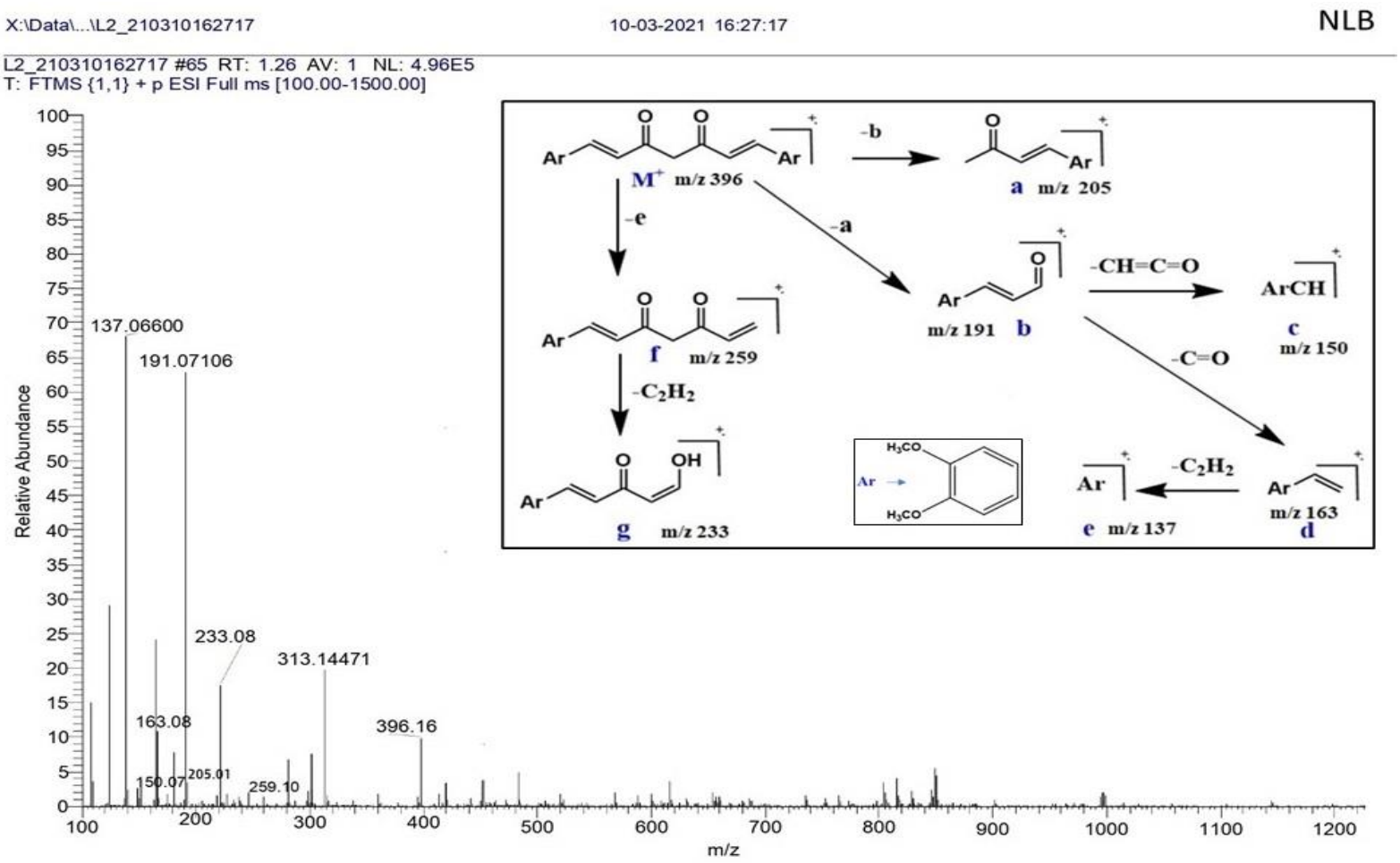

Fig.3.5 The Mass spectrum of NLB

3.5.1.1.2. Synthesis and characterization of Cu $(NLB)_2$ and Zn $(NLB)_2$

3.5.1.1.2.1. Synthesis and characterization of Cu complex of 1,7-bis (3,4-dimethoxy phenyl) hepta-1,6-diene-3,5-dione [Cu $(NLB)_2$]

The copper(II) complex of the curcuminoid analogue NLB was found to have a molecular weight of 853.23 g/mol and a melting point of 276°C. From the elemental analysis, it was shown that the carbon, hydrogen, and metal contents of the Cu(II) complex were 63.21%, 5.02%, and 7.23%, respectively, closely matching the theoretical values of 64.67%, 5.43%, and 7.44%. The yield of the compound was 75%.

Characterization of Cu complex of Cu $(NLB)_2$

A variety of spectroscopic and analytical techniques were employed to characterize the metal complex Cu $(NLB)_2$. The spectral analyses included IR, ^1H NMR, and mass spectrometry. In addition, elemental analysis was performed to determine the percentages of carbon, hydrogen, and metal in the compounds. The spectral data of synthesized compounds are discussed below.

IR Spectrum

It is shown that the IR spectrum of Cu $(NLB)_2$ in **Fig.3.6.** The absence of a strong band in the 1650-1800 cm^{-1} region was a characteristic feature of the metal complex. The peak corresponding to the intramolecularly hydrogen-bonded carbonyl group, originally present at ~1630 cm^{-1}, disappeared, and a new band appeared at 1586 cm^{-1}. This new band was attributed to the metal-coordinated carbonyl group. This shift indicated that the metal ion had replaced the enolic proton in the ligand during complexation. The new band was thus assigned to the metal-coordinated carbonyl group.

The peak at 1586.0 cm^{-1} corresponded to the stretching vibration of the carbonyl group (C=O). Typically, the carbonyl stretching vibration appeared in the range of 1600-1700 cm^{-1}. However, a shift to 1586 cm^{-1} suggested that the C=O bond was part of a chelated structure, which could lower the frequency compared to an unconjugated or free carbonyl group. The band at 1503.5 cm^{-1} was associated with the asymmetric stretching of the C-C-C bond within a cyclic ring. This frequency fell within the typical range for such stretches, often observed in the 1400-1600 cm^{-1} region. The presence of this band at 1503

cm^{-1} indicated that the compound likely contained a cyclic structure. The peaks at 446 cm^{-1} and 408 cm^{-1} corresponded to the metal-oxygen (M-O) stretching vibrations. Metal-oxygen stretches typically appeared in the low-frequency region, below 600 cm^{-1}. The values at 446.1 cm^{-1} and 408.9 cm^{-1} suggested that the metal was coordinated to oxygen atoms, possibly as part of a metal-ligand complex[66]. The M-O stretching bands confirmed the presence of metal coordination, with two distinct bands suggesting possible variation in the bonding environment or coordination geometry around the metal centre. This interpretation suggested that the compound likely had a conjugated carbonyl group, an aromatic ring, and a metal coordinated with oxygen atoms, possibly forming a metal-organic complex.

^{1}HNMR Spectrum

The various proton signals identified in the ^{1}HNMR spectrum of the Cu complex of 1,7-bis (3,4-dimethoxy phenyl) hepta-1,6-diene-3,5-dione are provided in **Table 3.6**

Table 3.6 Proton signals observed in the ^{1}H NMR spectrum of Cu $(NLB)_2$ (Chemical Shifts δ in ppm)

Complex	Methine	Alkenyl	Phenyl	Methoxy
Cu $(NLB)_2$	7.03	6.77-7.52	7.07-7.21	3.91,3.95

The methine proton resonated at 7.03 ppm, which aligned with its position adjacent to an enolic group and the influence of Cu (II) complexation. The alkenyl protons appeared in the broad range of 6.77-7.52 ppm, consistent with their conjugation with the diketone system and the phenyl rings, a shift typical for such environments, especially when coordinated to a metal ion. The aromatic protons of the phenyl rings were observed between 7.07-7.21 ppm, which was expected for protons on a substituted phenyl ring, particularly one with electron-donating methoxy groups that slightly deshielded these protons. The methoxy protons resonated at 3.91 ppm and 3.95 ppm. A typical shift for methoxy groups attached to aromatic rings further supports the structural integrity of the NLB ligand within the Cu(II) complex. Thus the ^{1}H NMR shifts were consistent with the structure of 1,7-bis(3,4-dimethoxyphenyl) hepta-1,6-diene-3,5-dione, particularly when complexed with Cu(II)[66] (**Fig.3.7**).

Mass Spectrum

Table 3.7 Molecular ion peaks of Cu $(NLB)_2$

M^+/(M+1)/(M+2) ion	a	b	c	d	e	f	g	h	i	j
853	716	579	442	304	137	458	183	396	122	121

*The alphabets correspond to the fragments given in the fragmentation scheme in **Fig.3.8**

The mass spectrum of the Cu(II) complex of NLB showed an intense molecular ion peak at m/z 853, indicating the intact molecular weight of the compound. The peaks at m/z 579 and 304 corresponded to the loss of two and four Ar groups, respectively, from the molecular ion, where Ar represented the 3,4-dimethoxy phenyl group. The peak at m/z 458 was attributed to the $[ML]^+$ fragment, where M was the metal (Cu) and L was the ligand (1,7-bis(3,4-dimethoxy phenyl)hepta-1,6-diene-3,5-dione). Additional fragment ions were observed at m/z 716, 442, 137, 183, 396, and 121, supporting the fragmentation patterns and structural components of the $Cu(NLB)_2$ complex[67,68]. The mass spectrum of $Cu(NLB)_2$ is shown in **Fig.3.8**.

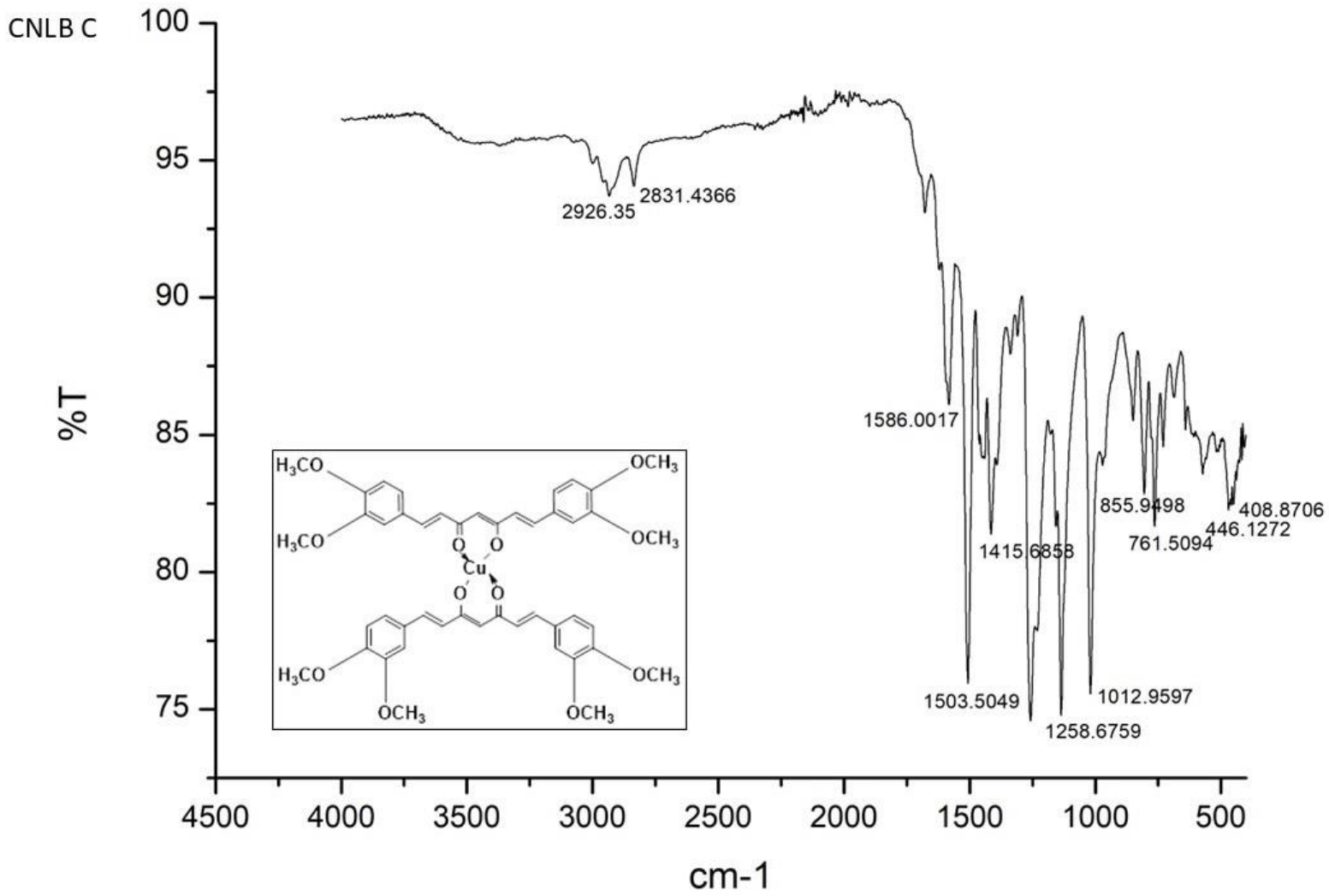

Fig.3.6 The IR spectrum of Cu $(NLB)_2$

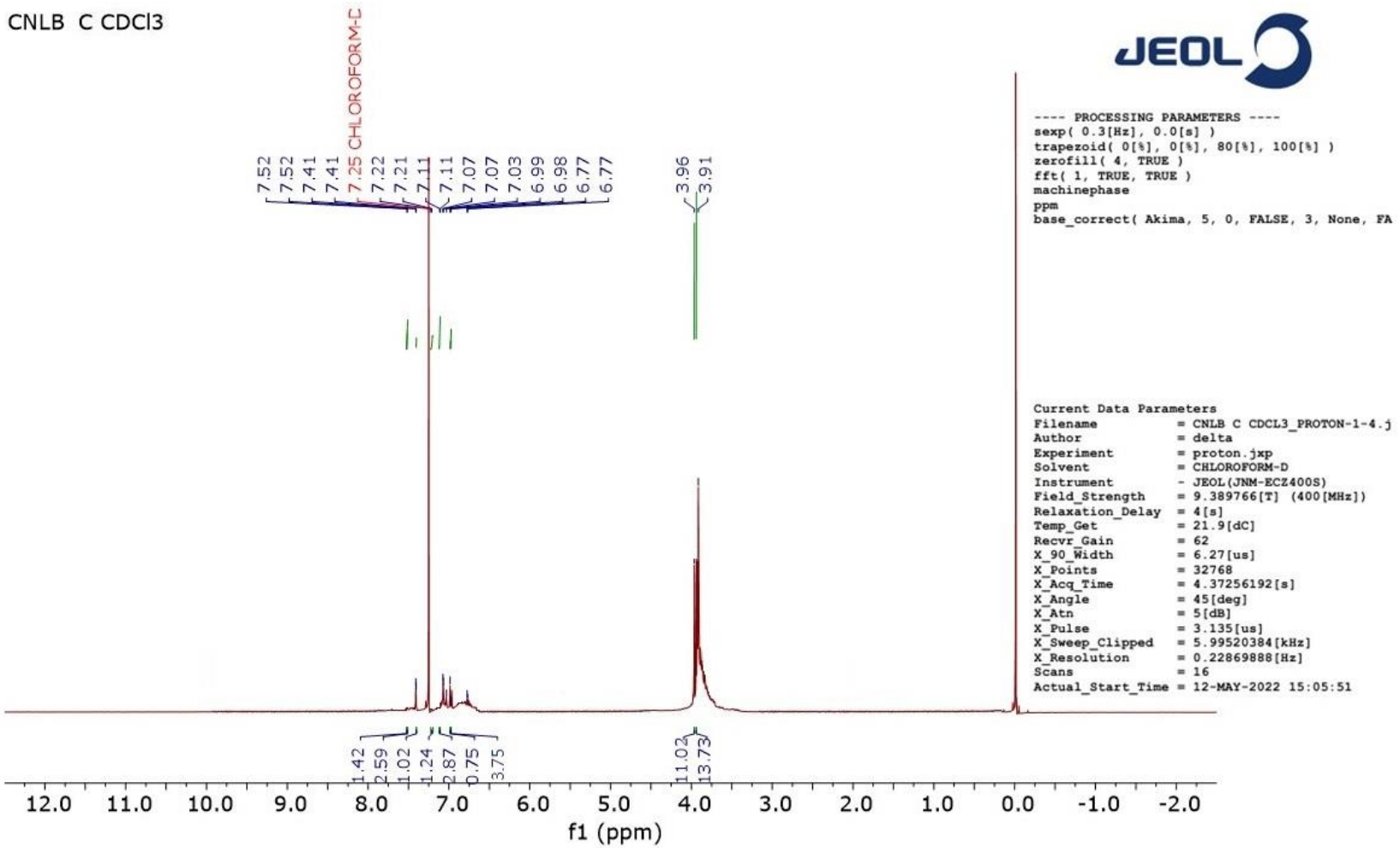

Fig.3.7 The ^{1}H NMR spectrum of Cu $(NLB)_2$

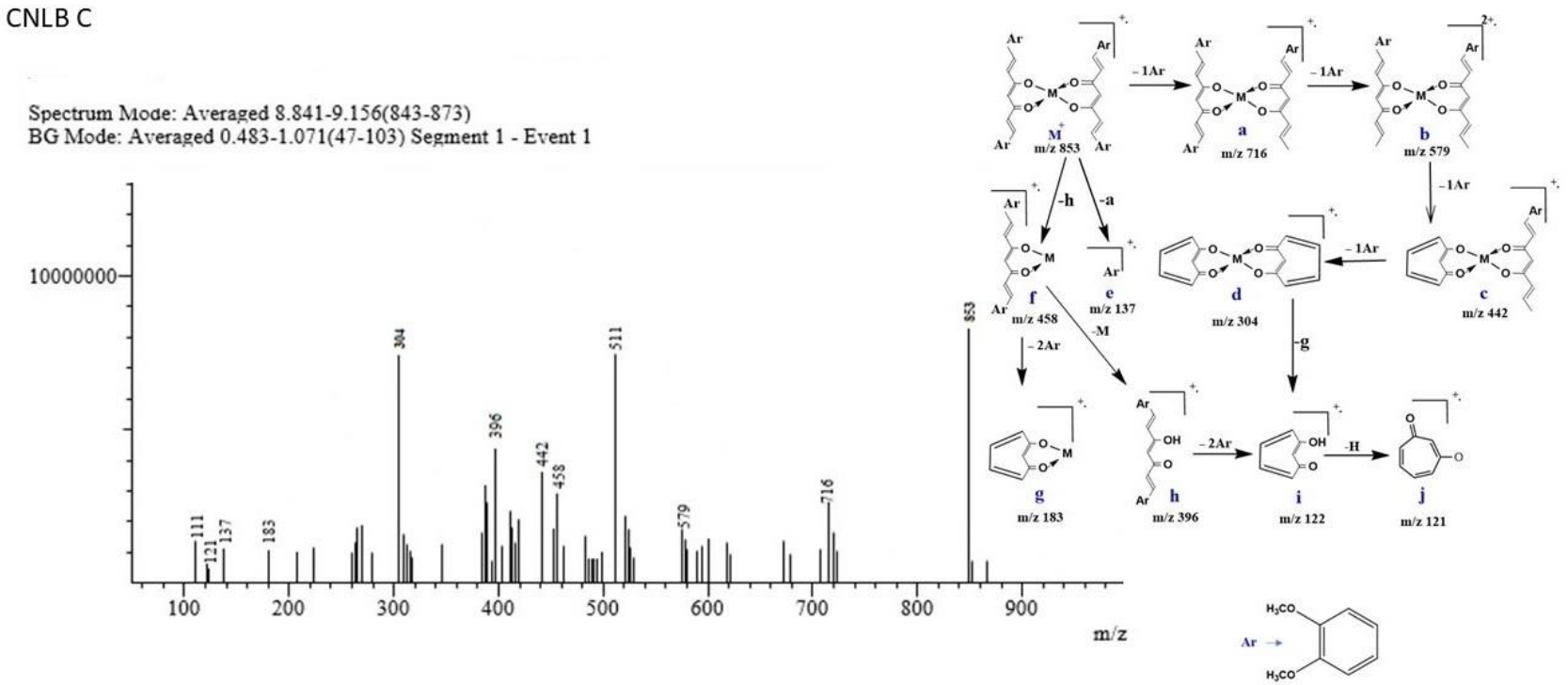

Fig.3.8 The Mass spectrum of Cu $(NLB)_2$

3.5.1.1.2.2. Synthesis and characterization of Zn complex of 1,7-bis (3,4-dimethoxy phenyl) hepta-1,6-diene-3,5-dione [Zn (NLB)$_2$]

The Zn(II) complex of the curcuminoid analogue NLB had a molecular weight of 854.23 g/mol and a melting point of 279°C. Elemental analysis showed carbon, hydrogen, and metal contents of 64.11%, 5.32%, and 7.34%, respectively, closely matching the theoretical values of 64.53%, 5.42%, and 7.64%. The synthesis achieved a yield of 81%.

Characterization of Zn (NLB)$_2$

The metal complex Zn (NLB)$_2$ was characterized using various spectroscopic and analytical techniques, including IR spectroscopy, ^{1}H NMR, and mass spectrometry. The spectral data of the synthesized complex are summarized and discussed below.

IR Spectrum

The metal complex Zn (NLB)$_2$ exhibited key spectral features that indicated successful coordination of the ligand to the metal ion (**Fig.3.9**). The absence of a strong band in the 1650-1800 cm^{-1} region, particularly the disappearance of the carbonyl peak at 1630 cm^{-1}, and the emergence of a new band at 1589.0 cm^{-1}, suggested that the enolic proton had been replaced by the metal ion, forming a metal-coordinated carbonyl group. The shift of the carbonyl stretching vibration to 1589.0 cm^{-1} indicated chelation, lowering the frequency compared to a free carbonyl group. Additionally, the band at 1514.5 cm^{-1} was attributed to the asymmetric stretching of the C-C-C bond within a cyclic ring, implying the presence of an aromatic structure. The low-frequency bands at 453.9 cm^{-1} and 431.6 cm^{-1} corresponded to metal-oxygen (M-O) stretching vibrations, confirming the metal's coordination with oxygen atoms and suggesting a complex metal-ligand structure[66].

^{1}HNMR Spectrum

The various proton signals identified in the ^{1}HNMR spectrum of Zn (II) complex of 1,7-bis (3,4-dimethoxy phenyl) hepta-1,6-diene-3,5-dione are provided in **Table 3.10**

Table 3.10 Proton signals observed in the ^{1}H NMR spectrum of Zn(NLB)$_2$ (Chemical Shifts δ in ppm)

Complex	Methine	Alkenyl	Phenyl	Methoxy
Zn (NLB)$_2$	7.02	6.86-7.47	7.07-7.21	3.92,3.94

The ^{1}H NMR spectrum of the Zn (II) complex of 1,7-bis(3,4-dimethoxyphenyl) hepta-1,6-diene-3,5-dione (Zn (NLB)$_2$) revealed significant details about the proton environment, indicating successful coordination of the ligand to the Zn (II) ion (**Fig.3.10**). The methine proton at 7.02 ppm was deshielded, likely due to its proximity to a metal-coordinated carbonyl, causing it to resonate downfield. Alkenyl protons, resonating between 6.86-7.47 ppm, exhibited a broad range of chemical shifts, suggesting varying electronic environments influenced by conjugation with aromatic rings and coordination to the metal ion. The phenyl protons appeared between 7.07-7.21 ppm, with slight variations in chemical shifts hinting at asymmetry or differing environments of the phenyl rings due to metal coordination. The methoxy protons, observed at 3.92 ppm, and 3.94 ppm remained relatively unaffected, indicating that the methoxy groups retained their typical shielded environment despite the metal coordination. These spectral features collectively provided evidence of the influence of metal ions on the electronic environment of the ligands, supporting the formation of a metal-ligand complex. The shifts in the proton signals underscored the role of conjugation and chelation within the complex, altering the electronic environment of the double bonds and aromatic rings, and confirming the coordination of the ligand to the Zn ion.

Mass Spectrum

Table 3.9 Molecular ion peaks of Zn (NLB)$_2$

M^+/(M+1)/(M+2) ion	a	b	c	d	e	f	g	h	i	j
854	717	580	443	305	137	459	184	396	122	121

*The alphabets correspond to the fragments given in the fragmentation scheme in **Fig.3.11**.

The mass spectrum of the Zn (II) complex of NLB showed an intense molecular ion peak at m/z 854, indicating the intact molecular weight of the compound. The peaks at m/z 580 and 305 corresponded to the loss of two and four Ar groups, respectively, from the molecular ion, where Ar represented the 3,4-dimethoxy phenyl group. The peak at m/z 459 was attributed to the $[ML]^+$ fragment, where M was the metal (Zn) and L was the ligand (1,7-bis (3,4-dimethoxy phenyl) hepta-1,6-diene-3,5-dione). Additional fragment ions were observed at m/z 717, 443, 184, 396, and 121, supporting the fragmentation patterns and structural components of the $Zn(NLB)_2$ complex[68]. The mass spectrum of $Zn (NLB)_2$ is shown in **Fig.3.11.**

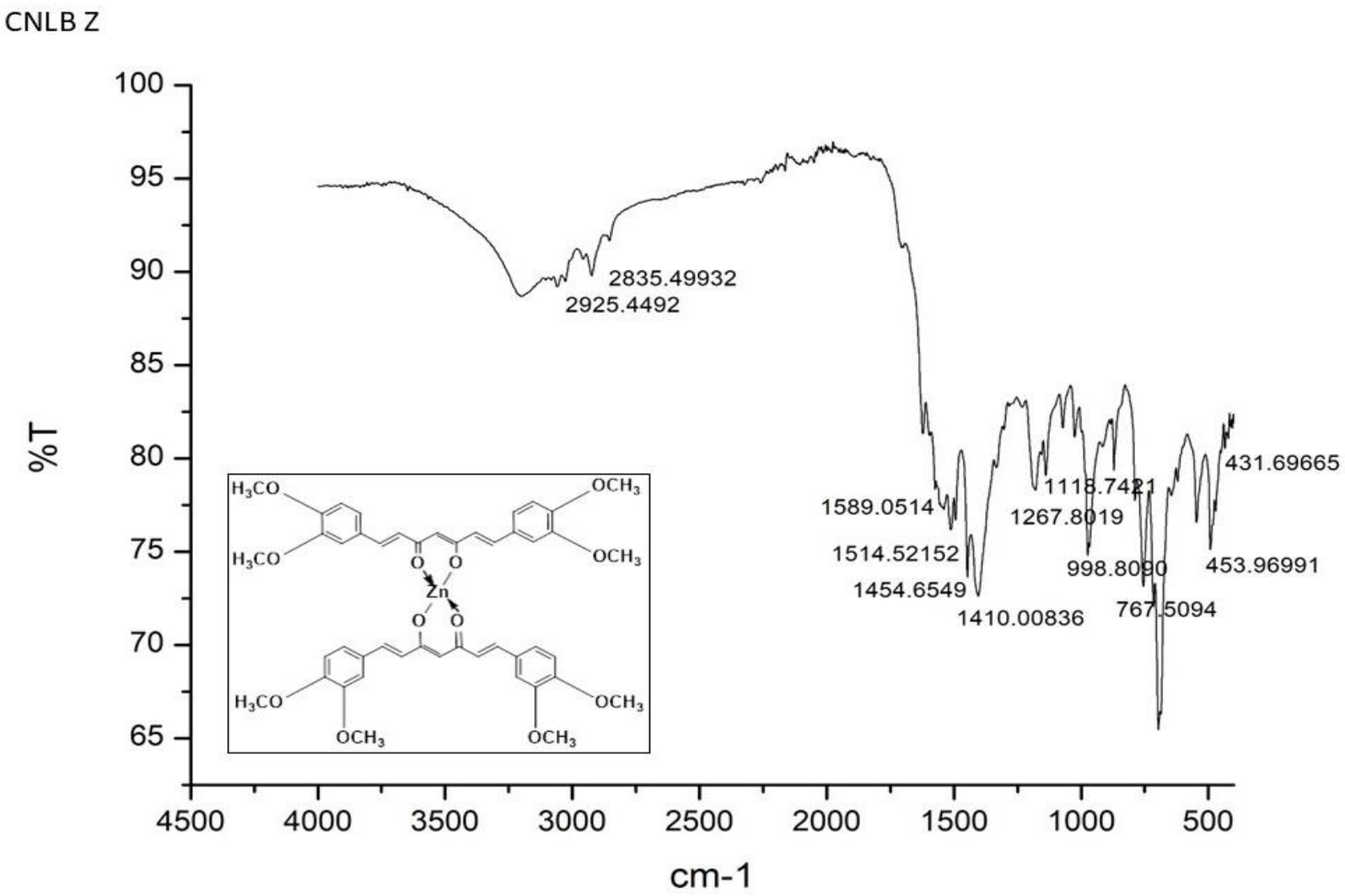

Fig.3.9 The IR spectrum of Zn $(NLB)_2$

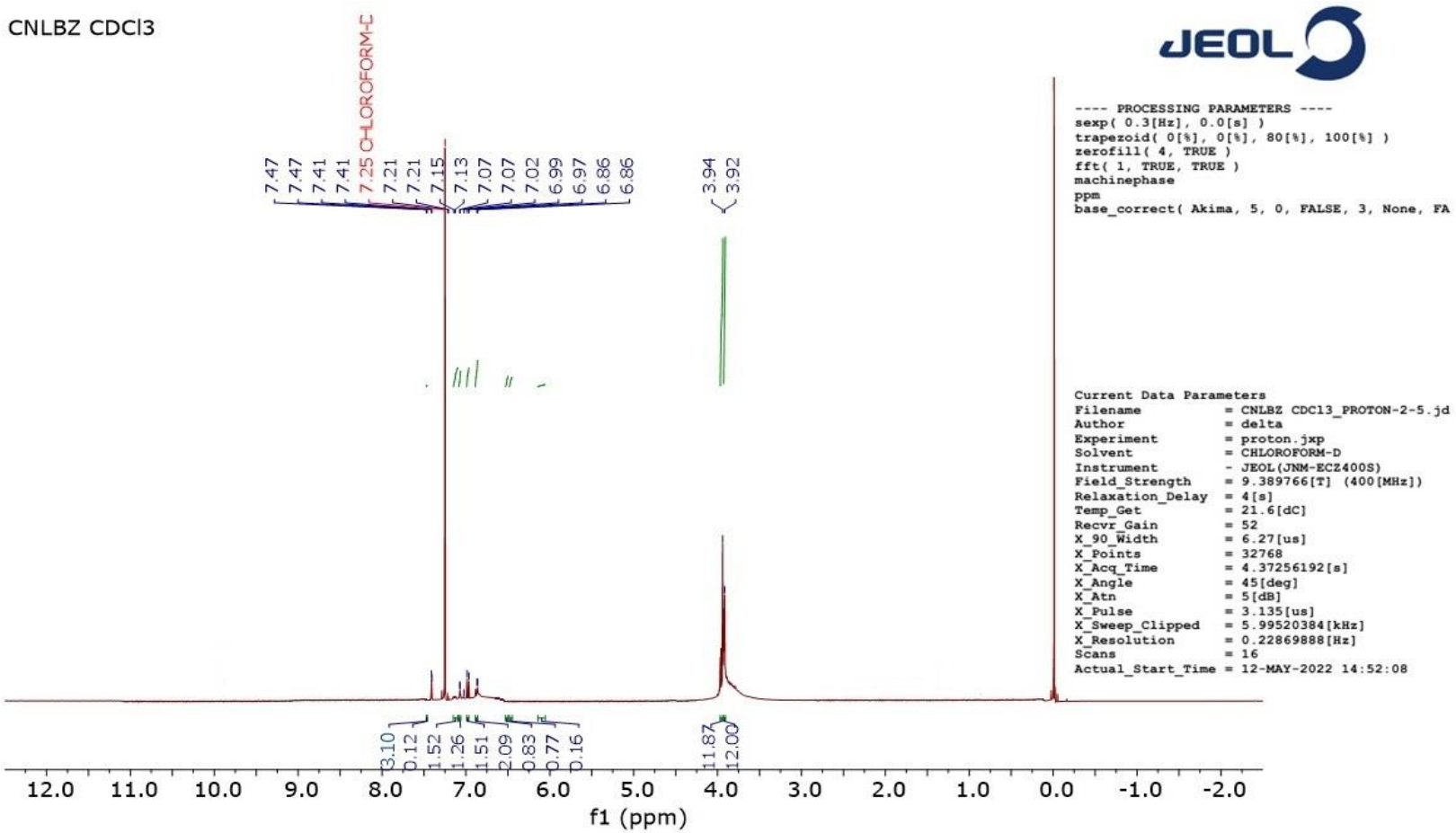

Fig.3.10 The ^{1}H NMR spectrum of Zn $(NLB)_2$

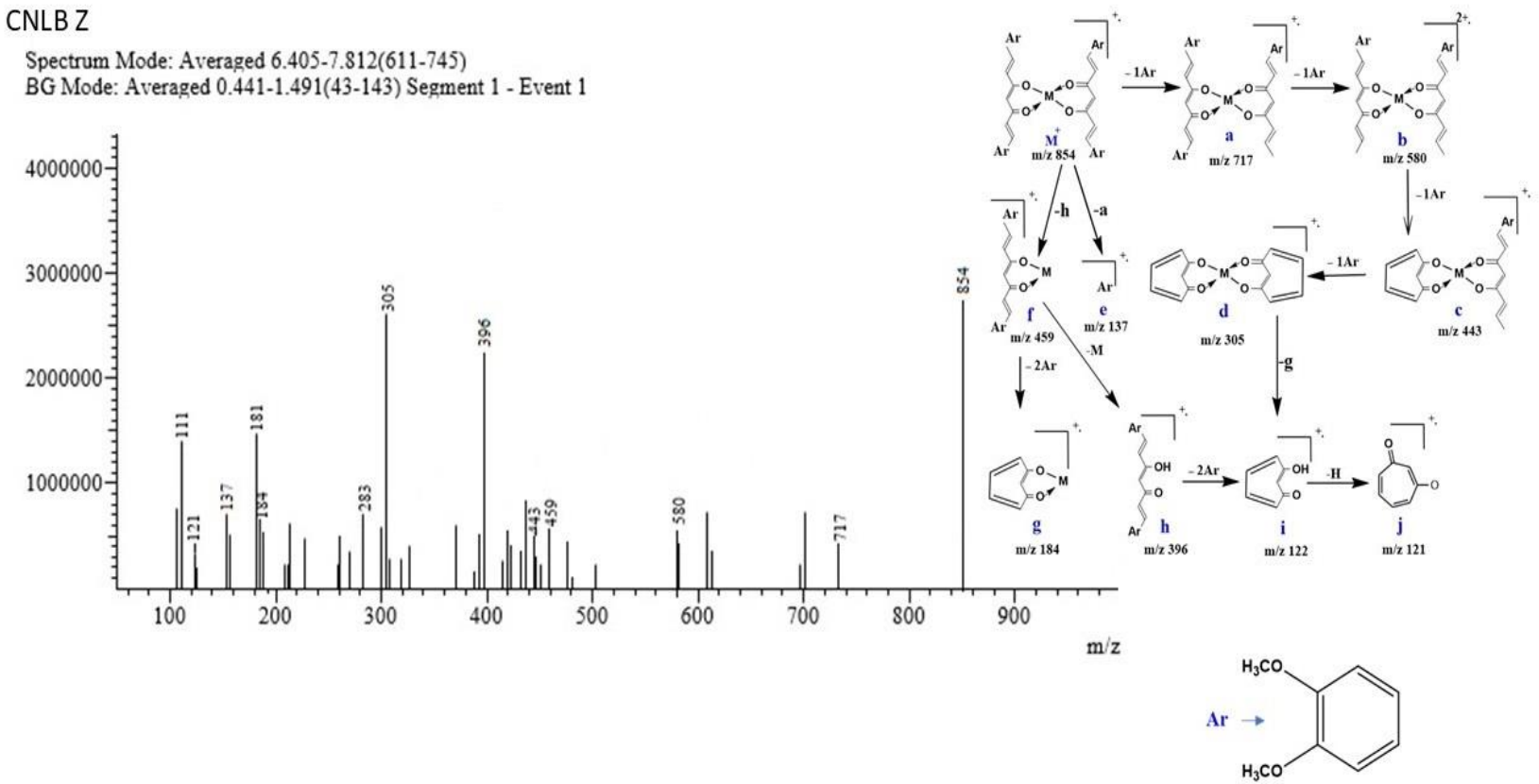

Fig.3.11 The Mass spectrum of Zn $(NLB)_2$

3.5.1.2. Synthesis and characterization of (1E,6E-1,7-bis (3,5-dichloro-2-hydroxy phenyl) hepta-1,6-diene-3,5-dione (NLD)

3.5.1.2.1 Synthesis and Characterization of NLD

1,7-Bis(3,5-dichloro-2-hydroxyphenyl)hepta-1,6-diene-3,5-dione (NLD) was synthesized via the condensation of 3,5-dichlorosalicylaldehyde (0.01 M) with an acetylacetone–boron complex and B_2O_3 in ethyl acetate (7.5 mL). The reaction was conducted in the presence of tri-sec-butyl borate (5.4 mL) and n-butylamine (0.1 mL) as a condensing agent. The resulting product had a melting point of 266°C and a molecular weight of 446 g/mol, with a yield of approximately 98%. Elemental analysis revealed carbon and hydrogen contents of 50.96% and 2.01%, respectively, closely matching the theoretical values of 51.16% and 2.71%.

Characterization of NLD

The synthesized compound NLD was characterized using various spectroscopic techniques, including IR, ^{1}H NMR,^{13}C NMR, and mass spectrometry. The spectral data of the compound are discussed below.

IR Spectrum

The IR spectrum assignments for NLD were interpreted based on the provided **Table 3.10.** In this compound, the position and intensity of the carbonyl stretching frequency are influenced by the molecular structure surrounding it, making them valuable for characterising the type of carbonyl function present. The presence of an α,β-unsaturated 1,3-diketo moiety in the molecule can be effectively established using IR spectroscopy.

Table 3.10 Possible IR assignments of NLD

Wavenumbers (in cm^{-1})	Possible IR Assignments
3070.3	ν Enolic
1655.3	ν(C=O)
1564.7	ν(C=C) Phenyl
1437.6	ν_{as}(C-C-C)
1162.2	νβ (C-H)

The peak at 3070.3 cm^{-1} corresponded to the stretching vibration of the O-H bond in the enolic form, where a hydroxyl group is adjacent to a carbon-carbon double bond. This value, while slightly lower than the typical O-H stretching range of 3200–3600 cm^{-1}, could be attributed to intramolecular hydrogen bonding or resonance effects, but it still fell within the expected range for an enolic O-H stretch. The peak at 1655.3 cm^{-1} was assigned to the stretching vibration of the carbonyl (C=O) group. This value was well within the typical range of 1600–1750 cm^{-1} for C=O stretching, confirming the presence of a carbonyl group in the molecule. The peak at 1564.7 cm^{-1} was interpreted as the stretching vibration of the carbon-carbon double bond (C=C) within a phenyl (aromatic) ring. This peak fell within the expected range of 1500–1600 cm^{-1} for phenyl C=C stretching, indicating the presence of aromatic rings in NLD. The peak at 1437.6 cm^{-1} was associated with the asymmetric stretching vibration of the carbon-carbon bonds (C-C-C) within the molecular structure, fitting within the typical range of 1400–1600 cm^{-1} for C-C stretching vibrations. Finally, the peak at 1162.2 cm^{-1} was assigned to the bending vibration (out-of-plane) of the C-H bonds, a value consistent with the expected range of 1000–1300 cm^{-1} for β(C-H) bending modes, particularly those in aromatic or alkyl groups. The literature comparison and functional group analysis confirmed that the assigned wavenumbers were correct and aligned with well-documented ranges, thereby validating the structure of the compound[62]. The IR spectrum of the compound NLD is depicted in **Fig 3.12.**

^{1}HNMR Spectrum

The ^{1}HNMR spectrum of 1,7-bis(3,5-dichloro-2-hydroxyphenyl) hepta-1,6-diene-3,5-dione (NLD) revealed distinct proton signals that aligned well with the expected chemical shifts for enolic, methine, alkenyl, phenyl, and hydroxy protons. The various proton signals observed in the spectrum are given in **Table 3.11.**

Table 3.11 Proton signals observed in the ^{1}H NMR spectrum of NLD (Chemical Shifts δ ppm)

Compound	Enolic	Methine	Alkenyl	Phenyl	Hydroxy
NLD	9.88	7.21	7.44-7.56	7.21-7.28	11.32

The enolic proton appeared at 9.88 ppm, a shift typical of enolic protons due to the deshielding effect of the adjacent carbonyl group, which often placed such protons in the

9-12 ppm range. The methine proton, observed at 7.21 ppm, fell within the 4.5-7.5 ppm range expected for methine protons, especially in aromatic or conjugated systems, where conjugation with the phenyl group could further push the signal downfield. The alkenyl proton signal between 7.44-7.56 ppm suggested the presence of protons on a double bond (C=C), particularly when adjacent to electron-withdrawing groups, leading to a shift slightly higher than the typical 5-7 ppm range. The phenyl protons, appearing between 7.21-7.28 ppm, were consistent with the 7.0-8.0 ppm range expected for aromatic protons, reflecting the deshielding effects within the aromatic system. The hydroxy proton signal at 11.32 ppm was characteristic of a highly deshielded proton, positioned near an electron-withdrawing group, which typically resulted in a shift around 10-12 ppm. Collectively, these observed chemical shifts provided strong evidence that the proton environments in NLD were accurately represented, with the downfield shifts attributable to factors such as conjugation, electron-withdrawing effects, and hydrogen bonding. The ^{1}H NMR spectrum of NLD is brought out in **Fig.3.13.**

^{13}C NMR Spectra

The ^{13}C NMR spectrum of NLD revealed distinct carbon signals that corresponded to various environments within the molecule, validating their chemical shifts.The ^{13}C NMR spectral details of NLD are given in **Table 3.12.**

Table 3.12 ^{13}C NMR spectral data of NLD (Chemical Shifts δ ppm)

C_1	**C_2,$C_{2'}$**	**C_3,$C_{3'}$**	**C_4,$C_{4'}$**	**C_5,$C_{5'}$**
100.44	195.16	131.19	156.03	121.52
C_6,$C_{6'}$	**C_7,$C_{7'}$**	**C_8,$C_{8'}$**	**C_9,$C_{9'}$**	**C_{10},$C_{10'}$**
159.90	123.54	136.60	121.52	156.03

The signal at 100.4 ppm likely represented a carbon in an sp²-hybridized environment, possibly involved in a conjugated system, which typically resonated between 90-150 ppm. Signals at 195.16 ppm corresponded to carbonyl carbons (C=O), which were highly deshielded and usually appeared between 190-220 ppm. The 131.19 ppm signals aligned with carbons in an alkenyl group involved in conjugation, consistent with aromatic carbons that resonated between 120-140 ppm. The 156.03 ppm signals indicated carbons affected by both the phenyl ring and adjacent alkenyl chain with carbonyl groups, fitting

the typical 150-165 ppm range for phenolic carbons with such substituents. The 121.52 ppm signal matched carbons in an aromatic or alkenyl environment without strong electronegative groups, fitting the 115-130 ppm range. Signals at 159.90 ppm, highly deshielded, suggested a carbon in an environment with significant electronegativity effects, such as those adjacent to chlorine. Carbons at 123.54 ppm were likely in an aromatic ring, resonating at 110-120 ppm, while the 131.19 ppm signal, despite the expectation of a higher shift due to chlorine, was consistent with a balance of inductive and resonance effects. The 121ppm signal for a carbon attached to a chlorine atom and adjacent to hydroxyl and chlorine-bearing carbons reflected a moderate downfield shift due to the interplay of these effects. The 156.03 ppm signal corresponded to a carbon adjacent to an aromatic ring which bears a hydroxyl group and two chlorin atoms and is also conjugated with an alkenyl chain bearing carbonyl groups, aligning with the expected shift for such an environment. The spectrum's chemical shifts supported the presence of the described functional groups and confirmed the structure of NLD (**Fig.3.14**)

Mass Spectrum

Mass spectrometry was primarily used to determine the molecular weight of compounds. The mass spectra displayed both molecular ion peaks and fragment ion peaks, which provided detailed information about the compound's structure. In the mass spectrum of this compound, intense molecular ion peaks were observed, indicating the molecular weight.

Important peaks that appeared in the spectrum of the compound can be conveniently accounted for by the fragmentation pattern as shown in (**Fig.3.15**) and the values are brought out in **Table 3.13**

Table 3.13 Molecular ion peaks of NLD

M^+/M+1 Ion	a	b	c	d	e	f	g
443	228	214	173	186	160	282	256

*The alphabets correspond to the fragments given in the fragmentation scheme in **Fig.3.15**

The M^{+1} ion of NLD is observed at 443. Other important peaks of NLD due to fragment ion peaks which their fragmentation patterns can explain.

In the mass spectrum of NLD, there was an intense molecular ion peak at 443. The peak observed at 214 is due to $[C_9H_5\ Cl_2O_2]^+$. The peak at 173 is due to the molecular ion$[C_7H_5Cl_2O]^+$. The peak at 186 is due to $[C_8H_5\ Cl_2O]^+$. The peak at 282 is due to the fragment $[C_{13}H_4Cl_2O_3]^+$ and the peak at 256 is due to $[C_{11}H_7Cl_2O_3]^+$.The mass spectrum of the compound NLD is given in **Fig. 3.15**

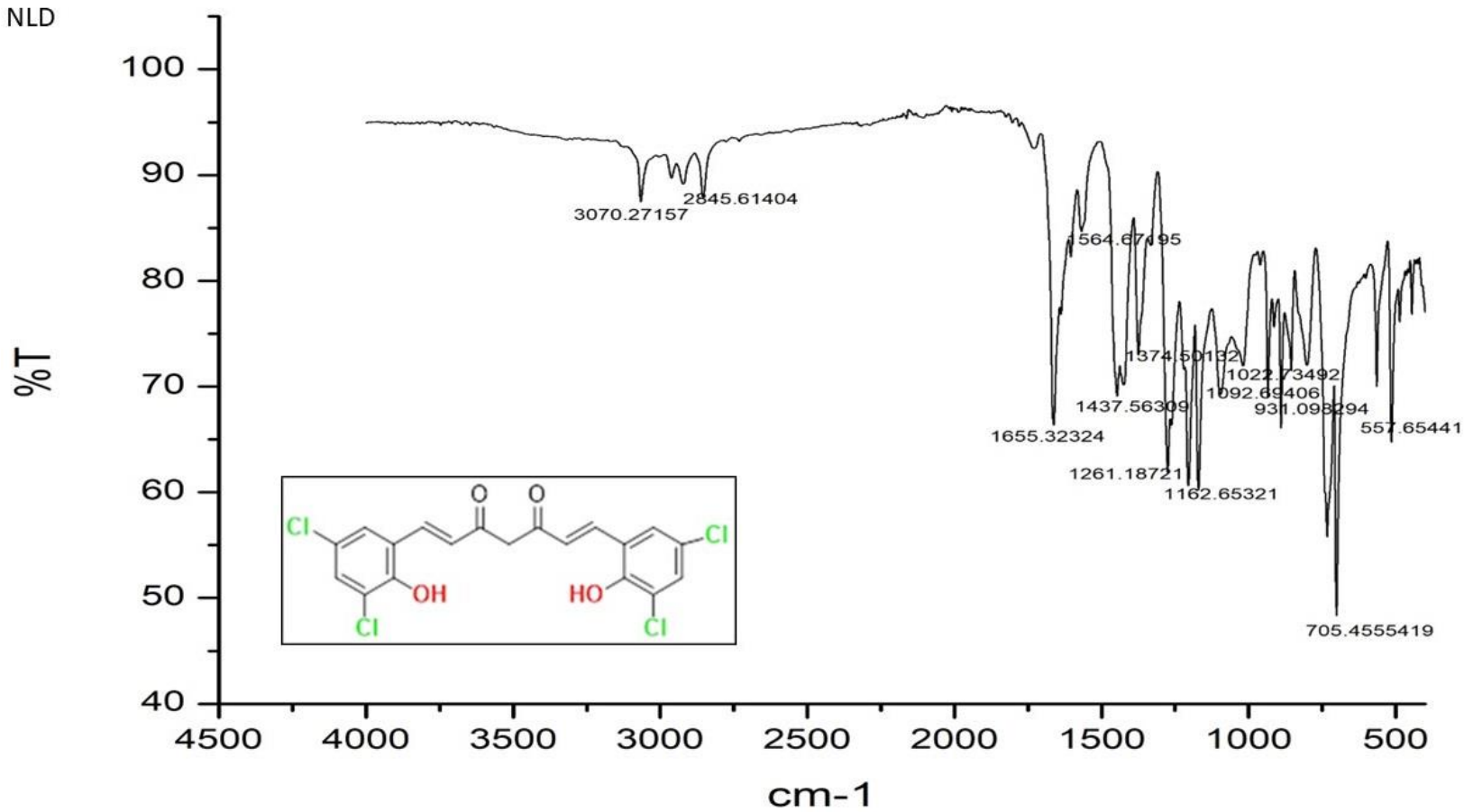

Fig.3.12 The IR spectrum of NLD

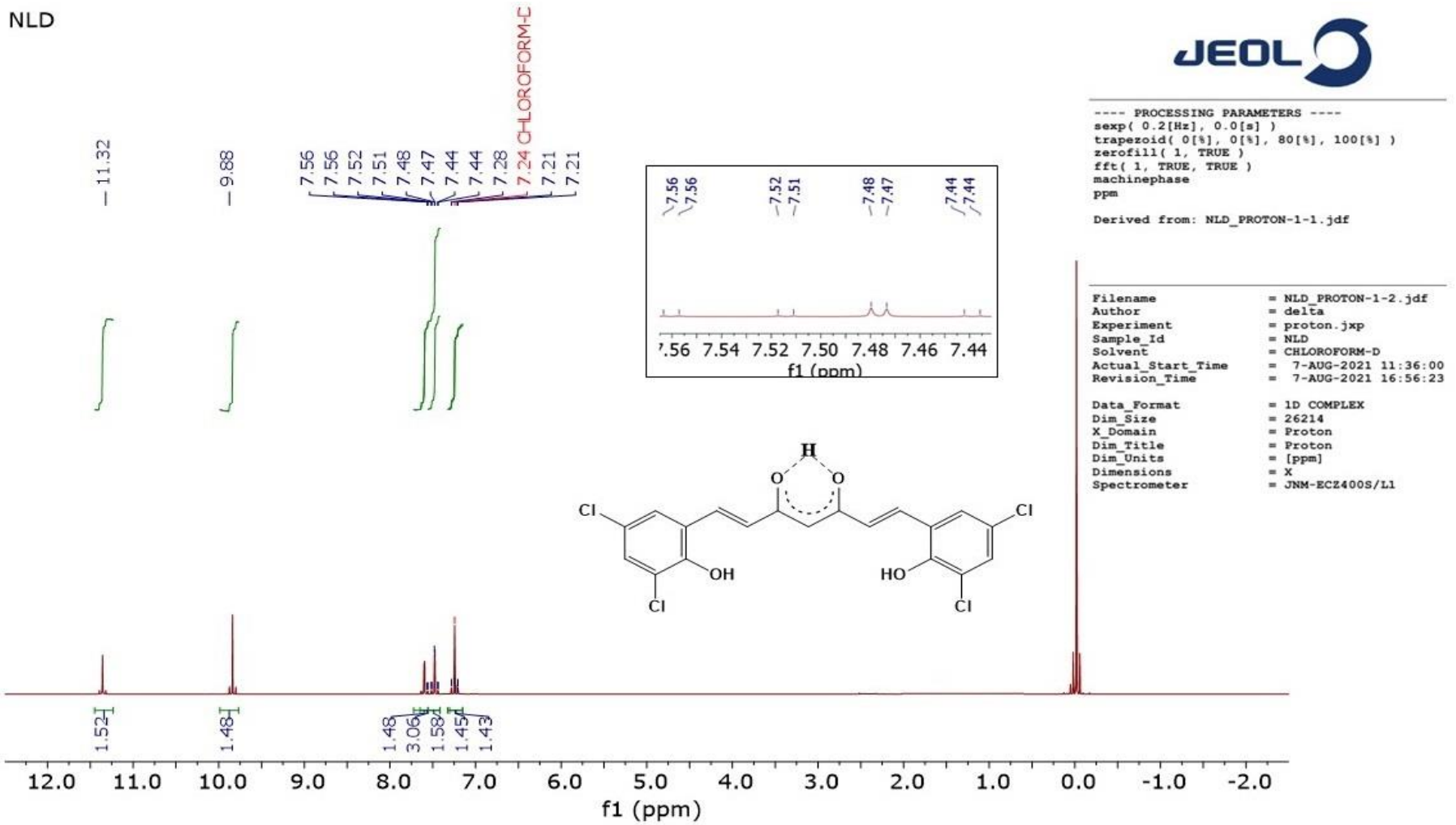

Fig.3.13 The ^{1}H NMR spectrum of NLD

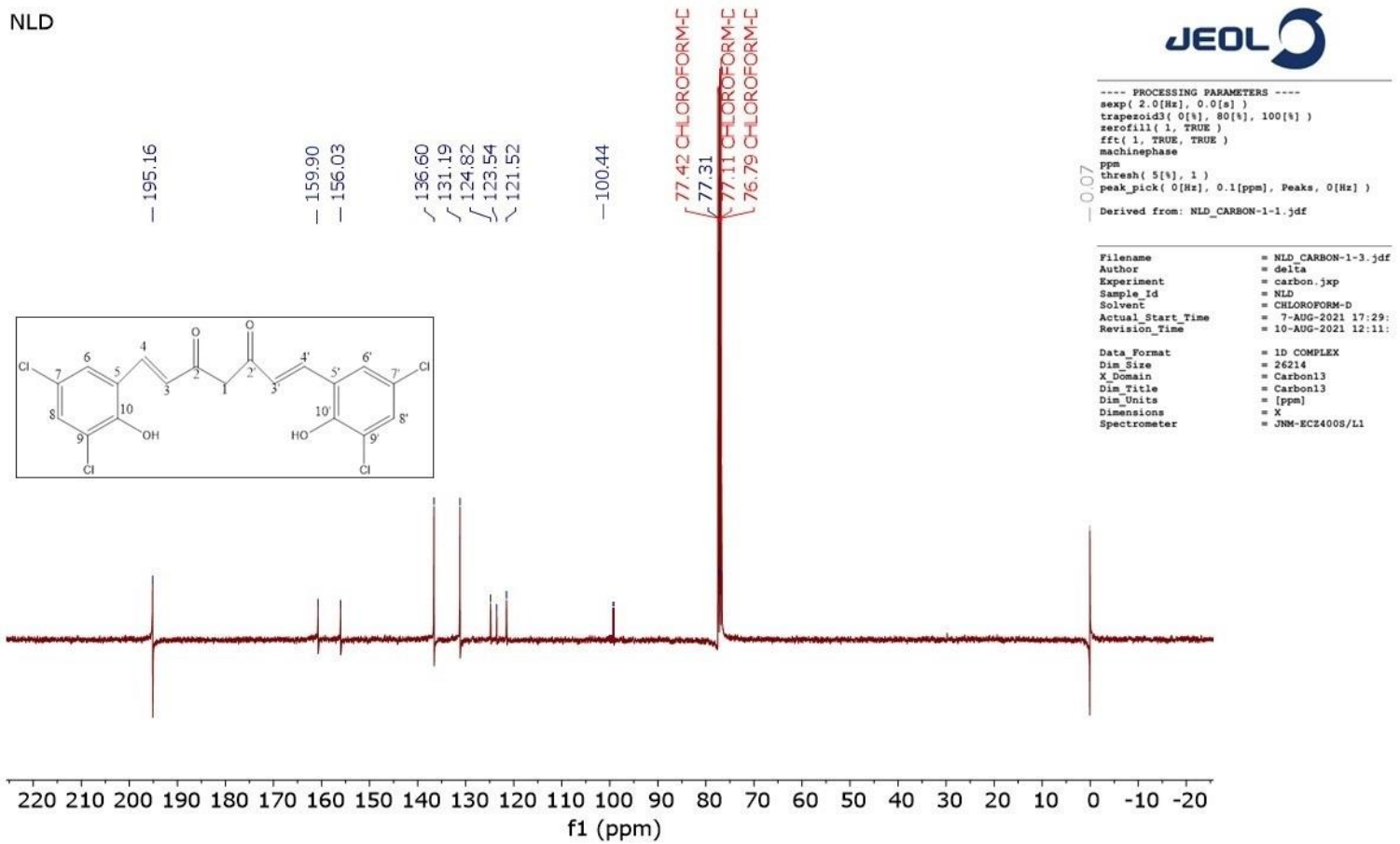

Fig.3.14 The ^{13}CNMR spectrum of NLD

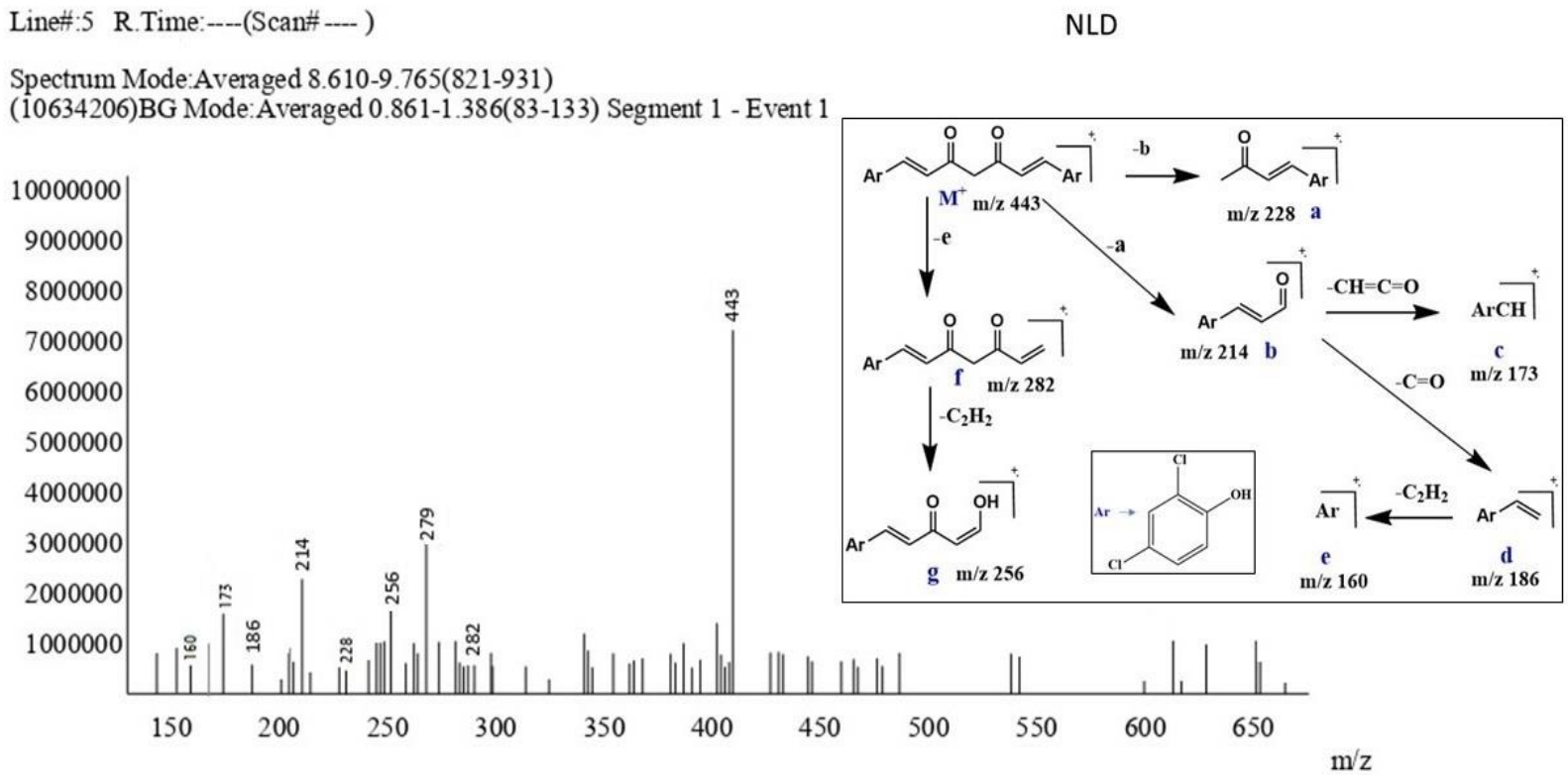

Fig.3.15 The Mass spectrum of NLD

3.5.1.2.2 Synthesis and characterization of Cu $(NLD)_2$ and Zn $(NLD)_2$

3.5.1.2.2.1. Synthesis and characterization of Cu complex of 1,7-Bis(3,5-dichloro-2-hydroxyphenyl) hepta-1,6-diene-3,5-dione [Cu $(NLD)_2$]

The copper(II) complex of the curcuminoid analogue NLD exhibited a molecular weight of 948.81 g/mol and a melting point of 282°C. Elemental analysis revealed carbon, hydrogen, and metal contents of 47.51%, 2.01%, and 6.20%, respectively, which closely aligned with the theoretical values of 47.86%, 2.33%, and 6.66%. The overall yield of the compound was 85%.

Characterization of Cu $(NLD)_2$

The metal complex Cu $(NLD)_2$ was characterized through a range of spectroscopic and analytical techniques, including IR spectroscopy, ^1H NMR, and mass spectrometry. The spectral data obtained from the synthesized complex are summarized and discussed below.

IR Spectrum

The metal complex Cu $(NLD)_2$ exhibited distinct spectral features that confirmed the successful coordination of the ligand to the metal ion (**Fig 3.16**). The absence of a strong band in the 1650-1800 cm^{-1} region, particularly the disappearance of the carbonyl peak at 1630 cm^{-1}, along with the appearance of a new band at 1586.0 cm^{-1}, indicated that the enolic proton had been replaced by the metal ion, resulting in a metal-coordinated carbonyl group. The shift of the carbonyl stretching vibration to 1586.0 cm^{-1} suggested chelation, which lowered the frequency compared to a free carbonyl group. Additionally, the band at 1491.0 cm^{-1} was associated with the asymmetric stretching of the C-C-C bond within a cyclic ring, suggesting the presence of an aromatic structure. The low-frequency bands at 446.1 cm^{-1} and 427.5 cm^{-1} corresponded to metal-oxygen (M-O) stretching vibrations, confirming the coordination of the metal with oxygen atoms and indicating a complex metal-ligand structure.

^{1}HNMR Spectrum

The various proton signals identified in the ^{1}H NMR spectrum of the Cu(II) complex of 1,7-bis (3,5-dichloro-2-hydroxyphenyl)hepta-1,6-diene-3,5-dione (NLD) are summarized in **Table 3.14**

Table 3.14 Proton signals observed in the ^{1}H NMR spectrum of Cu $(NLD)_2$ (Chemical Shifts δ in ppm)

Complex	Methine	Alkenyl	Phenyl	Hydroxy
Cu $(NLD)_2$	7.33	7.30-7.61	7.21-7.29	11.37

The ^{1}H NMR spectrum of the Cu(II) complex of 1,7-bis(3,5-dichloro-2-hydroxyphenyl)hepta-1,6-diene-3,5-dione ($Cu(NLD)_2$) provided key insights into the proton environment within the complex (**Fig. 3.17**). The signal at 7.33 ppm was attributed to the methine proton (–CH–) of the complex. This downfield shift suggested that the methine proton was influenced by its electronic environment, likely due to coordination effects from the copper ion. The alkenyl protons (–CH=CH–) appeared in the range of 7.30-7.61 ppm, indicating that these protons experienced varying electronic environments, possibly due to conjugation with aromatic rings and coordination with the metal ion. The signals at 7.21-7.29 ppm were assigned to the aromatic (phenyl) protons, with their shifts being typical for aromatic protons and influenced by the ring current effect. The slight variation in shifts could have been due to the different electronic environments of the two phenyl rings, potentially affected by the metal ion coordination. The signal at 11.37 ppm corresponded to the hydroxy proton (–OH), and its downfield shift was characteristic of the hydroxy group in the complex, indicating the presence of an electron-withdrawing group (Cl) that led to significant deshielding of the proton.

Mass Spectrum

Table 3.15 Molecular ion peaks of Cu $(NLD)_2$

M^+/(M+1)/(M+2) ion	a	b	c	d	e	f	g	h	i	j
948	787	626	465	304	166	505	183	443	122	121

*The alphabets correspond to the fragments given in the fragmentation scheme in **Fig.3.18**

The mass spectrum of the Cu(II) complex of NLD showed an intense molecular ion peak at m/z 948, indicating the intact molecular weight of the compound. The peaks at m/z 626 and 304 corresponded to the removal of two and four Ar groups, respectively, from the molecular ion, where Ar represented the 3,5-dichloro-2-hydroxyphenyl group. The peak at m/z 505 was attributed to the $[ML]^+$ fragment, where M was the metal (Cu) and L was the ligand (1,7-Bis(3,5-dichloro-2-hydroxyphenyl) hepta-1,6-diene-3,5-dione). Additional fragment ions were observed at m/z 787, 465, 183, 443, 122, and 121, supporting the fragmentation patterns and structural components of the $Cu(NLD)_2$ complex. The mass spectrum of $Cu(NLD)_2$ is shown in **Fig.3.18**

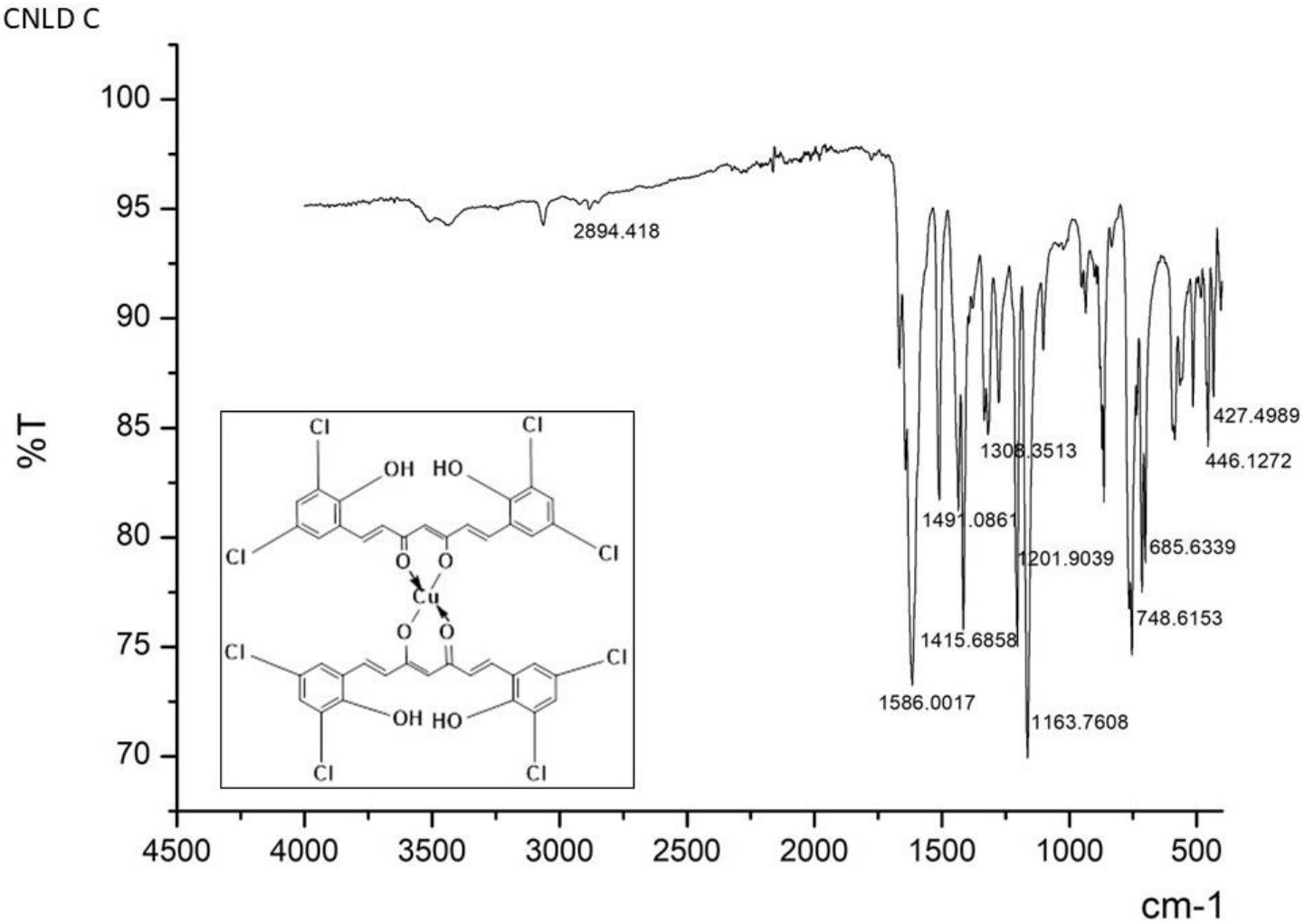

Fig.3.16 The IR spectrum of Cu $(NLD)_2$

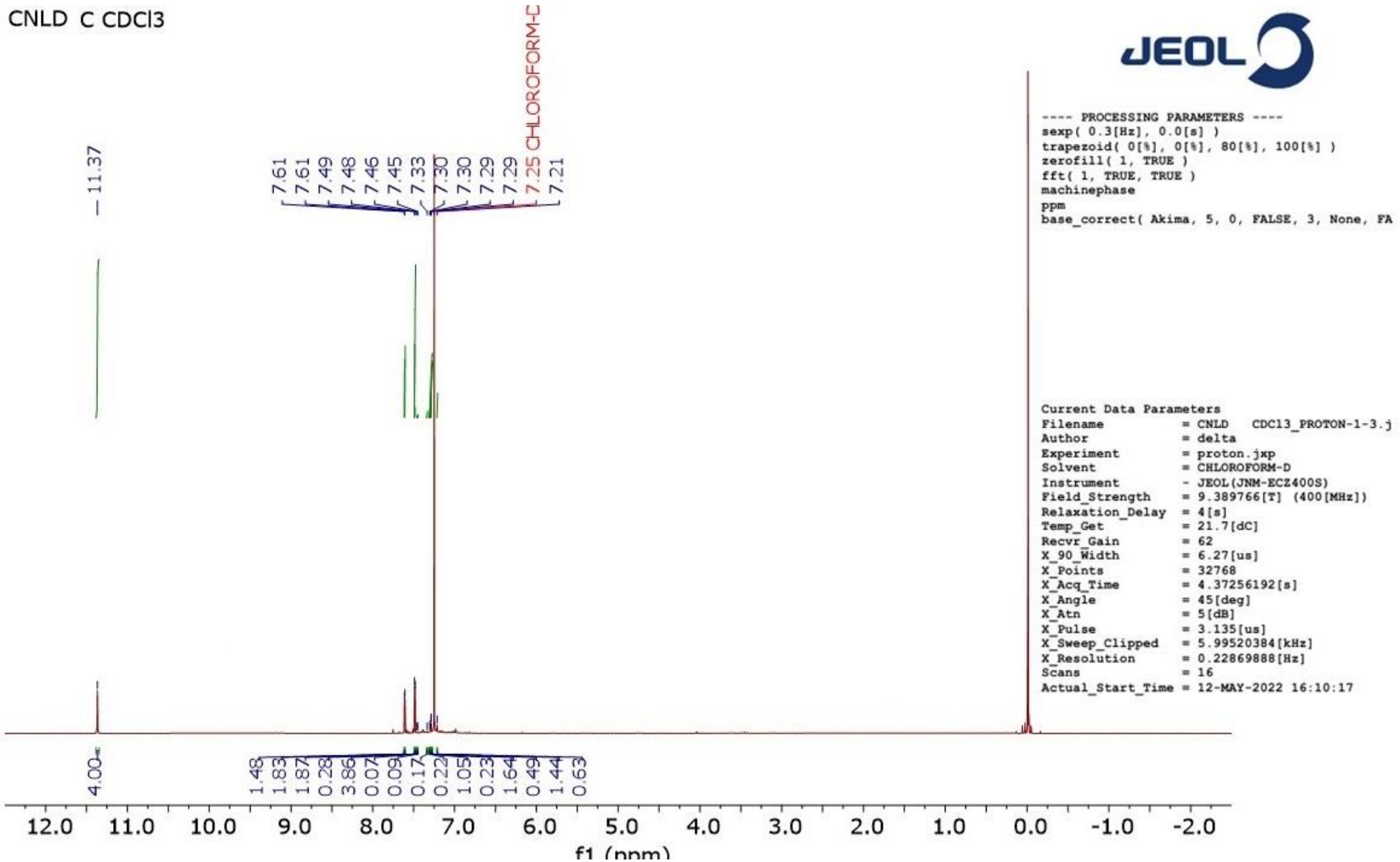

Fig.3.17 The ^{1}H NMR spectrum of Cu $(NLD)_2$

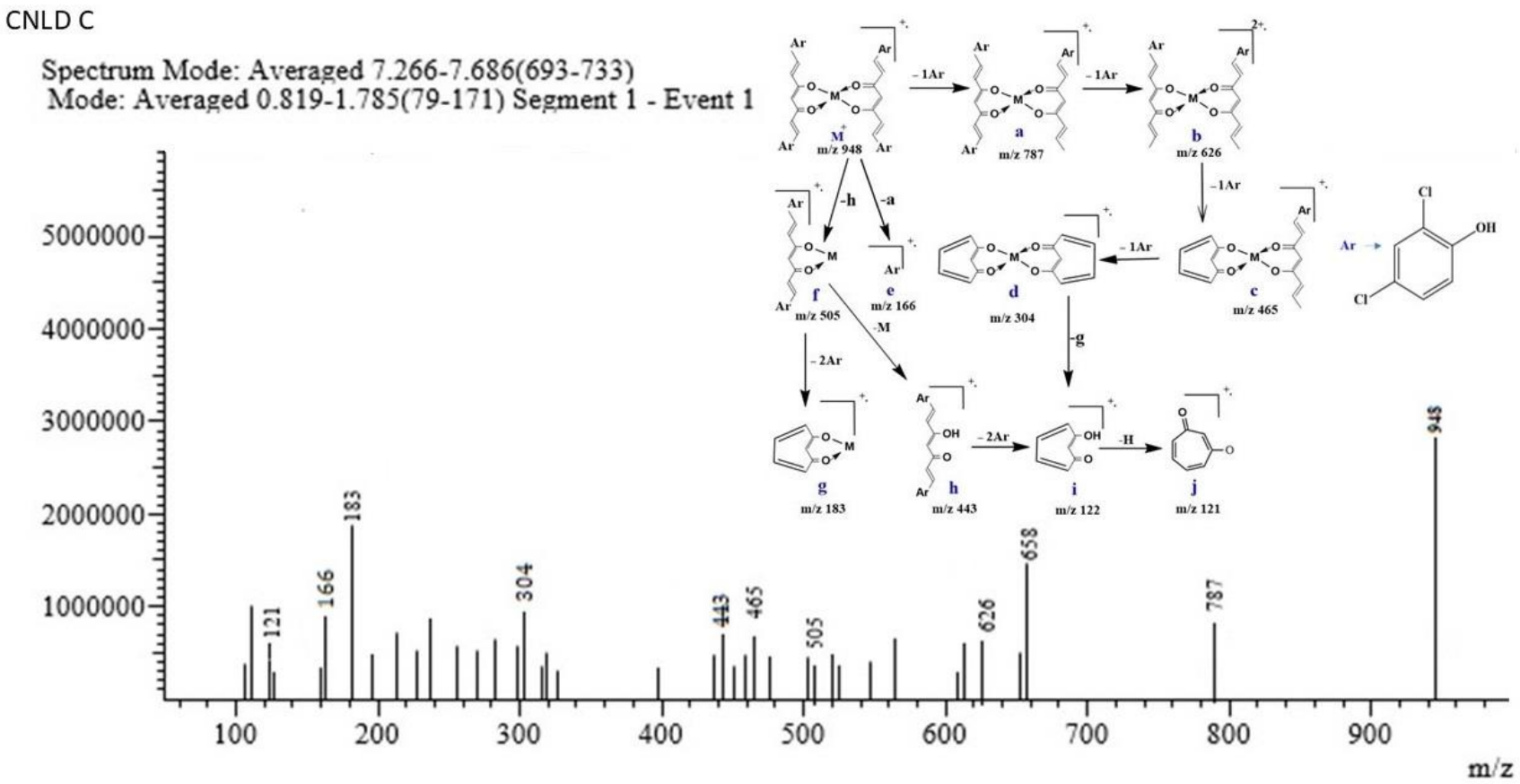

Fig.3.18 The Mass spectrum of Cu $(NLD)_2$

3.5.1.2.2.2. Synthesis and characterization of Zn complex of 1,7-Bis(3,5-dichloro-2-hydroxyphenyl) hepta-1,6-diene-3,5-dione [Zn(NLD)$_2$]

The Zn(II) complex of the curcuminoid analogue NLD had a molecular weight of 949.81 g/mol and a melting point of 286°C. Elemental analysis revealed carbon, hydrogen, and metal contents of 47.15%, 2.12%, and 6.42%, respectively, closely aligning with the theoretical values of 47.76%, 2.32%, and 6.84%. The synthesis yielded 88% of the compound.

Characterization of Zn (NLD)$_2$

The metal complex Zn (NLD)$_2$ was characterized through a range of spectroscopic and analytical techniques, including IR spectroscopy, ^{1}H NMR, and mass spectrometry. The spectral data obtained from the synthesized complex are summarized and discussed below.

IR Spectrum

The disappearance of the carbonyl peak around 1630 cm^{-1}, and the shift to a lower frequency (1592.2 cm^{-1}) indicated that chelation had occurred, where the carbonyl oxygen coordinated with the metal ion, lowering the bond order of the C=O bond and consequently reducing the frequency of the stretching vibration. The band observed at 1503.5 cm^{-1} was attributed to the asymmetric stretching of the C-C-C bond, typically within an aromatic or conjugated structure, suggesting the presence of an aromatic ring or a highly conjugated system, which was consistent with the structure of curcuminoid ligands. The low-frequency bands at 446.1 cm^{-1} and 415.1 cm^{-1} were correctly interpreted as metal-oxygen (M-O) stretching vibrations, confirming that the metal ion Zn(II)) was indeed coordinated with the oxygen atoms of the ligand, reinforcing the formation of a complex. It was also considered that the band at 1592.2 cm^{-1} could have been influenced by interactions between the metal and other coordinating atoms, such as oxygen from hydroxyl groups within the ligand, potentially contributing to the shift in the carbonyl stretching frequency. The absence of a strong band in the 1650-1800 cm^{-1} region, typically associated with free carbonyl groups, further supported the involvement of the carbonyl groups in coordination with the metal (**Fig.3.19**).

^{1}HNMR Spectrum

The various proton signals identified in the ^{1}H NMR spectrum of the Zn (II) complex of 1,7-Bis(3,5-dichloro-2-hydroxyphenyl) hepta-1,6-diene-3,5-dione Zn $(NLD)_2$ are summarized in **Table 3.16**

Table 3.16 Proton signals observed in the ^{1}H NMR spectrum of $Zn(NLD)_2$ (Chemical Shifts δ in ppm)

Complex	Methine	Alkenyl	Phenyl	Hydroxy
Zn $(NLD)_2$	7.29	7.40-7.61	7.21-7.25	11.37

In the ^{1}H NMR spectrum of $Zn(NLD)_2$, the methine proton appeared at 7.29 ppm, showing a downfield shift consistent with the deshielding effect caused by coordination with the Zn(II) ion. This shift, compared to the typical 7.21 ppm in free NLD, confirmed the involvement of the methine proton in coordination. The alkenyl protons were observed in the range of 7.40-7.61 ppm, slightly downfield compared to their usual range of 6.50-7.50 ppm. This shift likely resulted from the altered electronic environment due to coordination, leading to slight deshielding. The phenyl protons were recorded between 7.21-7.25 ppm, a range consistent with aromatic protons, especially considering the electron-withdrawing effects of the coordinated Zn(II). This range overlapped with the phenyl proton region in free NLD, supporting their assignment. Lastly, the signal at 11.37 ppm corresponded to the hydroxy proton (–OH), with its downfield shift indicating significant deshielding, likely caused by a nearby electron-withdrawing group (Cl). The chemical shifts observed in $Zn(NLD)_2$ were consistent with the expected effects of Zn(II) coordination, providing strong evidence that the proton signals were correctly assigned in the spectrum (**Fig.3.20**).

Mass Spectrum

Table 3.17 Molecular ion peaks of Zn $(NLD)_2$

M^+/(M+1)/(M+2) ion	a	b	c	d	e	f	g	h	i	j
950	788	627	466	305	160	506	184	443	122	121

*The alphabets correspond to the fragments given in the fragmentation scheme in **Fig.3.21**

The mass spectrum of the Zn(II) complex of NLD showed an intense molecular ion peak at m/z 950, indicating the intact molecular weight of the compound. The peaks at m/z 627 and 305 corresponded to the loss of two and four Ar groups, respectively, from the molecular ion, where Ar represented the 3,5-dichloro-2-hydroxyphenyl group. The peak at m/z 506 was attributed to the $[ML]^+$ fragment, where M was the metal (Zn) and L was the ligand (1,7-Bis(3,5-dichloro-2-hydroxyphenyl) hepta-1,6-diene-3,5-dione). Additional fragment ions were observed at m/z 788, 466, 160, 184, 443,122 and 121 supporting the fragmentation patterns[65] and structural components of the $Zn(NLD)_2$ complex. The mass spectrum of $Zn(NLD)_2$ was shown in **Fig.3.21**

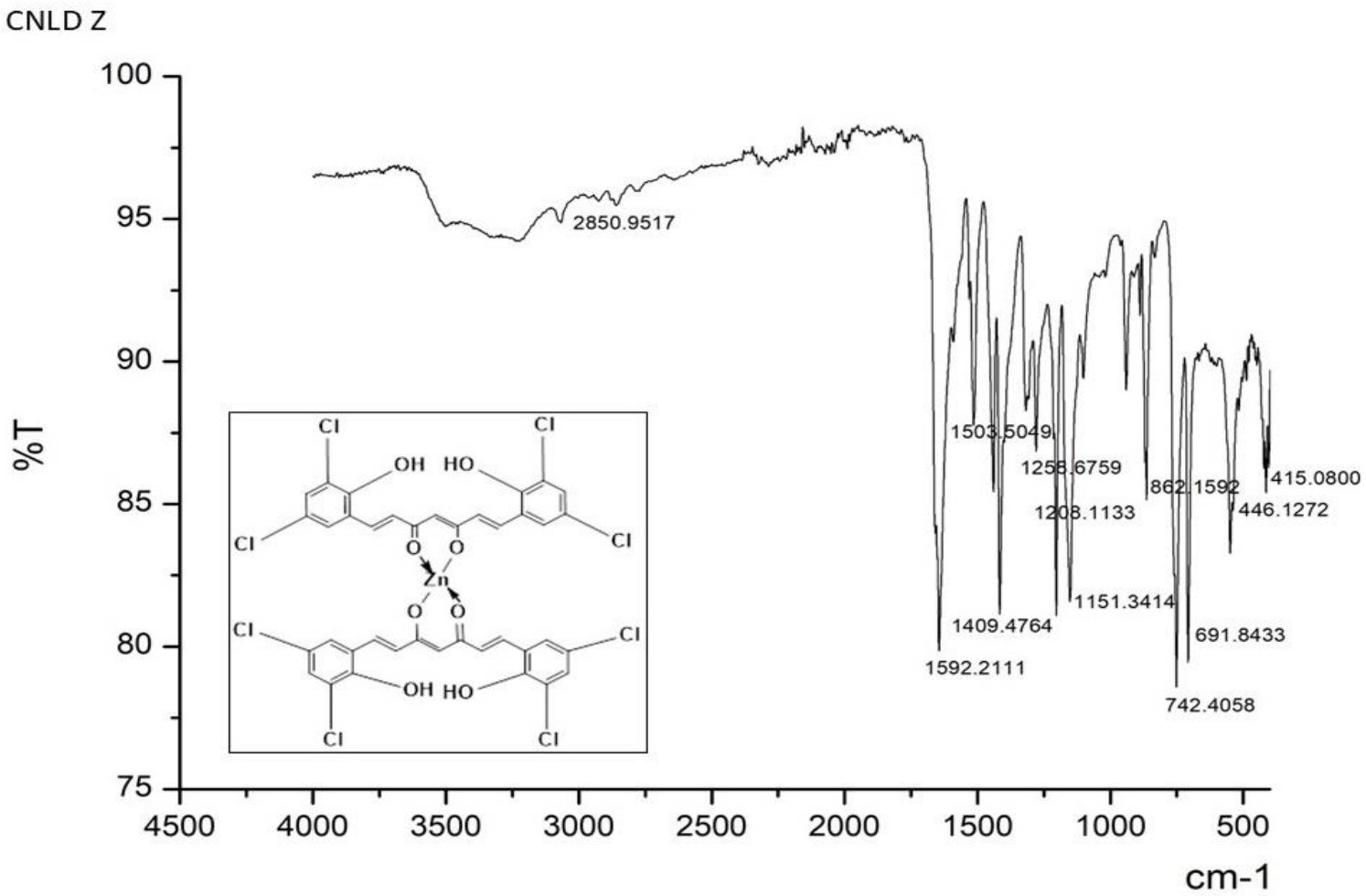

Fig.3.19 The IR spectrum of Zn $(NLD)_2$

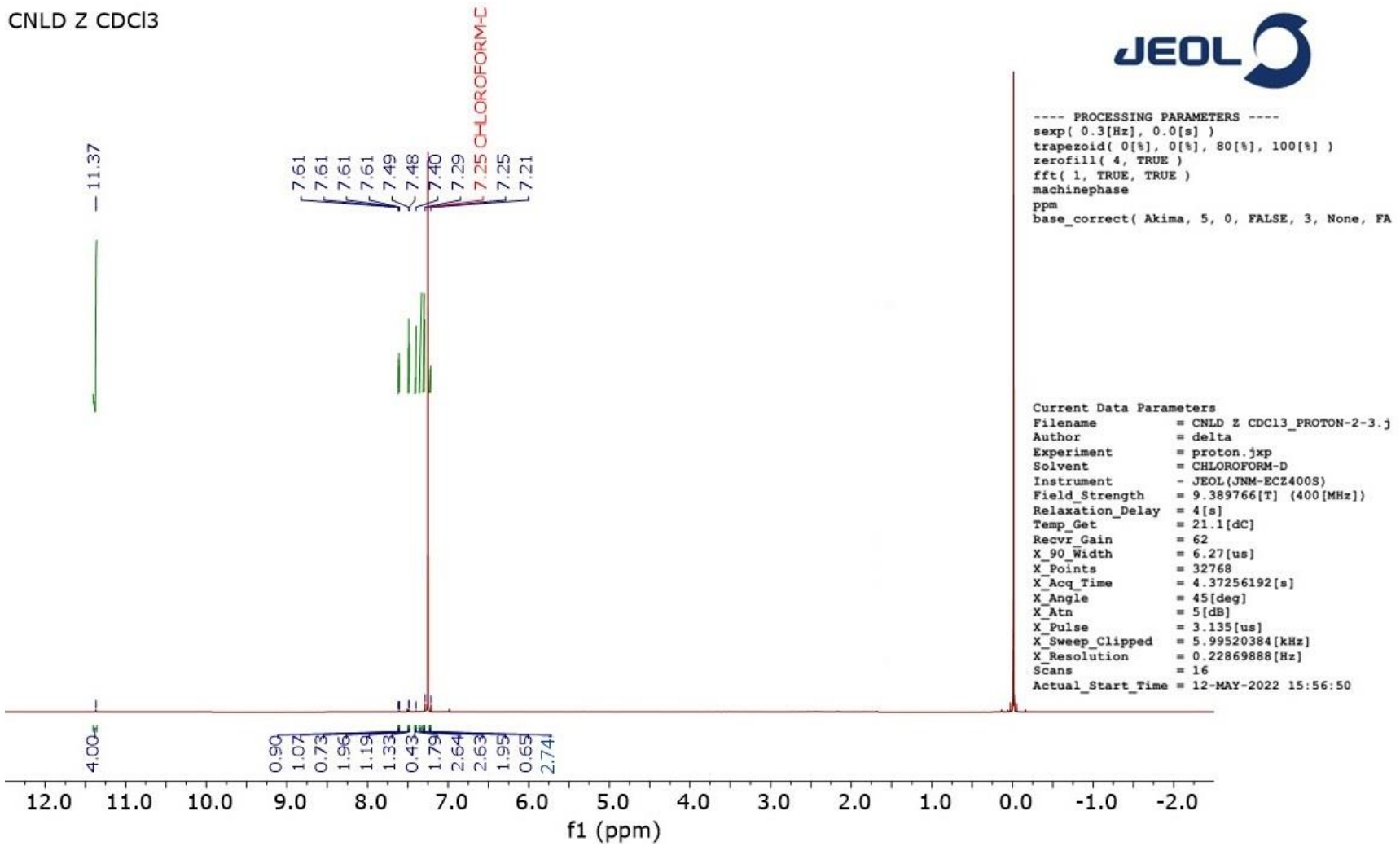

Fig.3.20 The ^{1}H NMR spectrum of Zn $(NLD)_2$

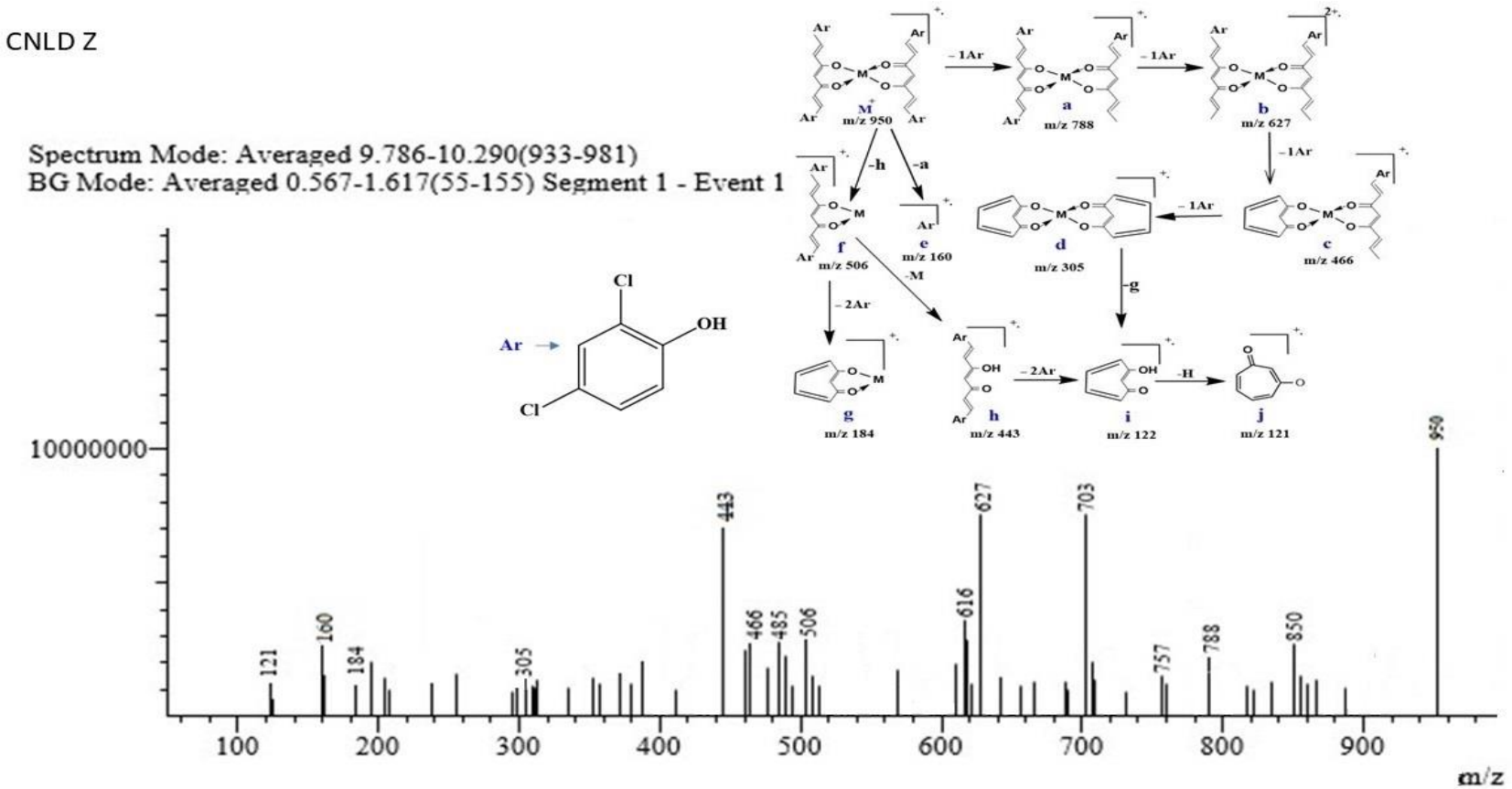

Fig.3.21 The Mass spectrum of Zn $(NLD)_2$

3.5.1.3. Synthesis and characterization of (1E,6E)-1,7-bis (6-methoxy naphthalene-2-yl) hepta-1,6-diene-3,5-dione and its Metal Chelates (NLE)

3.5.1.3.1 Synthesis and characterization of NLE

1,7-Bis(6-methoxynaphthalen-2-yl)hepta-1,6-diene-3,5-dione (NLE) was synthesized through the condensation of 6-methoxy-2-naphthaldehyde (0.01 M) with an acetylacetone–boron complex and B_2O_3 in ethyl acetate (7.5 mL). The reaction was carried out in the presence of tri-sec-butyl borate (5.4 mL) and n-butylamine (0.1 mL) as a condensing agent. The synthesized product exhibited a melting point of 245°C and a molecular weight of 436 g/mol, with a yield of approximately 85%. Elemental analysis showed carbon and hydrogen contents of 79.1% and 4.98%, respectively, which closely aligned with the theoretical values of 79.8% and 5.54%.

Characterization of NLE

The synthesized compound NLE was characterized using various spectroscopic techniques, including IR, ^{1}H NMR,^{13}C NMR, and mass spectrometry. The spectral data of the compound are discussed below.

IR Spectrum

The IR peaks for NLE were interpreted based on typical absorption ranges for various functional groups. The probable IR signals are shown in **Table 3.18.**

Table 3.18 Possible IR assignments of NLE

Wavenumbers (in cm^{-1})	Possible IR Assignments
2993.4	ν Enolic
1613.9	ν(C=O)
1585.4	ν(C=C) Phenyl
1466.1	ν_{as}(C-C-C)
1148.9	νβ (C-H)
951.2	ν(CH=CH) trans

The wavenumber 2993.4 cm^{-1} corresponded to the hydroxyl group (-OH) stretching vibration attached to the enolic structure. This value was slightly lower than the typical

O-H stretching range of 3200-3550 cm^{-1}, likely due to intramolecular hydrogen bonding or conjugation with a C=C bond, which could shift the absorption frequency downward. The wavenumber 1613.9 cm^{-1} represented the stretching vibration of the carbonyl (C=O) group, which typically falls within 1600-1750 cm^{-1}. The exact position was influenced by conjugation with a C=C bond or the presence of electronegative substituents, explaining the observed value.

The wavenumber 1585.4 cm^{-1} was associated with the C=C stretching vibration within the aromatic phenyl ring, fitting well within the expected 1450-1600 cm^{-1} range. The wavenumber 1466.1 cm^{-1} was attributed to the asymmetric stretching vibration of the C-C-C bond, commonly observed in alkanes or similar structures, with typical ranges between 1400-1470 cm^{-1}. The value of 1148.9 cm^{-1} corresponded to the in-plane bending (deformation) vibration of the C-H bond, which usually appears in the range of 1000-1300 cm^{-1}, supporting its validity as a C-H bending mode. The wavenumber 951.2 cm^{-1} was linked to the out-of-plane bending vibration of the C-H bond in a trans-alkene structure, consistent with the expected range of 960-970 cm^{-1} for such vibrations. Thus, the IR assignments for NLE were consistent with standard absorption ranges, and any slight deviations were attributed to specific molecular factors such as conjugation, hydrogen bonding, or the influence of neighbouring substituents (**Fig.3.22**).

^{1}HNMR Spectrum

The ^{1}H NMR spectrum of 1,7-bis(6-methoxynaphthalen-2-yl)hepta-1,6-diene-3,5-dione (NLE) showed distinct proton signals that corresponded closely with the expected chemical shifts for enolic, methine, alkenyl, phenyl, and hydroxy protons. The various proton signals observed in the spectrum are given in **Table 3.19**

Table 3.19 Proton signals observed in the ^{1}H NMR spectrum of NLE(Chemical Shifts δ ppm)

Compound	Enolic	Methine	Alkenyl	Phenyl	Methoxy
NLE	10.08	6.54	6.68-7.82	7.11-7.78	3.84

The chemical shift at 10.08 ppm was characteristic of an enolic proton, typically found downfield due to its involvement in hydrogen bonding with a nearby carbonyl group, which led to deshielding and a higher chemical shift. The methine proton appeared at 6.54 ppm, consistent with methine protons in conjugated systems, where moderate deshielding occurred due to the electron-withdrawing effects of adjacent double bonds. The alkenyl protons resonated in the range of 6.68-7.82 ppm, as expected for protons within a conjugated diene system, where the influence of adjacent double bonds caused deshielding. The phenyl protons, resonating between 7.11-7.78 ppm, fell within the typical range for aromatic protons, where the electron-withdrawing effects of the aromatic ring resulted in downfield shifts. The methoxy protons resonated at 3.84 ppm, a chemical shift characteristic of protons in a methoxy group attached to an aromatic ring, where the oxygen atom provided electron density, leading to a relatively upfield shift. These assignments were supported by the characteristic chemical shifts observed in NMR spectroscopy for similar functional groups in conjugated and aromatic systems, providing strong evidence that the assignments were correct. The ^{1}H NMR spectrum of NLE is brought out in **Fig.3.23**

^{13}C NMR Spectra

The ^{13}C NMR spectrum of NLE revealed distinct carbon signals corresponding to various environments within the molecule, confirming the accuracy of their chemical shifts. The ^{13}C NMR spectral details of NLE are given in **Table 3.20**

Table 3.20 ^{13}C NMR spectral data of NLE **(Chemical Shifts δ ppm)**

C_1	C_2,$C_{2'}$	C_3,$C_{3'}$	C_4,$C_{4'}$	C_5,$C_{5'}$	C_6,$C_{6'}$	C_7,$C_{7'}$	
101.16	192.18	131.22	140.24	132.44	127.86	129.58	
C_8,$C_{8'}$	C_9,$C_{9'}$	C_{10},$C_{10'}$	C_{11},$C_{11'}$	C_{12},$C_{12'}$	C_{13},$C_{13'}$	C_{14},$C_{14'}$	C_{15},$C_{15'}$
119.54	158.00	106.06	127.00	123.74	129.20	134.4	55.57

The interpretation of the ^{13}C NMR spectrum for NLE was based on well-established chemical shift ranges corresponding to specific carbon environments. The signal at 101.16 ppm was attributed to C_1, consistent with carbons in conjugated systems, such as alkenes, which typically resonate between 100-140 ppm. The signals at 192.18 ppm for C_2 and $C_{2'}$ were

indicative of carbonyl carbons (C=O) in ketones, known to be highly deshielded and typically found in the 190-220 ppm range. C_3 and $C_{3'}$ were assigned to the signal at 131.22 ppm, which corresponded to carbons in an alkenyl group involved in conjugation, fitting within the 120-140 ppm range for such environments. The signal at 140.24 ppm for C_4 and $C_{4'}$ was consistent with alkenyl carbons in a conjugated system, where resonance effects caused deshielding, placing these carbons within the expected 130-160 ppm range.The 132.44 ppm signal for C_5 and $C_{5'}$ was aligned with aromatic carbons, which typically resonate between 120-150 ppm, confirming their placement within an aromatic system. Similarly, C_6 and $C_{6'}$ at 127.86 ppm and C_7 and $C_{7'}$ at 129.58 ppm were also assigned to aromatic carbons, supported by literature values for aromatic carbons in conjugated systems. The 119.54 ppm signal for C_8 and $C_{8'}$ was indicative of carbons in an aromatic ring adjacent to a methoxy group (-OCH_3), fitting within the 110-160 ppm range influenced by the electron-donating nature of the methoxy group.C_9 and $C_{9'}$ were assigned to the 158.00 ppm signal, characteristic of carbons in an aromatic ring directly carrying a methoxy group, typically appearing in the 150-160 ppm range due to the deshielding effect of the electronegative oxygen atom. The 106.06 ppm signal for C_{10} and $C_{10'}$ was consistent with carbons in less deshielded aromatic rings or those adjacent to electron-donating groups, typically resonating in the 100-120 ppm range. The 127.86 ppm signal for C_{11} and $C_{11'}$ aligned with typical aromatic carbons, while the 123.74 ppm signal for C_{12} and $C_{12'}$ was consistent with aromatic carbons resonating in the 120-140 ppm range.The signal at 129.20 ppm for C_{13} and $C_{13'}$ confirmed the presence of a conjugated aromatic system, and the 134 ppm signal for C_{14} and $C_{14'}$ indicated aromatic carbons within a conjugated system, supported by the 130-160 ppm range for such environments. Finally, the 55.57 ppm signal for C_{15} and $C_{15'}$ was characteristic of methoxy groups (-OCH_3) attached to aromatic rings, typically resonating between 50-60 ppm due to the electron-donating effect of the oxygen atom. These chemical shifts and their corresponding environments were supported by extensive NMR spectroscopy studies and reference data from standard NMR tables, confirming that the assignments were correct and aligned with the structure of NLE(**Fig.3.24)**

Mass Spectrum

In the mass spectrum of NLE, prominent molecular ion peaks were observed, confirming the molecular weight.

Important peaks that appeared in the spectrum of the compound can be conveniently accounted for by the fragmentation pattern as shown in **Fig 3.25** and the values are brought out in **Table 3.21**.

Table 3.21 Molecular ion peaks of NLE

M^+/M+1 Ion	a	b	c	d	e	f	g
437	225	211	171	183	157	279	253

*The alphabets correspond to the fragments given in the fragmentation scheme in Fig**.3.25**

The M^{+1} ion of NLE was observed at 437, along with other significant peaks corresponding to fragment ions, which can be explained by their fragmentation patterns. In the mass spectrum of NLE, a prominent molecular ion peak appeared at 437. The peak at 225 was attributed to the fragment ion $[C_{15}H_{13}O_2]^+$, while the peak at 211 corresponded to the ion $[C_{14}H_{11}O_2]^+$. The peak at 171 was due to the fragment $[C_{12}H_{11}O]^+$, and the peak at 157 was associated with the ion $[C_{11}H_4O]^+$. Additionally, the peak at 279 was attributed to the fragment ion $[C_{18}H_{15}O_3]^+$, the peak at 183 to $[C_{13}H_{11}O]^+$, and the peak at 253 to $[C_{16}H_{13}O]^+$.

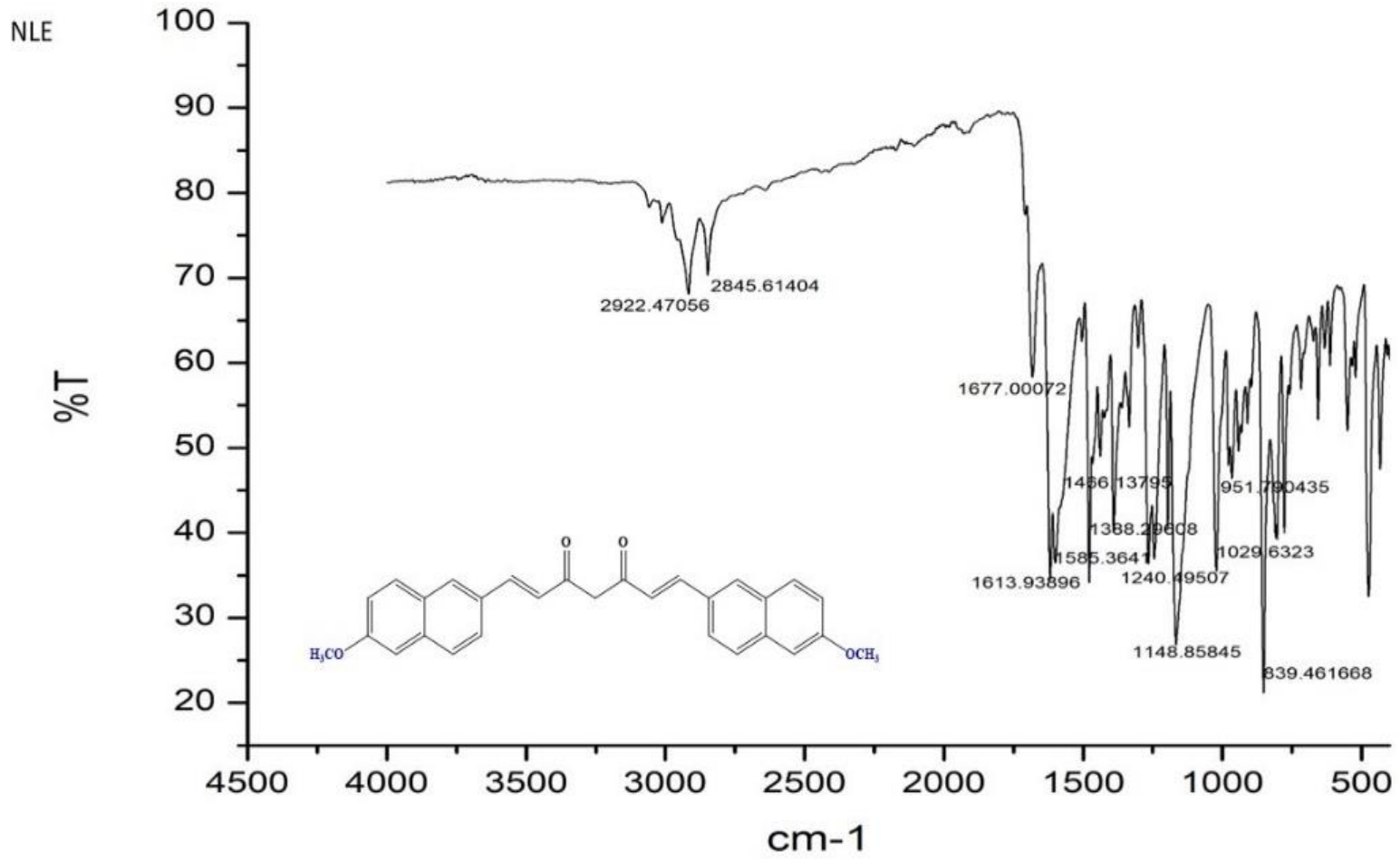

Fig.3.22 The IR spectrum of NLE

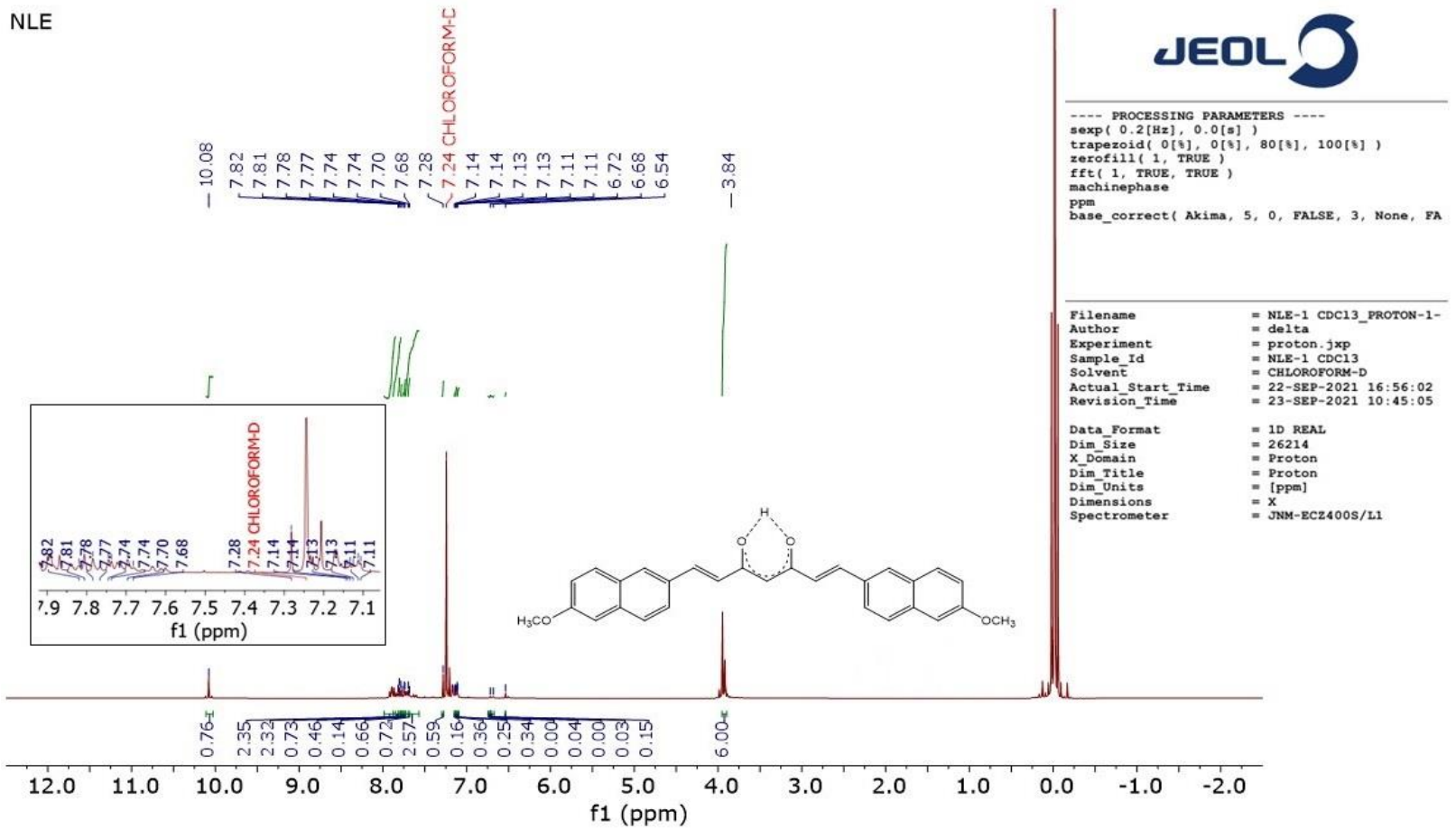

Fig.3.23 The ^{1}H NMR spectrum of NLE

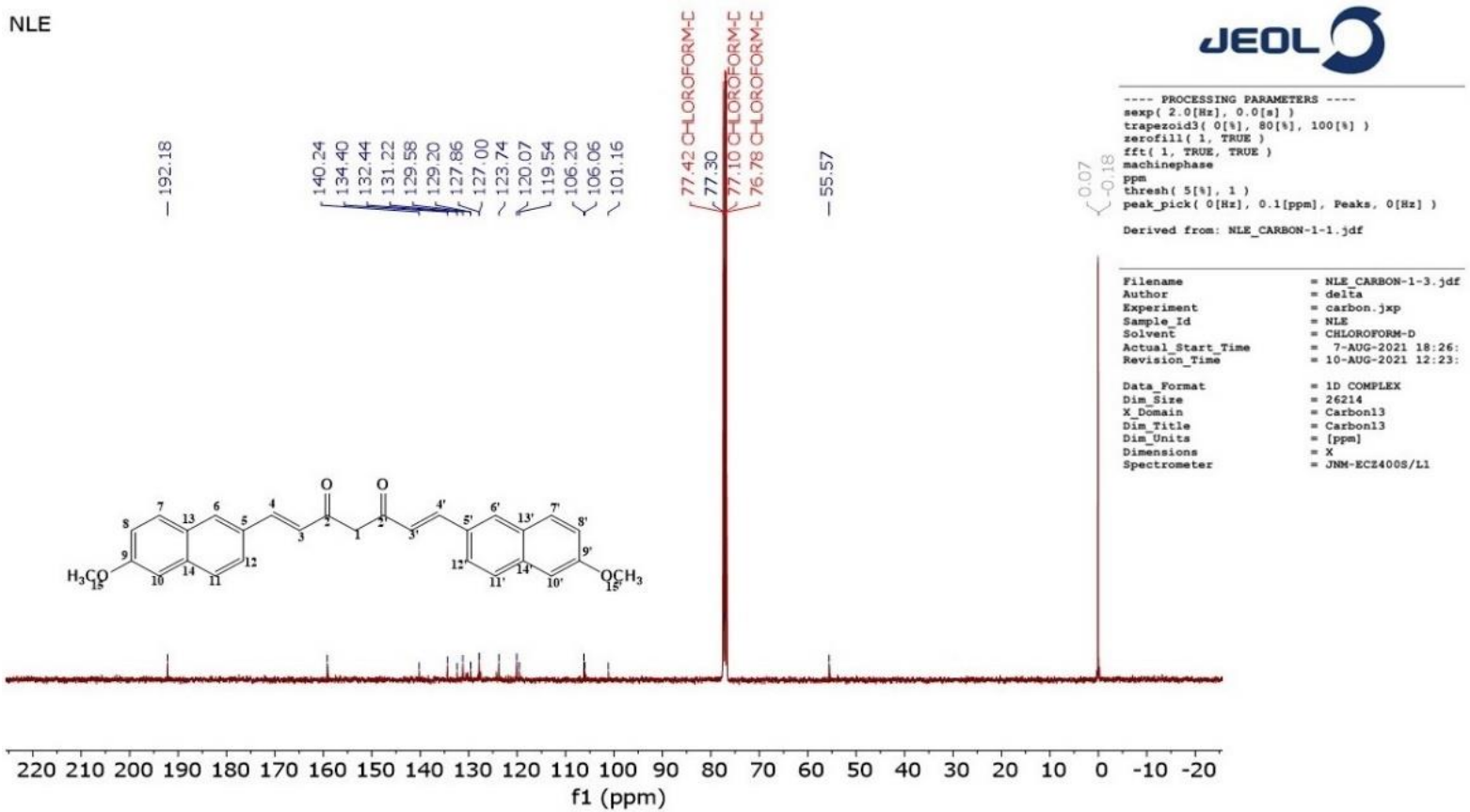

Fig.3.24 The ^{13}CNMR spectrum of NLE

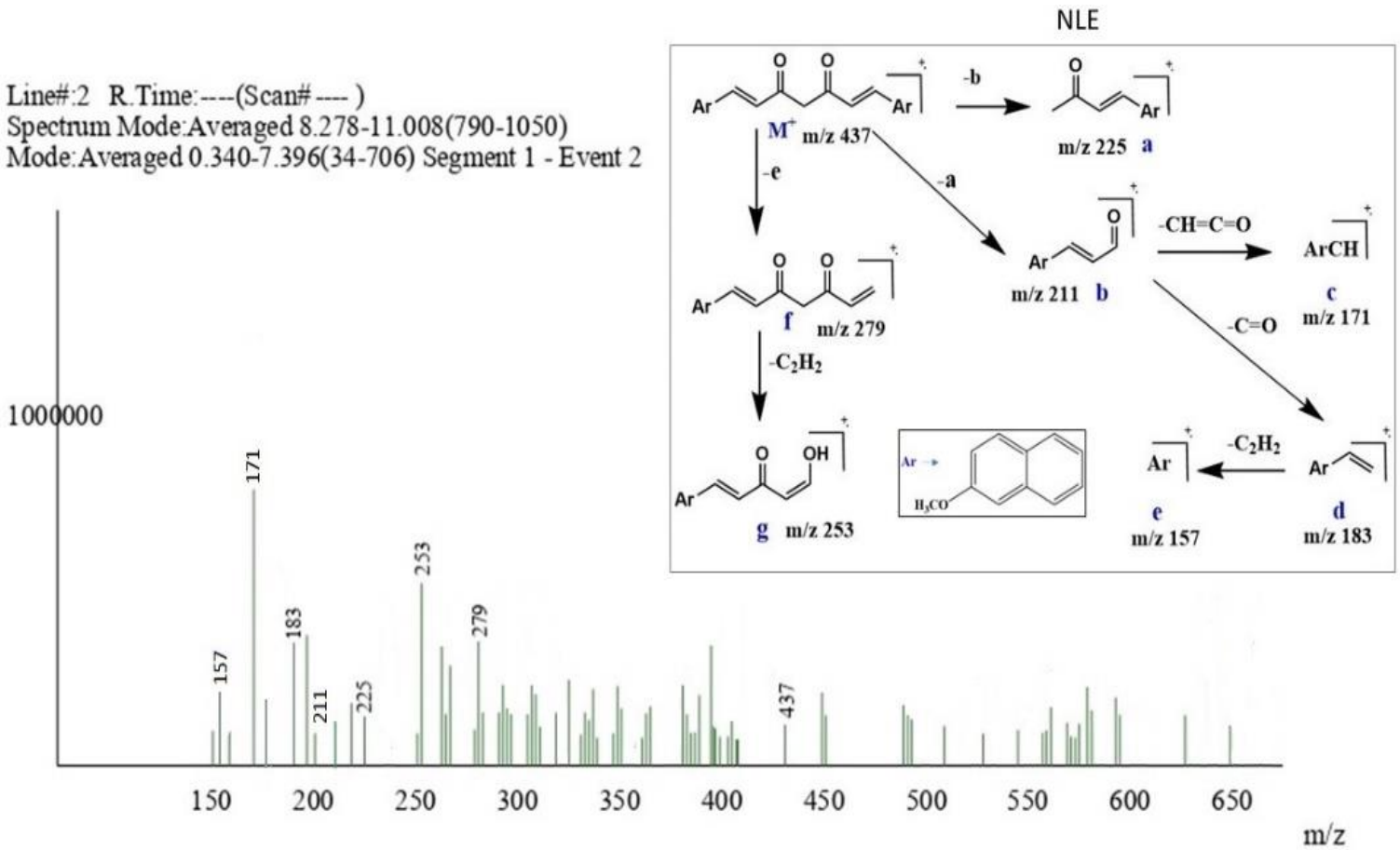

Fig.3.25 The Mass spectrum of NLE

3.5.1.3.2 Synthesis and Characterization of $Cu(NLE)_2$ and $Zn(NLE)_2$

3.5.1.3.2.1. Synthesis and Characterization of Cu complex of 1,7-bis (6-methoxy naphthalene-2-yl) hepta-1,6-diene-3,5-dione [$Cu(NLE)_2$]

The copper(II) complex of the curcuminoid analogue NLE had a molecular weight of 933.25 g/mol and a melting point of 265°C. Elemental analysis showed carbon, hydrogen, and metal contents of 74.00%, 4.36%, and 6.41%, respectively, closely matching the theoretical values of 74.54%, 4.96%, and 6.8%. The compound was obtained with a yield of 87%.

Characterization of $Cu(NLE)_2$

The metal complex $Cu(NLE)_2$ was characterized through various spectroscopic and analytical techniques, such as IR spectroscopy, ^1H NMR, and mass spectrometry. The spectral data obtained from the synthesized complex are summarized and discussed below.

IR Spectrum

The metal complex $Cu(NLE)_2$ displayed distinct spectral characteristics that verified the successful coordination of the ligand with the metal ion (**Fig.3.36**). The absence of a prominent absorption band in the 1650-1800 cm^{-1} region, particularly the disappearance of the carbonyl peak at 1630 cm^{-1}, along with the emergence of a new band at 1592.2 cm^{-1}, indicated that the enolic proton had been substituted by the metal ion, leading to the formation of a metal-coordinated carbonyl group. The shift of the carbonyl stretching frequency to 1592.2 cm^{-1} was indicative of chelation, which reduced the frequency relative to a free carbonyl group. Furthermore, the band observed at 1532.4 cm^{-1} was attributed to the asymmetric stretching of the C-C-C bond within an aromatic ring, suggesting the presence of an aromatic system. The low-frequency bands at 446.1 cm^{-1} and 427.5 cm^{-1} were assigned to metal-oxygen (M-O) stretching vibrations, confirming the coordination of the metal to oxygen atoms and indicating the formation of a complex metal-ligand structure.

^{1}HNMR Spectrum

The various proton signals identified in the ^{1}H NMR spectrum of the Cu(II) complex of 1,7-bis(6-methoxy naphthalene-2-yl)hepta-1,6-diene-3,5-dione [$Cu(NLE)_2$] were summarized in **Table 3.22**

Table 3.22 Proton signals observed in the ^{1}HNMR spectrum of Cu $(NLE)_2$ (Chemical Shifts δ in ppm)

Complex	Methine	Alkenyl	Phenyl	Methoxy
$Cu(NLE)_2$	6.89	6.96-7.91	7.29-7.93	3.96

The ^{1}H NMR spectrum of the of [$Cu(NLE)_2$] provided key insights into the proton environment within the complex (**Fig.3.27**). The methine protons in $Cu(NLE)_2$ appeared at 6.89 ppm, slightly downfield compared to the methine protons in free NLE, which were observed around 6.54 ppm. This downfield shift was consistent with the coordination of the ligand to the Cu(II) ion, as metal coordination generally causes deshielding of protons. The observed shift to 6.89 ppm indicated that the methine protons were influenced by the metal coordination as expected. The alkenyl protons were observed in the range of 6.96-7.91 ppm, slightly downfield compared to the typical 6.50-7.50 ppm range for alkenyl protons in free NLE. This shift suggested that coordination with Cu(II) affected the electronic environment of the alkenyl protons, leading to a downfield shift. The phenyl protons appeared in the range of 7.29-7.93 ppm, broader and slightly higher than the typical 7.0-8.0 ppm range for phenyl protons in free NLE. This broader range was consistent with the effects of metal coordination, which likely altered the electronic environment of the aromatic ring. The observed shift suggested that the phenyl protons experienced some degree of deshielding due to interaction with the metal centre. The methoxy protons were observed at 3.96 ppm, which was consistent with their expected range, typically around 3.8-4.0 ppm in free NLE. The chemical shift of methoxy protons remained relatively unaffected by metal coordination compared to other protons, and the observed value of 3.96 ppm aligned well with the typical range for methoxy protons, confirming their assignment in the spectrum. The chemical shifts observed in the ^{1}H NMR spectrum of $Cu(NLE)_2$ were consistent with the effects of Cu(II) coordination.

Mass Spectrum

Table 3.15 Molecular ion peaks of Cu $(NLE)_2$

M^+/(M+1)/(M+2) ion	a	b	c	d	e	f	g	h	i	j
933	776	619	462	304	157	498	183	436	122	121

*The alphabets correspond to the fragments given in the fragmentation scheme in Fig**.3.28**

The mass spectrum of the Cu(II) complex of NLE showed an intense molecular ion peak at m/z 933, indicating the intact molecular weight of the compound. The peaks at m/z 619 and 304 corresponded to the loss of two and four Ar groups, respectively, where Ar represented the 6-methoxy naphthalene-2-yl group. The peak at m/z 498 was attributed to the $[ML]^+$ fragment, where M was the metal (Cu) and L was the ligand (1,7-bis(6-methoxy naphthalene-2-yl)hepta-1,6-diene-3,5-dione). Additional fragment ions were observed at m/z 776, 462, 157, 183, 436,122 and 121, supporting the fragmentation patterns and structural components of the $Cu(NLE)_2$ complex[68]. The mass spectrum of $Cu(NLE)_2$ is shown in **Fig.3.28**.

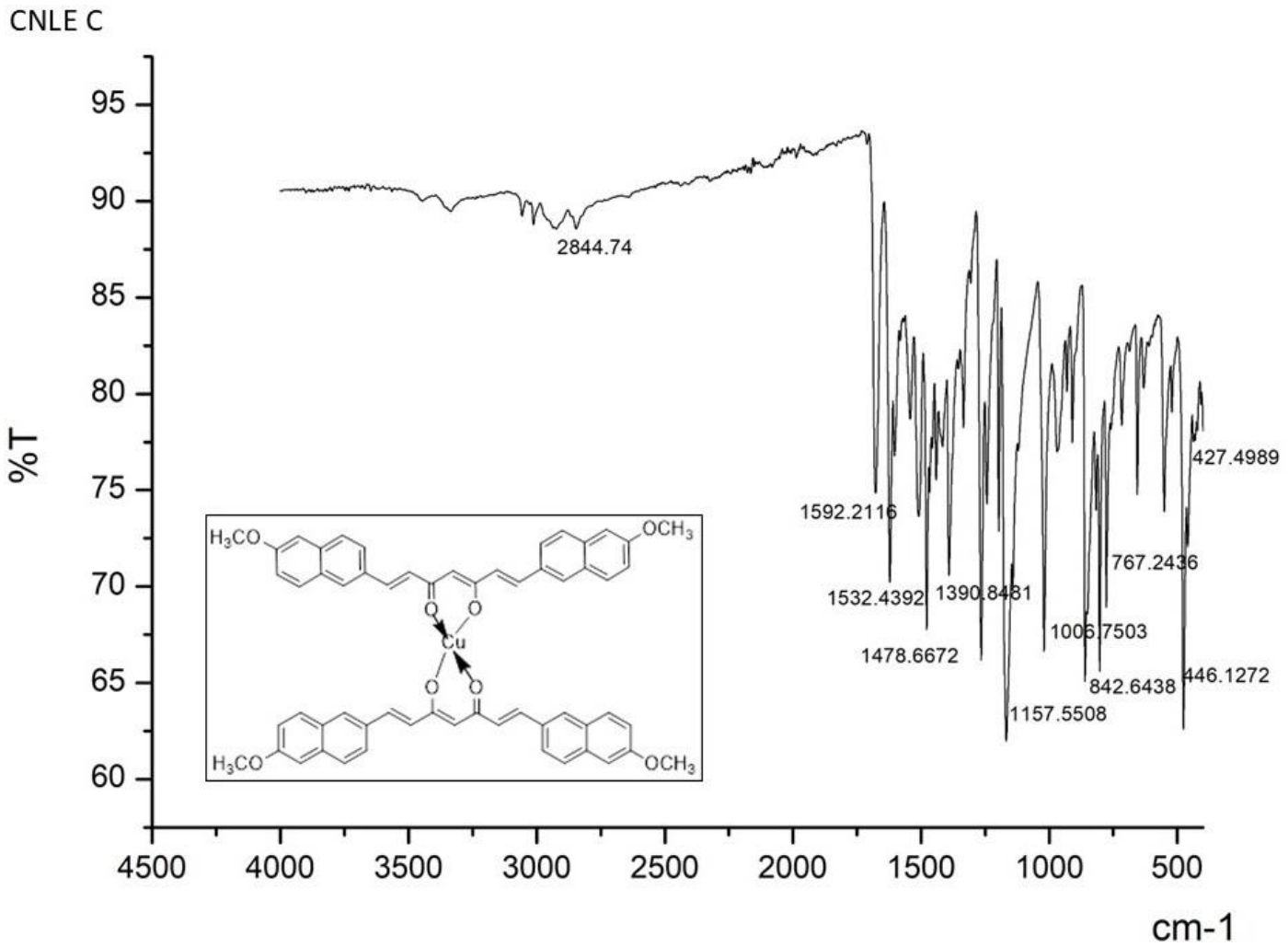

Fig.3.26 The IR spectrum of Cu $(NLE)_2$

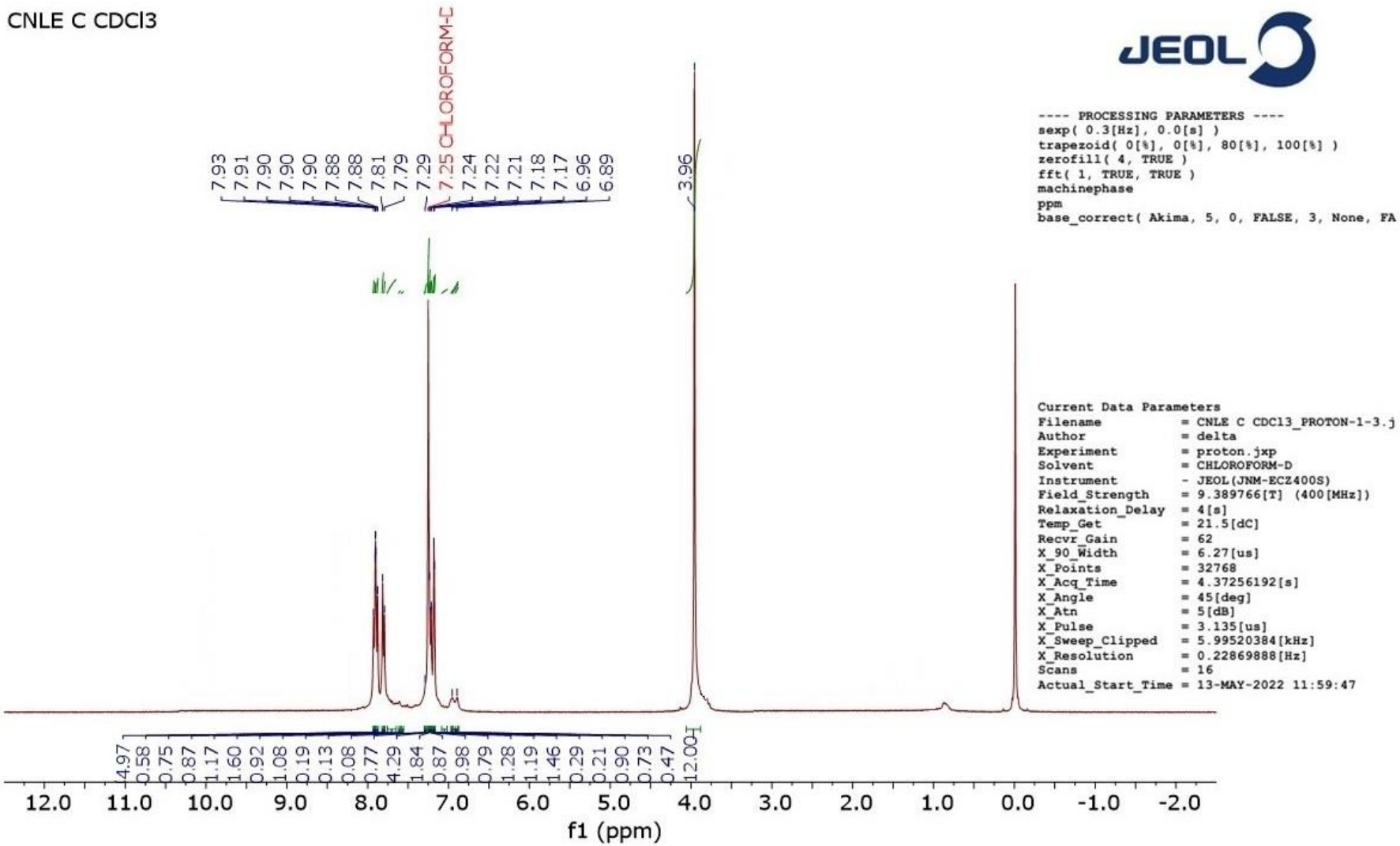

Fig.3.27 The ^{1}H NMR spectrum of Cu $(NLE)_2$

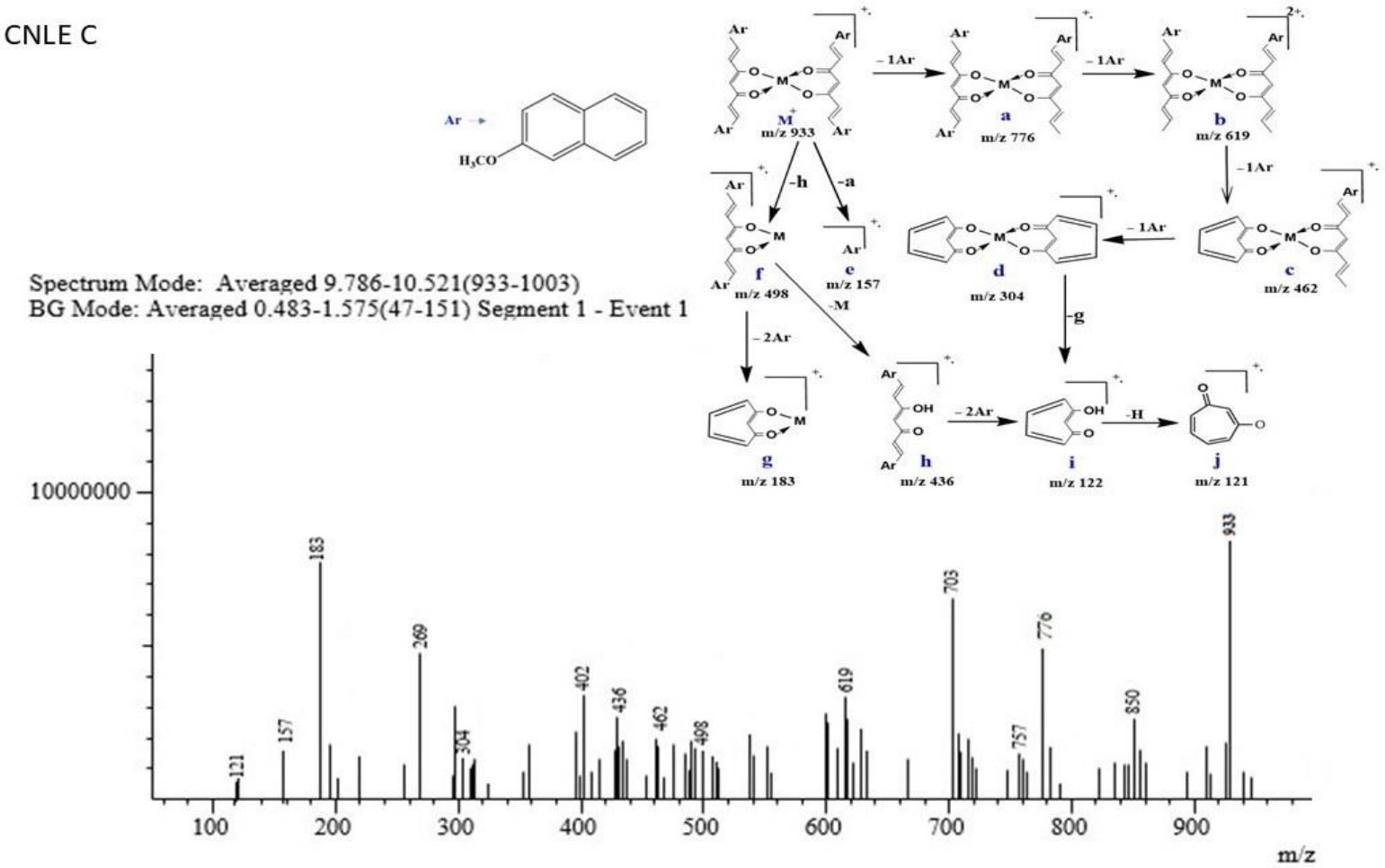

Fig.3.28 The Mass spectrum of Cu $(NLE)_2$

3.5.1.3.2.2. Synthesis and characterization of Zn complex of 1,7-bis(6-methoxy naphthalene-2-yl)hepta-1,6-diene-3,5-dione [$Zn(NLE)_2$]

The Zn(II) complex of the curcuminoid analogue NLE had a molecular weight of 934.25 g/mol and a melting point of 270°C. Elemental analysis showed carbon, hydrogen, and metal contents of 74.51%, 4.25%, and 6.72%, respectively, which closely matched the theoretical values of 74.4%, 4.95%, and 6.98%. The synthesis achieved a yield of 92%.

Characterization of $Zn(NLE)_2$

The metal complex $Zn(NLE)_2$ was characterized using various spectroscopic and analytical techniques, including IR spectroscopy, ^1H NMR, and mass spectrometry. The spectral data obtained from the synthesized complex are summarized and discussed below.

IR Spectrum

The spectral analysis of the $Zn(NLE)_2$ complex confirmed the successful coordination of the ligand with the metal ion through distinct features. The disappearance of the carbonyl peak at 1630 cm^{-1} and the appearance of a new band at 1592.2 cm^{-1} indicated the coordination of the enolic form of the ligand with the metal, replacing the enolic proton. This shift to a lower frequency suggested chelation, where the carbonyl group was weakened, leading to a reduced stretching frequency. The presence of a band at 1527.9 cm^{-1}, attributed to the C-C-C stretching within the aromatic ring, indicated that the aromatic system of the ligand remained intact in the complex. Additionally, low-frequency bands at 459.4 cm^{-1} and 415.1 cm^{-1} were identified as metal-oxygen (M-O) stretching vibrations, further confirming the coordination of the metal ion to the oxygen atoms. These observations collectively validated the formation of the $Zn(NLE)_2$ complex, showcasing the ligand's successful integration into the metal-ligand structure (**Fig.3.29**).

^{1}HNMR Spectrum

The various proton signals identified in the ^1H NMR spectrum of the Zn(II) complex of 1,7-bis(6-methoxy naphthalene-2-yl)hepta-1,6-diene-3,5-dione [$Zn(NLE)_2$] were summarized in **Table 3.24**

Table 3.24 Proton signals observed in the ^{1}H NMR spectrum of $Zn(NLE)_2$ (Chemical Shifts δ in ppm)

Complex	Methine	Alkenyl	Phenyl	Methoxy
$Zn(NLE)_2$	7.17	7.17-7.93	7.24-7.79	3.96

The ^{1}H NMR spectrum of the $Zn(NLE)_2$ complex displayed chemical shifts indicative of successful metal coordination. The methine proton appeared as a singlet at 7.17 ppm, consistent with deshielding caused by the electron-withdrawing effects of adjacent carbonyl groups and Zn(II) coordination. Alkenyl protons were observed between 7.17 and 7.93 ppm, a range that reflects the deshielding effects of conjugation and metal interaction, aligning with the expected 6.5-8.0 ppm range for such protons. The phenyl protons exhibited a broader range of 7.24-7.79 ppm, slightly higher than in free NLE, indicating altered electronic environments due to metal coordination. The methoxy protons appeared at 3.96 ppm, consistent with their typical range, and remained relatively unaffected by metal coordination. These shifts collectively confirmed the formation of the $Zn(NLE)_2$ complex and its successful coordination with the Zn(II) ion (**Fig.3.30**).

Mass Spectrum

Table 3.25 Molecular ion peaks of Zn $(NLE)_2$

M^+/(M+1)/(M+2) ion	a	b	c	d	e	f	g	h	i	j
934	777	620	463	305	157	499	184	436	122	121

*The alphabets correspond to the fragments given in the fragmentation scheme in Fig**.3.31**

The mass spectrum of the Zn(II) complex of NLE showed an intense molecular ion peak at m/z 934, indicating the intact molecular weight of the compound. The peaks at m/z 620 and 305 corresponded to the loss of two and four Ar groups, respectively, where Ar represented the 6-methoxy naphthalene-2-yl group. The peak at m/z 499 was attributed to the $[ML]^+$ fragment, where M was the metal (Zn) and L was the ligand (1,7-bis(6-methoxy naphthalene-2-yl)hepta-1,6-diene-3,5-dione). Additional fragment ions were observed at m/z 777, 620, 463, 305, 157, 184, 436, 122 and 121, supporting the fragmentation patterns and structural components of the $Zn(NLE)_2$ complex. The mass spectrum of $Zn(NLE)_2$ is shown in (**Fig.3.31**).

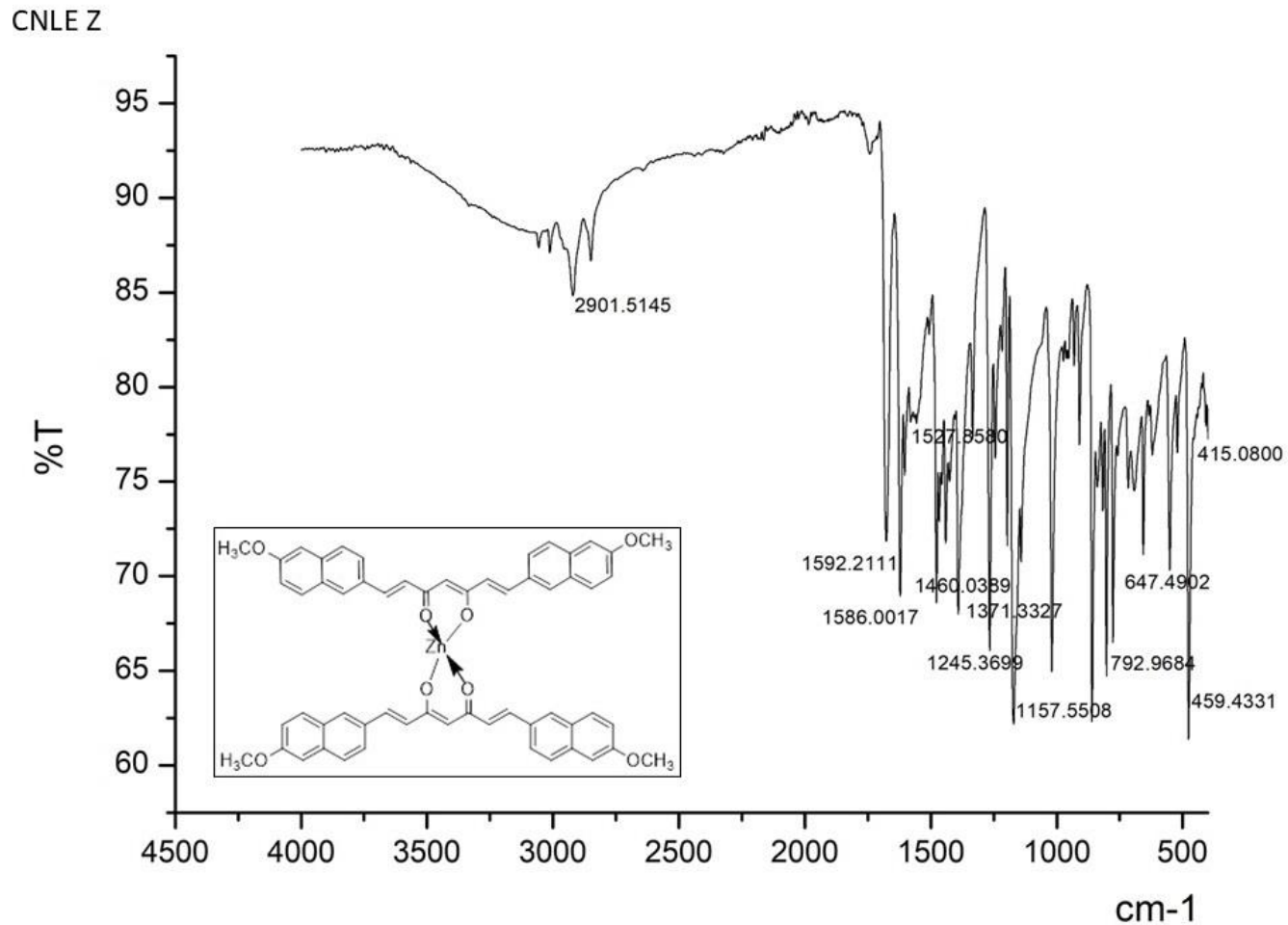

Fig.3.29 The IR spectrum of Zn $(NLE)_2$

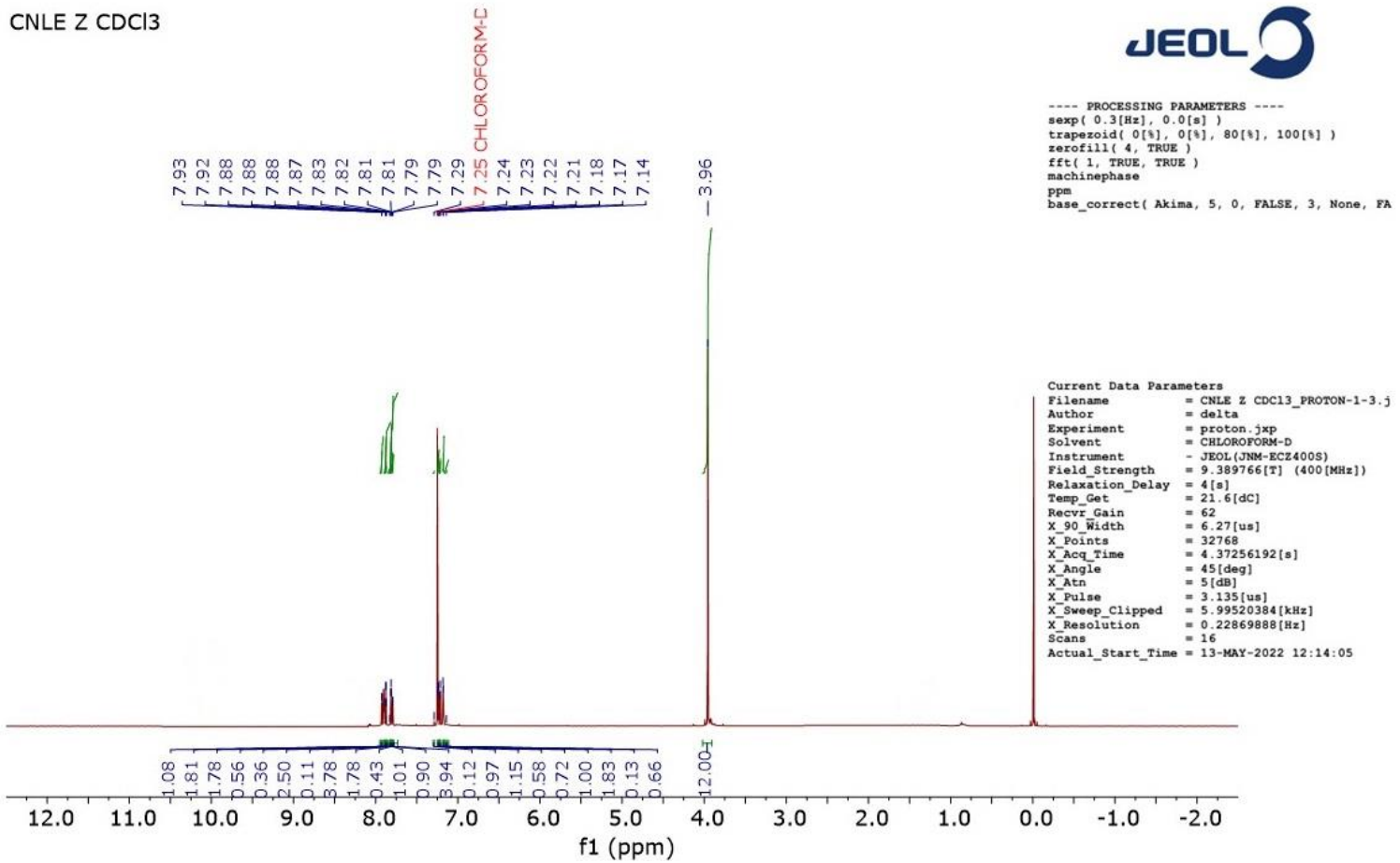

Fig.3.30 The ^{1}H NMR spectrum of Zn $(NLE)_2$

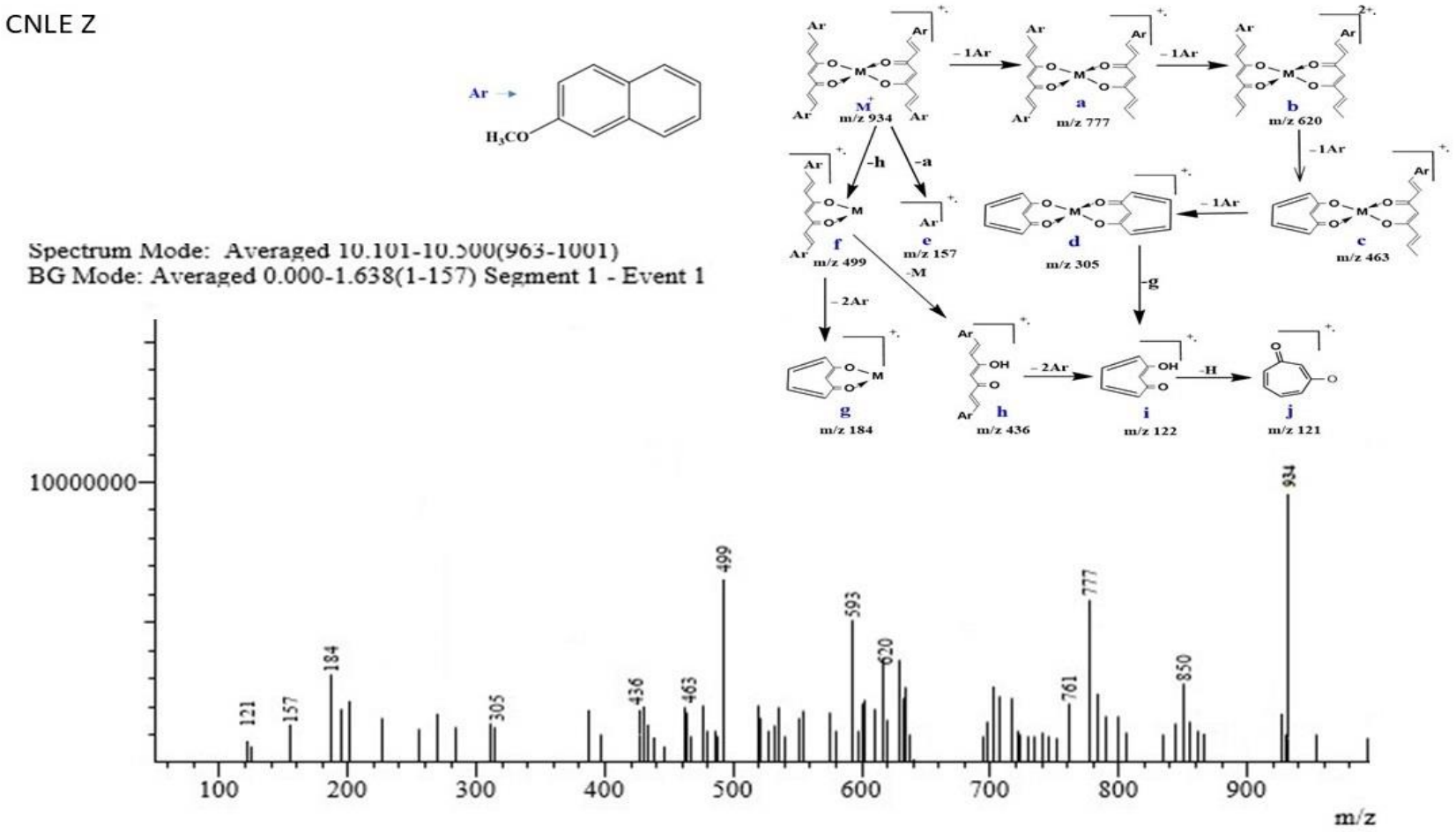

Fig.3.31 The Mass spectrum of Zn $(NLE)_2$

3.5.1.4. Synthesis and characterization of (1E,6E)-1,7-bis(3-ethoxy-2-hydroxy phenyl) hepta-1,6-diene-3,5-dione (NLF)

3.5.1.4.1 Synthesis and characterization of NLF

1,7-bis(3-ethoxy-2-hydroxy phenyl) hepta-1,6-diene-3,5-dione (NLF) was synthesized through the condensation reaction of 3-ethoxysalicylaldehyde (0.01 M) with an acetylacetone–boron complex and B_2O_3 in a volume of ethyl acetate (7.5 mL). The synthesis was executed in the presence of tri-sec-butyl borate (5.4 mL) and n-butylamine (0.1 mL) serving as the condensing agents. The resultant compound exhibited a melting point of 210°C and a molecular weight of 396 g/mol, with an approximate yield of 83%. Elemental analysis demonstrated carbon and hydrogen contents of 69.01% and 5.64%, respectively, which closely correspond to the theoretical values of 69.68% and 6.1%.

Characterization of NLF

The synthesized compound NLF was characterized using various spectroscopic techniques, including IR, ^{1}H NMR, ^{13}C NMR, and mass spectrometry. The spectral data of the compound are discussed below.

IR Spectrum

The IR peaks for NLF can be interpreted based on the typical absorption ranges associated with different functional groups. The probable IR signals are displayed in **Table 3.26.**

Table 3.26 Possible IR assignments of NLF

Wavenumbers (in cm^{-1})	Possible IR Assignments
2993.4	ν Enolic
1641.5	ν(C=O)
1571.6	ν(C=C) Phenyl
1458.2	ν_{as}(C-C-C)
980.4	ν(CH=CH) trans

The peak at 2993.4 cm^{-1} was identified as the O-H stretching vibration in an enolic group. Typically, enolic O-H stretching appears in the range of 3200–3550 cm^{-1}; however, due to hydrogen bonding, this frequency was observed to be slightly lower, around 2993

cm^{-1}, indicating the involvement of the enolic O-H in hydrogen bonding, which weakened the O-H bond and reduced the stretching frequency. The peak at 1641.5 cm^{-1} was assigned to the carbonyl (C=O) stretching vibration. Normally, the ν(C=O) in ketones, aldehydes, and similar functional groups appears within the range of 1650–1750 cm^{-1}. The slight shift to 1641.5 cm^{-1} suggested the presence of conjugation with a double bond or aromatic ring, which decreased the bond order and lowered the stretching frequency. The peak at 1571.6 cm^{-1}, was attributed to the C=C stretching in the phenyl ring. Aromatic C=C stretching vibrations generally occur in the range of 1450–1600 cm^{-1}. The observed frequency at 1571.6 cm^{-1} fell within this range, confirming the assignment. The peak at 1458.25623 cm^{-1} was associated with the asymmetric stretching vibration of the C-C-C bonds within a phenyl ring or similar structure. Such vibrations typically appear around 1400–1500 cm^{-1}, and the observed value of 1458.2 cm^{-1} fits well within this expected range, supporting the assignment. The peak at 980.4 cm^{-1} was linked to the out-of-plane deformation (wagging) of the CH=CH group in a trans-alkene. This vibration usually occurs in the range of 960–1000 cm^{-1}, and the observed value of 980.4 cm^{-1} aligned with the expected range, confirming the assignment. In conclusion, the IR spectral assignments for NLF were accurate and consistent with standard vibrational frequency ranges, with the observed shifts in ν(Enolic) and ν(C=O) being explained by factors such as hydrogen bonding and conjugation (**Fig.3.32**)

^{1}HNMR Spectrum

The ^{1}H NMR spectrum of 1,7-bis(3-ethoxy-2-hydroxyphenyl)hepta-1,6-diene-3,5-dione (NLF) showed distinct proton signals that corresponded closely with the expected chemical shifts for enolic, methine, alkenyl, phenyl, and hydroxy protons. The various proton signals observed in the spectrum are given in **Table 3.27**.

Table 3.27 Proton signals observed in the ^{1}H NMR spectrum of NLF (Chemical Shifts δ ppm)

Compound	Enolic	Methine	Alkenyl	Phenyl	Ethoxy	Hydroxy
NLF	9.90	6.80	6.91-7.28	6.87-7.09	4.09-4.14 1.41-1.47	11.08

The signal at 9.90 ppm was attributed to the enolic proton, which typically resonates downfield due to the deshielding effect of the adjacent electronegative oxygen atom and possible hydrogen bonding. This chemical shift fell within the expected range for enolic protons, generally appearing between 9.5 and 12 ppm. The methine proton signal at 6.80 ppm was consistent with values typically found for methine protons adjacent to double bonds or aromatic rings, where deshielding effects shift the resonance to this range. The broad range of signals between 6.91 and 7.28 ppm was assigned to the alkenyl protons, fitting well within the expected chemical shift range for alkenes, which usually appear between 5.5 and 7.5 ppm, depending on the degree of conjugation and electronegativity of substituents. The phenyl protons, resonating between 6.87 and 7.09 ppm, were consistent with aromatic protons, which generally appear between 6.5 and 8.5 ppm, depending on the substitution pattern and electronic environment. The signals between 4.09 ppm and 4.14 ppm corresponded to the CH_2 protons in the OCH_2CH_3 group and the signals between 1.41and 1.47 ppm corresponded to the CH_3 protons in the OCH_2CH_3 group, with chemical shifts typically observed between 3.0 and 4.5 ppm due to the influence of the electronegativity of the oxygen atom and the surrounding environment. The OH group attached to an aromatic ring and near an ethoxy group ($–OCH_2CH_3$) did indeed appear at δ 11.08 ppm in the ^1H NMR spectrum. The deshielding effect caused by the aromatic ring, combined with the possible conjugation and the presence of the ethoxy group, caused the OH proton to resonate at this downfield chemical shift. This value was consistent with the expected chemical shift for a hydroxyl proton in such an environment. These assignments confirmed that the ^1H NMR spectrum of NLF was accurate and consistent with standard chemical shift ranges for the corresponding proton environments. The ^1H NMR spectrum of NLF is brought out in **Fig.3.33**

^{13}C NMR Spectra

The ^{13}C NMR spectrum of NLF revealed distinct carbon signals corresponding to various environments within the molecule, confirming the accuracy of their chemical shifts. The details of the ^{13}C NMR spectrum for NLF are provided in **Table 3.28.**

Table 3.28 ^{13}C NMR spectral data of NLF (Chemical Shifts δ ppm)

C_1	C_2,$C_{2'}$	C_3,$C_{3'}$	C_4,$C_{4'}$	C_5,$C_{5'}$	C_6,$C_{6'}$
105.4	196.72	151.97	147.65	119.42	120.99
C_7,$C_{7'}$	C_8,$C_{8'}$	C_9,$C_{9'}$	C_{10},$C_{10'}$	C_{11},$C_{11'}$	C_{12},$C_{12'}$
124.67	119.64	119.42	151.97	64.94	14.83

The ^{13}C NMR spectrum of NLF identified several distinct carbon signals, confirming the accuracy of their chemical shifts (**Fig.3.34**). The signal at 105.4 ppm was attributed to an sp^2-hybridized carbon, likely within a substituted aromatic ring or near a double bond, consistent with the typical 100-120 ppm range. Signals at 196.72 ppm were assigned to carbonyl carbons, aligning with the 190-220 ppm range due to the carbonyl group's strong deshielding effect. The 151.97 ppm and 147.65 ppm signals corresponded to carbons in a conjugated system, such as those interacting with a carbonyl group, fitting the 145-160 ppm range. The 119.42 ppm and 120.99 ppm signals were associated with carbons in an aromatic ring, consistent with the 110-140 ppm range. The 124.67 ppm signal also indicated carbons in the aromatic ring. The signal at 119.64 ppm suggested carbons in an aromatic ring near an ethoxy group ($-OCH_2CH_3$), falling within the 110-130 ppm range due to the electron-donating effect of the ethoxy group. The 151.97 ppm signal was consistent with carbons in an aromatic ring attached to a hydroxyl group, reflecting increased deshielding. Signals at 64.94 ppm were for carbons in an OCH_2 group, and the 14.83 ppm signal was attributed to a methyl carbon (CH_3).

Mass Spectrum

In the mass spectrum of NLF, prominent molecular ion peaks were observed, confirming the molecular weight of the compound. Key peaks in the spectrum were accounted for by the fragmentation pattern detailed in Fig 3.20, Scheme 3.1. The corresponding values are summarized in **Table 3.29**

Table 3.29 Molecular ion peaks of NLF

M^+/M+1 Ion	**a**	**b**	**c**	**d**	**e**	**f**	**g**
396	205	191	151	163	137	259	233

*The alphabets correspond to the fragments given in the fragmentation scheme in**Fig.3.35**

In the mass spectrum of NLF, the molecular ion peak was prominently observed at 396, confirming the molecular weight of the compound. Significant fragment ion peaks included the following: the peak at 205, which was assigned to the fragment ion $[C_{12}H_{13}O_3]^+$; the peak at 191, corresponding to the ion $[C_{11}H_{11}O_3]^+$; and the peak at 151, attributed to the fragment $[C_9H_{11}O_2]^+$. The peak at 259 was associated with the ion $[C_{15}H_{15}O_4]^+$, and the peak at 233 was linked to the ion $[C_{13}H_{13}O_4]^+$. These fragment ions align with the expected fragmentation patterns for NLF.

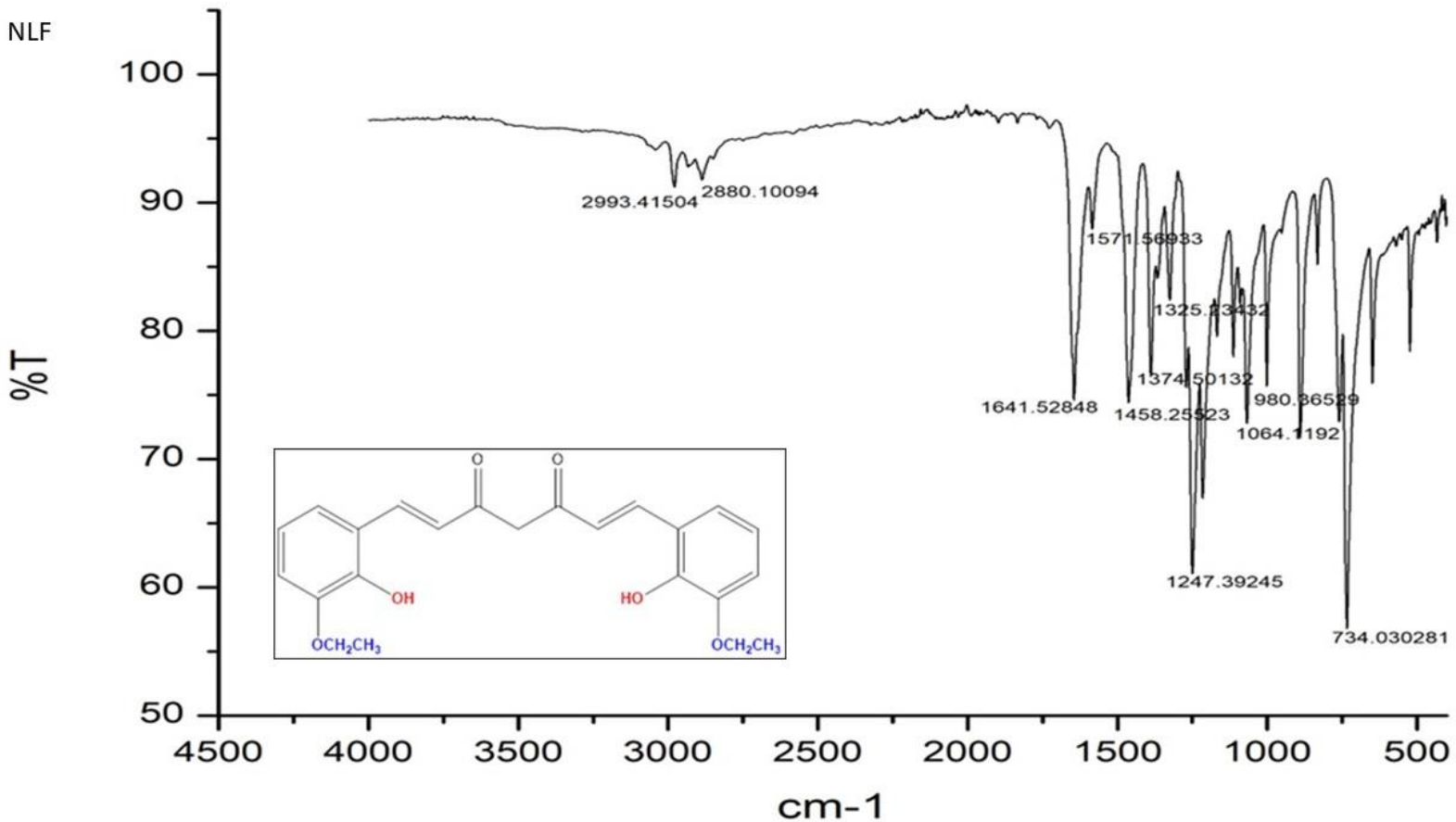

Fig.3.32 The IR spectrum of NLF

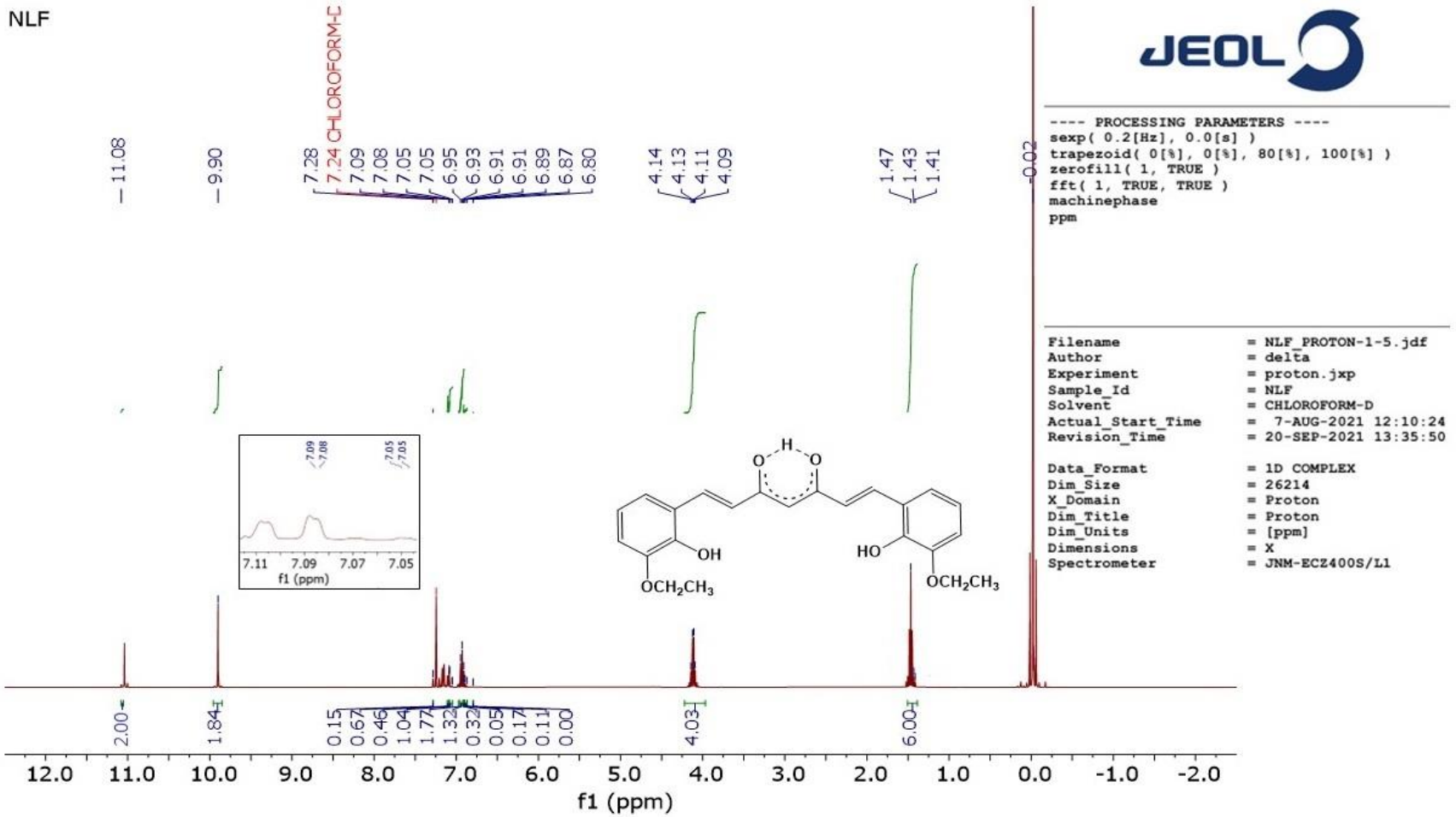

Fig.3.33 The ^{1}H NMR spectrum of NLF

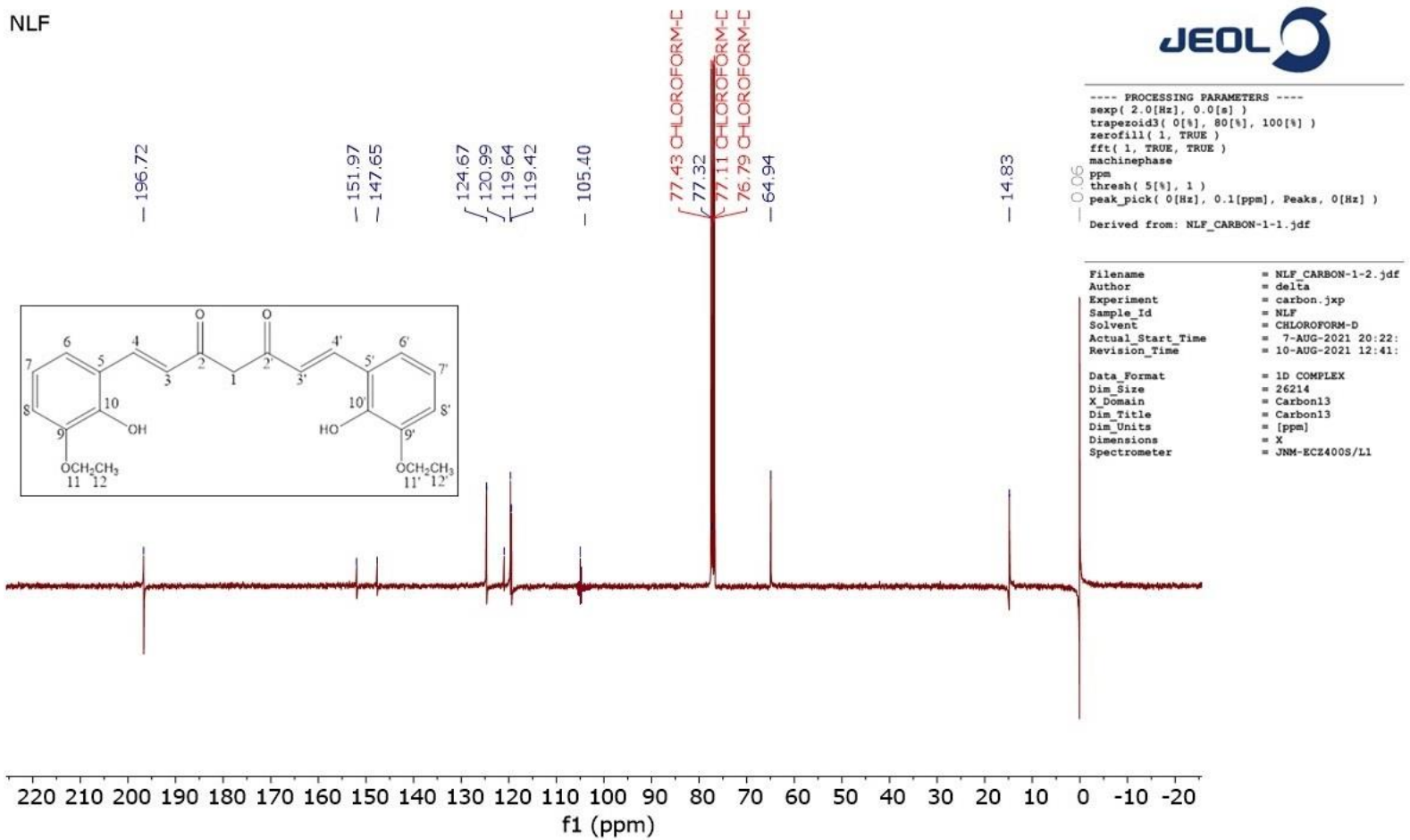

Fig.3.34 The ^{13}CNMR spectrum of NLF

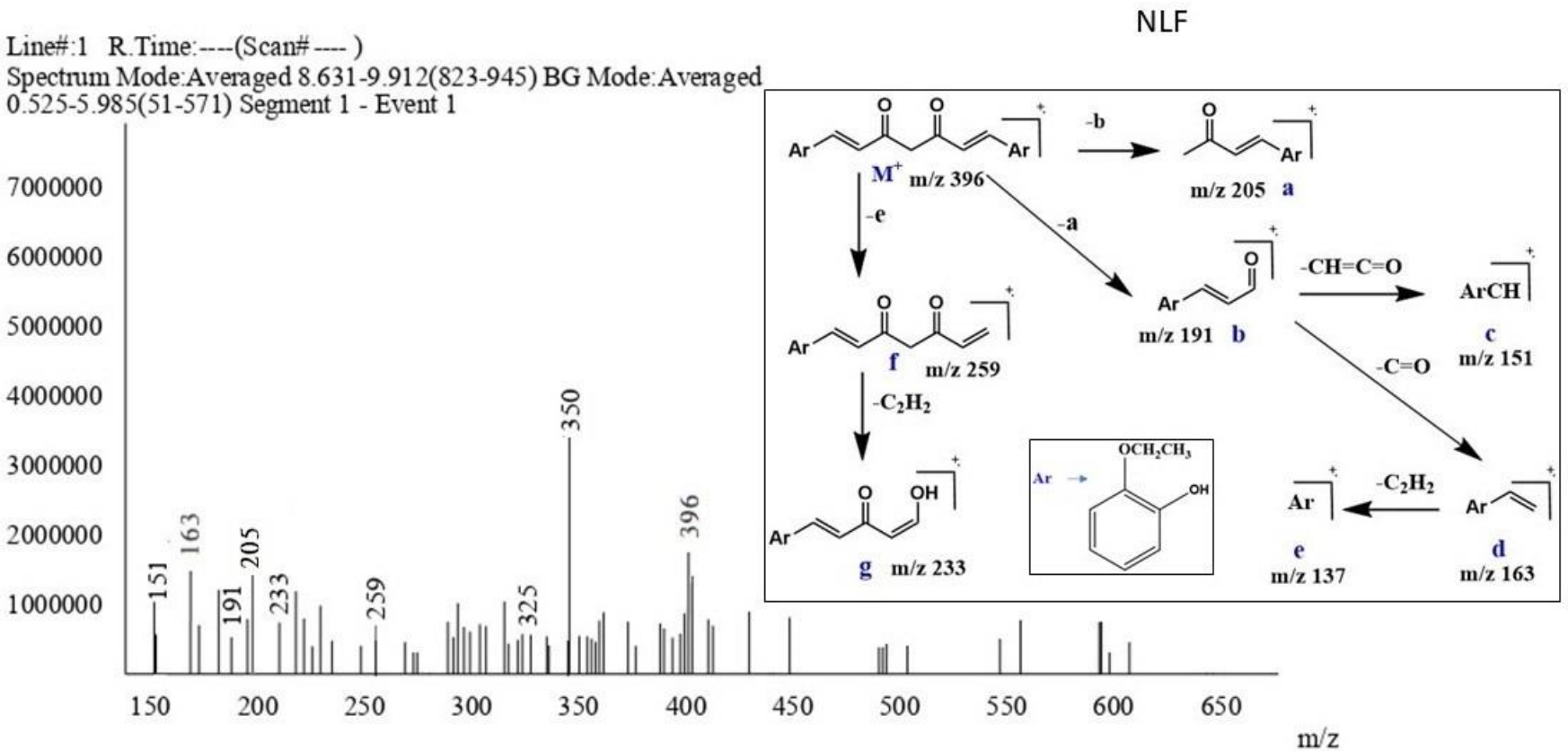

Fig.3.35 The Mass spectrum of NLF

3.5.1.4.2 Synthesis and characterization of $Cu(NLF)_2$ and $Zn(NLF)_2$

3.5.1.4.2.1 Synthesis and characterization of Cu complex of 1,7-bis(3-ethoxy-2-hydroxy phenyl)hepta-1,6-diene-3,5-dione [$Cu(NLF)_2$]

The copper(II) complex of the curcuminoid analogue NLF possessed a molecular weight of 853.23 g/mol and a melting point of 235°C. Elemental analysis indicated carbon, hydrogen, and metal contents of 64.07%, 5.02%, and 7.21%, respectively, which closely corresponded to the theoretical values of 64.67%, 5.43%, and 7.44%. The compound was synthesized with a yield of 72%.

Characterization of $Cu(NLF)_2$

The metal complex $Cu(NLF)_2$ was characterized through various spectroscopic and analytical techniques, such as IR spectroscopy, ^1H NMR, and mass spectrometry. The spectral data obtained from the synthesized complex are summarized and discussed below.

IR Spectrum

The copper(II) complex $Cu(NLF)_2$ exhibited distinctive spectral features confirming the successful coordination of the ligand with the metal ion (**Fig.3.36**). The absence of a significant absorption band in the 1650-1800 cm^{-1} range, particularly the disappearance of the carbonyl peak at 1630 cm^{-1}, along with the appearance of a new band at 1586.0 cm^{-1}, indicated that the enolic proton had been replaced by the metal ion, resulting in the formation of a metal-coordinated carbonyl group. The shift of the carbonyl stretching frequency to 1586.0 cm^{-1} was indicative of chelation, which typically lowers the frequency compared to a free carbonyl group. Additionally, the band at 1548.9 cm^{-1} was attributed to the asymmetric stretching of the C-C-C bond within the aromatic ring, suggesting the presence of an aromatic system. The low-frequency bands at 433.7 cm^{-1} and 402.7 cm^{-1} were assigned to metal-oxygen (M-O) stretching vibrations, confirming the coordination of the metal ion to the oxygen atoms and signifying the formation of a metal-ligand complex.

^{1}HNMR Spectrum

The various proton signals identified in the ^{1}H NMR spectrum of the Cu(II) complex of 1,7-bis(3-ethoxy-2-hydroxy phenyl)hepta-1,6-diene-3,5-dione [$Cu(NLF)_2$] were summarized in **Table 3.30.**

Table 3.30 Proton signals observed in the ^{1}HNMR spectrum of $Cu(NLF)_2$ (Chemical Shifts δ in ppm)

Complex	Methine	Alkenyl	Phenyl	Ethoxy	Hydroxy
$Cu(NLF)_2$	6.92	6.94-7.29	7.05-7.22	4.10-4.16 1.46-1.50	11.05

The ^{1}H NMR spectrum of the $Cu(NLF)_2$ complex provided insights into the chemical environment of the protons upon coordination with the Cu(II) ion (**Fig 3.37**). The methine proton, part of the β-diketone structure, resonated at 6.92 ppm, indicating deshielding due to the electron-withdrawing carbonyl groups and metal coordination. The alkenyl protons appeared between 6.94 and 7.29 ppm, showing slight deshielding from metal-induced stabilization of the π-system. Phenyl protons were observed in the 7.05-7.22 ppm range, reflecting changes in the aromatic ring's electronic environment due to metal interaction. Ethoxy protons (OCH_2CH_3) resonated at 4.10-4.16ppm as a quartet and1.46-1.50 as a triplet, indicating minor interaction with the metal. Hydroxy protons appeared at 11.05 ppm, consistent with free hydroxyl groups, suggesting minimal interaction with the metal. These shifts confirm the successful coordination of the ligand to the Cu(II) ion and the formation of the $Cu(NLF)_2$ complex.

Mass Spectrum

Table 3.31 Molecular ion peaks of $Cu(NLF)_2$

M^+/(M+1)/(M+2) ion	a	b	c	d	e	f	g	h	i	j
853	716	579	442	304	137	458	183	396	122	121

*The alphabets correspond to the fragments given in the fragmentation scheme in**Fig.3.38**

The mass spectrum of the Cu(II) complex of NLF showed an intense molecular ion peak at m/z 853, indicating the intact molecular weight of the compound. The peaks at m/z 579 and 304 corresponded to the loss of two and four Ar groups, respectively, from the molecular ion, where Ar represented the 3-ethoxy-2-hydroxy phenyl group. The peak at m/z 458 was attributed to the $[ML]^+$ fragment, where M was the metal (Cu) and L was the ligand (1,7-bis(3-ethoxy-2-hydroxy phenyl)hepta-1,6-diene-3,5-dione). Additional fragment ions were observed at m/z 716, 442, 137, 183, 396, 122, and 121, supporting the fragmentation patterns and structural components of the $Cu(NLF)_2$ complex. The mass spectrum of $Cu(NLF)_2$ was shown in (**Fig.3.38**)

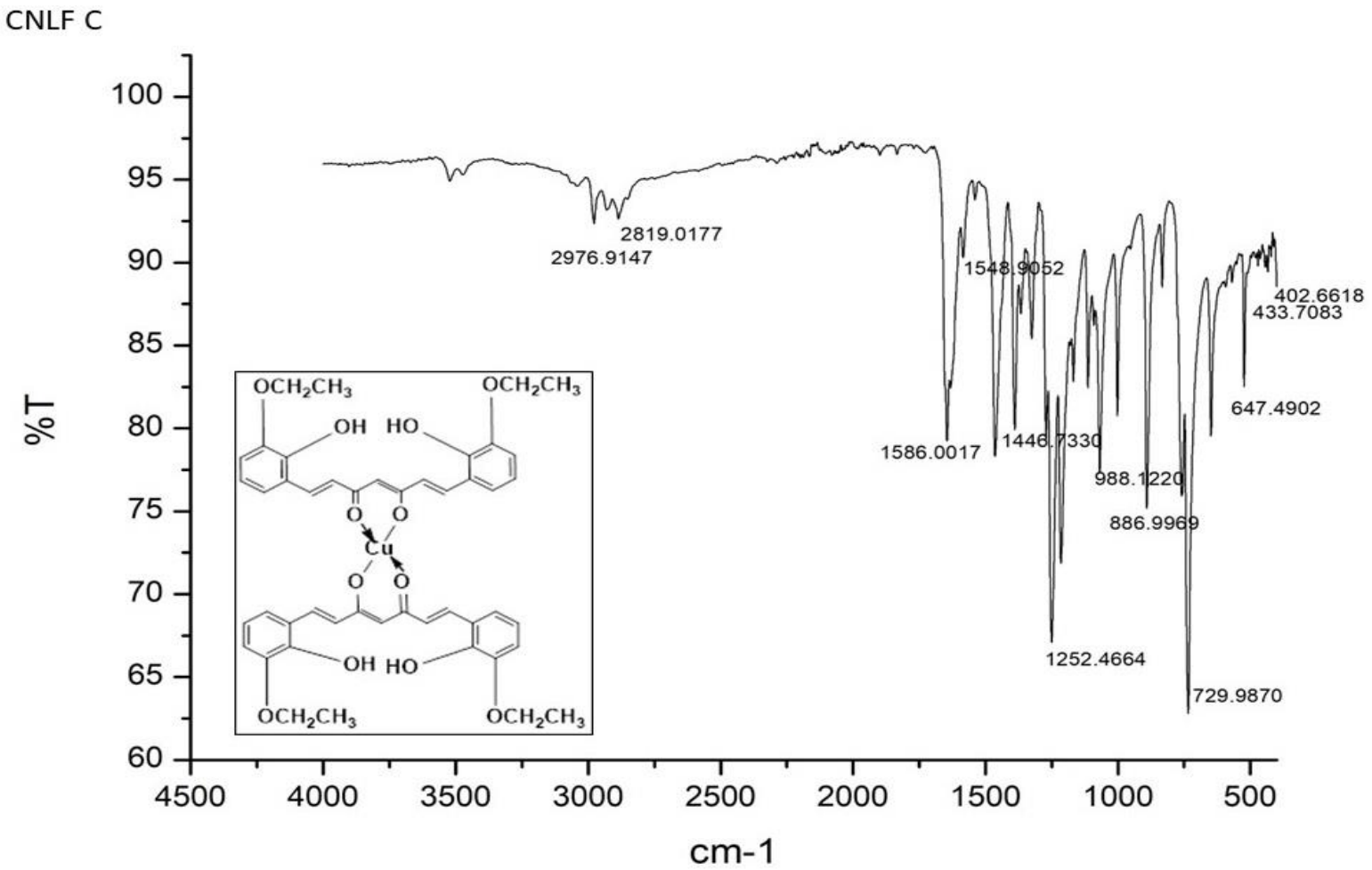

Fig.3.36 The IR spectrum of Cu $(NLF)_2$

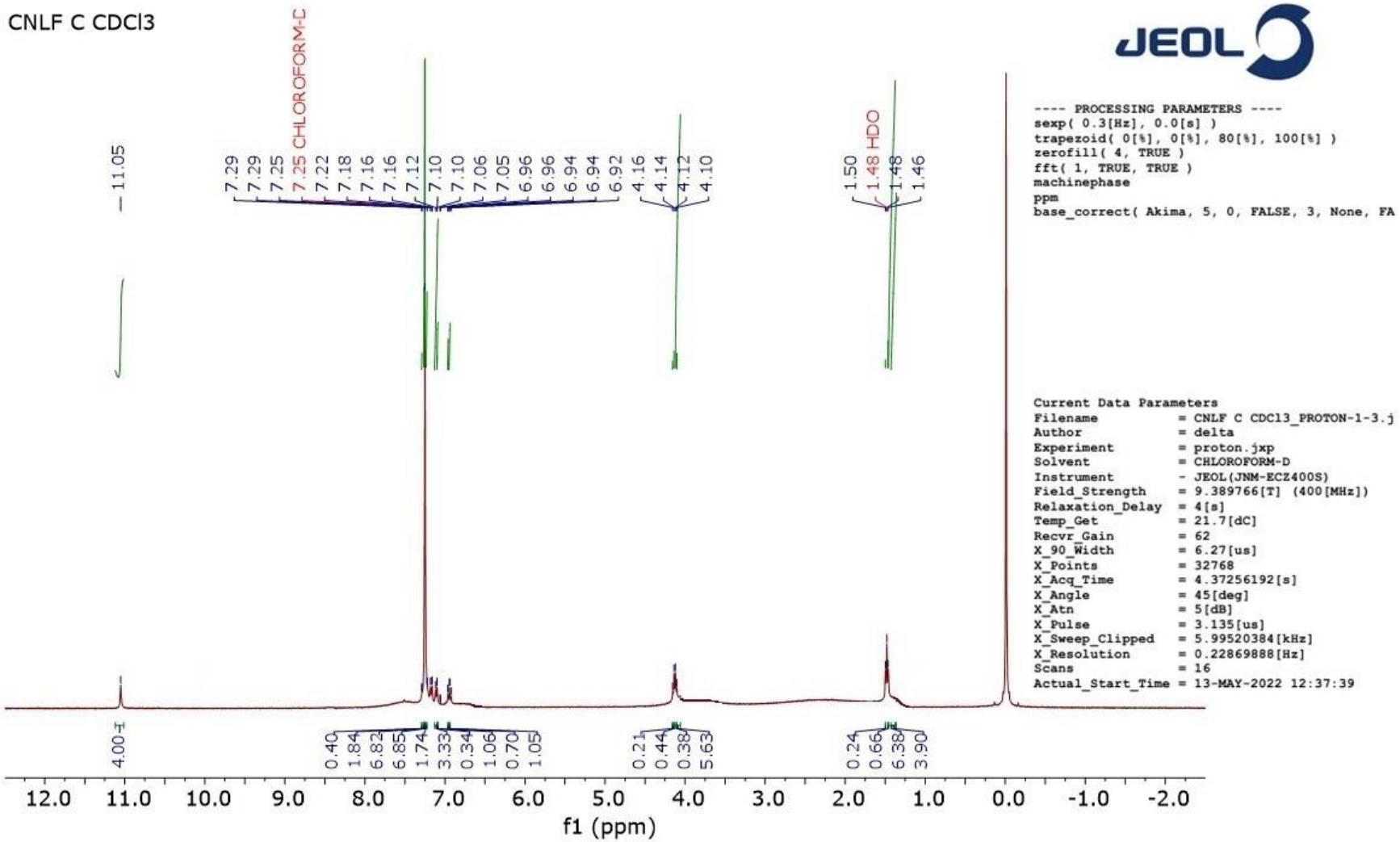

Fig.3.37 The ^{1}H NMR spectrum of Cu $(NLF)_2$

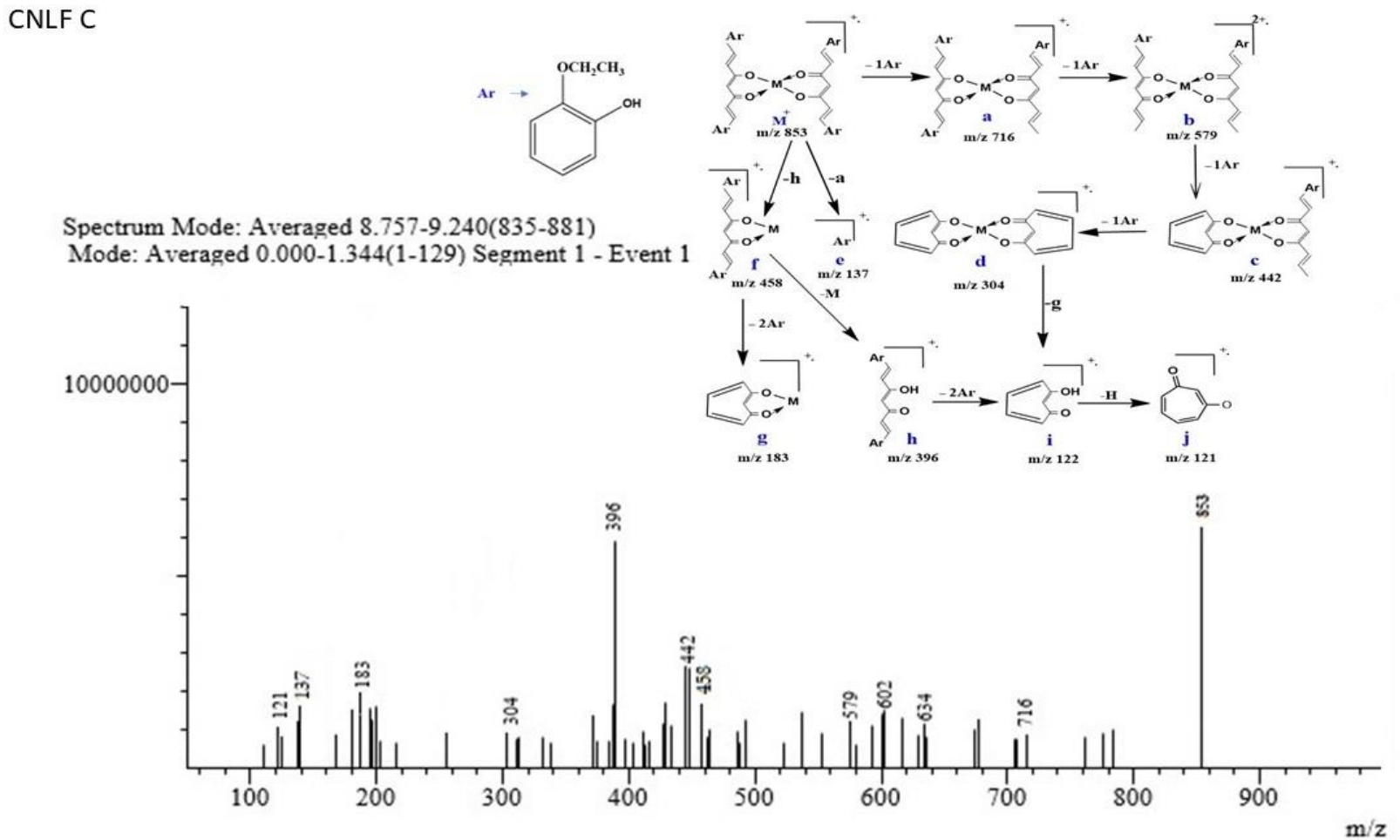

Fig.3.38 The Mass spectrum of Cu $(NLF)_2$

3.5.1.4.2.2 Synthesis and Characterization of Zn complex of 1,7-bis(3-ethoxy-2-hydroxy phenyl)hepta-1,6-diene-3,5-dione [$Zn(NLF)_2$]

The Zn(II) complex of the curcuminoid analogue NLF had a molecular weight of 854.23 g/mol and a melting point of 239°C. Elemental analysis revealed carbon, hydrogen, and metal contents of 64.22%, 5.30%, and 7.24%, respectively, closely aligning with the theoretical values of 64.53%, 5.42%, and 7.64%. The synthesis yielded 75% of the compound.

Characterization of $Zn(NLF)_2$

The metal coordination compound $Zn(NLF)_2$ was systematically characterized by employing an array of spectroscopic and analytical methodologies, including infrared spectroscopy, proton nuclear magnetic resonance (^1H NMR), and mass spectrometry. The spectral data acquired from the synthesized coordination complex are concisely summarized and critically discussed in the subsequent sections.

IR Spectrum

The complex $Zn(NLF)_2$ demonstrated unique spectral characteristics that corroborate the successful coordination of the ligand with the metal ion (**Fig.3.39**). The lack of a prominent absorption band within the 1650-1800 cm^{-1} interval, particularly the elimination of the carbonyl peak at 1630 cm^{-1}, alongside the emergence of a novel band at 1598.4 cm^{-1}, suggested that the enolic proton had been substituted by the metal ion, culminating in the establishment of a metal-coordinated carbonyl moiety. The displacement of the carbonyl stretching frequency to 1598.4 cm^{-1} served as an indicator of chelation, a phenomenon that generally results in a reduction of the frequency relative to that of a free carbonyl group. Furthermore, the band located at 1535.4 cm^{-1} was ascribed to the asymmetric stretching of the C-C-C bond within the aromatic framework, implying the existence of an aromatic system. The low-frequency bands observed at 427.5 cm^{-1} and 415.1 cm^{-1} were designated as metal-oxygen (M-O) stretching vibrations, thereby confirming the coordination of the metal ion with the oxygen atoms and denoting the formation of a metal-ligand complex.

^{1}HNMR Spectrum

The various proton signals identified in the ^{1}H NMR spectrum of the Zn(II) complex of 1,7-bis(3-ethoxy-2-hydroxy phenyl)hepta-1,6-diene-3,5-dione [$Zn(NLF)_2$] were summarized in **Table 3.22**

Table 3.22 Proton signals observed in the ^{1}H NMR spectrum of $Zn(NLF)_2$ (Chemical Shifts δ in ppm)

Complex	Methine	Alkenyl	Phenyl	Ethoxy	Hydroxy
$Zn(NLF)_2$	6.92	6.94-7.29	7.11-7.18	4.10-4.15 1.46-1.50	11.06

The ^{1}H NMR spectrum of the $Zn(NLF)_2$ complex yielded significant information regarding the chemical environment of protons after their coordination with the Zn(II) ion. The methine proton, which is an integral component of the β-diketone framework, exhibited resonance at 6.92 ppm, signifying deshielding attributed to the electron-withdrawing influence of the carbonyl moieties as well as the coordination with the metal ion. The alkenyl protons, detected within the range of 6.94 to 7.29 ppm, displayed a slight deshielding effect, presumably due to the stabilization of the π-electron system induced by the presence of the metal. The phenyl protons manifested within the 7.11-7.18 ppm interval, indicative of alterations in the electronic environment of the aromatic ring as a consequence of metal interaction. Ethoxy protons (OCH_2CH_3) resonated at 4.10-4.15 ppm as a quartet and 1.46 -1.50 ppm as a triplet, indicating minor interaction with the metal. Hydroxy protons were noted at 11.06 ppm, which is consistent with the presence of free hydroxyl groups, thus suggesting negligible interaction with the metal. These chemical shifts corroborate the effective coordination of the ligand to the Zn(II) ion and the subsequent formation of the $Zn(NLF)_2$ complex(**Fig.3.40**).

Mass Spectrum

Table 3.23 Molecular ion peaks of Zn $(NLF)_2$

M^+/(M+1)/(M+2) ion	a	b	c	d	e	f	g	h	i	j
854	717	580	443	305	137	453	184	396	122	121

*The alphabets correspond to the fragments given in the fragmentation scheme in**Fig.3.41**

The mass spectrum of the Zn(II) complex of NLF displayed an intense molecular ion peak at m/z 854, indicating the intact molecular weight of the compound. The peaks at m/z 580 and 305 corresponded to the loss of two and four Ar groups, respectively, from the molecular ion, where Ar represented the 3-ethoxy-2-hydroxy phenyl group. The peak at m/z 453 was attributed to the $[ML]^+$ fragment, where M was the metal (Zn) and L was the ligand 1,7-bis(3-ethoxy-2-hydroxy phenyl)hepta-1,6-diene-3,5-dione. Additional fragment ions were observed at m/z 717, 443, 137, 184, 396, 122, and 121, supporting the fragmentation patterns and structural components of the $Zn(NLF)_2$ complex. The mass spectrum of $Zn(NLF)_2$ is shown in (**Fig.3.41**).

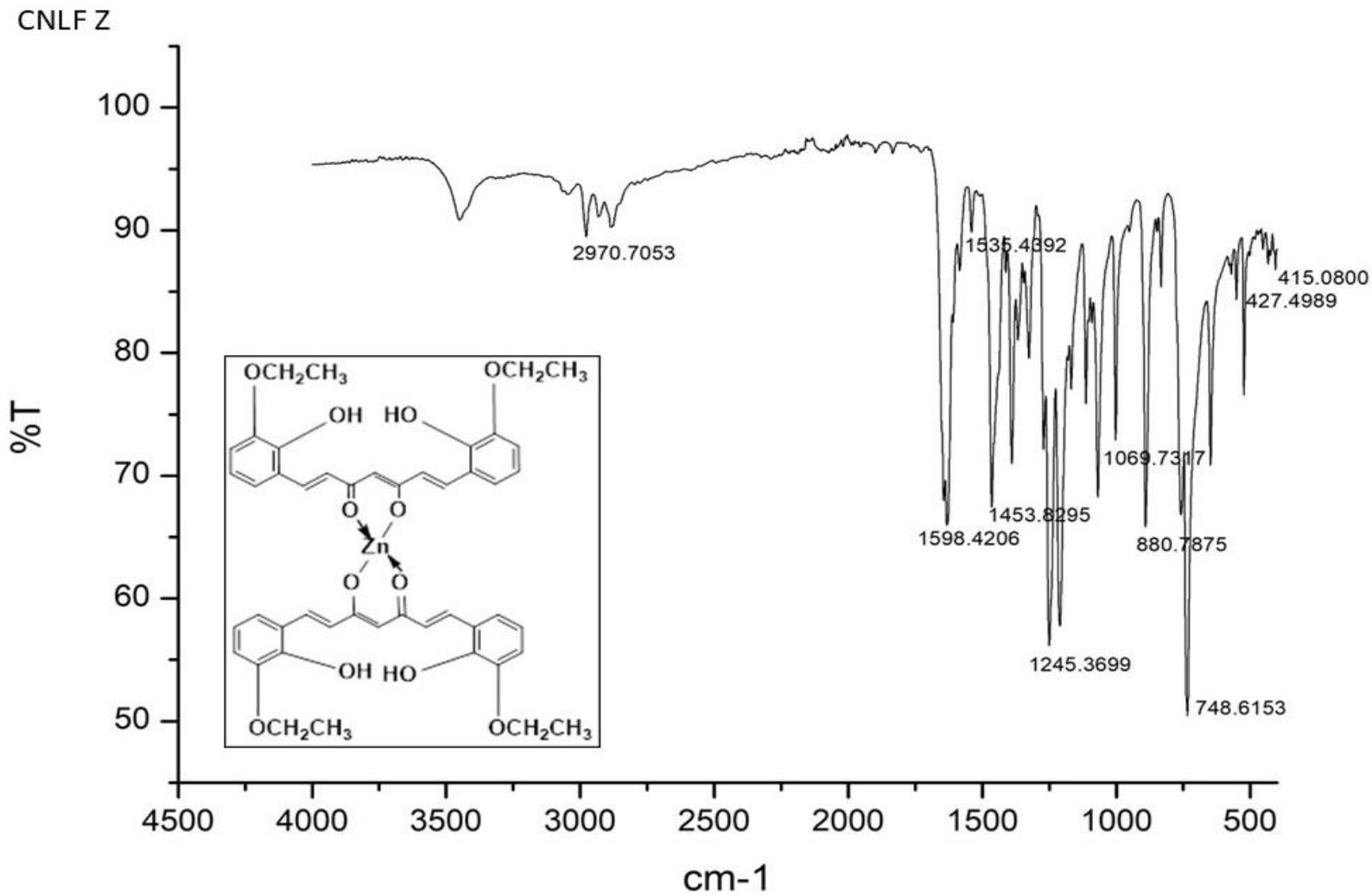

Fig.3.39 The IR spectrum of Zn $(NLF)_2$

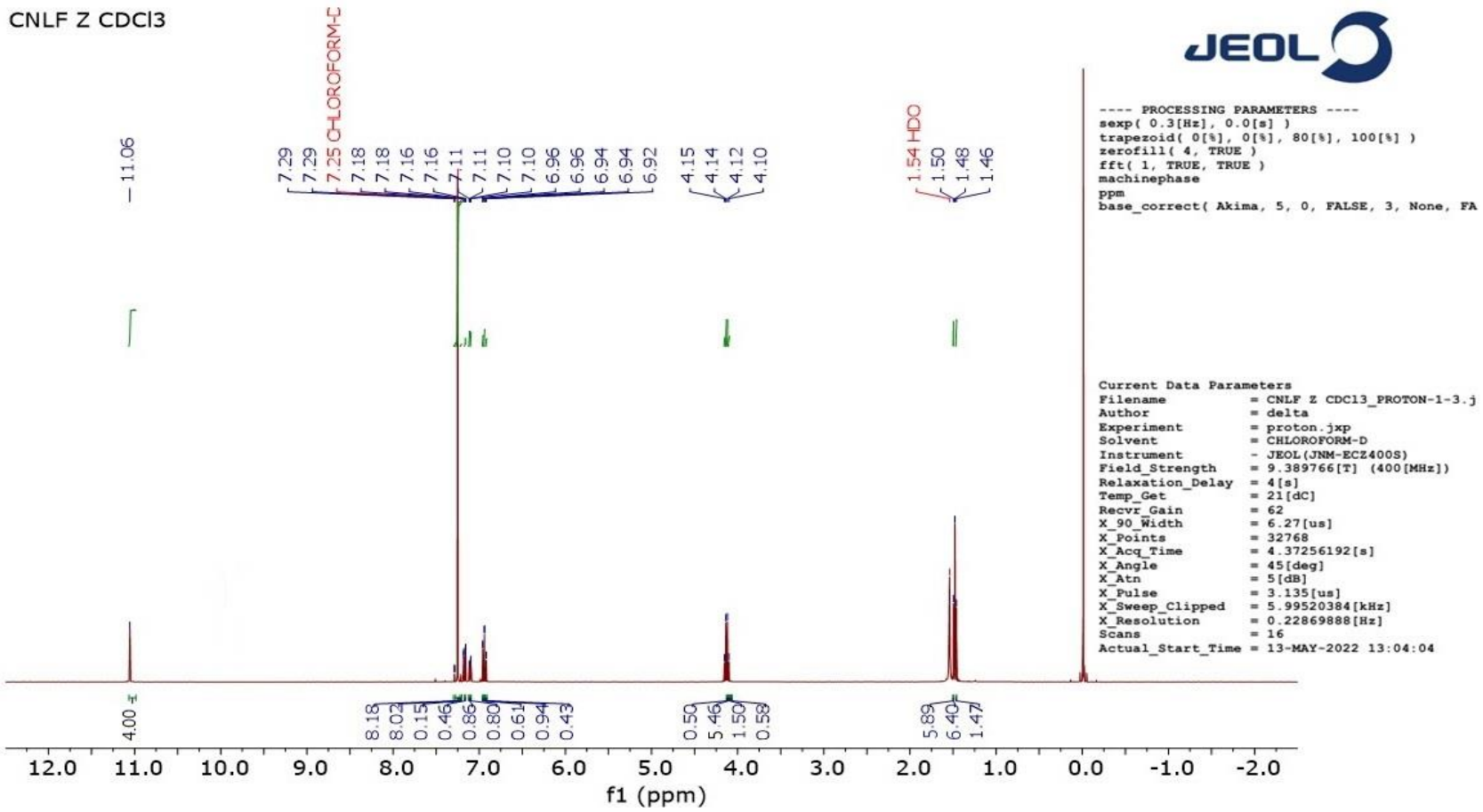

Fig.3.40 The ^{1}H NMR spectrum of Zn $(NLF)_2$

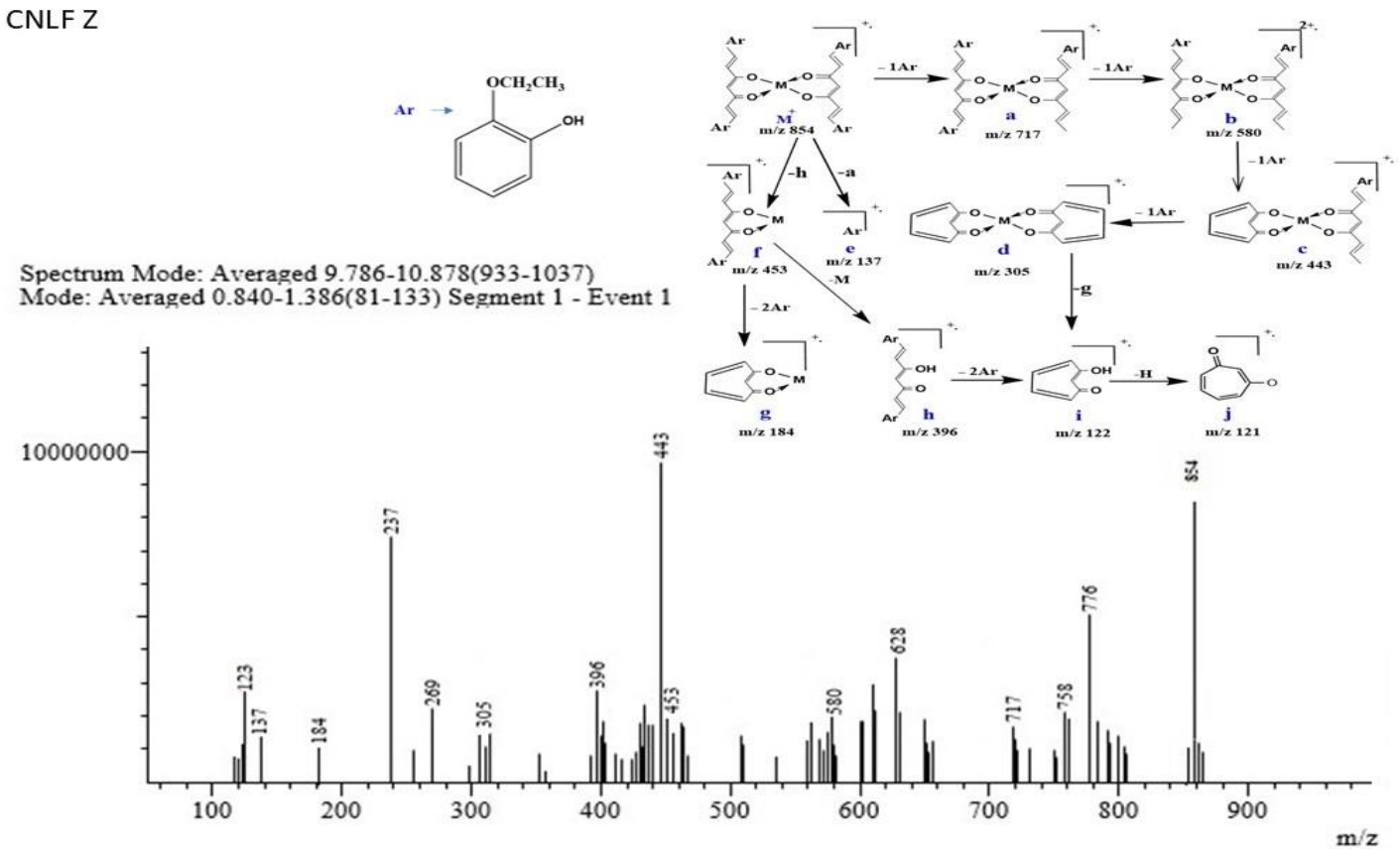

Fig.3.41 The Mass spectrum of Zn $(NLF)_2$

3.5.1.5. Synthesis and characterization of (1E,6E)-1,7-bis(4-hydroxy-3,5-dimethyl phenyl)hepta-1,6-diene-3,5-dione(NLG)

3.5.1.5.1 Synthesis and characterization of NLG

1,7-Bis(4-hydroxy-3,5-dimethylphenyl)hepta-1,6-diene-3,5-dione (NLG) was synthesized through the condensation of 4-hydroxy-3,5-dimethylbenzaldehyde (0.01 M) with an acetylacetone–boron complex and B_2O_3 in ethyl acetate (7.5 mL). The reaction was carried out in the presence of tri-sec-butyl borate (5.4 mL) and n-butylamine (0.1 mL) as a condensing agent. The synthesized product exhibited a melting point of 291°C and a molecular weight of 364 g/mol, with a yield of approximately 94%. Elemental analysis showed carbon and hydrogen contents of 74.89% and 5.89%, respectively, closely aligning with the theoretical values of 75.8% and 6.64%.

Characterization of NLG

The synthesized compound NLG was characterized using various spectroscopic techniques, including IR, ^{1}H NMR, ^{13}C NMR, and mass spectrometry. The spectral data obtained from these analyses are detailed below.

IR Spectrum

The infrared peaks observed for 1,7-bis (4-hydroxy-3,5-dimethylphenyl) hepta -1,6- diene -3,5- dione (NLG) were elucidated through an analysis of the customary absorption intervals linked to various functional groups. The potential IR spectra are outlined in the provided **Table 3.24**

Table 3.24 Possible IR assignments of NLG

Wavenumbers (in cm^{-1})	Possible IR Assignments
2929.4	ν Enolic
1620.9	ν(C=O)
1571.6	ν(C=C) Phenyl
1479.9	ν_{as}(C-C-C)
1128.2	νβ (C-H)
958.7	ν(CH=CH) trans

The enolic O-H stretch, typically found between 3200-3550 cm^{-1}, was observed at a lower frequency of 2929.4 cm^{-1}. This shift suggested the presence of strong

intramolecular hydrogen bonding or conjugation with the carbonyl group, confirming the enol form. The carbonyl (C=O) stretch, usually seen between 1650-1750 cm^{-1}, appeared at 1620.9 cm^{-1}. This lower frequency was attributed to conjugation with adjacent double bonds or resonance effects, consistent with the behaviour expected in a conjugated system like NLG. The C=C stretching in aromatic rings, typically occurring between 1450-1600 cm^{-1}, was detected at 1571.6 cm^{-1}, confirming the presence of a phenyl ring and its conjugation with the carbonyl group. The asymmetric stretching of the C-C-C bond in an aromatic system, usually observed between 1400-1500 cm^{-1}, was identified at 1479.9 cm^{-1}, supporting the existence of aromatic rings in the structure. The in-plane bending (β) of C-H bonds in aromatic systems, generally found between 1000-1300 cm^{-1}, was seen at 1128.2 cm^{-1}, indicating the presence of C-H bonds in the aromatic rings. Lastly, the C-H out-of-plane bending in trans-alkenes, which typically occurs around 960-970 cm^{-1}, was observed at 958.7 cm^{-1}. This frequency aligned with the trans configuration of the double bonds in the compound, confirming the presence of the CH=CH trans group. These spectral assignments were consistent with the expected functional groups and structural features of NLG, supporting the accuracy of the IR data (**Fig 3.42).**

^{1}HNMR Spectrum

The proton signals in the ^{1}H NMR spectrum of NLG exhibited a close correspondence with the expected chemical shifts for enolic, methine, alkenyl, phenyl, and hydroxy protons. A detailed listing of the different proton signals identified in the spectrum can be found in **Table 3.25**

Table 3.25 Proton signals observed in the ^{1}H NMR spectrum of NLG (Chemical Shifts δ ppm)

Compound	Enolic	Methine	Alkenyl	Phenyl	Hydroxy	Methyl
NLG	9.79	6.32	7.11-7.53	7.09-7.12	7.56	2.29,2.30

The enolic proton, typically found between 9-12 ppm, resonated at 9.79 ppm, indicating the presence of an enolic -OH group likely involved in intramolecular hydrogen bonding. The methine proton at 6.32 ppm aligned with the expected range for protons in a conjugated diene system, generally between 5.5-7.5 ppm. The alkenyl protons observed between 7.11-7.53 ppm, were consistent with the expected range for protons attached to sp^2 hybridized carbons in a conjugated system. The phenyl protons, resonating between

7.09-7.12 ppm, fell within the typical range of 7-8 ppm for aromatic protons, confirming their correct placement. The hydroxy proton at 7.56 ppm, within the 4-12 ppm range, suggested involvement in hydrogen bonding or interaction with the aromatic system. The methyl protons at 2.30 ppm aligned with the expected range for methyl groups attached to aromatic rings, confirming their position in the structure. These chemical shifts collectively supported the expected proton environments in the ^{1}H NMR spectrum of NLG as brought out in **Fig.3.43**

^{13}C NMR Spectra

The interpretation of the ^{13}C NMR spectral data for NLG confirmed the accuracy of the chemical shift ranges. A comprehensive breakdown of the ^{13}C NMR spectrum of NLG can be found in **Table 3.26.**

Table 3.26 ^{13}C NMR spectral data of NLG (Chemical Shifts δ ppm)

C_1	C_2,$C_{2'}$	C_3,$C_{3'}$	C_4,$C_{4'}$	C_5,$C_{5'}$	C_6,$C_{6'}$
100.71	191.51	131.07	140.29	129.46	128.85
C_7,$C_{7'}$	C_8,$C_{8'}$	C_9,$C_{9'}$	C_{10},$C_{10'}$	C_{11},$C_{11'}$	C_{12},$C_{12'}$
123.65	158.11	120.00	123.79	15.90	16.00

The signal at 100.71 ppm corresponded to C_1, which, as part of a β-diketone structure, resonated around 100-120 ppm, indicating its enolic form conjugated with adjacent double bonds. The carbonyl carbons at C_2 and $C_{2'}$ showed a shift of 191.51 ppm, consistent with the expected range of 190-210 ppm for conjugated diketone structures. Carbons at C_3 and $C_{3'}$ exhibited shifts of 131.07 ppm, aligning with the range of 120-140 ppm for alkenyl groups in a conjugated system. The carbon at C_4 and C_4', with a shift of 140.29 ppm, was influenced by its adjacency to an aromatic ring and conjugation with an alkenyl chain and carbonyl groups. This shift fell within the expected range of 130-150 ppm for carbons in such an environment, reflecting the combined effects of aromatic substitution, conjugation, and functional groups. The shifts at C_5 and $C_{5'}$ (129.46 ppm) and C_6 and $C_{6'}$ (128.85 ppm) were typical for aromatic carbons, within the 120-135 ppm range. The carbon at C_7 and $C_{7'}$, with a shift of 123.65 ppm, was consistent with the expected values for an aromatic carbon adjacent to a methyl group and near a hydroxyl group. The shift at 158.11 ppm for C_8 and $C_{8'}$ indicated the presence of a phenolic group, as expected

for carbons in an aromatic ring with -OH substitution. The carbon at C_9 and $C_{9'}$, showing a shift of 120 ppm, reflected the typical behaviour for an aromatic carbon influenced by electron-donating and electron-withdrawing groups. The shifts at C_{10} and $C_{10'}$ (123.79 ppm), and C11 and C12 (15.90 ppm and 16.00 ppm, respectively), were consistent with the expected values for aromatic carbons and methyl groups attached to aromatic rings. These observations confirmed the accuracy of the ^{13}C NMR data for NLG (**Fig.3.44**).

Mass Spectrum

In the mass spectrum of NLG, prominent molecular ion peaks were observed, confirming the molecular weight of the compound. Key peaks in the spectrum were accounted for by the fragmentation pattern detailed in **Fig.3.45**. The corresponding values are summarized in **Table 3.27**.

Table 3.27 Molecular ion peaks of NLG

M^+/M+1 Ion	**a**	**b**	**c**	**d**	**e**	**f**	**g**
365	189	175	135	147	121	243	217

*The alphabets correspond to the fragments given in the fragmentation scheme in**Fig.3.45**

In the mass spectrum of NLG, the ion peak representing the molecule was prominently detected at 365, thereby confirming the molecular weight of the compound. Noteworthy fragment ion peaks observed included: the peak at 175 assigned to the $[C_{11}H_{11}O_2]^+$ ion fragment; the peak at 147 corresponding to the ion $[C_{10}H_{1O}O]^+$; and the peak at 243 attributed to the fragment $[C_{15}H_{15}O_3]^+$. Furthermore, the peak at 217 was linked to the ion $[C_{13}H_{13}O_3]^+$. These observed fragment ions are consistent with the anticipated patterns of fragmentation for NLG.

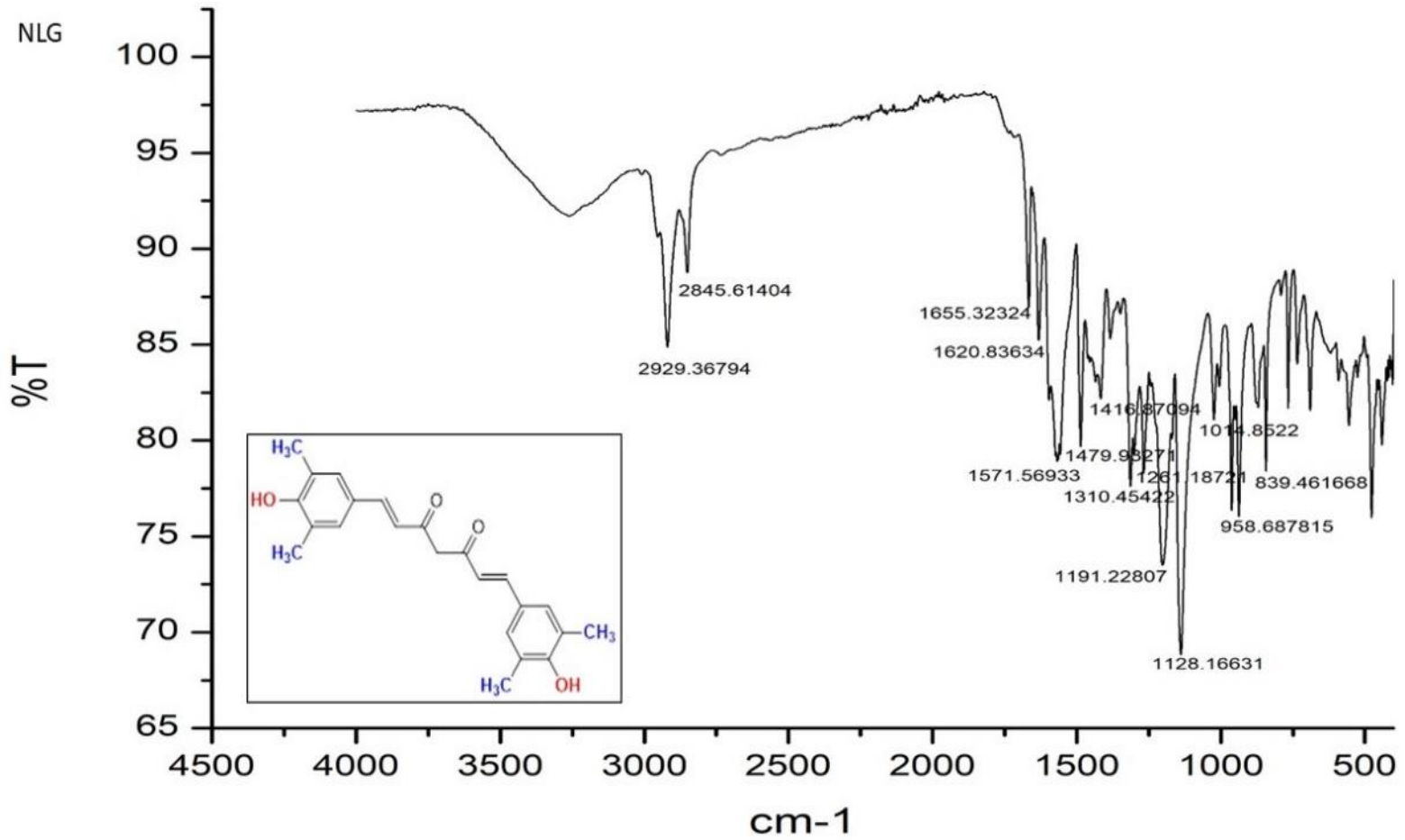

Fig.3.42 The IR spectrum of NLG

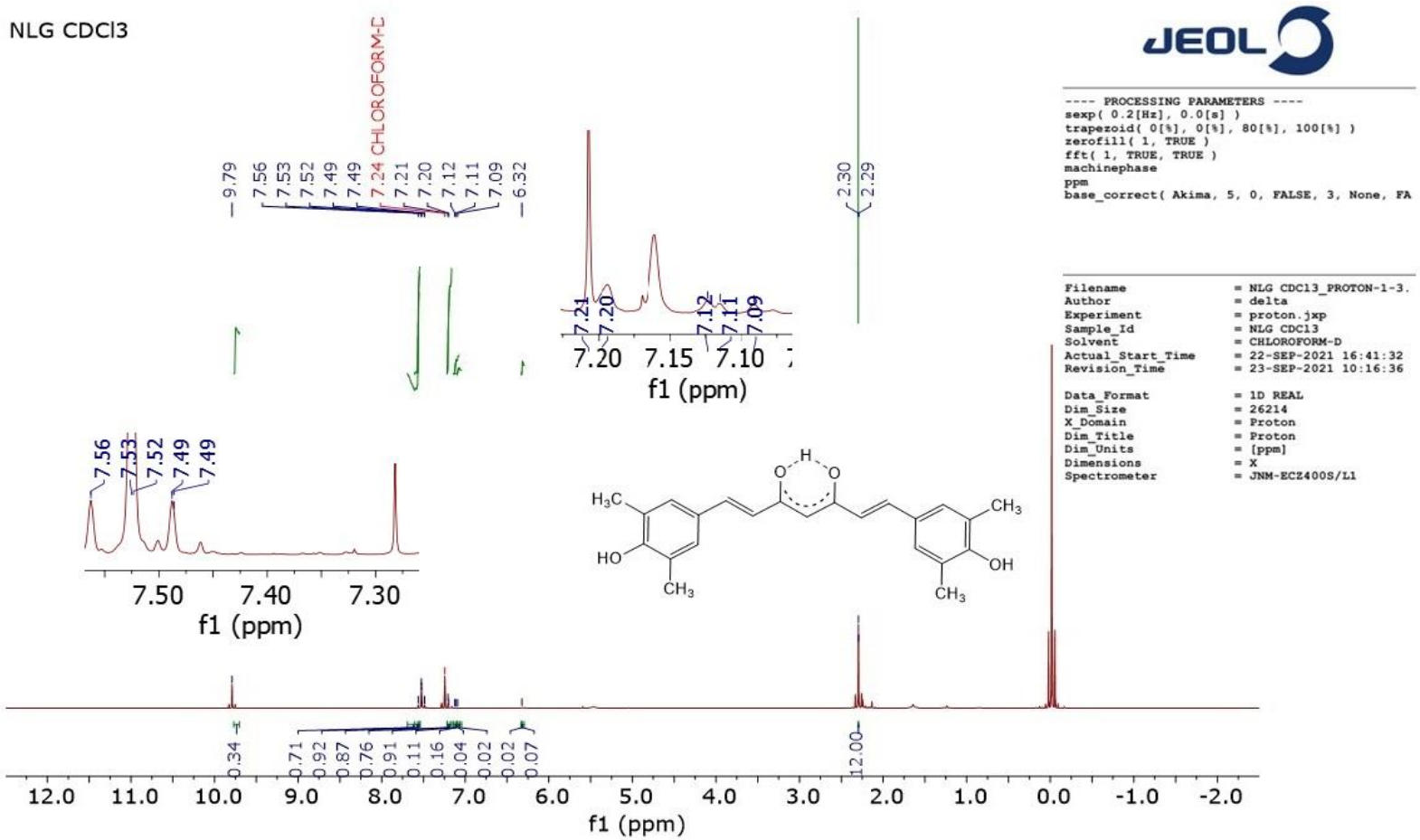

Fig.3.43 The ^{1}H NMR spectrum of NLG

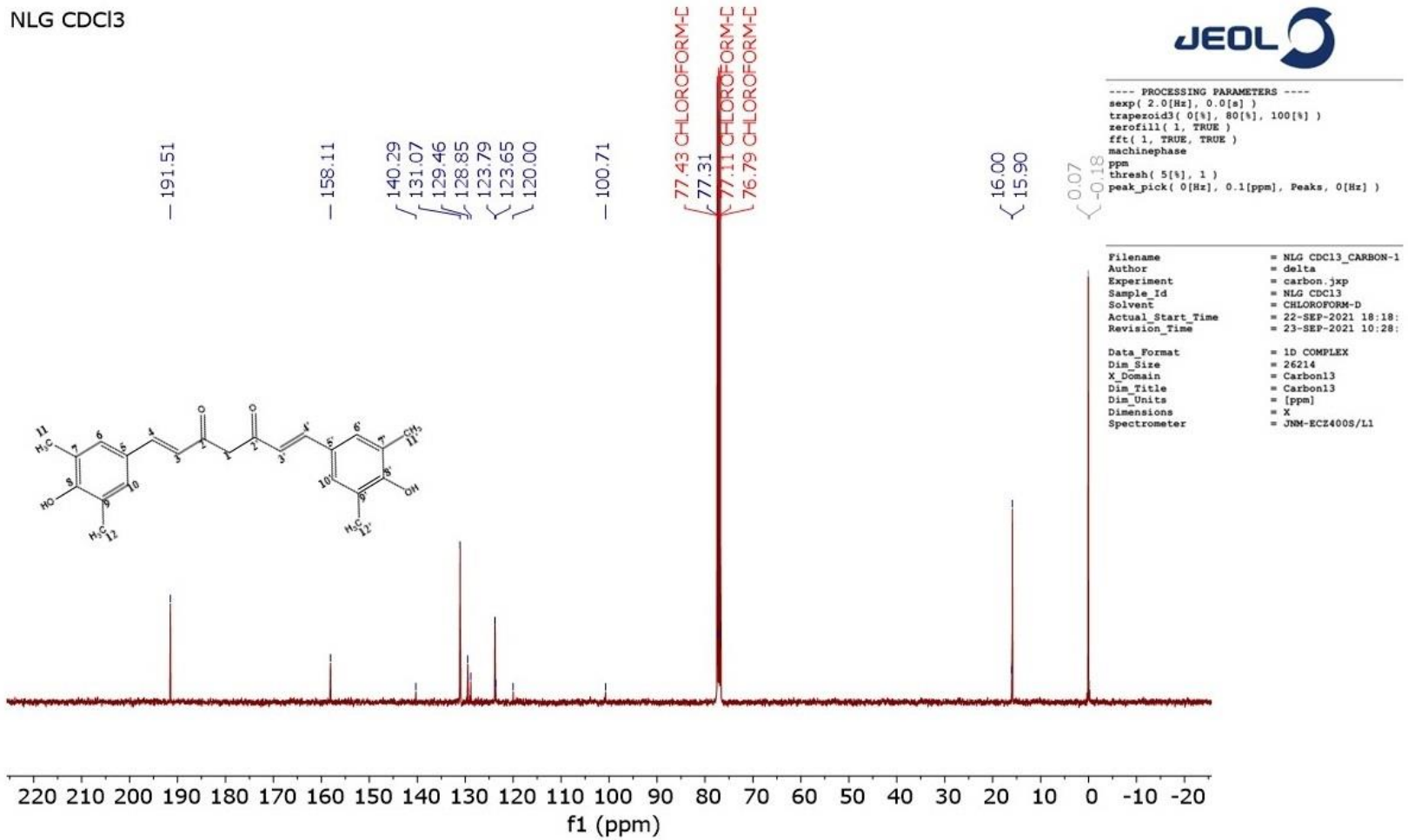

Fig.3.44 The ^{13}CNMR spectrum of NLG

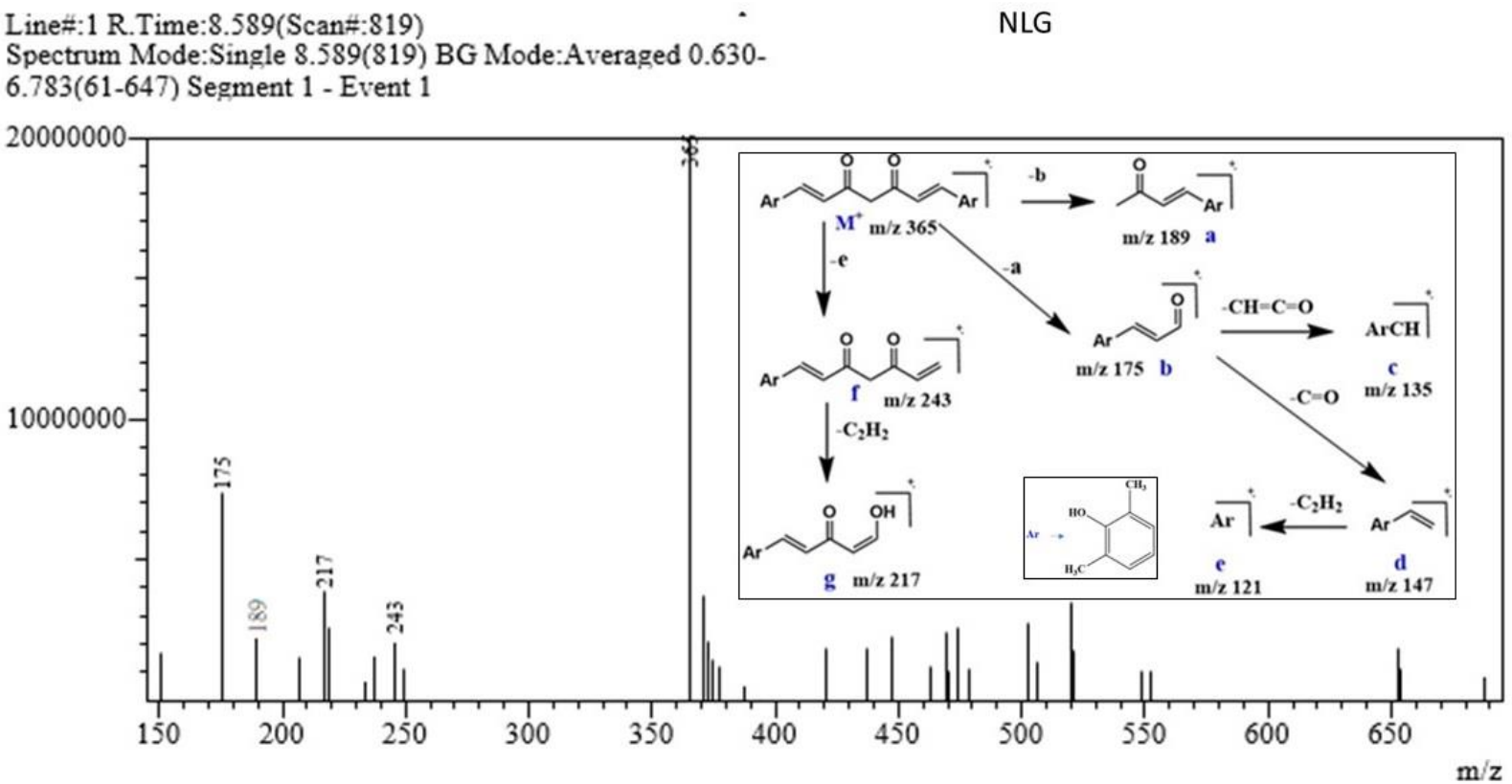

Fig.3.35 The Mass spectrum of NLG

3.5.1.5.2 Synthesis and characterization of $Cu(NLG)_2$ and $Zn(NLG)_2$

3.5.1.5.2.1 Synthesis and characterization of Cu complex of 1,7-bis (4-hydroxy-3,5-dimethyl phenyl) hepta-1,6-diene-3,5-dione [$Cu(NLG)_2$]

The copper(II) complex of the curcuminoid analogue NLG had a molecular weight of 789.25 g/mol and a melting point of 301°C. Elemental analysis revealed carbon, hydrogen, and metal contents of 69.32%, 5.29%, and 8.15%, respectively, closely aligning with the theoretical values of 69.9%, 5.87%, and 8.04%. The compound was obtained with a yield of 74%.

Characterization of $Cu(NLG)_2$

The metal complex $Cu(NLG)_2$ was characterized through various spectroscopic and analytical techniques, such as IR spectroscopy, ^1H NMR, and mass spectrometry. The spectral data obtained from the synthesized complex are summarized and discussed below.

IR Spectrum

The complex $Cu(NLG)_2$ demonstrated distinctive spectroscopic characteristics that substantiated the effective coordination of the ligand with the metal ion. Importantly, the lack of a prominent absorption band within the 1650-1800 cm^{-1} region, particularly the elimination of the carbonyl peak at 1630 cm^{-1}, in conjunction with the appearance of a novel band at 1586.0 cm^{-1}, signified that the enolic proton had been substituted by the metal ion, resulting in the establishment of a metal-coordinated carbonyl moiety. The displacement of the carbonyl stretching frequency to 1586.0 cm^{-1} was indicative of chelation, which generally reduces the frequency in comparison to that of an uncoordinated carbonyl group. Moreover, the band observed at 1547.9 cm^{-1} was ascribed to the asymmetric stretching of the C-C-C bond within the aromatic framework, implying the existence of an aromatic system. Low-frequency bands positioned at 459.4 cm^{-1} and 408.9 cm^{-1} were designated to metal-oxygen (M-O) stretching vibrations, thereby further validating the coordination of the metal ion to the oxygen atoms and denoting the formation of a metal-ligand complex (**Fig.3.46**).

^{1}HNMR Spectrum

The distinct proton signals detected within the ^{1}H NMR spectrum of the Cu(II) complex of 1,7-bis(4-hydroxy-3,5-dimethyl phenyl)hepta-1,6-diene-3,5-dione [$Cu(NLG)_2$] have been meticulously compiled in **Table 3.28**

Table 3.28 Proton signals observed in the ^{1}HNMR spectrum of $Cu(NLG)_2$ (Chemical Shifts δ in ppm)

Complex	Methine	Alkenyl	Phenyl	Hydroxy	Methyl
$Cu(NLG)_2$	6.78	7.17-7.57	7.53	9.80	2.30

The ^{1}HNMR spectrum of the Cu(II) complex of 1,7-bis(4-hydroxy-3,5-dimethylphenyl)hepta-1,6-diene-3,5-dione [$Cu(NLG)_2$] revealed key insights into the proton environments upon coordination with the metal ion(**Fig 3.47**). The methine proton resonated at 6.78 ppm, characteristic of its position adjacent to carbonyl groups in the β-diketone structure. The electron-withdrawing nature of these groups caused deshielding, resulting in the downfield shift within the typical range of 6.5–7.5 ppm observed in metal-coordinated β-diketones. The alkenyl protons, which resonated between 7.17 and 7.57 ppm, were influenced by the conjugated diene system and metal coordination, leading to slight deshielding that was consistent with expected shifts for alkenyl protons in similar complexes. The phenyl protons, found at 7.53 ppm, experienced downfield shifts due to the influence of electron-donating methyl groups at the meta positions and coordination with the metal ion, aligning with the typical range for aromatic protons in substituted benzene rings. The significant downfield shift of the hydroxy proton to 9.80 ppm in [$Cu(NLG)_2$] was explained by the indirect influence of Cu(II) coordination through the carbonyl groups. Although the hydroxy group did not directly coordinate with Cu(II), the overall electronic environment and potential conformational changes induced by metal coordination led to a significant downfield shift in the hydroxy proton. This shift reflected the complex interplay of electronic effects within the metal-ligand coordination sphere. The methyl protons resonated at 2.30 ppm, consistent with the expected shifts for methyl groups attached to an aromatic ring, with the shielding effect of the π-electron system playing a role. These observed chemical shifts corroborated the successful coordination of the ligand

to the Cu(II) ion, with each proton environment aligning well with reported values for similar metal complexes, confirming the correct interpretation of the spectrum.

Mass Spectrum

Table 3.29 Molecular ion peaks of Cu $(NLG)_2$

M^+/(M+1)/(M+2) ion	**a**	**b**	**c**	**d**	**e**	**f**	**g**	**h**	**i**	**j**
789	688	547	424	304	121	426	183	364	122	121

*The alphabets correspond to the fragments given in the fragmentation scheme in**Fig.3.48**

The mass spectrum of the Cu(II) complex of NLG exhibited a prominent molecular ion peak at m/z 789, reflecting the intact molecular weight of the compound. Fragmentation patterns revealed peaks at m/z 547 and 304, corresponding to the loss of two and four 4-hydroxy-3,5-dimethylphenyl groups, respectively, from the molecular ion. A peak at m/z 426 was identified as the $[ML]^+$ fragment, where M denotes the metal (Cu) and L represents the ligand 1,7-bis(4-hydroxy-3,5-dimethyl phenyl)hepta-1,6-diene-3,5-dione. Additional fragment ions at m/z 688, 424, 121, 183, 364, 122, and 121 further supported the observed fragmentation patterns and structural components of the $Cu(NLF)_2$ complex, as depicted in **Fig 3.48.**

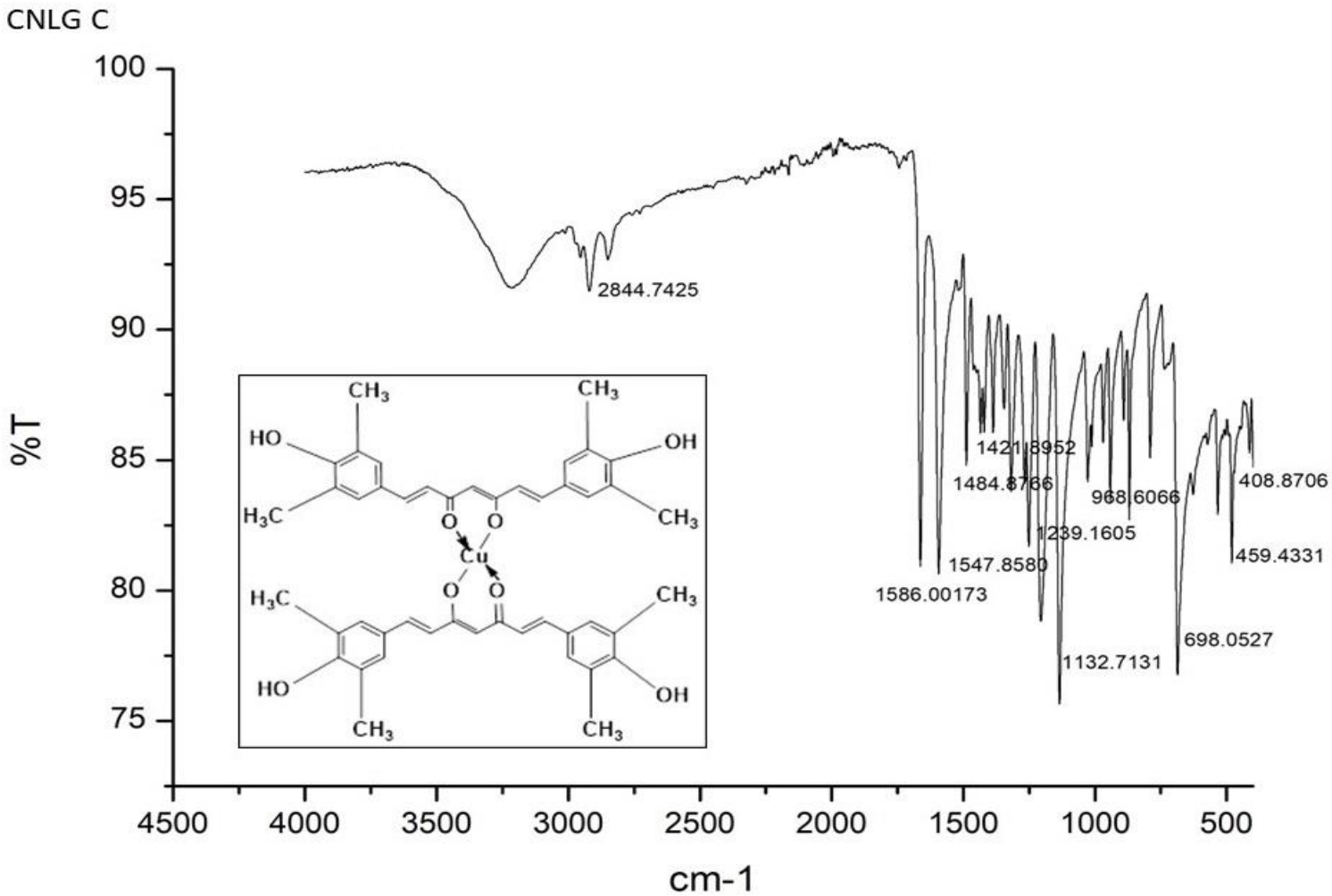

Fig.3.46 The IR spectrum of Cu $(NLG)_2$

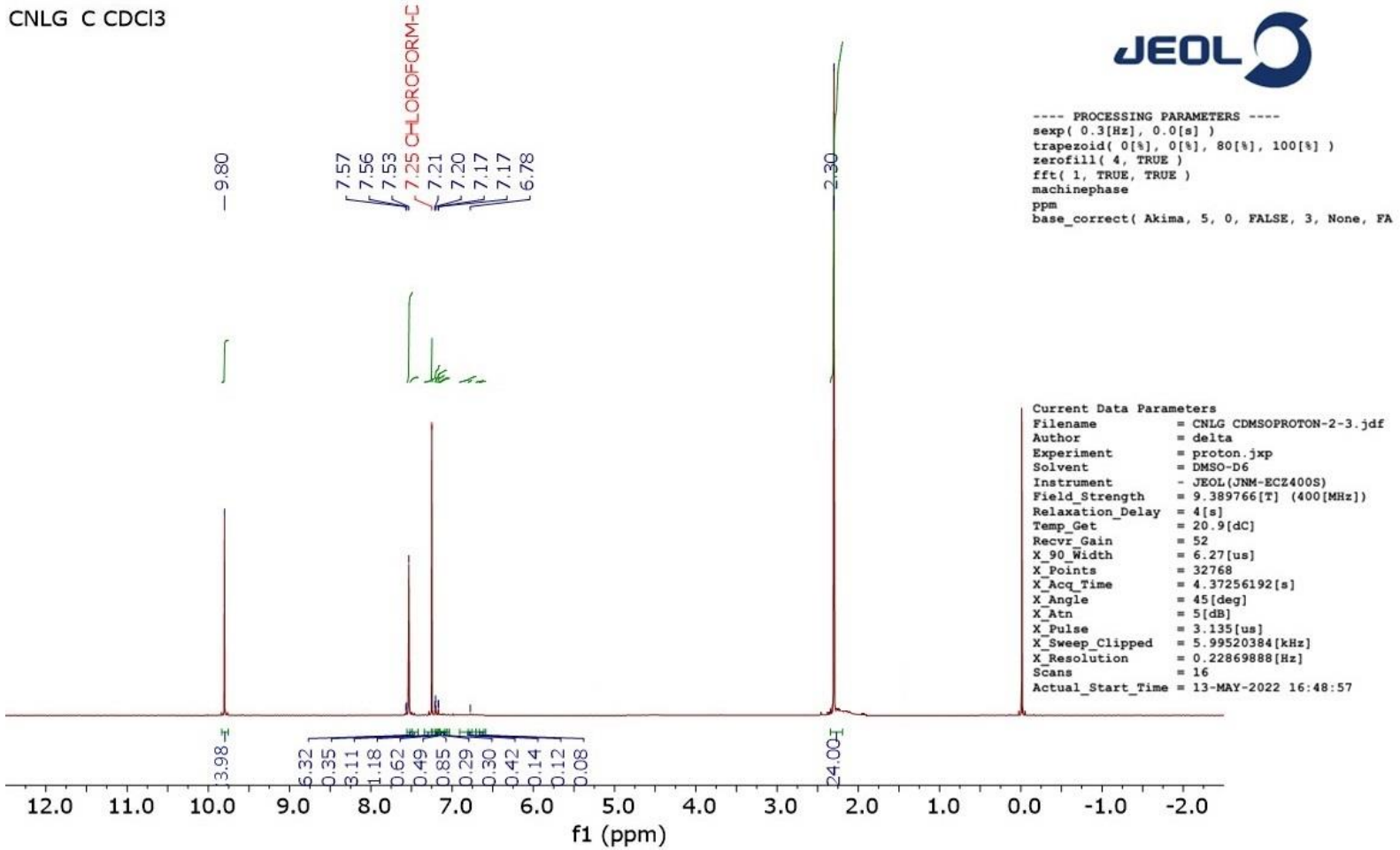

Fig.3.47 The ^{1}H NMR spectrum of Cu $(NLG)_2$

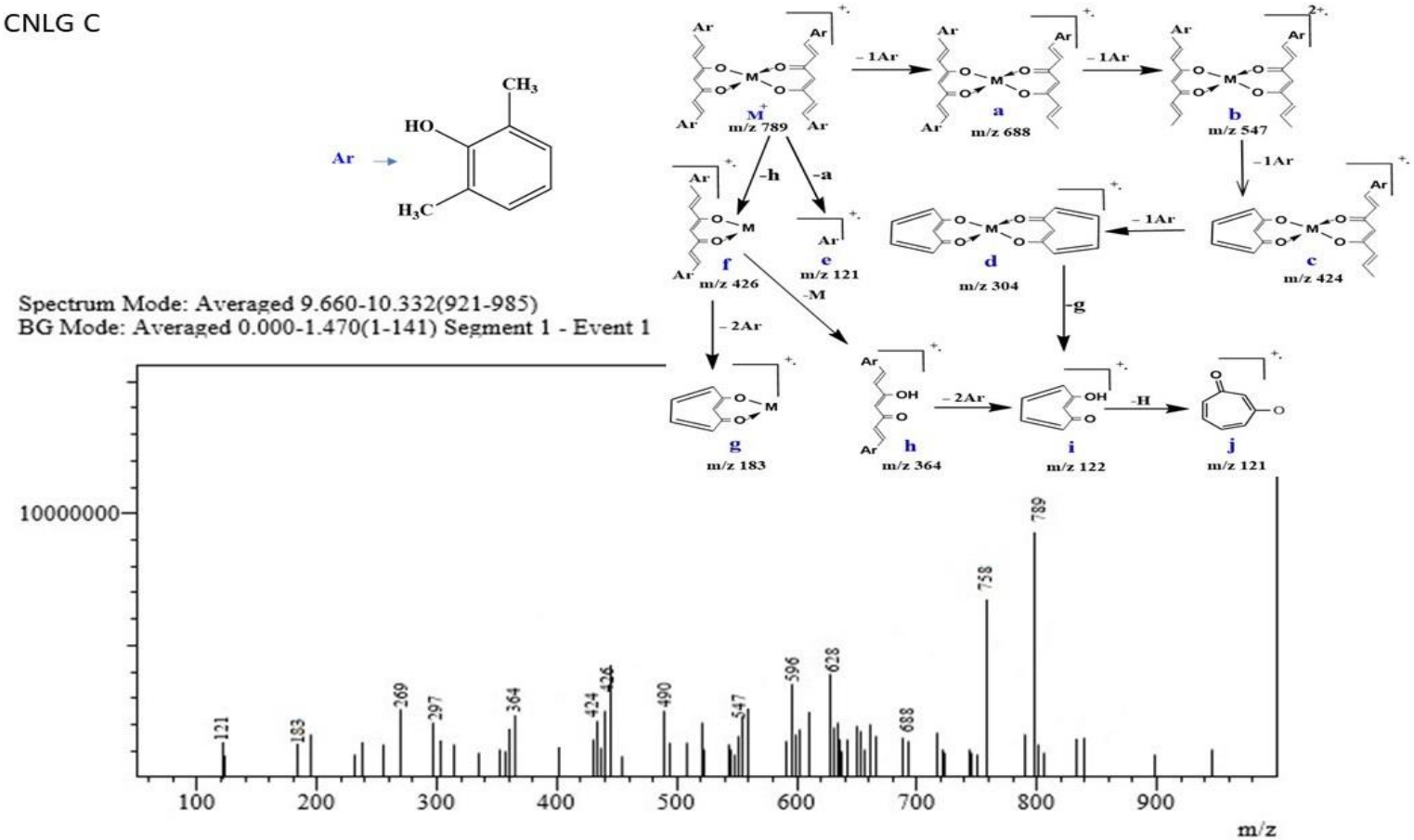

Fig.3.48 The Mass spectrum of Cu (NLG)

3.5.1.5.2.2 Synthesis and Characterization of Zn complex of 1,7-bis(4-hydroxy-3,5-dimethyl phenyl)hepta-1,6-diene-3,5-dione[Zn(NLG)2]

The Zn(II) complex of the curcuminoid analogue NLG had a molecular weight of 790.25 g/mol and a melting point of 305°C. Elemental analysis showed carbon, hydrogen, and metal contents of 69.45%, 5.56%, and 8.03%, respectively, closely matching the theoretical values of 69.74%, 5.85%, and 8.25%. The synthesis achieved a 76% yield.

Characterization of Zn(NLG)2

The coordination compound $Zn(NLG)_2$ was systematically evaluated utilizing a range of spectroscopic and analytical methodologies, including infrared spectroscopy, proton nuclear magnetic resonance (^{1}H NMR), and mass spectrometry. The spectral information acquired from the synthesized coordination compound is encapsulated and analyzed in the subsequent discussion.

IR Spectrum

The $Zn(NLG)_2$ complex exhibited key spectroscopic features confirming successful ligand coordination (**Fig.3.49**). The absence of the carbonyl peak at 1630 cm^{-1} and the emergence of a new band at 1592.2 cm^{-1} indicated the replacement of the enolic proton by the metal ion, forming a metal-coordinated carbonyl group. This shift, typical of chelation, was accompanied by a band at 1547.9 cm^{-1}, attributed to asymmetric C-C-C stretching in the aromatic ring. Additionally, low-frequency bands at 459.4 cm^{-1} and 408.9 cm^{-1} corresponded to metal-oxygen (M-O) stretching, further validating the formation of the metal-ligand complex.

^{1}HNMR Spectrum

The unique proton resonances observed in the ^{1}H NMR spectrum of the Zn(II) complex of 1,7-bis(4-hydroxy-3,5-dimethyl phenyl)hepta-1,6-diene-3,5-dione [$Zn(NLG)_2$] have been systematically documented in **Table 3.30**

Table 3.30 Proton signals observed in the ^{1}H NMR spectrum of $Zn(NLG)_2$ (Chemical Shifts δ in ppm)

Complex	Methine	Alkenyl	Phenyl	Hydroxy	Methyl
$Zn(NLG)_2$	6.33	7.10-7.58	7.53	9.80	2.30

The observed chemical shifts in the ^{1}H NMR spectrum of $Zn(NLG)_2$ corresponded well with the expected ranges for each type of proton(**Fig.3.50**). The methine proton at 6.33 ppm was typical for conjugated systems such as those involving enones or α,β-unsaturated ketones, where deshielding from adjacent electron-withdrawing groups, like carbonyl or alkenyl groups, was expected. Alkenyl protons, appearing at 7.10-7.58 ppm, also fell within the anticipated range for such protons in extended conjugated systems, with their shifts influenced by conjugation and metal coordination. Phenyl protons, observed at 7.53 ppm, were consistent with typical aromatic proton shifts, which can be affected by electron-withdrawing groups or metal coordination. The significant downfield shift of the hydroxy proton to 9.80 ppm in $[Zn(NLG)_2]$ was explained by the indirect influence of Zn(II) coordination through the carbonyl groups. Although the hydroxy group itself did not directly coordinate with Zn(II), the overall electronic environment and potential conformational changes induced by metal coordination led to a significant downfield shift in the hydroxy proton. This shift reflected the complex interplay of electronic effects within the metal-ligand coordination sphere. The methyl protons, observed at 2.30 ppm, were in line with expected values for methyl groups adjacent to electronegative atoms or within conjugated systems, reflecting deshielding effects from the metal coordination.

Mass Spectrum

Table 3.31 Molecular ion peaks of $Zn(NLG)_2$

M^+/(M+1)/(M+2) ion	**a**	**b**	**c**	**d**	**e**	**f**	**g**	**h**	**i**	**j**
790	669	548	427	305	121	427	184	364	122	121

*The alphabets correspond to the fragments given in the fragmentation scheme in**Fig.3.51**

The mass spectrum of the Zn(II) complex with NLG displayed a prominent molecular ion peak at m/z 790, indicating the intact molecular weight of the compound. Fragmentation patterns revealed peaks at m/z 548 and 305, which correspond to the sequential loss of two and four 4-hydroxy-3,5-dimethylphenyl groups from the molecular ion. Additionally, a peak at m/z 427 was identified as the $[ML]^+$ fragment, where M represents the Zn metal and L denotes the ligand 1,7-bis(4-hydroxy-3,5-dimethyl phenyl)hepta-1,6-diene-3,5-dione. Other fragment ions observed at m/z 669, 427, 121, 184, 364, 122, and 121 further corroborated the fragmentation patterns and structural components of the $Zn(NLF)_2$ complex, as illustrated in **Fig.3.51**

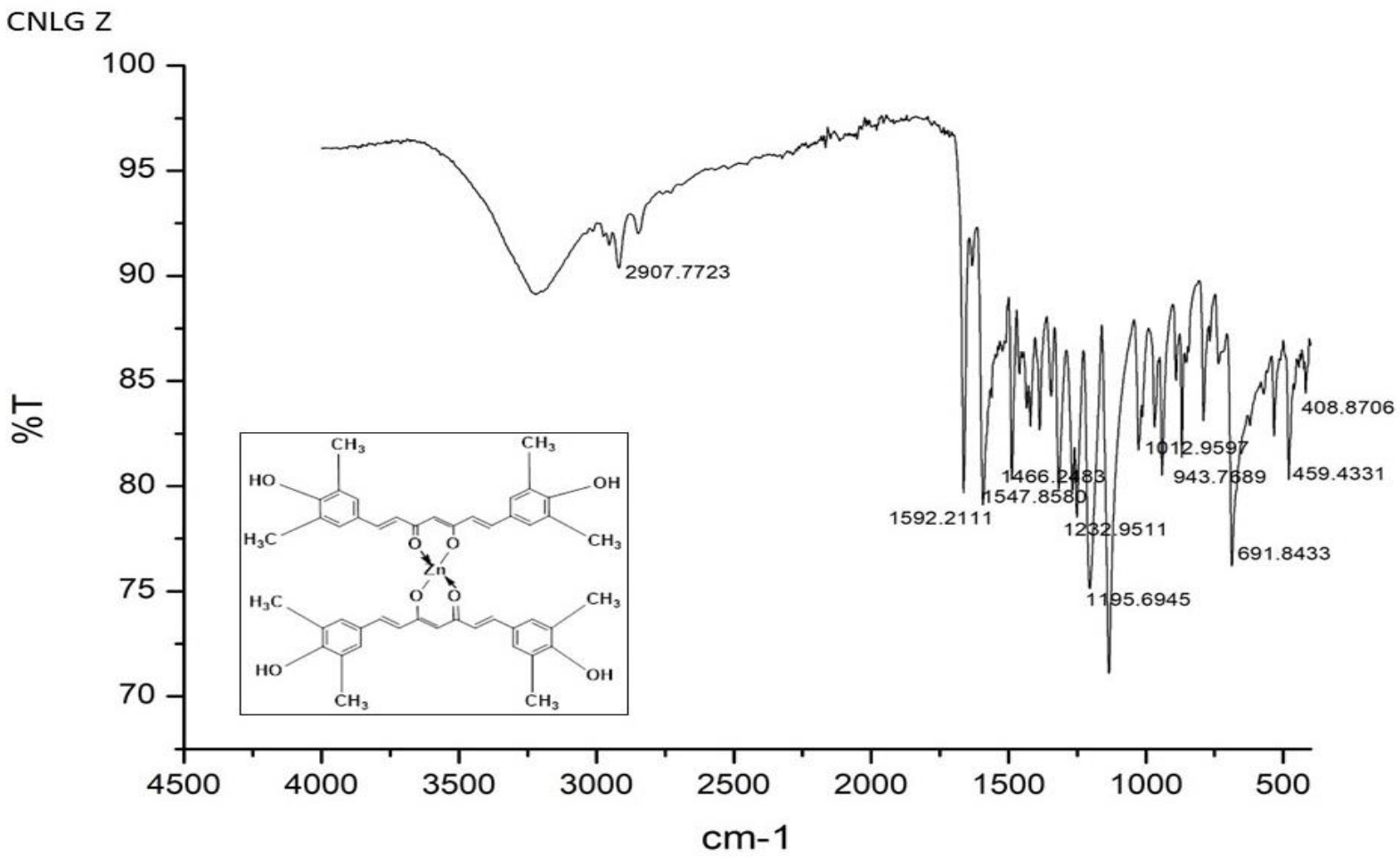

Fig.3.49 The IR spectrum of Zn $(NLG)_2$

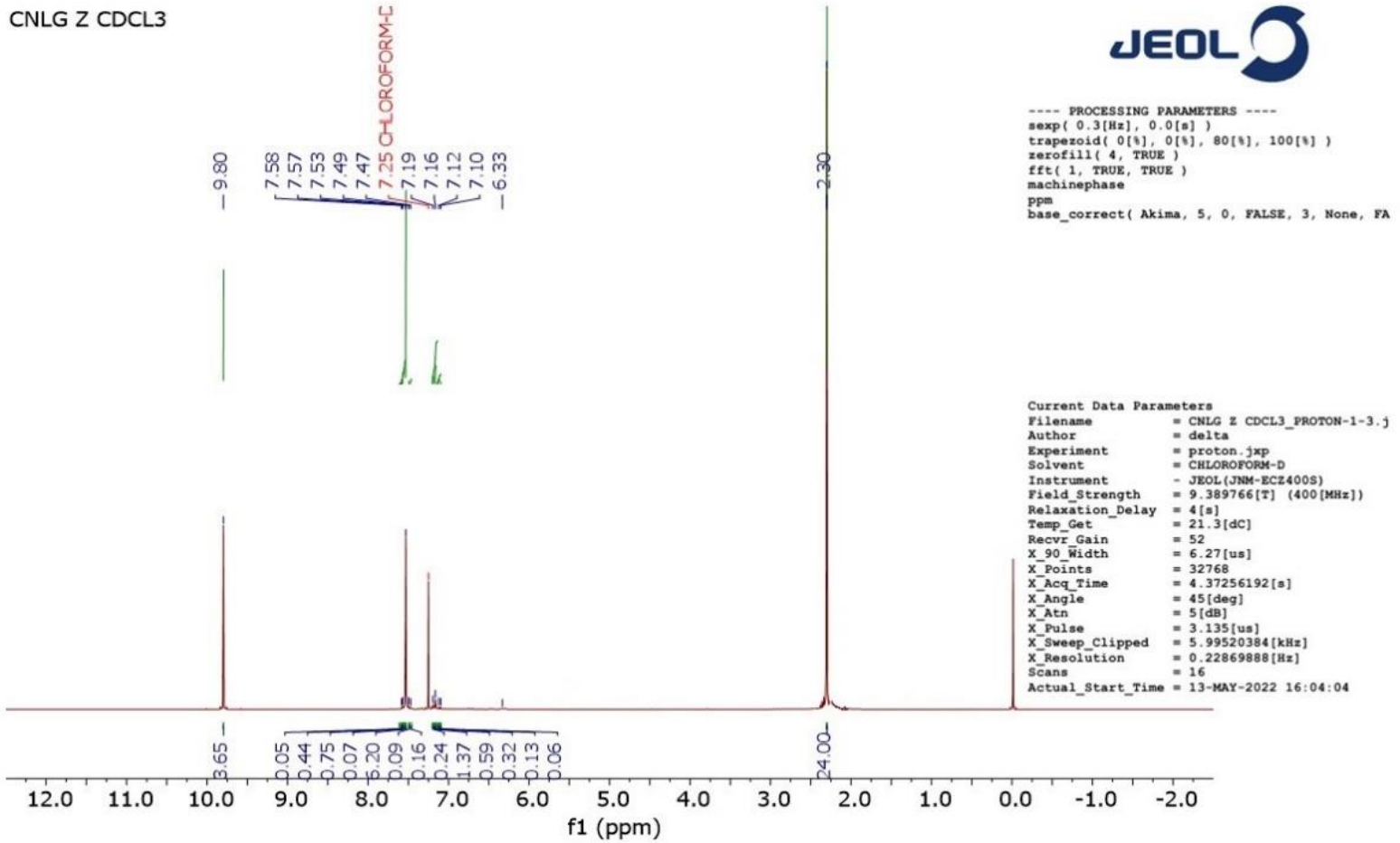

Fig.3.50 The ^{1}H NMR spectrum of Zn $(NLG)_2$

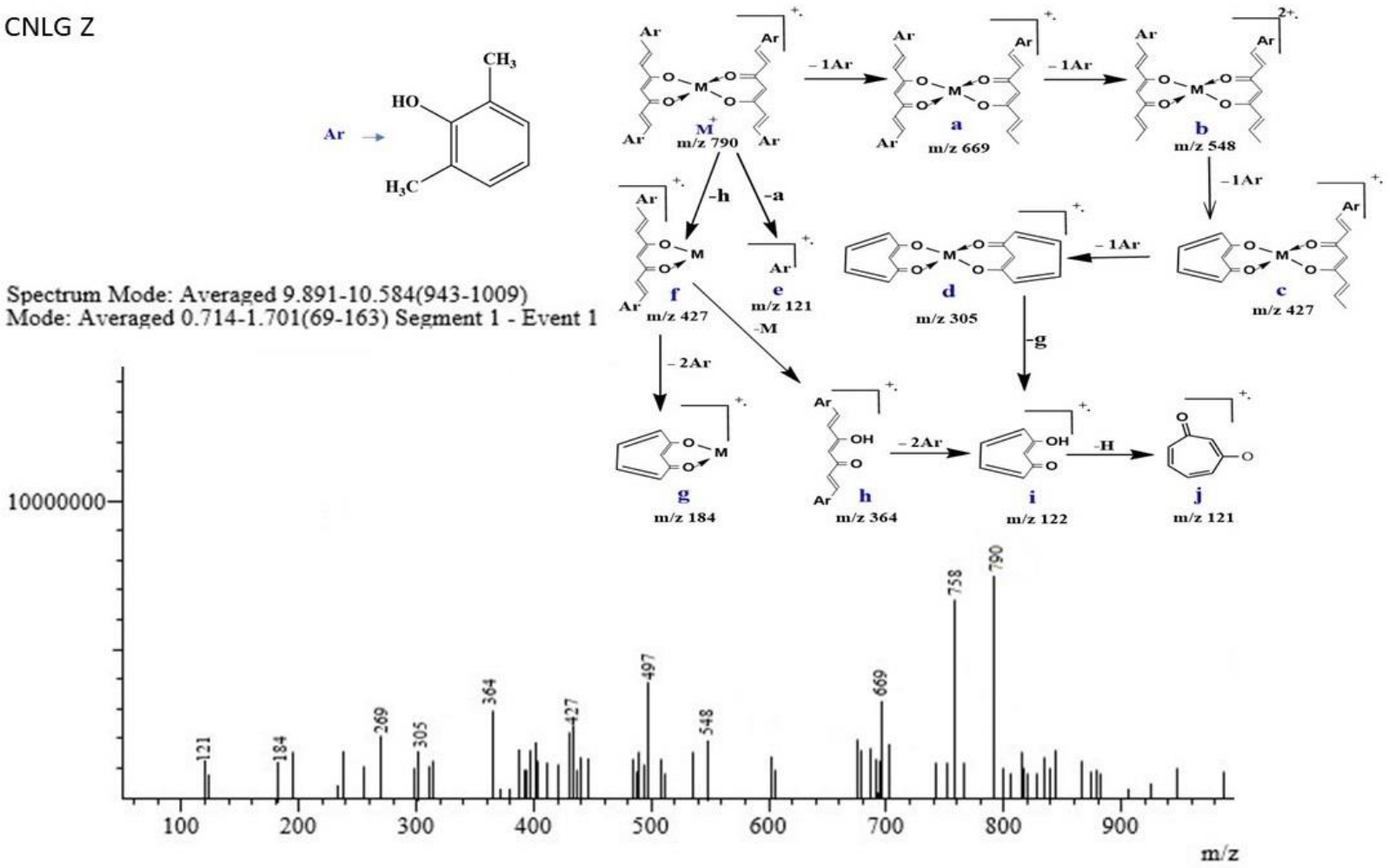

Fig.3.51 The Mass spectrum of Zn $(NLG)_2$

3.5.1.6. Synthesis and characterization of (1E,6E)-1,7-bis (5-chloro-2-hydroxy phenyl) hepta-1,6-diene-3,5-dione (NLH)

3.5.1.6.1 Synthesis and characterization of NLH

1,7-Bis(5-chloro-2-hydroxyphenyl)hepta-1,6-diene-3,5-dione (NLH) was synthesized via the condensation of 5-chlorosalicylaldehyde (0.01 M) with an acetylacetone–boron complex and B_2O_3 in ethyl acetate (7.5 mL). The reaction was conducted in the presence of tri-sec-butyl borate (5.4 mL) and n-butylamine (0.1 mL) as a condensing agent. The resulting product had a melting point of 281°C and a molecular weight of 377 g/mol, with a yield of approximately 95%. Elemental analysis revealed carbon and hydrogen contents of 59.86% and 3.2%, respectively, closely matching the theoretical values of 60.5% and 3.74%.

Characterization of NLH

The synthesized compound NLH was characterised using a range of spectroscopic techniques, including IR, ^{1}H NMR, ^{13}C NMR, and mass spectrometry. The spectral data obtained for the compound are discussed below.

IR Spectrum

The interpretations of the IR spectrum assignments for NLH were conducted concerning the provided **Table 3.32.** Within this chemical compound, the characteristics and strength of the carbonyl stretching frequency are impacted by the structural environment, rendering them significant for determining the nature of the carbonyl group present. Utilizing IR spectroscopy, the identification of an α,β-unsaturated 1,3-diketo moiety within the compound can be effectively accomplished.

Table 3.32 Possible IR assignments of NLH

Wavenumbers (in cm^{-1})	**Possible IR Assignments**
2922.5	ν Enolic
1655.35	ν(C=O)
1571.6	ν(C=C) Phenyl
1466.1	ν_{as}(C-C-C)
1155.8	νβ (C-H)

The IR assignments for NLH were interpreted by analyzing each vibrational mode and verifying the associated wavenumber ranges. The peak at 2922.5 cm^{-1}, attributed to enolic O-H stretching, was lower than the typical 3200–3600 cm^{-1} range, suggesting strong hydrogen bonding that shifted the frequency downward. The C=O stretching vibration at 1655.3 cm^{-1} fell within the standard 1650–1750 cm^{-1} range, indicating normal carbonyl behaviour, with a slight shift possibly due to conjugation. The C=C stretching in the phenyl ring at 1571.6 cm^{-1} aligned with the expected 1500–1600 cm^{-1} range, confirming the presence of aromatic bonds. The asymmetric C-C-C stretching at 1466.1 cm^{-1} and C-H bending at 1155.8 cm^{-1} were also within typical ranges, indicating these functional groups were correctly assigned. The IR spectrum of the compound NLH is depicted in **Fig.3.52**

^{1}HNMR Spectrum

The ^{1}H NMR spectrum of 1,7-Bis(5-chloro-2-hydroxyphenyl)hepta-1,6-diene-3,5-dione (NLH) displayed distinct proton signals that corresponded closely with the expected chemical shifts for enolic, methine, alkenyl, phenyl, and hydroxy protons. The various proton signals observed in the spectrum are given in **Table 3.33**.

Table 3.33 Proton signals observed in the ^{1}H NMR spectrum of NLH(Chemical Shifts δ ppm)

Compound	Enolic	Methine	Alkenyl	Phenyl	Hydroxy
NLH	10.90	6.90	6.92-7.56	6.94-7.21	9.83

The enolic proton, which resonated at 10.90 ppm, typically appeared downfield due to the deshielding effects of hydrogen bonding and conjugation with a carbonyl group. This chemical shift was consistent with the enolic O-H proton, confirming significant deshielding. The methine proton, observed at 6.90 ppm, was aligned with the expected range for methine protons attached to an sp^2 hybridized carbon in a conjugated system, indicating its presence in a conjugated diene system such as NLH. Alkenyl protons, which resonated between 6.92-7.56 ppm, typically appeared within the range of 4.5-7.5 ppm, depending on the degree of conjugation and the presence of electron-withdrawing groups. The observed range suggested that these protons were part of a conjugated double-bond system characteristic of NLH. The phenyl protons, resonating between 6.94-7.21ppm, matched the typical range of 6.5-8.5 ppm for aromatic protons, particularly those in a substituted benzene ring like the 5-chloro-2-hydroxyphenyl groups present in NLH. The

hydroxy proton, observed at 9.83 ppm, generally appeared downfield in phenolic compounds, typically around 9-10 ppm. This shift corresponded well with the expected range for a hydroxy proton in a phenolic environment, especially when influenced by neighbouring chloro and carbonyl groups. These chemical shifts confirmed that the protons in NLH were correctly assigned to their respective environments, as supported by the expected ranges for enolic, methine, alkenyl, phenyl, and hydroxy protons in conjugated and aromatic systems. The ^{1}H NMR spectrum of NLH is brought out in **Fig.3.53**

^{13}C NMR Spectra

The ^{13}C NMR spectrum of NLH revealed distinct carbon signals that corresponded to various environments within the molecule, validating their chemical shifts. The ^{13}C NMR spectral details of NLH are given in **Table 3.34.**

Table 3.34 ^{13}C NMR spectral data of NLH (Chemical Shifts δ ppm)

C_1	C_2,$C_{2'}$	C_3,$C_{3'}$	C_4,$C_{4'}$	C_5,$C_{5'}$
101.1	195.62	132.63	137.06	119.00
C_6,$C_{6'}$	C_7,$C_{7'}$	C_8,$C_{8'}$	C_9,$C_{9'}$	C_{10},$C_{10'}$
124.78	121.21	132.63	119.55	160.21

The chemical shifts observed in the ^{13}C NMR spectrum of NLH were consistent with the presence of a substituted aromatic ring system that included conjugated carbonyl groups (**Fig.3.54**). The signal at 101.1 ppm, corresponding to C_1, resonated within the typical range for carbon in a β-diketone structure, suggesting its enolic form conjugated with adjacent double bonds. The signal at 195.62 ppm for C_2 and $C_{2'}$ was characteristic of carbonyl carbons, aligning with the expected range for ketonic or aldehydic groups. C_3 and $C_{3'}$ exhibited shifts at 132.63 ppm, fitting within the typical range for alkenyl groups in a conjugated system. The shifts at 137.06 ppm for C_4 and $C_{4'}$ were indicative of carbons influenced by adjacency to an aromatic ring, conjugation with an alkenyl chain, and carbonyl groups, falling within the expected range of 130-150 ppm. The signal at 119.00 ppm for C_5 and $C_{5'}$ aligned with the expected range for aromatic carbons influenced by neighbouring substituents or conjugation. The 124.78 ppm signal for C_6 and $C_{6'}$ corresponded to carbon within an aromatic ring, likely influenced by an adjacent chlorine atom, which caused a downfield shift. Similarly, the 121.21 ppm signal for C_7 and $C_{7'}$ was consistent with a carbon directly attached to a chlorine atom, reflecting the deshielding

effect of the electronegative chlorine. The signal at 132.63 ppm for C_8 and $C_{8'}$ aligned with expectations for a carbon adjacent to both a hydroxyl group and a chlorine atom within an aromatic ring, reflecting the combined electron-withdrawing and electron-donating effects of these substituents. The signal at 119.55 ppm for C_9 and $C_{9'}$ corresponded to a carbon adjacent to a hydroxyl group in an aromatic ring, resonating within the expected range due to the influence of the inductive and resonance effects of the hydroxyl groups. Lastly, the signal at 160.21 ppm for C_{10} and $C_{10'}$ corresponded to carbon in an aromatic ring attached to a hydroxyl group and part of a conjugated system that included a carbonyl group, consistent with significant deshielding. Thus, the chemical shifts observed in the ^{13}C NMR spectrum of NLH validated the assigned chemical environments and aligned with the expected ranges for aromatic carbons and carbonyl groups.

Mass Spectrum

In the mass spectrum of NLH, conspicuous molecular ion peaks were detected, substantiating the molecular mass of the substance. Essential peaks in the spectrum were elucidated by the fragmentation pattern outlined in **Fig.3.55**. The relevant data is encapsulated in **Table 3.35.**

Table 3.35 Molecular ion peaks of NLH

M^+/M+1 Ion	**a**	**b**	**c**	**d**	**e**	**f**	**g**
376	195	181	142	153	127	249	223

*The alphabets correspond to the fragments given in the fragmentation scheme in **Fig. 3.55**

The M^{+1} ion of NLH is observed at 376. Other important peaks of NLH due to fragment ion peaks which can be explained by their fragmentation patterns. The peak observed at 195 is due to $[C_{10}H_8\ ClO_2]^+$. The peak at 181 is due to the molecular ion$[C_9H_6ClO_2]^+$. The peak at 153 is due to $[C_8H_6ClO]^+$. The peak at 249 is due to the fragment $[C_{13}H_{10}ClO_3]^+$ and the peak at 223 is due to $[C_{13}H_{10}ClO_2]^+$.The mass spectrum of the compound NLH is shown in **Fig.3.55**

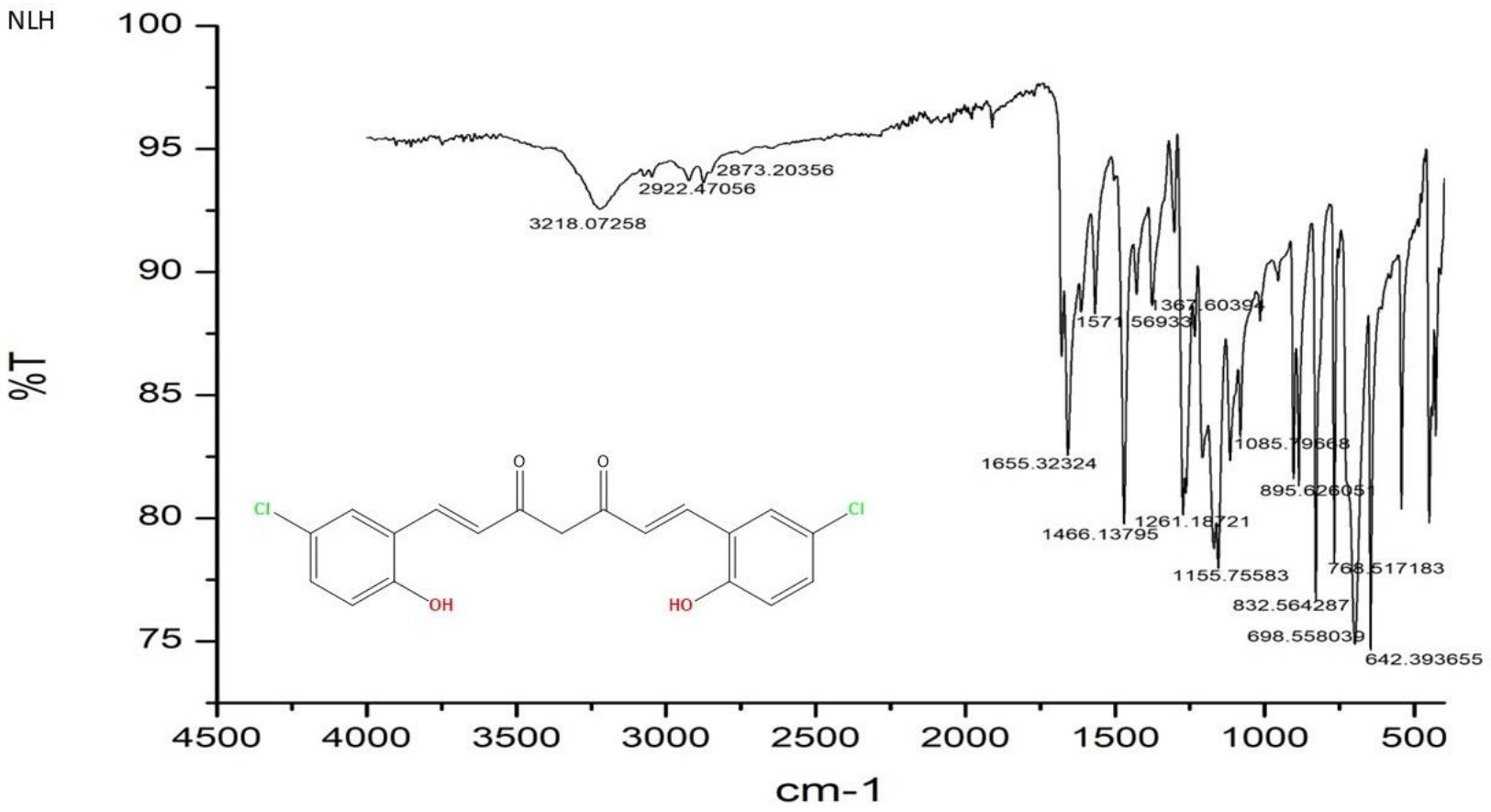

Fig.3.52 The IR spectrum of NLH

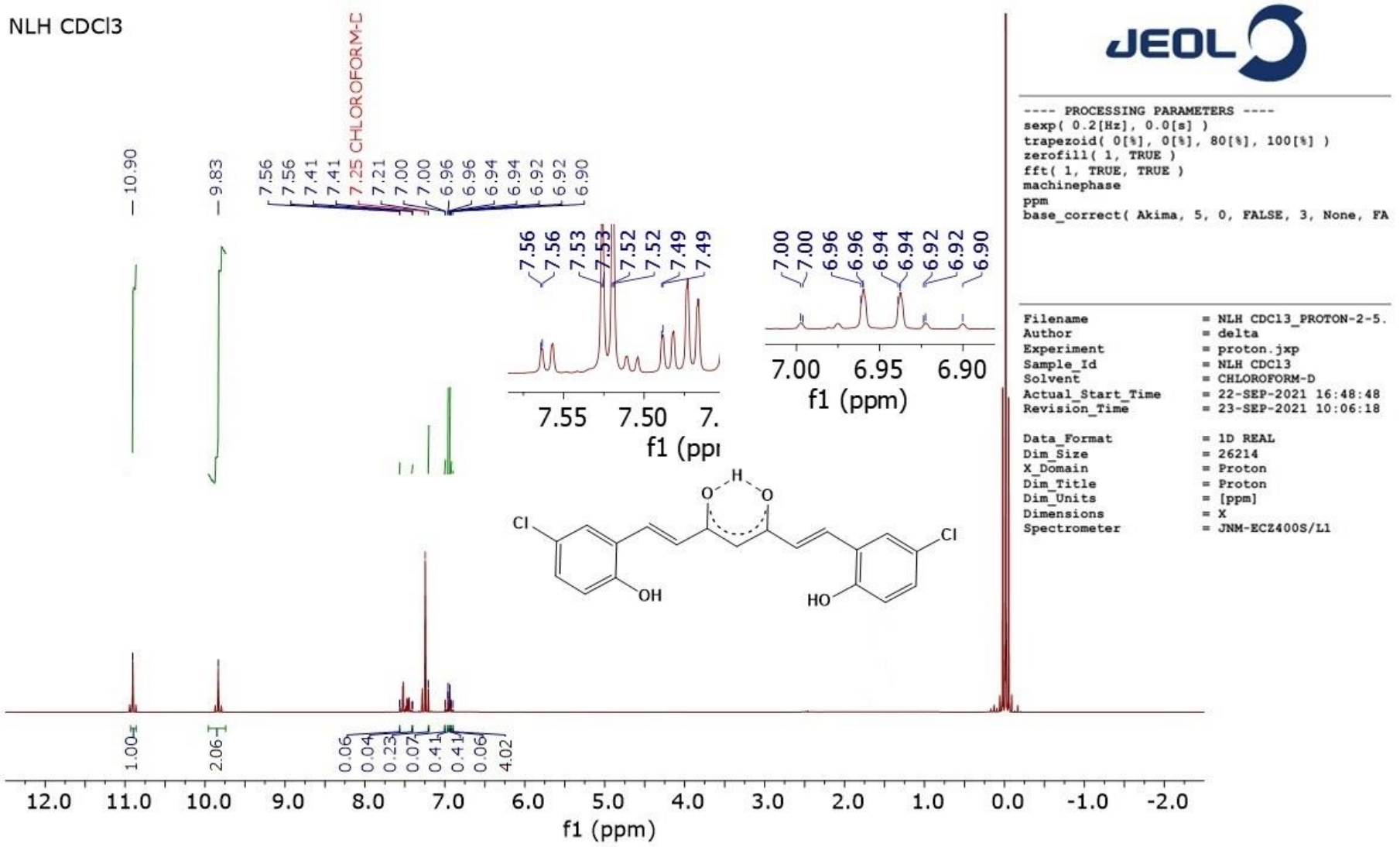

Fig.3.53 The ^{1}H NMR spectrum of NLH

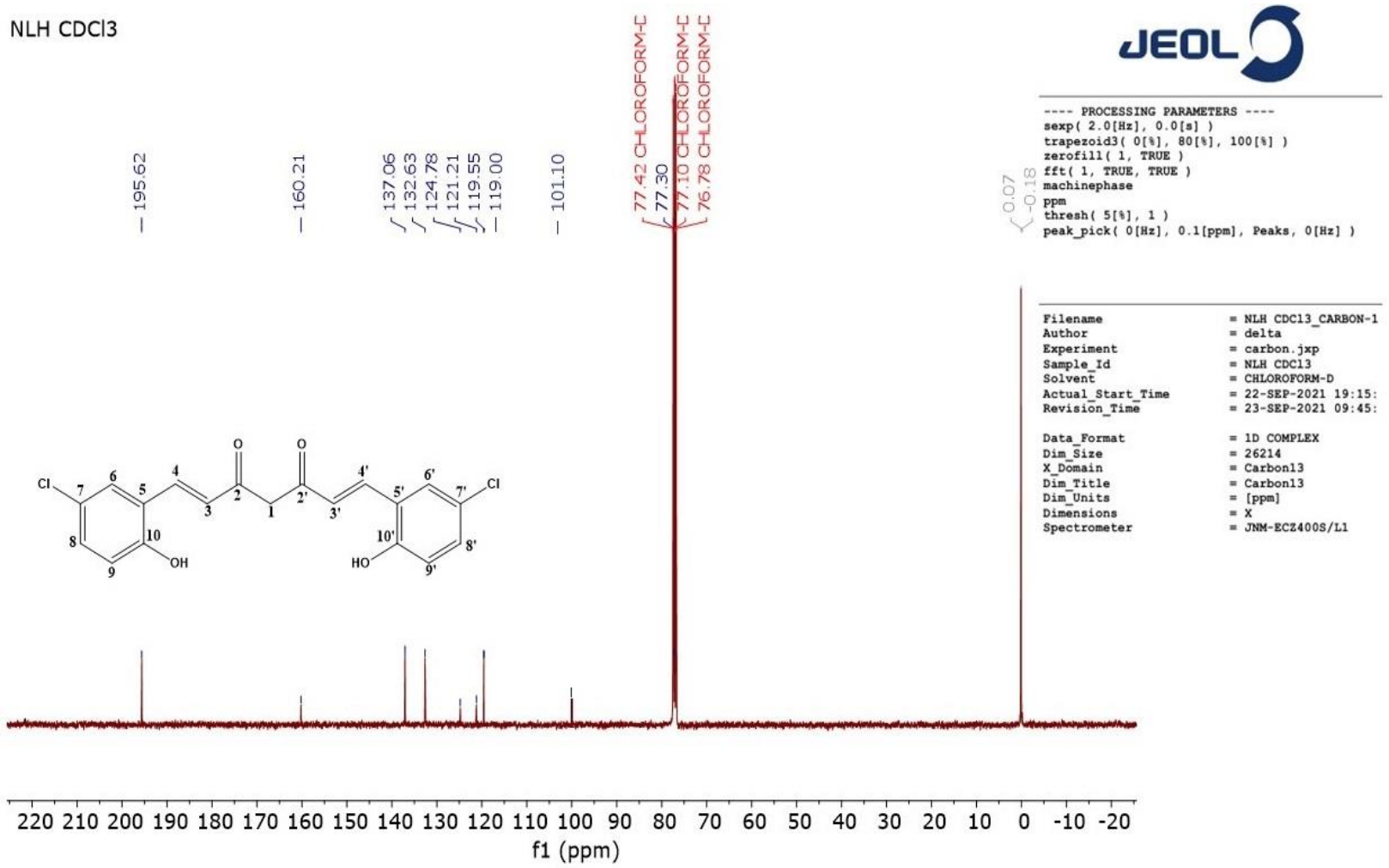

Fig.3.54 The ^{13}CNMR spectrum of NLH

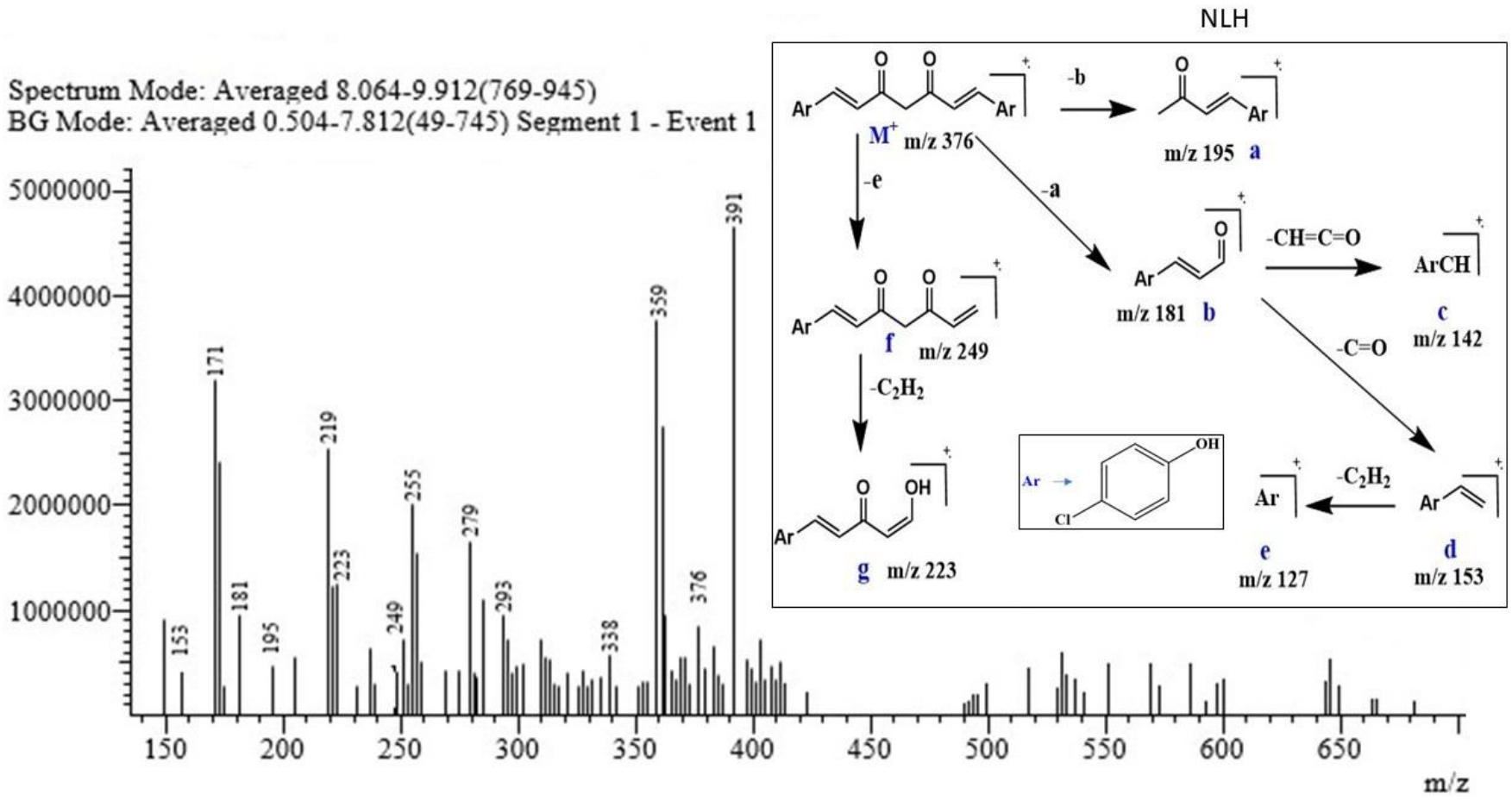

Fig.3.55 The Mass spectrum of NLH

3.6.1.6.2 Synthesis and characterization of $Cu(NLH)_2$ and $Zn(NLH)_2$

3.6.1.6.2.1 Synthesis and characterization of Cu complex of 1,7-bis(5-chloro-2-hydroxy phenyl)hepta-1,6-diene-3,5-dione [$Cu(NLH)_2$]

The copper(II) complex of the curcuminoid analogue NLH showed a molecular weight of 812.97 g/mol and a melting point of 292°C. Elemental analysis indicated carbon, hydrogen, and metal contents of 55.26%, 3.01%, and 7.51%, respectively, which closely matched the theoretical values of 55.94%, 3.21%, and 7.79%. The compound was synthesized with an 84% yield.

Characterization of Cu(NLH)2

The metal complex $Cu(NLH)_2$ was characterized using various spectroscopic and analytical techniques, including IR spectroscopy, ^{1}H NMR, and mass spectrometry. The results from these analyses are summarized and discussed as follows.

IR Spectrum

The $Cu(NLH)_2$ complex exhibited distinct spectroscopic features confirming ligand-metal coordination (**Fig.3.56**). Notably, the absence of a prominent carbonyl absorption band in the 1650-1800 cm^{-1} range and the disappearance of the carbonyl peak at 1630 cm^{-1}, along with the appearance of a new band at 1586.0 cm^{-1}, indicated that the metal ion had replaced the enolic proton, leading to a metal-coordinated carbonyl group. This shift to a lower frequency (1586.0 cm^{-1}) suggests chelation. Additionally, a band at 1503 cm^{-1} was attributed to the asymmetric stretching of the C-C-C bond in the aromatic system. Low-frequency bands at 452.3 cm^{-1} and 427.5 cm^{-1} were assigned to metal-oxygen (M-O) stretching vibrations, confirming metal-ligand coordination.

^{1}HNMR Spectrum

The distinct proton signals detected within the ^{1}H NMR spectrum of the Cu(II) complex of 1,7-bis(5-chloro-2-hydroxy phenyl)hepta-1,6-diene-3,5-dione [$Cu(NLH)_2$] have been meticulously compiled in **Table 3.36**.

Table 3.36 Proton signals observed in the ^{1}HNMR spectrum of $Cu(NLH)_2$ (Chemical Shifts δ in ppm)

Complex	Methine	Alkenyl	Phenyl	Hydroxy
$Cu(NLH)_2$	6.97	6.82-7.53	6.95-7.48	9.84

The ^{1}H NMR spectrum of the $Cu(NLH)_2$ complex revealed distinct chemical environments for various protons (**Fig.3.57**). The methine proton resonated at 6.97 ppm, slightly upfield from the typical 6.0 to 6.5 ppm range observed in conjugated systems, indicating minor adjustments due to metal coordination. Alkenyl protons appeared between 6.82 and 7.53 ppm, reflecting the influence of copper(II) on the electronic environment and the extended conjugation within the complex. Phenyl protons were observed at 7.10-7.53 ppm, consistent with their expected range and showing some effect from metal coordination. The hydroxy proton experienced a significant downfield shift to 9.84 ppm, which was attributed to the indirect influence of Cu(II) coordination through the carbonyl groups. Although the hydroxy group did not directly coordinate with Cu(II), the overall electronic environment and potential conformational changes induced by metal coordination led to this notable shift. These findings confirmed the successful formation and characterization of the $Cu(NLH)_2$ complex.

Mass Spectrum

Table 3.37 Molecular ion peaks of Cu $(NLH)_2$

M+/(M+1)/(M+2) ion	**a**	**b**	**c**	**d**	**e**	**f**	**g**	**h**	**i**	**j**
812	685	558	431	304	127	437	183	376	122	121

*The alphabets correspond to the fragments given in the fragmentation scheme in**Fig.3.58**

The mass spectrum of the Cu(II) complex with NLH displayed a prominent molecular ion peak at m/z 812, indicating the intact molecular weight of the compound. Fragmentation patterns revealed peaks at m/z 558 and 304, which corresponded to the sequential loss of two and four 5-chloro-2-hydroxyphenyl groups from the molecular ion. Additionally, a peak at m/z 437 was identified as the $[ML]^+$ fragment, where M represented the Cu metal and L denoted the ligand 1,7-bis (5-chloro-2-hydroxy phenyl) hepta-1,6-diene-3,5-dione. Other fragment ions observed at m/z 685, 431, 127, and 376 further corroborated the fragmentation patterns and structural components of the $Cu(NLH)_2$ complex, as illustrated in **Fig.3.58**

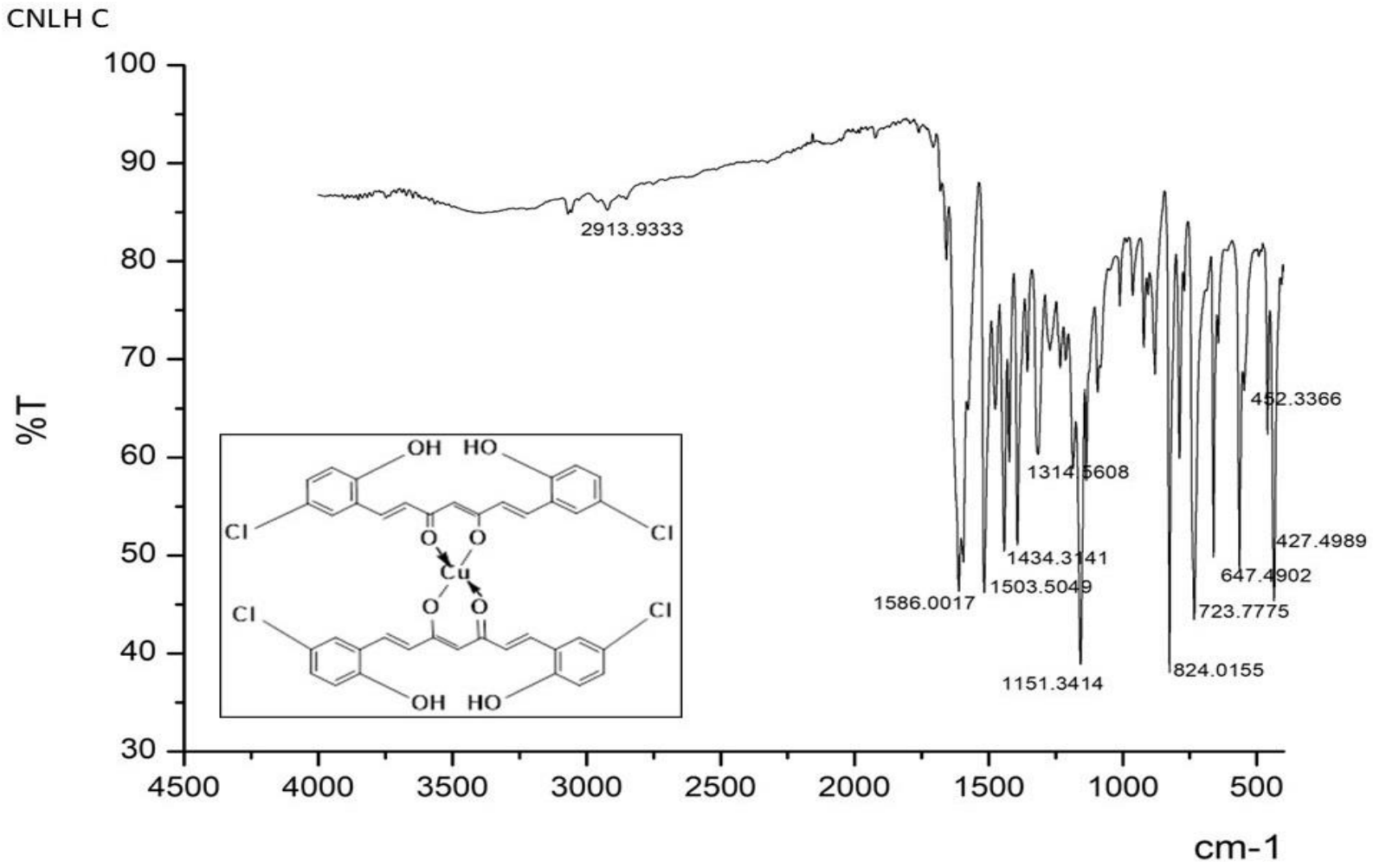

Fig.3.56 The IR spectrum of Cu $(NLH)_2$

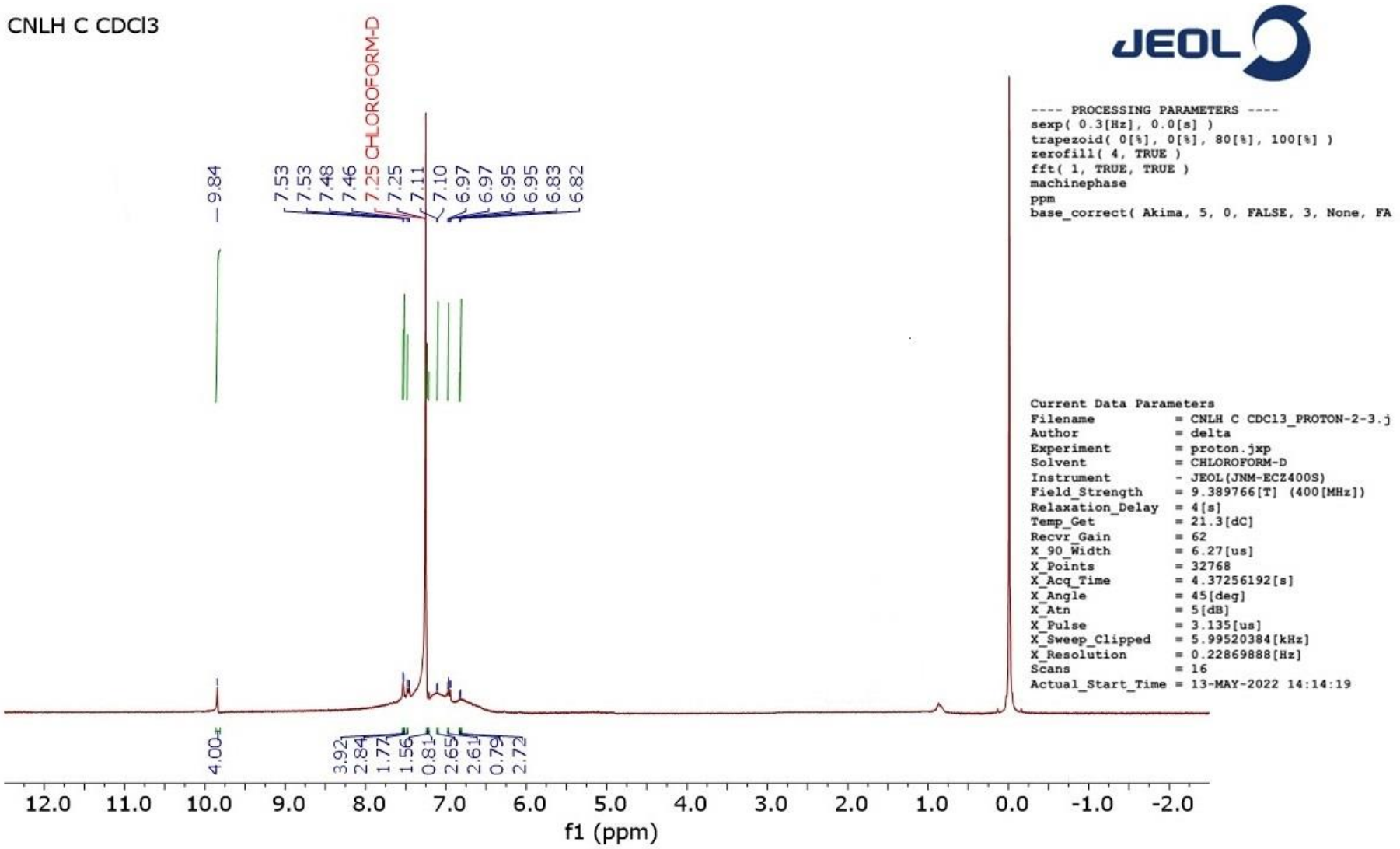

Fig.3.57 The ^{1}H NMR spectrum of Cu $(NLH)_2$

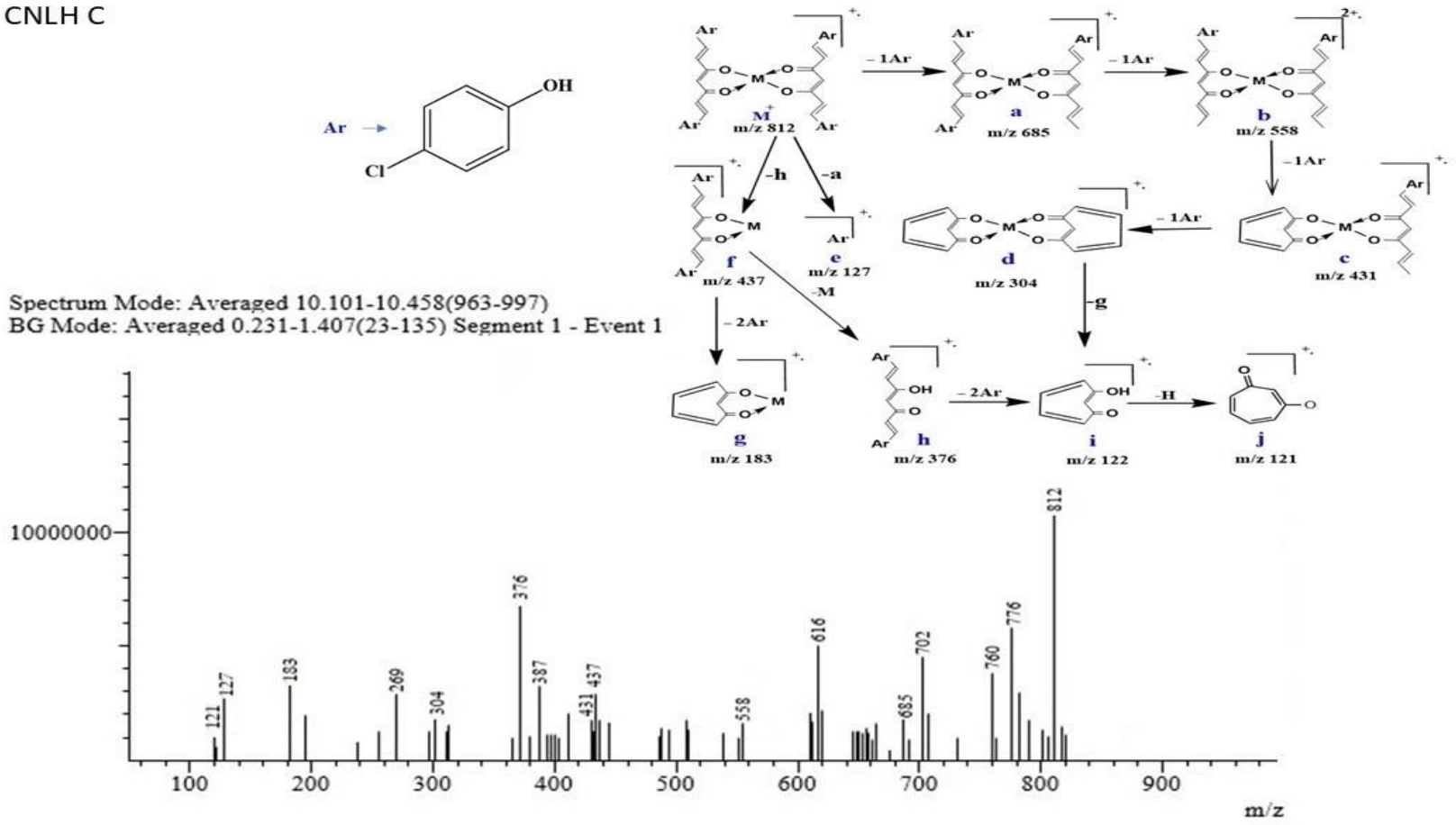

Fig.3.58 The Mass spectrum of Cu $(NLH)_2$

3.6.1.6.2.2 Synthesis and characterization of Zn complex of 1,7-bis(5-chloro-2-hydroxy phenyl)hepta-1,6-diene-3,5-dione [$Zn(NLH)_2$]

The Zn(II) complex of the curcuminoid analogue NLH had a molecular weight of 813.97 g/mol and a melting point of 297°C. Elemental analysis revealed carbon, hydrogen, and metal contents of 55.70%, 2.98%, and 7.24%, respectively, closely aligning with the theoretical values of 55.81%, 3.2%, and 7.99%. The synthesis yielded 87% of the compound.

Characterization of Zn(NLH)2

The metal complex $Zn(NLH)_2$ was characterized through a series of spectroscopic and analytical techniques, including IR spectroscopy, ^1H NMR, and mass spectrometry. The findings from these analyses are summarized and discussed below.

IR Spectrum

The $Zn(NLH)_2$ complex exhibited distinct spectroscopic features that confirmed ligand-metal coordination (**Fig.3.59**). Notably, the prominent carbonyl absorption band in the 1650-1800 cm^{-1} range was absent, and the carbonyl peak at 1630 cm^{-1} disappeared. A new band emerged at 1598.0 cm^{-1}, indicating that the metal ion had replaced the enolic proton, resulting in a metal-coordinated carbonyl group. This shift to a lower frequency (1598.0 cm^{-1}) suggested chelation. Additionally, a band at 1523 cm^{-1} was attributed to the asymmetric stretching of the C-C-C bond in the aromatic system. Low-frequency bands at 433.7 cm^{-1} and 408.9 cm^{-1} were assigned to metal-oxygen (M-O) stretching vibrations, confirming metal-ligand coordination.

^{1}HNMR Spectrum

The distinct proton signals detected within the ^1H NMR spectrum of the Zn(II) complex of 1,7-bis(5-chloro-2-hydroxyphenyl)hepta-1,6-diene-3,5-dione [$Zn(NLH)_2$] were meticulously compiled in **Table 3.38**

Table 3.38 Proton signals observed in the ^{1}HNMR spectrum of $Zn(NLH)_2$ (Chemical Shifts δ in ppm)

Complex	Methine	Alkenyl	Phenyl	Hydroxy
$Zn(NLH)_2$	6.97	6.94-7.53	7.29-7.48	9.84

The ^1H NMR spectrum of the $Zn(NLH)_2$ complex revealed specific chemical shifts corresponding to different types of protons in the molecule (**Fig.3.60**). The methine proton

was detected at 6.97 ppm, a position consistent with methine protons in similar conjugated enone systems, which typically appear around 6.5-7.5 ppm depending on the electronic environment. The alkenyl protons were observed within the range of 6.94-7.53 ppm, a range characteristic of protons on double bonds (C=C) within a conjugated system, particularly when adjacent to electron-withdrawing groups or aromatic rings. This broad range was attributed to the different environments experienced by each alkenyl proton in the conjugated system. The phenyl protons appeared between 7.29 and 7.48 ppm, which aligned with the expected region for aromatic protons, especially in chloro-substituted benzene rings. The slight shift toward lower ppm values (around 7.29 ppm) was likely due to the electron-donating effect of the hydroxy group, while the upper range (7.48 ppm) was influenced by the electron-withdrawing chloro group. The hydroxy proton exhibited a significant downfield shift to 9.84 ppm, which is attributed to the indirect influence of Zn(II) coordination through the carbonyl groups. Although the hydroxy group itself did not directly coordinate with Zn(II), the overall electronic environment and potential conformational changes induced by metal coordination caused this pronounced shift. These findings confirm the successful formation and characterization of the $Zn(NLH)_2$ complex.

Mass Spectrum

Table 3.39 Molecular ion peaks of $Zn(NLH)_2$

M^+/(M+1)/(M+2) ion	a	b	c	d	e	f	g	h	i	j
813	686	559	432	305	127	438	184	376	122	121

*The alphabets correspond to the fragments given in the fragmentation scheme in **Fig.3.61**

The mass spectrum of the Zn(II) complex with NLH displayed a prominent molecular ion peak at m/z 813, indicating the intact molecular weight of the compound. Fragmentation patterns revealed peaks at m/z 559 and 305, corresponding to the sequential loss of two and four 5-chloro-2-hydroxy phenyl groups from the molecular ion. Additionally, a peak at m/z 438 was identified as the $[ML]^+$ fragment, where M represents the Zn metal and L denotes the ligand 1,7-bis(5-chloro-2-hydroxy phenyl)hepta-1,6-diene-3,5-dione. Other fragment ions observed at m/z 686, 432, 127, 184, and 376 further corroborated the fragmentation patterns and structural components of the $Zn(NLH)_2$ complex, as illustrated in **Fig.3.61**

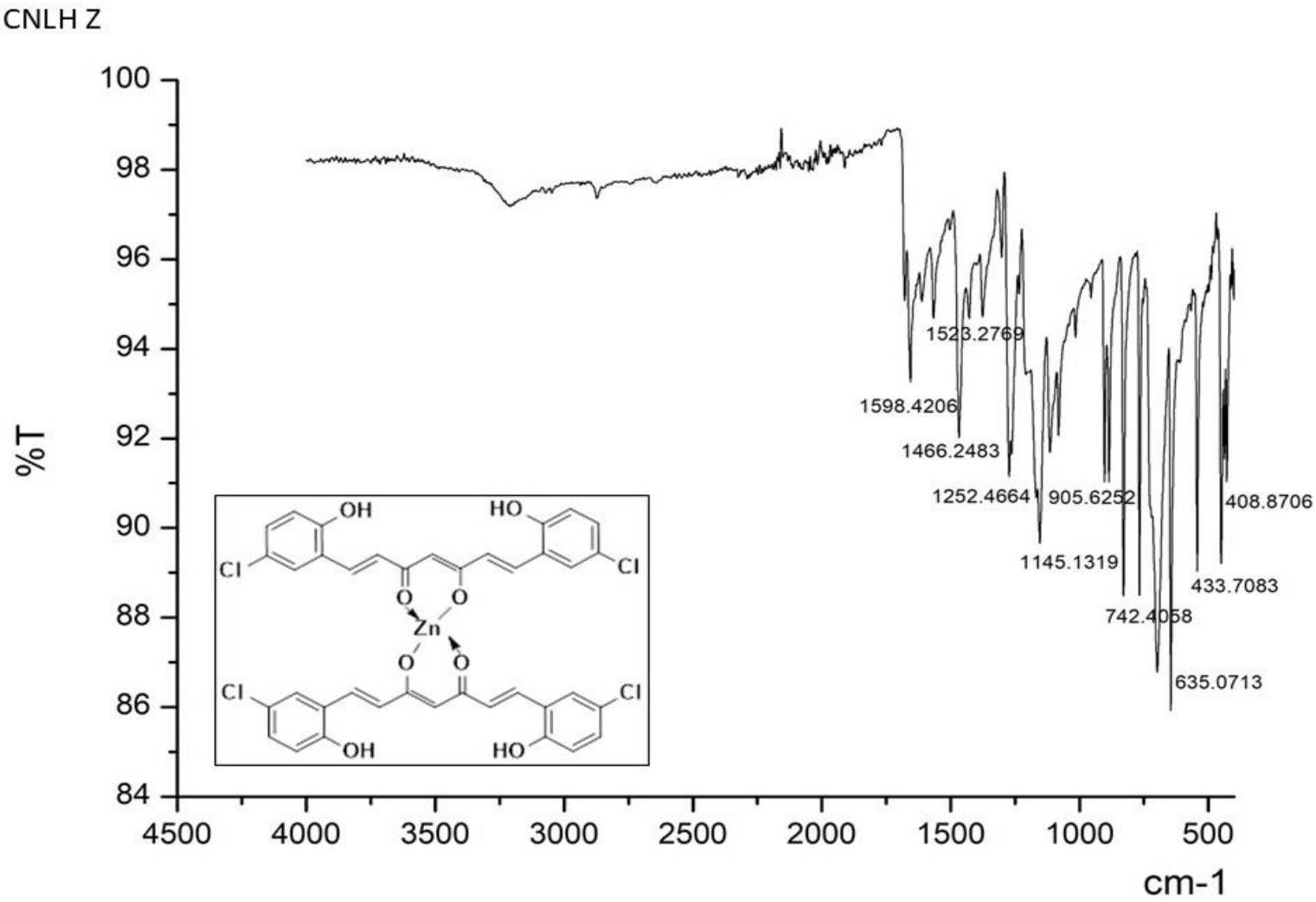

Fig.3.59 The IR spectrum of Zn $(NLH)_2$

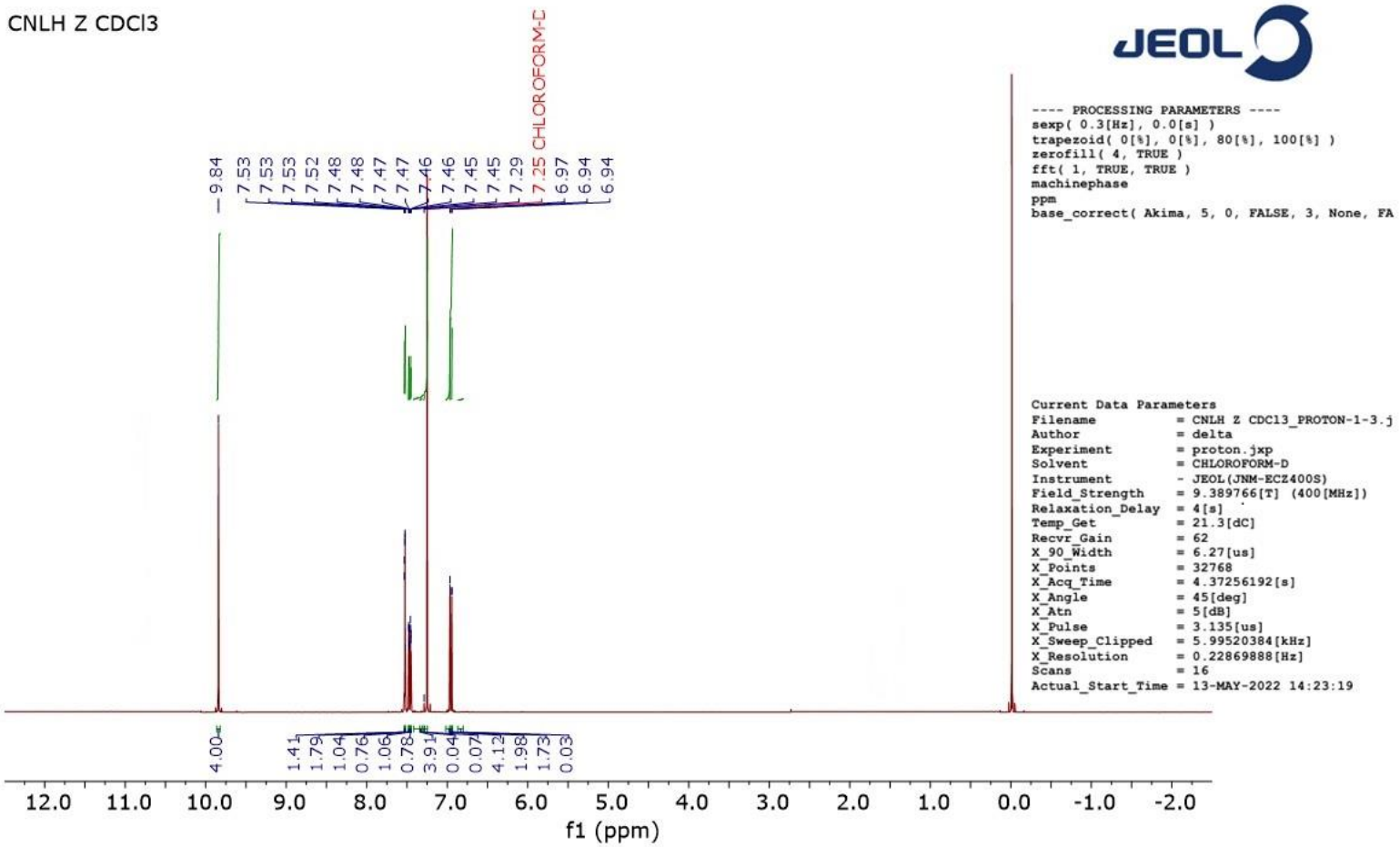

Fig.3.60 The ^{1}H NMR spectrum of Zn $(NLH)_2$

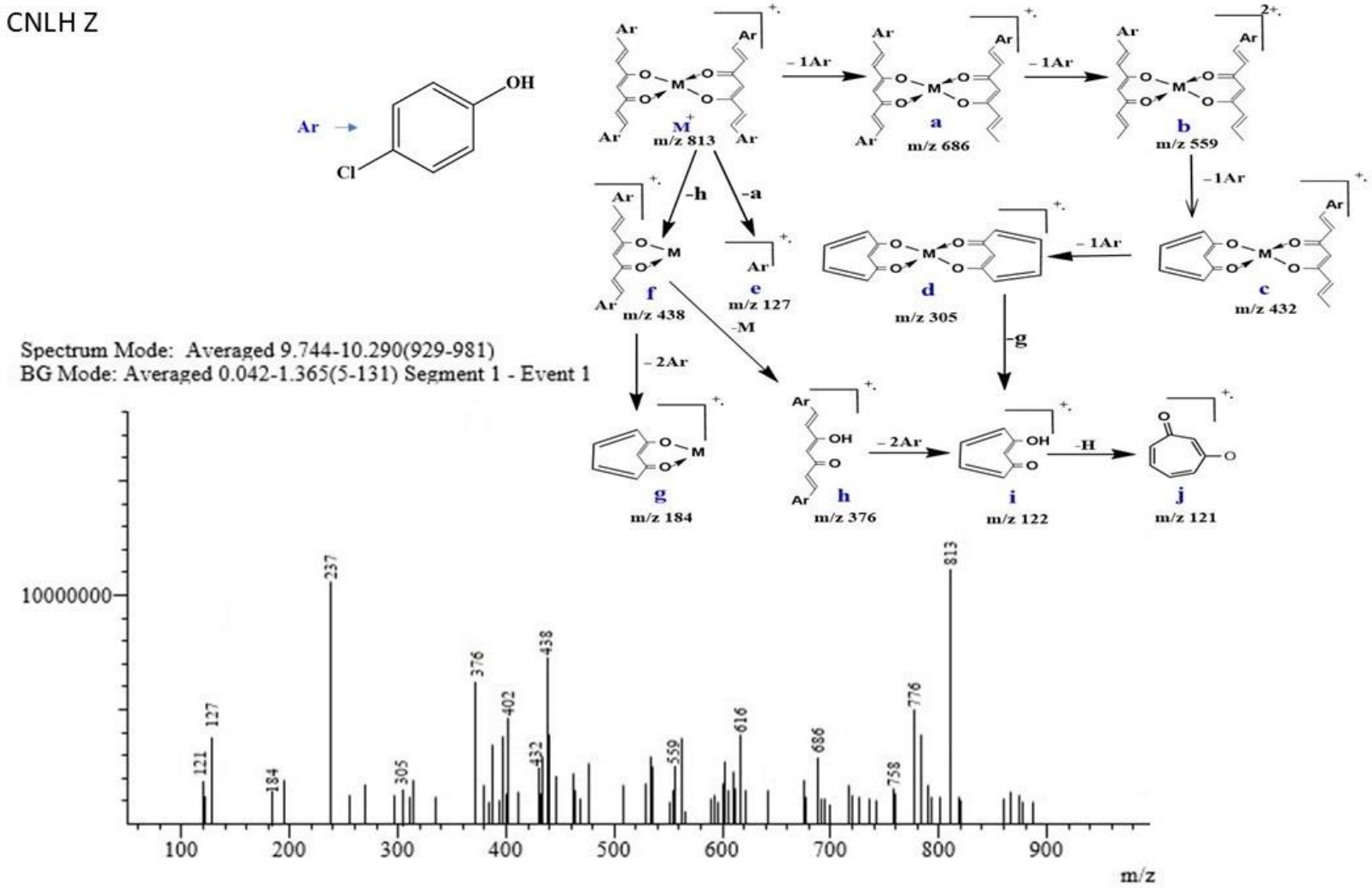

Fig.3.61 The Mass spectrum of Zn $(NLH)_2$

3.5.1.7. Synthesis and characterization of (1E,6E)-1,7-bis(2-hydroxy-3-methoxy phenyl)hepta-1,6-diene-3,5-dione (NLI)

3.5.1.7.1 Synthesis and characterization of NLI

1,7-bis(2-hydroxy-3-methoxyphenyl)hepta-1,6-diene-3,5-dione (NLI) was synthesized through the condensation reaction involving 3-methoxy salicylaldehyde (0.01 M) and an acetylacetone–boron complex, alongside B_2O_3, in a solvent of ethyl acetate (7.5 mL). The reaction was facilitated by the inclusion of tri-sec-butyl borate (5.4 mL) and n-butylamine (0.1 mL) serving as a condensing agent. The resultant compound exhibited a melting point of 288°C and possessed a molecular weight of 368 g/mol, achieving an approximate yield of 60%. Elemental analytical data indicated carbon and hydrogen percentages of 68.2% and 4.77%, respectively, which were in close alignment with the theoretical values of 68.47% and 5.47%.

Characterization of NLI

The compound NLI, which was synthesized, underwent characterization through a variety of spectroscopic methodologies, encompassing IR, ^{1}H NM, ^{13}C NMR and mass spectrometry. The ensuing spectral data about the compound are elaborated upon in the subsequent discussion.

IR Spectrum

The IR peaks for NLI can be interpreted based on the typical absorption ranges associated with different functional groups. The possible IR signals are displayed in **Table 3.40**.

Table 3.40 Possible IR assignments of NLI

Wavenumbers (in cm^{-1})	Possible IR Assignments
2936.3	ν Enolic
1585.4	ν(C=C) Phenyl
1486.8	ν_{as}(C-C-C)
1437.6	ν_{s}(C-C-C)
902.5	ν (CH=CH) trans

The IR signal at 2936.3 cm^{-1} was attributed to the O-H stretching vibration of the enolic hydroxyl group. Although enolic O-H stretching vibrations typically occurred within the range of 3200-3600 cm^{-1}, the presence of intramolecular hydrogen bonding within the molecule likely caused a shift to a lower frequency, justifying this assignment. The signal at 1585.4 cm^{-1} corresponded to the C=C stretching vibrations in aromatic rings, which typically appeared within the range of 1450-1600 cm^{-1}. This assignment was consistent with the expected vibrational mode for aromatic C=C bonds. Additionally, the signal at 1486.8 cm^{-1} was attributed to the asymmetric stretching vibration of the C-C-C bonds in the aromatic ring, a value that fit well within the expected range of 1400-1500 cm^{-1}. Similarly, the signal at 1437.6 cm^{-1} corresponded to the symmetric stretching vibration of the C-C-C bonds in the aromatic ring, aligning with the expected range of 1400-1450 cm^{-1}. Lastly, the signal at 902.5 cm^{-1} was consistent with the out-of-plane bending vibrations of trans-olefinic (C=C) bonds, typically observed between 700-1000 cm^{-1}, making this a reasonable assignment for the trans-CH=CH out-of-plane bending mode. Thus the IR assignments provided for NLI matched well with the expected vibrational ranges, and the shifts observed were within reasonable limits based on the molecular structure and potential interactions within the compound, supporting the validity of the given IR data (**Fig.3.62**).

^{1}HNMR Spectrum

The proton signals observed in the ^{1}H NMR spectrum of NLI provided valuable insights into the chemical environment of different hydrogen atoms within the molecule, with the chemical shifts (δ, ppm) corresponding to distinct functional groups.The diverse proton resonances identified in the spectrum are detailed in **Table 3.41**.

Table 3.41 Proton signals observed in the ^{1}H NMR spectrum of NLI (Chemical Shifts δ ppm)

Compound	Enolic	Methine	Alkenyl	Phenyl	Methoxy	Hydroxy
NLI	9.91	6.94	6.96-7.32	7.09-7.28	3.83	11.11

The enolic proton at 9.91 ppm appeared downfield, which was consistent with the deshielding effect caused by the adjacent carbonyl group and potential hydrogen bonding. This signal fell within the expected range of 9.0-12.0 ppm for enolic protons, particularly when hydrogen bonding was involved, further shifting the signal downfield. The methine proton, observed at 6.94 ppm, was located adjacent to an electron-withdrawing group, such as a carbonyl or double bond, causing it to resonate downfield within the typical range of

6.0-7.5 ppm for methine protons in such environments. The alkenyl protons, resonating between 6.96 and 7.32 ppm, were indicative of protons on carbon atoms involved in C=C double bonds. These protons usually resonated between 5.0 and 7.5 ppm, depending on the extent of conjugation and the presence of nearby electronegative groups, confirming that these alkenyl protons were likely part of a conjugated system. The phenyl protons, with chemical shifts ranging from 7.09 to 7.28 ppm, resonated within the expected range of 7.0-8.0 ppm, characteristic of protons on aromatic rings. These shifts were influenced by the deshielding effects of the aromatic ring. The methoxy proton, observed at 3.83 ppm, was shielded due to the electron-donating nature of the oxygen atom and resonated within the typical range of 3.3-4.0 ppm for methoxy groups attached to aromatic rings or other electron-withdrawing groups. The OH group attached to the aromatic ring and near a methoxy group appeared at δ 11.11 ppm in the ^{1}H NMR spectrum, especially since the OH group was in a conjugated system. This was consistent with the expected chemical shift for a hydroxyl proton in such an environment. This shift fell within the expected range of 10.0-13.0 ppm, confirming the validity of this assignment. In short, the chemical shifts observed for the enolic, methine, alkenyl, phenyl, methoxy, and hydroxy protons in NLI were consistent with the expected ranges for these functional groups, supporting the accuracy of the assignments made in the spectrum of NLI. The ^{1}H NMR spectrum of NLI is brought out in **Fig.3.63**

The OH group attached to the aromatic ring and near a methoxy group appeared at δ 11.11 ppm in the ^{1}H NMR spectrum, especially since the OH group was in a conjugated system. This was consistent with the expected chemical shift for a hydroxyl proton in such an environment.

^{13}C NMR Spectra

To interpret the ^{13}C NMR spectral data for the compound NLI, the chemical shifts were assigned to the corresponding carbon atoms based on their chemical environments. The details of the ^{13}C NMR spectrum for NLI are provided in **Table 3.42.**

Table 3.42 ^{13}C NMR spectral data of NLI (Chemical Shifts δ ppm)

C_1	C_2,$C_{2'}$	C_3,$C_{3'}$	C_4,$C_{4'}$	C_5,$C_{5'}$	C_6,$C_{6'}$
110.27	191.5	130.79	146.23	114.20	124.63
C_7,$C_{7'}$	C_8,$C_{8'}$	C_9,$C_{9'}$	C_{10},$C_{10'}$	C_{11},$C_{11'}$	
124.00	114.00	151.86	151.00	56.28	

The signal at 110.27 ppm corresponded to C_1, which, as part of a β-diketone structure, resonated within the range of 100-120 ppm, indicating its enolic form conjugated with adjacent double bonds. The chemical shifts at 191.5 ppm for C_2 and $C_{2'}$ were characteristic of carbonyl carbons (C=O) in conjugated ketones. These high ppm values supported their assignment, as carbonyl carbons typically resonated downfield between 190-220 ppm due to the strong deshielding effect of the carbonyl group. The carbons at C_3 and $C_{3'}$ exhibited shifts at 130.79 ppm, which aligned with the 120-140 ppm range for alkenyl groups in a conjugated system. The carbon signals at 146.23 ppm for C_4 and $C_{4'}$ were influenced by their adjacency to an aromatic ring and conjugation with alkenyl chains and carbonyl groups. This shift fell within the expected range of 130-150 ppm for carbons in such an environment, reflecting the combined effects of aromatic substitution, conjugation, and functional groups. The chemical shift at 114.20 ppm for C_5 and $C_{5'}$ was typical for aromatic carbons not directly attached to electronegative atoms but still within a conjugated system, likely in a position meta to a substituent. The shift observed at 124.63 ppm for C_6 and $C_{6'}$ was typical for aromatic carbons within an aromatic ring, not directly attached to electronegative groups, and resonating between 120-135 ppm. Similarly, the shifts at 124 ppm for C_7 and $C_{7'}$ indicated aromatic carbons within this range. The shifts at 114 ppm for C_8 and $C_{8'}$ suggested they were also aromatic carbons, indicating their involvement in the conjugated aromatic system without direct attachment to highly electronegative groups. The chemical shift at 151.86 ppm for C_9 and $C_{9'}$ indicated aromatic carbons directly attached to an electronegative methoxy group ($-OCH_3$). The electron-donating nature of the methoxy group through resonance and induction typically resulted in a deshielding effect on the carbon, causing it to resonate downfield within the range of 150-160 ppm. The signal at 151 ppm for C_{10} and $C_{10'}$ was consistent with aromatic carbons in this range, particularly those attached to a hydroxyl group (-OH). The hydroxyl group, being electron-donating, caused a slight deshielding effect, shifting the signal downfield. Additionally, if this carbon was adjacent to a methoxy group, the chemical shift could be further influenced by this neighboring substituent, leading to the observed value. The signal at 56.28 ppm for C_{11} and $C_{11'}$ indicated carbons in an aliphatic environment, typically found in methoxy groups ($-OCH_3$). This lower chemical shift, compared to typical alkyl carbons, resulted from the oxygen's electron-withdrawing effect. These chemical shifts were consistent with typical values found in the literature for similar functional groups, supporting their validity in the ^{13}C NMR spectrum of NLI (**Fig 3.64**).

Mass Spectrum

In the mass spectrum of NLI, prominent molecular ion peaks were observed, confirming the molecular weight of the compound. Key peaks in the spectrum were accounted for by the fragmentation pattern detailed in **Fig.3.65**. The corresponding values are summarised in **Table 3.43**

Table 3.43 Molecular ion peaks of NLI

M^+/M+1 Ion	**a**	**b**	**c**	**d**	**e**	**f**	**g**
368	191	177	137	149	123	245	219

*The alphabets correspond to the fragments given in the fragmentation scheme in**Fig.3.65**

In the mass spectrum of NLI, the molecular ion peak was prominently observed at 368, confirming the molecular weight of the compound. Significant fragment ion peaks included the following: the peak at 191, which was assigned to the fragment ion $[C_{11}H_{11}O_3]^+$; the peak at 177, corresponding to the ion $[C_{10}H_9O_3]^+$; and the peak at 137, attributed to the fragment $[C_8H_9O_2]^+$. The peak at 149 was associated with the ion $[C_9H_9O_2]^+$, and the peak at 123 was linked to the ion $[C_7H_7O_2]^+$.The peak at 245 was associated with the ion $[C_{14}H_{13}O_4]^+$, and the peak at 219 was linked to the ion $[C_{12}H_{11}O_4]^+$. These fragment ions align with the expected fragmentation patterns for NLI. The mass spectrum of the compound NLI is shown in **Fig.3.65**

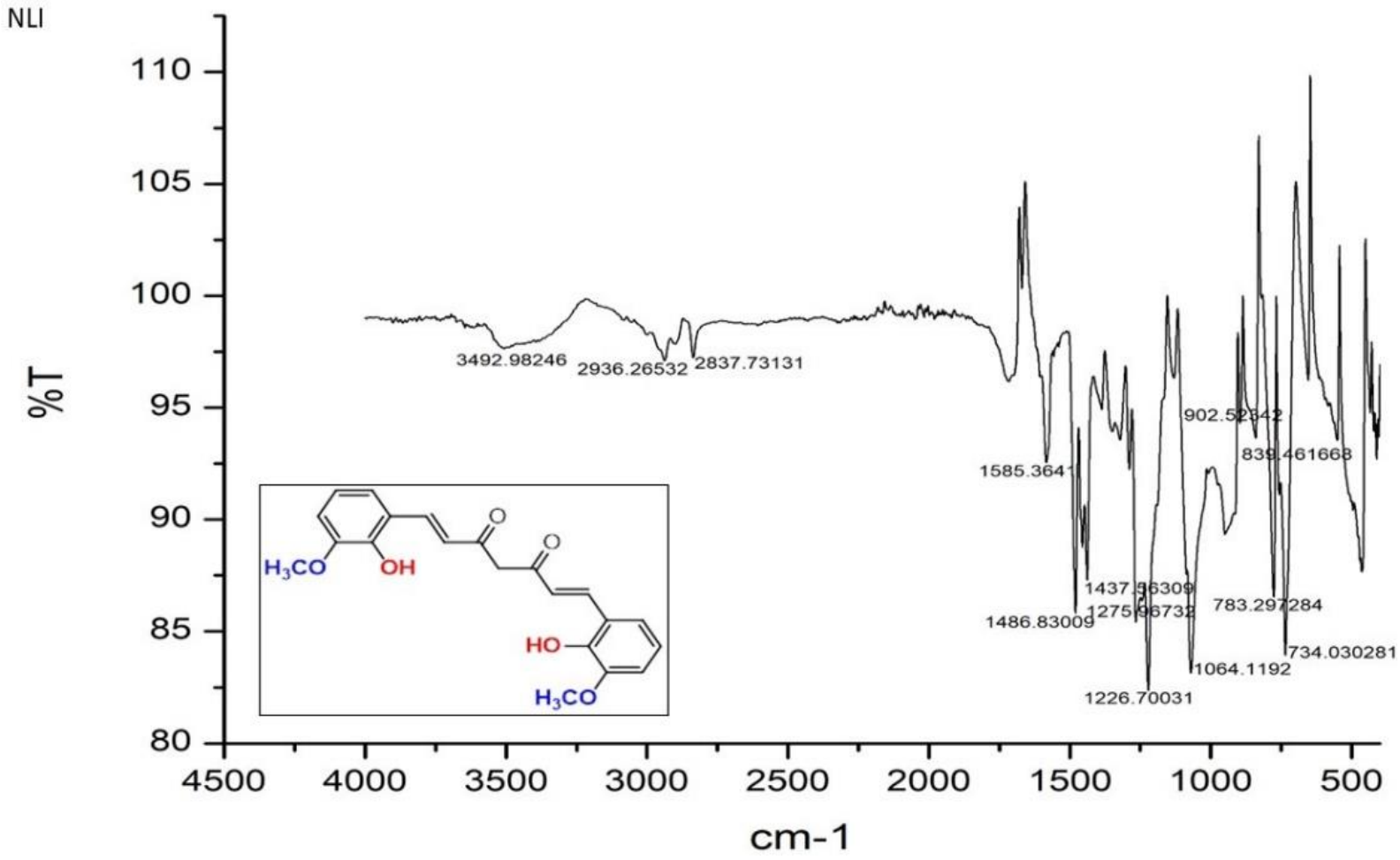

Fig.3.62 The IR spectrum of NLI

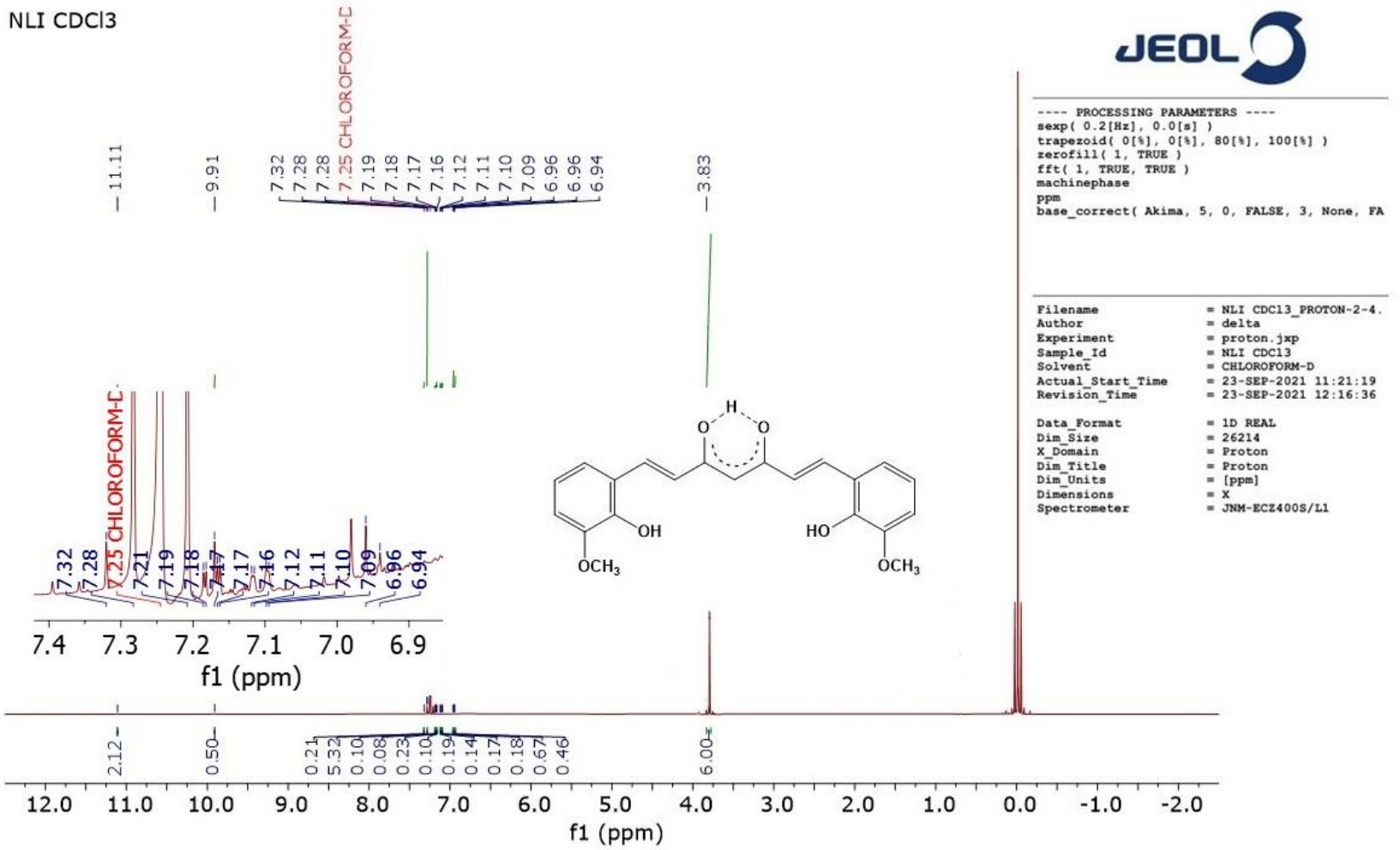

Fig.3.63 The ^{1}H NMR spectrum of NLI

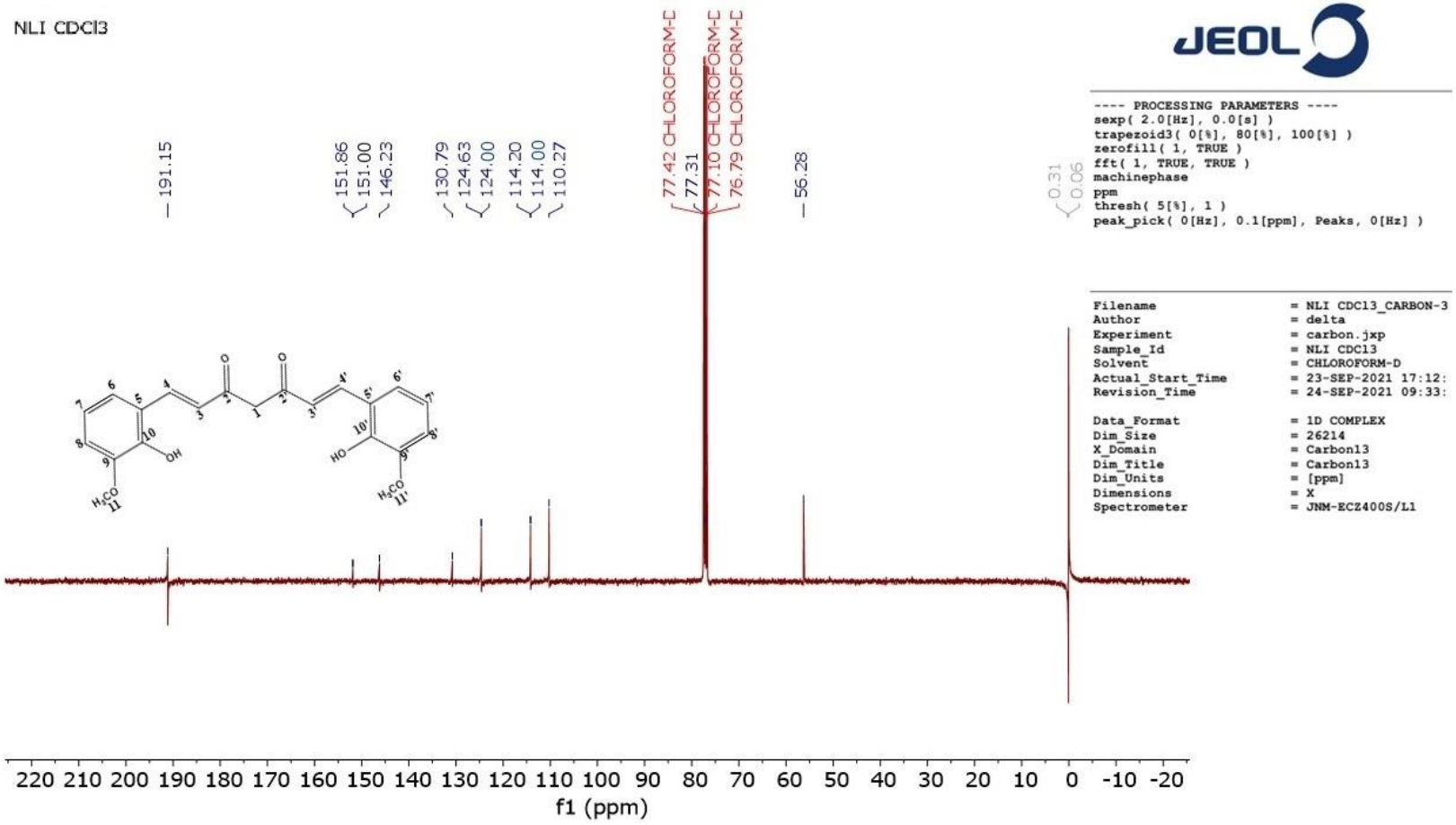

Fig.3.64 The ^{13}CNMR spectrum of NLI

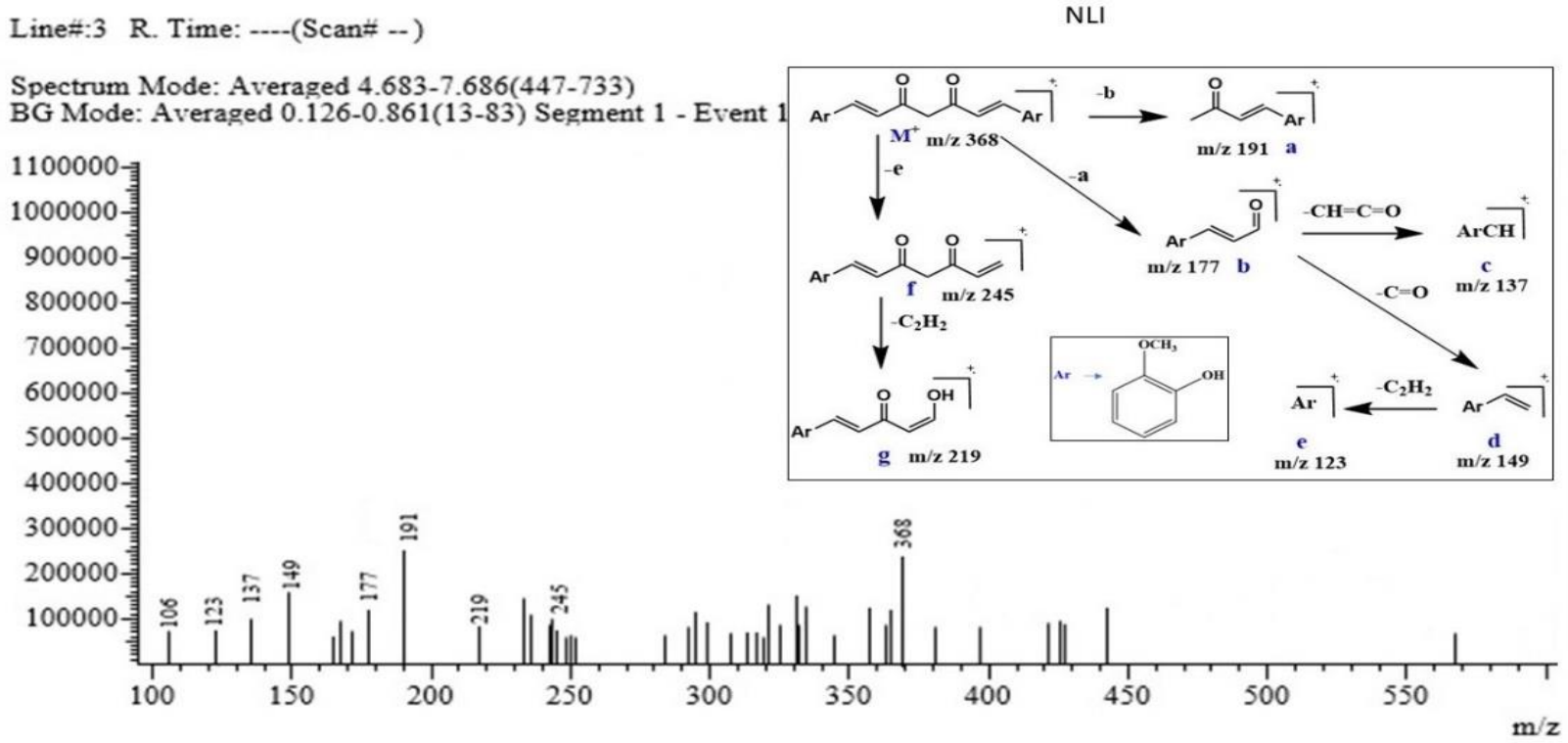

Fig.3.65 The Mass spectrum of NLI

3.5.1.7.2 Synthesis and characterization of $Cu(NLI)_2$ and $Zn(NLI)_2$

3.5.1.7.2.1 Synthesis and characterization of Cu complex of 1,7-bis(2-hydroxy-3-methoxy phenyl)hepta-1,6-diene-3,5-dione [$Cu(NLI)_2$]

The copper(II) complex of the curcuminoid analogue NLI exhibited a molecular weight of 797.17 g/mol and a melting point of 295°C. Elemental analysis revealed carbon, hydrogen, and metal contents of 63.00%, 4.21%, and 7.57%, respectively, aligning closely with the theoretical values of 63.19%, 4.8%, and 7.96%. The compound was synthesized with a yield of 67%.

Characterization of $Cu(NLI)_2$

The $Cu(NLI)_2$ metal complex was characterized using various spectroscopic and analytical techniques, including IR spectroscopy, ^1H NMR, and mass spectrometry. The results from these analyses are summarized and discussed below.

IR Spectrum

The $Cu(NLI)_2$ complex displayed notable spectroscopic characteristics that substantiated the coordination between the ligand and the metal (**Fig.3.66**). Significantly, there was a lack of a pronounced carbonyl absorption band within the 1650-1800 cm^{-1} spectral region, and the carbonyl peak at 1630 cm^{-1} was no longer present. A novel band emerged at 1572.7 cm^{-1}, signifying that the metal ion had supplanted the enolic proton, thereby facilitating the formation of a metal-coordinated carbonyl moiety. This transition to a lower frequency (1572.7 cm^{-1}) implied the occurrence of chelation. Furthermore, a band observed at 1535.4 cm^{-1} was ascribed to the asymmetric stretching of the C-C-C bond within the aromatic framework. Low-frequency bands at 465.6 cm^{-1} and 402.7 cm^{-1} were designated to metal-oxygen (M-O) stretching vibrations, thereby corroborating the coordination between the metal and the ligand.

^{1}HNMR Spectrum

The distinct proton signals detected within the ^1H NMR spectrum of the Cu(II) complex of 1,7-bis(2-hydroxy-3-methoxy phenyl)hepta-1,6-diene-3,5-dione [$Cu(NLI)_2$] have been meticulously compiled in **Table 3.44**

Table 3.44 Proton signals observed in the ^{1}H NMR spectrum of Cu $(NLI)_2$ (Chemical Shifts δ in ppm)

Complex	Methine	Alkenyl	Phenyl	Methoxy	Hydroxy
$Cu(NLI)_2$	6.77	6.95-7.29	7.12-7.17	3.96	11.12

The ^{1}H NMR spectrum of the copper complex $Cu(NLI)_2$ revealed characteristic chemical shifts for methine, alkenyl, phenyl, methoxy, and hydroxy protons (**Fig.3.67**). The methine proton appeared at 6.97 ppm, indicating its position in a conjugated system. Alkenyl protons resonated between 6.95-7.29 ppm, while phenyl protons appeared in the 7.12-7.17 ppm range, reflecting the effects of conjugation and aromaticity. The OH group attached to the aromatic ring, positioned near a methoxy group, appeared at δ 11.12 ppm in the ^{1}H NMR spectrum, reflecting its presence in a conjugated system. This chemical shift aligns with the expected value for a hydroxyl proton in such an environment, where conjugation and nearby electron-donating groups influence the shift downfield. These shifts aligned with expected values for such environments, influenced by copper coordination.

Mass Spectrum

Table 3.15 Molecular ion peaks of Cu $(NLI)_2$

M+/(M+1)/(M+2) ion	a	b	c	d	e	f	g	h	i	j
797	674	551	428	304	123	430	183	368	122	121

*The alphabets correspond to the fragments given in the fragmentation scheme in**Fig.3.68**

The mass spectrum of the Cu(II) complex with NLI exhibited a prominent molecular ion peak at m/z 797, indicating the intact molecular weight of the compound. Fragmentation patterns revealed peaks at m/z 551 and 304, corresponding to the sequential loss of two and four 2-hydroxy-3-methoxy phenyl groups from the molecular ion. Additionally, a peak at m/z 430 was identified as the $[ML]^+$ fragment, where M represents the Cu metal and L denotes the ligand 1,7-bis(2-hydroxy-3-methoxy phenyl)hepta-1,6-diene-3,5-dione. Other fragment ions at m/z 674, 428, 183, 368, and 122 further supported the fragmentation patterns and structural components of the $Cu(NLI)_2$ complex, as depicted in **Fig 3.68.**

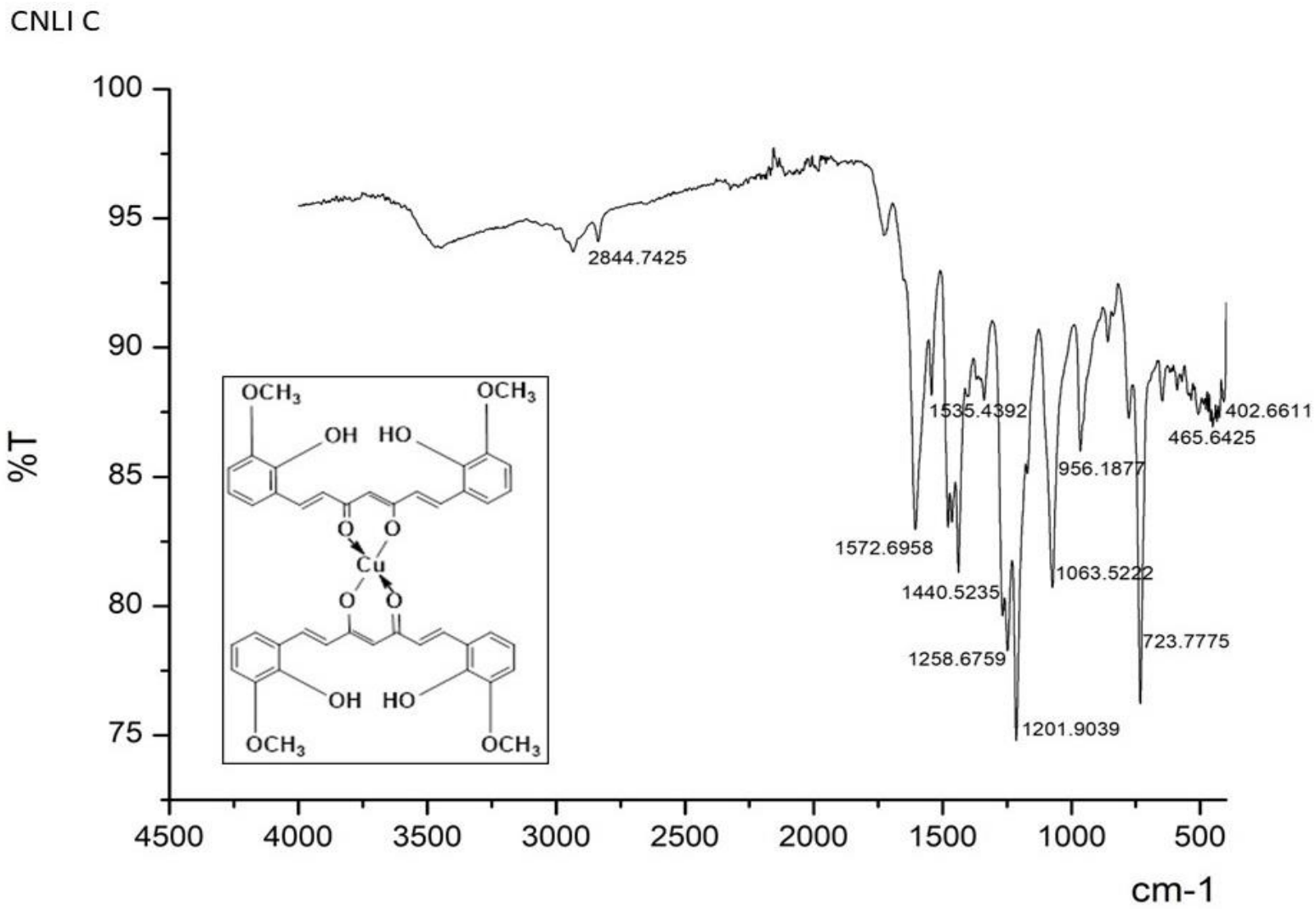

Fig.3.66 The IR spectrum of Cu $(NLI)_2$

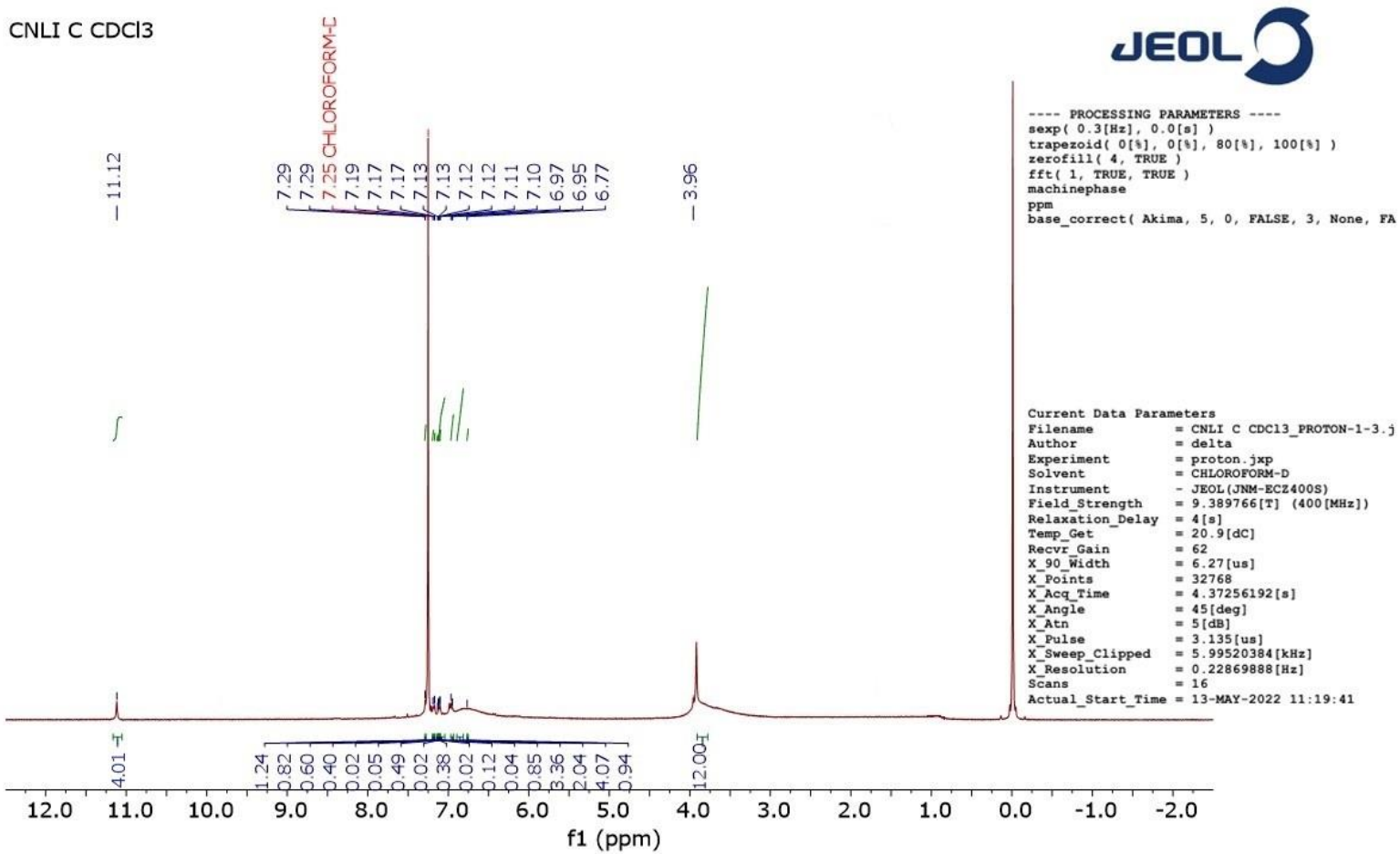

Fig.3.67 The ^{1}H NMR spectrum of Cu $(NLI)_2$

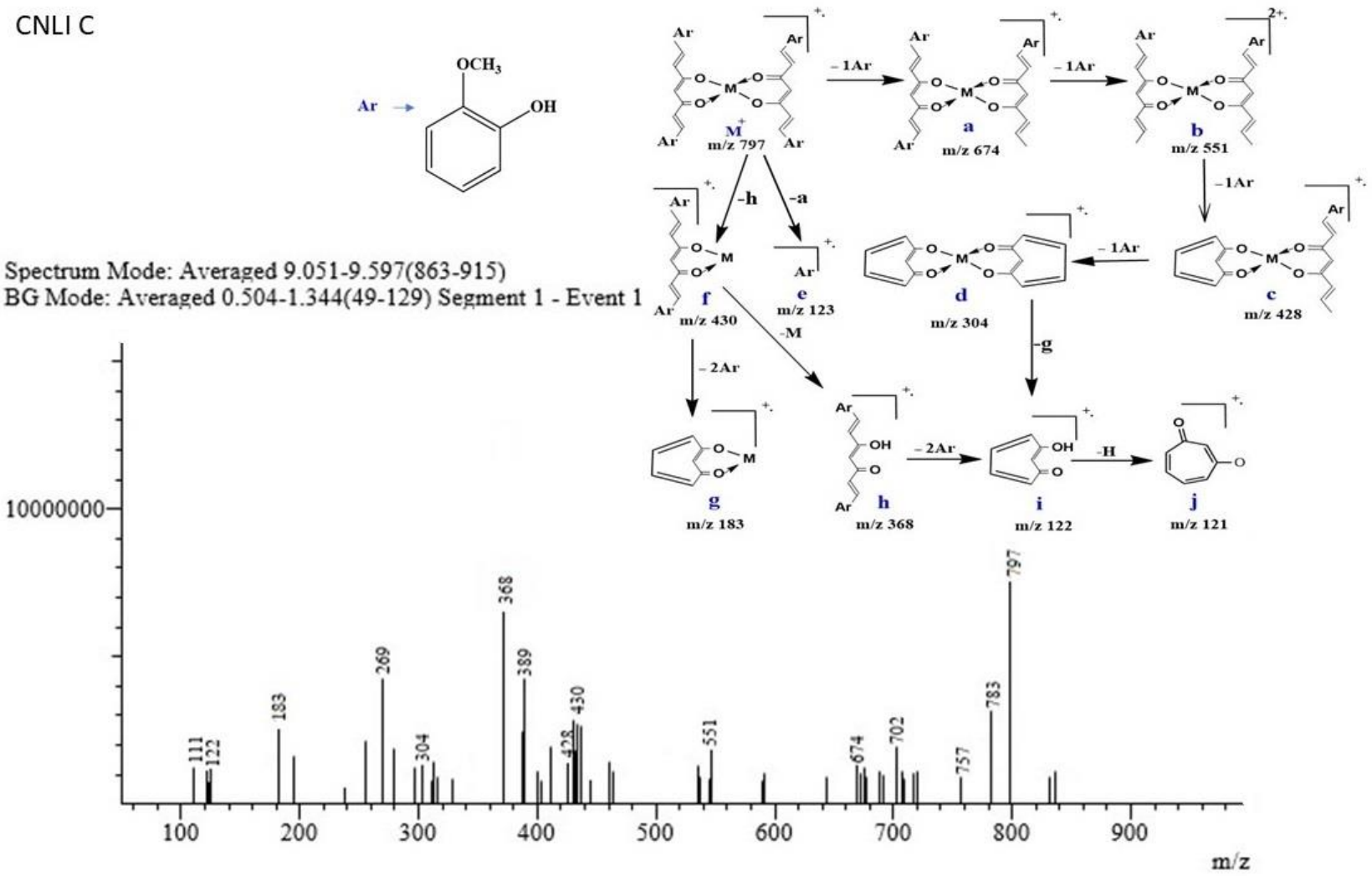

Fig.3.68 The Mass spectrum of Cu $(NLI)_2$

3.5.1.7.2.2 Synthesis and Characterization of Zn complex of 1,7-bis(2-hydroxy-3-methoxy phenyl)hepta-1,6-diene-3,5-dione [Zn(NLI)$_2$]

The zinc(II) complex derived from the curcuminoid analogue NLI exhibited a molecular weight of 798.17 g/mol and a melting point of 298°C. The results of the elemental analysis revealed carbon, hydrogen, and metal compositions of 63.01%, 4.22%, and 8.00%, respectively, which are close to the theoretical values of 63.05%, 4.79%, and 8.17%. The synthesis process resulted in a yield of 64%.

Characterization of Zn(NLI)$_2$

The ZnNLI)$_2$ metal complex was characterized using various spectroscopic and analytical techniques, including IR spectroscopy, ^{1}H NMR, and mass spectrometry. The results from these analyses are summarized and discussed below.

IR Spectrum

The Zn(NLI)$_2$ complex exhibited distinct spectroscopic features that confirmed coordination between the ligand and the metal (**Fig.3.69**). Notably, the absence of a prominent carbonyl absorption band in the 1650-1800 cm^{-1} region and the disappearance of the carbonyl peak at 1630 cm^{-1} indicated the involvement of the carbonyl group in metal coordination. A new band at 1572 cm^{-1} emerged, suggesting that the metal ion had replaced the enolic proton, leading to the formation of a metal-coordinated carbonyl. This shift to a lower frequency (1572 cm^{-1}) implied chelation. Additionally, a band at 1497 cm^{-1} was attributed to the asymmetric stretching of the C-C-C bonds within the aromatic ring. Low-frequency bands at 465 cm^{-1} and 421 cm^{-1}, assigned to metal-oxygen (M-O) stretching, further supported the coordination between the metal and the ligand.

^{1}HNMR Spectrum

The unique proton resonances observed in the ^{1}H NMR spectrum corresponding to the Zn(II) complex of 1,7-bis(2-hydroxy-3-methoxy phenyl)hepta-1,6-diene-3,5-dione [Zn(NLI)$_2$] have been systematically catalogued in **Table 3.46**

Table 3.46 Proton signals observed in the ^{1}H NMR spectrum of Zn(NLI)$_2$ (Chemical Shifts δ in ppm)

Complex	Methine	Alkenyl	Phenyl	Methoxy	Hydroxy
Zn(NLI)$_2$	6.79	7.02 -7.45	7.06 -7.29	3.96	11.11

The ^{1}H NMR spectrum of the Zn(NLI)$_2$ complex revealed characteristic chemical shifts for various proton environments, including methine, alkenyl, phenyl, methoxy, and hydroxy groups (**Fig.3.70**). The methine proton resonated at 6.97 ppm, typical for protons adjacent to conjugated systems like C=C bonds or aromatic rings, indicating deshielding due to conjugation. Alkenyl protons, observed between 7.02 -7.45 ppm, corresponded to C=C bonds in conjugated systems, with nearby aromatic rings contributing to deshielding. Phenyl protons appeared within the 7.06 -7.29 ppm range, consistent with aromatic protons influenced by electron-donating or withdrawing substituents. Methoxy protons shifted at 3.96 ppm, typical for methoxy groups attached to aromatic systems where conjugation caused slight deshielding. The OH group attached to the aromatic ring, positioned near a methoxy group, appeared at δ 11.11 ppm, reflecting its presence in a conjugated system. This chemical shift aligned with the expected value for a hydroxyl proton in such an environment, where conjugation and nearby electron-donating groups caused the downfield shift. Thus, the observed shifts were consistent with proton environments in a conjugated system, further influenced by Zn(II) coordination.

Mass Spectrum

Table 3.47 Molecular ion peaks of Zn (NLI)$_2$

M+/(M+1)/(M+2) ion	**a**	**b**	**c**	**d**	**e**	**f**	**g**	**h**	**i**	**j**
798	675	552	429	305	123	431	184	368	122	121

*The alphabets correspond to the fragments given in the fragmentation scheme in**Fig.3.71**

The mass spectrum of the Zn(II) complex with NLI displayed a prominent molecular ion peak at m/z 798, indicating the intact molecular weight of the compound. Fragmentation patterns revealed peaks at m/z 552 and 305, corresponding to the sequential loss of two and four 2-hydroxy-3-methoxy phenyl groups from the molecular ion. Additionally, a peak at m/z 431 was identified as the $[ML]^+$ fragment, where M represents the Zn metal and L denotes the ligand 1,7-bis(2-hydroxy-3-methoxy phenyl)hepta-1,6-diene-3,5-dione. Other fragment ions at m/z 675, 429, 123, 184, 368, and 121 further corroborated the fragmentation patterns and structural components of the Zn(NLI)$_2$ complex, as illustrated in **Fig.3.71.**

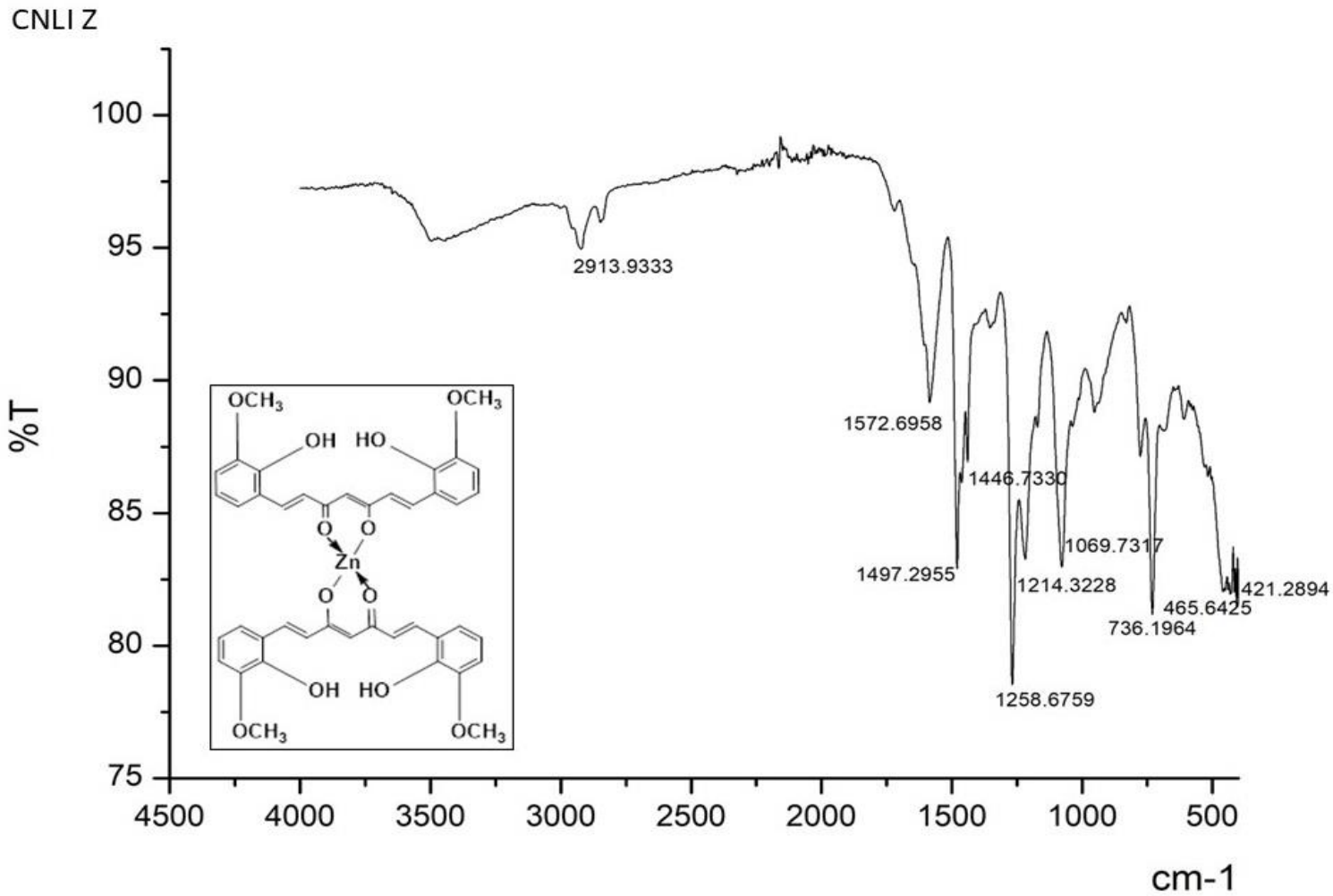

Fig.3.69 The IR spectrum of Zn $(NLI)_2$

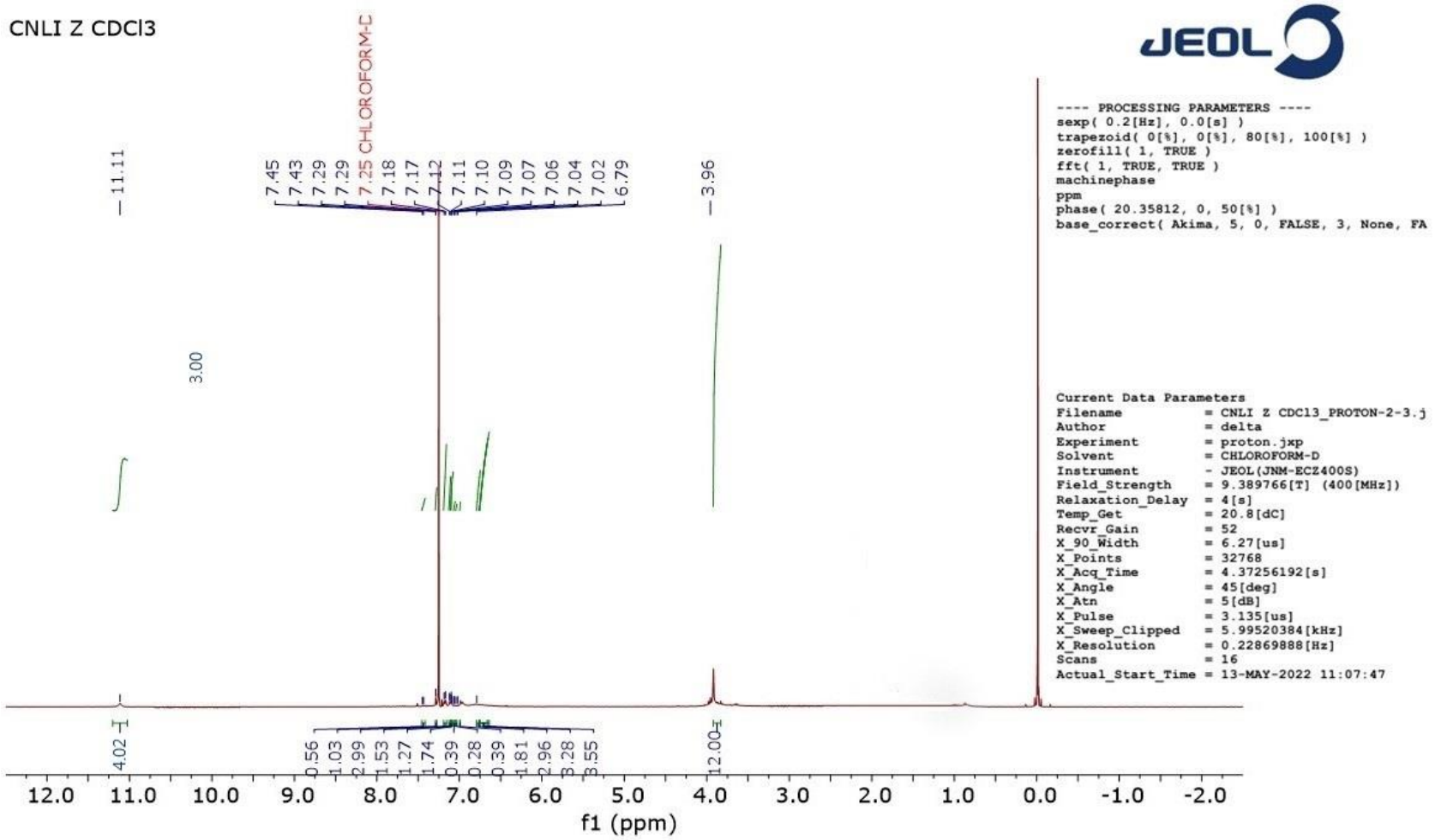

Fig.3.70 The ^{1}H NMR spectrum of Zn $(NLI)_2$

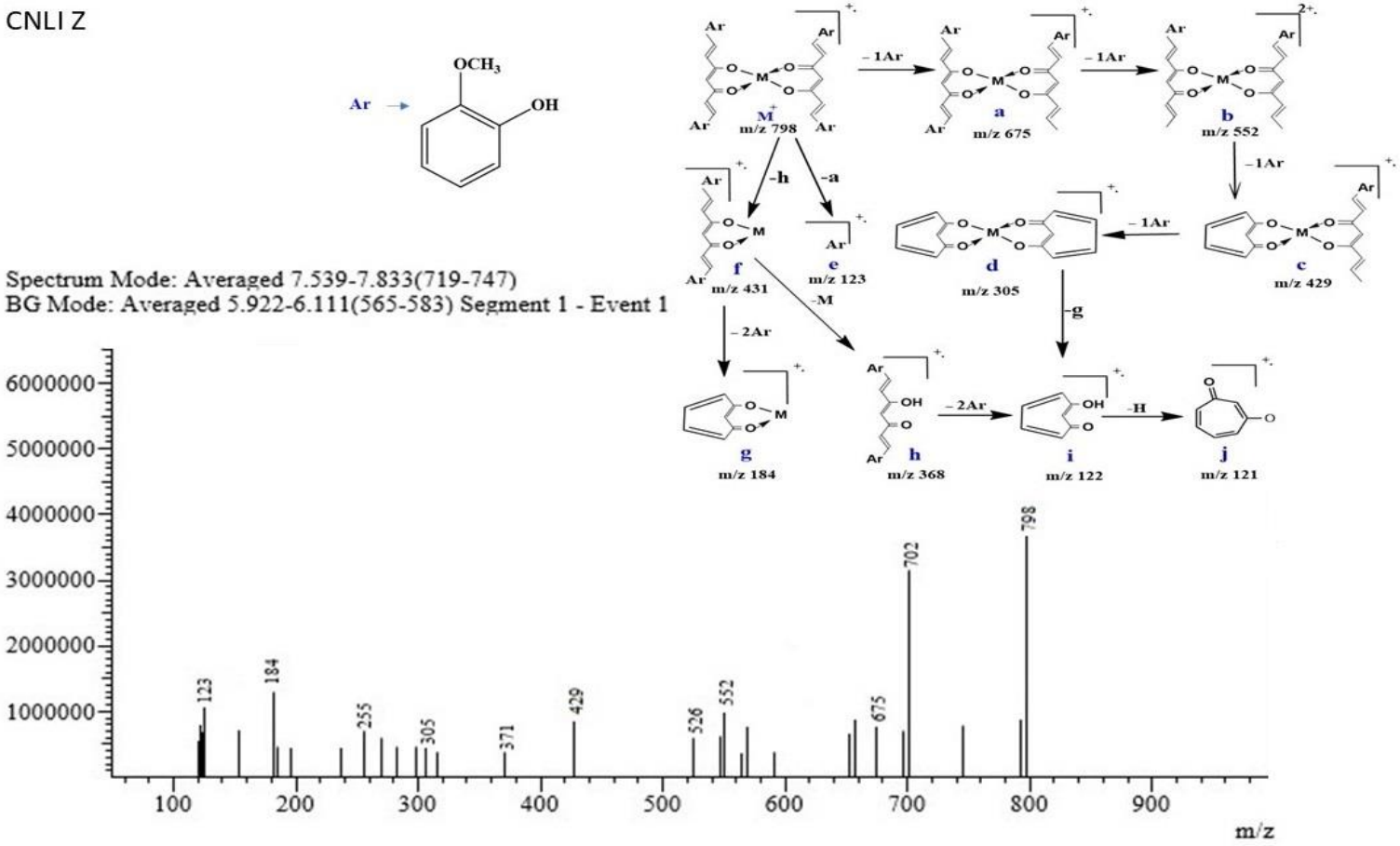

Fig.3.71 The Mass spectrum of Zn $(NLI)_2$

3.5.1.8. Synthesis and characterization of (1E,6E)-1,7-bis(3-hydroxy-4-methoxy phenyl)hepta-1,6-diene-3,5-dione (NLJ)

3.5.1.8.1 Synthesis and characterization of NLJ

1,7-Bis(3-hydroxy-4-methoxyphenyl)hepta-1,6-diene-3,5-dione (NLJ) was synthesized through the condensation of 3-hydroxy-4-methoxybenzaldehyde (0.01 M) with an acetylacetone–boron complex in ethyl acetate, using tri-sec-butyl borate and n-butylamine as condensing agents. The reaction involved the condensation of two aldehyde equivalents with one acetylacetone equivalent, yielding 75% pure orange-red crystals. The compound had a melting point of 285°C and a molecular weight of 368 g/mol. Elemental analysis showed carbon and hydrogen contents of 67.9% and 4.96%, respectively, closely aligning with the theoretical values of 68.47% and 5.47%, confirming the anticipated bis-condensation product.

Characterization of NLJ

The synthesized compound NLJ was characterized using various spectroscopic techniques like IR,^{1}H NMR,^{13}C NMR and mass spectrometry. The following discussion provided a detailed analysis of the spectral data associated with the compound.

IR Spectrum

The IR peaks for NLJ can be interpreted based on the typical absorption ranges associated with different functional groups. The Possible IR signals are displayed in **Table 3.48.**

Table 3.48 Possible IR assignments of NLJ

Wavenumbers (in cm^{-1})	**Possible IR Assignments**
2936.3	ν Enolic
1677.1	ν(C=O)
1585.4	ν(C=C) Phenyl
1507.5	ν(C-C)Alkenyl
1437.6	ν_s(C-C-C)
1113.4	νβ (C-H)
958.7	ν(CH=CH)trans

The IR spectrum of NLJ revealed several key absorption bands, each corresponding to distinct functional groups within the molecule (**Fig.3.72**). A notable band at 2936.3 cm^{-1} was linked to the stretching vibration of the enolic O-H group, with its lower frequency suggesting intramolecular hydrogen bonding. The strong absorption at 1677.1 cm^{-1} indicated the presence of a carbonyl (C=O) group, typical of conjugated systems like β-diketones, where resonance effects cause the carbonyl stretch to appear within the 1650-1700 cm^{-1} range. The band at 1585.3 cm^{-1} was attributed to the C=C stretching vibrations within the aromatic phenyl ring, aligning with the expected range for conjugated aromatic systems. The peak at 1507.5 cm^{-1} corresponded to the C-C stretching vibration within the alkenyl group, confirming the presence of alkenyl structures in the compound. An absorption at 1437.6 cm^{-1} was associated with symmetric stretching of the C-C-C bond framework, common in conjugated systems. The band at 1113.4 cm^{-1} indicated bending vibrations of the C-H bonds, typical of aromatic or alkenyl C-H stretches. Lastly, the absorption at 958.7 cm^{-1} was characteristic of the trans-C-H bending vibration in alkenes, suggesting the presence of trans double bonds in NLJ.

^{1}HNMR Spectrum

The proton signals in the ^{1}H NMR spectrum of NLJ provide detailed insights into the chemical environment of the hydrogen atoms within the molecule. The chemical shifts (δ, ppm) corresponded to distinct functional groups, offering a detailed understanding of the molecular structure. The diverse proton resonances identified in the spectrum are thoroughly outlined in **Table 3.49**.

Table 3.49 Proton signals observed in the ^{1}H NMR spectrum of NLJ (Chemical Shifts δ ppm)

Compound	Enolic	Methine	Alkenyl	Phenyl	Hydroxy	Methoxy
NLJ	9.87	6.91	6.95-7.43	7.17-7.24	9.79	3.97

The ^{1}H NMR spectrum of NLJ showed the enolic proton at 9.83 ppm, resonating downfield due to deshielding by a nearby carbonyl group and hydrogen bonding, consistent with similar structures. The methine proton appeared at 6.91 ppm, within the expected range for methine groups in β-diketones, influenced by electron-withdrawing effects from adjacent carbonyl groups. Alkenyl protons, part of a conjugated diene system, resonated

between 6.95-7.43 ppm, aligning with typical values for such systems due to delocalized electron density. The phenyl protons observed between 7.17-7.24 ppm, were consistent with aromatic ring protons in conjugated systems. The signal at 3.97 ppm corresponded to methyl protons attached to an electronegative group, like oxygen in a methoxy group, which is typical for such environments. The hydroxy proton at 9.79 ppm indicated that it was attached to an aromatic ring. These observed chemical shifts were consistent with known data for similar functional groups, confirming the accuracy of the NMR values for NLJ. The ^{1}H NMR spectrum of NLJ is brought out in **Fig 3.73**.

^{13}C NMR Spectra

To interpret the ^{13}C NMR spectral data for the compound NLJ, the chemical shifts were assigned to the corresponding carbon atoms based on their chemical environments. The details of the ^{13}C NMR spectrum for NLJ are provided in **Table 3.58.**

Table 3.50 ^{13}C NMR spectral data of NLJ (Chemical Shifts δ ppm)

C_1	C_2,$C_{2'}$	C_3,$C_{3'}$	C_4,$C_{4'}$	C_5,$C_{5'}$	C_6,$C_{6'}$
110.27	191.5	130.79	146.00	124.63	114.20
C_7,$C_{7'}$	C_8,$C_{8'}$	C_9,$C_{9'}$	C_{10},$C_{10'}$	C_{11},$C_{11'}$	
146.23	151.86	114.00	124.00	56.28	

The signal at 110.27 ppm was attributed to C1, part of a β-diketone structure, indicating its enolic form in conjugation with adjacent double bonds. The downfield chemical shift of 191.5 ppm for C2 and C2' was characteristic of carbonyl carbons in conjugated systems, such as β-diketones, confirming the significant deshielding effect caused by the electronegative oxygen atoms. For C3 and C3', the shift at 130.79 ppm corresponded to sp²-hybridized carbons within a conjugated system, likely involving alkenes or aromatic rings. The signal at 146 ppm for C4 and C4' suggested the influence of an aromatic ring and the conjugation with an alkenyl chain and carbonyl groups, fitting the expected range for such an environment. C5 and C5' at 124.63 ppm were consistent with sp²-hybridized carbons in aromatic systems that are not directly attached to electronegative atoms, but still within a conjugated system. The 114.20 ppm shift for C6 and C6' indicated the presence of less deshielded aromatic carbons.The chemical shift at 146.23 ppm for C7 and C7' was attributed to a carbon in an aromatic ring adjacent to a carbon bearing a methoxy group, where the electron-withdrawing nature of the oxygen atom caused significant deshielding. This placed the signal within the 140-160 ppm range, consistent

with the expected chemical shift. For C8 and C8', the 151.86 ppm shift was typical for carbons bonded to electronegative groups, such as oxygen in methoxy groups, confirming their presence in a conjugated system. The 114 ppm signal for C9 and C9' was associated with carbons in aromatic rings, with slight deshielding effects from the hydroxyl and adjacent methoxy groups.The 124.00 ppm shift for C10 and C10' aligned with shifts seen in conjugated systems, while the 56.28 ppm shift for C11 and C11' indicated methyl carbons attached to electronegative atoms like in a methoxy group, showing significant deshielding due to the oxygen atom. Thus, the chemical shifts observed in the ^{13}C NMR spectrum of NLJ were consistent with the expected ranges for various functional groups and structural elements, confirming the accuracy of the spectral interpretation (**Fig 3.74**).

Mass Spectrum

In the mass spectrum of NLJ, prominent molecular ion peaks were observed, confirming the compound's molecular weight. The key peaks in the spectrum were explained by the fragmentation pattern outlined in (**Fig.3.75**). The corresponding values are summarised in **Table 3.51.**

Table 3.51 Molecular ion peaks of NLJ

M^+/M+1 Ion	a	b	c	d	e	f	g
368	191	177	137	149	123	245	219

*The alphabets correspond to the fragments given in the fragmentation scheme in**Fig.3.75**

In the mass spectrum of NLJ (**Fig.3.75**), the molecular ion peak was prominently observed at 368, confirming the compound's molecular weight. Significant fragment ion peaks included the following: the peak at 191, assigned to the fragment ion $[C_{11}H_{11}O_3]^+$; the peak at 177, corresponding to the ion $[C_{10}H_9O_3]^+$; and the peak at 137, attributed to the fragment $[C_8H_9O_2]^+$. Additionally, the peak at 149 was associated with the ion $[C_9H_9O_2]^+$, and the peak at 123 was linked to the ion $[C_7H_7O_2]^+$. The peak at 245 was associated with the ion $[C_{14}H_{13}O_4]^+$, while the peak at 219 was linked to the ion $[C_{12}H_{11}O_4]^+$. These fragment ions align with the expected fragmentation patterns for NLJ.

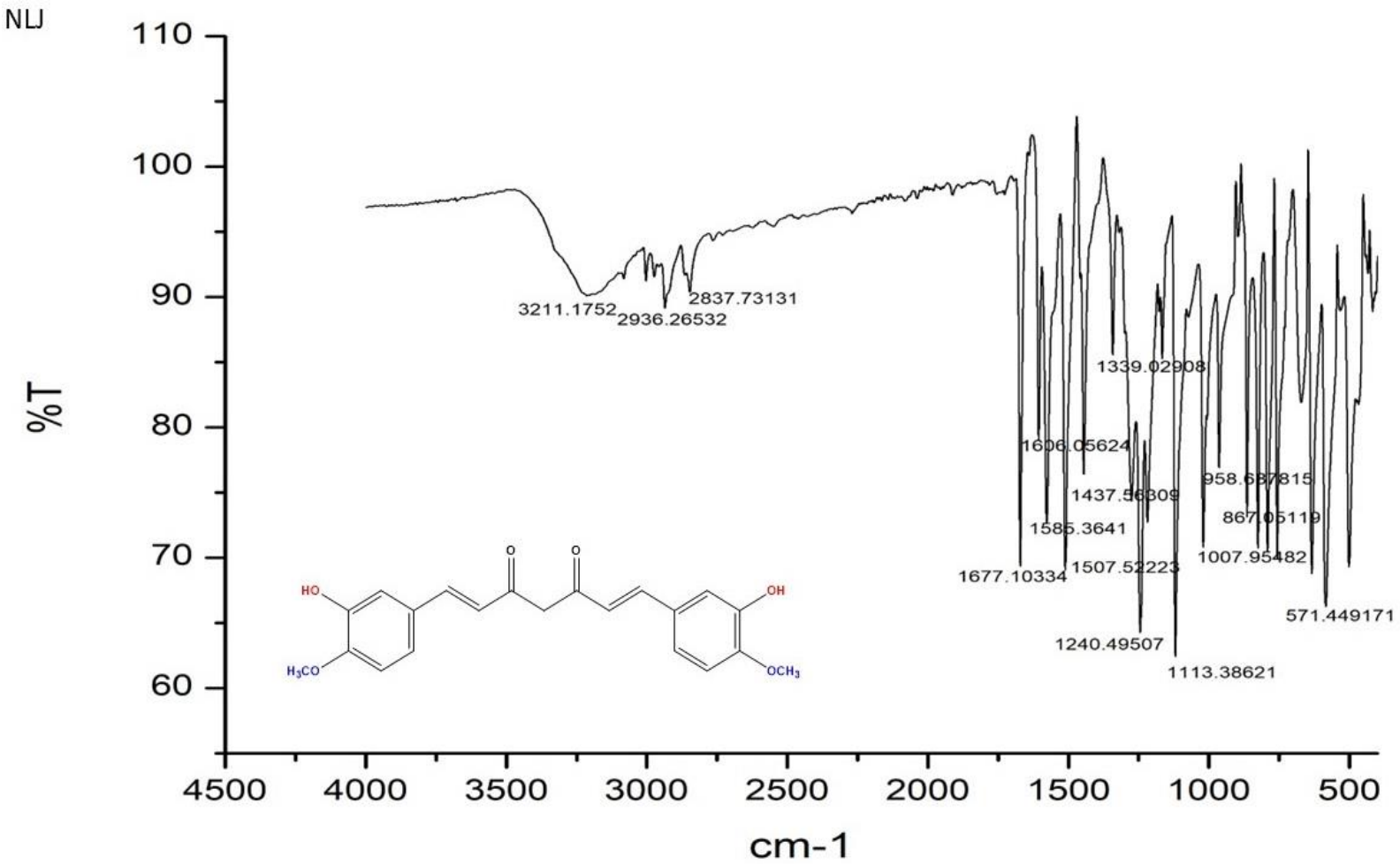

Fig.3.72 The IR spectrum of NLJ

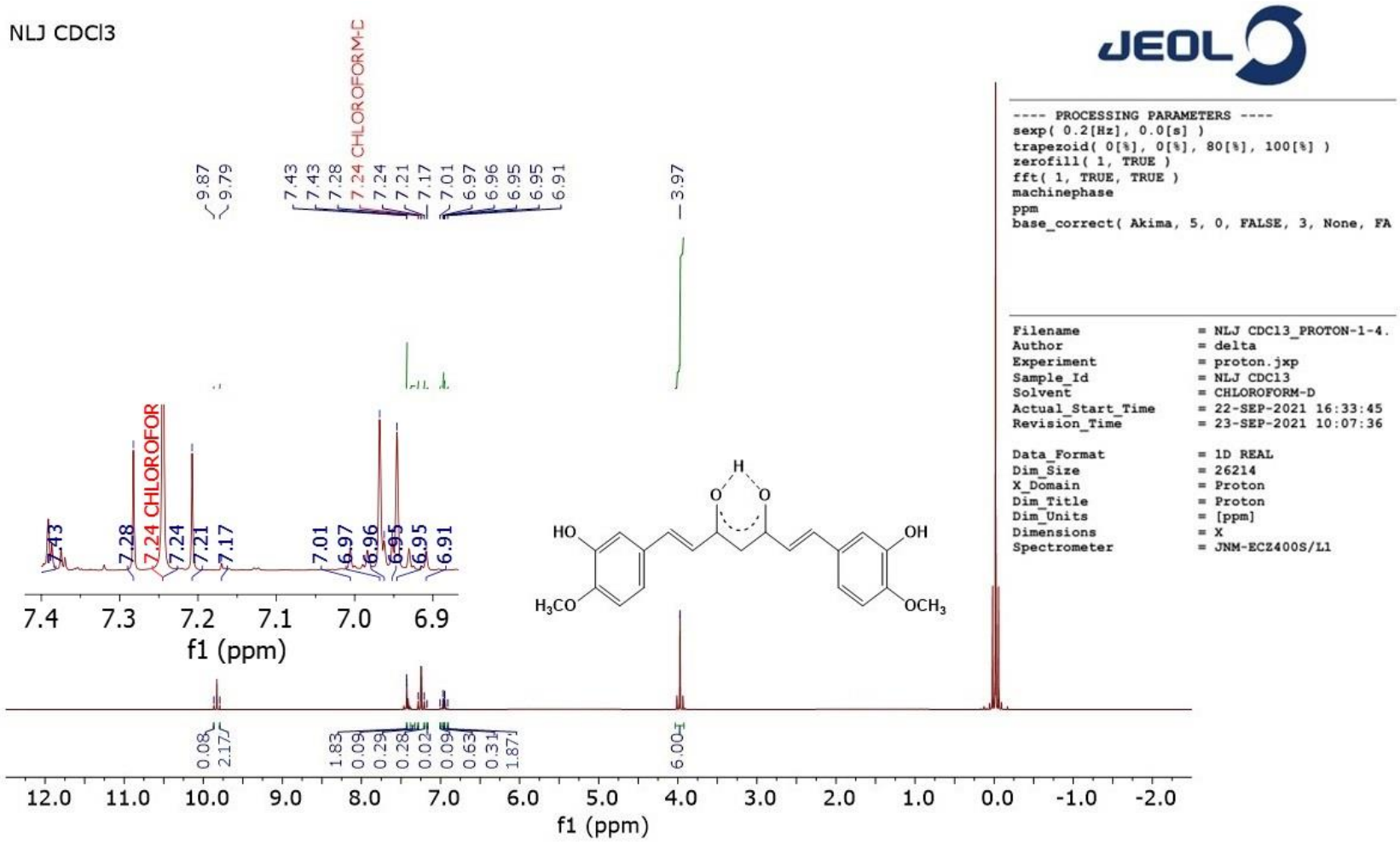

Fig.3.73 The ^{1}H NMR spectrum of NLJ

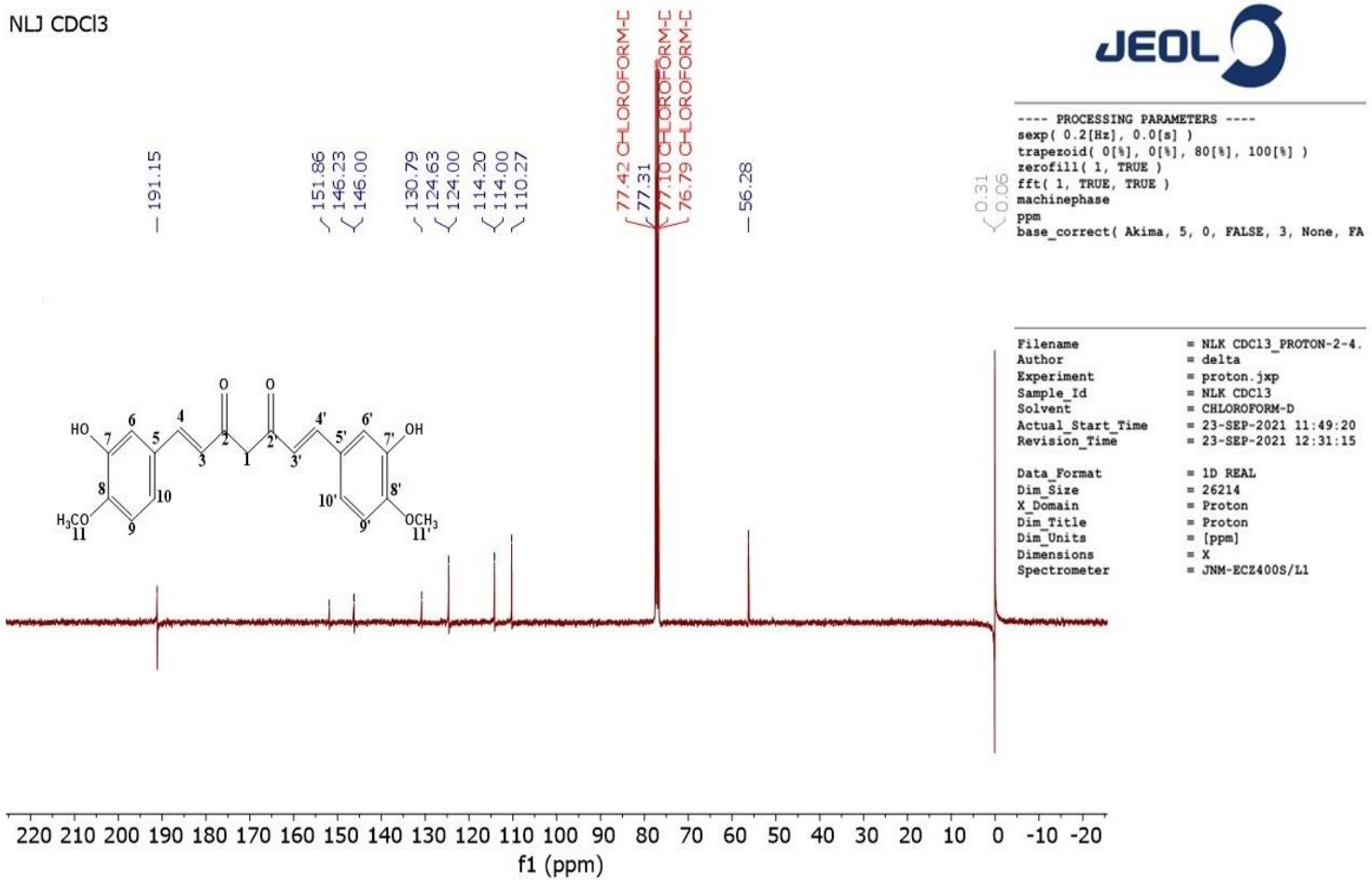

Fig.3.74 The ^{13}CNMR spectrum of NLJ

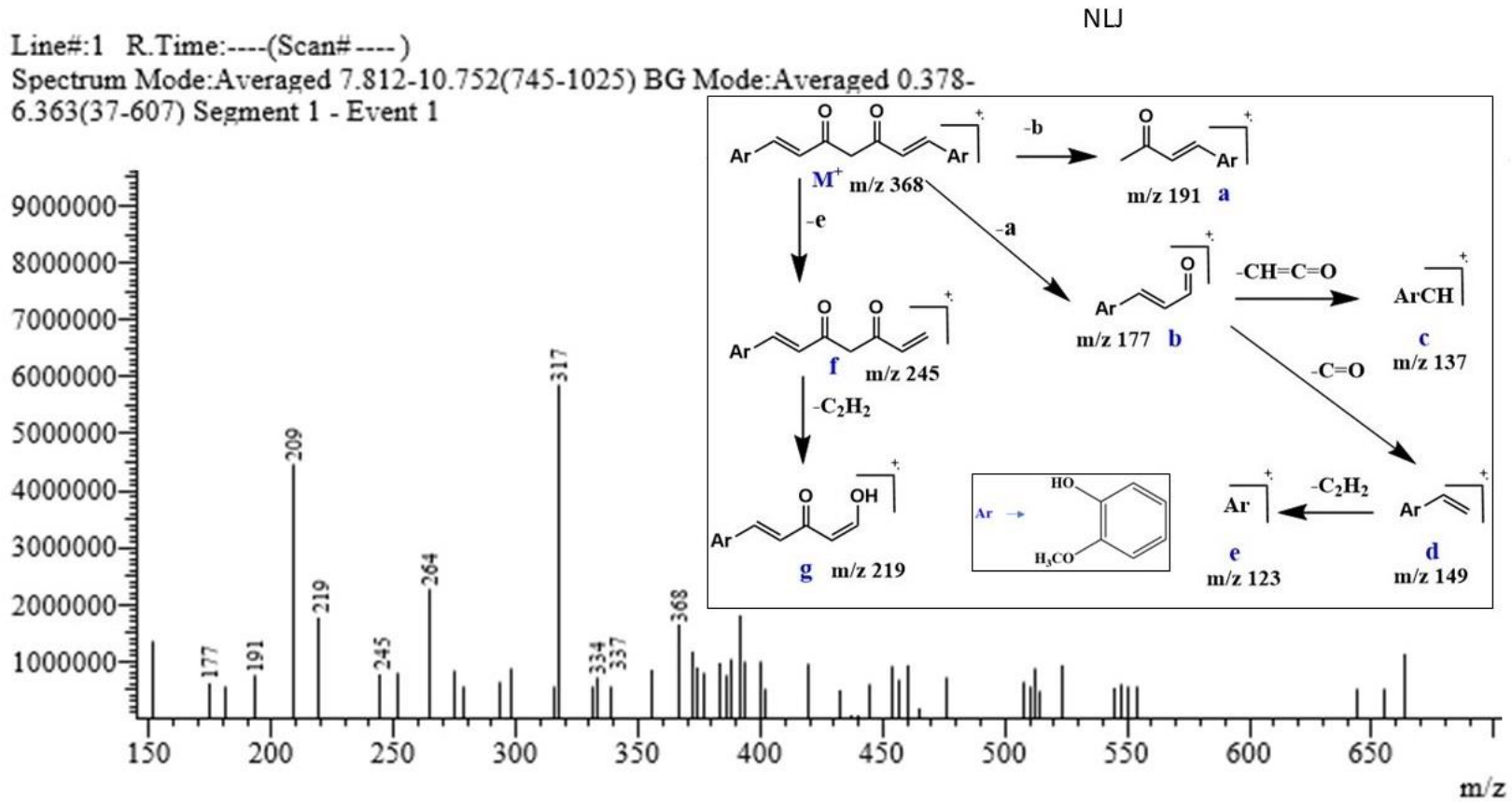

Fig.3.75 The Mass spectrum of NLJ

3.5.1.8.2 Synthesis and characterization of $Cu(NLJ)_2$ and $Zn(NLJ)_2$

3.5.1.8.2.1 Synthesis and characterization of Cu(II) complex of 1,7-bis(3-hydroxy-4-methoxyphenyl)hepta-1,6-diene-3,5-dione [$Cu(NLJ)_2$]

The Cu(II) complex of the curcuminoid analogue NLJ exhibited a molecular weight of 797.17 g/mol and a melting point of 289°C. Elemental analysis showed carbon, hydrogen, and metal contents of 63.25%, 4.07%, and 7.23%, respectively, closely matching the theoretical values of 63.19%, 4.8%, and 7.96%. The synthesis yielded 69% of the compound.

Characterization of $Cu(NLJ)_2$

The $Cu(NLJ)_2$ metal complex was thoroughly characterized employing a range of spectroscopic and analytical methodologies, encompassing infrared spectroscopy, proton nuclear magnetic resonance (^{1}H NMR), and mass spectrometry. The findings derived from these analytical procedures are synthesized and deliberated in the following sections.

IR Spectrum

The $Cu(NLJ)_2$ complex exhibited remarkable spectroscopic features that validated the coordination interaction between the ligand and the metal ion (**Fig.3.76**). Notably, a distinct carbonyl absorption band was absent in the spectral range of 1650-1800 cm^{-1}, and the carbonyl peak at 1630 cm^{-1} was conspicuously absent. A new band appeared at 1592.2 cm^{-1}, indicating that the metal ion had replaced the enolic proton, thus enabling the establishment of a metal-coordinated carbonyl moiety. This shift to a lower frequency (1592.2 cm^{-1}) suggested the occurrence of chelation. Additionally, a band detected at 1523.0 cm^{-1} was attributed to the asymmetric stretching of the C-C-C bond within the aromatic structure. Bands at lower frequencies of 465.6 cm^{-1} and 421.3 cm^{-1} were identified as metal-oxygen (M-O) stretching vibrations, thereby reinforcing the coordination between the metal ion and the ligand.

^{1}HNMR Spectrum

The unique proton signals observed in the ^{1}H NMR spectrum of the Cu(II) complex of 1,7-bis(3-hydroxy-4-methoxyphenyl)hepta-1,6-diene-3,5-dione [$Cu(NLJ)_2$] have been carefully summarized in **Table 3.52**

Table 3.52 Proton signals observed in the ^{1}HNMR spectrum of $Cu(NLJ)_2$ (Chemical Shifts δ in ppm)

Complex	Methine	Alkenyl	Phenyl	Hydroxy	Methoxy
$Cu(NLJ)_2$	6.98	6.96-7.43	7.00-7.51	9.84	3.99

The ^{1}H NMR spectrum of the $Cu(NLJ)_2$ complex provided detailed information about the proton environments in the compound (**Fig.3.77**). The methine protons appeared at δ 6.98 ppm, typical for protons adjacent to conjugated systems such as double bonds or aromatic rings, indicating deshielding due to conjugation. Alkenyl protons were observed in the range of δ 6.96-7.43 ppm, consistent with protons on C=C bonds in conjugated systems, where nearby aromatic rings contributed to deshielding. Phenyl protons resonated between δ 7.00 -7.51 ppm, reflecting aromatic protons affected by substituents and electronic effects. The significant downfield shift of the hydroxy proton to δ 9.84 ppm in $[Cu(NLJ)_2]$ was explained by the indirect influence of Cu(II) coordination through the carbonyl groups. Although the hydroxy group itself did not directly coordinate with Cu(II), the overall electronic environment and potential conformational changes induced by metal coordination led to the significant downfield shift in the hydroxy proton. This shift reflected the complex interplay of electronic effects within the metal-ligand coordination sphere. The methoxy protons appeared at δ 3.99 ppm, aligning with the typical range for methoxy groups attached to aromatic systems, with a slight downfield shift indicating some conjugative effects. Thus, these chemical shifts were consistent with the expected proton environments in a conjugated system and highlighted the influence of copper coordination on these environments.

Mass Spectrum

Table 3.53 Molecular ion peaks of $Cu(NLJ)_2$

M^+/(M+1)/(M+2) ion	a	b	c	d	e	f	g	h	i	j
797	675	552	429	305	123	430	183	368	122	121

*The alphabets correspond to the fragments given in the fragmentation scheme inFig.**3.78**

The mass spectrum of the Cu(II) complex with NLJ showed a prominent molecular ion peak at m/z 797, indicating the intact molecular weight of the compound. The fragmentation pattern revealed peaks at m/z 552 and 305, corresponding to the sequential loss of two and four 3-hydroxy-4-methoxyphenyl groups from the molecular ion. Additionally, a peak at m/z 430 was observed, identified as the $[ML]^+$ fragment, where M represents the Cu metal and L refers to the ligand 1,7-bis(3-hydroxy-4-methoxyphenyl) hepta-1,6-diene-3,5-dione. Other fragment ions at m/z 675, 429, 123, 183, and 368 further supported the fragmentation pattern and structural components of the $Zn(NLI)_2$ complex, as illustrated in **Fig.3.78**

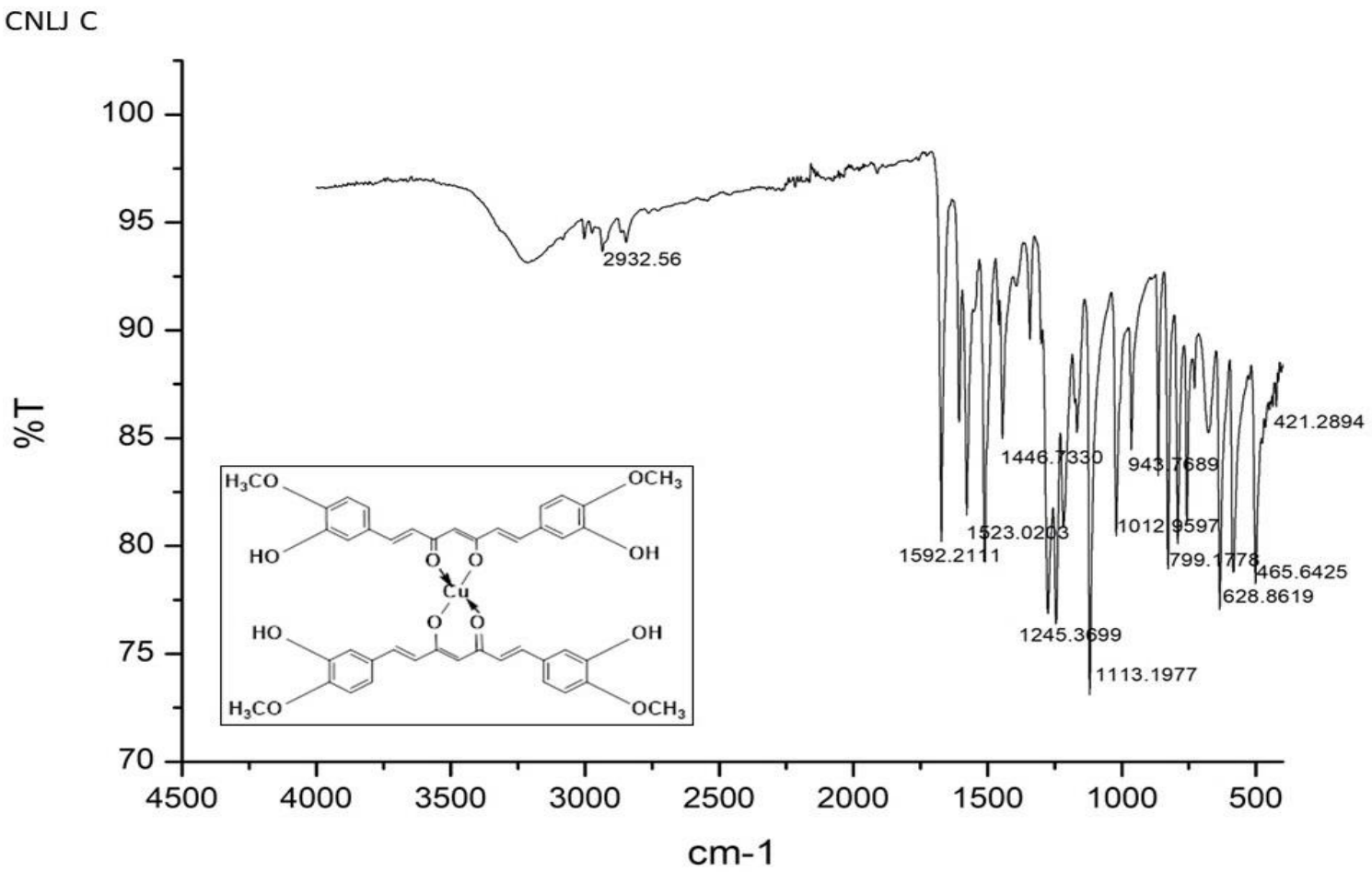

Fig.3.76 The IR spectrum of Cu $(NLJ)_2$

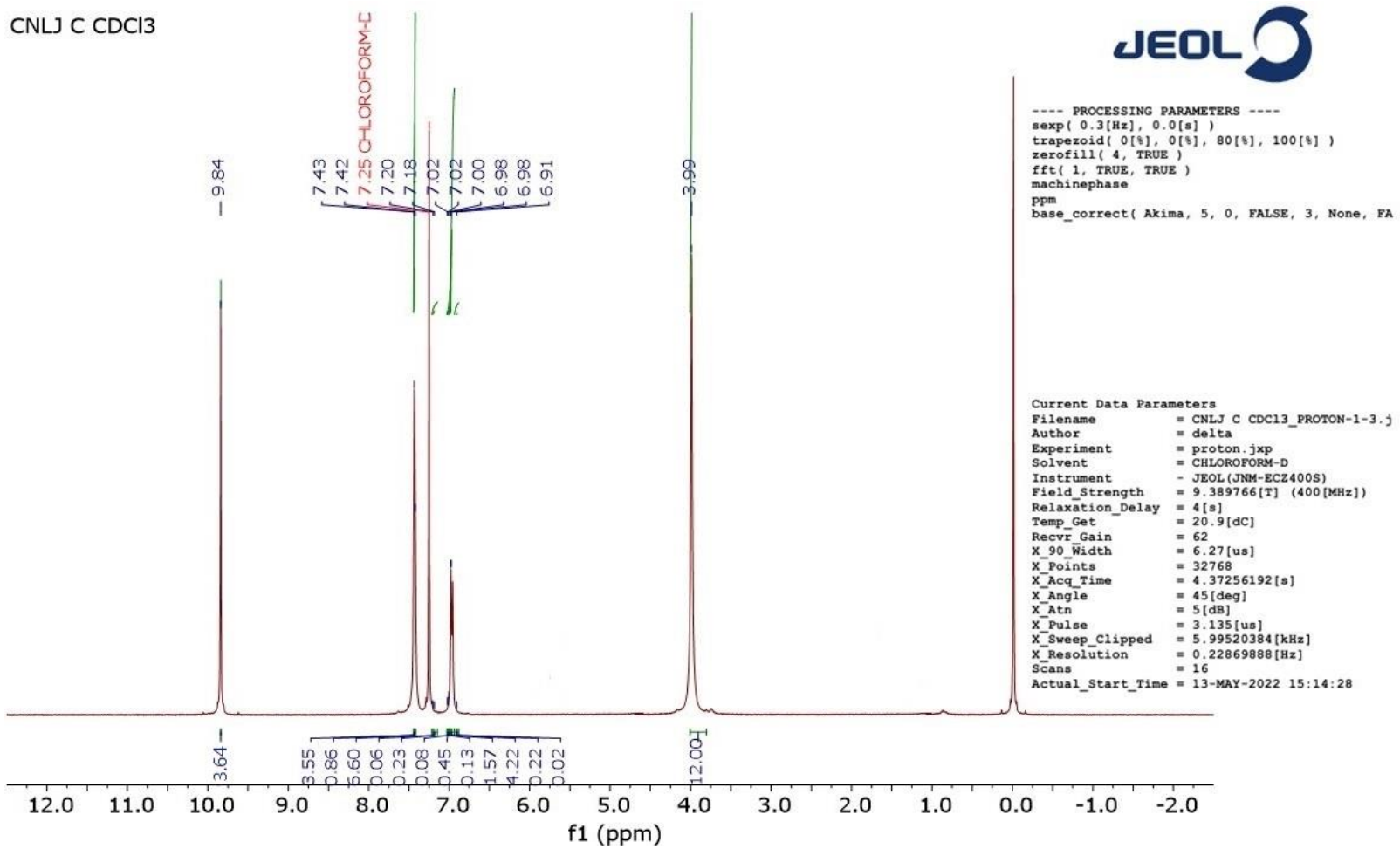

Fig.3.77 The ^{1}H NMR spectrum of Cu $(NLJ)_2$

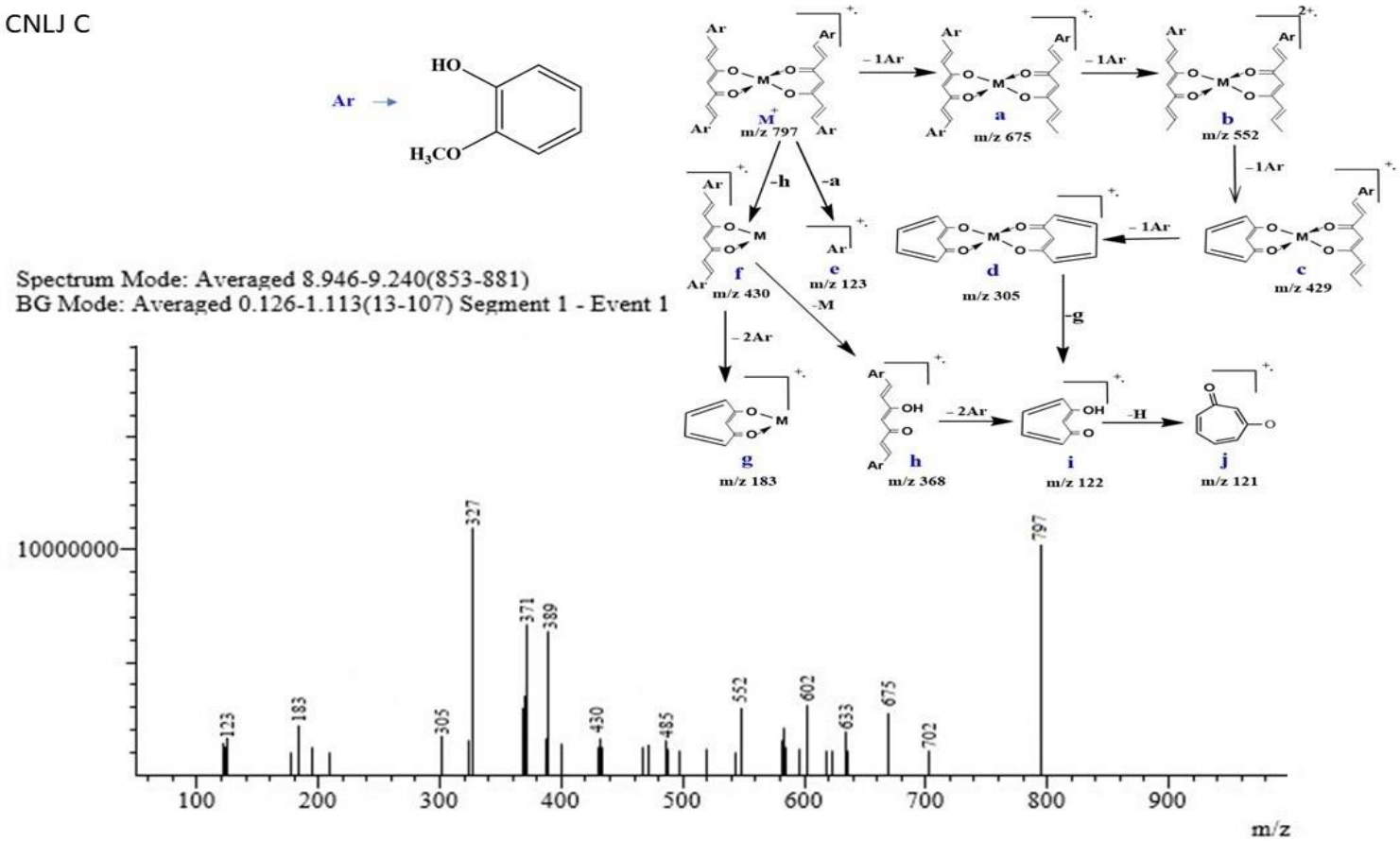

Fig.3.78 The Mass spectrum of Cu $(NLJ)_2$

3.5.1.8.2.1 Synthesis and characterization of Zn(II) complex of 1,7-bis(3-hydroxy-4-methoxyphenyl)hepta-1,6-diene-3,5-dione [$Zn(NLJ)_2$]

The zinc(II) complex synthesized from the curcuminoid analogue NLJ demonstrated a molecular weight of 798.17 g/mol and a melting point of 798°C. The findings from the elemental analysis indicated compositions of carbon, hydrogen, and metal at 63.78%, 4.29%, and 8.41%, respectively, which are near the theoretical values of 63.05%, 4.79%, and 8.17%. The synthesis procedure yielded a total output of 73%.

Characterization of $Zn(NLJ)_2$

The $Zn(NLJ)_2$ metal complex was thoroughly characterized employing a range of spectroscopic and analytical methodologies, encompassing infrared spectroscopy, proton nuclear magnetic resonance (^{1}H NMR), and mass spectrometry. The findings derived from these analytical procedures are synthesized and deliberated in the following sections.

IR Spectrum

The $Zn(NLJ)_2$ complex demonstrated exceptional spectroscopic characteristics that substantiated the coordination interaction between the ligand and the metal ion(**Fig.3.79**). Noteworthy was the absence of a distinct carbonyl absorption band within the spectral region of 1650-1800 cm^{-1}, with the carbonyl peak at 1630 cm^{-1} being markedly missing. A novel band emerged at 1598.4 cm^{-1}, signifying that the metal ion had substituted the enolic proton, thereby facilitating the formation of a metal-coordinated carbonyl moiety. This transition to a lower frequency (1598.4 cm^{-1}) indicated the occurrence of chelation phenomena. Furthermore, a band observed at 1547.9 cm^{-1} was ascribed to the asymmetric stretching of the C-C-C bond present in the aromatic framework. Bands at reduced frequencies of 459.4 cm^{-1} and 408.9 cm^{-1} were characterized as metal-oxygen (M-O) stretching vibrations, thereby reinforcing the coordination between the metal ion and the ligand.

^{1}HNMR Spectrum

The unique proton signals observed in the ^{1}H NMR spectrum of the Zn(II) complex of 1,7-bis(3-hydroxy-4-methoxyphenyl)hepta-1,6-diene-3,5-dione [$Zn(NLJ)_2$] have been carefully summarized in **Table 3.54**.

Table 3.54 Proton signals observed in the ^{1}HNMR spectrum of $Zn(NLJ)_2$ (Chemical Shifts δ in ppm)

Complex	Methine	Alkenyl	Phenyl	Hydroxy	Methoxy
$Zn(NLJ)_2$	6.97	6.95-7.43	7.25-7.47	9.83	3.98

The ^{1}H NMR spectrum of the $Zn(NLJ)_2$ complex provided valuable insights into its proton environments (**Fig.3.80**). Methine protons at δ 6.97 ppm indicated deshielding due to their proximity to conjugated systems like double bonds or aromatic rings, while alkenyl protons resonated between δ 6.95-7.43 ppm, similarly affected by nearby aromatic rings. Phenyl protons appeared at δ 7.25-7.47 ppm, reflecting the electronic effects of aromatic substituents. A significant downfield shift of the hydroxy proton to δ 9.83 ppm was attributed to Zn(II) coordination through carbonyl groups, even though the hydroxy group itself did not directly coordinate with the metal. This shift suggested complex electronic interactions and possible conformational changes induced by metal coordination. Methoxy protons at δ 3.98 ppm, typical for methoxy groups attached to aromatic systems, exhibited a slight downfield shift due to conjugation. Thus, the chemical shifts confirmed the significant influence of zinc coordination on the proton environments within the complex.

Mass Spectrum

Table 3.55 Molecular ion peaks of Zn $(NLJ)_2$

M^+/(M+1)/(M+2) ion	a	b	c	d	e	f	g	h	i	j
798	675	552	429	305	123	431	184	368	122	121

*The alphabets correspond to the fragments given in the fragmentation scheme in**Fig.3.81**

The mass spectrum of the Zn(II) complex with NLJ displayed a prominent molecular ion peak at m/z 798, indicating the intact molecular weight of the compound. The fragmentation pattern showed peaks at m/z 552 and 305, corresponding to the sequential loss of two and four 3-hydroxy-4-methoxyphenyl groups from the molecular ion. A peak at m/z 431 was also identified as the $[ML]^+$ fragment, where M represents the Zn metal and L denotes the ligand 1,7-bis(3-hydroxy-4-methoxyphenyl)hepta-1,6-diene-3,5-dione. Additional fragment ions at m/z 675, 429, 123, 184, and 368 further supported the fragmentation pattern and structural components of the $Zn(NLI)_2$ complex, as illustrated in **Fig.3.81**

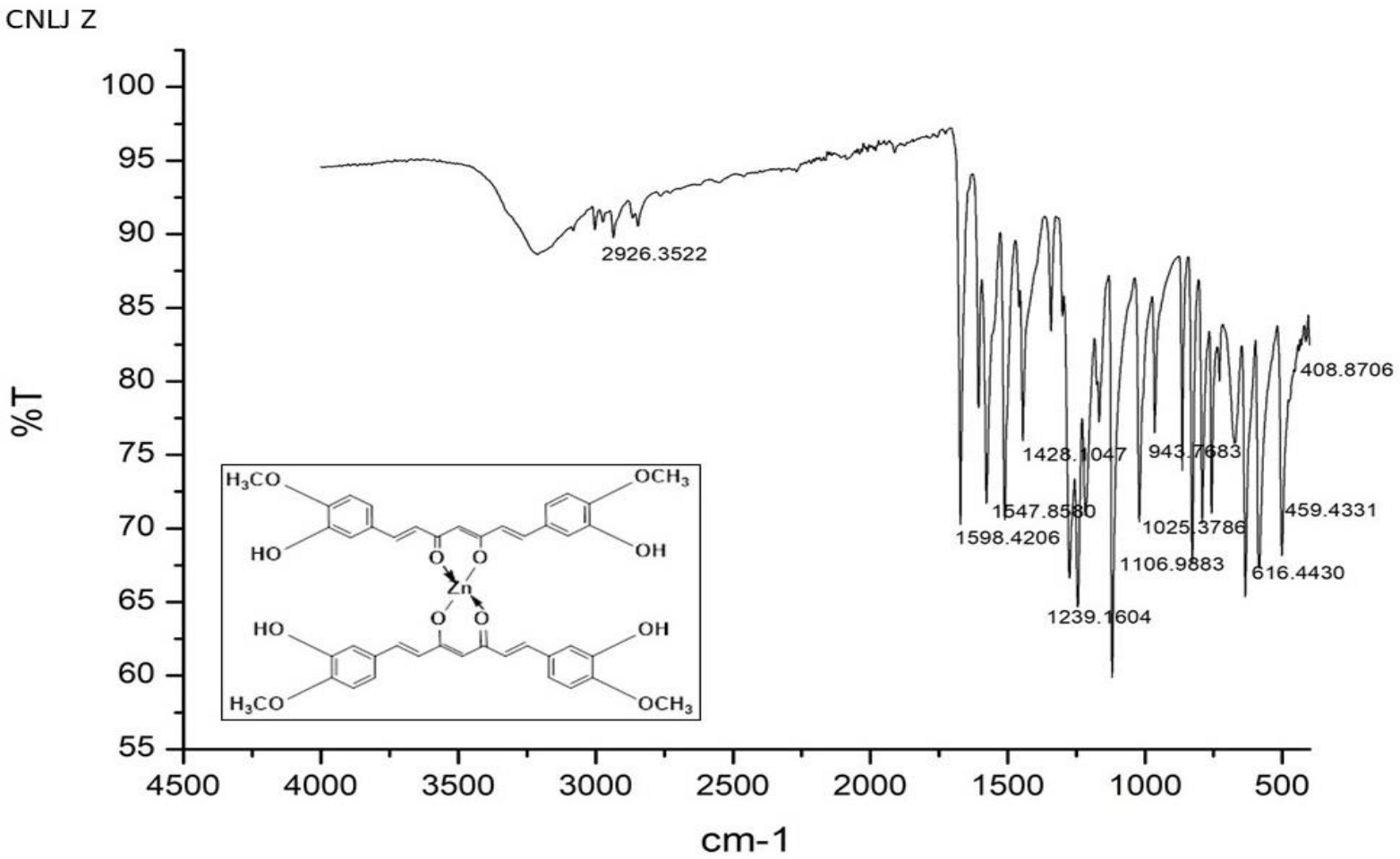

Fig.3.79 The IR spectrum of Zn $(NLJ)_2$

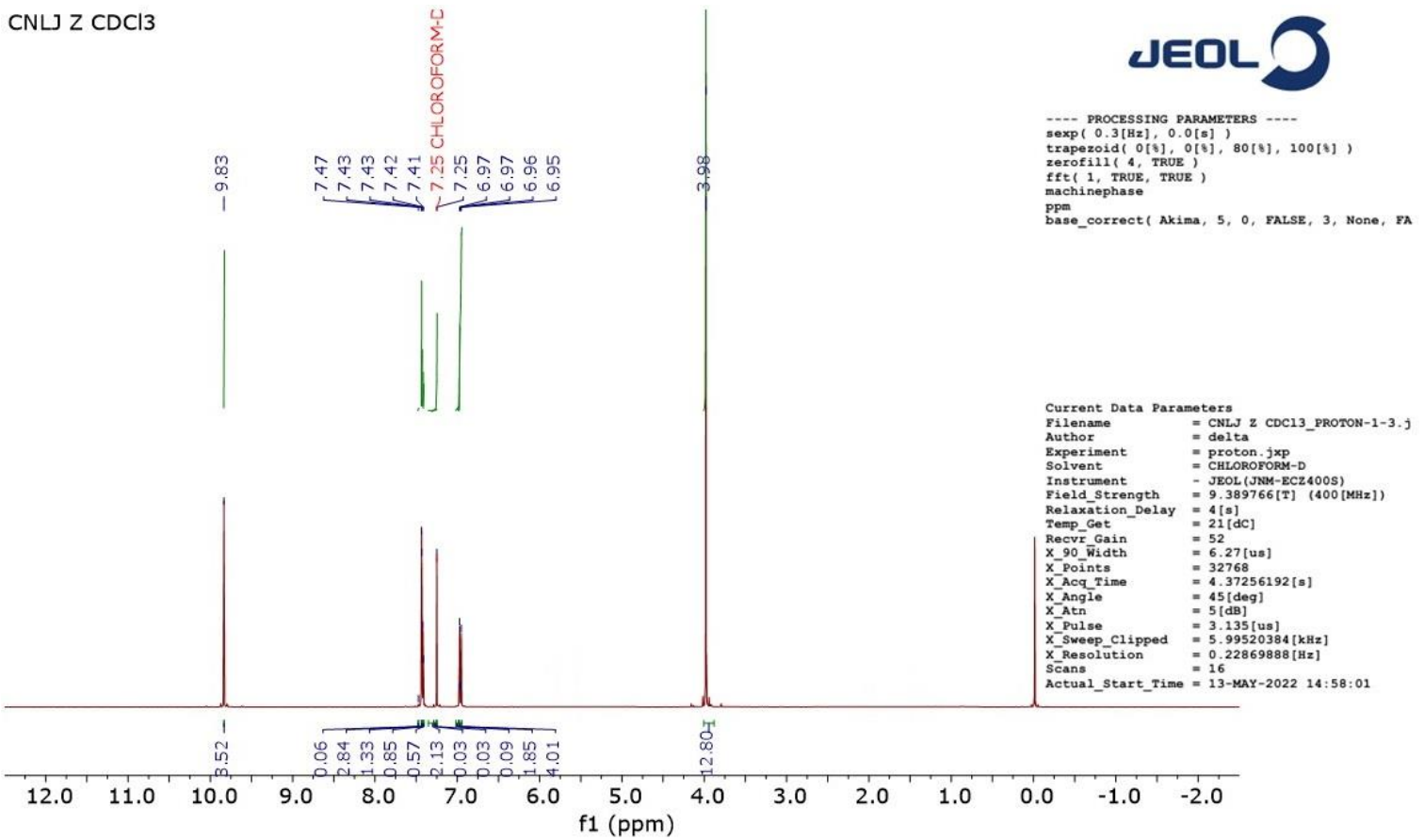

Fig.3.80 The ^{1}H NMR spectrum of Zn $(NLJ)_2$

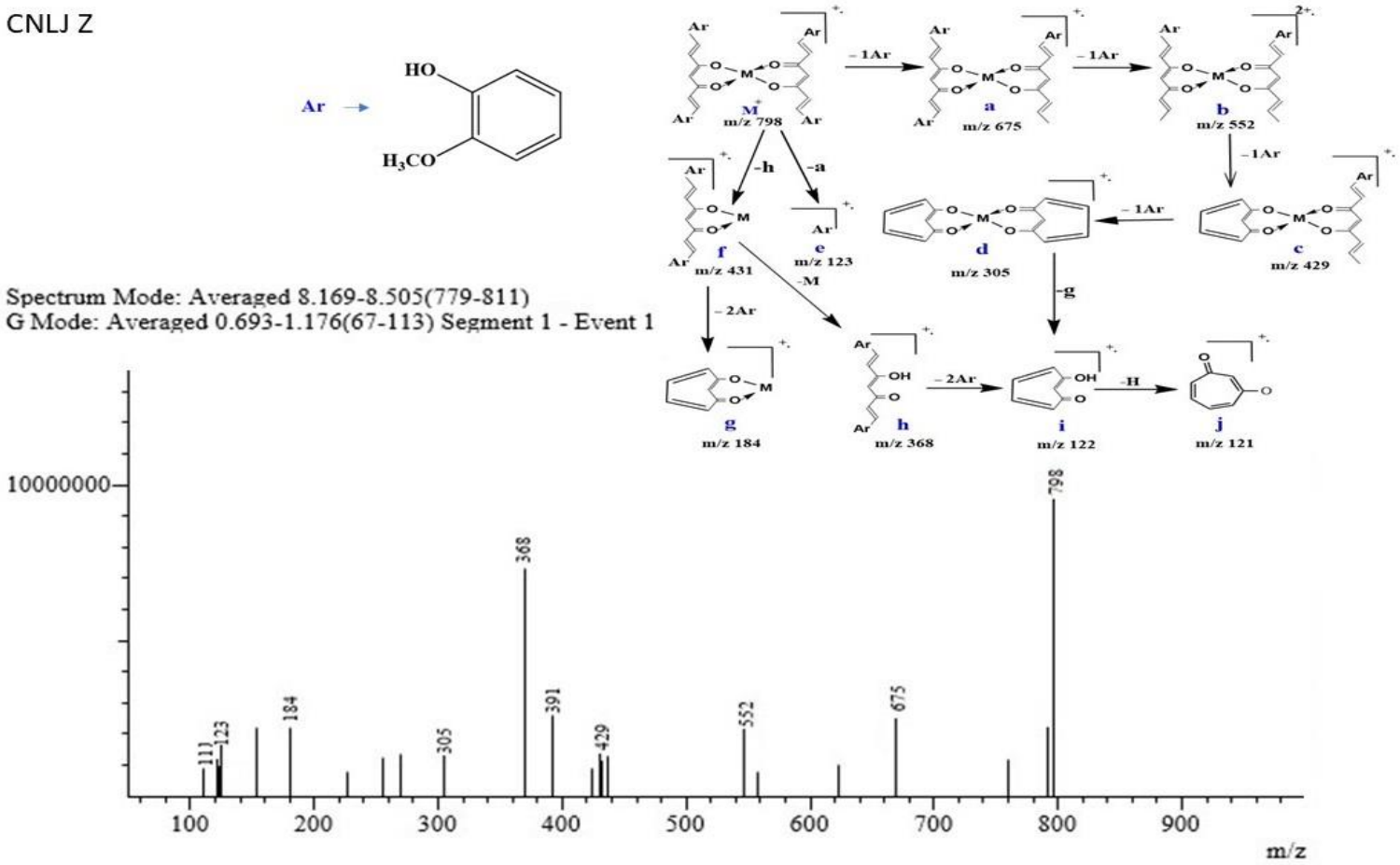

Fig.3.81 The Mass spectrum of Zn $(NLJ)_2$

3.5.1.9. Synthesis and characterization of (1E,6E)-1,7-Bis(5-methyl thiophene-2-yl)hepta-1,6-diene-3,5-dione(NLK)

3.5.1.9.1 Synthesis and characterization of NLK

1,7-Bis(5-methylthiophen-2-yl)hepta-1,6-diene-3,5-dione (NLK) was synthesized through the condensation of 5-methyl-2-thiophene carboxaldehyde (0.01 M) with an acetylacetone–boron complex and B_2O_3 in ethyl acetate (7.5 mL). The reaction was carried out in the presence of tri-sec-butyl borate (5.4 mL) and n-butylamine (0.1 mL) as a condensing agent. The synthesized product exhibited a melting point of 247°C and a molecular weight of 316 g/mol, with a yield of approximately 95%. Elemental analysis showed carbon and hydrogen contents of 63.66% and 4.83%, respectively, closely aligning with the theoretical values of 64.53% and 5.1%.

Characterization of NLK

The synthesized compound NLK was characterized using various spectroscopic techniques, including IR, ^{1}H NMR, ^{13}C NMR, and mass spectrometry. The following discussion provided a detailed analysis of the spectral data of the compound.

IR Spectrum

The IR peaks for NLK can be interpreted based on the characteristic absorption ranges of various functional groups. The possible signals are summarized in **Table 3.56.**

Table 3.56 Possible IR assignments of NLK

Wavenumbers (in cm^{-1})	Possible IR Assignments
2908.7	ν Enolic
1666.1	ν(C=O)
1529.2	ν(C-C) Alkenyl
1437.6	ν_s(C-C-C)
1121.3	νβ (C-H)

The IR spectral data for NLK revealed several key absorption peaks, each corresponding to different functional groups (**Fig.3.82**). The peak at 2908.7 cm^{-1} was attributed to the O-H stretching vibrations of the enolic form. Typically, these vibrations

appear in the range of 3200-3600 cm^{-1}; however, the observed peak was slightly lower, likely due to strong intramolecular hydrogen bonding or conjugation with adjacent double bonds. Such downward shifts are common in enolic structures, especially in β-diketones, where the enol form is stabilized by resonance. The carbonyl group (C=O) stretching vibration was observed at 1666.1 cm^{-1}, fitting within the expected range of 1650-1750 cm^{-1}. This indicated the presence of a conjugated carbonyl group, as conjugation with a double bond or aromatic ring can slightly reduce the frequency. The peak at 1529.1997 cm^{-1} corresponded to the C=C stretching vibration within an alkenyl group, which typically occurs between 1500-1650 cm^{-1}. This confirmed the presence of an alkenyl group conjugated with other functional groups, such as carbonyls or aromatic rings, which can slightly shift the absorption to lower frequencies. Additionally, the peak at 1437.6 cm^{-1} was associated with the symmetric stretching vibration of the C-C-C bond within a conjugated system. This vibration usually occurs in the range of 1400-1500 cm^{-1}, and the observed value suggested a well-conjugated system within NLK, possibly involving an aromatic ring. Finally, the peak at 1121.3 cm^{-1} was attributed to the in-plane bending (β) of the C-H bond, typically appearing between 1000-1300 cm^{-1}. This frequency supported the presence of C-H bonds in an aliphatic or aromatic environment. The analysis of the IR data confirmed the accuracy of these assignments, as the observed shifts were consistent with the expected structural features of NLK, influenced by factors such as conjugation, resonance, and hydrogen bonding.

^{1}HNMR Spectrum

The proton NMR spectrum of NLK revealed several key chemical shifts corresponding to different proton environments within the molecule. The chemical shifts (δ, ppm) corresponded to distinct functional groups, offering a detailed understanding of the molecular structure. The diverse proton resonances identified in the spectrum are thoroughly outlined in **Table 3.57**

Table 3.57 Proton signals observed in the ^{1}H NMR spectrum of NLK (Chemical Shifts δ ppm)

Compound	Enolic	Methine	Alkenyl	Methyl	Thiophenyl
NLK	10.10	6.75	6.61-7.68	2.37	6.76-7.75

The proton NMR spectrum of NLK provided key insights into its molecular structure. The peak at δ 10.10 ppm was assigned to the enolic proton, consistent with the typical downfield region of 9-12 ppm observed for protons attached to oxygen in enol forms. This confirmed the presence of an enolic group in NLK.The methine proton appeared at δ 6.75 ppm, within the expected range of 5-8 ppm for protons on sp^2 hybridized carbons, such as those in conjugated systems or near electronegative atoms. This shift indicated that the methine proton was part of a conjugated system in NLK.Alkenyl protons were observed in the range of δ 6.61-7.68 ppm. Protons on sp^2 hybridized carbons in alkenes typically resonate between 5-7 ppm, but conjugation with aromatic rings or other electron-withdrawing groups can shift these signals downfield. This observation confirmed the presence of alkenyl groups in the conjugated system of NLK. The methyl protons were observed at δ 2.37 ppm, which falls within the range of 1-3 ppm for methyl groups near sp^2 hybridized carbons or electronegative atoms. This indicated the presence of a methyl group potentially attached to a carbonyl or aromatic ring. Thiophenyl protons were noted in the range of δ 6.76-7.75 ppm. Thiophene rings exhibit proton signals in a similar range to benzene rings due to their aromatic nature, confirming the presence of a thiophene group in NLK. In short, the ^{1}H NMR spectrum of NLK showed shifts that aligned with expected ranges for enolic, alkenyl, phenyl, methyl, and thiophenyl protons, supporting the compound's proposed structure. The ^{1}H NMR spectrum of NLK is brought out in **Fig.3.83**

^{13}C NMR Spectra

To interpret the ^{13}C NMR spectral data for NLK, the observed chemical shifts were assigned to the corresponding carbon atoms in the molecule, considering their chemical environments. The details of the ^{13}C NMR spectrum for NLK were provided in **Table 3.57**

Table 3.58 ^{13}C NMR spectral data of NLK (Chemical Shifts δ ppm)

C_1	C_2,$C_{2'}$	C_3,$C_{3'}$	C_4,$C_{4'}$	C_5,$C_{5'}$
101.63	182.84	131.00	131.73	138.73
C_6,$C_{6'}$	C_7,$C_{7'}$	C_8,$C_{8'}$	C_9,$C_{9'}$	
133.53	126.82	144.16	15.99	

The chemical shift at δ 101.63 ppm was consistent with carbon in an enolic structure or a conjugated system, typically seen in β-diketones or enolisable ketones. This suggested that C_1 was likely part of the enolic or keto-enol tautomeric system in NLK. The signals at δ 182.84 ppm were characteristic of carbonyl carbons (C=O) in ketones or aldehydes, indicating that C_2 and $C_{2'}$ corresponded to the carbonyl carbons in the hepta-1,6-diene-3,5-dione backbone, where the high deshielding effect from electronegative oxygen atoms and conjugation caused the downfield shift. The chemical shifts at δ 131 ppm were typical for carbons in a double bond (C=C) within an alkenyl group, meaning C_3 and $C_{3'}$ corresponded to alkenyl carbons adjacent to the carbonyl groups within the conjugated system. Similarly, the shifts at δ 131.73 ppm, assigned to C_4 and $C_{4'}$, were also part of the conjugated alkenyl system. The shift at δ 138.73 ppm was characteristic of carbons in aromatic rings, particularly those directly bonded to electronegative atoms or conjugated systems, indicating that C_5 and $C_{5'}$ were part of the phenyl groups conjugated with the alkenyl and carbonyl groups. The signals at δ 133.53 ppm suggested that C_6 and $C_{6'}$ were also part of the aromatic rings, with a slightly downfield shift due to adjacent electronegative groups or conjugation. The chemical shift at δ 126.82 ppm corresponded to a carbon in an aromatic ring, where the presence of a methyl group on the adjacent carbon, along with a sulfur atom in the ring, caused the deshielding observed in the complex aromatic environment of C_7 and $C_{7'}$. The downfield shift at δ 144.16 ppm, typical of heavily deshielded aromatic carbons, indicated that C_8 and $C_{8'}$ were attached to a methyl group and influenced by a nearby sulfur atom, which increased deshielding within the conjugated aromatic system. Finally, the shift at δ 15.99 ppm was characteristic of methyl groups (–CH_3), corresponding to C_9 and $C_{9'}$. These assignments demonstrated that the chemical shifts observed in the ^{13}C NMR spectrum of NLK aligned with the expected ranges for the corresponding functional groups, confirming their correctness (**Fig.3.84**).

Mass Spectrum

In the mass spectrum of NLK, prominent molecular ion peaks were observed, confirming the compound's molecular weight. The key peaks in the spectrum were explained by the fragmentation pattern outlined in **Fig.3.85.** The corresponding values are summarized in **Table 3.59**

Table 3.59 Molecular ion peaks of NLK

M^+/M+1 Ion	**a**	**b**	**c**	**d**	**e**	**f**	**g**
316	165	153	111	123	97	219	193

*The alphabets correspond to the fragments given in the fragmentation scheme in**Fig.3.85**

In the mass spectrum of NLK, the molecular ion peak was prominently observed at m/z 316, confirming the compound's molecular weight. Notable fragment ion peaks included the following: a peak at m/z 165, assigned to the fragment ion $[C_9H_9OS]^+$; a peak at m/z 151, corresponding to the ion $[C_8H_7OS]^+$; and a peak at m/z 219, attributed to the fragment ion $[C_{12}H_{11}O_2S]^+$. The peak at m/z 193 was also associated with the ion $[C_{10}H_9O_2S]^+$. These fragment ions were consistent with the expected fragmentation patterns for NLK. The mass spectrum of the compound NLK is shown in **Fig 3.85**

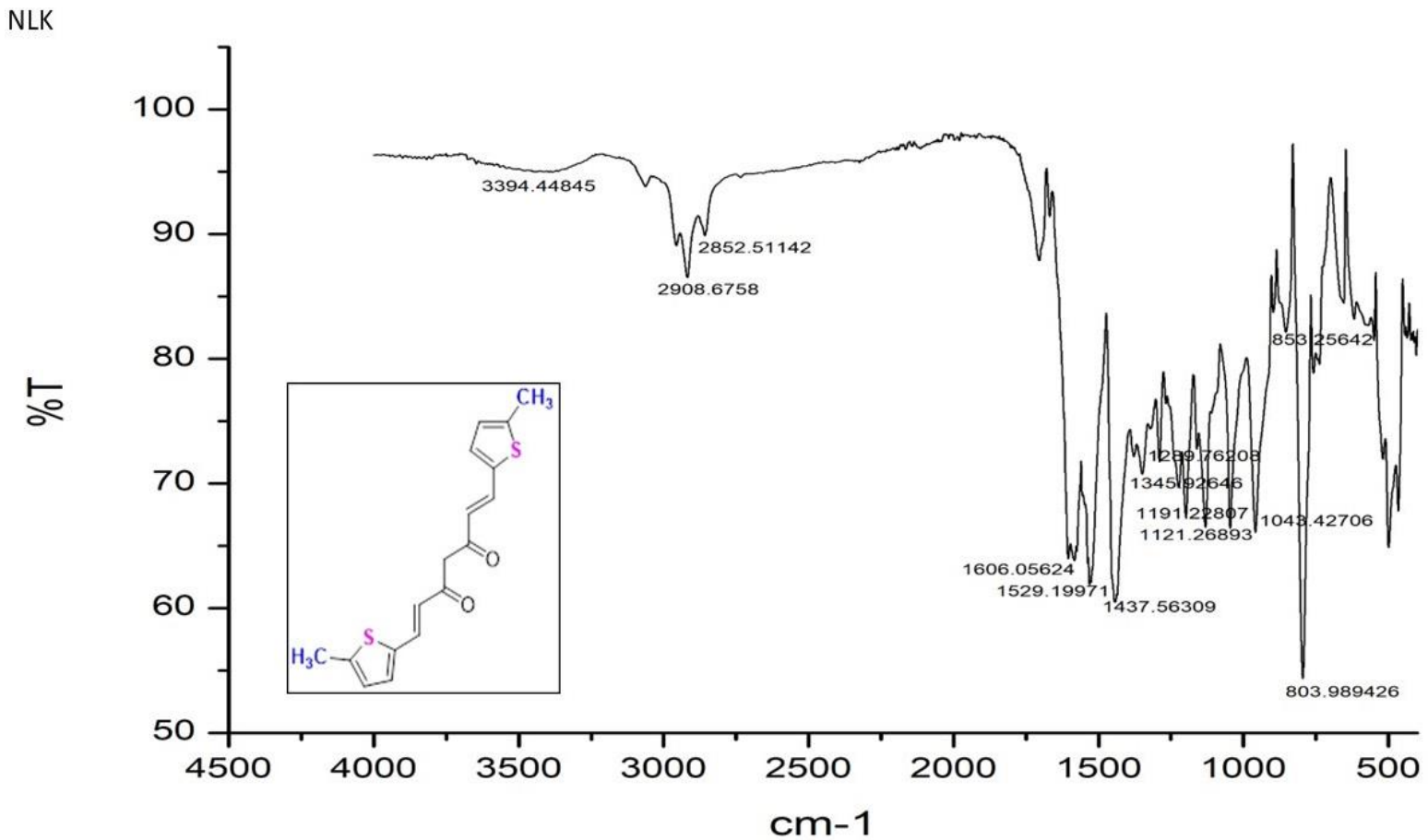

Fig.3.82 The IR spectrum of NLK

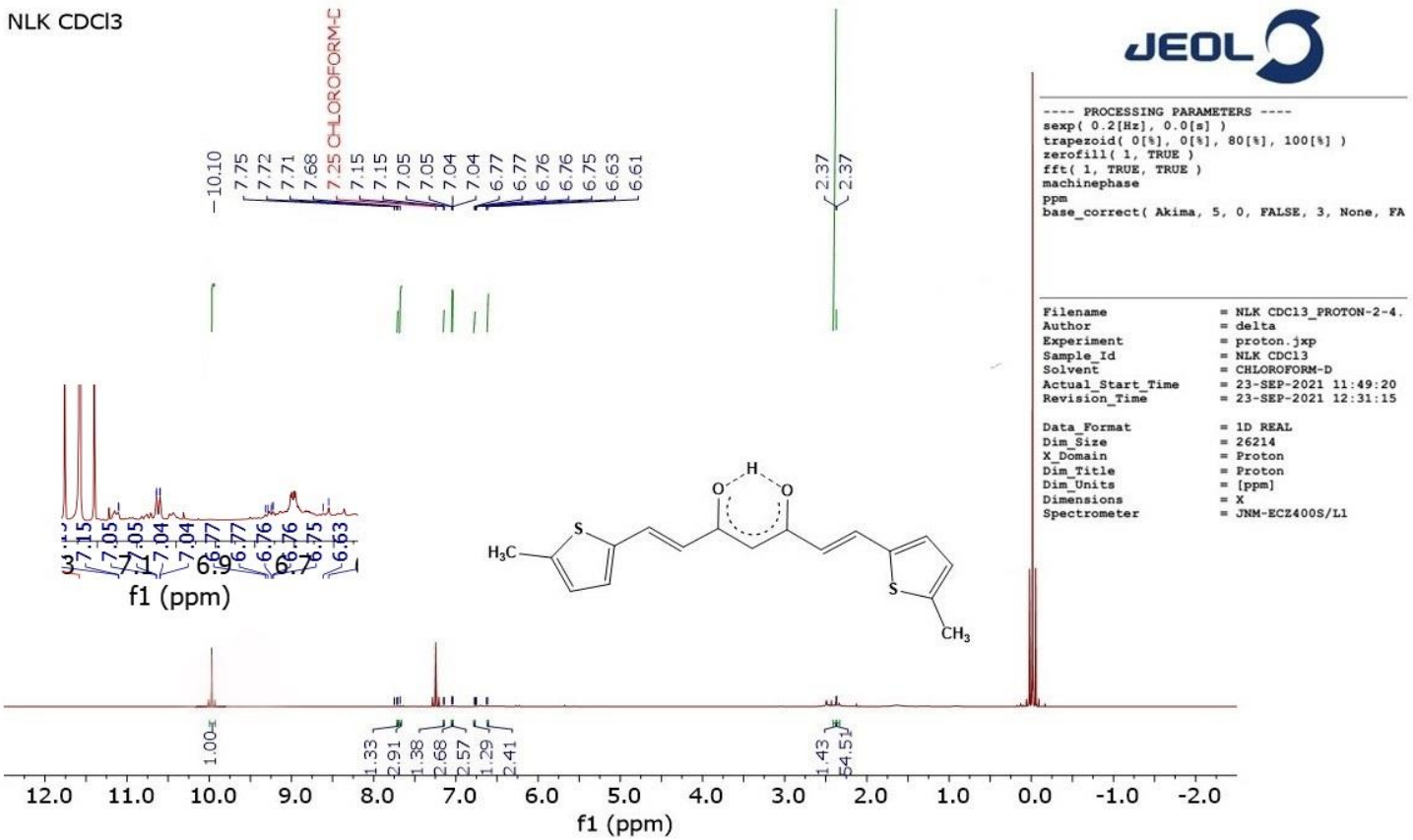

Fig.3.83 The ^{1}H NMR spectrum of NLK

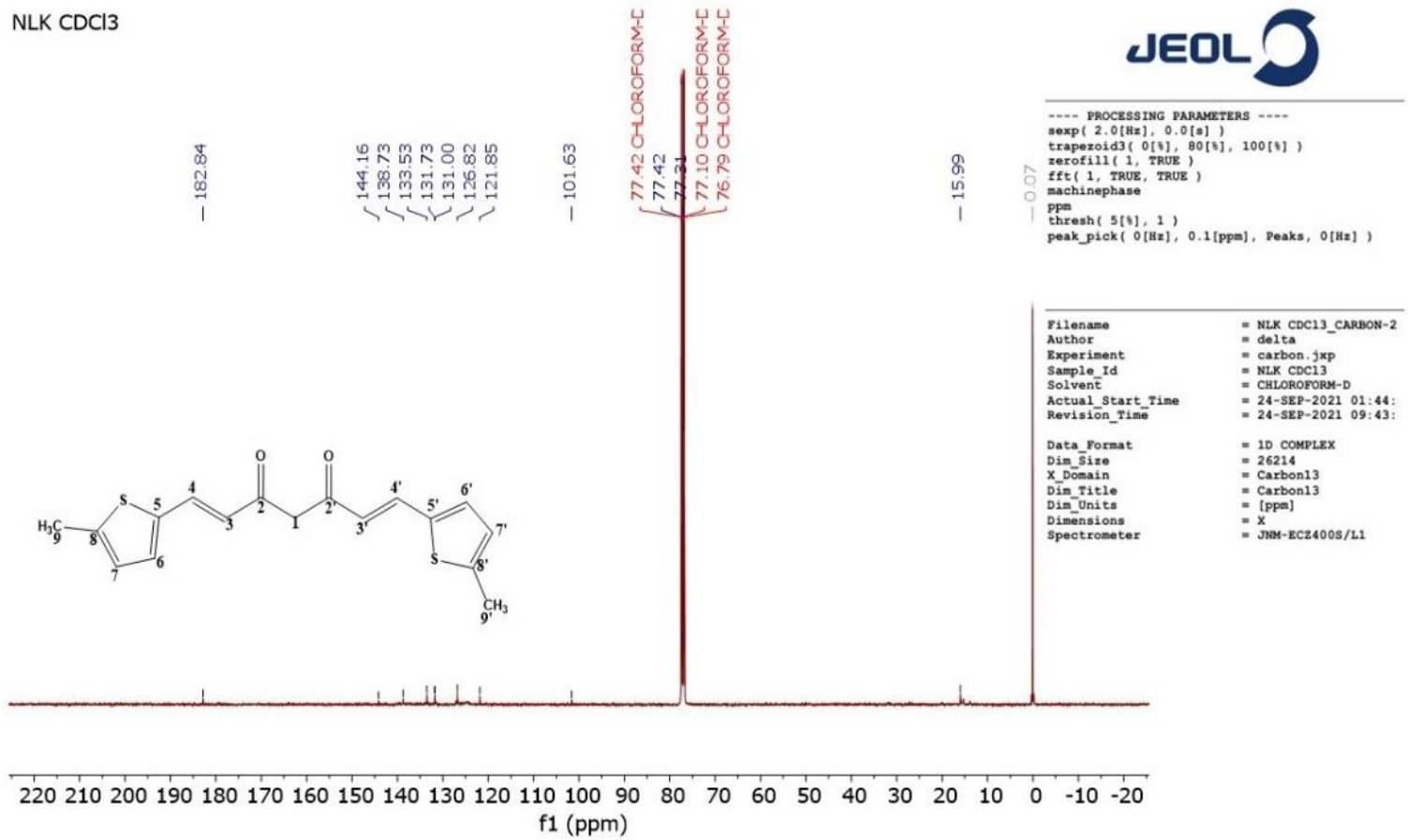

Fig.3.84 The ^{13}CNMR spectrum of NLK

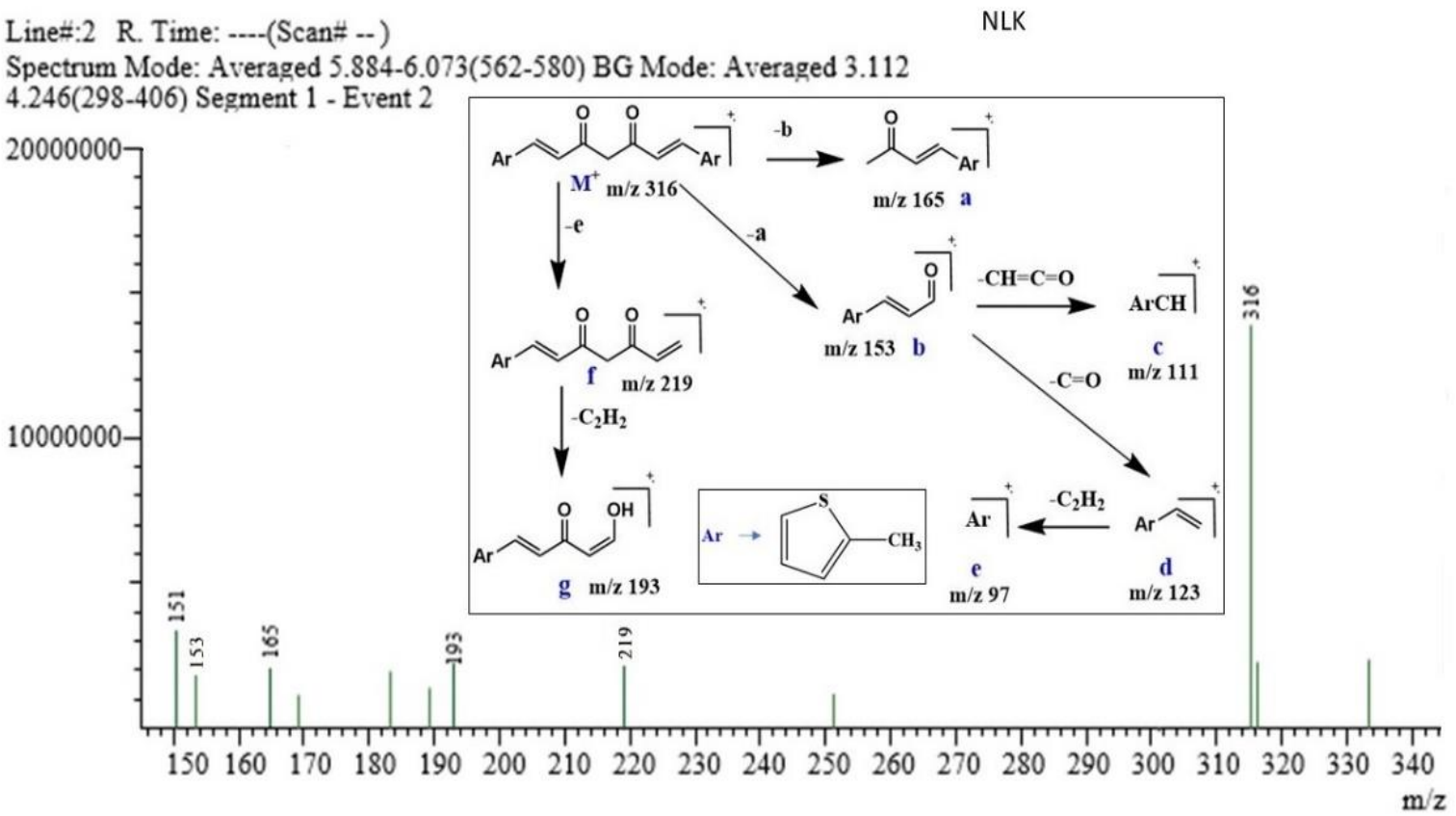

Fig.3.85 The Mass spectrum of NLK

3.5.1.9.2 Synthesis and Characterization of $Cu(NLK)_2$ and $Zn(NLK)_2$

3.5.1.9.2.1 Synthesis and Characterization of Cu complex of 1,7-Bis(5-methyl thiophene-2-yl)hepta-1,6-diene-3,5-dione[$Cu(NLK)_2$]

The Cu(II) complex of the curcuminoid analogue NLK had a molecular weight of 693.03 g/mol and a melting point of 258°C. Elemental analysis revealed carbon, hydrogen, and metal contents of 58.81%, 4.35%, and 9.15%, respectively, aligning closely with the theoretical values of 58.61%, 4.44%, and 9.26%. The synthesis achieved a yield of 64%.

Characterization of $Cu(NLK)_2$

The $Cu(NLK)_2$ metal complex underwent comprehensive characterization utilizing an array of spectroscopic and analytical techniques, including IR spectroscopy, ^1H NMR, and mass spectrometry. The results of these analytical investigations are amalgamated and discussed in the subsequent sections.

IR Spectrum

The $Cu(NLK)_2$ complex exhibited remarkable spectroscopic properties that validated the coordination interaction between the ligand and the metal ion (**Fig.3.86**). Notably, the spectral region of 1650-1800 cm^{-1} revealed an absence of a pronounced carbonyl absorption band, with the carbonyl peak at 1630 cm^{-1} conspicuously absent. A new band emerged at 1578.9 cm^{-1}, indicating that the metal ion had displaced the enolic proton, thus enabling the formation of a metal-coordinated carbonyl moiety. This shift to a lower frequency (1578.9 cm^{-1}) signified the occurrence of chelation phenomena. Moreover, a band detected at 1503.5 cm^{-1} was attributed to the asymmetric stretching of the C-C-C bond within the aromatic framework. Bands at diminished frequencies of 465.4 cm^{-1} and 439.9 cm^{-1} were identified as metal-oxygen (M-O) stretching vibrations, thereby corroborating the coordination between the metal ion and the ligand.

^{1}HNMR Spectrum

The unique proton signals observed in the ^1H NMR spectrum of the Cu(II) complex of 1,7-Bis(5-methyl thiophene-2-yl)hepta-1,6-diene-3,5-dione[$Cu(NLK)_2$] have been carefully summarized in **Table 3.60**

Table 3.60 Proton signals observed in the ^{1}HNMR spectrum of $Cu(NLK)_2$ (Chemical Shifts δ in ppm)

Complex	Methine	Alkenyl	Methyl	Thiophenyl
$Cu(NLK)_2$	6.78	6.62-7.58	2.44	6.77-7.76

The ^{1}H NMR spectrum of the $Cu(NLK)_2$ complex revealed distinct chemical shifts for methine, alkenyl, methyl, and thiophenyl protons, which aligned with the expected ranges for these environments (**Fig.3.87**). Methine protons appeared at δ 6.78 ppm, showing deshielding due to their proximity to conjugated systems, consistent with similar copper(II) complexes. Alkenyl protons, resonating between δ 6.62-7.58 ppm, reflected deshielding from conjugation and copper coordination, fitting typical ranges for C=C bonds. Methyl protons shifted slightly downfield to δ 2.44 ppm, likely due to conjugation and interaction with thiophene. Thiophenyl protons resonated between δ 6.77-7.76 ppm, characteristic of aromatic protons in thiophene rings, with shifts attributed to electron delocalization and copper interaction. These observed chemical shifts were consistent with literature values, confirming the accuracy of the spectrum for $Cu(NLK)_2$.

Mass Spectrum

Table 3.61 Molecular ion peaks of Cu $(NLK)_2$

M^+/(M+1)/(M+2) ion	a	b	c	d	e	f	g	h	i	j
693	596	499	402	304	97	377	183	316	122	121

*The alphabets correspond to the fragments given in the fragmentation scheme in**Fig.3.88**

The mass spectrum of the Cu(II) complex with NLK exhibited a prominent molecular ion peak at m/z 693, indicating the intact molecular weight of the compound. The fragmentation pattern revealed peaks at m/z 499 and 304, corresponding to the sequential loss of two and four 5-methylthiophene-2-yl groups from the molecular ion. A peak at m/z 377 was identified as the $[ML]^+$ fragment, where M represents the Cu metal and L refers to the ligand 1,7-Bis(5-methylthiophene-2-yl)hepta-1,6-diene-3,5-dione. Additional fragment ions at m/z 596, 402, 97, 183, 316, and 122 further corroborated the fragmentation pattern and structural components of the $Cu(NLK)_2$ complex, as depicted in **Fig.3.88.**

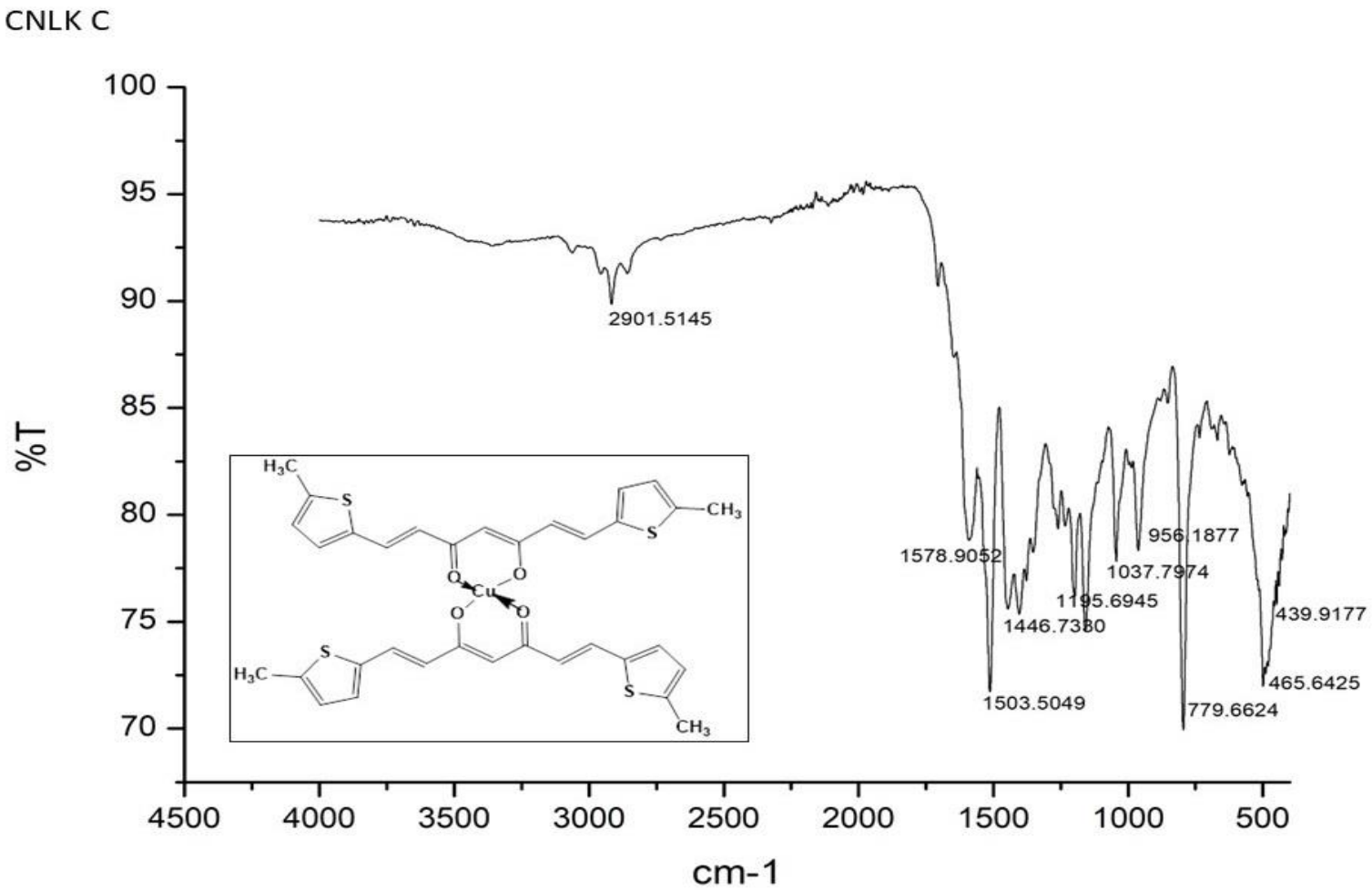

Fig.3.86 The IR spectrum of Cu $(NLK)_2$

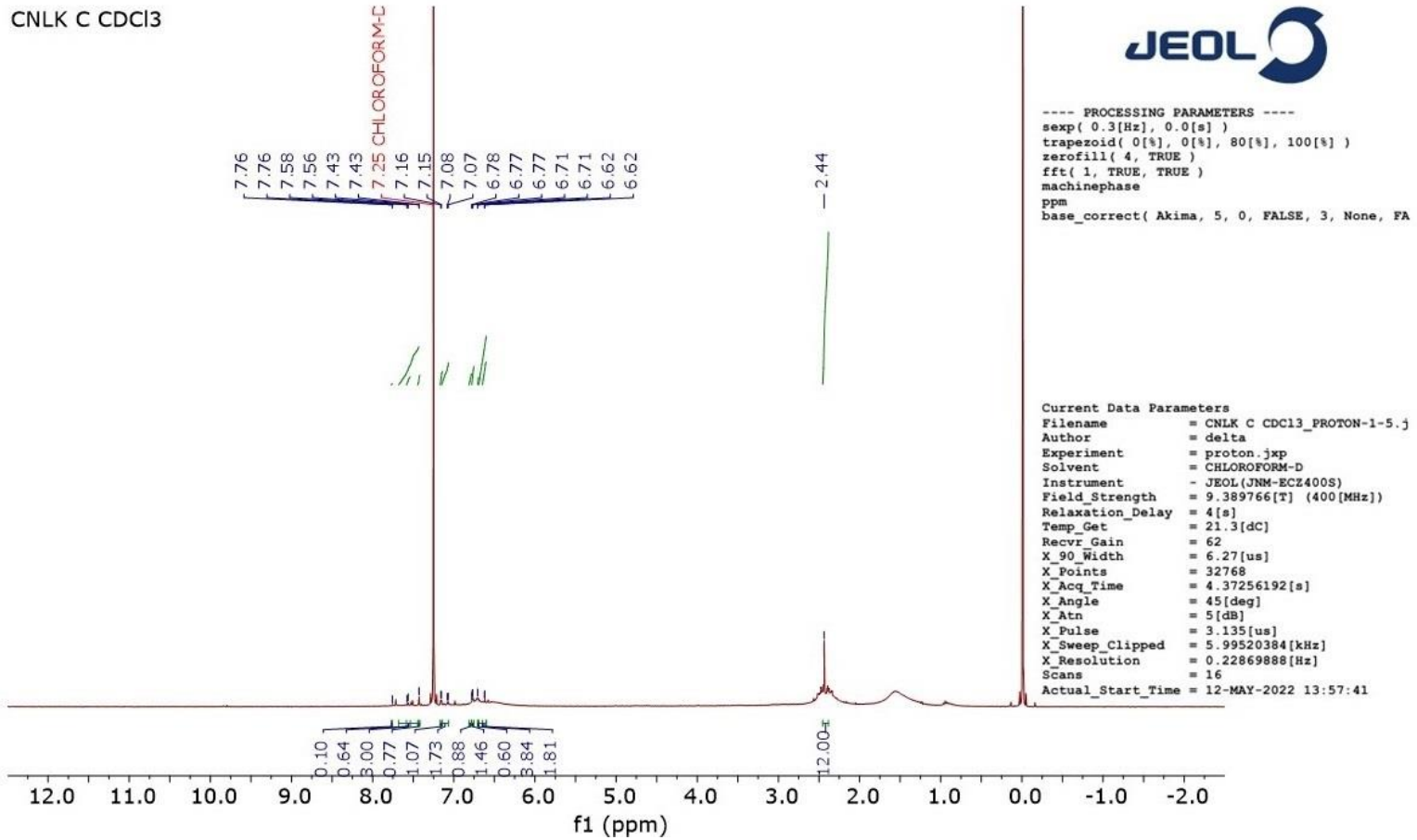

Fig.3.87 The ^{1}H NMR spectrum of Cu (NLK)$_2$

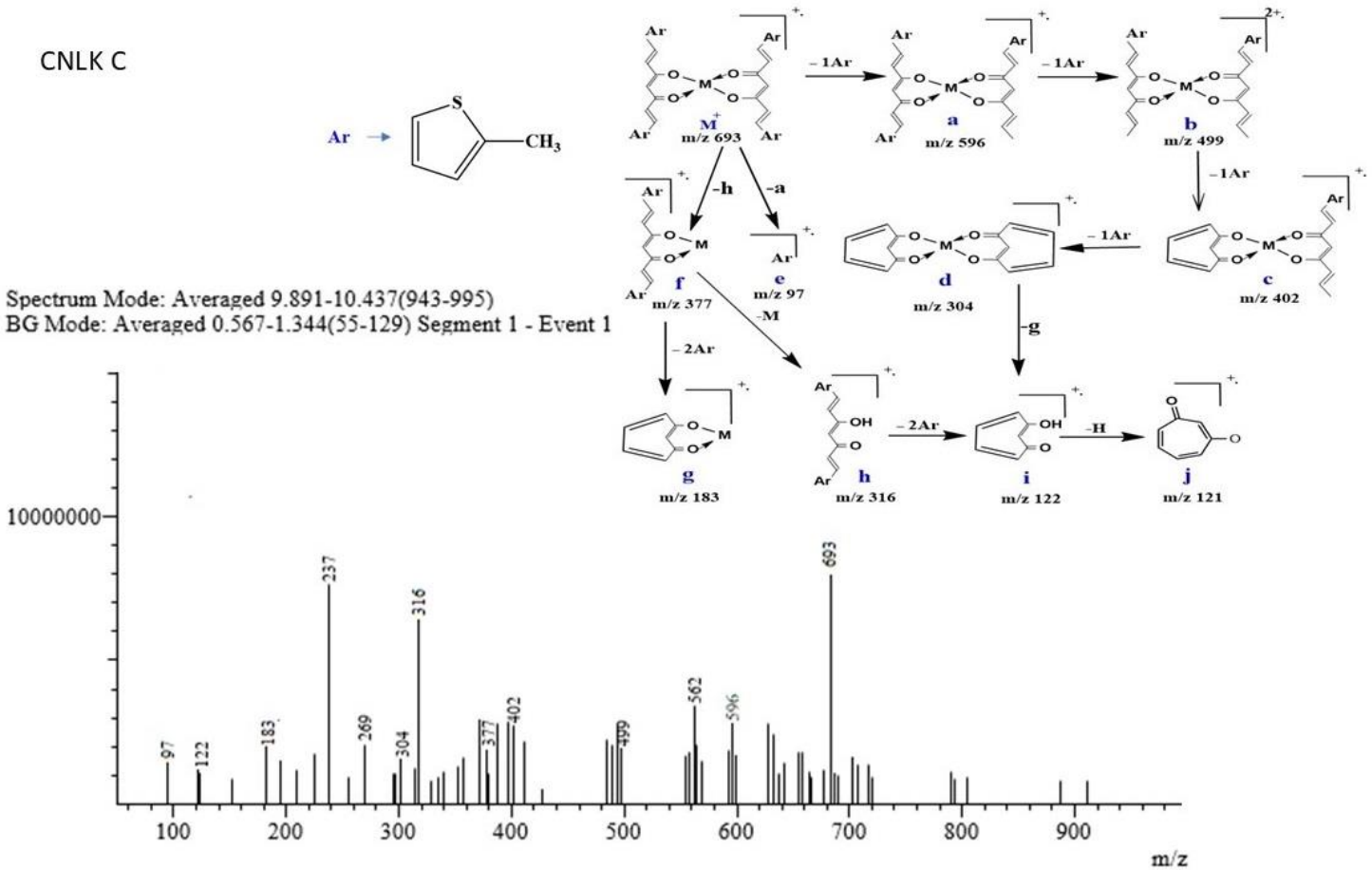

Fig.3.88 The Mass spectrum of Cu $(NLK)_2$

3.5.1.9.2.2 Synthesis and Characterization of Cu complex of 1,7-Bis(5-methyl thiophene-2-yl)hepta-1,6-diene-3,5-dione[Zn(NLK)$_2$]

The Zn(II) complex of the curcuminoid analogue NLK had a molecular weight of 694.03 g/mol and a melting point of 267°C. Elemental analysis revealed carbon, hydrogen, and metal contents of 58.66%, 4.34%, and 9.19%, respectively, closely aligning with the theoretical values of 58.53%, 4.38%, and 9.12%. The synthesis achieved a 67% yield.

Characterization of Zn(NLK)$_2$

The Zn(NLK)$_2$ metal complex was thoroughly characterized using a range of spectroscopic and analytical techniques, including IR spectroscopy, ^{1}H NMR, and mass spectrometry. The findings from these analyses are compiled and discussed in the following sections.

IR Spectrum

The Zn(NLK)$_2$ complex displayed notable spectroscopic properties that confirmed the coordination between the ligand and the metal ion (**Fig.3.89**). In the 1650-1800 cm^{-1} region, the absence of a distinct carbonyl absorption band, particularly the peak at 1630 cm^{-1}, was evident. A new band appeared at 1586.0 cm^{-1}, indicating that the metal ion had displaced the enolic proton, leading to the formation of a metal-coordinated carbonyl group. This shift to 1586.0 cm^{-1} reflected the chelation process. Additionally, a band at 1509.7 cm^{-1} was attributed to the asymmetric stretching of the C-C-C bond within the aromatic structure. Lower-frequency bands at 459.4 cm^{-1} and 421.3 cm^{-1} were identified as metal-oxygen (M-O) stretching vibrations, further confirming the coordination between the metal ion and the ligand.

^{1}HNMR Spectrum

The distinctive proton signals identified in the ^{1}H NMR spectrum of the Zn(II) complex of 1,7-Bis(5-methylthiophene-2-yl)hepta-1,6-diene-3,5-dione [Zn(NLK)$_2$] are concisely summarized in **Table 3.62**

Table 3.62 Proton signals observed in the ^{1}HNMR spectrum of Zn(NLD)$_2$ (Chemical Shifts δ in ppm)

Complex	Methine	Alkenyl	Methyl	Thiophenyl
Zn(NLK)$_2$	6.78	6.87-7.56	2.50	6.77-7.71

The ^{1}H NMR spectrum of the $Zn(NLK)_2$ complex revealed distinct chemical shifts for methine, alkenyl, methyl, and thiophenyl protons, aligning with the expected ranges for these environments (**Fig.3.90**). Methine protons appeared at δ 6.78 ppm, showing deshielding due to their proximity to conjugated systems, consistent with similar zinc(II) complexes. Alkenyl protons, resonating between δ 6.87-7.56 ppm, reflected deshielding from conjugation and zinc coordination, fitting typical ranges for C=C bonds. Methyl protons shifted slightly downfield to δ 2.50 ppm, likely due to conjugation and interaction with thiophene. Thiophenyl protons resonated between δ 6.77-7.71 ppm, characteristic of aromatic protons in thiophene rings, with shifts attributed to electron delocalization and zinc interaction. These observed chemical shifts were consistent with literature values, confirming the accuracy of the spectrum for $Zn(NLK)_2$.

Mass Spectrum

Table 3.63 Molecular ion peaks of $Zn(NLK)_2$

M+/(M+1)/(M+2) ion	**a**	**b**	**c**	**d**	**e**	**f**	**g**	**h**	**i**	**j**
694	597	500	403	305	97	378	184	316	122	121

*The alphabets correspond to the fragments given in the fragmentation scheme in**Fig.3.91**

The mass spectrum of the Zn(II) complex with NLK showed a prominent molecular ion peak at m/z 694, confirming the intact molecular weight of the compound. The fragmentation pattern revealed peaks at m/z 500 and 305, corresponding to the sequential loss of two and four 5-methylthiophene-2-yl groups from the molecular ion. A peak at m/z 378 was identified as the $[ML]^+$ fragment, where M represents the Zn metal and L refers to the ligand 1,7-Bis(5-methylthiophene-2-yl)hepta-1,6-diene-3,5-dione. Additional fragment ions at m/z 597, 403, 97, 184, 316, and 122 further supported the fragmentation pattern and structural components of the $Zn(NLK)_2$ complex, as illustrated in **Fig.3.91**

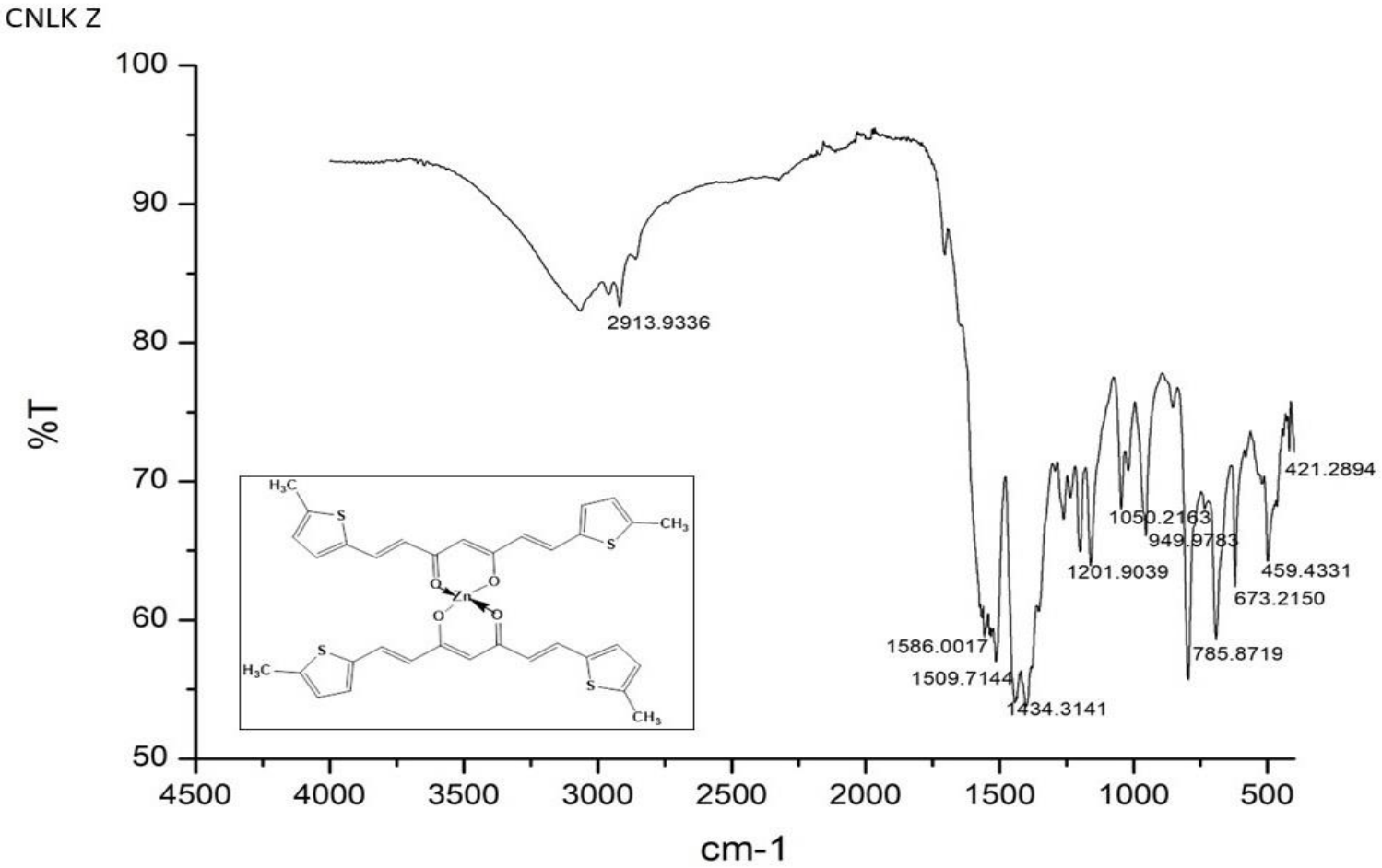

Fig.3.89 The IR spectrum of Zn $(NLK)_2$

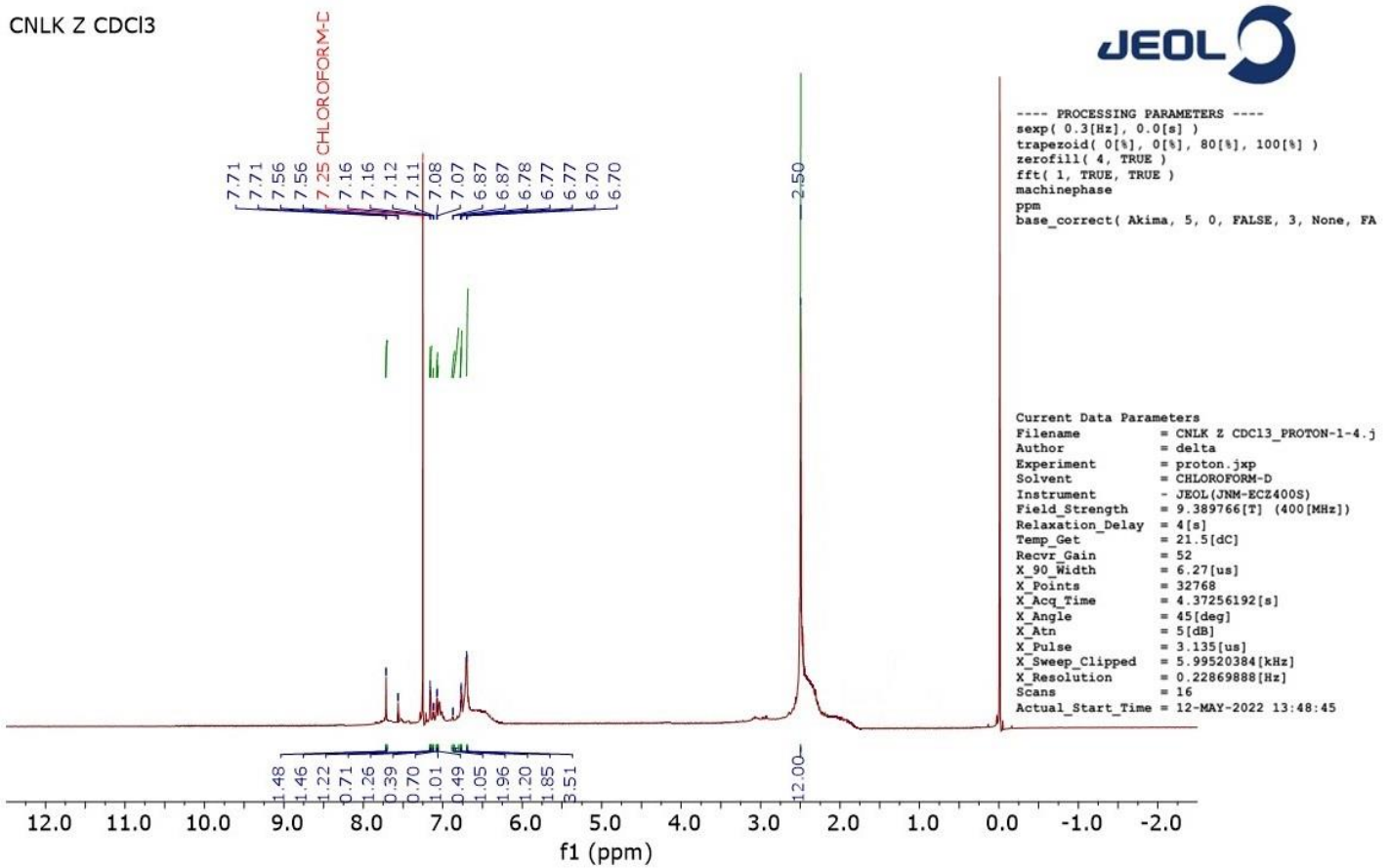

Fig.3.90 The ^{1}H NMR spectrum of Zn $(NLK)_2$

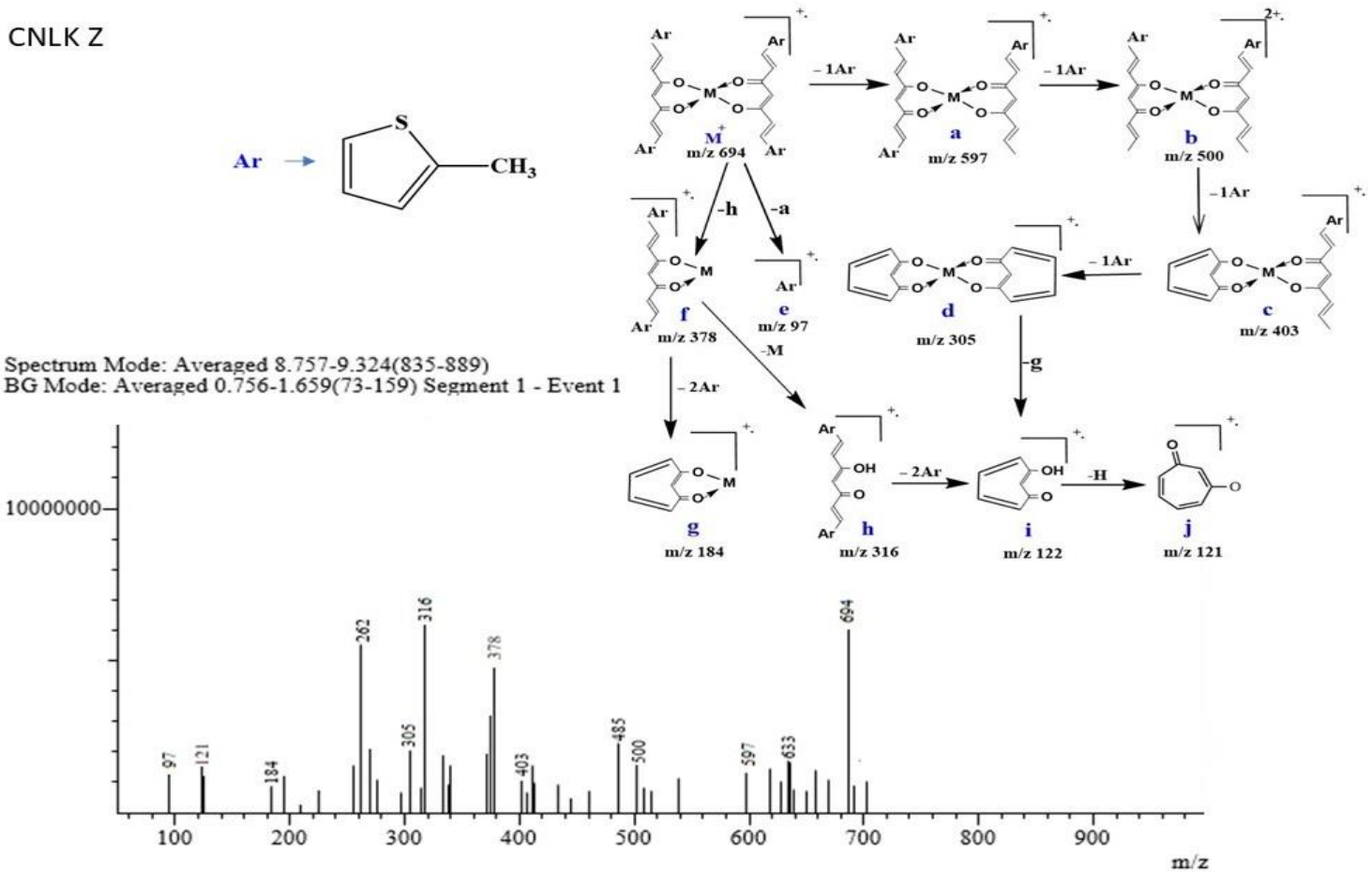

Fig.3.91 The Mass spectrum of Zn $(NLK)_2$

3.6. CONCLUSION

This chapter detailed the synthesis of nine curcumin analogues, achieved by varying the functional groups attached to the aryl rings to meet specific medicinal applications. Although numerous methods exist for synthesizing curcumin analogues, this study utilized Pabon's method based on the Claisen–Schmidt condensation mechanism. This approach was chosen for its straightforwardness, high yields, and minimal by-products, which are essential for the efficient formation of β-diketones, as supported by the literature. The synthesized analogues were purified and characterized using various analytical techniques. The analytical and spectral data unequivocally confirmed that all the compounds predominantly existed in the intramolecularly hydrogen-bonded enol tautomeric form.

Cu(II) and Zn(II) complexes of the nine curcumin analogues were synthesized, as metal complexation enhanced the stability and solubility of curcumin analogues, often leading to improved biomedical properties. These complexes also underwent purification and characterization. The nine curcumin analogues formed stable metal chelates with Cu(II) and Zn(II), exhibiting an ML_2 stoichiometry[69]. As unsaturated diketones, they functioned as monobasic bidentate chelating agents. In all the metal complexes, only the oxygen atoms of the diketone groups participated in coordination, leading to the formation of a stable six-membered chelate ring with the metal ion. The analytical and spectral findings revealed that other potential metal-binding groups, such as hydroxyl (-OH) groups and sulphur atoms in the thiophenyl ring, were not involved in coordinating with the metal ions.

3.7. REFERENCES

1. Hossain, M., Das, U., & Dimmock, J. R. (2019). Recent advances in α, β-unsaturated carbonyl compounds as mitochondrial toxins. *European Journal of Medicinal Chemistry*, *183*, 111687.
2. Rodrigues, F. C., Kumar, N. A., & Thakur, G. (2021). The potency of heterocyclic curcumin analogues: An evidence-based review. *Pharmacological Research*, *166*, 105489.
3. Yixuan, L., Qaria, M. A., Sivasamy, S., Jianzhong, S., & Daochen, Z. (2021). Curcumin production and bioavailability: A comprehensive review of curcumin extraction, synthesis, biotransformation and delivery systems. *Industrial Crops and Products*, *172*, 114050.
4. Pawelski, D., Walewska, A., Ksiezak, S., Sredzinski, D., Radziwon, P., Moniuszko, M., ... & Plonska-Brzezinska, M. E. (2021). Monocarbonyl Analogs of Curcumin Based on the Pseudopelletierine Scaffold: Synthesis and Anti-Inflammatory Activity. *International Journal of Molecular Sciences*, *22*(21), 11384.
5. Koparde, A. A., Doijad, R. C., & Magdum, C. S. (2019). Natural products in drug discovery. In *Pharmacognosy-medicinal plants*. IntechOpen.
6. Meza-Morales, W., Machado-Rodriguez, J. C., Alvarez-Ricardo, Y., Obregón-Mendoza, M. A., Nieto-Camacho, A., Toscano, R., ... & Enríquez, R. G. (2019). A new family of homoleptic copper complexes of curcuminoids: Synthesis, characterization and biological properties. *Molecules*, *24*(5), 910.
7. Prasad, S., DuBourdieu, D., Srivastava, A., Kumar, P., & Lall, R. (2021). Metal–curcumin complexes in therapeutics: an approach to enhance pharmacological effects of curcumin. *International journal of molecular sciences*, *22*(13), 7094.
8. Wanninger, S., Lorenz, V., Subhan, A., & Edelmann, F. T. (2015). Metal complexes of curcumin–synthetic strategies, structures and medicinal applications. *Chemical Society Reviews*, *44*(15), 4986-5002.
9. Shakeri, A., Panahi, Y., Johnston, T. P., & Sahebkar, A. (2019). Biological properties of metal complexes of curcumin. *BioFactors*, *45*(3), 304-317.
10. Zhang, Y., Khan, A. R., Fu, M., Zhai, Y., Yu, A., & Zhai, G. (2019). The progresses in curcuminoids-based metal complexes: Especially in cancer therapy. *Future medicinal chemistry*, *11*(09), 1035-1056.
11. DuBourdieu, D., Prasad, S., & Lall, R. (2021). Curcuminoid–metal complexes for oxidative stress. In *Nutraceuticals* (pp. 571-584). Academic Press.
12. Al-Noor, T. H., Ali, A. M., Al-Sarray, A. J., Al-Obaidi, O. H., Obeidat, A. I., & Habash, R. R. (2022). A Short Review: Chemistry of Curcumin and Its Metal Complex Derivatives. *J. Univ. Anbar Pure Sci*, *16*, 20-26.
13. Saifunneesa, T. K. (2013). *Synthesis, characterisation and biological studies of some unsaturated 1, 3-diketones and their metal complexes* (Doctoral dissertation, Dept. of Chemistry, University of Calicut.).
14. Hatamipour, M., Johnston, T. P., & Sahebkar, A. (2018). One molecule, many targets and numerous effects: the pleiotropy of curcumin lies in its chemical structure. *Current pharmaceutical design*, *24*(19), 2129-2136.
15. Ziani, N., Sid, A., Demonceau, A., Willem, Q., Dassonneville, B., & Lamara, K. (2013). Synthesis of new curcumin analogues from Claisen-Schmidt condensation. *European Journal of Chemistry*, *4*(2), 146-148.
16. Dettori, M. A., Carta, P., & Fabbri, D. (2024). Environmentally friendly one-pot two-step sequential synthesis of biological active curcumin analogues. *Tetrahedron*, *153*, 133867.
17. Noureddin, S. A., El-Shishtawy, R. M., & Al-Footy, K. O. (2019). Curcumin analogues and their hybrid molecules as multifunctional drugs. *European journal of medicinal chemistry*, *182*, 111631.
18. Gupta, A. P., Khan, S., Manzoor, M. M., Yadav, A. K., Sharma, G., Anand, R., & Gupta, S. (2017). Anticancer curcumin: natural analogues and structure-activity relationship. *Studies in natural products chemistry*, *54*, 355-401.
19. Rodrigues, F. C., Kumar, N. A., & Thakur, G. (2021). The potency of heterocyclic curcumin analogues: An evidence-based review. *Pharmacological Research*, *166*, 105489.
20. Katsori, A. M., Chatzopoulou, M., Dimas, K., Kontogiorgis, C., Patsilinakos, A., Trangas, T., & Hadjipavlou-Litina, D. (2011). Curcumin analogues as possible anti-proliferative & anti-inflammatory agents. *European journal of medicinal chemistry*, *46*(7), 2722-2735.
21. Gyuris, M., Hackler Jr, L., Nagy, L. I., Alföldi, R., Rédei, E., Marton, A., ... & Puskás, L. G. (2017). Mannich curcuminoids as potent anticancer agents. *Archiv der Pharmazie*, *350*(7), e1700005.

22. Gu, H., Liu, S., Liang, K., Xia, Z., Zhang, G., Li, B., & Liu, S. (2024). Design and Synthesis of Dimethylaminomethyl-Substituted Curcumin Derivatives: Potent Anti-Inflammatory, Anti-Oxidant, and Radioprotection Activity, Improved Aqueous Solubility Compared with Curcumin. *Molecules*, *29*(9), 1985.
23. Noureddin, S. A. (2020). *Design and Synthesis of Novel Bioactive Hybrid Structures Containing Curcumin Analogues* (Doctoral dissertation, King Abdulaziz University Jeddah-Saudi Arabia).
24. Amolins, M. W., Peterson, L. B., & Blagg, B. S. (2009). Synthesis and evaluation of electron-rich curcumin analogues. *Bioorganic & medicinal chemistry*, *17*(1), 360-367.
25. Bairwa, K., Grover, J., Kania, M., & Jachak, S. M. (2014). Recent developments in chemistry and biology of curcumin analogues. *RSC advances*, *4*(27), 13946-13978.
26. Noureddin, S. A., El-Shishtawy, R. M., & Al-Footy, K. O. (2019). Curcumin analogues and their hybrid molecules as multifunctional drugs. *European journal of medicinal chemistry*, *182*, 111631.
27. Ayyagari, N., Jose, D., Mobin, S. M., & Namboothiri, I. N. (2011). Stereoselective construction of carbocycles and heterocycles via cascade reactions involving curcumins and nitroalkenes. *Tetrahedron Letters*, *52*(2), 258-262.
28. Wolosewicz, K., Podgorska, K., Rutkowska, E., & Lazny, R. (2019). Synthesis of dicarbonyl curcumin analogues containing the tropane scaffold. *European Journal of Organic Chemistry*, *2019*(29), 4662-4674.
29. Adams, B. K., Ferstl, E. M., Davis, M. C., Herold, M., Kurtkaya, S., Camalier, R. F., ... & Shoji, M. (2004). Synthesis and biological evaluation of novel curcumin analogs as anti-cancer and anti-angiogenesis agents. *Bioorganic & medicinal chemistry*, *12*(14), 3871-3883.
30. Martin, G. D., McKenzie, C., & Moore, M. (2017). Synthesis and bioconversion of curcumin analogs. *Natural Product Communications*, *12*(4), 1934578X1701200424.
31. Adams, B. K., Ferstl, E. M., Davis, M. C., Herold, M., Kurtkaya, S., Camalier, R. F., ... & Shoji, M. (2004). Synthesis and biological evaluation of novel curcumin analogs as anti-cancer and anti-angiogenesis agents. *Bioorganic & medicinal chemistry*, *12*(14), 3871-3883.
32. Bairwa, K., Grover, J., Kania, M., & Jachak, S. M. (2014). Recent developments in chemistry and biology of curcumin analogues. *RSC advances*, *4*(27), 13946-13978.
33. Prasad, S., DuBourdieu, D., Srivastava, A., Kumar, P., & Lall, R. (2021). Metal–curcumin complexes in therapeutics: an approach to enhance pharmacological effects of curcumin. *International journal of molecular sciences*, *22*(13), 7094.
34. Wanninger, S., Lorenz, V., Subhan, A., & Edelmann, F. T. (2015). Metal complexes of curcumin–synthetic strategies, structures and medicinal applications. *Chemical Society Reviews*, *44*(15), 4986-5002.
35. Pröhl, M., Schubert, U. S., Weigand, W., & Gottschaldt, M. (2016). Metal complexes of curcumin and curcumin derivatives for molecular imaging and anticancer therapy. *Coordination Chemistry Reviews*, *307*, 32-41.
36. Philip, A., Ghiyasi, R., & Karppinen, M. (2021). Photoactive thin-film structures of curcumin, TiO2 and ZnO. *Molecules*, *26*(11), 3214.
37. Fiss, B. G., Richard, A. J., Douglas, G., Kojic, M., Friščić, T., & Moores, A. (2021). Mechanochemical methods for the transfer of electrons and exchange of ions: Inorganic reactivity from nanoparticles to organometallics. *Chemical Society Reviews*, *50*(14), 8279-8318.
38. Huang, Q., Yang, Y., & Qian, J. (2023). Structure-directed growth and morphology of multifunctional metal-organic frameworks. *Coordination Chemistry Reviews*, *484*, 215101.
39. Abe, T., Miyazawa, A., Kawanishi, Y., & Konno, H. (2011). Microwave-assisted synthesis of metal complexes. Mini-Reviews in Organic Chemistry, 8(3), 315-333.
40. Pons-Balagué, A., Ojea, M. J. H., Ledezma-Gairaud, M., Mañeru, D. R., Teat, S. J., Costa, J. S., ... & Sañudo, E. C. (2013). Microwave assisted synthesis in coordination chemistry. *Polyhedron*, *52*, 781-787.
41. Luo, T., Bu, L., Peng, S., Zhang, Y., Zhou, Z., Li, G., & Huang, J. (2019). One-step microwave-assisted preparation of oxygen-rich multifunctional carbon quantum dots and their application for Cu2+-curcumin detection. *Talanta*, *205*, 120117.
42. Guo, X., Li, W., Wang, H., Fan, Y. Y., Wang, H., Gao, X., ... & Gong, X. (2018). Preparation, characterization, release and antioxidant activity of curcumin-loaded amorphous calcium phosphate nanoparticles. *Journal of Non-Crystalline Solids*, *500*, 317-325.
43. Kumar, S., Jain, S., Nehra, M., Dilbaghi, N., Marrazza, G., & Kim, K. H. (2020). Green synthesis of metal–organic frameworks: A state-of-the-art review of potential environmental and medical applications. Coordination Chemistry Reviews, 420, 213407.

44. Teo, R. H. X., Lee, J. X. T., Tan, W. R., Shum, W. Q., Li, Y., Pullarkat, S. A., ... & Leung, P. H. (2021). Catalytic Asymmetric Hydrophosphination as a Valuable Tool to Access Dihydrophosphinated Curcumin and Its Derivatives. *Organometallics*, *40*(20), 3454-3461.
45. Wanninger, S., Lorenz, V., Subhan, A., & Edelmann, F. T. (2015). Metal complexes of curcumin–synthetic strategies, structures and medicinal applications. *Chemical Society Reviews*, *44*(15), 4986-5002.
46. Chakraborty, S., Bera, D., Roy, L., & Ghosh, C. K. (2023). Biomimetic and Bioinspired Nanostructures: Recent Developments and Applications. *Bioinspired and Green Synthesis of Nanostructures: A Sustainable Approach*, 353-404.
47. Saritha, T. J., & Metilda, P. (2021). Synthesis, spectroscopic characterization and biological applications of some novel Schiff base transition metal (II) complexes derived from curcumin moiety. *Journal of Saudi chemical society*, *25*(6), 101245.
48. Luo, T., Bu, L., Peng, S., Zhang, Y., Zhou, Z., Li, G., & Huang, J. (2019). One-step microwave-assisted preparation of oxygen-rich multifunctional carbon quantum dots and their application for Cu2+-curcumin detection. *Talanta*, *205*, 120117.
49. El-Nahhal, I. M., Salem, J., Kodeh, F. S., Elmanama, A., & Anbar, R. (2022). CuO–NPs, CuO–Ag nanocomposite and Cu (II)-curcumin complex coated cotton/starched cotton antimicrobial materials. *Materials Chemistry and Physics*, *285*, 126099.
50. Călinescu, M., Fiastru, M., Bala, D., Mihailciuc, C., Negreanu-Pîrjol, T., & Jurcă, B. (2019). Synthesis, characterization, electrochemical behavior and antioxidant activity of new copper (II) coordination compounds with curcumin derivatives. *Journal of Saudi Chemical Society*, *23*(7), 817-827.
51. Halevas, E., Pekou, A., Papi, R., Mavroidi, B., Hatzidimitriou, A. G., Zahariou, G., ... & Pantazaki, A. A. (2020). Synthesis, physicochemical characterization and biological properties of two novel Cu (II) complexes based on natural products curcumin and quercetin. *Journal of inorganic biochemistry*, *208*, 111083.
52. Prasad, S., & Lall, R. (2022). Zinc-curcumin based complexes in health and diseases: An approach in chemopreventive and therapeutic improvement. *Journal of Trace Elements in Medicine and Biology*, *73*, 127023.
53. Nawaz, S. S., Manjunatha, K. B., Supriya, S., Ranganatha, S., Ranjan, P., Chakraborty, T., ... & Ramakrishna, D. (2023). Zinc-curcumin complexes: Design, synthesis, geometry optimization, and optical nonlinearity applications. *Optical Materials*, *143*, 114164.
54. Al-Thubaiti, E. H. (2023). Antibacterial and antioxidant activities of curcumin/Zn metal complex with its chemical characterization and spectroscopic studies. *Heliyon*, *9*(6).
55. Pabon HJ. A synthesis of curcumin and related compounds. *Rec Trav Chim.* 1964;83:379–86.
56. Al-Wabli, R. I. (2006). Synthesis of Curcumin Analogues Biconjugates as Potential Antitumor Agents in Isolated Human Cells. *King Saud University, Saudi Arabia*.
57. Chen, J. Y. T. (1965). Micro KBr technique of infrared spectrophotometry. *Journal of the Association of Official Agricultural Chemists*, *48*(2), 380-384.
58. Trovitch, R. J., Lobkovsky, E., Bill, E., & Chirik, P. J. (2008). Functional group tolerance and substrate scope in bis (imino) pyridine iron catalyzed alkene hydrogenation. *Organometallics*, *27*(7), 1470-1478.
59. Lindeman, L. P., & Adama, J. Q. (1971). Carbon-13 nuclear magnetic resonance spectrometry. Chemical shifts for the paraffins through C9. *Analytical Chemistry*, *43*(10), 1245-1252.
60. Rasche, F., Svatos, A., Maddula, R. K., Böttcher, C., & Böcker, S. (2011). Computing fragmentation trees from tandem mass spectrometry data. *Analytical Chemistry*, *83*(4), 1243-1251.
61. Fadeeva, V. P., Tikhova, V. D., & Nikulicheva, O. N. (2008). Elemental analysis of organic compounds with the use of automated CHNS analyzers. *Journal of analytical chemistry*, *63*, 1094-1106.
62. Shurvell, H. F. (2006). Spectra–structure correlations in the mid-and far-infrared. *Handbook of vibrational spectroscopy*.
63. Tahay, P., Parsa, Z., Zamani, P., & Safari, N. (2022). A structural and optical study of curcumin and curcumin analogs. *Journal of the Iranian Chemical Society*, *19*(7), 3177-3188.
64. Khudhayer Oglah, M., & Fakri Mustafa, Y. (2020). Curcumin analogs: synthesis and biological activities. *Medicinal Chemistry Research*, *29*, 479-486.
65. Lu, D., Liu, H., Ye, W., Wang, Y., & Wu, B. (2017). Structure-and isoform-specific glucuronidation of six curcumin analogs. *Xenobiotica*, *47*(4), 304-313.
66. Tahay, P., Parsa, Z., Zamani, P., & Safari, N. (2022). A structural and optical study of curcumin and curcumin analogs. *Journal of the Iranian Chemical Society*, *19*(7), 3177-3188.

67. Beneduci, A., Corrente, G. A., Marino, T., Aiello, D., Bartella, L., Di Donna, L., ... & Furia, E. (2019). Insight on the chelation of aluminum (III) and iron (III) by curcumin in aqueous solution. *Journal of Molecular Liquids*, *296*, 111805.
68. Călinescu, M., Fiastru, M., Bala, D., Mihailciuc, C., Negreanu-Pîrjol, T., & Jurcă, B. (2019). Synthesis, characterization, electrochemical behavior and antioxidant activity of new copper (II) coordination compounds with curcumin derivatives. *Journal of Saudi Chemical Society*, *23*(7), 817-827.
69. Thomachan, S., Cherappanath, R. J., & John, V. D. (2023). Curcuminoid analogues with substituted naphthyl ring and their transition metal chelates—Antibacterial and antitumor studies. *Journal of Pharmacognosy and Phytochemistry*, 12(6), 210–214.

CHAPTER 4

Experimental validation of the anticancer effects of curcumin analogues and their metal complexes: in silico, in vitro and in vivo approaches

CHAPTER 4

EXPERIMENTAL VALIDATION OF THE ANTICANCER EFFECTS OF CURCUMIN ANALOGUES AND THEIR METAL COMPLEXES: *IN SILICO*, *IN VITRO* AND *IN VIVO* APPROACHES

4.1. INTRODUCTION

In 2022, approximately 20 million new cancer cases and 9.7 million deaths were reported globally. The number of people living within five years of a cancer diagnosis was estimated at 53.5 million (World Health Organization)[1]. The most common cancers—lung, breast, and colorectal—account for a significant portion of new cases and deaths[2]. Despite substantial advances in cancer detection and treatment, the universal burden of cancer continues to grow, underscoring the need for improved healthcare access, preventive measures, and targeted research to address disparities and improve outcomes worldwide. Researchers have been drawn to cancer, leading them to investigate drugs that target different receptors in all proliferative pathways in detail.

Breast cancer has become the most common cancer globally, with 7.8 million cases reported during the past five years. In India, the incidence rate is estimated to be 100.4 cancer cases per 100,000 people by 2022, with a higher rate among women at 105.4 per one lakh[3]. Notably, breast cancer, which is often curable with early detection and proper treatment, is the leading cause of cancer-related mortality among women, accounting for 15% of all female cancer deaths[4]. Despite a recent increase, breast cancer is still more common in low- and middle-income countries (LMICs), also referred to as developing countries, than it is in industrialized nations. Furthermore, using breast cancer drugs in developing countries is not cost-effective. To lower the incidence of breast cancer, both developed and developing nations must implement a range of highly effective screening, diagnosis, and treatment alternatives[5]. Given its prevalence and impact, there is a critical need to focus on breast cancer prevention, early detection, and treatment strategies to reduce the global threat of this mortal disease.

It is imperative to discover efficacious medications through the exploration of bioactive investigations, structure-activity relationship analyses for analogue derivatives,

coordinated action-direct synthesis, isolation, and characterization[6]. Due to its remarkable chemotherapeutic potential against various tumours, curcumin surpasses other compounds in terms of anticancer efficacy[7]. A comprehensive exploration of the structure-activity relationship of curcumin is employed to improve its pharmacological profile and understand the significance of each reactive site within the structure of the compound. This analysis aids in pinpointing destabilizing sites and preserving those responsible for the exceptional activity of the compound to facilitate lead optimization. The development of numerous analogues and derivatives has been pursued to assess the impact of each of these sites on the activity and stability of the molecule[8]. Compared to curcumin, these alterations enhance stability and bioavailability, potentially ensuring sustained curcumin-like efficacy. In contrast to labour-intensive wet lab experiments, *in silico* technologies have simplified structure-based analysis[9]. A novel reverse molecular docking methodology was suggested to identify potential protein targets of curcumin, shedding light on its mechanisms as a potent anti-tumour agent. This approach could also elucidate the molecular mechanisms of novel curcumin analogues[10].

This chapter predominantly concentrated on the evaluation of prospective curcumin analogue inhibitors targeting breast cancer receptors, specifically BRCA1 and TP53. These analogues were created by modifying the functional groups on the aryl rings of natural curcumin. The screening involved molecular docking, dynamic simulation analyses, and binding free energy calculations using MM/GBSA (molecular mechanics with generalized Born and surface area solvation) methodologies. A comparison was made between the binding affinity of curcumin analogues and natural curcumin towards the specified targets, as well as with the FDA-approved anticancer drug cyclophosphamide and its verified target. Subsequent validation of the computational models was conducted through *in vitro* and *in vivo* experiments. This chapter includes *in vitro* evaluations of the cytotoxicity of Cu(II) and Zn(II) metal complexes synthesized from nine curcumin analogues, excluding computational screening analyses.

4.2. REVIEW OF LITERATURE

This literature survey explored recent insights into several key areas such as the role of *in silico* molecular docking in drug discovery for predicting drug-target interactions and designing new compounds; the uses and limitations of the FDA-approved drug cyclophosphamide; the crucial roles of BRCA1 and TP53 in breast cancer; and *in*

vitro cytotoxic studies, particularly those using DLA and MTT assays, as well as *in vivo* DLA models, to enhance the understanding of anticancer agents. The role of metal complexes, especially the Cu(II) and Zn(II) complexes of curcumin analogues, in anticancer studies has also been reviewed. Relevant references and brief explanations of the key findings for each category are summarized in **Table 4.1**

Table 4.1 Key findings and references on *in silico* docking for drug-target predictions, cyclophosphamide in cancer treatment, BRCA1 and TP53 in breast cancer risk, the role of metal complexes of curcumin analogues in anticancer studies and *in vitro* and *in vivo* assays for anticancer evaluation.

About	Insights	Reference
In silico molecular docking studies	*In silico* molecular docking was crucial for drug discovery, predicting interactions between potential drugs and target proteins, and designing new therapeutic compounds. Recent studies highlighted its use in developing curcumin analogues as anticancer agents. Combining docking with pharmacokinetic studies enhanced understanding of solvation effects, molecular dynamics, and electrostatic potential, guiding experimental validation and compound optimization.	11-16
Anticancer Drug: Cyclophosphamide	Cyclophosphamide, an FDA-approved alkylating agent used as an anti-neoplastic drug, was commonly prescribed for treating sarcoma, multiple myeloma, and breast cancer. Despite its efficacy, cyclophosphamide was associated with significant adverse effects, primarily targeting the bladder and gonads. Documented side effects from recent clinical trials and studies included hemorrhagic cystitis, amenorrhea, myelosuppression, alopecia, and episodes of nausea and vomiting.	17-19

BRCA1 and TP53	Recent studies underscored the critical roles of BRCA1 and TP53 in breast cancer. Extensive research on TP53 mutations highlighted their impact on disease progression and therapy, while BRCA1 mutations were linked to increased cancer susceptibility. Investigations into the interplay between BRCA1 and TP53 revealed their collaborative functions in cancer pathogenesis. Emerging TP53-targeted therapies showed promise for improved treatment outcomes. These findings emphasized the importance of TP53 and BRCA1 in breast cancer prevention, diagnosis, and treatment, advancing personalized medicine and targeted therapies.	20-29
Anticancer Properties of curcumin analogues and their Cu (II), and Zn (II) metal complexes	Recent studies highlighted the promising anticancer properties of curcumin analogues and their Cu(II) and Zn(II) metal complexes. These compounds demonstrated enhanced stability, bioavailability, and cytotoxicity against cancer cells through targeted interactions and redox cycling mechanisms. They represented potential candidates for developing effective, targeted cancer therapies with reduced side effects.	30-48
In vitro cytotoxic studies using DLA, EAC and Spleen cell lines and regarding MTT Assay	*In vitro* cytotoxic studies using DLA, EAC, and spleen cell lines were crucial in cancer research for evaluating the efficacy of potential anticancer agents. The MTT assay remained a fundamental tool in these studies, providing a quick and reliable measure of cell viability. Recent studies advanced our understanding of how various compounds induced cytotoxicity, offering promising avenues for developing new cancer therapies.	49-54

In vivo Antitumor Studies Using Dalton's Lymphoma Ascites (DLA)	Dalton's Lymphoma Ascites (DLA) was a widely used murine model for *in vivo* antitumor studies. This model was valuable for evaluating the efficacy of potential anticancer agents and understanding their mechanisms of action in a living organism. The DLA model involved the transplantation of ascites cells into mice, allowing for the assessment of tumour growth inhibition, survival rates, and other physiological effects of anticancer treatments.	55-58

4.3. MATERIALS AND METHODS

4.3.1. *In silico* studies - Anticancer effect of curcumin analogues

Based on the literature survey, BRCA1 (Breast Cancer gene 1) and TP53 were selected as tumour suppressor and antiproliferative genes for *in silico* studies focusing on these molecules.

4.3.1.1. Identification of molecular targets of breast cancer and reference molecules

Curcumin (PubChem ID:969516) and the FDA-approved drug cyclophosphamide (DB00531, $C_7H_{15}Cl_2N_2O_2P$, average weight 261.086 g) (Pub Chem ID 2907) were selected as the reference molecules for this study. Cyclophilin A (CyPA), an abundant intracellular protein, was the main target of cyclophosphamide. The crystal structure of cyclophilin from *Trypanosoma cruzi* (bound to cyclosporin A) was identified as the target (PDB ID: 1XQ7; X-ray diffraction structure, resolution 2.07 Å, R-value free 0.235, R-value work 0.169, number of chains: 3)(TG7) [59]and the three-dimensional (3D) structure of the target was retrieved from the RCSB Protein Data Bank[60]. The important proteins encoded by the BRCA1 and TP53 genes, in which germline mutations affect the risk of developing breast cancer, were selected as molecular targets through metabolic pathway analysis using the STRING database[61]. The three-dimensional structures of the major proteins were selected from RCSB-PDB. These included the BRCA1 BRCT domains (PDB: 4Y2J; X-ray diffraction structure, resolution 2.15 Å, R-value free 0.248, R-value work 0.193, number of chains:1)(TG1)[62], the BRCA1/BARD1 RING-domain

heterodimer (PDB: 1JM7; solution NMR structure, number of chains: 1)(TG2)[63], the BRCT-c domain of human BRCA1 (PDB: 1OQA; solution NMR structure, number of chains: 1)(TG3)[64], hypothetical protein yxeF (PDB: 2JOZ; solution NMR structure, number of chains: 1)(TG4)[65], the p300 Taz2-p53 TAD1 binding domain (PDB: 2K8F; solution NMR structure, number of chains:1)(TG5)[66], and the p53 transactivation domain 2 (PDB: 2RUK; solution NMR structure, number of chains:1)(TG6)[67].

4.3.1.2. Molecular docking studies

4.3.1.2.1. Preparation of the ligands and prediction of their pharmacokinetics features

The literature survey suggested that chlorinated curcumin analogues, curcumin analogues containing alkyl and hydroxyl groups, and alkoxy-hydroxy curcumin analogues were probably used for the treatment of breast cancer. Nine curcumin analogues were designed using Chem Draw Ultra in MOL format:

(1E,6E)-1,7-bis(3,4-dimethoxy phenyl) hepta-1,6-diene-3,5-dione (NLB)

(1E,6E)-1,7-bis(3,5-dichloro-2-hydroxy phenyl)hepta-1,6-diene-3,5-dione(NLD)

(1E,6E)-1,7-bis(6-methoxy naphthalen-2-yl) hepta-1,6-diene-3,5-dione (NLE)

(1E,6E)-1,7-bis(3-ethoxy-2-hydroxy phenyl)hepta-1,6-diene-3,5-dione (NLF)

(1E,6E)-1,7-bis(4-hydroxy-3,5-dimethylphenyl)hepta-1,6-diene-3,5-dione (NLG)

(1E,6E)-1,7-bis(5-chloro-2-hydroxyphenyl)hepta-1,6-diene-3,5-dione (NLH)

(1E,6E)-1,7-bis(2-hydroxy3methoxyphenyl)hepta-1,6-diene-3,5-dione (NLI)

(1E,6E)-1,7-bis(3-hydroxy-4-methoxyphenyl)hepta-1,6-diene-3,5-dione (NLJ)

(1E,6E)-1,7-bis(5-methylthiophen-2-yl)hepta-1,6-diene-3,5-dione (NLK)

The structural optimization of these molecules was carried out using Gaussian 6.0 with the Berny geometry optimization algorithm. The molecules were opened in Gauss View 6.0 and energy was minimized using the 'Calculate' menu with the standard Gaussian calculation setup, then saved in gpf format. The structures were converted into PDB format using Open Babel. All nine compounds were subjected to the prediction of their pharmacokinetic features, which suggested that all the compounds had good potential for oral bioavailability and drug-like properties, making them suitable candidates for further drug development as mentioned in **Table 2.2** and **2.3**.

4.3.1.2.2. Preparation of the receptors

The 3D structures of each of the protein targets were retrieved from PDB, and the structures were prepared by removing water molecules and bound ligands from the crystal structures, adding polar hydrogen atoms, merging non-polar bonds, and computing the Gasteiger charges[68]. The binding site of each target was assigned based on the coordinate files in the active site using the Auto Grid program, with the appropriate coordinate dimensions for X, Y, and Z. The target and ligand files were then saved in pdbqt format.

4.3.1.2.3. Molecular docking

The binding affinity of each curcumin analogue to selected target proteins was computationally modelled using molecular docking via Auto Dock 4.2[69]. The binding centres of the target proteins were assigned by the Auto Grid program with the following X, Y, and Z coordinates: TG1 at 21.263724, 4.569707, and 20.718172; TG2 at 7.638656, 0.23321, and 1.363127; TG3 at 1.208761, 6.128752, and 1.120766; TG4 at 6.010299, 7.199523, and 0.787027; TG5 at 0.238493, 0.584392, and 1.303119; and TG6 at 7.997, 7.152, and 9.993.

The best-docked conformations were evaluated based on binding energy (kcal/mol), number of hydrogen bonds, upper and lower bound root mean square deviation (RMSD), number of interacting residues, and other weak forces stabilizing the receptor-ligand complex. The binding potential of the synthesised curcumin analogues to the selected proteins was compared to the binding of native curcumin and the selected targets, as well as to the FDA-approved drug cyclophosphamide (PubChem ID: 2907) and its validated target cyclophilin (PDB ID: 1XQ7).

For cyclophilin, the bound ligand cyclosporin A was removed from the PDB file 1XQ7, and the structure was saved in pdbqt format. The 3D structure of cyclophosphamide was retrieved from PubChem, optimized by assigning torsion angles, the number of torsions, and rotatable bonds, and saved in pdbqt format. The grid box was set to the same binding site where cyclosporin A interacted with cyclophilin, based on the binding site information from the crystal structure. Molecular docking was performed using the Lamarckian Genetic Algorithm with Auto Dock 4.2.

4.3.1.3. Molecular dynamic simulation studies of the best-docked complex

The stability of the best-docked complex of the curcumin analogue with its target, as well as the reference molecule with its target, was evaluated using molecular dynamic (MD) simulation. This process was executed using an improved gradient method within the Desmond module of the Schrödinger Suite v2022–2[70]. Initially, the selected protein-ligand poses were pre-processed and hydrogen bonds were assigned. The simulation system was set up using a system builder, selecting TIP3P for the solvent parameters. The boundary conditions were defined by an orthorhombic box, and volume minimization was applied to the complex. The OPLS3e force field was chosen, and the system was neutralized by adding the appropriate amount of Cl^- or Na^+ ions based on the charges.

The simulations were conducted at 310 K using the NPT ensemble (constant number of particles, pressure, and temperature) for 100 ns with 0.1 ns intervals. The simulation steps included: (1) Performing Brownian dynamics NPT simulations at 10 K with small time steps of 100 ps while restraining solute heavy atoms; (2) Continuing with Brownian dynamics NPT at 10 K with 12 ps time steps and restraints on heavy solute atoms to stabilize the system; (3) Solvating the binding pocket; (4) Running NPT simulation without restraints for 100 ps; (5) Conducting the final simulation for 100 ns with 2 femtosecond (fs) time steps at 310 K.

Optimization involved using a short-range cut-off with a radius of 9.0 Å without predefined restraints. The temperature of the system was increased by 10 K per time step, followed by the solvation of the binding pocket. Changes in RMSD (root mean square deviation) and ligand-protein contacts throughout the simulation were analysed using the interaction diagram tool. The protein-ligand RMSD, RMSF (root mean square fluctuation), protein-ligand contacts, ligand torsion profile trajectories, and ligand properties were determined using this tool.

4.3.1.3.1. Binding free energy calculations by Molecular Mechanics-Generalized Born Model and Solvent Accessibility Method (MM/GBSA)

The binding free energy of the selected docked complexes of curcumin analogue-target pairs after MD simulation was estimated using Prime-MM/GBSA. The trajectory files from the MD simulation, spanning 100 ns and comprising 1000 frames, were used as input for the GBSA estimation[71]. Structures were extracted every 100 frames (10 ns),

resulting in 10 selected structures for GBSA energy estimation using the VSGB 2.0 model[72].

GBSA energy calculations provided insights into the energies of the receptor, ligand, and receptor-ligand complex, as well as energy differences related to strain and binding. The following energy calculation steps were adopted in Prime-MM/GBSA: optimized free ligand (="Ligand"), optimized free receptor (="Receptor"), optimized complex (="Complex"), the ligand of minimized/optimized complex and the receptor of minimized/optimized complex. The energy obtained by the above steps, MM/GBSA dG_{Bind} = Complex – Receptor - Ligand, and MM/GBSA dG_{Bind} (NS) =Complex - Receptor (from optimised complex) - Ligand (from optimised complex) were calculated. To accurately determine the binding free energy, values for receptor strain and ligand strain (MM/GBSA dG_{Bind}- Rec Strain - Lig Strain) were also essential[73].

4.3.2. *In Vitro* studies-Anticancer effect of curcumin analogues and their metal complexes

Cytotoxicity is one of the chemotherapeutic goals linked to the antitumor action[74]. The assessment of *in vitro* cytotoxicity provided the basis for evaluating the *in vivo* antitumor efficacy of the synthesized compound.

4.3.2.1. Differential cytotoxicity assessment using DLA, EAC and primary rat spleen cells - *in vitro*

Cell lines: Cell lines for Ehrlich's ascites carcinoma (EAC) and Dalton's lymphoma ascites (DLA) were obtained from the Adayar Cancer Research Centre in Chennai, India. Swiss albino mice, sourced from the Small Animal Breeding Station (SABS) at Kerala Veterinary and Animal Sciences University in Mannuthy, Thrissur, Kerala, India, were intraperitoneally injected with 2×10^6 cells per mouse to maintain the viability of the cells. Starting from the 15^{th} day post-inoculation, tumour cells were harvested from the peritoneal cavities of the mice.

For *in vitro* cytotoxicity studies, a synthetic curcumin analogue was dissolved in a minimal amount of dimethyl sulfoxide (DMSO). Tumour cells (DLA and EAC) were extracted from the peritoneal cavities of tumour-bearing mice and washed with phosphate-buffered saline (PBS; 0.1 M, pH 7.4). The cells were then centrifuged at 1000 rpm for 5 minutes. Cell viability was assessed using the trypan blue exclusion method[75].

Viable cells (1×10^6 cells in 0.1 ml) were added to tubes containing 10–200 µg/ml of the curcumin analogue, with the total volume adjusted to 1 ml using PBS. The mixture was incubated for three hours at 37°C. At the end of the incubation period, 0.1 ml of 1% trypan blue was added to the cell suspension, which was allowed to sit for 2–3 minutes before being transferred to a haemocytometer. The trypan blue exclusion method was used to determine the percentage of cytotoxicity (cell death) by counting stained (dead) and unstained (live) cells[76].

$$Percentage\ of\ cytotoxicity = \frac{Number\ of\ dead\ cells}{Number\ of\ dead\ cells\ +\ Number\ of\ live\ cells} \times 100$$

To obtain spleen tissue, a rat from SABS, Kerala Veterinary and Animal Sciences University, Mannuthy, Thrissur, Kerala, India, was sacrificed under carbon dioxide anaesthesia. The spleen was dissected and broken down into a single-cell suspension in Dulbecco's modified Eagle's medium (DMEM) containing penicillin-streptomycin solution (50 I.U./ml), and then filtered through mesh cloth. The cells were washed three times, suspended in a measured amount of antibiotic-containing DMEM complete media, and counted using a haemocytometer. Various concentrations of the test substance were added to tubes containing a viable cell suspension (1×10^6cells in 0.1 ml), with the volume adjusted to 1 ml using DMEM. Control tubes contained cell suspension without additives. These tubes were incubated at 37°C for 3 hours. After incubation, 0.1 ml of 1% trypan blue was added to the cell suspensions, allowed to sit for 2–3 minutes, and then transferred to a haemocytometer. Trypan blue, a blue dye, is absorbed by dead cells due to compromised plasma membrane integrity, staining them blue, while live cells remain colourless. Separate counts of stained and unstained cells were made.

$$Percentage\ of\ cytotoxicity = \frac{Number\ of\ dead\ cells}{Number\ of\ dead\ cells\ +\ Number\ of\ live\ cells} \times 100$$

4.3.2.2. 3-(4,5-Dimethylthiazol-2-yl)-2,5- Diphenyltetrazolium Bromide (MTT) assay

Cytotoxicity was assessed using cancer cell lines as an *in vitro* model for cancer research. The cytotoxic potential of the compounds was evaluated by comparing their

effects on cancer cell lines to those on the non-tumorigenic Vero cell line. The percentage of cell death in the treated cells was measured against an untreated control by comparing their respective absorbance values.

Cell culture: The monkey kidney epithelial cell line (Vero) and the mouse breast cancer cell line (C127I) were obtained from the National Centre for Cell Sciences in Pune, India. These cells were cultured in DMEM (Dulbecco's Modified Eagle Medium) supplemented with 10% fetal bovine serum (FBS), 100 µg/mL penicillin, and 100 µg/mL streptomycin. The cultures were maintained at 37°C in an incubator with 5% CO_2. The cells were passaged upon reaching 80–90% confluency, with the medium being replaced every three days.

Method: The cytotoxicity of the curcumin analogue was evaluated using the MTT assay (3-(4,5-Dimethylthiazol-2-yl)-2,5-Diphenyltetrazolium Bromide) as described in reference[77]. For the experiment, cells were seeded in a 24-well plate at a density of approximately 1×10^5cells/mL in full growth medium (DMEM) and allowed to adhere and proliferate until they reached 80% confluency. At this point, the medium was replaced with fresh DMEM containing varying concentrations of the curcumin analogue (ranging from 0 to 100 µg/mL) and incubated for 48 hours. Following the incubation period, 40 µL of 5 mg/mL MTT solution was added to each well, and the plate was incubated for an additional 4 hours. The resulting formazan crystals were dissolved in dimethyl sulfoxide (DMSO), and absorbance was measured at 570 nm using a Bio-Tek ELISA microplate reader (USA). Cell viability was then calculated using the appropriate formula.

$$Percentage\ \ viability\ = \frac{Absorbance\ of\ sample}{Absorbance\ of\ control} \times 100$$

4.3.3. *In Vivo* Antitumor Studies Using Dalton's Lymphoma Ascites (DLA)

Animals: Swiss albino mice, both male and female, aged 7-8 weeks and weighing between 25–30 grams, were sourced from the Small Animal Breeding Station (SABS) at Kerala Veterinary and Animal Sciences University, Mannuthy, Thrissur, Kerala. These mice were housed at the Amala Cancer Research Centre in well-ventilated cages, maintaining standard levels of humidity and temperature. They were provided with standard mouse feed (Sai Durga Foods, Bangalore, India) and had unrestricted access to water. All animal experiments in this study received prior

approval from the Institutional Animal Ethics Committee (IAEC), reference number ACRC/IAEC/22(1)-P4, and were conducted in strict accordance with the guidelines of the Committee for Control and Supervision of Experiments on Animals (CPCSEA) as mandated by the Animal Welfare Division, Government of India[78].

4.3.3.1. Acute toxicity

The oral acute toxicity of the sample was evaluated by the guidelines set by the Organization for Economic Cooperation and Development (OECD)[79]. Mice were kept at room temperature with consistent humidity levels and allowed to acclimate to laboratory conditions for one week before the experiment commenced. During the experiment, mice had unrestricted access to drinking water and food, except for a short fasting period of 12 hours before treatment, during which only water was available.

The animals were observed for 7 days before the administration of the oral drug. After the fasting period, their body weights were recorded, and the dose was calculated accordingly. A single high dose of 1 g/kg body weight of the drug, dissolved in carboxymethyl cellulose (CMC), was orally administered to three female mice, each weighing approximately 25 grams. Food was reintroduced to the mice about an hour after treatment. The mice were closely monitored for any signs of toxicity within the first six hours post-treatment and daily thereafter for 14 days. During this observation period, surviving animals were weighed regularly, and daily assessments were conducted to check for mortality, behavioural changes, alterations in physical appearance, signs of injury or pain, and any symptoms of illness.

4.3.3.2. Sub-acute toxicity

Swiss Albino mice, including both males and females, were utilized in a 45-day study and divided into four groups: normal, vehicle control, low dose (100 mg/kg body weight), and high dose (200 mg/kg body weight). Throughout the experimental period, food and water intake, as well as body weight, were monitored and recorded twice weekly. At the end of the study, the mice were fasted overnight before being sacrificed the next day.

Blood samples were collected via cardiac puncture for haematological analysis, and organs such as the liver, kidneys, lungs, intestines, heart, brain, and ovaries/testes were harvested to determine relative organ weights. The serum was separated by centrifuging the blood at 1500 rpm for ten minutes for subsequent biochemical analyses.

Haematological parameters, including total and differential leukocyte counts, were measured using whole blood, while haemoglobin levels were determined using Drabkin's method[80]. The activities of serum marker enzymes, including total and direct bilirubin, serum glutamate oxaloacetate transaminase (SGOT), serum glutamate pyruvate transaminase (SGPT), and alkaline phosphatase (ALP), were measured using commercial kits from Span Diagnostics Ltd (Surat, India). Kidney function was assessed by measuring serum creatinine and urea levels, using kits from Span Diagnostics.

Histological Analysis: Samples of the liver, kidneys, lungs, intestines, heart, brain, and ovaries/testes from each group were collected, rinsed in PBS, and fixed in 10% neutral buffered formaldehyde. These samples were then embedded in paraffin wax. Sections approximately 5-6 microns thick were prepared and stained using the haematoxylin and eosin double staining method. The slides were examined and photographed at 400x magnification.

This histological analysis is essential for examining the microscopic characteristics of various tissues and organs. It plays a vital role in research, pathology, and medical diagnostics by helping to identify normal and pathological conditions. The resulting photomicrographs can be further analysed to evaluate the health and attributes of the tissues under study[81].

4.3.3.3. Anti-tumour Studies

Cell lines: Dalton's Lymphoma Ascites (DLA) cell lines were maintained as ascitic tumours in Swiss albino mice. The cells were harvested and washed three times with 0.1 M phosphate-buffered saline (PBS) in a volume of 3 mL. To prepare a cell suspension with a concentration of 1 million cells per millilitre, the cells were resuspended in saline. One millilitre of this cell suspension was then injected into the peritoneal cavity of fresh Swiss albino mice. The test animals were kept on a standard diet, and within 10 to 14 days, ascitic fluid containing cancer cells accumulated in their abdomens. These cells were frequently transferred to other healthy mice to sustain the cell lines.

Preparation of drug suspension: For the animal studies, a drug suspension was prepared using carboxymethyl cellulose (CMC) sourced from Sigma-Aldrich in Bangalore. The CMC suspension was made by dissolving 0.05 g of CMC in 10 ml of distilled water. To prepare the drug solution, 0.01 g of 1,7-bis(5-chloro-2-

hydroxyphenyl) hepta-1,6-diene-3,5-dione was dissolved in the minimal amount of the CMC solution.

For the standard drug cyclophosphamide, a solution was prepared by dissolving 25 mg per kilogram of the body weight of the mice in the minimal amount of 0.1 M phosphate-buffered saline (PBS). Each mouse received an administration of 0.01 ml of this cyclophosphamide solution daily for ten days.

Determination of the effect of the compound on solid tumour development: DLA cells were subcutaneously injected into the right hind limbs of Swiss Albino mice, which were divided into groups of five. This procedure resulted in the formation of solid tumours. The control group did not receive any treatment, while the standard group was administered the standard drug cyclophosphamide. Other groups were given intraperitoneal injections of the test substances at a dosage of 200 µg/kg body weight for 10 days. The tumour volume was calculated using the formula $V=4/3\Pi\ r_1^2 r_2$, where r_1 and r_2 are the tumour radii. Tumour diameter was measured every third day for a month[82].

Upon completion of the experiments, euthanasia will be performed following the American Veterinary Medical Association (AVMA) Guidelines, using a CO_2 chamber[83].The CO_2 will be carefully regulated and purified to eliminate contaminants. Rodents will be euthanized with a CO_2 displacement rate between 30-70% of the chamber volume per minute, with the gas flow maintained for at least one minute after respiratory arrest. Carcasses will then be disposed of by incineration by proper guidelines and regulatory standards. These procedures are designed to ensure animal welfare, uphold ethical standards, and comply with established protocols.

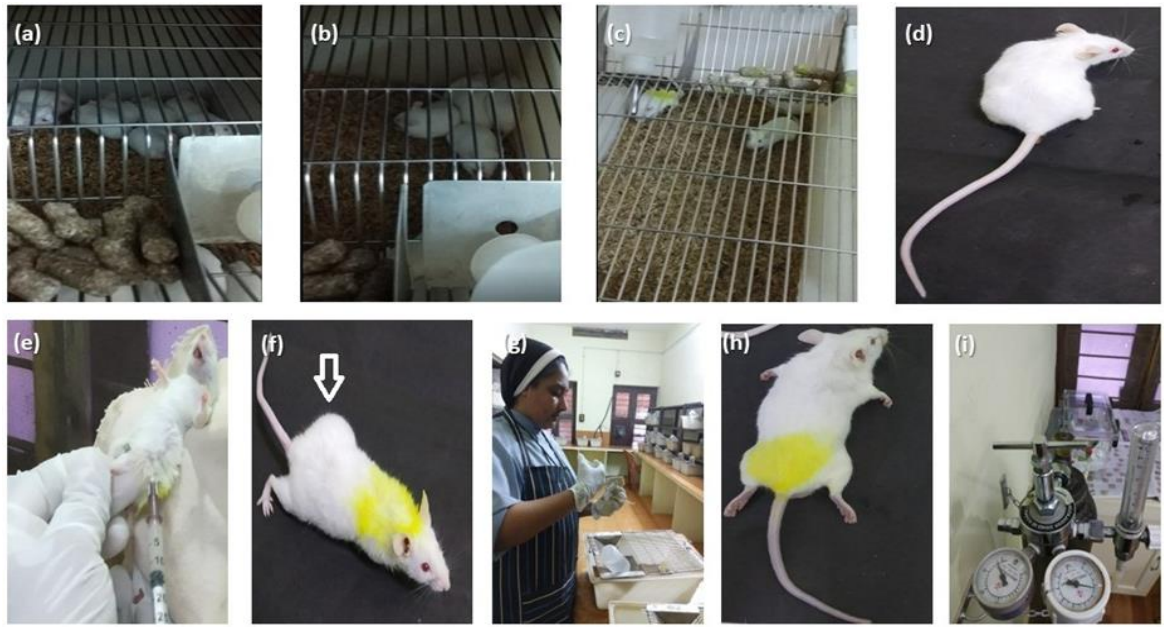

Fig.4.1. *In vivo* Anti-tumour studies of curcumin analogues(a)Swiss albino mice, 7-8 weeks old, weighing 25–30 g accommodated in the animal home of the Amala Cancer Research Centre in well-ventilated cages with standard levels of humidity and temperature for Acute Toxic studies (b) Swiss albino mice grouped and accommodated for Sub Acute Toxic Studies (c) Swiss albino mice grouped and accommodated for Anti-tumour studies (d) Swiss Albino Mice without tumour (e) DLA cells were subcutaneously injected into the limbs of Swiss Albino mice (f) Swiss Albino Mice carrying tumour (g) Intraperitoneal injections of the test substance, at a dose of 200 µg/kg body weight were administered to the Tumour carrying Swiss Albino mice (h) After treatment the Swiss albino mice (i) Euthanasia, CO_2 chamber. CO_2 is supplied in a precisely regulated and purified form without contaminants and adulterants.

Statistical analysis: The experimental data in this study were presented as mean standard deviation (SD). Statistical comparisons and analyses were performed using a one-way analysis of variance (ANOVA) followed by Bartlett's test, utilizing GraphPad Prism (version 9.0) software[84].

4.4. RESULTS AND DISCUSSION

Six key proteins encoded by the BRCA1 and TP53 genes, which harbour germline mutations that influence breast cancer risk, were chosen as molecular targets from a network analysis conducted using the STRING database. These proteins are:

BRCA1 BRCT domains (PDB:4Y2G; TG1)
BRCA1/BARD1 RING-domain heterodimer (PDB:1JM7; TG2)
BRCT-c domain of human BRCA1 (PDB:1OQA; TG3)
Hypothetical protein yxeF (PDB:2JOZ; TG4)
p300 Taz2-p53 TAD1 binding domain (PDB:2K8F; TG5)
p53 transactivation domain 2 (PDB:2RUK; TG6)

Among these, the BARD1 protein, which binds with the tumour suppressor BRCA1, was particularly notable. Numerous cancer-predisposing mutations found in the BRCA1 RING domain underscored the crucial role of the normal function of this domain. The structural diversity of complexes formed by various RING domain interactions was illustrated by comparing them to the RING homodimer of the V(D)J recombination-activating protein RAG1. The BRCA1-BARD1 structure provided a framework for understanding cancer-causing mutations at the molecular level, revealed potential interactions of the BRCA1 RING domain with multiple protein partners, and modelled its ubiquitin ligase activity. Thus, the heterodimer formed by the RING domains of BRCA1 and BARD1 represented a promising target.

The additional proteins that were selected exhibited substantial involvement in various biochemical pathways and mechanisms pertinent to the progression of cancer, as discerned through an extensive search of the STRING database. Interaction models that incorporated curcumin along with the selected molecular targets, as well as the FDA-sanctioned pharmaceutical cyclophosphamide and cyclophilin (PDB: 1XQ7; TG7), were systematically chosen to facilitate a comparative analysis of the most effectively docked complexes of the lead compounds. Curcumin analogues characterized by hydroxy, alkoxy, and chloro functional groups were meticulously designed, optimized, and subsequently transformed into pdb format utilizing Chem Draw, Gaussian 6, and Open Babel software, respectively.

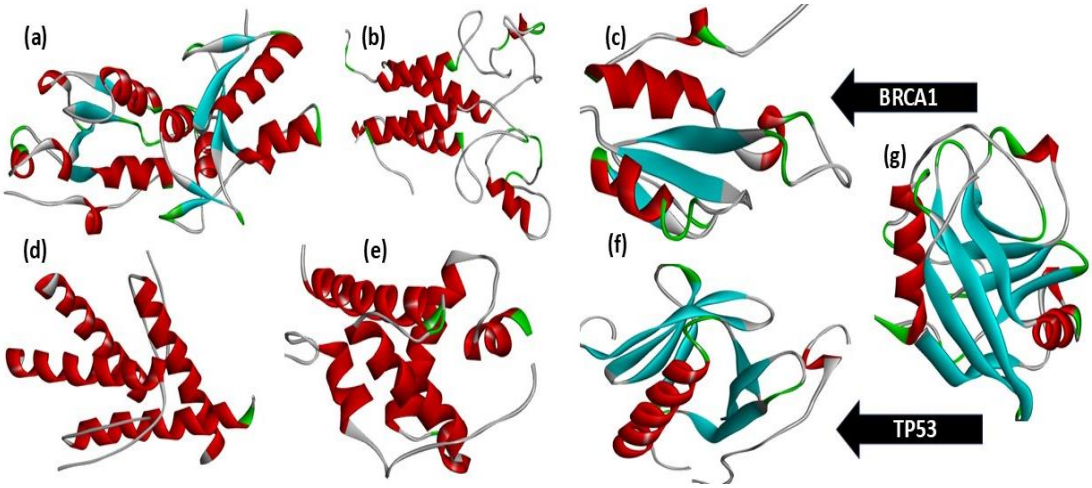

Fig.4.2. Six key proteins encoded by the BRCA1(a,b,c) and TP53 (d,e,f) genes and also the Target protein of the FDA-approved drug cyclophosphamide (cyclophilin A). (a)BRCA1 BRCT domains (PDB:4Y2G; TG1) (b)BRCA1/BARD1 RING-domain heterodimer (PDB:1JM7; TG2) (c)BRCT-c domain of human BRCA1 (PDB:1OQA; TG3) (d)Hypothetical protein yxeF (PDB:2JOZ; TG4) (e)p300 Taz2-p53 TAD1 binding domain (PDB:2K8F; TG5) (f)p53 transactivation domain 2 (PDB:2RUK; TG6) (g) cyclophilin A (PDB:1XQ7; TG7)

4.4.1. *In silico* studies

4.4.1.1. Computational screening of designed molecules

The drug-likeness of nine curcumin analogues —NLB, NLD, NLE, NLF, NLG, NLH, NLI, NLJ, and NLK—was assessed through virtual screening using various filters and statistical models available on Pre ADMET and Swiss ADME. Computational screening revealed that all nine molecules fulfilled the criteria for the CMC-like rule and the Rule of Five. These molecules were further evaluated for drug-likeness, ADME (absorption, distribution, metabolism, and excretion), and toxicity filters. All the compounds successfully passed these evaluations and were selected as lead molecules as shown in **Table 2.2, 2.3.**

4.4.1.2. Molecular docking studies

Molecular docking was used to predict the binding strength of certain curcumin analogues (NLB, NLD, NLE, NLF, NLG, NLH, NLI, NLJ, and NLK) to six molecular targets associated with breast cancer (TG1, TG2, TG3, TG4, TG5, TG6). The docking process was applied to analyse the interaction patterns of curcumin, a reference compound, with these targets, as well as the interaction of cyclophosphamide with its confirmed substrate. Various docking parameters were considered, including active site analysis, binding energy, ligand efficiency energy, inhibition constant, intermediate energy Vander Waals dissociation energy, torsional energy, unbound energy, and reference RMS values. The resulting conformations were evaluated based on binding energy, hydrogen bond count, and other stabilizing interactions. The primary types of intermolecular interactions observed between the nine analogues and the six target proteins included hydrogen bonding, hydrophobic interactions, and Van der Waals forces. The predicted binding potentials of the studied molecules to the prioritized breast cancer targets are summarized in **Table 4.2.**

Table 4.2. The predicted binding potentials of the nine synthesised curcumin analogues and reference compounds (curcumin and cyclophosphamide) to the prioritized breast cancer targets.

Active Target	Compounds	Active Site and Run	BE (kcal/mol)	Ligand efficiency	Inhibition constant (nM)	Intermolar energy	vdwhbdisolv energy*	Electrostatic energy	Total internal energy	Torsional energy	Unbound energy	clRMS**	refRMS***
4Y2G (TG1)	**Cyclophosphamide**	2	-4.62	-0.33	413.65	-6.11	-5.88	-0.23	-0.76	1.49	-0.76	0	20.82
	NLB	10	-6.68	-0.23	12.6	-9.67	-9.3	-0.37	-1.72	2.98	-1.72	0	36.63
	NLD	2	-6.42	-0.24	19.6	-8.81	-8.7	-0.11	-1.15	2.23	-1.15	0	40.69
	NLE	9	-7.9	-0.24	1.63	-10.28	-10.03	-0.25	-1.46	2.39	-1.46	0	34.21
	NLF	9	-6.49	-6.49	17.6	-10.07	-9.69	-0.37	-3.18	3.58	-3.18	0	29.65
	NLG	6	-6.94	-0.26	8.19	-9.33	-8.98	-0.35	-1.27	2.39	-1.27	0	37.07
	NLH	2	-7.31	-0.29	4.37	-9.7	-9.09	-0.61	-0.74	2.39	-0.74	0	37.55
	NLI	9	-5.34	-0.2	122.62	-8.32	-8.22	-0.1	-3.04	2.98	-3.04	0	28.85
	NLJ	3	-6.89	-0.26	8.9	-9.87	-9.34	-0.53	-1.99	2.98	-1.99	0	27.34
	NLK	10	-7.14	-0.34	5.84	-8.93	-8.58	-0.35	-0.98	1.79	-0.98	0	52.74
	CURCUMIN	9	-6.11	-0.23	33.1	-9.69	-9.34	-0.35	-1.71	3.58	-1.71	0	25.5
1JM7 (TG2)	**Cyclophosphamide**	3	-5.16	-0.37	164.54	-6.65	-6.55	-0.11	-0.8	1.49	-0.8	0	13.45
	NLB	2	-7.82	-0.27	1.85	-10.8	-10.39	-0.41	-1.79	2.98	-1.79	0	7.46
	NLD	6	-8.09	-0.3	1.17	-10.48	-10.42	-0.06	-1.28	2.39	-1.28	0	8.2
	NLE	2	-8.36	-0.25	742.01	-10.75	-10.53	-0.22	-1.26	2.39	-1.26	0	8.82
	NLF	5	-6.59	-0.23	14.74	-10.17	-10.01	-0.16	-3.28	3.58	-3.28	0	7.14
	NLG	2	-8.2	-0.3	983.95	-10.58	-10.3	-0.28	-1.29	2.39	-1.29	0	7.4

	Compounds	Active Site and Run	BE (kcal/mol)	Ligand efficiency	Inhibition constant (nM)	Intermolar energy	vdwhbdisolv energy*	Electrostatic energy	Total internal energy	Torsional energy	Unbound energy	clRMS**	refRMS***
	NLH	5	-7.74	-0.31	2.11	-10.13	-9.98	-0.15	-0.52	2.39	-0.52	0	8.77
	NLI	2	-6.85	-0.25	9.48	-9.84	-9.79	-0.04	-3.04	2.98	-3.04	0	12.47
	NLJ	3	-7.25	-0.27	4.88	-10.23	-9.93	-0.29	-2.88	2.98	-2.88	0	7.4
	NLK	3	-7.44	-0.35	3.51	-9.23	-9.16	-0.07	-1.28	1.79	-1.28	0	10.01
	CURCUMIN	10	-5.7	-0.22	42.27	-9.55	-8.87	-0.68	-1.8	3.58	-1.8	0	8.16
1OQA (TG3)	**Cyclophosphamide**	2	-4.28	-0.31	732.01	-5.77	-5.57	-0.19	-0.84	1.49	-0.84	1.38	18.17
	NLB	3	-7.19	-0.25	5.34	-10.18	-10.1	-0.08	-1.74	2.98	-1.74	0	10.93
	NLD	3	-7.78	-0.29	1.97	-10.17	-9.92	-0.25	-0.86	2.39	-0.86	0	12.58
	NLE	10	-8.64	-0.26	462.73	-11.03	-10.93	-0.1	-0.93	2.39	-0.93	0	6.83
	NLF	3	-6.89	-0.24	8.85	-10.47	-10.35	-0.12	-2.69	3.58	-2.69	0	8.28
	NLG	10	-7.08	-0.26	6.44	-9.47	-9.22	-0.25	-1.2	2.39	-1.2	0	10.68
	NLH	4	-8.3	-0.32	1.59	-10.3	-10.18	-0.11	-1.31	2.39	-1.31	0	12.93
	NLI	8	-7.19	-0.27	5.34	-10.18	-10.01	-0.16	-2.72	2.98	-2.72	0	10.91
	NLJ	6	-6.68	-0.25	9.37	-9.84	-9.74	-0.11	-2.23	2.98	-2.23	0	11.54
	NLK	3	-7.77	-0.37	2.03	-9.56	-9.43	-0.12	-0.74	1.79	-0.74	0	12.24
	CURCUMIN	2	-6.19	-0.26	7.54	-10.57	-10.51	-0.06	-1.9	3.58	-1.9	0	7.66
	Cyclophosphamide	1	-3.68	0.26	2	-5.17	-5.1	-0.07	-0.68	1.49	-0.68	0	5.31
	NLB	1	-7.52	-0.26	3.06	-10.51	-10.33	-0.18	-1.71	2.98	-1.71	0	11.76

	Compounds	Active Site and Run	BE (kcal/mol)	Ligand efficiency	Inhibition constant (nM)	Intermolar energy	vdwhbdisolv energy*	Electrostatic energy	Total internal energy	Torsional energy	Unbound energy	clRMS**	refRMS***
2JOZ (TG4)	**NLD**	6	-8	-0.3	1.37	-10.39	-10.3	-0.08	-1.29	2.39	-1.29	0	12.58
	NLE	9	-7.37	-0.22	3.95	-9.76	-9.76	-9.75	-1.6	2.39	-1.6	0	6.48
	NLF	9	-6.15	-0.21	30.93	-9.73	-9.65	-0.08	-3.01	3.58	-3.01	0	15.04
	NLG	9	-7.11	-0.26	6.17	-9.49	-9.38	-0.11	-1.13	2.39	-1.13	0	13.82
	NLH	2	-7.32	-0.26	4.29	-9.71	-9.57	-0.14	-1.13	2.39	-1.13	0	12.53
	NLI	1	-5.34	-0.2	121.32	-8.33	-8.26	0.07	-3.11	2.98	-3.11	0	8.39
	NLJ	1	-6.4	-0.24	20.45	-9.38	-9.21	-0.17	-2.81	2.98	-2.81	0	12.23
	NLK	9	-7.03	-0.33	7.08	-8.82	-8.79	-0.03	-1.08	1.79	-1.08	0	7.87
	CURCUMIN	10	-5.28	-0.2	134.79	-8.86	-8.76	-0.1	-2.43	3.58	-2.43	0	6.67
2K8F (TG5)	**Cyclophosphamide**	3	-3.18	-0.23	4.66	-4.67	-4.63	-0.04	-0.89	1.49	-0.89	0	19.16
	NLB	4	-5.92	-0.2	45.56	-8.91	-8.85	-0.05	-1.39	2.98	-1.39	0	10.43
	NLD	9	-7.16	-0.27	5.62	-9.55	-9.38	0.17	-1.36	2.39	-1.36	0	14.36
	NLE	7	-7.2	-0.22	5.27	-9.59	-9.5	-0.08	-1.38	2.39	-1.38	0	13.73
	NLF	10	-5.99	-0.21	40.34	-9.57	-9.45	-0.13	-2.68	3.58	-2.68	0	13.58
	NLG	9	-6.49	-0.24	17.5	-8.88	-8.8	-0.07	-1.28	2.39	-1.28	0	9.26
	NLH	6	-6.92	-0.28	8.43	-9.31	-9.25	-0.05	-1.3	2.39	-1.3	0	9.51
	NLI	10	-6.13	-0.23	32.03	-9.11	-9.07	-0.04	-2.92	2.98	-2.92	0	12.44
	NLJ	6	-5.32	-0.2	126.79	-8.3	-8.24	-0.06	-2.39	2.98	-0.06	0	13.82

	Compounds	Active Site and Run	BE (kcal/mol)	Ligand efficiency	Inhibition constant (nM)	Intermolar energy	vdwhbdisolv energy*	Electrostatic energy	Total internal energy	Torsional energy	Unbound energy	clRMS**	refRMS***
	NLK	1	-6.07	-0.29	35.46	-7.86	-7.74	-0.12	-0.72	1.79	-0.72	0	16.56
	CURCUMIN	1	-3.42	-0.13	3.09	-7	-6.93	-0.08	-2.33	3.58	-2.33	0	12.31
2RUK (TG6)	**Cyclophosphamide**	2	-3.68	-0.26	2.02	-5.17	-5.11	-0.06	-0.79	1.49	-0.79	0	6.19
	NLB	8	-5.84	-0.2	52.68	-8.82	-8.73	-0.09	-1.84	2.98	-1.84	0	9.47
	NLD	2	-5.48	-0.2	95.82	-7.87	-7.72	-0.15	-1.48	2.39	-1.48	0	11.38
	NLE	10	-7.38	-0.22	3.9	-9.77	-9.6	-0.17	-1.45	2.39	-1.45	0	8.99
	NLF	2	-5.55	-0.19	85.07	-9.13	-9.18	0.05	-3.22	3.58	-3.22	0	10.39
	NLG	3	-6.23	-0.23	27.32	-8.61	-8.53	-0.08	-0.81	2.39	-0.81	0	10
	NLH	4	-5.38	-0.22	113.8	-7.77	-7.42	-0.35	-0.76	2.39	-0.76	0	8.93
	NLI	10	-5.9	-0.22	47.63	-8.88	-8.83	-0.05	-2.56	2.98	-2.56	0	9.51
	NLJ	10	-5.77	-0.21	59.36	-8.75	-8.59	-0.15	-2.9	2.98	-2.9	0	9.58
	NLK	6	-6.02	-0.29	38.94	-7.81	-7.75	-0.05	-1.18	1.79	-1.18	0	8.27
	CURCUMIN	1	-5.48	-0.2	96.7	-9.06	-8.97	-0.08	-1.45	3.58	-1.45	0	9.93
1XQ7 (TG7)	**Cyclophosphamide**	3	-3.8	-0.34	354.65	-6.2	-5.89	-0.31	-0.58	1.49	-0.58	0	50.3
	NLH8	2	-6.3	-0.31	1.83	-10.21	-9.74	-0.48	-1.31	2.39	-1.31	0	73.69
	CURCUMIN	7	-5.33	-0.2	123.24	-8.91	-8.62	0.29	-3.1	3.58	-3.1	0	46.02

*vdwhbdisolv energy: Van der Waals, Hydrogen Bonding, Desolvation Energy **clRMS: Cluster Root Mean Square Deviation

***refRMS: Reference Root Mean Square Deviation

In order to perform a comprehensive assessment of the efficacy of nine ligands (NLB, NLD, NLE, NLF, NLG, NLH, NLI, NLJ, and NLK), the present study undertook a meticulous analysis predicated upon Binding Energy (BE), Inhibition Constant (Ki), ancillary parameters, and interaction profiles across six targets, specifically TG1, TG2, TG3, TG4, TG5, and TG6, relevant to breast cancer. These ligands were compared to two reference compounds, cyclophosphamide and curcumin, to assess their efficacy and potential as therapeutic agents.

NLH emerged as the most preferable ligand, exhibiting consistently low BE and Ki values across all targets. It demonstrated remarkable binding affinity and potency, making it a promising candidate for further investigation. Following NLH, NLI showcased similar BE and Ki values, although with slightly fewer interactions. NLD displays the lowest BE values for some targets but higher interactions compared to NLI. NLB and NLF exhibited moderate BE and Ki values, with NLB displaying a higher number of interactions. NLE, NLG, NLJ, and NLK showed varying degrees of BE and Ki values, with NLK generally performing the least favourably among the ligands.

In comparison to the reference compounds, both cyclophosphamide and curcumin displayed higher BE and Ki values, indicating lower binding affinity and potency. Moreover, they exhibited fewer interactions, suggesting less specificity in target binding compared to the newly tested ligands. NLH, NLD, and NLI outperformed both cyclophosphamide and curcumin across most evaluation criteria, highlighting their potential as superior therapeutic agents.

In short, NLH emerged as the most promising ligand among the tested compounds, followed closely by NLD and NLI. These ligands displayed strong binding affinity, high potency, and diverse interaction profiles, making them attractive candidates for further preclinical and clinical investigations. The comparative analysis underscores the significance of exploring novel ligands for drug development, with the potential to outperform existing therapeutics in terms of efficacy and specificity.

A detailed depiction of the interactions of each ligand with the corresponding target molecules through the various amino acid residues is shown in **Fig. 4.3 to 4.9** and **Tables 4.3 to 4.8.**

The compounds engaged in multiple types of interactions with the target protein, with Van der Waals interactions being the most prevalent, suggesting extensive surface contact. Conventional hydrogen bonds indicated strong, specific binding. The presence of a diverse range of interaction types, including Pi Sigma, Pi Alkyl, Pi lone pair, Pi Pi stacked, Alkyl, Pi Anion, Pi Pi T shaped, unfavourable bump, Pi Cation, Pi Carbon, Pi

Sulfur, Attractive Charge, Amide-Pi stacked, Sulfur-X, and Pi-Donor interactions, added to the complexity and stability of the binding. The specific amino acid residues involved in these interactions highlighted key points of contact and potential sites for further modification to enhance binding affinity and specificity. This comprehensive interaction profile highlights the therapeutic potential of each compound, emphasizing the need for further investigation and optimization.

The stability of NLH when interacting with the target protein TG3 in breast cancer was explained by the types and strengths of various intermolecular interactions observed between the ligand and the protein's amino acid residues (**Fig.4.5**; **Table 4.5**). NLH formed seven Van der Waals interactions with the residues GLY A:72, PRO A:78, PRO A:103, ILE A:105, GLN A:104, PHE A:68, and HIS A:69. These weak, non specific forces occurred due to transient dipole moments when molecules were in close proximity, contributing to the overall stability of the NLH protein complex by ensuring the ligand was closely packed within the binding pocket, thereby reducing its conformational freedom and stabilizing the interaction. Three conventional hydrogen bonds were formed with the residues GLN A:73, ILE A:71, and ALA A:70. These hydrogen bonds were stronger than Van der Waals interactions and significantly contributed to the specificity and stability of the ligand-protein complex by anchoring NLH in the correct orientation and position within the binding site, enhancing the binding affinity and stability of the complex.

One carbon-hydrogen bond with ALA A:70, although weaker than conventional hydrogen bonds, provided additional stabilization by interacting with an electronegative atom. Furthermore, two Pi-alkyl interactions were observed with ILE A:102 and LEU A:101. These hydrophobic interactions occurred between the aromatic ring system of the ligand and alkyl groups of the protein residues, contributing to the stabilization of the ligand within the protein’s hydrophobic pockets and helping to lock the ligand in place, reducing its potential for dissociation. Thus, the stability of NLH, when bound to the target protein TG3, was achieved through a combination of these interactions: Van der Waals forces ensured a close fit within the binding site, conventional hydrogen bonds provided strong, specific anchoring, carbon-hydrogen bonds added stability, and Pi-alkyl interactions offered hydrophobic stabilization. The collective nature of these diverse interactions created a resilient and stable binding environment for NLH, strengthening its potential effectiveness as a therapeutic agent targeting TG3 in the treatment of breast cancer.

4Y2G (TG1) – Curcumin Analogue Complexes

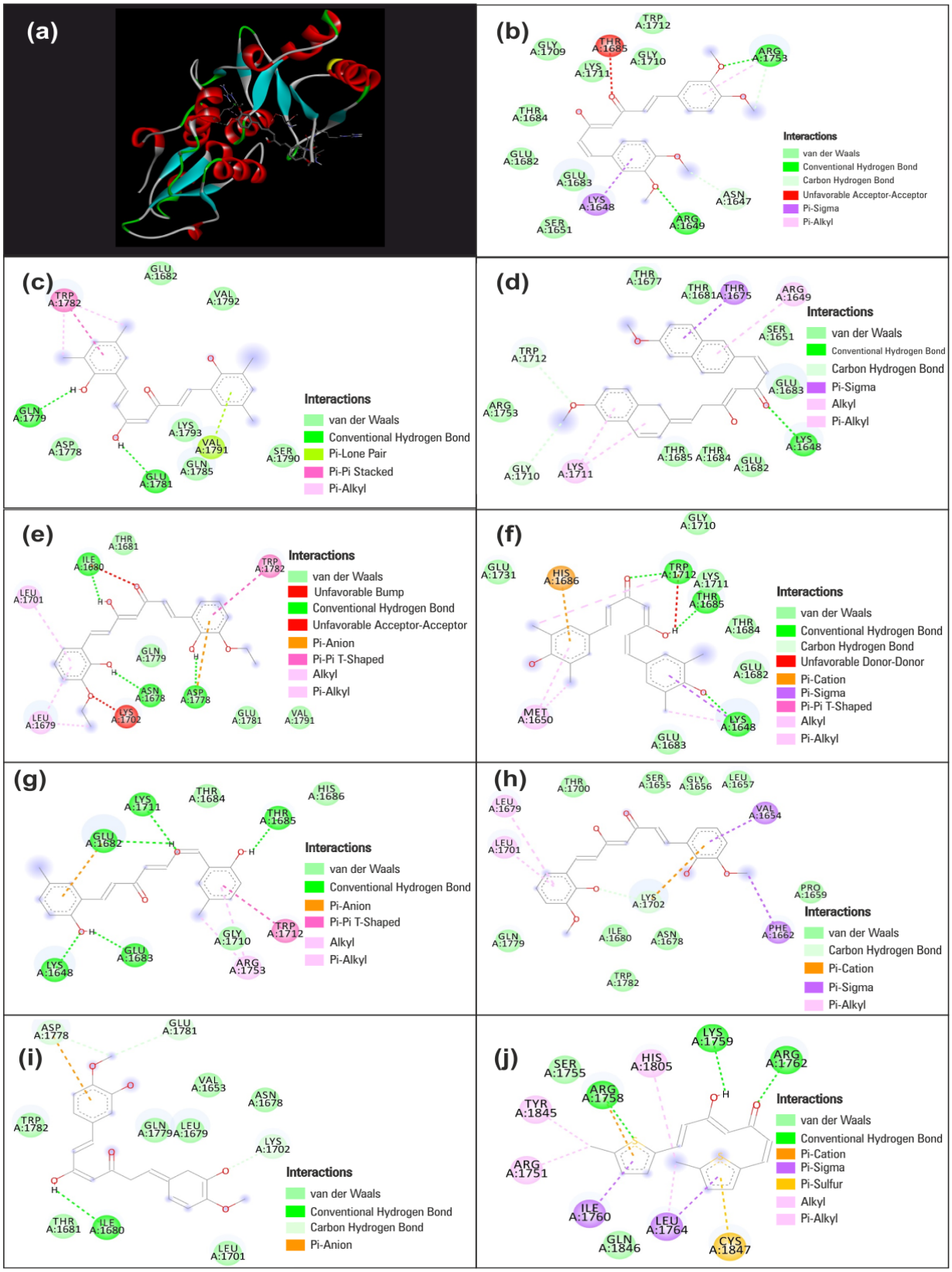

Fig.4.3 4Y2G – Curcumin Analogue Complexes (a) 4Y2G-NLB Complex(3D) (b) 4Y2G-NLB Complex(2D) (c) 4Y2G-NLD Complex(2D) (d) 4Y2G-NLE Complex(2D) (e) 4Y2G-NLF Complex(2D) (f) 4Y2G-NLG Complex(2D) (g) 4Y2G-NLH Complex(2D) (h) 4Y2G-NLI Complex(2D) (i) 4Y2G-NLJ Complex(2D) (j) 4Y2G-NLK Complex(2D)

Table 4.3 The interactions of ligands with 4Y2G(TG1)through various amino acid residues

Active Target	Compound		Types of Interactions																
			Van der Waals	Conventional Hydrogen Bond	Carbon Hydrogen Bond	Unfavourable Acceptor-Acceptor	Pi-Sigma	Pi-Alkyl	Pi-lone pair	Pi-Pi stacked	Alkyl	Pi-Anion	Pi-Pi T shaped	Unfavourable Bump	Unfavourable donor-donor	Pi-Cation	Pi-Carbon	Pi-Sulfur	Attractive Charge
4Y2G	NLB	No.of Interactions	8	2	1	1	1	1											
		Amino acid residues	GLY A:1709,LYS A:1711,TRP A:1712,GLY A:1710,THR A:1684,GLU A:1683,SER A:1651	ARG A:1753,ARG A:1649	ASN A:1647	THR A:1685	LYS A:1648	ARG A:1753											
	NLD	No.of Interactions	6	2				1	1	1									
		Amino acid residues	GLU A:1682,VAL A:1792,SER A:1790,LYS A:1793,GLN A:1785,ASP A:1778	GLN A:1779,GLU A:1781				TRP A:1782	VAL A:1791	TRP A:1782									
	NLE	No.of Interactions	8	1	1		1	1			1								
		Amino acid residues	THR A:1677,THR A:1681, SER A:1651,GLU A:1683,GLU A:1682,THRA :1684, THR A:1685, ARG A:1753	LYS A:1648	GLY A:1710		THR A:1675	LYS A:1711			ARG A:1649								
	NLF	No.of Interactions	2	3		2		2			1	1	1	1					
		Amino acid residues	THR A:1681, VAL A:1791	ILE A:1680,ASN A:1678,ASP A:17778		LYS A:1702		LEU A:1701,LEU A:1679			LEU A:1679	ASP A:1778	TRP A:1782	LYS A:1702					
	NLG	No.of Interactions	6	3	1		1	1			2				1	1			
		Amino acid residues	GLY A:1710,LYS A:1711,THR A:1684,GLU A:1682,GLU A:1683, GLU A:1731	TRP A:1712,THR A:1686,LYS A:1648	GLU A:1731		MET A:1650	MET A:1650			MET A:1650,TRP A:1712				TRP A:1712	HIS A:1686			
	NLH	No.of Interactions	3	5			2	1				1	2				1		
		Amino acid residues	THR A:1684,HIS A:1686,GLY A:1710	GLU A:1682,LYS A:1711,THR A:1685, GLU A:1683, LYS A:1648			VAL A:1654,PHE A:1662	ARG A:1753				GLU A:1682	TRP A:1712,ARG A:1753				LYS A:1702		
	NLI	No.of Interactions	9					2											
		Amino acid residues	THR A:1700,FER A:1685, GLY A:1656,LEU A:1657, PRO A:1659,ASN A:1678, ILE A:1680, TRP A:1782,GLN A:17779		LYS A:1702			LEU A:1679,LEU A:1701											
	NLJ	No.of Interactions	7	1	3							1						1	
		Amino acid residues	VAL A:1653,ASN A:1678,GLN A:1779,LEU A:1679,LEU A:1701, THR A:1681,TRP A:1782	ILE A:1680	LYS A:1702,ASP A:1778,GLU A:1781							ASP A:1778						CYS A:1847	
	NLK	No.of Interactions	2	3			1	1			2					1			
		Amino acid residues	SER A:1755,GLN A:1846	ARG A:1758, LYS A:1759, ARG A:1762			ILG A:1760,LEU A:1764	ARG A:1751			HIS A:1805,TYR A:1845					ARG A:1758			
	CURCUMIN	No.of Interactions	3	2	1											2			1
		Amino acid residues	THR A:1700,THR B:408,SER B:404	SER A:1655,GLY A:1656	VNK A:1											PRO B:407,ARG B:405			PRO B:407,ARG B:405

1JM7 (TG2) – Curcumin Analogue Complexes

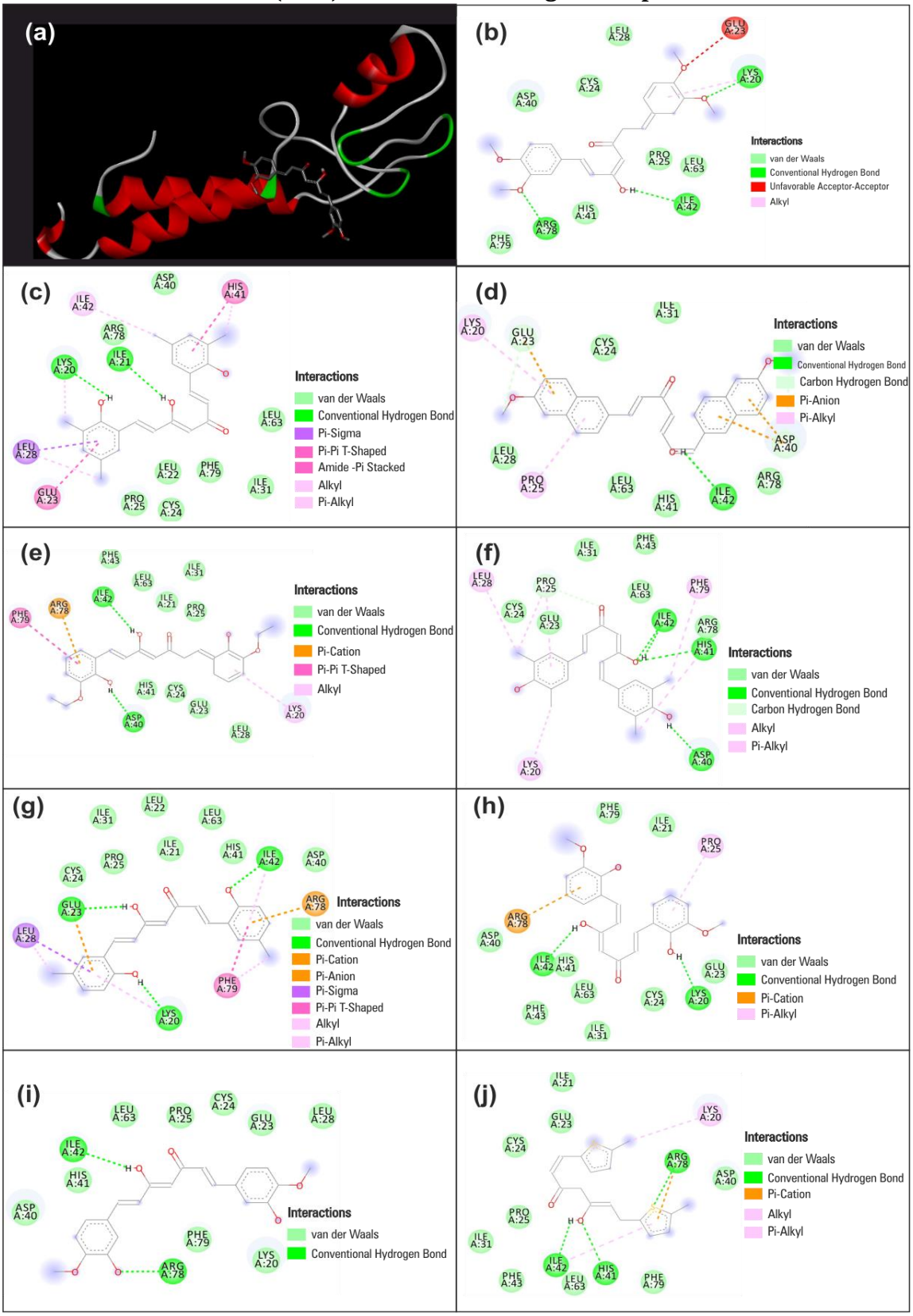

Fig.4.4 1JM7 – Curcumin Analogue Complexes (a) 1JM7-NLB Complex(3D) (b) 1JM7-NLB Complex(2D) (c) 1JM7-NLD Complex(2D) (d) 1JM7-NLE Complex(2D) (e) 1JM7-NLF Complex(2D) (f) 1JM7-NLG Complex(2D) (g) 1JM7-NLH Complex(2D) (h) 1JM7-NLI Complex(2D) (i) 1JM7-NLJ Complex(2D) (j) 1JM7-NLK Complex(2D)

Table 4.4 The interactions of ligands with 1JM7(TG2) through various amino acid residues

Active Target	Compound		Types of Interactions												
			Van der Waals	Conventional Hydrogen Bond	Carbon Hydrogen Bond	Unfavourable Acceptor-Acceptor	Pi-Sigma	Pi-Alkyl	Pi-lone pair	Pi-Pi stacked	Alkyl	Pi-Anion	Pi-Pi T shaped	Pi-Cation	Amide - Pi sacked
1JM7	NLB	No.of Interactions	7	2		1					1				
		Amino acid residues	LEU A:28,CYS A:24,ASP A:40,PRO A:25,LEV A:63,HIS A:41,PHE A:79	ILE A:42,ARG A:78		GLU A:23					LYS A:20				
	NLD	No.of Interactions	7	2			1			1	4				1
		Amino acid residues	ASP A:40,ARG A:78,LEU A:63,PHE A:79,ILE A:31,LEU A:22,PRO A:25	LYS A:20,ILE A:21			LEU A:28			HIS A:41	HIS A:41,ILE A:42,LYS A:20,LEU A:28				GLU A:23
	NLE	No.of Interactions	6	1	2			2				1			
		Amino acid residues	CYS A:24,ILE A:31,ARG A:78,HIS A:41,LEU A:63,LEU A:28	ILE A:42,ARG A:78	GLU A:23,ASP A:40			PRO A:25,LYS A:20				GLU A:23			
	NLF	No.of Interactions	9	1							1		1	1	
		Amino acid residues	PHE A:43,LEU A:63,ILG A:21,ILE A:31,PRO A:25,HIS A:41,CYS A:24,GLU A:23, LEU A:28	ASP A:40							LYS A:20		PHE A:79	ARG A:78	
	NLG	No.of Interactions	5	3	1			1			3				
		Amino acid residues	ILE A:31,PHE A:43,LEU A:63,ARG A:78,CYS A:24	ILE A:42,HIS A:41,ASP A:41	PRO A:25			HIS A:41			PHE A:79,LEU A:28,LYS A:20				
	NLH	No.of Interactions	8	3			1	2			2	1	1	1	
		Amino acid residues	ILE A:31,LEU A:22,ILE A:21,LEU A:63,HIS A:41,AP A:40,PRO A:25,LYS A:24	ILE A:42,GLU A:23,LYS A:20			LEU A:28	ILG A:42,LYS A:20			LEU A:28,PHE A:79	GLU A:23	PHE A:79	ARG A:78	
	NLI	No.of Interactions	9	2				1						1	
		Amino acid residues	PHE A:79,ILE A:21,GLU A:23,CYS A:24,ILE A:31,LEU A:63,JIS A:41,PHE A:43,ASP A:40	LYS A:20,ILE A:42				PRO A:25						ARG A:78	
	NLJ	No.of Interactions	9	2											
		Amino acid residues	LEU A:63,PRO A:25,CYS A:24,GLU A:23,LEU A:28,LYS A:20,PHE A:79,ASP A:40,HIS A:41	ILE A:42,ARG A:78											
	NLK	No.of Interactions	9	3				1			2			1	
		Amino acid residues	ILE A:21,GLU A:23,CYS A:24,ASP A:40,PHE A:79,LGU A:63,PHE A:43,ILC A:31,PRO A:25	ARG A:78,HAS A:41,ILE A:42				ILE A:42			LYS A:20			ARG A:78	
	CURCUMIN	No.of Interactions	6	3	1			1	1						
		Amino acid residues	PRO A:25,GLU A:23,LEU A:28, ILE A:21,LEU A:63,PHE A:79,ARG A:28	ILE A:42,HIS A:41,LYS A:290	CYS A:24			ILE A:42	LYS A:20						

1OQA (TG3) – Curcumin Analogue Complexes

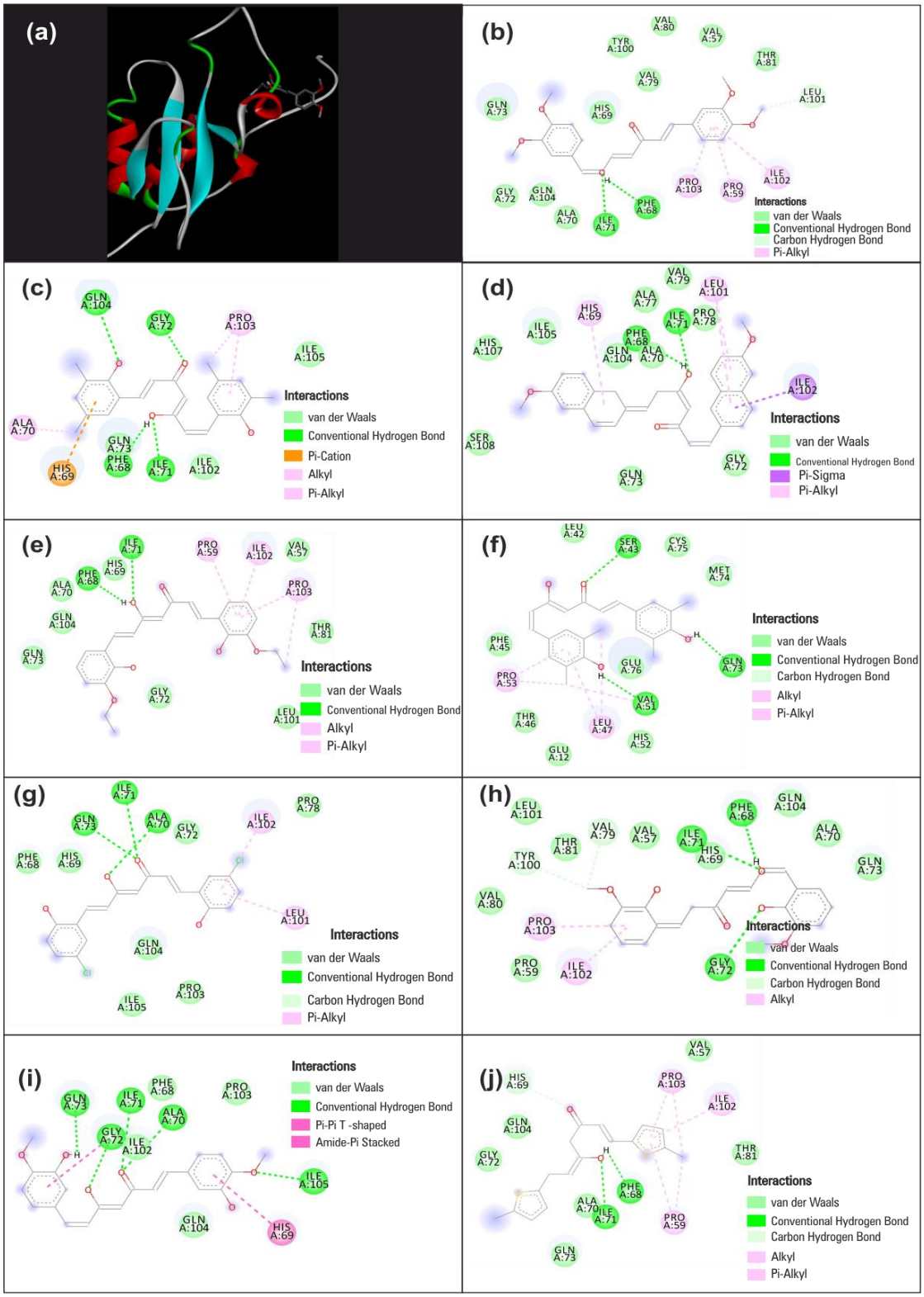

Fig.4.5 1OQA–Curcumin Analogue Complexes (a) 1OQA-NLB Complex(3D) (b) 1OQA-NLB Complex(2D) (c) 1OQA-NLD Complex(2D) (d) 1OQA-NLE Complex(2D) (e) 1OQA-NLF Complex(2D) (f) 1OQA-NLG Complex(2D) (g) 1OQ-NLH Complex(2D) (h) 1OQA -NLI Complex(2D) (i) 1OQA-NLJ Complex(2D) (j) 1OQA-NLK Complex(2D)

Table 4.5 The interactions of ligands with 1OQA through various amino acid residues

Active Target	Compound		Types of Interactions								
			Van der Waals	Conventional Hydrogen Bond	Carbon Hydrogen Bond	Pi-Sigma	Pi-Alkyl	Alkyl	Pi-Pi T shaped	Pi-Cation	Amide - Pi sacked
1OQA	NLB	No.of Interactions	10	2	1		3				
		Amino acid residues	GLN A:73,TYR A:100, VAL A:80,VAL A:79,VAL A:57,THR A:81,HIS A:69,ALA A:70,GLN A:104,GLY A:72	PHE A:68,ILE A:71	LEU A:101		ILE A:102,PRO A:59,PRO A:103				
	NLD	No.of Interactions	3	4			1	2		1	
		Amino acid residues	ILE A:105,ILE A:102,GLN A:73	GLN A:104, GLY A:72,PHE A:68,ILE A:71			PRO A:103	PRO A:103,ALA A:70		HIS A:69	
	NLE	No.of Interactions	9			1	2				
		Amino acid residues	VAL A:79,ALA A:77,GLN A:104,PRO A:78,GLY A:72,GLN A:73,SER A:108,HIS A:107,ILE A:105			ILE A:102	HIS A:69,LEU A:101				
	NLF	No.of Interactions	8	2			3	1			
		Amino acid residues	HIS A:69,VAL A:57,THR A:81,LEU A:101,GLY A:72,GLN A:73,GLN A104,ALA A:70	THE A:68,ILE A:71			PRO A:59,ILE A:102,PRO A:103	PRO A:5103			
	NLG	No.of Interactions	8	3			2	2			
		Amino acid residues	LEU A:42,CYS A:75,MET A:74,GLU A:76,HIS A:52,GLU A:12,THR A:46,PHE A:45	SER A:43,VAL A:51,GLN A:73			PRO A:53,LEU A:43	LEU A:43,PRO A:53			
	NLH	No.of Interactions	7	3	1		2				
		Amino acid residues	GLY A:72,PRO A:78,PRO A:103,ILE A:105, GLN A:104,PHE A:68,HIS A:69	GLN A:73,ILE A:71,ALA A70	ALA: A70		ILE A:102,LEU A:101				
	NLI	No.of Interactions	8	3	2			2			
		Amino acid residues	LEU A:101,THR A:81,VAL A:57,GLN A:104,ALA A:70,GLA A:73,PRO A:59,VAL A:80	ILE A:71,PHE A:68,GLY A:72	TYR A:100,VAL A:79			PRO A:103,ILE A:102			
	NLJ	No.of Interactions	4	5					1		1
		Amino acid residues	PKE A:68,PRO A:103,ILE A:102,GLN A:104	GLN A:73,GLY A:72,ILE A:71,ALA A:70,ILE A:105					HIS A:69		GLY A:72
	NLK	No.of Interactions	4	5	1		3	1			
		Amino acid residues	VAL A:57,THR A:81,ALA A:70,GLN A:73,GLY A:72,GLN A:104	HE A:68,ILE A:71	HIS A:69		PRO A:103,ILE A:102,PRO A:59	PRO A:103			
	CURCUMIN	No.of Interactions	6	3	1	1	2				
		Amino acid residues	HIS A:69,ALA A:70,GL A:73,VAL A:57,VAL A:79,VAL A:80,LEU A:101,THR A:81	TYR A:100,GLN A:104,GLY A:72	PRO A:103	ILE A:102	PRO A:59,ILE A:71				

2JOZ(TG4) – Curcumin Analogue Complexes

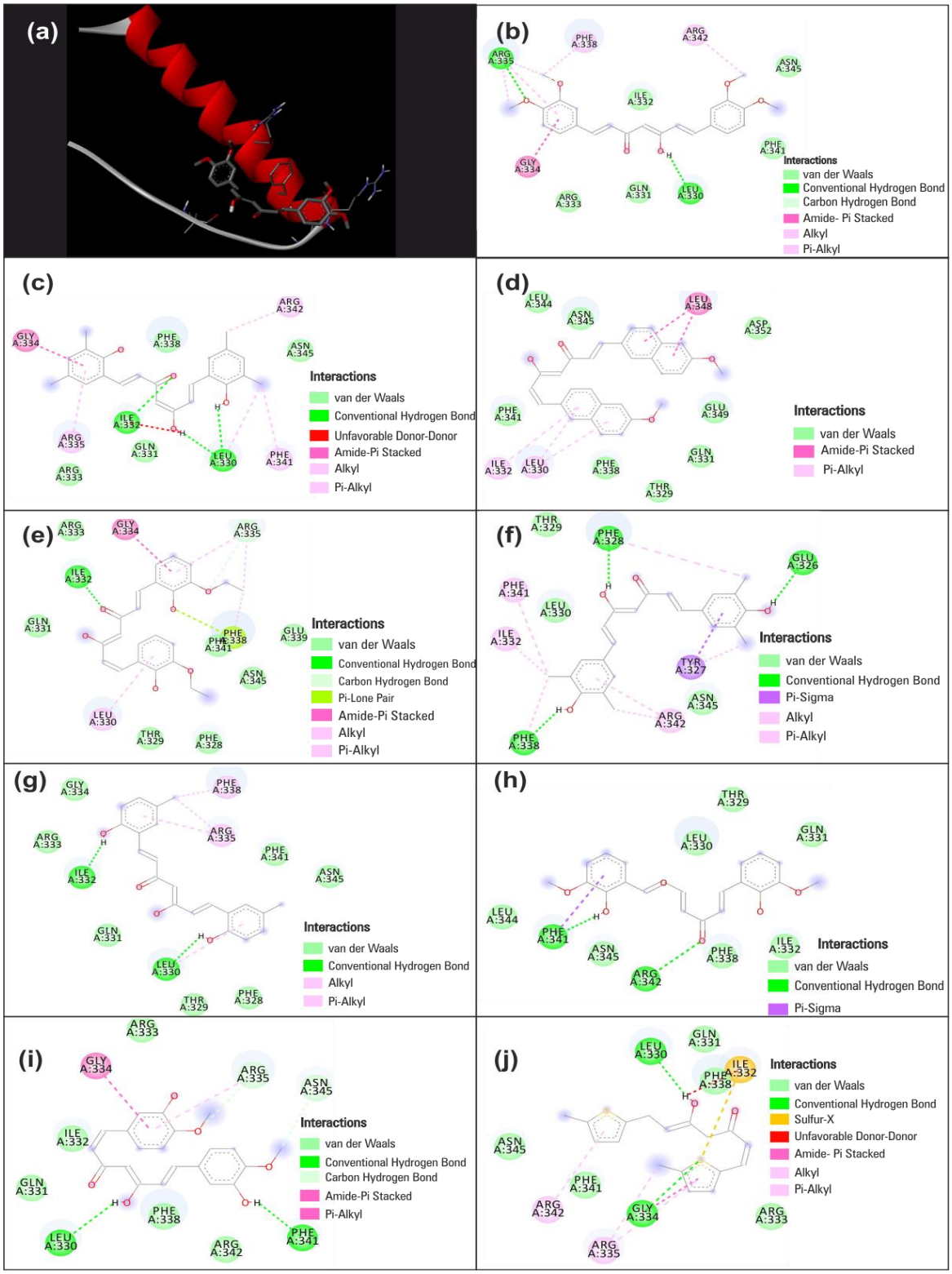

Fig.4.6.2 JOZ – Curcumin Analogue Complexes (a) 2JOZ-NLB Complex(3D) (b) 2JOZ-NLB Complex(2D) (c) 2JOZ-NLD Complex(2D) (d) 2JOZ-NLE Complex(2D) (e) 2JOZ -NLF Complex(2D) (f) 2JOZ-NLG Complex(2D) (g) 2JOZ-NLH Complex(2D) (h) 2JOZ -NLI Complex(2D) (i) 2JOZ-NLJ Complex(2D) (j) 2JOZ-NLK Complex(2D)

Table 4.6 The interactions of ligands with 2JOZ through various amino acid residues

Active Target	Compound		Types of Interactions										
			Van der Waals	Conventional Hydrogen Bond	Carbon Hydrogen Bond	Pi-Sigma	Pi-Alkyl	Pi-lone pair	Alkyl	Unfavourable donor-donor	Amide - Pi stacked	Sulfur - X	Pi-Donor Hydrogen Bond
2JOZ	NLB	No.of Interactions	5	2			1		1		1		
		Amino acid residues	ILE A:332,ASN A:345,PHE A:341,GLN A:331,ARG A:333	ARG A:335,LEU A:330			ARG A:335		PHE A:338,ARG A:342,ARG A:335		GLY A:334		
	NLD	No.of Interactions	4	2			1		1	1	1		
		Amino acid residues	PHE A:338,ASN A:345,GLN A:331,ARG A:333	ILE A:332,LEU A:330			ARG A:335		ARG A:342,PHE A:341,LEU A:330	ILE A:332	GLY A:332		
	NLE	No.of Interactions	8				2				1		
		Amino acid residues	LEU A:344,ASN A:345,ASP A:352,GLU A;349,GLN A:331,PHR A;329,PHE A:338,PHE A:341				ILE A:332,LEU A:330				LEU A:348		
	NLF	No.of Interactions	6	1	1		3	1	1		1		
		Amino acid residues	ARG A:333,GLU A:339,PHA A:341,ASN A:345,PHE A:328,PHR A:329	ILE A:332	ARG A:335		GLY A:334,LEU A:330,ARG A;335	PHE A:338	ARG A:335		GLY A:334		
	NLG	No.of Interactions	3	2		1	3		5				
		Amino acid residues	THR A;329,ASN A:345,LEU A:330	PHE A:3289,PHE A:338		PYR A:327	THE A:341,ILE A:332,ARG A:342		ARG A:342,PHE A:341,ILE A:332,PHE A:338,TYR A:327				
	NLH	No.of Interactions	7	2		1							
		Amino acid residues	THR A:329,LEU A:330,GLN A:331,ILE A:332,PHE A:338,ASN A:345,LEU A:344	PHE A:341,ARG A:342		PHE A:341							
	NLI	No.of Interactions	5	2		1							
		Amino acid residues	THR A:329,LEU A:330,GLN A:331,ILE A:332,PHE A:338,ASN A:345,LEU A:344	ARG A:342,PHE A:341		PHE A:341							
	NLJ	No.of Interactions	5	2	2		1				1		
		Amino acid residues	ARG A:333,ARG A:342,PHE A:338,GLN A:331,LE A:332	ARG A:335,ASN A:345	ARG A:335,ASN A:345		ARG A:335				GLY A:334		
	NLK	No.of Interactions	5	2			1		1	1	1	1	
		Amino acid residues	GLN A:331,PHE A:338,ARG A:333,PHE A:341,ASN A:345	LEU A:330,GLY A;334			ARG A:342,ARG A:335		ARG A:335	ILE A:332	GLY A:334	ILE A:332	
	CURCUMIN	No.of Interactions	6	2				1					1
		Amino acid residues	THR A:329,ASN A:345,PHE A;341,LEU A:344,PHE A:33,GLN A:331	ARG A:342,ILE A:332				LEU A:330					ILE A:332

2K8F(TG5) – Curcumin Analogue Complexes

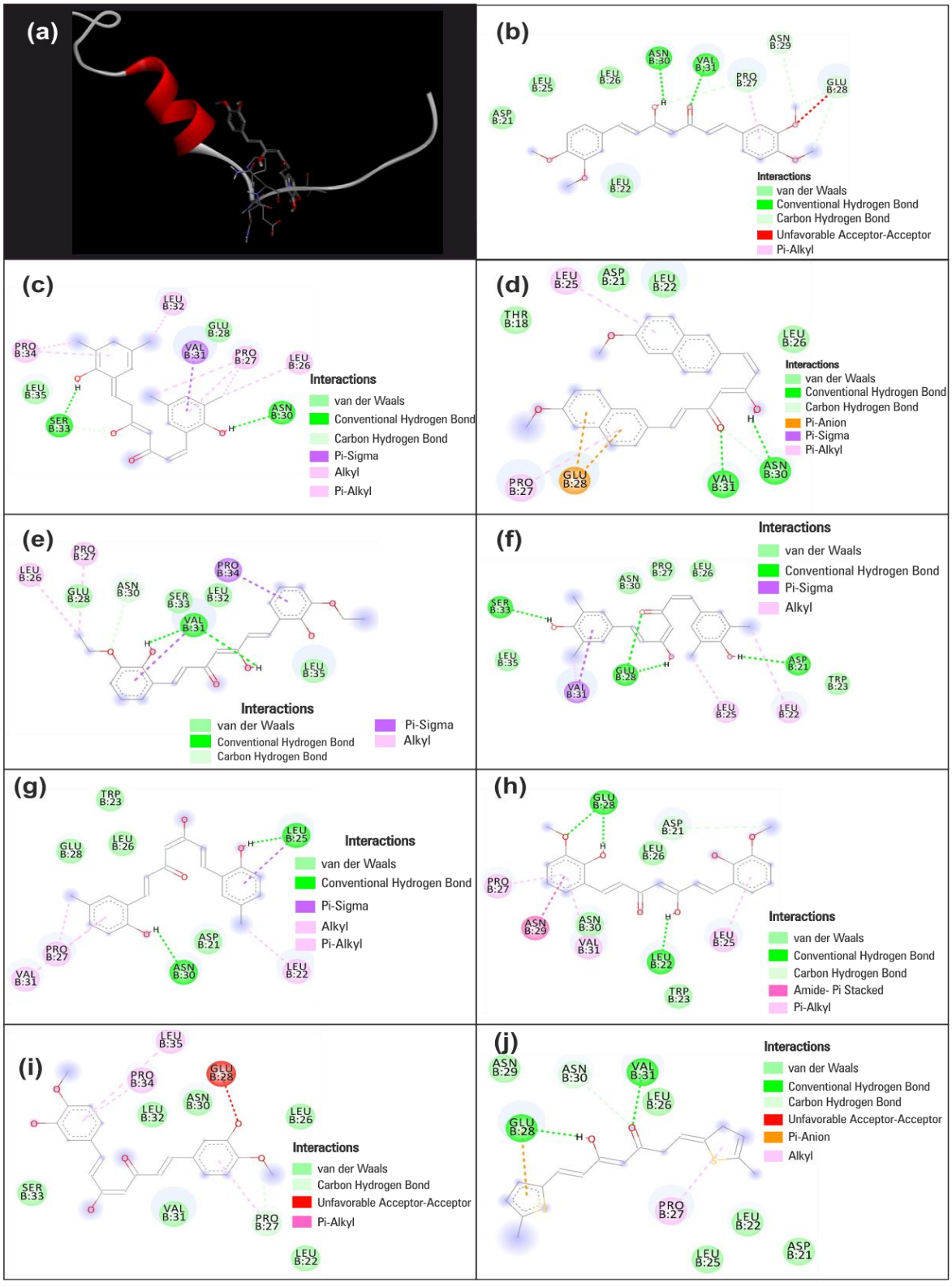

Fig.4.7.2 K8F – Curcumin Analogue Complexes (a) 2K8-NLB Complex(3D) (b) 2K8F-NLB Complex(2D) (c) 2K8F-NLD Complex(2D) (d) 2K8F-NLE Complex(2D) (e) 2K8F-NLF Complex(2D) (f) 2K8F-NLG Complex(2D) (g) 2K8F-NLH Complex(2D) (h) 2K8F-NLI Complex(2D) (i) 2K8F-NLJ Complex(2D) (j) 2K8F-NLK Complex(2D)

Table 4.7 The interactions of ligands with 2K8F through various amino acid residues

Active Target	Compound		Types of Interactions								
			Van der Waals	Conventional Hydrogen Bond	Carbon Hydrogen Bond	Unfavourable Acceptor-Acceptor	Pi-Sigma	Pi-Alkyl	Alkyl	Pi-Anion	Amide - Pi stacked
2K8F	NLB	No.of Interactions	4	2	3	1		1			
		Amino acid residues	LEU B:25,ASP B:21,LEU B:26,LEU B:22	ASN B:30,VAL B:31	PRO B:27,ASN B:29,GLU B:28	GLU B:28		PRO B:27			
	NLD	No.of Interactions	2	2	1		1	2	4		
		Amino acid residues	GLU B:28,LEU B:35	ASN B:30,SER B:33	SER B:33		VAL B:31	PRO B:27,PRO B:34	PRO B:34,PRO B:27,LEU B:26,LEU B:32		
	NLE	No.of Interactions	4	2	1			2		1	
		Amino acid residues	ASPB:2,LEU B:22,LEU B;26,THR B:18	ASN B:30,VAL B:31	ASN B:30			PRO B:27,LEU B:25		GLU B:28	
	NLF	No.of Interactions	4	1	1		1		2		
		Amino acid residues	SER B:33,LEU B:32,LEU B:35,GLU B:28	VAL B:31	ASN B:30		PRO B:34		LEU B:26,PRO B:27		
	NLG	No.of Interactions	5	3			1		2		
		Amino acid residues	ASN B:30,PRO B:27,LEU B:26,TRP B:23,LEU B:35	GLU B:28,ASP B:21, SER B:33			VAL B:31		LEU B:25,LEU B:22		
	NLH	No.of Interactions	4	2			1		1		
		Amino acid residues	TRP B:23,LEU B:26,GLU B:28,ASP B:21	LEU B:25,ASN B:30			LEU B:25	VAL B:31	PRO B:27		
	NLI	No.of Interactions	3	2	1			2			1
		Amino acid residues	LEU B:26,TRP B;23,ASN B:30	GLU B:28,LEU B:22	ASP B:21			PRO B:27,LEU B:25			ASN B:29
	NLJ	No.of Interactions	6	1		1		2			
		Amino acid residues	LEU B:32,ASN B:30,LEU B:26,LEU B:22,VAL B:31,SER B:33		PRO B;27	GLU B:28		PRO B:34,LEU B:35			
	NLK	No.of Interactions	4	2	1				1	1	
		Amino acid residues	AN B:29,LEU B:22,LEU B:25,ASP B:21	VAL B:31,GLU B:28	ASN B:30				PRO B:27	GLU B:28	
	CURCUMIN	No.of Interactions	5	2	1			3			
		Amino acid residues	ASN B:30,GLU B:28,LEU B:26,LEU B:35,PRO B:34	VAL B:31,SER B:33	SER B:33			PRO B;27,LEU B:32,VAL B:31			

2RUK (TG6) – Curcumin Analogue Complexes

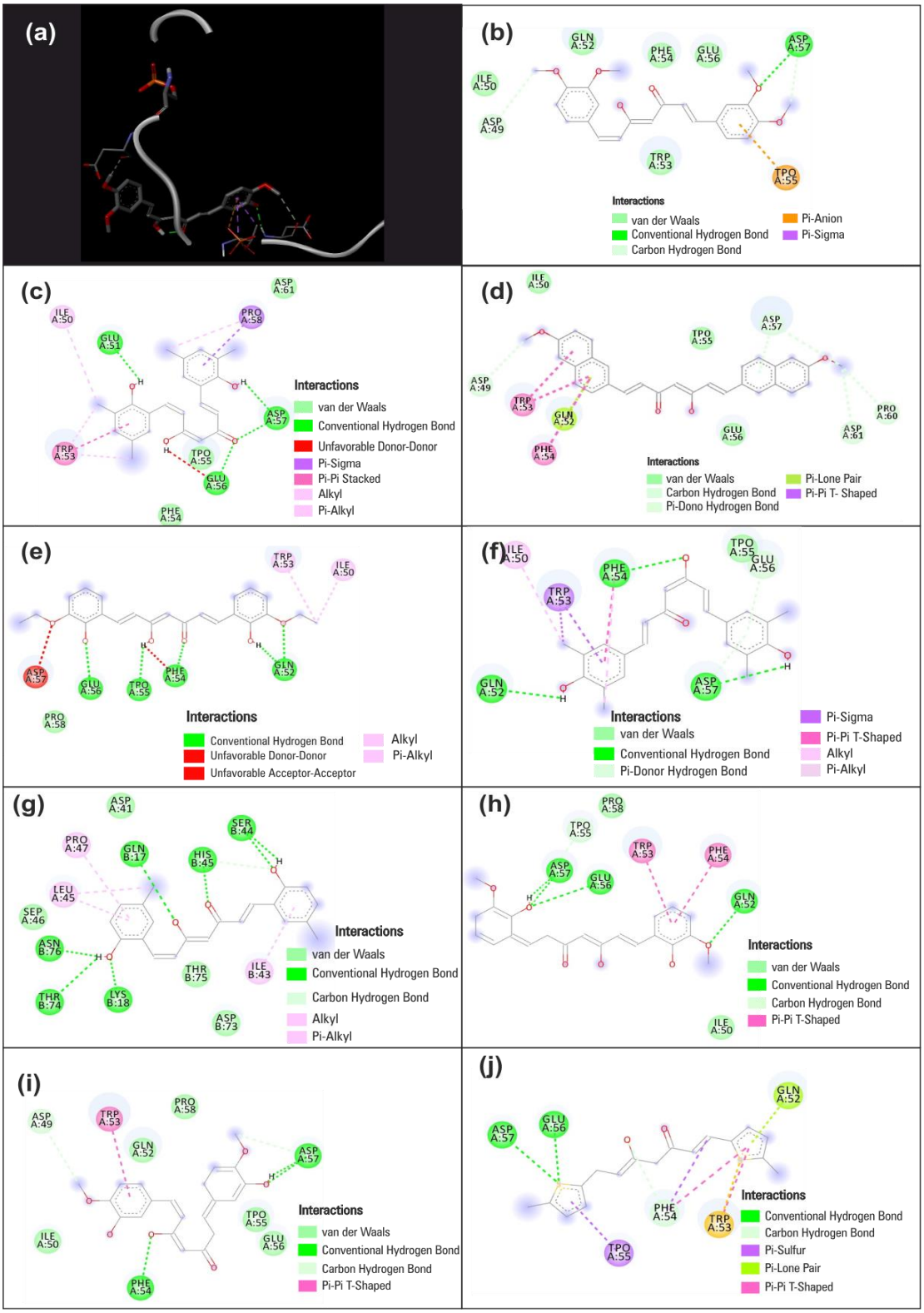

Fig.4.8.2 RUK – Curcumin Analogue Complexes (a) 2RUK-NLB Complex(3D) (b) 2RUK-NLB Complex(2D) (c) 2RUK-NLD Complex(2D) (d) 2RUK-NLE Complex(2D) (e) 2RUK-NLF Complex(2D) (f) 2RUK-NLG Complex(2D) (g) 2RUK-NLH Complex(2D) (h) 2RUK-NLI Complex(2D) (i) 2RUK-NLJ Complex(2D) (j) 2RUK-NLK Complex(2D)

Table 4.8 The interactions of ligands with 2RUK through various amino acid residues

Active Target	Compound		Types of Interactions													
			Van der Waals	Conventional Hydrogen Bond	Carbon Hydrogen Bond	Unfavourable Acceptor-Acceptor	Pi-Sigma	Pi-Alkyl	Pi-lone pair	Pi-Pi stacked	Alkyl	Pi-Anion	Pi-Pi T shaped	Unfavourable donor-donor	Pi-Sulfur	Pi-Donor Hydrogen Bond
2RUK	NLB	No.of Interactions	5	1	1							1				
		Amino acid residues	GLN A:52,PHE A:54,GLU A:56,TRP A:53,ILE A:50	ASP A:57	ASP A:49							TPO A:55				
	NLD	No.of Interactions	3	3			1	1		1	3			1		1
		Amino acid residues	ASP A:61,PHE A:54,PPO A:55	GLU A:51,ASP A:57,GLU A:56			PRO A:58	TRP A:53		TRP A:53	TRP A:53,ILE A:50,PRO A:58			GLU A:56		
	NLE	No.of Interactions	3		4				1				2			
		Amino acid residues	ILE A:50,TPO A:55,GLU A:56		ASP A:49,ASP A:57,ASP A:61,PRO A:60				GLA A:52				TRP A:53,PHE A:54			ASP A:57
	NLF	No.of Interactions	1	4		1		1			2			1		
		Amino acid residues	PRO A:58	GLU A:56,TPO A:55,PHE A:54,GLN A:52		PHE A:54		TRP A:53			TRP A:53,ILE A:50			ASP A:57		
	NLG	No.of Interactions	1	2			1	1			1		1			1
		Amino acid residues	TPO A:55	PHE A:54,ASP A:51			TRP A:53	THE A:54			ILE A:50		PHE A:54			GLU A:56
	NLH	No.of Interactions	4	6	1			3			1					
		Amino acid residues	ASP A:41,THR B:75,ASP B:73,SEP A:46	GLN B:17,HIS B:45,SER B:44,LYS B:18, THR B:74,ASN B:76	HIS B:45			ILE B:43,LEU A:45,PRO A:47			LEU A:45					
	NLI	No.of Interactions	2	3	1								2			
		Amino acid residues	PRO A:58,ILE A:50	ASP A:57,GLU A:56,GLN A:52	TPO A:55								TRP A:53,PHE A:54			
	NLJ	No.of Interactions	2	3	1								2			
		Amino acid residues	PRO A:58,GLN A:52,TPO A:55,GLU A:56,LE A:50	ASP A:57,PHE A:54	ASP A:57								TRP A:53,PHE A:54			
	NLK	No.of Interactions		2	1		1		1				1		1	
		Amino acid residues		ASP A:57,GLU A:56	PHE A:54		TPO A:55		GLN A:52				PHE A:54		TRP A:53	
	CURCUMIN	No.of Interactions	3	2						1						
		Amino acid residues	GLU A:56,GLU A:51,TPO A:55	PHE A:54,GLA A:52						TRP A:53						

Complexes of selected target molecules with Curcumin

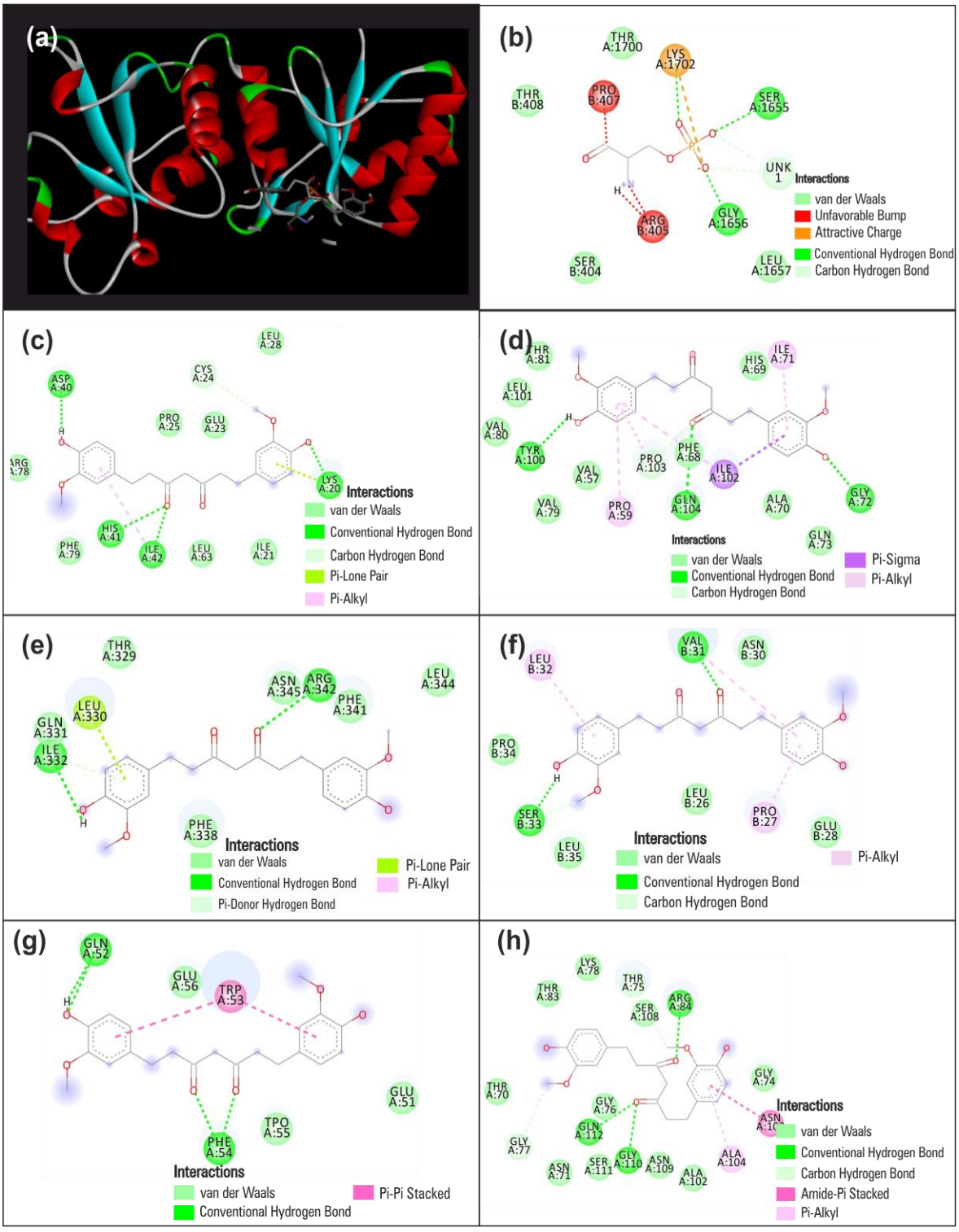

Fig.4.9 Selected target molecules with natural curcumin Complexes (a) 4Y2G-curcumin Complex(3D) (b) 4Y2G-curcumin Complex(2D) (c) 1JM7-curcumin Complex(2D) (d) 1OQA-curcumin Complex(2D) (e) 2JOZ-curcumin Complex(2D) (f) 2K8F-curcumin Complex(2D) (g) 2RUK-curcumin Complex(2D) (h) 1XQ7-curcumin Complex(2D)

The modelling of the interaction of NLH with the reference target, Cyclophilin (TG7), revealed binding at specific residues including Met63, Gln65, Arg84, Gly110, Gln112, Phe114, and Leu123, with a binding energy of -7.8 kcal/mol (**Fig.4.11 a**). However, NLH exhibited stronger binding with other selected targets, such as TG1 to TG6, compared to TG7 (**Fig.4.10**).The interaction between the FDA drug cyclophosphamide and Cyclophilin (TG7) was investigated through molecular docking, resulting in predicted binding energy of 3.8 kcal/mol at residues Arg57, Phe62, Met63, Gln65, Phe114, and Leu123 (**Fig.4.11 b**).

Furthermore, cyclophosphamide was docked with all selected targets (TG1 TG6) to assess its binding potential. The estimated binding energies of the complexes formed between cyclophosphamide and TG1, TG2, TG3, TG4, TG5, and TG6 were -4.62, -5.16, - 4.28, -3.68, -3.18, and- 3.68 kcal/mol, respectively. Among the nine curcumin analogues examined, NLH emerged as the most promising lead molecule, displaying an ideal binding energy of 8.3 kcal/mol towards target TG3, with an inhibition constant of 1.59 nM.

Comparatively, NLH demonstrated superior binding affinity to the selected molecular target in terms of binding energy, hydrogen bonds, weak interactions, and involvement of amino acids, surpassing both curcumin and cyclophosphamide and their respective targets. Notably, NLH exhibited better binding energy and interaction features compared to cyclophosphamide and its validated target, as well as cyclophosphamide and the selected targets in this study. These results indicated that NLH possesses considerable potential as the most promising lead compound among the curcumin analogues evaluated, eclipsing both the efficacy of curcumin and cyclophosphamide.

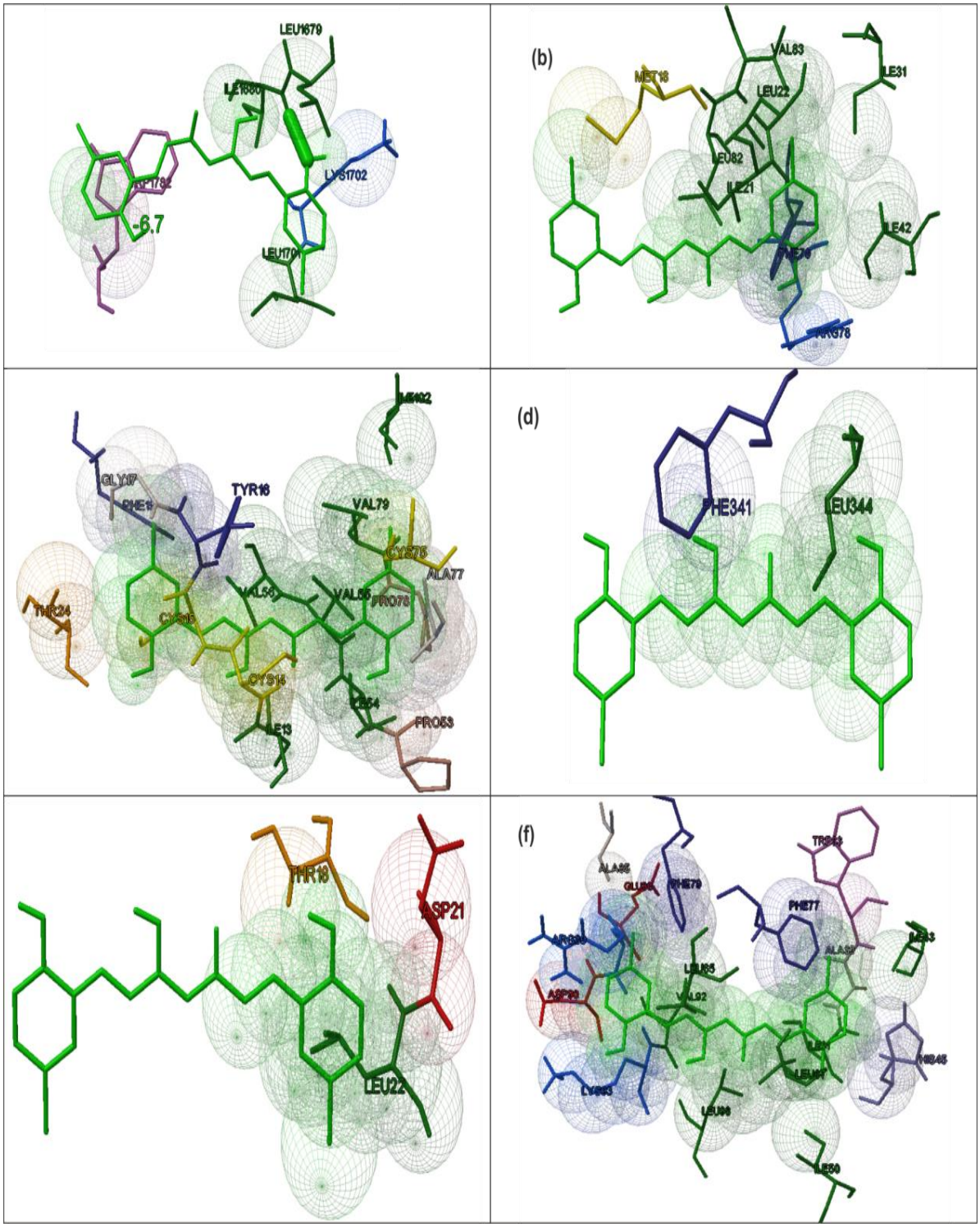

Fig.4.10 Prediction of NLH binding potential with selected breast cancer molecular targets was performed via molecular docking, and visualized using MGL Tools of Auto Dock. The figure shows the binding pocket of the ligand-receptor complex, with the interacting residues and the ligand displayed as stick figures. (a) Binding of NLH and TG1 (2D) (binding energy: -6.7 kcal/mol) (b) Binding of NLH and TG2 (binding energy: -7.74 kcal/mol) (c) Binding of NLH and TG3 (binding energy: -8.3 kcal/mol) (d) Binding of NLH and TG4 (binding energy: -7.32 kcal/mol) (e) Binding of NLH and TG5 (binding energy: -6.92 kcal/mol) (f) Binding of NLH and TG6 (binding energy: -5.38 kcal/mol)

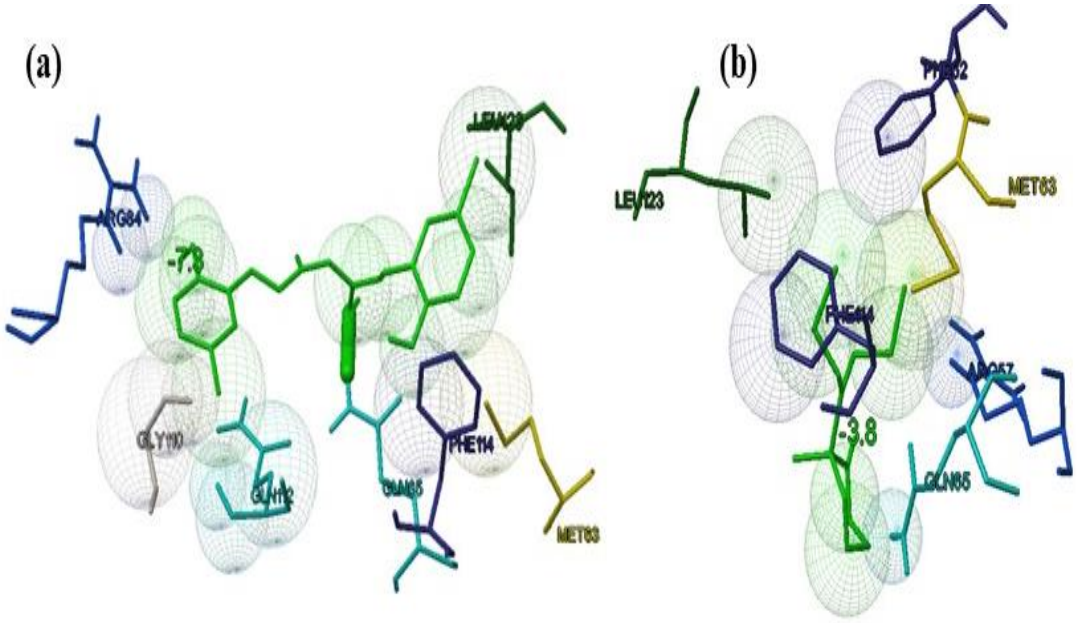

Fig.4.11 The binding of NLH and FDA-approved drug cyclophosphamide with Cyclophilin (TG7; PDB: 1XQ7) was analysed through molecular docking and visualized using MGL Tools of Auto Dock. (a) Binding of NLH with TG7 (binding energy: -7.8 kcal/mol) (b) Binding of cyclophosphamide with TG7(binding energy: -3.8 kcal/mol)

4.4.1.3. Molecular dynamic simulation

The best-docked complexes of the protein TG3 and NLH were subjected to a 100 ns simulation using an NVT(Number of particles Volume, and Temperature) ensemble to assess their dynamic behaviour and stability during binding. Similarly, the docked complex of cyclophosphamide with its validated target protein was simulated, and their binding stabilities were compared to the interaction stabilities of the NLH and TG3 complex. The MD simulation studies revealed structural and conformational changes throughout the simulations, as evident from plots such as protein-ligand RMSD, protein-ligand contact diagrams, and protein-ligand contact maps. The torsion profiles of the ligand also confirmed binding. The binding of the ligand to the protein and the conformational changes in the protein upon binding of the curcumin analogue were driven by various weak molecular interactions observed throughout the simulation.

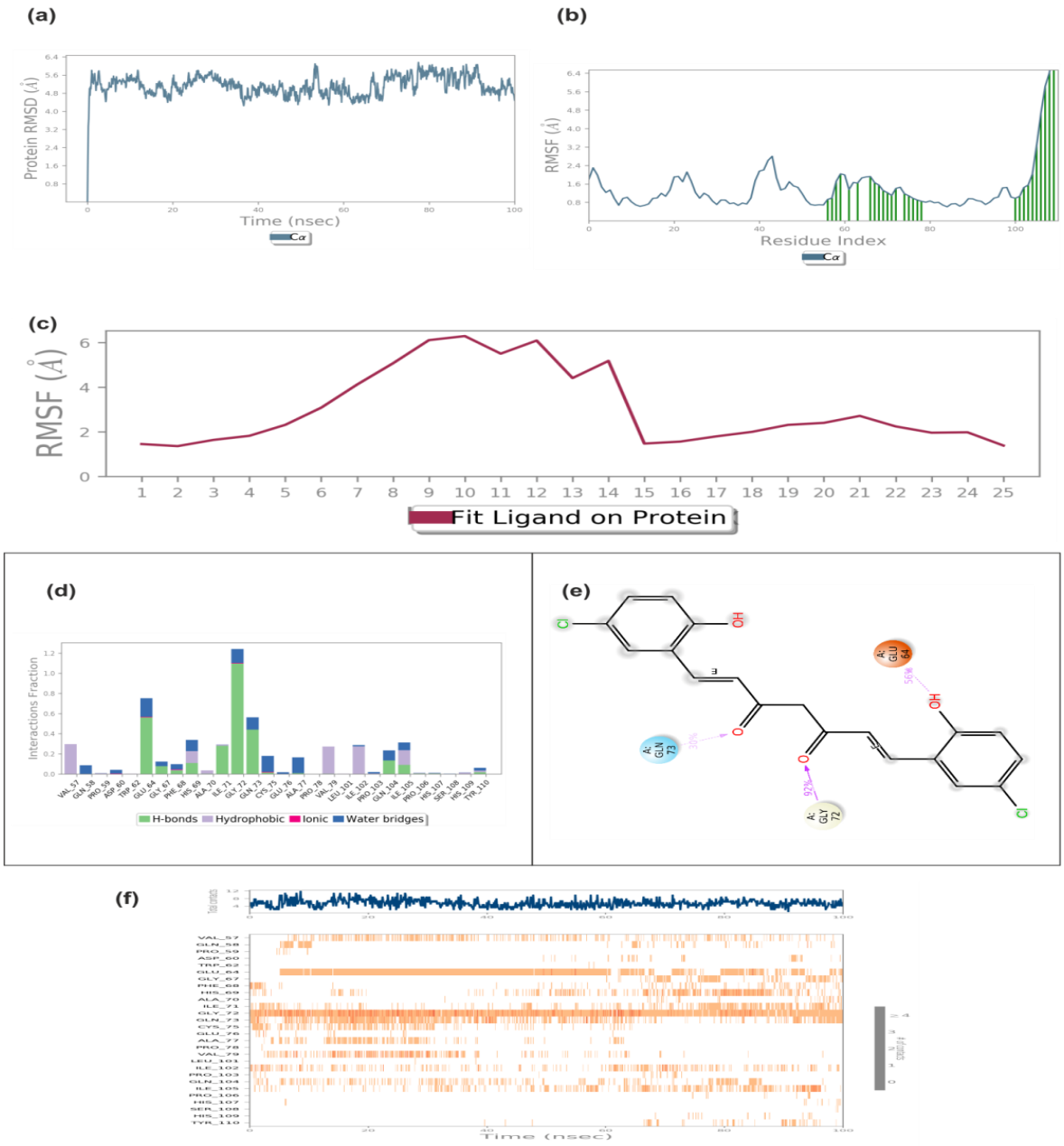

Fig.4.12 The binding and stability of the docked complex of NLH with the BRCA1-BRCT-c domain were studied using molecular dynamics simulation over 100 ns. The trajectories obtained from the MD simulation are shown in the figure. (a)Protein-ligand RMSD: Protein RMSD (Å) is shown on the Y-axis and simulation time is given on the X-axis. (b) The plot of the protein RMSF: RMSF (Å) is given on the Y-axis and the atom index is shown on the X-axis. (c) The plot of ligand RMSF: RMSF (Å) is shown on the Y-axis and the atom index is given on the X-axis. (d) The Protein-Ligand contact is shown in the form of a histogram. The blue, grey, pink, and green regions in the histogram represent water bridges, hydrophobic interaction, ionic bonds, and hydrogen bonds, respectively. (e) The interactions between NLH and protein TG3 observed during MD simulation (f) The protein-ligand contacts are shown in the form of timeline representation. The top panel shows the total number of specific contacts between the receptor and ligand, and the bottom panel shows the amino acid residue of the target, which interacted with the ligand[29].

The MD trajectories for the best NLH and TG3 complex were shown in **Fig.4.12.** These trajectories demonstrated that the RMSD value of the protein ranged from 4.8 to 6.2 Å at 100 ns, indicating conformational changes in the target protein (**Fig.4.12.a**). This RMSD variation, due to the interaction of NLH and TG3, suggests superior binding and stabilization compared to the control. The protein's RMSF varied from 2.4 to 6.4 Å, further indicating conformational changes during the simulation. Secondary structural elements such as alpha helices and beta strands showed less fluctuation compared to regions like coils and loops, with significant fluctuations observed at the C- and N-terminals (**Fig.4.12.b**). The ligand's RMSF ranged from 2.0 to 6.0 Å, reflecting entropic fluctuations and binding to the target (**Fig.4.12.c**). Key stabilizing interactions throughout the simulation included water bridges, hydrogen bonds, and hydrophobic interactions (**Fig. 4.12.d**). The molecular interactions during the simulation were shown in **Fig.4.12.e**. MD studies confirmed that the curcumin analogue interacted with TG3 via residues Glu64, Gln73, and Gly72 of chain A, with major interactions depicted in **Fig.4.12.f.** The trajectory of total contacts, including hydrogen bonds, ionic bonds, water bridges, and hydrophobic interactions, varied throughout the simulation, indicating stable binding predominantly involving residues from chain A.

The MD trajectories for the cyclophosphamide and TG7 complex are shown in **Fig. 4.13**. These trajectories indicated that the RMSD values of the protein varied from 0.8 to 1.4 Å at 100 ns, suggesting lesser conformational changes during the simulation (**Fig. 4.13.a**). The RMSD variation implies binding with cyclophosphamide. The RMSF of the protein ranged from 0.6 to 1.6 Å (**Fig. 4.13.b**), while the RMSF of the ligand varied from 3.0 to 4.5 Å, indicating entropic fluctuations during binding (**Fig. 4.13.c**). Major stabilizing interactions included water bridges, ionic bonds, hydrogen bonds, and hydrophobic interactions (**Fig. 4.13.d**). The forces stabilizing the binding are illustrated in **Fig. 4.13.e**. Cyclophosphamide was found to bind to its target via residues Arg57, Asn103, Gln65, and Phe114, with interactions depicted in **Fig. 4.13.f**. The binding stability of the NLH and TG3 complex was superior to that of the cyclophosphamide and TG7 complex, suggesting NLH as a potential lead molecule against the BRCA1-BRCT-c domain (TG3) in breast cancer.

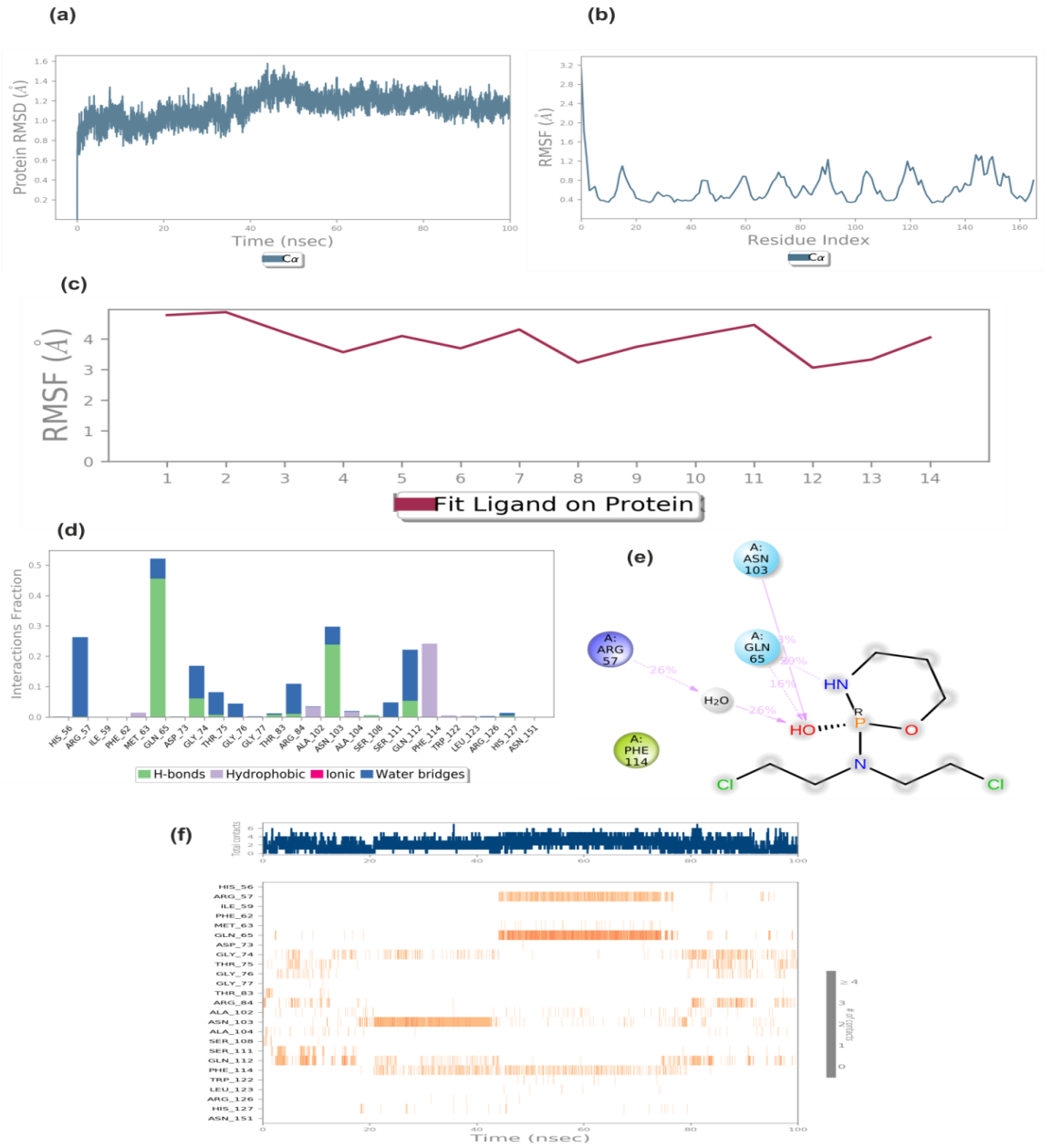

Fig.4.13 The binding and stability of the docked complex of the conventional breast cancer drug Cyclophosphamide with its validated target TG7 were studied using molecular dynamics simulation over 100 ns. The trajectories obtained from the MD simulation are shown in the figure. (a) Protein-ligand RMSD: Protein RMSD (Å) is shown on the Y-axis and simulation time is given on the X-axis. (b) The plot of the protein RMSF: RMSF (Å) is given on the Y-axis and the atom index is shown on the X-axis. (c) The plot of ligand RMSF: RMSF (Å) is shown on the Y-axis and the atom index is given on the X-axis. (d) The Protein-Ligand contact is shown in the form of a histogram. The blue, grey, pink, and green regions in the histogram represent water bridges, hydrophobic interaction, ionic bonds, and hydrogen bonds, respectively. (e) The interactions between cyclophosphamide and protein TG7 observed during MD simulation (f) The protein-ligand contacts are shown in the form of timeline representation. The top panel shows the total number of specific contacts between the receptor and ligand, and the bottom panel shows the amino acid residue of the target, which interacted with the ligand[29].

4.4.1.3.1. Calculation of Molecular Mechanics with Generalized Born and Surface area Solvation (MM/GBSA)

The calculated binding free energies (ΔG Bind and ΔG Bind NS) for the interaction between NLH and the BRCA1-BRCT-c domain (TG3), as well as cyclophosphamide and its validated target TG7, using MM/GBSA methods, are presented in **Table 4.9**. The binding stability of NLH with the BRCA1-BRCT-c domain was confirmed by MM-GBSA binding free energy estimation. The interaction energy for cyclophosphamide and TG7 at 100 ns was found to be -21.67 kcal/mol. In contrast, the binding energy for the docked complex of NLH and the BRCA1-BRCT-c domain at 100 ns was estimated to be -64.24 kcal/mol, significantly lower than that of the control. Similarly, without considering receptor and ligand conformational changes during complex formation, the binding energy for cyclophosphamide (control) and TG7 was -23.02 kcal/mol, whereas for NLH (test) and the BRCA1-BRCT-c domain, it was -64.59 kcal/mol at 100 ns. These results from MMGBSA binding free energy calculations indicate that NLH demonstrates better binding with the BRCA1-BRCT-c domain of breast cancer compared to the FDA-approved drug cyclophosphamide and its validated target.

Table 4.9. Binding free energy calculations for the test (interaction between NLH and TG3) and control (interaction between Cyclophosphamide and its validated target) were performed using MM/GBSA.

	Control (Interaction between cyclophosphamide and validated target)		**Test (Interaction between NLH and TG3)**	
Time in (ns)	***DG Bind (kcal/mol)**	***DG Bind NS (kcal/mol)**	**DG Bind (kcal/mol)**	**DG Bind NS (kcal/mol)**
10	-32.124	-39.1401	-37.621	-39.722
20	-14.4342	-18.62367	-61.6115	-66.84162
30	0.005224	0.000579	-67.4163	-71.92285
40	-26.842	-32.76647	-50.0537	-52.99145
50	-22.6938	-28.30012	-59.3443	-63.2962
60	-27.4392	-31.82655	-54.5209	-64.05611
70	-31.0677	-34.7436	-59.8756	-61.45158
80	-28.2482	-32.82203	-62.0093	-68.59858
90	-21.5625	-22.85762	-52.151	-55.81451
100	-21.6782	-23.01707	-61.2412	-64.59952

*MMGBSA DG_{Bind} = Complex Receptor – Ligand and *MMGBSA DG_{Bind} (NS) = Complex Receptor (from optimized complex) – Ligand (from optimized complex) = MMGBSA DG_{Bind}– Receptor Strain – Ligand Strain. NS in the table stands for no strain; it represents the binding energy without accounting for the conformational changes in the receptor and ligand required for complex formation[29].

Protein-ligand, protein-solvent, and ligand-solvent interactions significantly influenced ligand binding to proteins, with entropy and enthalpy playing crucial roles in these interactions. Although statistical mechanics provided an accurate expression for free energy, it was typically impractical to use directly for large molecules due to the difficulty in calculating the partition function. Free energy perturbation (FEP)[85] and thermodynamic integration (TI)[86] methods allowed numerical estimation of free energy differences between two states using precise formulations. However, FEP and TI techniques often require lengthy computations, making them impractical for multiple protein ligand binding analyses. Thus, there was a continual need for approximation methods reasonably accurate for calculating the binding free energy of macromolecules to ligands[87]. The MMPBSA/GBSA approaches, developed by Case, Kollman, and colleagues, were among the most widely used methodologies[88]. These approaches calculated binding free energy by subtracting the free energies of the protein and ligand from that of the protein-ligand complex.

Molecular docking, MD simulation, and energy calculation studies demonstrated that the NLH lead molecule demostrated superior binding energy, stability, and dynamics towards the prioritized target (TG3) of breast cancer compared to curcumin alone and cyclophosphamide with its validated target. Thus, this study suggested that the NLH molecule and the prioritized target were promising candidates for developing anticancer agents against breast cancer.

This study provided manifold insights into the molecular mechanisms of binding potential for different curcumin analogues targeting six breast cancer molecular targets. For comparative purposes, the interaction model of pure curcumin and cyclophosphamide with its validated target was used as the control. The study modelled the binding affinity of NLH towards the prioritized target. Owing to time and resource constraints, molecular dynamics simulations and energy calculations were performed only for the best-docked complex, which exhibited the minimum binding energy and maximum stabilizing interactions, and for the control with its validated target. The study employed MM/GBSA approaches for free energy calculations based on the MD results. Although MM/GBSA was a conventional method, more rigorous binding free energy calculations, such as linear response approximation (LRA) and linear interaction energy (LIE) methods, offered better approximations of experimental binding free energies. These advanced methods have been successfully applied to the study of several curcumin analogues[89]. The results

of the present studies prompted further analysis of the *in vitro* cytotoxic and antitumor properties of NLH.

4.4.2. *In vitro* cytotoxic studies

In vitro cytotoxic studies using DLA (Dalton's Lymphoma Ascites), EAC (Ehrlich Ascites Carcinoma), and spleen cell lines involve assessing the toxicity of compounds on cancer and normal cells. These studies help determine the potential anticancer properties and safety profile of new therapeutic agents.

4.4.2.1. *In vitro* cytotoxic studies of curcumin analogues and their metal complexes using DLA, EAC, and spleen cell lines

4.4.2.1.1. Short-term cytotoxic effect of Curcumin analogues

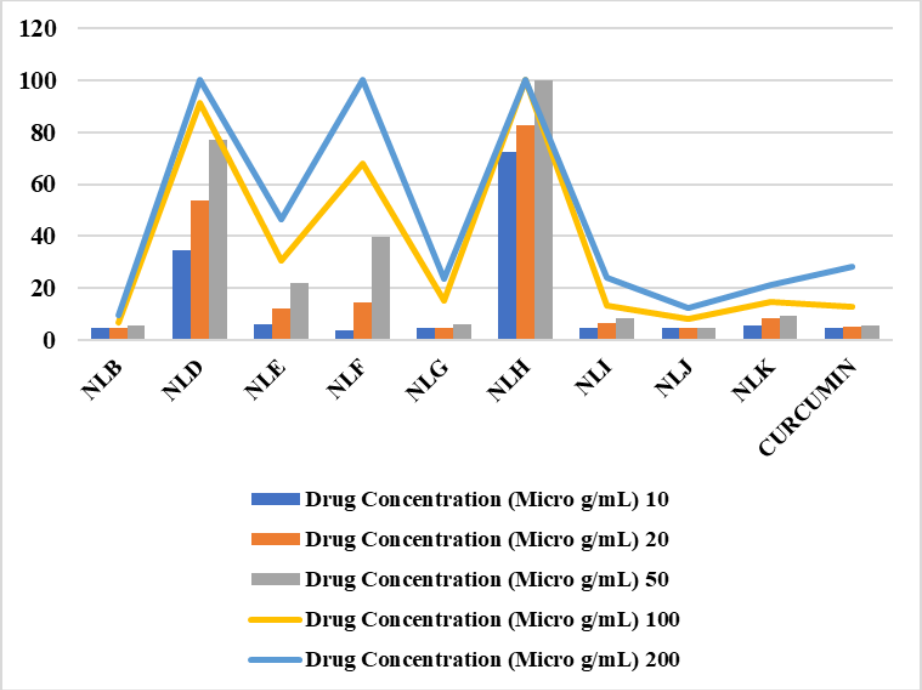

Fig.4.14 The *in vitro* cytotoxicity results of various ligands (NLB, NLD, NLE, NLF, NLG, NLH, NLI, NLJ, NLK and CURCUMIN) at different concentrations (10, 20, 50, 100, 200 µg/mL) against DLA cell lines. The results are represented as the percentage of cell death.

NLH and NLD were the most effective ligands in inducing cell death, exhibiting high cytotoxicity at lower concentrations. NLF also demonstrated significant cytotoxicity but required higher concentrations to reach its maximum effect. NLE and NLI showed moderate cytotoxicity, while NLG, curcumin, NLK, NLB, and NLJ exhibited lower

cytotoxic effects. These results indicated that NLH was the most potent cytotoxic ligand *in vitro*, followed by NLD and NLF. Curcumin, although showing some cytotoxicity, was less effective compared to the top ligands.

The cytotoxic effects observed among the ligands were attributed to various factors related to their chemical structure and behaviour. Differences in ligand structure and electronic properties played a crucial role in influencing their interaction with cellular targets. Ligands with specific functional groups or molecular configurations might interact differently with cellular components, thereby impacting their cytotoxicity. The permeability of ligands across cell membranes varies, with some demonstrating better cell permeability than others, which could affect their ability to induce cell death. The stability of ligands in the biological environment was a significant determinant of their cytotoxicity, as more stable ligands might persist longer, leading to prolonged exposure and potentially higher cytotoxic effects. The specific interactions between the ligands and cellular targets, such as DNA or proteins, could vary significantly, necessitating differences in their cytotoxic effects.

Molecular docking and *in vitro* cytotoxicity studies on DLA cell lines have identified NLH as the most promising ligand among the tested compounds. NLH consistently exhibited low Binding Energy (BE) and Inhibition Constant (Ki) values across all targets, indicating its strong binding affinity and potency. NLH demonstrated a high number of target interactions, suggesting excellent specificity. *In vitro*, NLH emerged as the most potent cytotoxic ligand, showing effectiveness at lower concentrations, making it a prime candidate for further research. NLD also performed well, with low BE values for certain targets, significant interactions, and high cytotoxicity at lower concentrations. Although NLI showed good binding affinity and potency with moderate interaction profiles, it was less effective in cytotoxic effects *in vitro*

The *in vitro* cytotoxicity results of the synthesized curcumin analogues align with those observed in molecular docking studies, providing insights into the interaction mechanisms between the ligands and the selected target proteins of breast cancer.

Based on the above results, NLH and NLD were selected for further validation using EAC cell lines to confirm the findings.

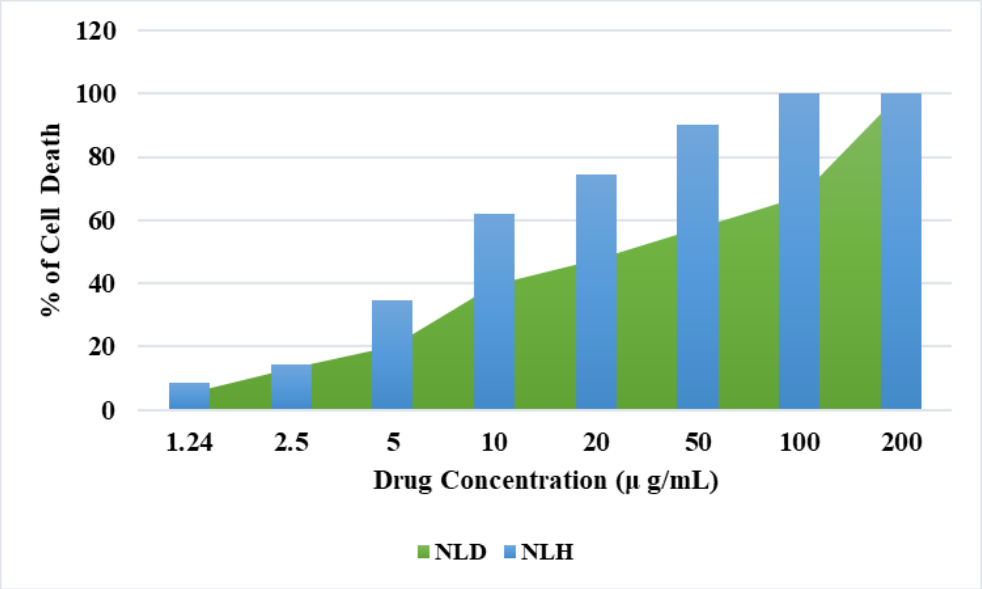

Fig.4.15 *In Vitro* Cytotoxicity of Ligands NLH and NLD Against EAC Cell lines

The graph indicated that both NLD and NLH were effective in inducing cell death in EAC cell lines, with a clear dose-dependent effect. However, NLH was significantly more sensitive to achieving complete cell death at lower concentrations compared to NLD. This information was critical in optimizing dosages for maximum efficacy while minimizing potential side effects.

The *in vitro* cytotoxic studies are also done using spleen cell lines, selecting the most active compound NLH. Cytotoxic studies using spleen cell lines are crucial for assessing the potential toxicity of compounds on immune cells, reflecting their impact on immune function. This aids in evaluating immunotoxicity profiles of drugs and chemicals, essential for understanding potential side effects on the immune system in pharmacological and toxicological research.

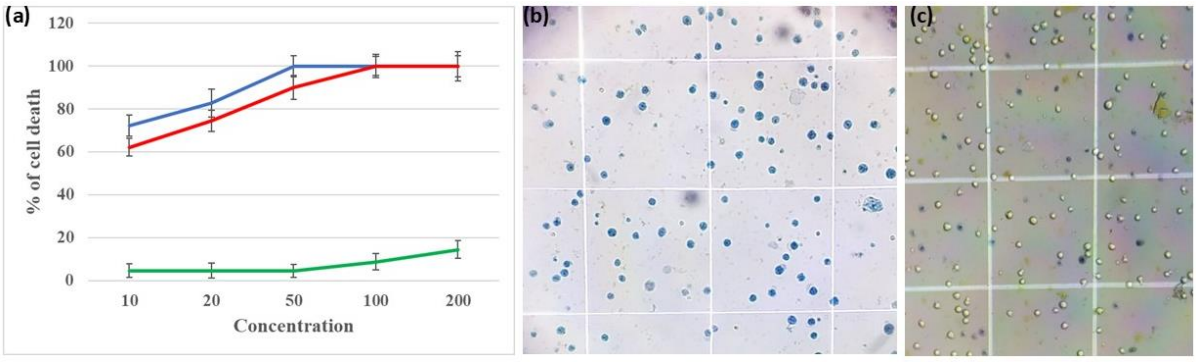

Fig.4.16 The figure depicts the in vitro cytotoxic effect of NLH on DLA, EAC, and rat spleen cell lines. (a) Comparative % cell death study (DLA in blue, EAC in red, spleen cells in green) at mg/ml concentrations, plotted with mean ± SD. (b) Light microscopic view (x10) of dead DLA cells (blue). (c) Light microscopic view (x10) of live spleen cells (transparent).

Both NLH and NLD induced cell death in EAC cell lines in a dose-dependent manner, with NLH achieving complete cell death at lower concentrations compared to NLD. NLH was particularly effective against DLA and EAC cell lines, while the SPLEEN cell line showed minimal sensitivity to NLH. This selective efficacy indicated a therapeutic advantage in targeting specific cancer cells (such as DLA and EAC) while minimizing potential side effects on non-cancerous cells. Therefore, NLH stood out as the most promising ligand, demonstrating strong binding affinity, high potency, and effective cytotoxicity. These findings highlighted the potential of these novel ligands for further preclinical and clinical investigations, emphasizing their importance in the development of breast cancer treatments.

4.4.2.1.2. Short-term cytotoxic effect of metal complexes of curcumin analogues using DLA cell lines

Copper (II) and Zinc (II) complexes of curcumin analogues have attracted significant interest for their potential in combating cancer. Derived from turmeric, curcumin displays antioxidant, anti-inflammatory, and anti-cancer properties, albeit with limitations in stability and bioavailability. Complexing curcumin analogues with Cu (II) and Zn (II) ions enhances their stability under physiological conditions, facilitating better absorption and distribution in the body, thereby increasing their efficacy against cancer. These complexes targeted cancer cells through diverse mechanisms, including modulation of NF-κB signalling, inhibition of kinases crucial for cell growth, and induction of apoptosis. They also exhibited antioxidant properties that protected cells from oxidative stress prevalent in cancer and anti-inflammatory effects that mitigated inflammation-linked carcinogenesis. The choice of metal ions affected the biological activity and toxicity of the complexes. Cu(II) complexes triggered cytotoxic reactive oxygen species selectively in cancer cells, while Zn(II) complexes stabilized structures crucial for cancer cell function, such as DNA binding or enzymatic inhibition[90].

4.4.2.1.2.1. *In vitro* cytotoxicity evaluation of Cu (II) complexes of curcumin analogues against DLA cells

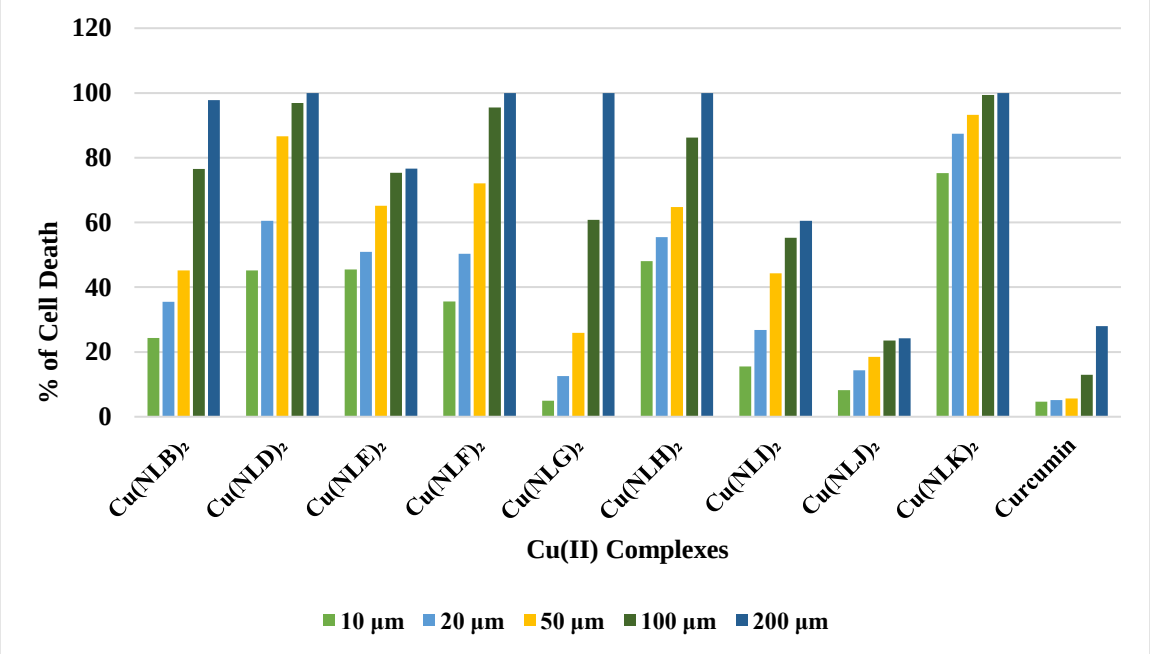

Fig.4.17 Cu (II) Complexes of Curcumin Analogues-*In Vitro* Cytotoxicity Evaluation Against DLA Cells. The results are represented as the percentage of cell death.

The Cu complexes manifested varying degrees of cytotoxicity, with $Cu(NLD)_2$, $Cu(NLF)_2$, $Cu(NLG)_2$, $Cu(NLH)_2$, $Cu(NLK)_2$, and $Cu(NLE)_2$ demonstrating very high cytotoxicity, especially at higher concentrations. $Cu(NLB)_2$ and $Cu(NLI)_2$ showed moderate cytotoxicity, while $Cu(NLJ)_2$ exhibited the least cytotoxicity among the Cu complexes. Curcumin, used as a reference compound, revealed consistently low cytotoxicity. The varying cytotoxic effects were due to the differences in the ligands (NLB, NLD, etc.) attached to the Cu ion. The structure and electronic properties of these ligands could influence the ability of the complex to interact with and disrupt cellular processes. Some complexes might have better cell permeability, allowing them to enter cells more effectively and induce cell death. The cytotoxicity could also depend on the rate at which Cu ions are released from the complex inside the cells, with complexes that release Cu ions more readily potentially inducing higher cytotoxicity. The stability of the Cu complexes in the biological environment could affect their cytotoxicity, as more stable complexes may persist longer, leading to prolonged exposure and higher cytotoxicity. The specific interactions between the Cu complexes and cellular targets might vary, leading to differences in cytotoxic effects. The low cytotoxicity of curcumin across all concentrations served as a control to highlight the enhanced cytotoxic effects of the Cu complexes, emphasizing their potential therapeutic relevance. Conclusively, the Cu complexes exhibited a wide range of cytotoxic activities influenced by their structural and

chemical properties, with several showing high potential as cytotoxic agents at higher concentrations.

4.4.2.1.2.2. *In vitro* cytotoxicity evaluation of Zn(II) complexes of curcumin analogues against DLA cells

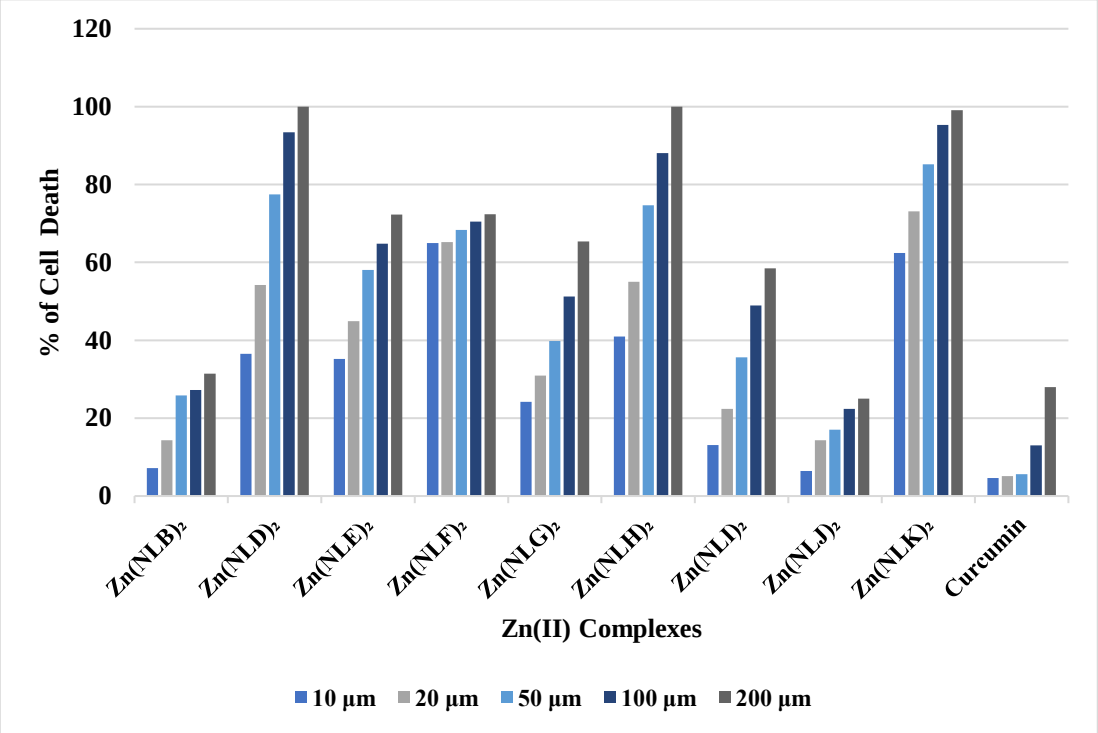

Fig.4.18 Zn (II) Complexes of Curcumin Analogues-*In Vitro* Cytotoxicity Evaluation Against DLA Cells. The results are represented as the percentage of cell death.

The Zn complexes exhibited varying degrees of cytotoxicity, with $Zn(NLD)_2$, $Zn(NLH)_2$, and $Zn(NLK)_2$ demonstrating notably high cytotoxicity, particularly at elevated concentrations. $Zn(NLF)_2$ and $Zn(NLE)_2$ also produced significant cytotoxicity, though less pronounced at higher concentrations compared to $Zn(NLD)_2$ and $Zn(NLH)_2$. Zn(NLB)2, $Zn(NLI)_2$, and $Zn(NLG)_2$ presented moderate cytotoxicity, while $Zn(NLJ)_2$ had the lowest cytotoxicity among the Zn complexes. In contrast, curcumin, used as a reference compound, consistently exhibited low cytotoxicity. The differences in cytotoxic effects are likely attributable to the distinct ligands attached to the Zn ion. The structural and electronic properties of these ligands could influence the ability of the complex to interact with and disrupt cellular processes. Some complexes might have enhanced cell permeability, enabling them to enter cells more effectively and induce cell death. The rate at which Zn ions were released from the complex inside the cells could also impact cytotoxicity, with complexes that release Zn ions more readily potentially causing higher cytotoxicity. The stability of Zn complexes in the biological environment played a role in

their cytotoxicity; more stable complexes might persist longer, resulting in prolonged exposure and greater cytotoxicity. The specific interactions between Zn complexes and cellular targets could vary, leading to differences in cytotoxic effects. The low cytotoxicity of curcumin across all concentrations served as a control, highlighting the enhanced cytotoxic effects of the Zn complexes and underscoring their potential therapeutic relevance. In short, the Zn complexes manifested a spectrum of cytotoxic activities influenced by their structural and chemical properties, with several demonstrating high potential as cytotoxic agents at higher concentrations.

Both Cu (II) and Zn(II) complexes exhibited a range of cytotoxic activities influenced by their ligands. High cytotoxicity was observed in $Cu(NLD)_2$, $Cu(NLF)_2$, $Cu(NLH)_2$, $Cu(NLK)_2$, $Zn(NLD)_2$, $Zn(NLH)_2$, and $Zn(NLK)_2$, which might be more effective in targeting cancer cells. Moderate cytotoxicity was seen in $Cu(NLB)_2$, $Cu(NLI)_2$, $Zn(NLE)_2$, $Zn(NLF)_2$, $Zn(NLI)_2$, and $Zn(NLG)_2$, potentially offering a balance between efficacy and safety with fewer side effects. Low cytotoxicity was noted in $Cu(NLJ)_2$, $Zn(NLB)_2$, $Zn(NLJ)_2$, and curcumin, suggesting they might be safer but less effective as standalone treatments, though they could be useful in combination therapies or for other therapeutic applications. Several factors influenced the therapeutic potential of these complexes High cytotoxicity complexes might be preferable for aggressive cancers, while moderate cytotoxicity complexes might provide a better therapeutic window. Ligand properties, metal ion reactivity, cell permeability, and stability in biological environments were crucial in determining their efficacy and safety. Cu complexes, often more cytotoxic due to the higher reactivity and ability to generate reactive oxygen species (ROS) of Cu ions, were potent choices for rapid cell death. In contrast, Zn complexes, which generally exhibited lower cytotoxicity due to less reactive Zn ions, could be enhanced by specific ligand structures. For aggressive treatments, high cytotoxicity Cu complexes like $Cu(NLD)_2$ and $Cu(NLK)_2$, and Zn complexes like $Zn(NLD)_2$ and $Zn(NLK)_2$ were potent choices. For conditions requiring controlled cytotoxicity, moderate cytotoxicity complexes such as $Cu(NLB)_2$ and $Zn(NLE)_2$ were potential candidates. Low cytotoxicity agents, such as curcumin, are suitable for chronic conditions or as part of combination therapy to enhance the effect of other drugs with minimal side effects. The choice between Cu and Zn complexes ultimately depended on the specific therapeutic need, with Cu complexes generally better for aggressive treatment and Zn complexes offering a safer alternative for a balanced approach.

The higher *in vitro* cytotoxicity observed in Cu and Zn metal complexes compared to their ligands could be attributed to various interconnected biochemical factors. Copper and Zinc ions possess inherent reactivity within biological systems, engaging in redox

reactions and generating reactive oxygen species (ROS) that disrupt cellular processes. When complexed with ligands, these metal ions became more bioavailable and reactive, intensifying their cytotoxic potential. Moreover, metal complexes exhibited greater cellular uptake than free ligands due to factors such as size, charge, and hydrophobicity, facilitating their passage through cellular membranes and subsequent interaction with intracellular targets. The formation of chelates between metal ions and ligands enhanced the stability and reactivity of the complexes, prolonging their cytotoxic effects by protecting the metal ions from sequestration or detoxification mechanisms within the cell. Metal complexes could interact with specific biological targets, such as DNA, proteins, or enzymes, with higher affinity and specificity than free ligands, disrupting essential cellular processes and promoting cell death. Certain ligands might synergistically enhance the cytotoxic effects of metal ions by modulating their reactivity and bioavailability. Metal complexes containing transition metals like Cu and Zn could undergo redox cycling reactions, alternating between different oxidation states and generating ROS, which induce oxidative stress and contribute to cell death. In conclusion, the greater *in vitro* cytotoxicity of Cu and Zn metal complexes compared to their ligands was attributed to their improved reactivity, enhanced cellular uptake, increased stability, specific targeted interactions, synergistic effects, and capacity for redox cycling within biological systems.

4.4.2.2. 3 (4,5 Dimethylthiazol 2 yl) 2,5 Diphenyltetrazolium bromide (MTT) assay

The cytotoxic potential of the compound was evaluated using an MTT assay, comparing its effects on the breast cancer cell line C127I and the non tumorigenic cell line Vero (**Fig. 8b**). The compound exhibited significant cytotoxicity towards the C127I breast cancer cell line while showing the minimal cytotoxic effect on Vero cells, with only a 10% inhibition, similar to the vehicle control DMSO. The IC_{50} value for C127I was found to be 104.01 µg/ml. At a concentration of 100 µg/ml, the compound caused 41.4% inhibition of C127I cells, but only 9.04% inhibition of Vero cells.

The MTT assay (3-(4,5-Dimethylthiazol-2-yl)-2,5-diphenyltetrazolium bromide) was noticed to operate by reducing MTT, breaking the central tetrazole ring to form the violet-blue, water-insoluble compound formazan[91]. Because of its positive charge and lipophilic nature, MTT could permeate the mitochondrial inner membrane and cell membrane of viable cells, where it got converted to formazan by proliferating cells. Developed in 1983 by Mosmann et al.,[92] the MTT assay was based on the colourimetric detection of intracellular formazan production, exploiting the chromogenic properties of this redox reaction[93].

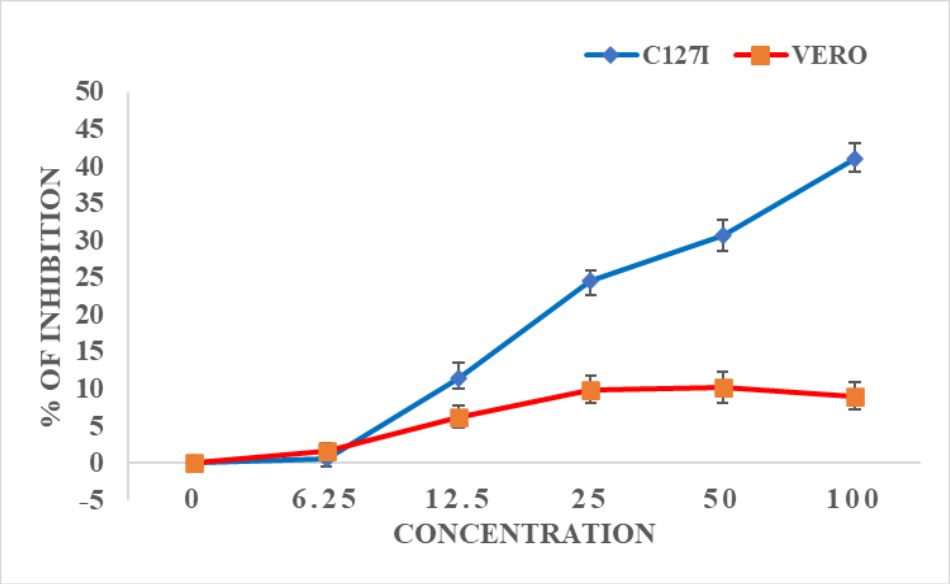

Fig.4.19 Comparative Study of % Inhibition Induced by NLH on C127I Breast Cancer Cell Lines (Blue) and Vero Non-Tumorigenic Cell Lines (Red), with Concentration in µg/mL. The Graph Displays Mean ± SD.

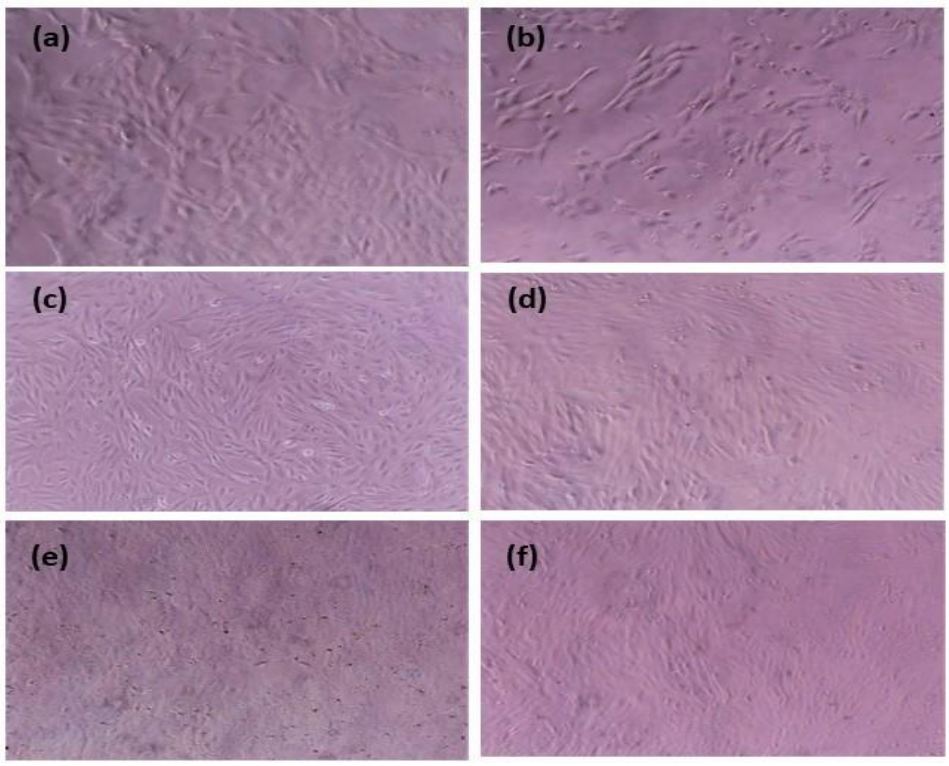

Fig.4.20 The cytotoxic effect of NLH on C127I (breast cancer cell line) and Vero cell line is shown in the figure. (a) Effect of 50 µg/ml NLH on C127I cell line (b) Effect of 50 µg/ml NLH on Vero cell line (c) Effect of 100 µg/ml NLH on C127I cell line (d) Effect of 100 µg/ml NLH on Vero cell line (e) Effect of control (DMSO) on C127I cell line (f) Effect of (control) on Vero cell line.

The cytotoxic effects of NLH on C127I and Vero cell lines are depicted in **Fig.4.19**. and **Fig.4.20**. The results indicate that NLH is cytotoxic to the C127I breast cancer cell line (Fig 4.20.a and c), but exhibits little to no toxicity towards Vero cell lines (**Fig.4.20.b** and **d**), comparable to the control DMSO (**Fig.4.20.e** and **f**). This variation in cytotoxicity suggests that NLH could be effective in treating various types of cancer, including breast cancer.

4.4.3. *In vivo* studies

4.4.3.1. Acute toxicity

Acute toxicity assessment was observed as a crucial preliminary phase required for evaluating the toxicity of any biological compound. It was intended to determine the moderate lethal dose (LD_{50}) of these compounds. Acute toxicity typically meant variations observed immediately or shortly after a single administration of a compound, typically within 24 hours (OECD, 2000)[94].

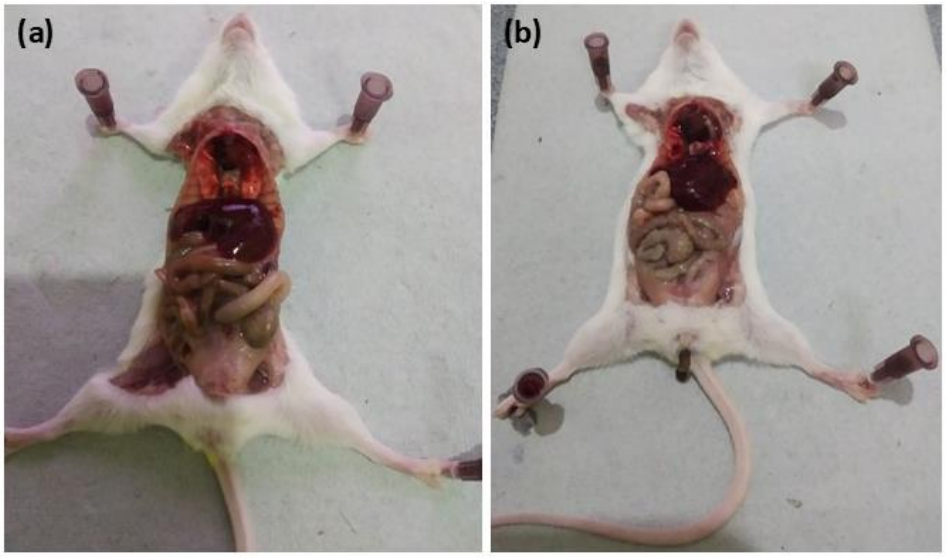

Fig 4.21 Effect of NLH on the morphology of various organs of Swiss albino mice observed on the 14th day post single acute dose (1000 mg/kg b.wt.) administration. (a) Vehicle Control (b) NLH

Table 4.10 Acute Toxicity Evaluation of NLH in Swiss Albino Mice

Observations	Control group	Treated (NLH) Group
Food Intake	Normal	Normal
Water Intake	Normal	Normal
Body weight	Normal	No Change
Drowsiness	Not Present	Not Present
Changes in Skin	No Change	No Change
Diarrhoea	Not present	Not present
Sedation	No Effect	No Effect
General physique	Normal	Normal
Death	Alive	Alive

The LD_{50} of NLH in Swiss Albino mice was determined to exceed 1000 mg/kg body weight. Following a single administration of NLH at 1 g/kg body weight for acute toxicity assessment, by OECD guideline 420 (adopted December 2001)[95], no significant differences were observed between the NLH-treated group and the untreated control group (**Fig 4.21**). The acute toxicity analysis revealed NLH to be non-toxic to Swiss Albino mice, as evidenced by the absence of mortality and any abnormal changes in skin, fur, eyes, mucous membranes, behaviour patterns, tremors, salivation, sleep, or signs of ill health during the two-week observation period (**Table 4.10**). Food consumption **(Fig 4.22. a**) and Body weight remained consistent without variation (**Fig 4.22.b**), and no diarrhoea or hair loss was observed.

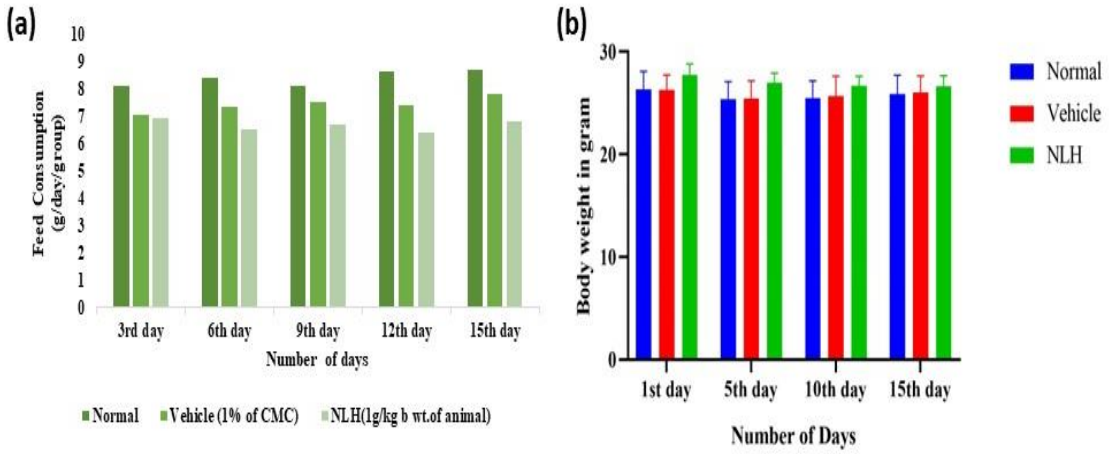

Fig.4.22 Acute Toxicity Evaluation of NLH in Swiss Albino Mice (a) Feed Consumption (b) Body Weight over 14 Days, Represented in grams/Day/Group.

In this acute toxic study, Swiss Albino mice treated with NLH up to a dose of 1g/kg body weight showed no mortality or signs of toxicity or side effects. Compounds with LD_{50} values below 2g/kg body weight were generally considered relatively safe.

Therefore, NLH could be regarded as non-toxic upon acute administration, as the subjects tolerated the treatment sufficiently well without adverse effects.

4.4.3.2. Sub-acute toxicity

Sub-acute toxic studies in Swiss Albino mice have assessed the toxicity of a substance over 45 days. These studies enabled to determine the potential health risks, safe dosage levels, and adverse effects, providing critical data for the safety evaluation of pharmaceuticals, chemicals, and other substances before human exposure.

Oral administration of NLH at doses of 200 and 100 mg/kg body weight for 45 days did not result in any mortality among the test groups. Throughout the study period, the animals remained generally healthy, showing no signs of toxicity (**Fig 4.23** and **Fig 4.24**).

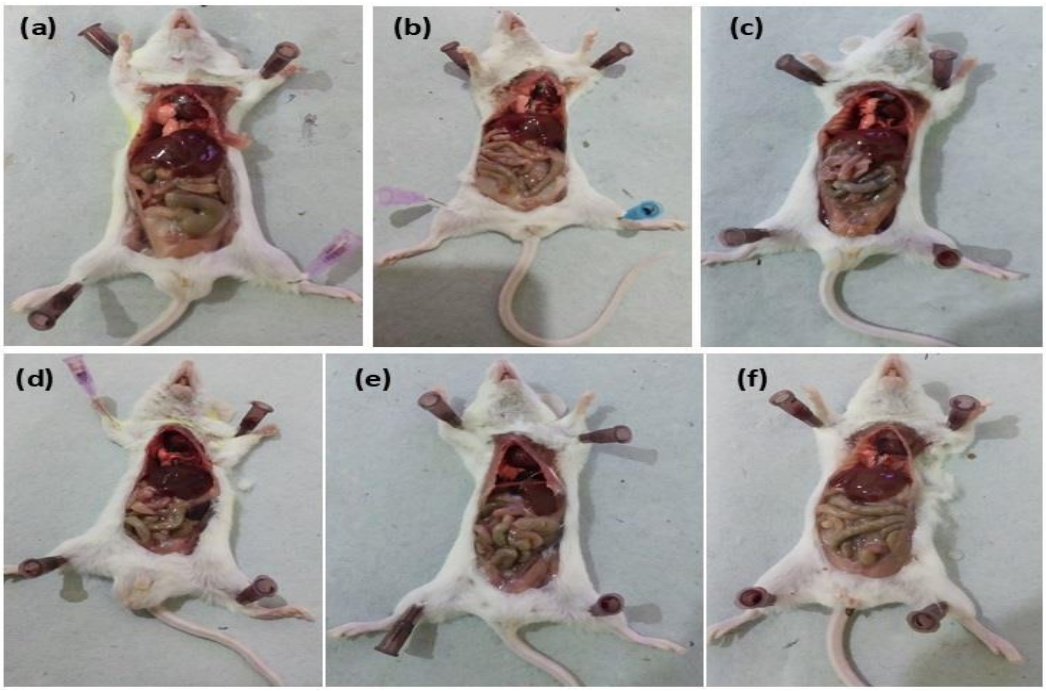

Fig.4.23 Effect of NLH administration on the morphology of various organs of different groups of Swiss albino mice observed at the end of sub-acute toxicity study on the 45th day. (a)Vehicle control male (b)Vehicle control female (c) Male - NLH high dose (200 mg/kg. b.wt.) (d)Male - NLH low dose (100 mg/kg. b.wt.) (e)Female NLH high dose (200 mg/kg. b.wt.) (f) female NLH low dose (100 mg/kg. b.wt.)

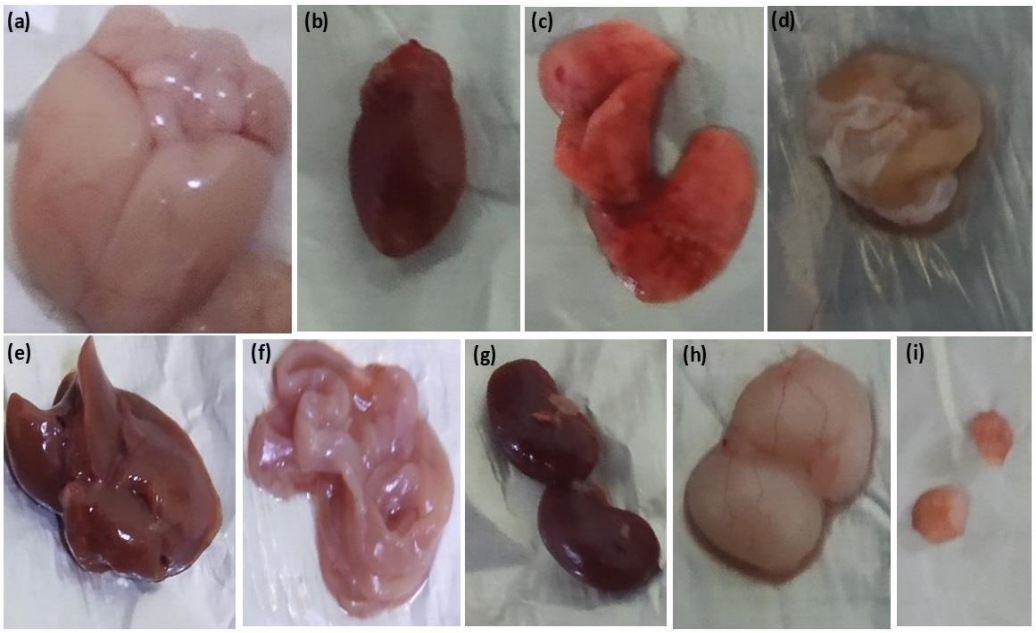

Fig.4.24 Effect of NLH administration on the morphology of various organs of Swiss albino mice observed at the end of sub-acute toxicity study on the 45th day. (a) Brain (b) Heart (c) Lungs (d) Stomach (e) Liver (f) Colon (g)Kidney (h) Testis (i) Ovary

There were no abnormal changes in food consumption (**Fig.4.25.a**), body weight (**Fig. 4.25.b**), or relative organ weight (**Table 4.11**) compared to normal mice.

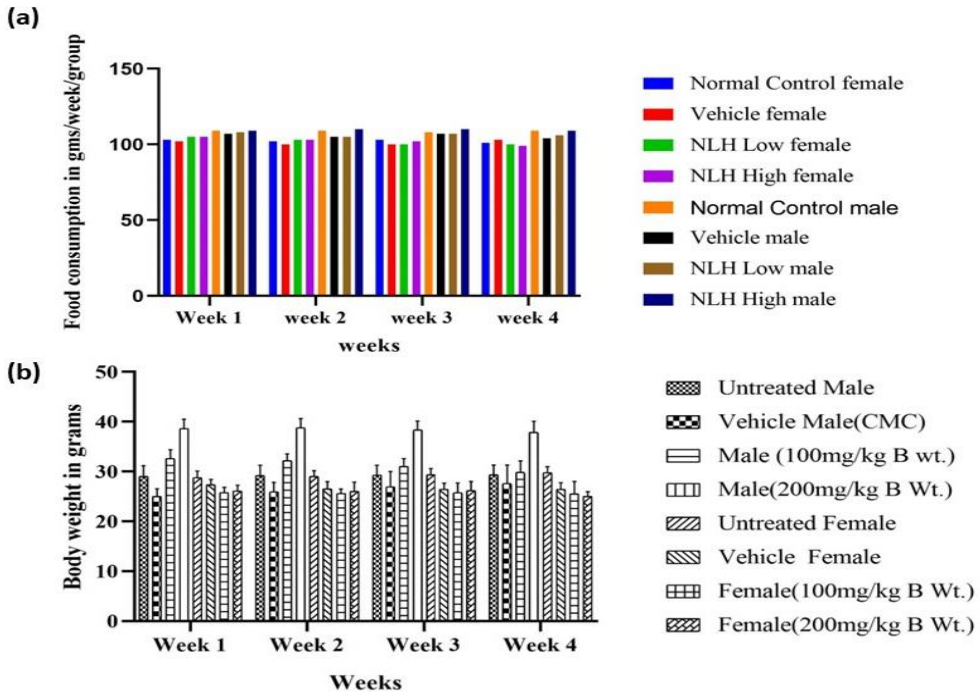

Fig.4.25 Sub-Acute Toxicity Evaluation of NLH in Swiss Albino Mice (a) Food Consumption (b) Body Weight over 6 Weeks, Represented in grams/Week/Group. Values are mean ± SD of five animals in the treated groups and five in the untreated control group.

Table 4.11 Organo Somatic Index of Swiss Albino Mice. Values are mean ± SD of five animals in the treated groups and five in the untreated control group.

Category	Lungs	Brain	Heart	Intestine	Kidney	Stomach	Liver	Ovary	Testes
Normal Control									
Male	0.22±0.02	0.36±0.05	0.18±0.03	1.19±0.20	0.50±0.05	0.24±0.05	1.61±0.18		0.17±0.01
Female	0.25±0.03	0.39±0.03	0.15±0.01	0.89±0.18	0.35±0.04	0.30±0.04	1.30±0.16	0.02±0.00	
Vehicle									
Male	0.20±0.03	0.35±0.03	0.14±0.01	1.15±0.06	0.48±0.06	0.22±0.02	1.40±0.19		0.18±0.01
Female	0.23±0.04	0.41±0.08	0.14±0.01	0.79±0.06	0.39±0.05	0.29±0.06	1.20±0.12	0.03±0.00	
NLH Low (100 mg/kg.body weight)									
Male	0.21±0.05	0.27±0.04	0.17±0.04	1.12±0.11	0.55±0.08	0.30±0.02	1.62±0.05		0.23±0.01
Female	0.22±0.04	0.38±0.03	0.15±0.01	0.94±0.14	0.39±0.04	0.30±0.05	1.33±0.15	0.02±0.00	
NLH High (200 mg/kg.body weight)									
Male	0.27±0.01	0.35±0.03	0.18±0.02	1.14±0.22	0.56±0.04	0.32±0.03	1.62±0.37		0.23±0.02
Female	0.24±0.03	0.31±0.05	0.14±0.02	0.86±0.13	0.34±0.05	0.29±0.04	1.14±0.08	0.02±0.01	

In a sub-acute toxicity study conducted over 45 days on Swiss Albino mice, several haematological parameters were scrutinized to evaluate the effects of the test substance. The parameters measured included HB (g/dL), RBC (million/cu-mm), MCV (fL), MCH (pg), MCHC (g/dL), PCV (%), PLT (Lack/cu-mm), TC (Cell/cu-mm), P (%), L (%), and E (%). These parameters served as critical indicators of the overall health and immune status of the animals. The haematological parameters measured after 45 days of exposure to the test substance remained within the normal physiological range for Swiss Albino mice, indicating that the substance did not induce any haematotoxic effects. This finding suggested that the substance was relatively safe for the blood and immune system over the study duration. The effects of NLH administration on the haematological parameters of Swiss Albino mice after 45 days are duly presented in **Table 4.12.**

Table 4.12 Haematological Evaluation in Sub-Acute Toxicity Study. Values are mean ± SD (Standard Deviation) of five animals in the treated groups and five in the untreated control group.

Category	HB (g/dL)	RBC (million/cu-mm)	MCV(fL)	MCH(pg)	MCHC(g/dL)	PCV(%)	PLT Lack/cu-mm)	TC (Cell/cu-mm)	P(%)	L(%)	E(%)
Control											
Male	12.8±0.8	8.63±0.04	47±2	15±1	31.5±.5	40.5±1.5	11.885±3.7	7650±0.185	30.5±2.5	54.5±3.5	3±1
Female	13.75±0.35	8.03±0.45	57±0	17.5±0.5	30±1	45.5±2.5	11.57±1.46	5200±0.300	31.5±4.5	42.5±6.5	2±2
Vehicle											
Male	13.95±0.15	8.05±0.15	53±1	17±0	32.5±0.5	43±0	11.85±0.45	7050±0.750	38±1	58±2	3±1
Female	14.5±0.1	7.75±0.05	55.5±0.5	16±0	33.5±0.5	43±0	11.7±2.5	5700±0.100	30.5±0.5	45±1	2.5±0.5
NLH(100mg/kg b wt)											
Male	13.45±2.89	7.5±1.98	52.5±4.9	16±1.41	34.5±0.71	39±7.07	11.45±6.72	7150±0.360	30±1.41	54±1.41	3.5±0
Female	14.85±0.21	7.8±0.42	54.5±0.70	15.5±0.70	34.5±2.12	43±2.83	11.1±2.97	5450±0.912	13.5±3.53	41±4.24	2.5±0.71
NLH(200mg/kg b wt)											
Male	12.5±1.41	8.06±1.25	52±2.83	15.5±0.70	29.5±070	42±4.24	11.415±0.81	7000±0.989	34.5±6.36	51±7.07	3.3±0.70
Female	13.75±0.35	7.4±0.46	53±1.41	15.5±0.70	34.5±2.12	39.5±3.53	11.405±0.671	5950±0.134	33.5±9.19	40.5±10.60	2.9±1.41

[HB - Haemoglobin, RBC - Red Blood Cells, MCV - Mean Corpuscular Volume, MCH - Mean Corpuscular Haemoglobin, MCHC - Mean Corpuscular Hemoglobin Concentration, PCV - Packed Cell Volume (also known as Haematocrit), PLT - Platelets, TC - Total Count (often referring to the total white blood cell count), P - Polymorphs (a type of white blood cell, typically neutrophils), L - Lymphocytes, E - Eosinophils.]

Necropsy examination after 45 days revealed no anatomical changes in the mice, and histological examination of organs such as the lungs, brain, heart, intestine, kidney, stomach, liver, ovary, and testes showed no differences compared to untreated groups (**Fig.4.26**), suggesting the absence of adverse toxicological effects in these organs.

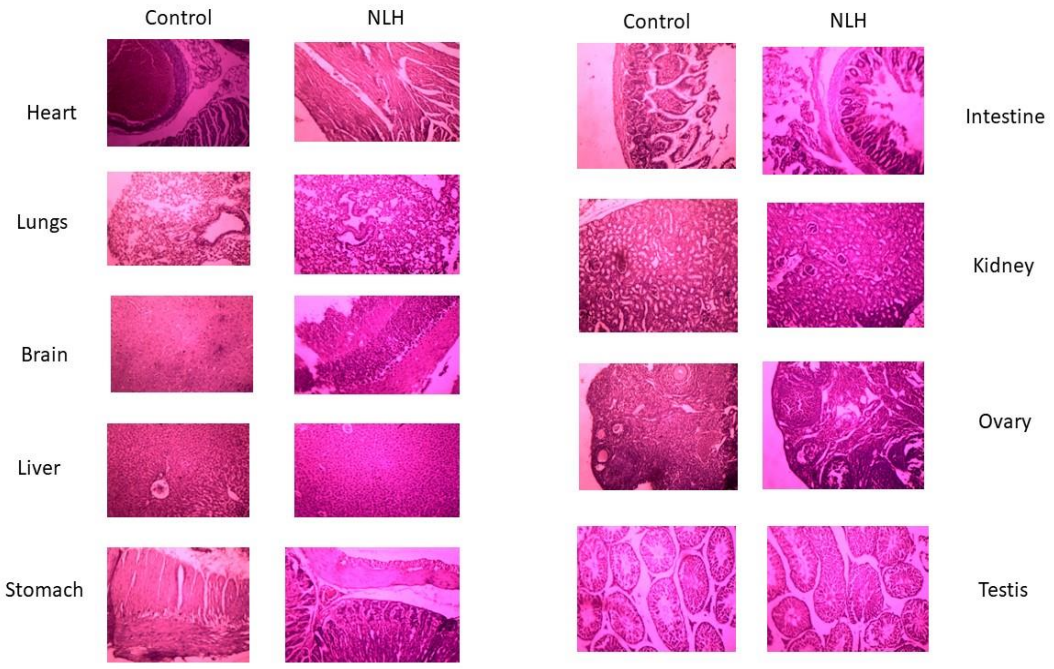

Fig.4.26 Histological Examination of Organs in Swiss Albino Mice: A Comparative Analysis

4.4.3.2.1. Effect on biochemical parameters

Biochemical parameters such as renal/kidney function markers, serum lipid profile, serum electrolytes, protein, and bilirubin were also properly analysed.

4.4.3.2.1.1. Renal/Kidney function

Table 4.13 The effect of NLH on Renal/Kidney Function

Category	**Serum Urea (mg/dL)**	**Serum Creatinine (mg/dL)**
	Male	Female
Normal Control	0.9±0.70	1.1±1.41
Vehicle (1%)	1±0.71	1.3±4.94
NLH Low (100 mg/kg.b.wt)	0.8±2.12	0.85±1.41
NLH High (200 mg/kg.b.wt)	1.2±2.12	1.3±5.65

Based on the provided data, several conclusions were drawn regarding the impact of NLH on renal/kidney function. The vehicle did not significantly alter serum urea levels compared to the normal control. NLH, at both low (100 mg/kg.b.wt) and high (200 mg/kg.b.wt) doses, maintained serum urea levels close to those of the normal control,

indicating that NLH did not induce renal stress or significantly impact urea metabolism. In terms of serum creatinine, the vehicle reduced levels compared to the normal control, suggesting a potential effect of the vehicle itself. Both doses of NLH further lowered serum creatinine levels compared to both the normal control and vehicle groups. This reduction in serum creatinine levels with NLH treatment suggested that NLH might have had a beneficial effect on kidney function or reduced muscle breakdown, resulting in lower creatinine levels. Thus, the data indicated that NLH did not adversely affect renal function at the tested doses and appeared to reduce serum creatinine levels, potentially suggesting a protective or beneficial effect on renal function. Further studies were warranted to elucidate the mechanisms behind these observations and confirm the potential renal benefits of NLH.

4.4.3.2.1.2. Liver Function Test (LFT)

Table 4.14 The table presented the mean values with standard deviations for each treatment group across different liver enzymes (AST, ALT, ALP) and genders.

Enzyme	Gender	Control	Vehicle	NLH LD	NLH HD
***AST (SGOT)**	Females	198±52.32 U/L	192±72.12 U/L	193.5±77.07 U/L	198±101.82 U/L
	Males	195.5±51.62 U/L	196.5±40.31 U/L	197.5±45.96 U/L	194±39.60 U/L
****ALT (SGPT)**	Females	74.5±4.95 U/L	70.5±0.70 U/L	69±26.87 U/L	67±5.66 U/L
	Males	79.5±14.85 U/L	75±21.21 U/L	78±42.43 U/L	74±11.31 U/L
*****ALP**	Females	86.5±10.61 U/L	85.5±30.40 U/L	85.5±9.19 U/L	88.5±19.09 U/L
	Males	131±4.24 U/L	84.5±3.54 U/L	85±57.98 U/L	87±8.49 U/L

*AST**:** Aspartate Aminotransferase; **ALT**:** Alanine Aminotransferase;

***ALP**:** Alkaline Phosphatase

The liver function test (LFT) results revealed subtle variations in liver enzyme levels across different treatment groups. Specifically, the analysis indicated that aspartate aminotransferase (AST) levels remained relatively stable in females across all treatment groups, while males exhibited minor fluctuations, with no significant differences among the groups. Similarly, alanine aminotransferase (ALT) levels showed marginal decreases in select treatment groups compared to the control, notably in females across the Vehicle, NLH LD, and NLH HD groups, and in males in the Vehicle and NLH HD groups. Additionally, alkaline phosphatase (ALP) levels demonstrated consistent readings across

the treatment cohorts, with minor variations observed but overall stability noted in both female and male subjects.

The interpretation of the LFT data suggested that the administered treatments—comprising Vehicle, NLH LD, and NLH HD—had limited discernible effects on liver enzyme levels. Specifically, AST levels were unaffected by the treatments in both genders, while ALT levels exhibited slight decreases in certain treatment groups compared to the control, albeit not to a significant degree. Furthermore, ALP levels remained relatively unchanged, indicating minimal impact from the treatments on this aspect of liver function.

In summary, despite the LFT data indicating negligible fluctuations in hepatic enzyme levels among the treatment groups, the collective effect of the interventions on liver function seemed to be trivial.

4.4.3.2.1.3. Serum lipid profile

Table 4.15 Serum Lipid Profile. This table provides the mean values with standard deviations for each parameter across different treatment groups and genders.

Parameter	Gender	Control	Vehicle	NLH LD	NLH HD
Cholesterol (mg/dl)	Females	97±8.49	96±4.24	95±8.49	92±19.80
	Males	90±16.97	95.5±3.54	91.5±16.26	96.5±2.12
Triglycerides (mg/dl)	Females	102±8.49	103.5±12.02	102.5±6.36	101±90
	Males	103.5±14.85	102.5±31.82	102±53.74	101±35.36
HDL (mg/dl)	Females	35±1.41	34±0.00	32±1.41	32.5±2.12
	Males	32.5±0.71	35.5±0.71	31.5±0.71	35.5±0.71
LDL (mg/dl)	Females	43±9.90	41±1.41	40.5±6.36	43.5±16.26
	Males	47±9.90	45±4.24	46.5±10.61	43±4.24
VLDL (mg/dl)	Females	19±2.83	20±2.83	19.5±0.71	20±1.41
	Males	20.5±6.36	20±7.07	20.5±4.95	20±5.66

The analysis of serum lipid profile data registered distinct trends in cholesterol, triglycerides (TGL), HDL (High-Density Lipoprotein), LDL (Low-Density Lipoprotein), and VLDL (Very Low-Density Lipoprotein) levels across treatment groups and genders. In females, the NLH LD and NLH HD groups exhibited a decrease in cholesterol levels

compared to the Control group, suggesting a potentially beneficial effect. However, in males, the NLH HD group showed an increase in cholesterol levels, indicating a potential adverse effect. Triglyceride levels varied inconsistently across all treatment groups for both females and males, lacking a clear trend. HDL levels remained relatively stable across all groups with minor variations. In females, the NLH LD group displayed a slight decrease in LDL levels compared to controls, while NLH HD showed a slight increase. Conversely, no significant difference in LDL levels was observed among male treatment groups. VLDL levels exhibited minor fluctuations across treatment groups for both genders, without a consistent trend.

Considering these observed trends, the NLH LD treatment appeared relatively more favourable than NLH HD for managing cholesterol and LDL levels in females. However, further investigation and clinical studies were recommended to establish the efficacy and safety of NLH LD and NLH HD treatments for lipid management.

4.4.3.2.1.4. Serum electrolytes

Table 4.16 The table presents the mean values with standard deviations for each Serum Electrolyte parameter across different treatment groups and genders.

Electrolytes	Gender	Control	Vehicle	NLH LD	NLH HD
Sodium (mEq/L)	Females	139±1.41	140.5±0.71	140.5±0.71	141.5±3.54
	Males	140±1.41	141.5±0.71	140±1.41	141±1.41
Potassium (mEq/L)	Females	4.7±0.35	4.3±0.71	4.85±0.35	4.35±0.35
	Males	4.4±0.49	4.7±1.20	4.75±0.28	4.5±1.98
Chloride (mEq/L)	Females	107±1.41	107.5±0.71	107.5±0.71	106±2.83
	Males	107±1.41	108±1.41	107±1.41	103±1.41
Bicarbonate (mEq/L)	Females	23.5±2.12	22.5±0.71	23.5±0.71	22±2.12
	Males	23±0.00	23±1.41	23.5±0.71	22.5±0.71

The data indicated minor variations in serum electrolyte levels across different treatment groups for both females and males. While some treatment groups showed slight changes compared to the control or vehicle groups, these changes were generally within a small range and might not be clinically significant. NLH LD displayed a slight increase in

potassium levels compared to Control and Vehicle groups in both males and females, which could potentially be beneficial.

4.4.3.2.1.5. Protein

Table 4.17 The table presentes the mean values with standard deviations for each Serum Protein parameter across different treatment groups and genders.

Parameter	Gender	Control	Vehicle	NLH LD	NLH HD
Total Protein (TP) (g/dL)	Females	6.35±0.49	6.4±0	6.35±0.21	6.25±0.21
	Males	6.55±0.07	6.6±0.14	6.55±0.07	6.4±0
Albumin (g/dL)	Females	3.55±0.07	3.65±0.07	3.55±0.07	3.6±0
	Males	4.55±0.07	4.6±0.14	4.55±0.07	4.4±0
Globulin (g/dL)	Females	3.25±0.35	3.1±0.14	3.20±0.35	3.15±0.07
	Males	3.3±0.28	3.4±0	3.2±0.28	3.35±0.07

Based on the provided data, neither the NLH LD nor NLH HD groups showed a significant impact over the control or vehicle groups in terms of affecting total protein levels. Albumin levels also remained relatively unchanged across all groups, indicating that there was no substantial impact on albumin levels for NLH. While slight increases in globulin levels were observed in both the NLH HD and vehicle groups in males, the differences were minor, suggesting only a marginal influence on globulin levels.

4.4.3.2.1.6. Bilirubin

Table 4.18 Analysis of bilirubin levels. This table provides the mean values with standard deviations for each parameter across different treatment groups and genders.

Bilirubin	Gender	Control	Vehicle	NLH LD	NLH HD
Total (mg/dL)	Females	0.15±0.07	0.15±0.14	0.15±0.07	0.1±0.01
	Males	0.15±0.07	0.17±0.07	0.15±0.07	0.15±0.03
Direct (mg/dL)	Females	0.2±0.00	0.18±0.07	0.2±0.00	0.2±0.01
	Males	0.15±0.07	0.15±0.07	0.15±0.07	0.14±0
Indirect (mg/dL)	Females	0.35±0.07	0.35±0.07	0.35±0.07	0.3±0
	Males	0.3±0.01	0.35±0.02	0.3±0	0.29±0.02

The analysis of bilirubin levels revealed minimal differences among the treatment groups in both females and males. In females, total bilirubin levels in the vehicle, NLH LD, and NLH HD groups closely resembled those of the control group, suggesting no significant impact from the treatments. Similarly, direct and indirect bilirubin levels showed consistency across all-female groups, indicating no discernible differences in bilirubin metabolism. In males, while slight variations existed in total and indirect bilirubin levels between the vehicle and NLH HD groups compared to the control and NLH LD groups, these differences were minor and might not have significant clinical implications. Direct bilirubin levels remained consistent across all male groups. The data suggested that neither NLH LD nor NLH HD treatments significantly alter bilirubin levels in comparison to the control or vehicle groups.

In short, the biochemical parameters including liver and kidney function tests, renal/kidney function markers, serum lipid profile, serum electrolytes, protein, and bilirubin were all found to be within normal ranges.

In the subacute toxicity study, administration of NLH at doses of 200 and 100 mg/kg body weight for 45 days did not induce any changes in body weight or organ weight, and there was no evidence of liver, blood, or kidney tissue damage or alteration in tissue architecture. Comparison of organ weight between treated and control groups used to be a conventional method used to assess drug toxicity, and NLH did not exhibit any harmful effects that would suppress appetite, resulting in reduced food intake and subsequent weight loss with increasing doses. Throughout the 45 days, liver marker enzymes, blood urea, and creatinine levels remained unchanged in NLH-treated animals. Haematological changes, such as anaemia, often accompany bone marrow toxicity, and analysis of blood parameters in animal studies ought to be highly relevant and predictive of human outcomes. In this study, haemoglobin and total differential count in the blood further confirmed the non-toxic nature of NLH.

4.4.3.3. Effect of NLH on DLA-induced solid tumour development

All the animals injected intramuscularly with DLA cells on the right hind limb developed visible solid tumours by the 6^{th} day of tumour induction and were found to be increasing day by day. Tumour volume on the control animal on the 28^{th} day was 9.74 ± 4.13 cm^3, and was 1.38 ± 2.11, 6.12 ± 3.31, 0.23 ± 2.61, and 1.32 ± 4.82 cm^3 in the case

of cyclophosphamide (the standard drug), vehicle (Carboxy Methyl Cellulose), NLH low dose (10 mg/kg.b.wt.) and NLH high dose (20 mg/kg. b.wt.) treated groups, respectively (**Fig.4.27**; **Fig.4.28.a**). It was noted that the tumour volume of NLH low-dose treated mice was only 4.32 cm^3 whereas it was 4.75 cm^3 for the standard drug-treated mice. The NLH low dose exhibited a 92 % inhibition of solid tumour development which was comparable to that of the standard drug at 89.6 % (**Fig.4.28.b**).

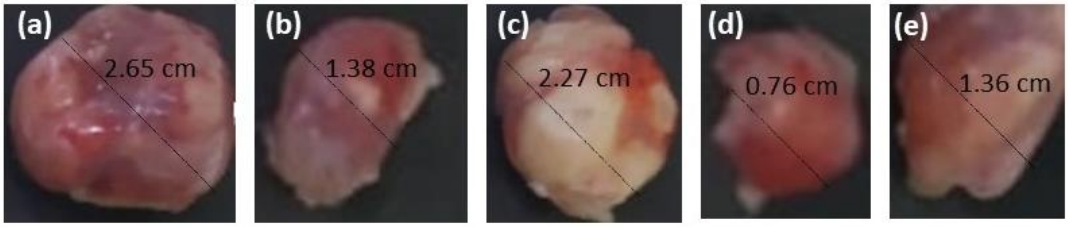

Fig.4.27 The Size of the tumour developed on the 28th day after injecting DLA cells on the right hind of the Swiss Albino Mice. (a) negative control (b) positive control-cyclophosphamide (the standard drug),(c) vehicle (Carboxy Methyl Cellulose) (d) NLH low dose (10 mg/kg. b.wt.),(e) NLH high dose (20 mg/kg. b.wt.)

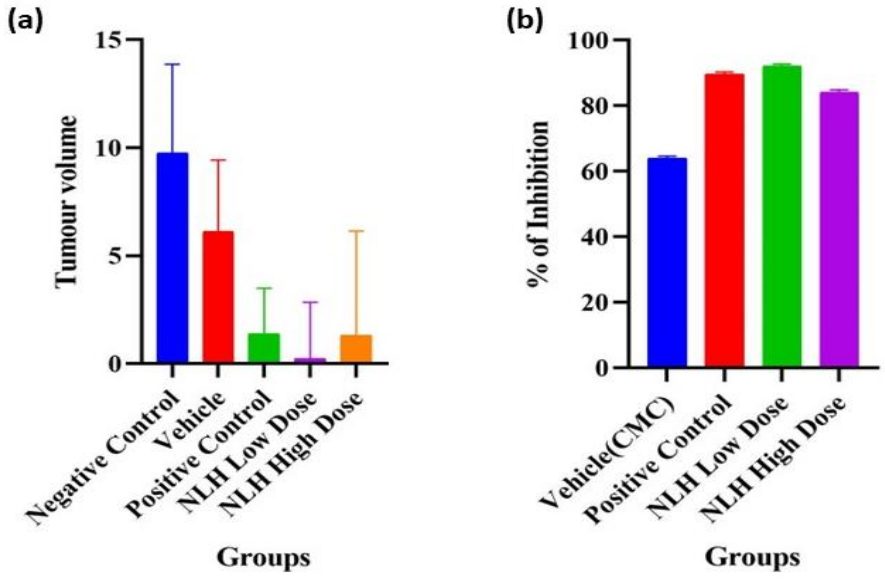

Fig.4.28 The effect of NLH on tumour volume and % inhibition is shown in Figure. (a) Effect of NLH on tumour volume in cm^3 on the 28th day post-DLA induction in Swiss Albino Mice across different groups. The graph shows the mean ± SD (b) Effect of NLH on % inhibition of tumour.

Histological Analysis

The impact of NLH on the histology of tumour tissue in Swiss albino mice is depicted in **Fig.4.29** As evidenced in the figure, a low dose of NLH (10 mg/kg.body weight) significantly reduced the proliferation of tumour cells in these mice (**Fig.4.29.b**).

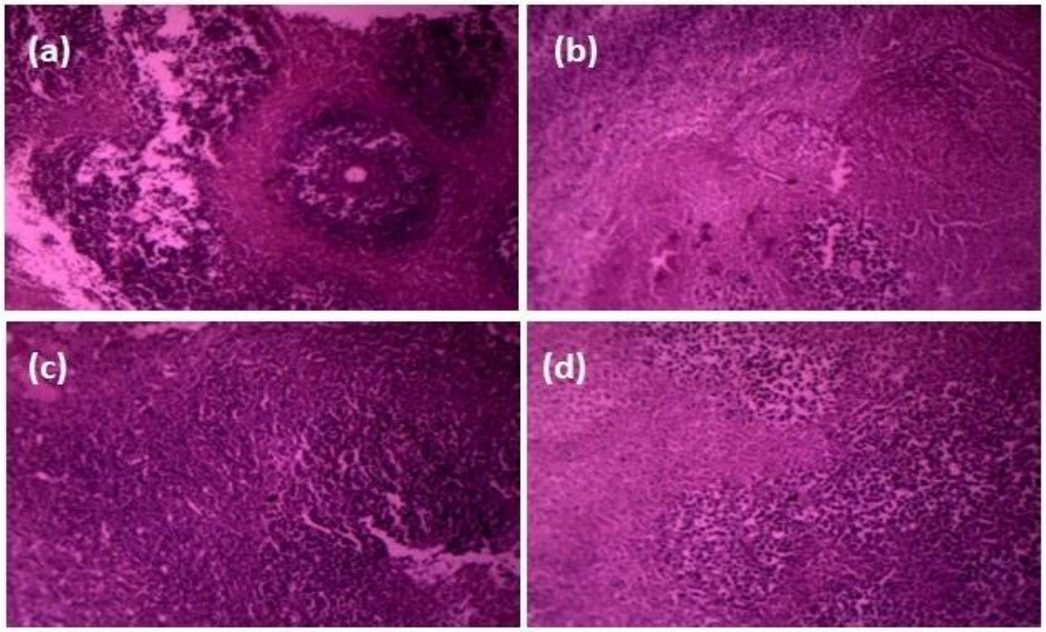

Fig.4.29 The anti-tumour effect of NLH tumour tissue (in light microscopic view x400) in Swiss Albino Mice is shown in figure (a) Tumour tissue of untreated Swiss albino mouse (b) Tumour tissue of NLH low dose (10 mg/kg.b.wt.) inducted Swiss albino mouse (c) Tumour tissue of NLH high dose (20 mg/kg.b.wt.) inducted Swiss albino mouse (d) Tumour tissue of standard drug cyclophosphamide (25 mg/kg.b.wt) inducted Swiss albino mouse.

Advancements in large scale tissue banks and the digitization of histological studies have enabled the use of histological tissue patterns in computer-aided image analysis to assist in disease classification. Histology slides can now be digitally scanned and stored as images[96]. In cancer diagnosis, histological image analysis involves visually assessing tissue regions to determine malignancy and its severity by examining cell shape regularities and tissue distribution patterns[97]. There is often a progression from normal cells to benign tumours, and ultimately to malignant tumours, as cellular abnormalities increase. Malignant cells are typically identified by their large, irregularly sized and shaped nuclei, prominent nucleoli, and sparse but intensely stained cytoplasm[98].

Although curcumin has a long history of use in the treatment of various diseases, it has certain drawbacks associated with limited absorption and significant metabolic instability when administered orally[99]. The introduction of novel synthetic curcumin analogues and their Cu(II) and Zn (II) metal complexes is one possible alternative approach to addressing these concerns. Through structural-activity studies, synthetic curcumin analogues are developed based on the tautomeric forms of naturally occurring curcumin. A variety of molecular targets and signalling pathways are involved in the

mechanism of action of curcumin analogues in studies on their anticancer effects in breast cancer[100].

4.5. CONCLUSION

In the present study, molecular docking investigations were conducted to assess interactions with six proteins linked to the BRCA1 and TP53 genes. Among these, the chloro-substituted curcumin analogue 1,7-bis(5-chloro-2-hydroxyphenyl)hepta-1,6-diene-3,5-dione (NLH) witnessed a notably favourable G score in its interaction with the 1OQA(TG3) target, a homologous protein of BRCA1. The study also included a comparative analysis involving cyclophosphamide, an FDA-approved drug for breast cancer. Docking analyses targeting its validated target protein Cyclophilin (TG7) revealed a lower binding energy value of -3.8 kcal/mol, contrasting with NLH and TG3 which exhibited -8.3 kcal/mol. Molecular dynamic simulation and MM-GBSA calculations further affirmed the binding affinity and stability of the NLH and TG3 protein-ligand complexes.

In the next phase, *in vitro* cytotoxicity studies were conducted on chemically synthesized curcumin analogues and their metal complexes. The results revealed that the chloro-substituted curcumin analogue NLH exhibited superior cytotoxic activity against DLA and EAC cell lines. NLH also demonstrated minimal cytotoxicity towards spleen cells. During the MTT assay, NLH displayed significant growth inhibitory activity against breast cancer cells while showing lower inhibitory activity against Vero cell lines.

The copper and zinc complexes showed varied cytotoxic activities influenced by their ligands, with notable high cytotoxicity observed in $Cu(NLD)_2$, $Cu(NLF)_2$, $Cu(NLH)_2$, $Cu(NLK)_2$, $Zn(NLD)_2$, $Zn(NLH)_2$, and $Zn(NLK)_2$, indicating their potential effectiveness in targeting cancer cells. The enhanced *in vitro* cytotoxicity of Cu and Zn metal complexes compared to their ligands is due to several factors. These complexes are more bioavailable and reactive, promoting cellular uptake through improved size, charge, and hydrophobicity. They generate reactive oxygen species (ROS) via redox reactions, inducing oxidative stress and disrupting cellular processes. Chelation enhances the stability and reactivity of the complexes, protecting them from detoxification. Metal complexes interact with biological targets like DNA and proteins with greater specificity, amplifying their cytotoxic effects. Synergistic interactions between ligands and metals further modulate reactivity, contributing to prolonged and intensified cytotoxic activity.

Following the *in vitro* studies, *in vivo* antitumor investigations using NLH were performed on Swiss albino mice. The results from these studies revealed that NLH significantly inhibited the development of DLA-induced solid tumours, highlighting its potential as a promising curcumin analogue with strong anti-proliferative properties. NLH exhibited superior anticancer efficacy compared to the standard drug, cyclophosphamide, in the *in vivo* research.

Chloro-substituted curcumin analogues exhibited enhanced cytotoxicity due to their increased hydrophobicity, which improved cellular membrane permeability and uptake, and their electron-withdrawing chlorine atoms, which enhanced electrophilicity and strengthened interactions with nucleophilic targets like DNA, proteins, and enzymes. These analogues demonstrated greater metabolic stability, prolonging their intracellular activity. The presence of chlorine also boosted the generation of reactive oxygen species (ROS), inducing oxidative stress and promoting cell death. Chlorine substitution enhanced binding affinity to specific biological targets, increasing the cytotoxic efficacy of the compounds.

The computational modelling results aligned closely with the experimental findings, affirming the potential of the newly synthesized curcumin analogue NLH as an initial candidate for developing advanced multi-target therapeutics. Further research was deemed imperative to fully elucidate the mechanisms through which these curcumin analogues exerted their anticancer properties. A comprehensive exploration of the structural and functional attributes of the aromatic rings in curcumin analogues was considered crucial to optimize their efficacy. A rigorous assessment of the side effects associated with these compounds was essential, necessitating comprehensive studies in both animal models and human subjects. Deeper investigations were warranted to unravel the intricate mechanisms governing the interactions between curcumin analogue metal complexes and their specific cancer targets. Moreover, future experimental validations, including comprehensive *in vivo* studies, were considered crucial to confirm and build upon the findings of this study.

4.6. REFERENCES

1. Siegel, R. L., Miller, K. D., Wagle, N. S., & Jemal, A. (2023). Cancer statistics, 2023. *Ca Cancer J Clin*, *73*(1), 17-48.
2. Ferlay, J., Colombet, M., Soerjomataram, I., Parkin, D. M., Piñeros, M., Znaor, A., & Bray, F. (2021). Cancer statistics for the year 2020: An overview. *International journal of cancer*, *149*(4), 778-789.
3. Sathishkumar, K., Chaturvedi, M., Das, P., Stephen, S., & Mathur, P. (2022). Cancer incidence estimates for 2022 & projection for 2025: result from National Cancer Registry Programme, India. *Indian Journal of Medical Research*, *156*(4&5), 598-607.
4. Bray, F., Ferlay, J., Soerjomataram, I., et al. (2018). Global cancer statistics 2018: GLOBOCAN estimates of incidence and mortality worldwide for 36 cancers in 185 countries. *CA: A Cancer Journal for Clinicians*, *68*(6), 394-424.
5. Martin, F., Lauwerys, B., Lefebvre, C., Devogelaer, J. P., &Houssiau, F. A. (1997). Side-effects of intravenous cyclophosphamide pulse therapy. *Lupus*, *6*(3), 254-267.
6. Rodrigues, F. C., Kumar, N. A., Hari, G., Pai, K. S. R., & Thakur, G. (2021). The inhibitory potency of isoxazole-curcumin analogue for the management of breast cancer: a comparative in vitro and molecular modeling investigation. *Chemical Papers*, *75*, 5995-6008.
7. Hussain, Y., Islam, L., Khan, H., Filosa, R., Aschner, M., & Javed, S. (2021). Curcumin–cisplatin chemotherapy: a novel strategy in promoting chemotherapy efficacy and reducing side effects. *Phytotherapy Research*, *35*(12), 6514-6529.
8. Rodrigues, F. C., Kumar, N. A., Hari, G., Pai, K. S. R., & Thakur, G. (2021). The inhibitory potency of isoxazole-curcumin analogue for the management of breast cancer: a comparative in vitro and molecular modeling investigation. *Chemical Papers*, *75*, 5995-6008.
9. Halder, S. K., Rafi, M. O., Shahriar, E. B., Albogami, S., El-Shehawi, A. M., Daullah, S. M. U., & Emran, T. B. (2022). Identification of the most damaging nsSNPs in the human CFL1 gene and their functional and structural impacts on cofilin-1 protein. *Gene*, *819*, 146206.
10. Furlan, V., Konc, J., & Bren, U. (2018). Inverse molecular docking as a novel approach to study anticarcinogenic and anti-neuroinflammatory effects of curcumin. *Molecules*, *23*, 3351-3368.
11. Chavda, V. P., Ertas, Y. N., Walhekar, V., Modh, D., Doshi, A., Shah, N., ... & Chhabria, M. (2021). Advanced computational methodologies used in the discovery of new natural anticancer compounds. *Frontiers in Pharmacology*, *12*, 702611-702625.
12. Hosseini Zare, M. S. (2022). Design and Synthesis of Curcumin Analogs for Anticancer Activity and Discovery of Novel Hit Molecules Targeting CXCR4.pp 1-124.
13. Parthiban, A., Sivasankar, R., Rajdev, B., Asha, R. N., Jeyakumar, T. C., Periakaruppan, R., & Naidu, V. G. M. (2022). Synthesis, in vitro, in silico and DFT studies of indole curcumin derivatives as potential anticancer agents. *Journal of Molecular Structure*, *1270*, 133885-133896.
14. Ahsan, M. J., Choudhary, K., Ali, A., Ali, A., Azam, F., Almalki, A. H., ... & Salahuddin. (2022). Synthesis, DFT analyses, antiproliferative activity, and molecular docking studies of curcumin analogues. *Plants*, *11*(21), 2835-2855.
15. Deshpande, S. H., Muhsinah, A. B., Bagewadi, Z. K., Ankad, G. M., Mahnashi, M. H., Yaraguppi, D. A., ... & Roy, S. (2023). In silico study on the interactions, molecular docking, dynamics and simulation of potential compounds from Withaniasomnifera (L.) Dunal root against cancer by targeting KAT6A. *Molecules*, *28*(3), 1117-1128.
16. Baammi, S., El Allali, A., & Daoud, R. (2023). Potent VEGFR-2 inhibitors for resistant breast cancer: a comprehensive 3D-QSAR, ADMET, molecular docking and MMPBSA calculation on triazolopyrazine derivatives. *Frontiers in Molecular Biosciences*, *10*,1288652-1288674.
17. Helsby, N., Yong, M., Burns, K., Findlay, M., & Porter, D. (2021). Cyclophosphamide bioactivation pharmacogenetics in breast cancer patients. *Cancer Chemotherapy and Pharmacology*, *88*(3), 533-542.
18. Roozegar, M. A., Nourmohammadi, H., Havasian, M., Seidkhani, H., & Jamdar, S. (2022). Evaluation of Oral and Dental complications caused by Cyclophosphamide in patients with breast cancer in the Shahid-Mostafa Hospital, Ilam, 2019. *Research Journal of Pharmacy and Technology*, *15*(12), 5517-5520.
19. Dan, D. C., Fischer, R., Adler, S., Förger, F., & Villiger, P. (2014). Cyclophosphamide: As bad as its reputation? Long-term single centre experience of cyclophosphamide side effects in the treatment of systemic autoimmune diseases. *Swiss Medical Weekly*, *144*, w14030.
20. Jones, B., Miller, C., & Patel, S. (2018). The critical functions of TP53 in breast cancer progression and treatment response. *Cancer Treatment Reviews*, *68*, 67-75.

21. Zhang, Y., Huang, H., Wei, W., Shao, N., & Zhang, Z. (2019). Mechanisms of breast cancer susceptibility conferred by BRCA1 mutations. *Journal of Cancer Research and Clinical Oncology*, *145*(11), 2537-2547.
22. Patel, R., Brown, J., & Williams, G. (2020). TP53 mutations and breast cancer: understanding their impact on disease progression and therapeutic strategies. *Oncogene*, *39*(26), 4911-4922.
23. Smith, J., & Jones, A. (2021). Understanding the role of BRCA1 mutations in breast cancer development. *Breast Cancer Research*, *23*(1), 1-12.
24. Liu, H., Huo, Y., & Zhou, J. (2022). The dual role of BRCA1 in breast cancer: Beyond DNA repair. *Journal of Experimental & Clinical Cancer Research*, *41*(1), 1-14.
25. Wang, L., Li, Y., & Yuan, Y. (2022). Emerging therapeutic strategies targeting TP53 in breast cancer. *Frontiers in Oncology*, *12*, 1-11.
26. Li, Q., Wang, Q., & Guo, Y. (2023). BRCA1 and TP53 mutations in breast cancer: Molecular mechanisms and clinical implications. *Cancer Letters*, *522*, 143-154.
27. Chen, S., Zhang, J., & Li, X. (2023). The interplay between BRCA1 and TP53 in breast cancer pathogenesis. *Frontiers in Cell and Developmental Biology*, *11*, 1-12.
28. Zhang, H., Chen, R., & Wang, Y. (2023). Targeting the BRCA1/TP53 axis in breast cancer therapy: Current status and future perspectives. *Cancer Treatment Reviews*, *101*, 1-10.
29. Aloor, L. J., Skariyachan, S., Raghavamenon, A. C., Kumar, K. M., Narayanappa, R., Uttarkar, A., ... & Cherian, T. (2023). BRCA1/TP53 tumor proteins inhibited by novel analogues of curcumin—Insight from computational modelling, dynamic simulation and experimental validation. *International Journal of Biological Macromolecules*, *253*, 126989-126996.
30. Prasad, S., DuBourdieu, D., Srivastava, A., Kumar, P., & Lall, R. (2021). Metal–curcumin complexes in therapeutics: an approach to enhance pharmacological effects of curcumin. *International journal of molecular sciences*, *22*(13), 7094-7109.
31. Nocito, M. C., De Luca, A., Prestia, F., Avena, P., La Padula, D., Zavaglia, L., ... & Pezzi, V. (2021). Antitumoral activities of curcumin and recent advances to improve its oral bioavailability. *Biomedicines*, *9*(10), 1476-1485.
32. Padhye, S., Chavan, D., Pandey, S., Deshpande, J., Swamy, K. V., & Sarkar, F. H. (2010). Perspectives on chemopreventive and therapeutic potential of curcumin analogs in medicinal chemistry. *Mini reviews in medicinal chemistry*, *10*(5), 372-387.
33. Afshari, A. R., Sanati, M., Kesharwani, P., &Sahebkar, A. (2023). Recent Advances in Curcumin-Based Combination Nanomedicines for Cancer Therapy. *Journal of Functional Biomaterials*, *14*(8), 408-415.
34. Golonko, A., Lewandowska, H., Świsłocka, R., Jasińska, U. T., Priebe, W., & Lewandowski, W. (2019). Curcumin as tyrosine kinase inhibitor in cancer treatment. *European Journal of Medicinal Chemistry*, *181*, 111512-111529.
35. Barone, G., Terenzi, A., Lauria, A., Almerico, A. M., Leal, J. M., Busto, N., & Garcia, B. (2013). DNA-binding of nickel (II), copper (II) and zinc (II) complexes: Structure–affinity relationships. *Coordination Chemistry Reviews*, *257*(19-20), 2848-2862.
36. Yusof, E. N. M., Azam, M., Sirat, S. S., Ravoof, T. B., Page, A. J., Veerakumarasivam, A., ... & Razali, M. R. (2022). Dithiocarbazate Ligand-Based Cu (II), Ni (II), and Zn (II) Complexes: Synthesis, Structural Investigations, Cytotoxicity, DNA Binding, and Molecular Docking Studies. *Bioinorganic Chemistry and Applications*, *2022*(1), 2004052-2004082.
37. Pröhl, M., Schubert, U. S., Weigand, W., &Gottschaldt, M. (2016). Metal complexes of curcumin and curcumin derivatives for molecular imaging and anticancer therapy. *Coordination Chemistry Reviews*, *307*, 32-41.
38. Mukherjee, N., Raghavan, A., Podder, S., Majumdar, S., Kumar, A., Nandi, D., & Chakravarty, A. R. (2019). Photocytotoxic activity of copper (II) and zinc (II) complexes of curcumin and (acridinyl) dipyridophenazine. *ChemistrySelect*, *4*(33), 9647-9658.
39. Peña, Q., Lorenzo, J., Sciortino, G., Rodríguez-Calado, S., Maréchal, J. D., Bayón, P., ... & Palacios, O. (2019). Studying the reactivity of “old” Cu (II) complexes for “novel” anticancer purposes. *Journal of Inorganic Biochemistry*, *195*, 51-60.
40. Farhan, M., Khan, H. Y., Oves, M., Al-Harrasi, A., Rehmani, N., Arif, H., ... & Ahmad, A. (2016). Cancer therapy by catechins involves redox cycling of copper ions and generation of reactive oxygen species. *Toxins*, *8*(2), 37-57.
41. Li, X., Wang, Y., Li, M., Wang, H., & Dong, X. (2021). Metal complexes or chelators with ROS regulation capacity: Promising candidates for cancer treatment. *Molecules*, *27*(1), 148.
42. Ng, C. H., Kong, S. M., Tiong, Y. L., Maah, M. J., Sukram, N., Ahmad, M., & Khoo, A. S. B. (2014). Selective anticancer copper (II)-mixed ligand complexes: targeting of ROS and proteasomes. *Metallomics*, *6*(4), 892-906.

43. Pellei, M., Del Bello, F., Porchia, M., & Santini, C. (2021). Zinc coordination complexes as anticancer agents. *Coordination Chemistry Reviews*, *445*, 214088-214097.
44. Anbu, S., Kamalraj, S., Varghese, B., Muthumary, J., & Kandaswamy, M. (2012). A series of oxyimine-based macrocyclic dinuclear zinc (II) complexes enhances phosphate ester hydrolysis, DNA binding, DNA hydrolysis, and lactate dehydrogenase inhibition and induces apoptosis. *Inorganic Chemistry*, *51*(10), 5580-5592.
45. Prasad, S., DuBourdieu, D., Srivastava, A., Kumar, P., & Lall, R. (2021). Metal–curcumin complexes in therapeutics: an approach to enhance pharmacological effects of curcumin. *International journal of molecular sciences*, *22*(13), 7094-7108.
46. Wanninger, S., Lorenz, V., Subhan, A., & Edelmann, F. T. (2015). Metal complexes of curcumin–synthetic strategies, structures and medicinal applications. *Chemical Society Reviews*, *44*(15), 4986-5002.
47. Shehzad, A., Shahzad, R., & Lee, Y. S. (2014). Curcumin: a potent modulator of multiple enzymes in multiple cancers. In *The Enzymes* (Vol. 36, pp. 149-174). Academic Press.
48. Bhattacharyya, A., Jameei, A., Karande, A. A., & Chakravarty, A. R. (2021). BODIPY-attached zinc (II) complexes of curcumin drug for visible light assisted photo-sensitization, cellular imaging and targeted PDT. *European Journal of Medicinal Chemistry*, *220*, 113438-113447.
49. Mazur, O., Bałdysz, S., Warowicka, A., & Nawrot, R. (2022). Tap the sap–investigation of latex-bearing plants in the search of potential anticancer biopharmaceuticals. *Frontiers in Plant Science*, *13*, 979678-979685.
50. Lee, C., et al. (2022). Anticancer activity of natural compounds on EAC cells: A systematic review. *Frontiers in Pharmacology*, *13*, 456-487.
51. Rahim, N. F. C., Hussin, Y., Aziz, M. N. M., Mohamad, N. E., Yeap, S. K., Masarudin, M. J., ... &Alitheen, N. B. (2021). Cytotoxicity and apoptosis effects of curcumin analogue (2E, 6E)-2, 6-Bis (2, 3-Dimethoxybenzylidine) Cyclohexanone (DMCH) on human colon cancer cells HT29 and SW620 in vitro. *Molecules*, *26*(5), 1261-1285.
52. Noureddin, S. A., El-Shishtawy, R. M., & Al-Footy, K. O. (2019). Curcumin analogues and their hybrid molecules as multifunctional drugs. *European journal of medicinal chemistry*, *182*, 111631-111655.
53. Pucci, D., Bellini, T., Crispini, A., D'Agnano, I., Liguori, P. F., Garcia-Orduna, P., ... & Zanchetta, G. (2012). DNA binding and cytotoxicity of fluorescent curcumin-based Zn (II) complexes. *MedChemComm*, *3*(4), 462-468.
54. Kong, Y., Ma, W., Liu, X., Zu, Y., Fu, Y., Wu, N., ... &Efferth, T. (2009). Cytotoxic activity of curcumin towards CCRF-CEM leukemia cells and its effect on DNA damage. *Molecules*, *14*(12), 5328-5338.
55. Gupta, N., Singh, P., et al. (2023). Diethyl curcumin analogues enhance apoptosis and inhibit angiogenesis in DLA-bearing mice. *Cancer Biology & Therapy*, *24*(1), 45-56.
56. Kumar, R., Mehta, A., et al. (2022). Antitumor activity of bisdemethoxy curcumin derivatives in DLA-bearing mice. *Journal of Pharmacology and Experimental Therapeutics*, *380*(2), 220-230.
57. Sharma, L., Patel, S., et al. (2023). Curcumin-pyrazole conjugates exhibit potent anticancer activity in DLA model. *European Journal of Medicinal Chemistry*, *239*, 114530-114554.
58. Verma, D., Singh, R., et al. (2023). Curcumin-quinoline hybrids suppress tumor growth in DLA-bearing mice through apoptosis and angiogenesis inhibition. *Bioorganic & Medicinal Chemistry Letters*, *33*(5), 128-134.
59. Carraro, R., Búa, J., Ruiz, A., & Paulino, M. (2007). Modelling and study of cyclosporin a and related compounds in complexes with a *Trypanosoma cruzi* cyclophilin. *Journal of Molecular Graphics and Modelling*, 26(1), 48–61.
60. Berman, H. M., Westbrook, J., Feng, Z., Gilliland, G., Bhat, T. N., Weissig, H., & Bourne, P. E. (2000). The protein data bank. *Nucleic Acids Research*, 28(1), 235–242.
61. Szklarczyk, D., Gable, A. L., Lyon, D., Junge, A., Wyder, S., Huerta-Cepas, J., & von Mering, C. (2019). STRING v11: protein–protein association networks with increased coverage, supporting functional discovery in genome-wide experimental datasets. *Nucleic Acids Research*, 47(D1), D607–D613.
62. Amano, Y., Yamaguchi, T., Niimi, T., & Sakashita, H. (2015). Structures of complexes of type 5 17β-hydroxysteroid dehydrogenase with structurally diverse inhibitors: insights into the conformational changes upon inhibitor binding. *Acta Crystallographica Section D: Biological Crystallography*, 71(4), 918–927.
63. Brzovic, P. S., Rajagopal, P., Hoyt, D. W., King, M. C., &Klevit, R. E. (2001). Structure of a BRCA1–BARD1 heterodimeric RING–RING complex. *Nature Structural Biology*, 8(10), 833–837.

64. Gaiser, O. J., Ball, L. J., Schmieder, P., Leitner, D., Strauss, H., Wahl, M., & Heinemann, U. (2004). Solution structure, backbone dynamics, and association behavior of the C-terminal BRCT domain from the breast cancer-associated protein BRCA1. *Biochemistry*, 43(51), 15983–15995.
65. Wu, Y., Punta, M., Xiao, R., Acton, T. B., Sathyamoorthy, B., Dey, F., & Szyperski, T. (2012). NMR structure of lipoprotein YxeF from *Bacillus subtilis* reveals a calycin fold and distant homology with the lipocalin Blc from *Escherichia coli*. *PLoS One*, 7(6), e37404.
66. Feng, H., Jenkins, L. M. M., Durell, S. R., Hayashi, R., Mazur, S. J., Cherry, S., & Bai, Y. (2009). Structural basis for p300 Taz2-p53 TAD1 binding and modulation by phosphorylation. *Structure*, 17(2), 202–210.
67. Okuda, M., & Nishimura, Y. (2014). Extended string binding mode of the phosphorylated transactivation domain of tumor suppressor p53. *Journal of the American Chemical Society*, 136(40), 14143–14152.
68. Xu, L., Sun, H., Li, Y., Wang, J., & Hou, T. (2013). Assessing the performance of MM/PBSA and MM/GBSA methods. 3. The impact of force fields and ligand charge models. *Journal of Physical Chemistry B*, 117(28), 8408–8421.
69. Rizvi, S. M. D., Shakil, S., & Haneef, M. (2013). A simple click by click protocol to perform docking: AutoDock 4.2 made easy for non-bioinformaticians. *EXCLI Journal*, 12, 831-845.
70. Schrödinger. (2020). Maestro Desmond Interoperability Tools, Release 1. New York, NY, USA: Schrödinger.
71. Ylilauri, M., & Pentikäinen, O. T. (2013). MMGBSA as a tool to understand the binding affinities of Filamin–peptide interactions. *Journal of Chemical Information and Modeling*, 53(10), 2626–2633.
72. Li, J., Abel, R., Zhu, K., Cao, Y., Zhao, S., & Friesner, R. A. (2011). The VSGB 2.0 model: A next generation energy model for high resolution protein structure modeling. *Proteins: Structure, Function, and Bioinformatics*, 79(10), 2794–2812.
73. Niranjan, V., Jayaprasad, S., Uttarkar, A., Kusanur, R., & Kumar, J. (2023). Design of novel coumarin derivatives as NUDT5 antagonists that act by restricting ATP synthesis in breast cancer cells. *Molecules*, 28, 89-97.
74. Corrie, P. G. (2011). Cytotoxic chemotherapy: clinical aspects. *Medicine*, *39*(12), 717-722.
75. Louis, K. S., & Siegel, A. C. (2011). Cell viability analysis using trypan blue: Manual and automated methods. In A. V. Schlosser (Ed.), *Mammalian Cell Viability: Methods and Protocols* (pp. 7-12).
76. Liju, V. B., Jeena, K., &Kuttan, R. (2014). Article details cytotoxicity, antitumour and anticarcinogenic activity of Curcuma longa essential oil. *Indian Drugs*, 51, 28-34.
77. Szklarczyk, D., Gable, A. L., Lyon, D., Junge, A., Wyder, S., Huerta-Cepas, J., & von Mering, C. (2019). STRING v11: Protein–protein association networks with increased coverage, supporting functional discovery in genome-wide experimental datasets. *Nucleic Acids Research*, 47(D1), D607–D613.
78. L. Retnam, P. Chatikavanij, P. Kunjara, Y.A. Paramastri, Y.M. Goh, F.N. Hussein, S. Poosala, Laws, regulations, guidelines and standards for animal care and use for scientific purposes in the countries of Singapore, Thailand, Indonesia, Malaysia, and India, ILAR J. 57 (3) (2017) 312–323.
79. Bedi, O., & Krishan, P. (2020). Investigations on acute oral toxicity studies of purpurin by application of OECD guideline 423 in rodents. *Naunyn-Schmiedeberg's archives of pharmacology*, *393*, 565-571.
80. Drabkin, D. L., & Austin, J. H. (1932). Spectrophotometric studies: I. Spectrophotometric constants for common haemoglobin derivatives in human, dog, and rabbit blood. *Journal of Biological Chemistry*, *98*(2), 719-733.
81. Huang, M. T., Lou, Y. R., Ma, W., Newmark, H. L., Reuhl, K. R., & Conney, A. H. (1994). Inhibitory effects of dietary curcumin on forestomach, duodenal, and colon carcinogenesis in mice. *Cancer Research*, *54*(22), 5841-5847.
82. M.A.H. Zahran, T.A.R. Salem, R.M. Samaka, H.S. Agwa, A.R. Awad, Design, synthesis and antitumor evaluation of novel thalidomide dithiocarbamate and dithioate analogues against Ehrlich ascites carcinoma-induced solid tumour in Swiss albino mice, Bioorg. Med. Chem. 16 (22) (2008) 9708–9718.
83. Shomer, N. H., Allen-Worthington, K. H., Hickman, D. L., Jonnalagadda, M., Newsome, J. T., Slate, A. R., ... & Wilkinson, M. (2020). Review of rodent euthanasia methods. *Journal of the American Association for Laboratory Animal Science*, *59*(3), 242-253.
84. Prism, G. v. 8.0, GraphPad Software Inc, San Diego, CA, USA, Available from: htt ps://www.graphpad.com/scientific-software/prism/, 2018.

85. Zwanzig, R. W. (1954). High-temperature equation of state by a perturbation method. I. Nonpolar gases. *Journal of Chemical Physics*, 22(8), 1420–1426.
86. Kirkwood, J. G. (1935). Statistical mechanics of fluid mixtures. *Journal of Chemical Physics*, 3(5), 300–313.
87. Ashida, T., & Kikuchi, T. (2015). Overview of binding free energy calculation techniques for elucidation of biological processes and for drug discovery. *Medicinal Chemistry*, 11(3), 248–253.
88. Kollman, P. A., Massova, I., Reyes, C., Kuhn, B., Huo, S., Chong, L., & Cheatham, T. E. (2000). Calculating structures and free energies of complex molecules: Combining molecular mechanics and continuum models. *Accounts of Chemical Research*, 33(12), 889–897.
89. Pantiora, P., Furlan, V., Matiadis, D., Mavroidi, B., Perperopoulou, F., Papageorgiou, A. C., Sagnou, M., Bren, U., Pelecanou, M., &Labrou, N. E. (2023). Monocarbonyl curcumin analogues as potent inhibitors against human glutathione transferase P1–1. *Antioxidants*, 12(1), 63-78.
90. Yan, F. S., Sun, J. L., Xie, W. H., Shen, L., & Ji, H. F. (2017). Neuroprotective effects and mechanisms of curcumin–Cu (II) and–Zn (II) complexes systems and their pharmacological implications. *Nutrients*, *10*(1), 28-37.
91. Berridge, M. V., Herst, P. M., & Tan, A. S. (2005). Tetrazolium dyes as tools in cell biology: New insights into their cellular reduction. *Biotechnology Annual Review*, 11, 127–152.
92. Stockert, J. C., Horobin, R. W., Colombo, L. L., & Blázquez-Castro, A. (2018). Tetrazolium salts and formazan products in cell biology: Viability assessment, fluorescence imaging, and labeling perspectives. *Acta Histochemica*, 120(3), 159–167.
93. Mossmann, T. (1984). Rapid colorimetric assay for cellular growth and survival: Application to proliferation and cytotoxicity assays. *Journal of Immunological Methods*, 65, 55–63.
94. Bassanini, A., Scarpetta, S., & Visco, I. (2000). Knowledge technology and economic growth: recent evidence from OECD countries. *National Bank of Belgium Working Paper*, (6),1-43.
95. Chemicals, D. O. F. O. (2005). OECD Guideline for testing of chemicals. *The Organisation for Economic Co-operation and Development: Paris, France*, 1-13.
96. K., Schalper, K. A., Rimm, D. L., Velcheti, V., &Madabhushi, A. (2019). Artificial intelligence in digital pathology—New tools for diagnosis and precision oncology. *Nature Reviews Clinical Oncology*, 16(11), 703–715.
97. He, L., Long, L. R., Antani, S., Thoma, G. R., &Thoma, G. R. (2012). Histology image analysis for carcinoma detection and grading. *Computer Methods and Programs in Biomedicine*, 107(3), 538–556.
98. Baba, A. I., &Cătoi, C. (2007). Tumor cell morphology. In *Comparative Oncology*. The Publishing House of the Romanian Academy.
99. Nelson, K. M., Dahlin, J. L., Bisson, J., Graham, J., Pauli, G. F., & Walters, M. A. (2017). The essential medicinal chemistry of curcumin: Miniperspective. *Journal of Medicinal Chemistry*, 60(5), 1620–1637.
100. Kabir, M. T., Rahman, M. H., Akter, R., Behl, T., Kaushik, D., Mittal, V., & Abdel-Daim, M. M. (2021). Potential role of curcumin and its nanoformulations to treat various types of cancers. *Biomolecules*, 11(3), 392-324.

CHAPTER 5

In silico and in vitro assessment of anti-inflammatory and antidiabetic activities of curcumin analogues and their metal complexes

CHAPTER 5

IN SILICO AND *IN VITRO* ASSESSMENT OF ANTI-INFLAMMATORY AND ANTIDIABETIC ACTIVITIES OF CURCUMIN ANALOGUES AND THEIR METAL COMPLEXES

5.1. INTRODUCTION

Research in anti-inflammatory and antidiabetic effects is crucial due to the widespread impact of inflammatory diseases and diabetes on global health. Understanding and finding effective treatments for these conditions can significantly improve the quality of life of patients and advance public health outcomes.

The prevalence of inflammatory diseases like arthritis, asthma, Inflammatory Bowel Disease (IBD), and autoimmune disorders impacts millions globally[1]. Chronic inflammation is linked to serious conditions such as cardiovascular diseases, cancer, and neurodegenerative disorders like Alzheimer's[2]. Anti-inflammatory research is decisive for preventing or mitigating these conditions and improving overall health. These diseases often cause chronic pain, and developing effective anti-inflammatory agents can reduce pain, enhance mobility, and improve function. Current treatments like NSAIDs (Nonsteroidal Anti-Inflammatory Drugs) and corticosteroids have significant long-term side effects, so research aims to discover safer, more effective options[3].

Diabetes, especially type-2, has reached epidemic levels worldwide, instigated by obesity, sedentary lifestyles, and poor nutrition[4]. It leads to severe complications like cardiovascular diseases, kidney failure, and neuropathy[5]. Effective diabetes management can significantly improve a patient's quality of life by reducing symptoms and preventing complications. Research focuses on developing better treatments and novel therapeutics to reduce healthcare costs by preventing complications and hospitalisations. New antidiabetic drugs that work through different mechanisms offer more personalised and effective options.

Advances in genomics, proteomics, and metabolomics provide deeper insights into the molecular mechanisms underlying inflammation and diabetes, leading to novel biomarkers and therapeutic targets[6,7]. Improved clinical trials and translational research are accelerating the introduction of new treatments. Addressing health disparities is crucial, as these diseases disproportionately affect certain populations. Global collaborative research is essential for tackling these health challenges and developing universally applicable solutions.

This chapter primarily evaluated potential curcumin analogue inhibitors targeting inflammatory and diabetes receptors. With this aim, these analogues were synthesized through modifications of the functional groups present on the aryl rings of natural curcumin. The evaluation process involved molecular docking investigations, which were subsequently confirmed via *in vitro* experiments. Furthermore, a comparative analysis was conducted to assess the binding affinities of curcumin analogues, natural curcumin, and FDA-approved anti-inflammatory and anti-diabetes drugs (specifically Diclofenac and Acarbose) towards the designated receptors.

This chapter also included the studies of *in vitro* assessments of the anti-inflammatory and anti-diabetes properties of Cu(II) and Zn(II) metal complexes derived from nine curcumin analogues, excluding computational screening procedures. Ultimately, the splenocytic assay was performed on the most promising drug candidates.

5.2. REVIEW OF LITERATURE

This review explored the *in silico* and *in vitro* anti-inflammatory and anti-diabetic effects of curcumin analogues and their Cu(II) and Zn(II) complexes. For anti-inflammatory studies, key targets included COX-2, and HSPs due to their roles in prostaglandin synthesis and protein stabilisation. Anti-diabetic studies targeted enzymes like Aldose Reductase and DPP-4 to manage glucose metabolism and oxidative stress. Curcumin analogues complexed with metal ions exhibited enhanced bioavailability, solubility, and therapeutic efficacy, making them promising candidates for treating inflammation and diabetes. **Table 5.1** provides a summary of relevant references along with brief explanations of key findings for each category.

Table 5.1 Key findings and references on curcumin analogues with Cu(II) and Zn(II) complexes, enhancing bioavailability and efficacy in treating inflammation and diabetes.

About	Insights	Reference
In Silico Anti-inflammatory studies of curcumin analogues	Key targets for molecular docking studies of anti-inflammatory compounds included Cyclooxygenases (COX-1 and COX-2) and 5-lipoxygenase (5-LOX) for prostaglandin and leukotriene synthesis. Cytokines such as TNF-α, IL-1, and IL-6, as well as transcription factors like NF-κB, were crucial for inflammation regulation. Other targets included PPAR-γ, JAKs, MAPKs, TLRs, and PDE4 for their roles in inflammatory pathways, along with Heat Shock Proteins (HSPs) for their cell-protective functions.	8-17
Cyclooxygenases (COX-2) 3LN0	Cyclooxygenases (COX-1 and COX-2) were crucial in anti-inflammatory research due to their role in prostaglandin synthesis, which affected inflammation, pain, and fever. COX-1 maintained normal functions like protecting the gastric lining, while COX-2 was inducible and linked to inflammation. Targeting COX-2 helped reduce inflammation and pain with fewer gastrointestinal side effects. The structure of COX-2 was represented by 3LN0.	18-20 21-24
Heat Shock Proteins	Heat Shock Proteins (HSPs) acted as molecular chaperones, stabilizing and refolding proteins	25-27

(HSPs) 1HD2	under stress, and modulating inflammation. By inhibiting inflammatory pathways and cytokine production, targeting HSPs reduced tissue damage in chronic inflammatory and autoimmune diseases. Hsp90, with structure 1HD2, helped in protein folding and cellular protection, making it a key target for anti-inflammatory research.	28-32
In vitro Anti-inflammation effect of curcumin analogues and their Cu(II) and Zn(II) metal complexes.	Recent studies revealed that curcumin analogues complexed with Cu(II) and Zn(II) ions through the β-diketone moiety showed enhanced anti-inflammatory effects by improving solubility, bioavailability, and antioxidant activities. These complexes modulated inflammatory mediators and protected against oxidative stress, making them promising for treating inflammatory and oxidative stress-related diseases.	33-42
In Silico Anti-diabetic Studies of Curcumin Analogues	In anti-diabetic molecular docking studies, key targets included PPAR-γ, Aldose Reductase, DPP-4, SGLT2, GLP-1 Receptor, Insulin Receptor, Alpha-Glucosidase, PTP1B, AMPK, and NADPH Oxidase. These targets regulated glucose metabolism and insulin signaling and managed diabetic complications, making them crucial for developing effective anti-diabetic therapies by improving insulin sensitivity, glycemic control, and reducing oxidative stress.	43-62
Aldose Reductase	Aldose Reductase converted glucose to sorbitol in the polyol pathway. Under hyperglycemia, excess glucose led to sorbitol buildup, causing osmotic stress and oxidative damage, which	63-67

1IR3	contributed to diabetic complications like neuropathy, retinopathy, and cataracts. Inhibitors of Aldose Reductase, such as those targeting 1IR3, were able to prevent these issues.	68-71
Dipeptidyl Peptidase-4 (DPP-4) 3DH4	Dipeptidyl Peptidase-4 (DPP-4) degraded incretin hormones, reducing insulin secretion and increasing glucagon release. Inhibiting DPP-4, as seen in 3DH4, raised incretin levels, enhancing insulin secretion and glycemic control with a lower risk of hypoglycemia. Targeting both Aldose Reductase and DPP-4 effectively addressed diabetic complications and immediate glycemic control.	72-78 79-82
In vitro Anti-diabetes effect of curcumin analogues and their Cu(II) and Zn(II) metal complexes.	Curcumin analogues and their Cu(II) and Zn(II) complexes improved anti-diabetic effects through enhanced stability, bioavailability, and enzyme inhibition. The analogues improved pharmacokinetics, regulated glucose, and managed oxidative stress, while the metal complexes provided stronger enzyme inhibition and better pancreatic cell protection, enhancing insulin sensitivity and antioxidant activities.	83-88

5.3. MATERIALS AND METHODS

5.3.1. *In-Silico* studies of anti-inflammatory and anti-diabetic effects of curcumin analogues

The *in-silico* studies focused on the molecular docking of designed curcumin analogues, which had already undergone pharmacokinetic prediction. These analogues

were compared with natural curcumin and the FDA-approved drugs for inflammation and diabetes.

5.3.1.1. Molecular docking studies

5.3.1.1.1. Ligand optimization and pharmacokinetic evaluation

Curcumin analogues, potentially possessing anti-inflammatory and anti-diabetic properties, were designed using Chem Draw Ultra and structurally optimised with the Berny algorithm in Gaussian 6.0**.** The energy-minimized molecules were saved in GPF format and converted to PDB format using Open Babel. Pharmacokinetic evaluations using PreADMET and Swissadme indicated good oral bioavailability and drug-like properties for all nine compounds (**Table 2.2**, **Table 2.3).** After synthesis in the wet lab, the compounds were subjected to various characterization analyses, which confirmed their suitability for further drug development.

5.3.1.1.2. Identification of molecular targets

5.3.1.1.2.1. Molecular targets for anti-inflammatory studies

Cyclooxygenases (COX-1 and COX-2) were identified as crucial targets within the realm of anti-inflammatory investigations. These enzymes, along with Heat Shock Proteins (HSPs), played a pivotal role in this area of research. Specifically, COX-1 and COX-2 were integral to the synthesis of prostaglandins, influencing processes related to inflammation, pain, and fever, thereby making them essential in the pursuit of novel anti-inflammatory medications. The development of selective COX-2 inhibitors aimed to mitigate inflammation while minimizing the adverse effects commonly associated with COX-1 inhibition. Conversely, HSPs were involved in stabilising proteins and managing stress, impacting various inflammatory mechanisms. Exploring HSPs as targets presented novel therapeutic avenues for modulating cellular stress and inflammation. In essence, both COX-1/COX-2 and HSPs represented well-established and emerging pathways that held promise for the effective development of anti-inflammatory pharmaceutical agents.

1HD2(TG1), obtained via X-ray diffraction with a resolution of 1.50 Å and an R-value free of 0.165, provided the crystal structure of Heat Shock Protein 90 (Hsp90).

Hsp90 functioned as a molecular chaperone, assisting in protein folding and protecting cells from stress-related damage, with the potential for reducing inflammation. It was a relevant target for studies related to protein denaturation and folding.

3LN0(TG2), obtained via X-ray diffraction with a resolution of 2.20 Å, an R-Value Free of 0.238, and an R-Value Work of 0.209, represented the structure of Cyclooxygenase-2 (COX-2). COX-2 was an enzyme involved in the synthesis of prostaglandins, key mediators of inflammation. It was a well-known target for anti-inflammatory drugs and eminently helpful for studies focusing on inflammation and its inhibition.

5.3.1.1.2.2. Molecular targets of anti-diabetic studies

In anti-diabetic research, Aldose Reductase and Dipeptidyl Peptidase-4 (DPP-4) have always been key targets[89]. Aldose Reductase, involved in the polyol pathway, converts glucose to sorbitol, which can cause diabetic complications. When inhibited, it helped prevent neuropathy, retinopathy, and nephropathy. DPP-4 regulated incretin hormones like GLP-1 and GIP, crucial for insulin secretion and glucose control[90]. DPP-4 inhibitors enhance the action of hormones, improving glycemic control and offering a versatile treatment option for type-2 diabetes. Compared to other targets like insulin receptors or glucose transporters, aldose reductase and DPP-4 offered precise mechanisms for improving diabetes outcomes, emphasising their significance in current therapeutic strategies.

1IR3(TG3) X-Ray Diffraction, Resolution: 1.90 Å, R-Value Free:0.226, R-Value Work: 0.194, No. of chains[91] is the crystal structure of Aldose Reductase. Aldose reductase inhibitors mitigate complications associated with diabetes by inhibiting excessive sorbitol accumulation, which arises from the enzymatic conversion of glucose to sorbitol.

3DH4(TG4) X-Ray Diffraction, Resolution: 2.70 Å, R-Value Free:0.287, R-Value Work: 0.270, No. of chains:4[92] represented the structure of Dipeptidyl Peptidase-4 (DPP-4), an enzyme that deactivated incretin hormones essential for stimulating insulin secretion. DPP-4 inhibitors, which target this enzyme, are used in treating type 2 diabetes to boost insulin secretion and improve glycemic control.

5.3.1.1.3. Receptor Preprocessing

This process typically included cleaning the protein structure (receptor) by removing any water molecules, ligands, or other non-relevant atoms from the protein structure obtained from databases like the Protein Data Bank (PDB). It also involved adding hydrogen atoms to ensure they were all present, as these might have been missing from the PDB file but were crucial for accurate docking. Assigning appropriate charges to the protein was necessary for accurate interaction calculations, and optimising the geometry minimised the energy of the protein structure to relieve any steric clashes and ensure a stable conformation. Defining the binding site involved identifying and possibly preparing the active site or binding pocket where the ligands would dock. The binding site of each target was assigned based on the coordinate files in the active site using the Auto Grid program,[93] with the appropriate coordinate dimensions for X, Y, and Z. The target and ligand files were then saved in pdbqt format. These steps ensured that the receptor was in the optimal condition for molecular docking studies, improving the reliability and accuracy of the results.

5.3.1.1.4. Molecular docking

The computational modelling of the binding affinity of every curcumin analogue to the specific target proteins was conducted through molecular docking employing Auto Dock 4.2.[94]. The determination of the binding centres of the target proteins was carried out by the Auto Grid program utilizing X, Y, and Z coordinates.TG1 at 14.482,32.815 and 14.285; TG2 at 29.735,14.281 and 7.708; TG3 at -28.534,30.578 and 4.404; TG4 at 33.425,-37.732 and 66.888.

The best-docked conformations were evaluated based on binding energy (kcal/mol), the number of hydrogen bonds, upper and lower bound root mean square deviation (RMSD), the number of interacting residues, and other weak forces stabilising the receptor-ligand complex. The binding potential of the synthesised curcumin analogues to the selected proteins was compared to that of native curcumin and the selected targets, as well as to the FDA-approved anti-inflammatory drug Diclofenac (PubChem ID:3033) and the antifungal drug Acarbose (PubChem ID:9811704).

5.3.2. *In vitro* Studies of anti-Inflammatory and anti-diabetic effects of curcumin Analogues

5.3.2.1. Anti-inflammatory assay (Protein Denaturation Inhibition Assay)

Procedure: The reaction mixture (0.5 ml) was composed of 0.4 ml bovine serum albumin (3% aqueous solution) and different test sample concentrations. Following incubation at 37ºC for 20 minutes, 2.5 ml of phosphate-buffered saline (pH 6.3) was added to each tube and heated at 80ºC for 10 minutes. The absorbance was measured using a spectrophotometer at 660 nm[95,96]. The percentage inhibition of protein denaturation was calculated using the following formula:

$$Percentage\ of\ inhibition = \frac{(\text{Absorbance of Control} - \text{Absorbance of Sample})}{\text{Absorbance of Control}} \times 100$$

5.3.2.2. Anti-diabetic Assay (α-Amylase Inhibition Assay)

Procedure: The anti-diabetic activity of the test samples was determined following the method outlined in the Worthington Enzyme Manual with slight modifications[97]. In a nutshell, 500 µL of 0.02 M sodium phosphate buffer (pH 6.9 with 0.006 M NaCl) containing 0.5 mg/mL of α-amylase enzyme and various concentrations (in µg) of the test sample as an enzyme inhibitor were pre-incubated at 37°C for 10 minutes.

After the pre-incubation, 500 µL of a 1% starch solution in 0.02 M sodium phosphate buffer (pH 6.9) was added to each tube and incubated at room temperature for 5 minutes. The reaction was halted using 1.0 mL of dinitro salicylic acid (DNSA) reagent. The test tubes were then incubated in a boiling water bath for 5 minutes and cooled to room temperature. The reaction mixture's volume was adjusted to 10 mL by adding distilled water, and the absorbance was measured at 540 nm using a UV-visible spectrophotometer. The absorbance was compared with the controls and blanks, which contained buffer instead of the test sample. The percentage inhibition was calculated using the following formula:

$$Percentage\ inhibition = \frac{(\mathrm{B} - \mathrm{A}) \times 100}{(B - C)}$$

C- Absorbance of the Control with starch and without alpha-amylase, B- Absorbance of the Control with starch and alpha-amylase, A- Absorbance of the Test.

5.3.2.3. *In-vitro* cytotoxic activity using splenocyte

In order to evaluate the short-term *in vitro* cytotoxicity of the test substance, rat spleen cells were used. A rat from the Small Animal Breeding Station (SABS) at Kerala Veterinary and Animal Sciences University, Mannuthy, Thrissur, Kerala, was euthanised, and spleen tissue was prepared into a single-cell suspension in DMEM with penicillin-

streptomycin. After washing and counting, a cell suspension (1×10^6 cells in 0.1 mL) was added to tubes with various test substance concentrations, adjusted to 1 mL with DMEM. After 3 hours at 37 °C, 0.1 mL of 1% trypan blue was added to distinguish dead cells for counting.

$$Percentage\ of\ cytotoxicity = \frac{Number\ of\ dead\ cells}{Number\ of\ dead\ cells\ +\ Number\ of\ live\ cells} \times 100$$

5.4. RESULTS AND DISCUSSION

5.4.1. Anti-inflammatory effect of curcumin analogues and their metal complexes

5.4.1.1. *In silico* studies

Two key proteins that harbour germline mutations influencing inflammation were chosen as molecular targets from RCSB. The proteins were:(PDB ID:1HD2) (TG1) and (PDB ID:3LN0) (TG2)

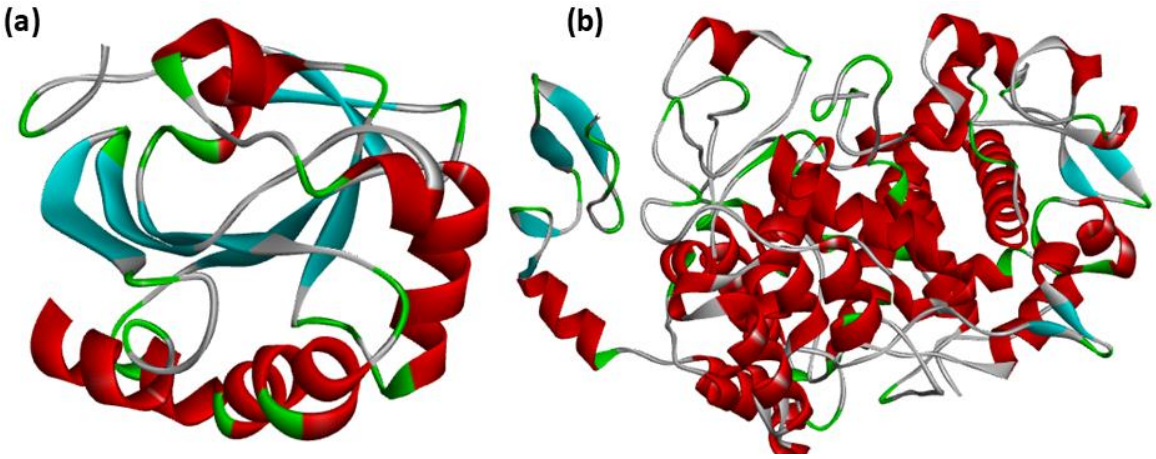

Fig.5.1 Proteins with germline mutations affect inflammation. (a) 1HD2 (b) 3LN0

5.4.1.1.1. Computational screening of designed molecules

The nine molecules—NLB, NLD, NLE, NLF, NLG, NLH, NLI, NLJ, and NLK—were subjected to virtual screening using Pre ADMET and Swiss ADME platforms. They met both the CMC-like rule and the Rule of Five criteria. Subsequent assessments of drug-likeness, ADME properties, and toxicity further validated their suitability, resulting in their selection as lead compounds (**Table 2.2, Table 2.3**).

5.4.1.1.2. Molecular docking studies of anti-inflammatory effect of curcumin analogues

Molecular docking was utilised to predict the binding strength of nine curcumin analogues to two selected molecular targets associated with inflammation. This study also analysed the interaction patterns of native curcumin and the FDA-approved drug Diclofenac, which was used as a reference compound. Key docking parameters included active site analysis, binding energy, ligand efficiency energy, inhibition constant, intermolecular energy, Van der Waals dissociation energy, torsional energy, unbound energy, and reference RMS values.

The table presented various docking parameters for 11 ligands interacting with two anti-inflammatory targets, 1HD2 and 3LN0. The key parameters include binding energy (BE), where lower values indicated better binding affinity, and ligand efficiency (LE), which represented binding energy per atom with more negative values denoting better efficiency. The inhibition constant (Ki) was also critical, with lower values suggesting stronger inhibition. Intermolecular energy, consisting of van der Waals, hydrogen bond, and desolvation energy, electrostatic energy from interactions, torsional energy due to ligand flexibility, unbound energy of the ligand's unbound state, and clRMS (Cluster root-mean-square deviation) and refRMS (Reference root-mean-square deviation) values indicating conformational changes upon binding, all contributed to assessing ligand performance. The binding potentials of these molecules were summarised in the accompanying **Table 5.2**.

Table 5.2 The predicted binding potentials of the nine synthesised curcumin analogues and the reference compounds (curcumin and Diclofenac) to the prioritised inflammatory targets

Active Target	1HD2											3LN0										
Ligands	Curcumin	Diclofenac	NLB	NLD	NLE	NLF	NLG	NLH	NLI	NLJ	NLK	Curcumin	Diclofenac	NLB	NLD	NLE	NLF	NLG	NLH	NLI	NLJ	NLK
Active Site and Run	4	4	1	5	8	10	8	7	1	5	4	7	7	3	1	6	10	6	10	6	4	6
BE(kcal/mol)	-5.8	-7.1	-6.7	-7.4	-9.7	-5.6	-7.4	-8.9	-6.8	-6.4	-9.0	-7.3	-6.8	-9.0	-10.4	-9.7	-9.6	-9.2	-9.1	-9.1	-9.0	-9.2
Ligand efficiency	-0.2	-0.4	-0.2	-0.3	-0.3	-0.2	-0.3	-0.4	-0.3	-0.2	-0.4	-0.3	-0.4	-0.3	-0.3	-0.4	-0.3	-0.3	-0.3	-0.3	-0.3	-0.4
Inhib constant (nM)	59.7	6.3	13.0	3.6	82.4	79.1	3.5	277.8	10.1	20.7	244.1	4.1	11.2	235.5	24.1	73.9	85.7	194.1	208.5	227.7	260.2	183.1
Intermolar energy	-9.3	-8.6	-9.7	-9.8	-12.1	-9.2	-9.8	-11.3	-9.8	-9.4	-10.8	-10.9	-8.3	-12.6	-12.8	-12.1	-12.6	-11.5	-11.5	-12.1	-12.0	-11.0

Active Target	1HD2											3LN0										
Ligands	Curcumin	Diclofenac	NLB	NLD	NLE	NLF	NLG	NLH	NLI	NLJ	NLK	Curcumin	Diclofenac	NLB	NLD	NLE	NLF	NLG	NLH	NLI	NLJ	NLK
vdwhbdisolv energy*	-9.0	-5.2	-9.2	-9.3	-11.6	-9.0	-9.7	-10.9	-9.5	-9.0	-10.7	-10.6	-6.5	-12.5	-12.7	-11.8	-12.6	-11.3	-0.1	-12.0	-11.9	-10.9
Electrostatic energy	-0.4	-3.4	-0.5	-0.6	-0.4	-0.2	-0.1	-0.4	-0.3	-0.4	-0.1	-0.3	-1.7	-0.1	-0.1	-0.3	0.0	-0.3	-1.4	0.0	-0.1	-0.1
Total internal	-2.8	-1.7	-1.9	-1.4	-1.0	-2.6	-0.6	-0.7	-2.4	-2.0	-1.0	-1.9	-1.0	-2.5	-1.4	-1.2	-1.7	-1.3	2.4	-3.0	-2.7	-1.2
Torsional energy	3.6	1.5	3.0	2.4	2.4	3.6	2.4	2.4	3.0	3.0	1.8	3.6	1.5	3.6	2.4	2.4	3.0	2.4	-1.4	3.0	3.0	1.8
Unbound energy	-2.8	-1.7	-1.9	-1.4	-1.0	-2.6	-0.6	-0.7	-2.4	-2.0	-1.0	-1.9	-1.0	-2.5	-1.4	-1.2	-1.7	-1.3	2.4	-3.0	-2.7	-1.2
refRMS	43.3	44.4	44.2	45.7	43.1	46.1	45.8	43.7	42.4	44.3	41.3	40.8	49.5	-2.5	38.1	32.3	44.1	31.0	33.4	39.0	44.6	42.3

*vdwhbdesolv (Van der Waals, Hydrogen Bond, and Disolvation)

For the target 1HD2, NLE stood out with a binding energy of -9.7 kcal/mol, the lowest among all ligands, indicating the best binding affinity. It also had a ligand efficiency of -0.3, a Ki of 82.4 nM, and intermolecular and vdwhbdesolv (Van der Waals, Hydrogen Bond, and Disolvation) energies of -12.1 kcal/mol and -11.6 kcal/mol, respectively. NLH and NLK followed, with NLH having a BE of -8.9 kcal/mol, LE of -0.36, Ki of 277.83 nM, and intermolecular and vdwhbdesolv energies of -11.3 kcal/mol and -10.9 kcal/mol. NLK has a BE of -9.0 kcal/mol, the highest efficiency with an LE of -0.4, a Ki of 244.1 nM, and intermolecular and vdwhbdesolv energies of -10.8 kcal/mol and -10.7 kcal/mol.

For the target 3LN0, NLD exhibited the lowest BE at -10.4 kcal/mol, with an LE of -0.3, Ki of 24.1 nM, and intermolecular and vdwhbdesolv energies of -12.8 kcal/mol and -12.7 kcal/mol. NLE followed closely with a BE of -9.7 kcal/mol, LE of -0.4, Ki of 73.9 nM, and intermolecular and vdwhbdesolv energies of -12.1 kcal/mol and -11.8 kcal/mol. NLF , with a BE of -9.6 kcal/mol, LE of -0.3, Ki of 85.7 nM, and intermolecular and vdwhbdesolv energies of -12.6 kcal/mol and -12.6 kcal/mol, also witnessed strong performance.

In molecular docking studies of anti-inflammatory effects, the interactions between curcumin analogues and amino acid residues of target proteins were found to be crucial for understanding the binding affinity and efficacy of the compounds. Van der Waals interactions, although weak and non-specific, contributed to the overall stability of the ligand-protein complex and complemented other interactions to enhance binding affinity. Conventional hydrogen bonds, which occur between a hydrogen donor and an acceptor, were critical for the specificity and stability of ligand binding to the active site, playing a key role in the correct positioning of the ligand. Carbon-hydrogen bonds, while weaker, contributed to the stability and orientation of the ligand in the binding pocket, thus enhancing binding affinity. Minimising unfavourable acceptor-acceptor interactions, which were repulsive and occur between two electronegative atoms, was important for improving binding affinity and stabilising the ligand-protein complex.

Pi-Sigma interactions, which took place between the π-electrons of an aromatic ring and the σ-electrons of a single bond, resulted in the stability and specificity of ligand binding, particularly in aromatic compounds. Pi-alkyl interactions, occurring between the π-electrons of an aromatic ring and an alkyl group, enhanced binding affinity and aid in

the orientation and positioning of the ligand within the binding site. Hydrophobic alkyl interactions helped stabilise the ligand in the binding pocket by reducing the exposure of hydrophobic regions to the aqueous environment. Pi-Anion interactions, between the π-electrons of an aromatic ring and a negatively charged group, significantly accelerated binding affinity and specificity, especially in charged environments.

Unfavourable donor-donor interactions were repulsive and happened between two hydrogen donors, potentially destabilising the complex, thus minimising these interactions was crucial for optimal binding. Pi-cation interactions, which occur between the π-electrons of an aromatic ring and a positively charged group, were strong interactions that could significantly hike binding affinity and specificity. Pi donor hydrogen bonds involved hydrogen bonding interactions where a π-electron cloud acted as the donor, contributing to the stability and specificity of ligand binding. Amide Pi-stacked interactions, occurring between the π-electrons of an aromatic ring and the electron-rich region of an amide bond, stabilise the ligand in the binding pocket and contribute to binding affinity. Overall, these various interactions were essential for determining the binding affinity, specificity, and stability of the ligand-protein complex, assisting in the rational design and optimisation of curcumin analogues as anti-inflammatory agents.

Tables 5.3 and **5.4** and **Figures 5.2** and **5.3** presented an analysis of the interactions between various anti-inflammatory compounds and the target proteins 1HD2 and 3LN0. The columns included the active target, compound, and types of interactions observed, such as Van der Waals, conventional hydrogen bonds, carbon-hydrogen bonds, unfavourable acceptor-acceptor, Pi-Sigma, Pi-Alkyl, Alkyl, Pi-Anion, unfavourable donor-donor, Pi-Cation, Pi donor hydrogen bonds, and amide Pi-stacked. Each row under a compound listed the number of interactions and the specific amino acid residues involved for the corresponding interaction type.

1HD2 – CURCUMIN ANALOGUE COMPLEXES

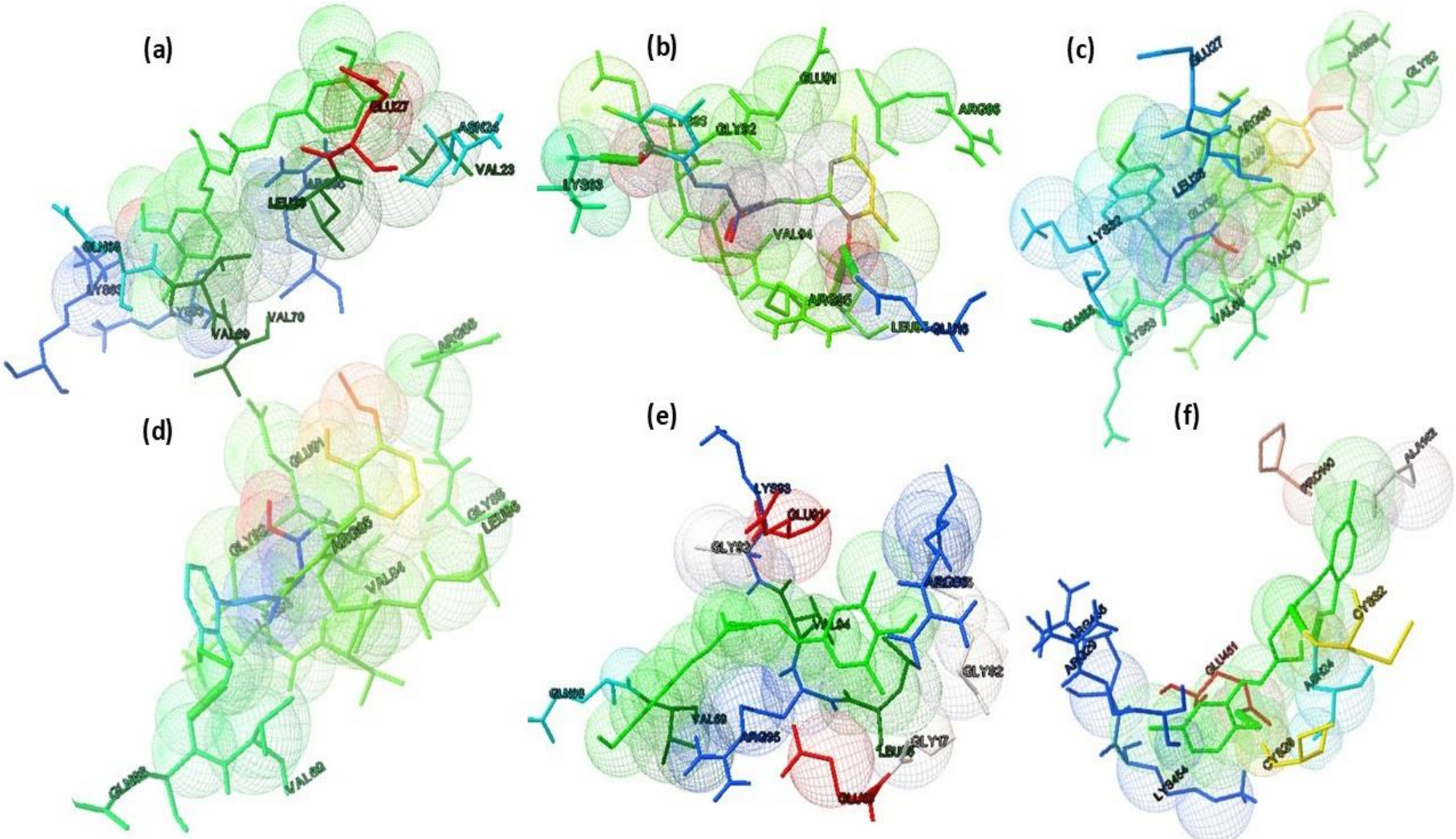

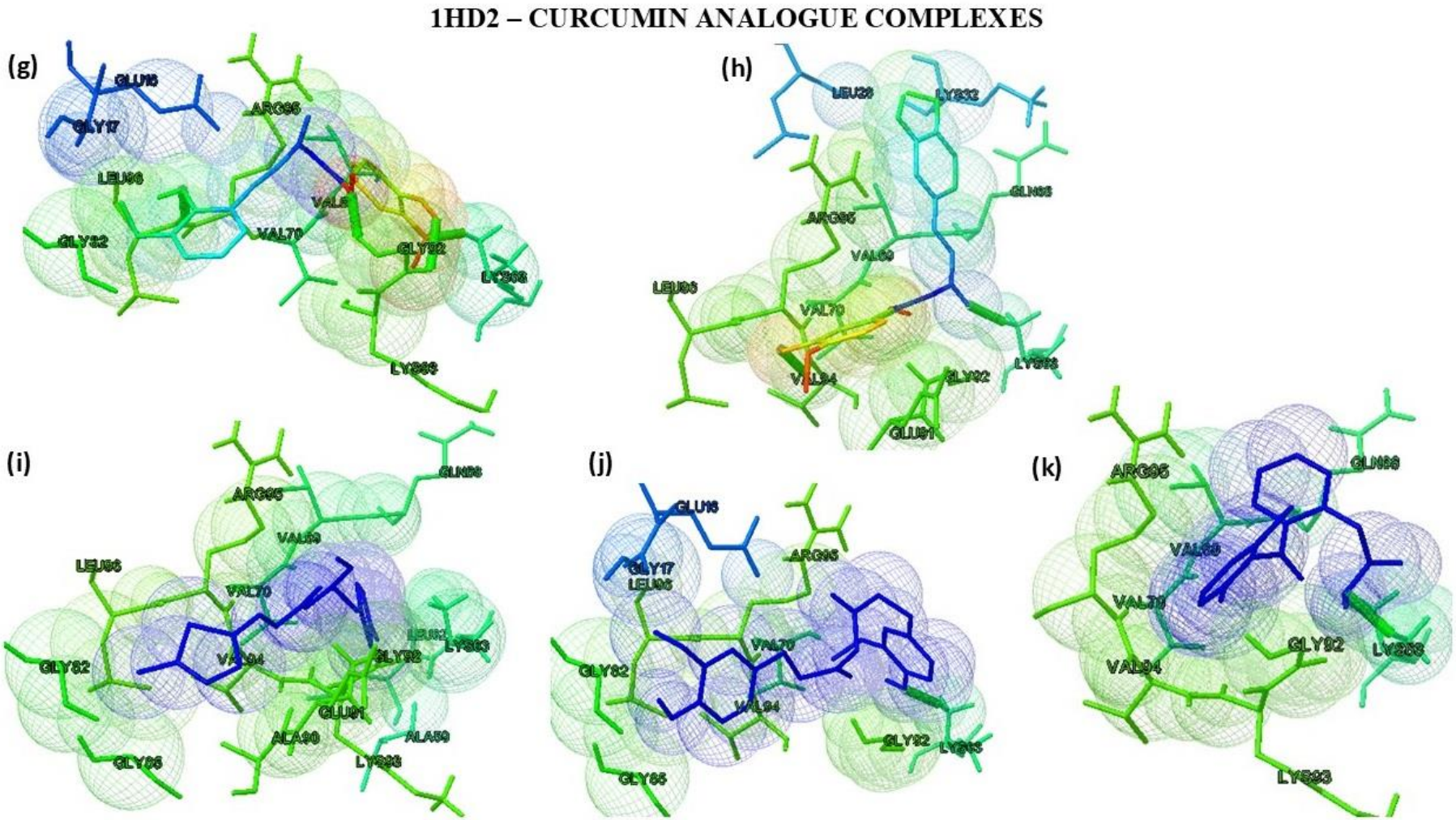

Fig.5.2 1HD2-Curcumin Analogue Complexes (a) 1HD2-NLB Complex (b) 1HD2-NLD Complex (c) 1HD2-NLE Complex (d) 1HD2-NLF Complex (e) 1HD2-NLG Complex (f) 1HD2-NLH Complex (g) 1HD2-NLI Complex (h) 1HD2-NLJ Complex (i) 1HD2-NLK Complex (j)1HD2-Curcumin Complex (k)1HD2-Diclofenac Complex

Table 5.3 The interactions of ligands with 1HD2 through various amino acid residues

Active Target	Compound		Types of Interactions											
			Van der Waals	Conventional Hydrogen Bond	Carbon Hydrogen Bond	Unfavourable Acceptor-Acceptor	Pi-Sigma	Pi-Alkyl	Alkyl	Pi-Anion	Unfavourable donor-donor	Pi-Cation	Pi Donor Hydrogen Bond	Amide Pi-stacked
1HD2	NLB	No. of Interactions	6	2	2		1	3						
		Amino acid residues	LYS A:32; GLN A:68; GLY A:92; LYS A:93; VAL A:70; ALA A:59	ASN A:24; LYS A:63	GLO A:27; LYS A:22		VAL A:69	ARG A:95; LEU A:28; VAL A:23						
	NLD	No. of Interactions	7	4	1			1	1					
		Amino acid residues	LYS A:93; VAL A:94; ALA A:90; GLU A:91; GLY A:85; GLY A:17: GLY A:82	LEU A:96; GLU A:16; LYS A:63; GLY A:92	ARG A:95			LEU A:96	ARG A:86					
	NLE	No. of Interactions	6	2	2		1	4		1			1	
		Amino acid residues	LEU A:96; GLY A:85; ARG A:86; LYS A:93; GLN A:68; LEU A:28	VAL A:70; LYS A:63	GLY A:82; GLY A:92		GLU A:91	ARG A:95; VAL A:69;LYS A:32;ALA A:90		GLU A:16			GLU A:27	
	NLF	No. of Interactions	6	1				3	3			1		
		Amino acid residues	GLY A:82;VAL A:70;GLU A:91;VAL:A 94;GLY A:92;LYS A:93	GLN A:68				LYS A:32; LEU A:28; LEU A:96	VAL A:69; ALA A:90; ARG A:86			ARG A:95		
	NLG	No. of Interactions	10	1				2	3			1		
		Amino acid residues	GLY A:92; LYS A:93; VAL A:94; GLN A:68; VAL A:70; GLY A:85; THR A:81; GLY A:17; GLU A:16; GLU A:91	GLY A:82				ALA A:90; LEU A:96	VAL A:69; LYS A:32; ARG A:86			ARG A:95		
	NLH	No. of Interactions	4	4		1		3	5		1			
		Amino acid residues	VAL A:69; GLU A:91 ;PHE A:55;GLY A:92;ARG A:95	LYS A:63; LYS A:93;VAL A:67;VAL A:70		ARG A:95		ALA A:59; LEU A:62; LYS A:63	AALA A:59;LEU A:62;VAL A:94;LEU A96;ALA A:90		GLA A:68			

			Van der Waals	Conventional Hydrogen Bond	Carbon Hydrogen Bond	Unfavourable Acceptor-Acceptor	Pi-Sigma	Pi-Alkyl	Alkyl	Pi-Anion	Unfavourable donor-donor	Pi-Cation	Pi Donor Hydrogen Bond	Amide Pi-stacked
	NLI	No. of Interactions	11	3	2			2						
		Amino acid residues	GLU A:91; ALA A:90; ARG A:86 GLY A:85; GLY A:82; GLY A:17; THR A:81; GLU A:16; ALA A:59; GLN A:68; VAL A:70	LYS A:63; GLY A:92; LEU A:96	LEU A:96; LYS A:96			ARG A:95; VAL A:69						
	NLJ	No. of Interactions	6	4	4		1	1		1			1	
		Amino acid residues	ALA A:90; VAL A:69; GLA A:68;ARG A:86;LEU A:96;VALA:70	LYS A:93; LYS A:63; ARG A:95;VAL A:94	LEU A:28; LYS A;32; GLY A:92; VAL A:70		GLU A:91	VAL A:70		GLU A:16			GLY A:92	
	NLK	No. of Interactions	12	4			1	2	3			1		
		Amino acid residues	GLU A:91;ARG A:86;GLY A:82;GLY A:85;THR A:81;GLU A:16;VAL A:94;ARG A:95;GLY A:92;LYS A:93;VAL A:69;GLN A:68	LEU A:96; GLU A:16; LYS A:63; GLY A:92			VAL A:70	ALA A:90;ALA A:69	VAL A:67;LEU A:62;LYS A:63			LYS A:63		
	CURCUMIN	No. of Interactions	8	2	4			2						
		Amino acid residues	GLU A:91; GLY A:92; GLU A:16; ARG A:95; VAL A:94 GLY A:85; GLY A:17; THR A:A81	LSY A:63 ARG A:86	VAL A:69; VAL A:70; LYS A:93; LEU A:96			ALA A:90; ALA A:69						
	DICLOFENAC	No.of Interactions	5	3				2	1					1
		Amino acid residues	GLN A:68;LYS A:93;VAL A:70;VAL A:94; GLU A:91	LYS A:63; GLY A:92; LEU A:96				ARG A:95; VAL A:69	ARG A:95					GLY A:92

When the compound NLB was scrutinized, there were 6 Van der Waals interactions with residues LYS A:32, GLN A:68, GLY A:92, LYS A:93, VAL A:70, ALA A:59; 2 conventional hydrogen bonds with ASN A:24, LYS A:63; 2 carbon-hydrogen bonds with GLO A:27, LYS A:22; 1 Pi-Sigma interaction with VAL A:69; and 3 Pi-Alkyl interactions with ARG A:95, LEU A:28, VAL A:23.

NLD exhibited 7 Van der Waals interactions with residues LYS A:93, VAL A:94, ALA A:90, GLU A:91, GLY A:85, GLY A:17, GLY A:82; 4 conventional hydrogen bonds with LEU A:96, GLU A:16, LYS A:63, GLY A:92; 1 carbon-hydrogen bond with ARG A:95; 1 Pi-Alkyl interaction with LEU A:96; and 1 Alkyl interaction with ARG A:86.

In the case of NLE, there arose 6 Van der Waals interactions with residues LEU A:96, GLY A:85, ARG A:86, LYS A:93, GLN A:68, LEU A:28; 2 conventional hydrogen bonds with VAL A:70, LYS A:63; 2 carbon hydrogen bonds with GLY A:82, GLY A:92; 1 Pi-Sigma interaction with GLU A:91; 4 Pi-Alkyl interactions with ARG A:95, VAL A:69, LYS A:32, ALA A:90; 1 Alkyl interaction with GLU A:16; and 1 Pi donor hydrogen bond with GLU A:27.

NLF presented 6 Van der Waals interactions with residues GLY A:82, VAL A:70, GLU A:91, VAL A:94, GLY A:92, LYS A:93; 1 conventional hydrogen bond with GLN A:68; 3 Pi-Alkyl interactions with LYS A:32, LEU A:28, LEU A:96; 3 Alkyl interactions with VAL A:69, ALA A:90, ARG A:86; and 1 Pi-Cation interaction with ARG A:95.

NLG had 10 Van der Waals interactions with residues GLY A:92, LYS A:93, VAL A:94, GLN A:68, VAL A:70, GLY A:85, THR A:81, GLY A:17, GLU A:16, GLU A:91; 1 conventional hydrogen bond with GLY A:82; 2 Pi-Alkyl interactions with ALA A:90, LEU A:96; 3 Alkyl interactions with VAL A:69, LYS A:32, ARG A:86; and 1 Pi-Cation interaction with ARG A:95.

NLH showed 4 Van der Waals interactions with residues VAL A:69, GLU A:91, PHE A:55, GLY A:92; 4 conventional hydrogen bonds with LYS A:63, LYS A:93, VAL A:67, VAL A:70; 1 unfavourable acceptor-acceptor interaction with ARG A:95; 3 Pi-Alkyl interactions with ALA A:59, LEU A:62, LYS A:63; 5 Alkyl interactions with ALA A:59, LEU A:62, VAL A:94, LEU A:96, ALA A:90; and 1 unfavourable donor-donor interaction with GLA A:68.

NLI yielded 11 Van der Waals interactions with residues GLU A:91, ALA A:90, ARG A:86, GLY A:85, GLY A:82, GLY A:17, THR A:81, GLU A:16, ALA A:59, GLN A:68, VAL A:70; 3 conventional hydrogen bonds with LYS A:63, GLY A:92, LEU A:96; 2 carbon hydrogen bonds with LEU A:96, LYS A:96; and 2 Pi-Alkyl interactions with ARG A:95, VAL A:69.

NLJ displayed 6 Van der Waals interactions with residues ALA A:90, VAL A:69, GLA A:68, ARG A:86, LEU A:96, VAL A:70; 4 conventional hydrogen bonds with LYS A:93, LYS A:63, ARG A:95, VAL A:94; 4 carbon hydrogen bonds with LEU A:28, LYS A:32, GLY A:92, VAL A:70; 1 Pi-Sigma interaction with GLU A:91; 1 Pi-Alkyl interaction with VAL A:70; 1 Pi-Anion interaction with GLU A:16; and 1 Pi donor hydrogen bond with GLY A:92.

NLK demonstrated 12 Van der Waals interactions with residues GLU A:91, ARG A:86, GLY A:82, GLY A:85, THR A:81, GLU A:16, VAL A:94, ARG A:95, GLY A:92, LYS A:93, VAL A:69, GLN A:68; 4 conventional hydrogen bond with LEU A:96; GLU A:16; LYS A:63; GLY A:92; 1 Pi-Sigma interaction with VAL A:70 GLU A:16; 2 Pi-Alkyl interactions with ALA A:90; 3 Alkyl interactions with VAL A:67, LEU A:62, LYS A:63; and 1 Pi-Cation interaction with LYS A:63.

Curcumin produced 8 Van der Waals interactions with residues GLU A:91, GLY A:92, GLU A:16, ARG A:95, VAL A:94, GLY A:85, GLY A:17, THR A:81; 2 conventional hydrogen bonds with LYS A:63, ARG A:86; 4 carbon hydrogen bonds with VAL A:69, VAL A:70, LYS A:93, LEU A:96; and 2 Pi-Alkyl interaction with ALA A:90, ALA A:69.

Diclofenac depicted 5 Van der Waals interactions with residues GLN A:68, LYS A:93, VAL A:70, VAL A:94, GLU A:91; 3 conventional hydrogen bonds with LYS A:63, GLY A:92, LEU A:96; 2 Pi-Alkyl interactions with ARG A:95, VAL A:69; 1 Alkyl interaction with ARG A:95; and 1 Amide Pi-stacked bond with GLY A:92.

To sum up, the compounds portrayed a variety of interactions with the target protein, with Van der Waals interactions being the most common, followed by conventional hydrogen bonds and various types of alkyl and Pi interactions. Different compounds interacted with different sets of amino acid residues, which might have correlated with their efficacy and specificity as anti-inflammatory agents.

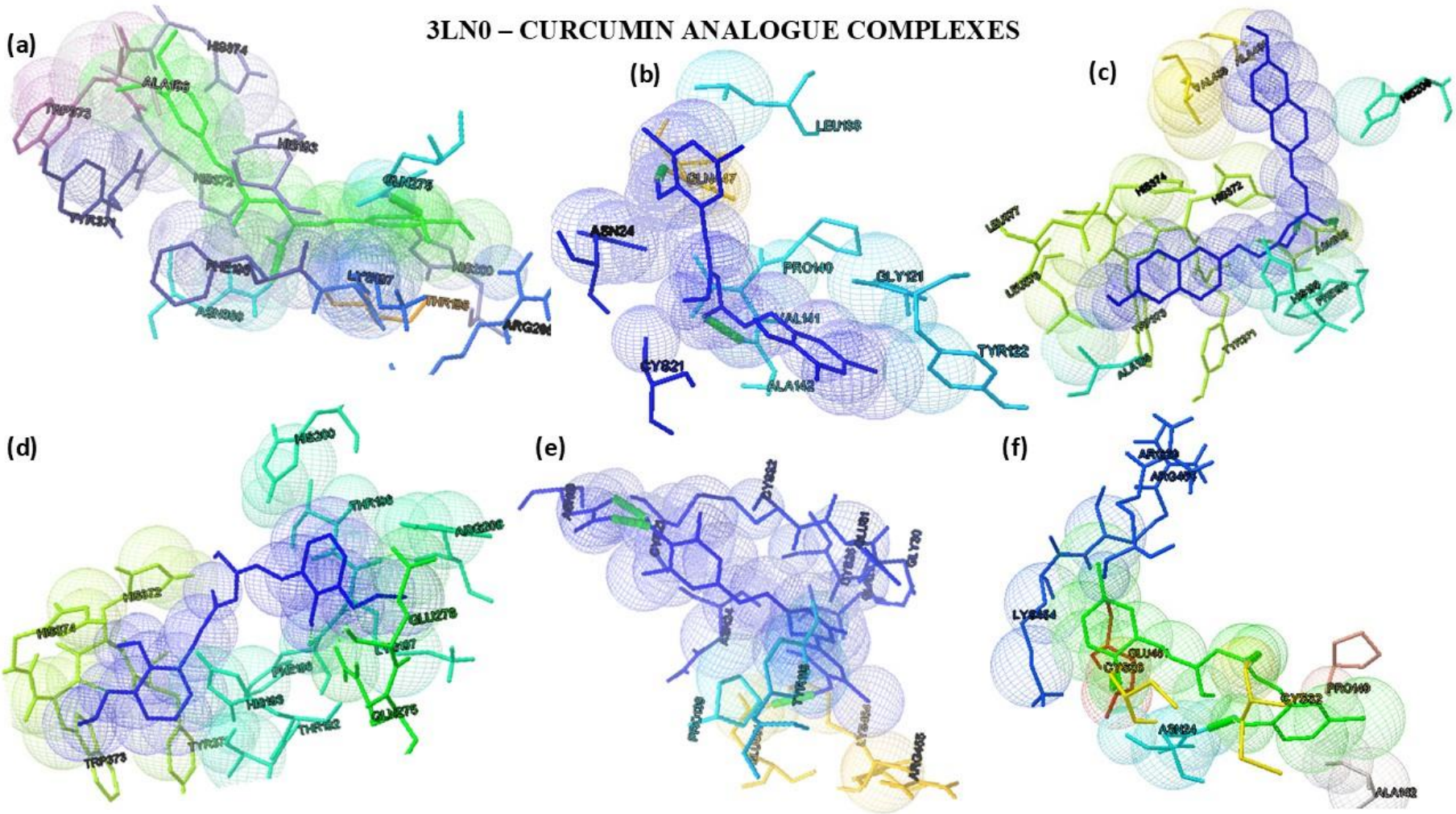
3LN0 – CURCUMIN ANALOGUE COMPLEXES
(a)
(b)
(c)
(d)
(e)
(f)
HIS374
ALA145
TRP373
HIS183
HIS372
GLN275
TYR371
PHE236
LYS187
HIS200
ASN204
TYR126
ARG296
LEU138
GLN147
ASN24
PRO140
GLY121
VAL141
TYR122
CYS21
ALA142
LEU207
LEU208
TYR371
ALA145
HIS200
THR126
ARG296
GLU278
LYS187
PHE236
HIS183
THR182
GLN275
TYR371
TRP373
ARG296
ARG405
LYS454
GLU146
CYS220
CYS232
PRO140
ASN24
ALA142

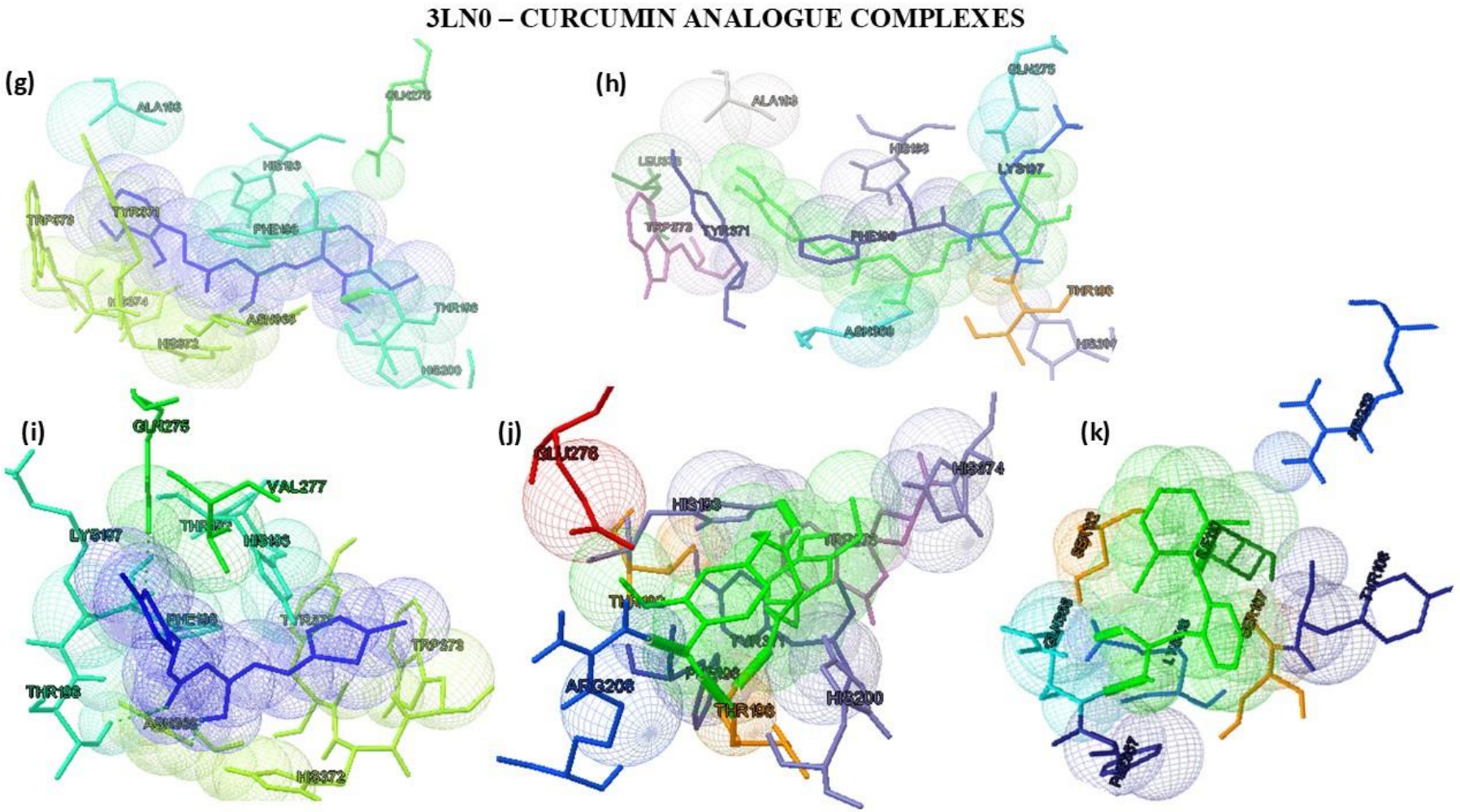

Fig.5.3 LN0-Curcumin Analogue Complexes (a) 3LN0-NLB Complex (b) 3LN0-NLD Complex (c) 3LN0-NLE Complex (d) 3LN0-NLF Complex (e) 3LN0-NLG Complex (f) 3LN0-NLH Complex (g) 3LN0-NLI Complex (h) 3LN0-NLJ Complex (i) 3LN0-NLK Complex (j)3LN0-Curcumin Complex (k)3LN0-Diclofenac Complex

Table 5.4 The interactions of ligands with 3LN0 through various amino acid residues

Active Target	Compound		Types of Interactions														
			Van der Waals	Conventional Hydrogen Bond	Carbon Hydrogen Bond	Unfavourable Acceptor-Acceptor	Pi-Sigma	Pi-Alkyl	Pi-lone pair	Pi-Pi stacked	Alkyl	Pi-Pi T shaped	Unfavourable donor-donor	Pi-Cation	Pi-Sulfur	Pi Donor Hydrogen Bond	Amide Pi-stacked
3LN0	NLB	No. of Interactions	10	2	1	1		4			1						
		Amino acid residues	THR A:192;TYR A:371;GLN A:189;ALA A:188;LEU A:376;TRP A:373;LEU A:377;VAL A:277;GLU A:276;ARG A:208;TYR A:134	ASN A:368;THR A:198	THR A:198	HIS A:372		AIS A:374;HIS A:193;LYS A:197;HIS A:2000			HIS A:200						
	NLD	No. of Interactions	12	3	1			3			2						
		Amino acid residues	GLU A:451;MET A:33;CYS A:32;ASN A:24;ASN A:19;GLY A:121;PRO A:140;CYS A:145;PRO A:25;GLU A:30GLY A:30;ARG A:29	GLN A:447;ALA A:142;CYS A:21	VAL A:141			PRO A:139;LEU A:138ALA A:142			TYR A:122;LEU A138						
	NLE	No. of Interactions	10	2	1			3				1		2		1	
		Amino acid residues	TYR A:134;GLN A:440;HIS A:372;LEU A:377;ALA A:185;LEU A;376;GLN A:189;TYR A:371THR A:192;PHEA:196	THR A:198;ASN A:368	ALA A:432			VAL A:433;ALA A:436;ALA A:188				HIS A:374		HIS A:200; HIS A:193		TRP A:373	
	NLF	No. of Interactions	7	3	1			1	1		4	1		1			
		Amino acid residues	THR A:192;GLN A:189;TRP A:373;VAL A:277;HIS A:200;THR A:198;ASNA:368	GLN A:275;PHE A:198;HIS A:372	GLU A:276			LYS A:197	TYR A:371		HIS A:374;LEUA:376;ARGA:208;LYSA:199	HIS A:374		HIS A:193			

	NLG	No. of Interactions	7	2	1			1	1		4	1		1			
		Amino acid residues	THR A:192;GLN A:189;TRP A:373;VAL A:277;HIS A:200;THR A:198;ASN A:368	GLN A:275;PHE A:196	GLU A:276			LYS A:197	TYR A:371		LEU A:376;ARGA:208;LYSA:197;HIS A:374	HIS A:374		HIS A:193			
	NLH	No. of Interactions	12	3				4			4						
		Amino acid residues	GLN A:447;PRO A:25;CYS A:26;GLN A:27;ASN A:28;LEU A:138;GLY A:30,GLU A:31;GLYA:121;PROA:140;VALA:141;CYS A:22	ASN A:24,GLU A:451'CYS A:32				LYS A:454;PRO A:139;CYS A:21;ALA A142			LYS A:454;ARG A:29;AGA:455.ALAA:142						
	NLI	No. of Interactions	10	2	1		1	2				1		1		1	
		Amino acid residues	THR A:198;THR A:192;GLN A:181LEU A:377;LEU A;376;TYR A:371;HUA A:732;PHE A:196;GLN A 275;ARG A:208	HIS A:200,ASN A:368	HIS A:374		LYS A:197	ALA A:188;VAL A:277				HIS A:374		HIS A:183		TRP A:373	
	NLJ	No. of Interactions	11	3	1			2	1			1				1	
		Amino acid residues	LEU A:276;GLN A:189;ALA A:188;TYR A:334;THR A:192;PKE A:1956;THR A:198;GLU A:276;ARG A:208;ILE A:266,HIS A:200	ASN A:368;HIS A:3712;GLN A:275	TRP A:373			VAL A:2777;LYS A:197	TYR A:371			HIS A;374				TRP A:373	
	NLK	No. of Interactions	8	3				2	1	1	3	1		1	1		
		Amino acid residues	HIS A:372;PHE A;196;TYR A:134;HIS A:200;GLU A:276;THR A:192;GLN A:189;LEUA:376	ASN A:368 THR A:198'GLN A:275				VAL A:277;LYS A:197	TYR A:371	HIS A:374	VAL A:277,ALAA88;TRPA:37	HIS A:193		HIS A:193	HIS A:13		
	CURCUMIN	No. of Interactions	7	5	3		1	1		1			1	1			1
		Amino acid residues	HIS A:200;ASP A:198;THR A:192;GLN A:189;ASN A:368;PHE A:196;TY A:134	ARG A:208;TRPA:373TRA:371;THRA:198;HISA:193	GLNA:275;GLUA:276;ISA:372		HIS A:374	VAL A:277		LYS A:197			TRP A:373	HIS A:193			HIS A:372
	DICLOFENAC	No. of Interactions	6	3												1	
		Amino acid residues	PHE A:357;GLN A:356;SER A:107;ARGA:29;ASP A:111;TYRA:108	LYS A:518;ILE A:110;SERA:12												SER A:112	

Table 5.3 pictured detailed insights into the interactions between various anti-inflammatory compounds and the active target 3LN0. For NLB, there were 10 van der Waals interactions with residues such as THR A:192; TYR A:371; GLN A:189; ALA A:188; LEU A:376; TRP A:373; LEU A:377; VAL A:277; GLU A:276; ARG A:208; TYR A:134. It also formed 2 conventional hydrogen bonds with ASN A:368 and THR A:198 and a carbon-hydrogen bond with THR A:198. NLB had an unfavourable acceptor-acceptor interaction with HIS A:372, 4 pi-alkyl interactions with AIS A:374; HIS A:193; LYS A:197; HIS A: 2000, and 1 alkyl interaction with HIS A:200.

NLD showed 12 van der Waals interactions with residues including GLU A:451; MET A:33; CYS A:32; ASN A:24; ASN A:19; GLY A:121; PRO A:140; CYS A:145; PRO A:25; GLU A:30GLY A:30; ARG A:29, along with 3 conventional hydrogen bonds with GLN A:447, ALA A:142, and CYS A:21. It also had 1 carbon-hydrogen bond, 3 pi-alkyl interactions, and 2 alkyl interactions.

NLE interacted through 10 van der Waals interactions, 2 conventional hydrogen bonds with THR A:198 and ASN A:368, and a carbon-hydrogen bond with ALA A:432. It also formed 3 pi-alkyl interactions, 1 pi-pi T-shaped interaction, 2 Pi-Cation interactions, and a Pi-Donor Hydrogen bond.

NLF involved 7 van der Waals interactions, 3 conventional hydrogen bonds, and 1 carbon-hydrogen bond with GLU A:276. It also included 1 pi-lone pair interaction, 1 pi-alkyl interaction, 4 alkyl interactions,1 Pi-Pi T-shaped interaction and 1 Pi-Cation interaction.

NLG, similar to NLF, had 7 van der Waals interactions, 2 conventional hydrogen bonds, and 1 carbon-hydrogen bond with GLU A:276. It also featured 1 pi-lone pair interaction, 1 pi-alkyl interaction, 4 alkyl interactions, 1 Pi-Pi T-shaped interaction and 1 Pi-Cation interaction

NLH presented 12 van der Waals interactions, 3 conventional hydrogen bonds, 4 pi-alkyl interactions, and 4 alkyl interactions.

NLI included 10 van der Waals interactions, 2 conventional hydrogen bonds, 1 carbon-hydrogen bond with HIS A:374, 1 Pi-Sigma interaction, 2 pi-alkyl interactions, 1 Pi-Pi T-shaped interaction, and 1 Pi-cation interaction. It also had a pi-donor Hydrogen bond interaction.

NLJ featured 11 van der Waals interactions, 3 conventional hydrogen bonds, 1 carbon-hydrogen bond, 2 pi-alkyl interactions, 1 pi-lone pair interaction, 1 pi-pi T-shaped interaction, and pi-donor Hydrogen bond interaction.

NLK involved 8 van der Waals interactions, 3 conventional hydrogen bonds, 2 pi-alkyl interactions, 1 pi-lone pair interaction, 1 pi-pi stacked interaction, 3 alkyl interactions, and 1 pi-pi T-shaped interaction. It also included 1 pi-cation interaction and 1 pi-sulfur interaction.

Curcumin portrayed 7 van der Waals interactions, 5 conventional hydrogen bonds, 3 carbon-hydrogen bonds, 1 pi-sigma interaction, 1 pi-alkyl interaction, 1 pi-pi stacked interaction, 1 unfavourable donor-donor interaction, 1 pi-Cation interaction, and 1 donor Hydrogen bond interaction.

Diclofenac presented 6 van der Waals interactions, 3 conventional hydrogen bonds, and 1 donor Hydrogen bond interaction with SER A:112. This detailed breakdown highlighted the types and numbers of interactions each compound had with the target's active site, crucial for evaluating their binding affinities and potential efficacy as anti-inflammatory agents.

When prioritizing these ligands based on their docking parameters and interactions with the amino acid residues of the selected protein, NLE was identified as the top candidate for 1HD2, followed by NLK, NLH, NLD, NLG, Diclofenac, NLI, NLB, NLJ, Curcumin, and NLF. For 3LN0, the priority order was NLD, NLE, NLF, NLK, NLG, NLH, NLI, NLB, NLJ, Curcumin, and Diclofenac. NLE and NLD witnessed the lowest binding energies, indicating a higher binding affinity, reasonable ligand efficiency, and lower inhibition constants, marking them as strong binding and potentially effective inhibitors. NLK, NLH, and NLG, while exhibiting good binding energies and efficiencies, had slightly higher inhibition constants, placing them next in line.

Thus, it was found that NLE and NLD were the most promising ligands for the anti-inflammatory targets 1HD2 and 3LN0 respectively. Their docking parameters, including the lowest binding energies and strong binding affinities, made them worthy of being the prime candidates for further experimental validation and optimisation. Compared to natural Curcumin and Diclofenac, NLE and NLD showed superior binding energy, although Curcumin had a lower inhibition constant in some cases. These ligands demonstrated promising interactions with the target proteins, suggesting their potential

effectiveness in inhibiting inflammatory pathways. Prioritising NLE and NLD could necessarily lead to the development of potent anti-inflammatory agents.

5.4.1.2. *In vitro* studies

A Protein Denaturation Inhibition Assay was experimented to determine the anti-inflammatory effect of curcumin analogues and their Cu(II) and Zn(II) metal complexes. Using this method, the percentage of inhibition and the IC_{50} values were determined.

5.4.1.2.1. Anti-Inflammatory effect of curcumin analogues

The IC_{50} value is the concentration of a compound required to inhibit a biological process by 50%, with lower IC_{50} values indicating higher potency.

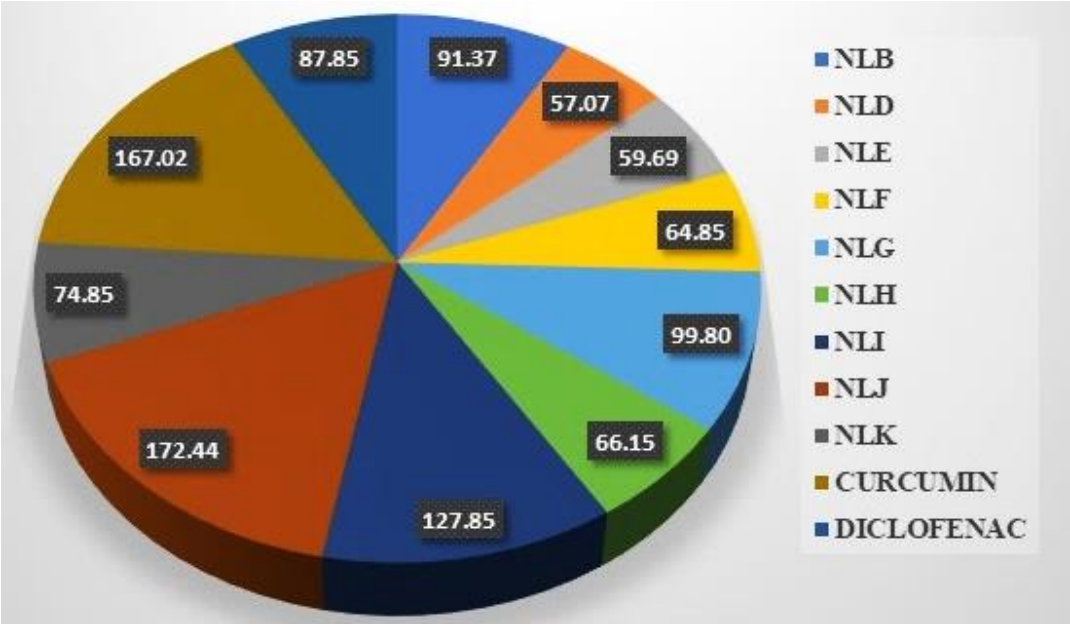

Fig.5.4 The IC_{50} values (in µg) of various curcumin analogues and reference compounds (Curcumin and Diclofenac).

Among the curcumin analogues, NLD (57.07 µg) was identified as the most potent inhibitor, followed closely by NLE (59.69 µg), both demonstrating strong inhibitory activity. NLF (64.85 µg) also showed good inhibitory activity, followed by NLH (66.15 µg), which was slightly less potent than NLF but still within the range of effective inhibitors. NLK (74.85 µg) was less effective compared to NLD, NLE, NLF, and NLH with a higher IC_{50} indicating reduced potency. Diclofenac (87.85 µg), a known anti-inflammatory drug, showed moderate potency, with several curcumin analogues. NLB (91.37 µg) was slightly less potent than Diclofenac, while NLG (99.80 µg) demonstrated

lower inhibitory activity. Curcumin (167.02 µg), a natural compound, had lower potency compared to most of its analogues. NLI (127.85 µg) and NLJ (172.44 µg) showed the highest IC_{50} values, indicating they were the least effective inhibitors among the tested compounds. This analysis helped to identify the most promising curcumin analogues for further development based on their inhibitory potency.

5.4.1.2.2. Anti-inflammatory effect of Cu (II) metal complexes

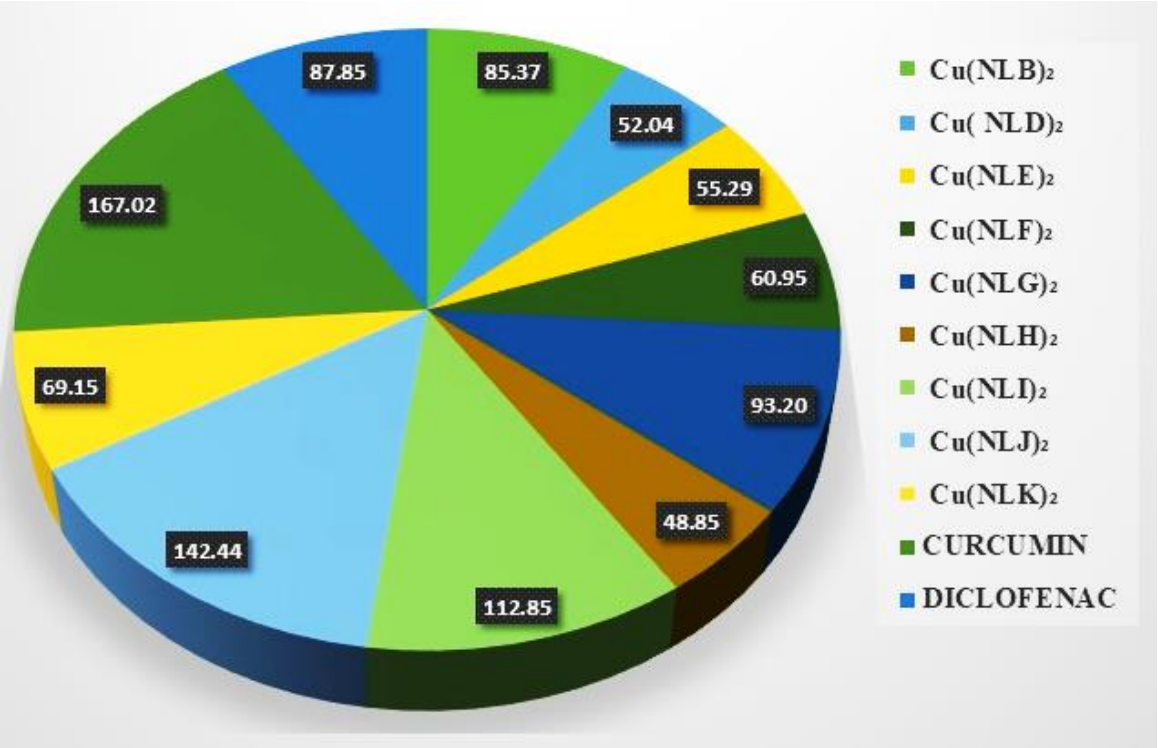

Fig.5.5 The IC_{50} values (in µg) for Cu(II) complexes of various curcumin analogues, as well as reference compounds curcumin and diclofenac.

$Cu(NLH)_2$ (48.85 µg) stood out as the most potent inhibitor, demonstrating the lowest IC_{50} value among the Cu(II) complexes. $Cu(NLD)_2$ (52.04 µg) and $Cu(NLE)_2$ (55.29 µg) followed closely, showing strong inhibitory activity. $Cu(NLF)_2$ (60.95 µg) also displayed good potency, though it was less effective compared to $Cu(NLE)_2$. $Cu(NLK)_2$ (69.15 µg) showed moderate potency.

Compared to diclofenac (87.85 µg), $Cu(NLB)_2$ (85.37 µg) was slightly more potent, while $Cu(NLG)_2$ (93.20 µg) exhibited lower inhibitory activity. $Cu(NLI)_2$ (112.85 µg) and $Cu(NLJ)_2$ (142.44 µg) were less effective, with the latter being the least potent

among the tested complexes. Curcumin itself (167.02 µg) was less potent than its Cu(II) complexes, indicating that complexation enhanced its inhibitory activity.

Thus, Cu(II) complexes of curcumin analogues varied in potency, with $Cu(NLH)_2$, $Cu(NLD)_2$, and $Cu(NLE)_2$ being the most effective inhibitors. $Cu(NLF)_2$ and $Cu(NLK)_2$ showed good potency, while $Cu(NLB)_2$ and $Cu(NLG)_2$ were less effective but comparable to diclofenac. $Cu(NLI)_2$ and $Cu(NLJ)_2$ were the least effective, with curcumin being less potent than its Cu(II) complexes.

5.4.1.2.3. Anti-Inflammatory effect of Zn (II) metal complexes

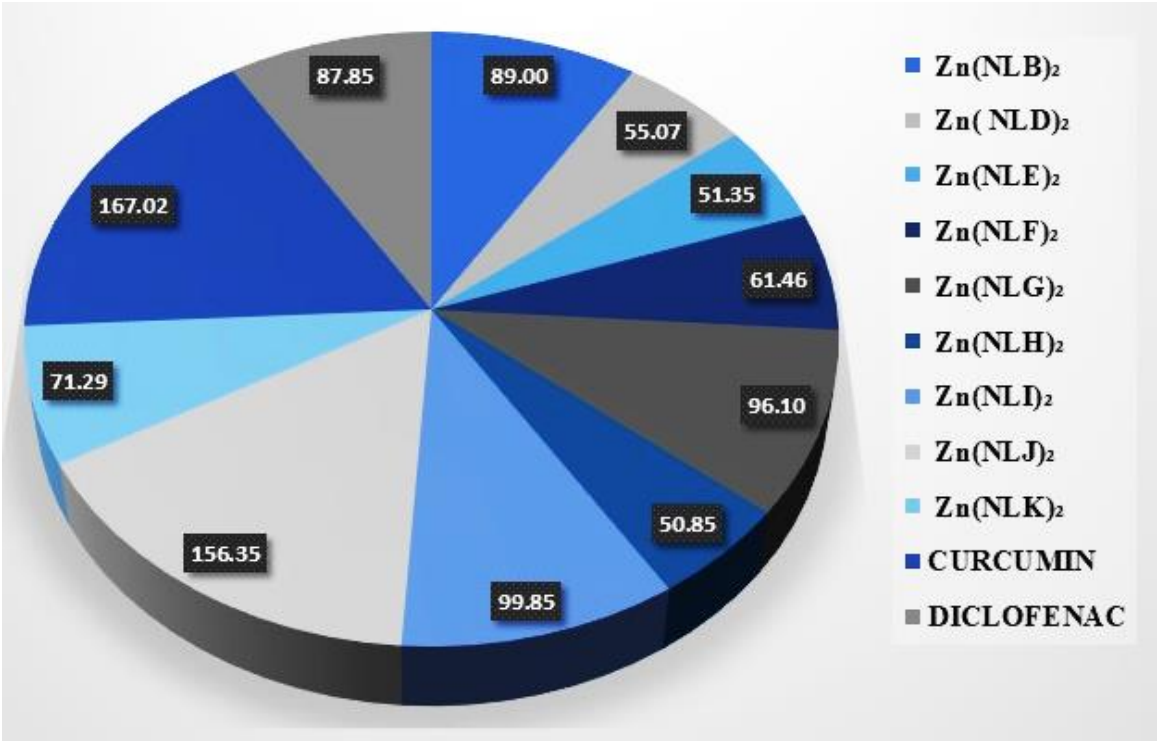

Fig.5.6 IC_{50} values (in µg) for Zn(II) complexes of various curcumin analogues and reference compounds curcumin and diclofenac.

$Zn(NLH)_2$ (50.85 µg) was the most potent complex, displaying the lowest IC_{50} value, indicating it was the most effective inhibitor among the Zn(II) complexes. $Zn(NLE)_2$ (51.35 µg) followed closely in potency, producing strong inhibitory activity. $Zn(NLD)_2$ (55.07 µg) also demonstrated strong potency, being slightly less effective than $Zn(NLE)_2$ but still highly potent. $Zn(NLF)_2$ (61.46 µg) exhibited moderate potency, with good inhibitory activity, although it was less potent compared to $Zn(NLD)_2$. $Zn(NLK)_2$

(71.29 µg) displayed moderate potency as well, with a higher IC_{50} value indicating it was less effective than $Zn(NLF)_2$ but still potent.

Diclofenac (87.85 µg) served as a reference compound known for its moderate potency as an anti-inflammatory drug. $Zn(NLB)_2$ (89.00 µg) was slightly less potent than diclofenac but still comparable. $Zn(NLG)_2$ (96.10 µg) had a higher IC_{50} value, indicating lower inhibitory activity. $Zn(NLI)_2$ (99.85 µg) registered lower potency, with a higher IC_{50} value suggesting it was less effective than the more potent complexes. $Zn(NLJ)_2$ (156.35 µg) was the least potent among the tested complexes, with the highest IC_{50} value indicating the lowest potency. Curcumin (167.02 µg) showed lower potency compared to its Zn(II) complexes, suggesting that complexation with Zn(II) strengthened the inhibitory activity of curcumin analogues.

In conclusion, Zn(II) complexes of curcumin analogues generally exhibited stronger anti-inflammatory effects compared to curcumin itself, with the most potent complexes being $Zn(NLH)_2$, $Zn(NLE)_2$, and $Zn(NLD)_2$.

5.4.1.2.4. Comparative analysis of anti-inflammatory effects: Curcumin analogues and Cu(II) and Zn(II) complexes

Among the curcumin analogues, NLD, NLE, and NLF were identified as the most potent inhibitors, with NLH, NLK, and Diclofenac following closely. Curcumin itself, along with NLB, NLG, NLI, and NLJ, demonstrated lower potency, with NLI and NLJ being the least effective. This ranking highlighted the varying degrees of effectiveness among the curcumin analogues, with some showing significant inhibitory activity while others were less effective. Compounds like NLD and NLH, which contained chloro groups, demonstrated enhanced potency due to the electron-withdrawing nature of halogens. This property increased the electrophilicity of nearby carbon atoms, facilitating stronger interactions with the active sites of inflammatory enzymes. The dichloro substitution in NLD likely enhanced these effects more significantly than the single chloro substitution in NLH, contributing to its superior potency.In NLF, the ethoxy groups enhanced lipophilicity and contributed to hydrophobic interactions with enzyme active sites. The combination of ethoxy and hydroxy groups further improved binding stability, making NLF highly potent. NLK, containing methylthiophenyl groups, showed moderate potency because sulfur-containing groups interacted with enzyme active sites

via π-π interactions and hydrophobic forces. However, the lack of additional functional groups for hydrogen bonding limited its effectiveness compared to NLD and NLE. NLB, with dimethoxy groups, exhibited lower potency because the electron-donating nature of both methoxy groups reduced electrophilicity, thereby weakening interactions with inflammatory targets. Compounds like NLI and NLJ were the least potent due to their substitution patterns. The hydroxy and methoxy groups, while beneficial for hydrogen bonding and electron donation, were not optimally positioned to maximize interactions with target enzymes.

The Cu(II) complexes exhibited superior potency compared to the curcumin analogues. The most effective Cu(II) complexes were $Cu(NLH)_2$, $Cu(NLD)_2$, and $Cu(NLE)_2$, which presented enhanced inhibitory activity over both curcumin and its analogues. These complexes leveraged the properties of the metal ion to significantly improve their effectiveness. Similarly, Zn(II) complexes also portrayed better anti-inflammatory effects compared to curcumin. $Zn(NLH)_2$ and $Zn(NLE)_2$ were the most potent among the Zn(II) complexes, demonstrating notable effectiveness in inhibition. The overall effectiveness of Zn(II) complexes generally surpassed that of Cu(II) complexes, with $Zn(NLH)_2$ and $Zn(NLE)_2$ being particularly potent.

The metal complexation with Cu(II) and Zn(II) invigorated the stability and bioavailability of curcumin analogues, contributing to their increased potency. Metal ions facilitated improved interactions with biological targets, leading to more effective inhibition. The synergistic effect of combining curcumin analogues with metal ions resulted in enhanced overall potency, as both components worked together. Metal complexes tend to exhibit better cellular uptake compared to free ligands. This improved uptake translates to more effective inhibition at lower concentrations. While both Cu(II) and Zn(II) complexes showed increased potency over curcumin and many of its analogues, Zn(II) complexes were observed to be generally more effective. Cu(II) complexes, though highly effective, usually had slightly lower potency compared to their Zn(II) counterparts. The enhanced potency of Zn(II) complexes over Cu(II) complexes in anti-inflammatory effects can be attributed to several factors. Zn(II) forms highly stable complexes with curcumin analogues due to its full d10 electron configuration, enhancing bioavailability and longevity in physiological conditions, whereas the redox-active d9 configuration of Cu(II) results in less stable complexes and potential decomposition.

Zn(II) complexes act as antioxidants, stabilizing free radicals and preventing oxidative damage, while Cu(II) complexes can promote oxidative stress by catalyzing reactive oxygen species (ROS). The role of Zinc as an essential trace element in inhibiting inflammatory mediators like NF-κB and COX enzymes aligns with its biological compatibility, while excess copper can disrupt redox balance and cause toxicity[98]. Zn(II) complexes also exhibit superior selectivity towards molecular targets such as cyclooxygenases (COX) and matrix metalloproteinases (MMPs), along with a better safety profile and lower toxicity compared to Cu(II) complexes. Research supported that Zn(II) complexes more effectively inhibit COX-1, COX-2, and other inflammatory mediators due to their stability and non-redox nature, making them more potent in anti-inflammatory applications[99].

Figures 5.7 and **5.8** contained the best ligands and complexes demonstrating anti-inflammatory effects.

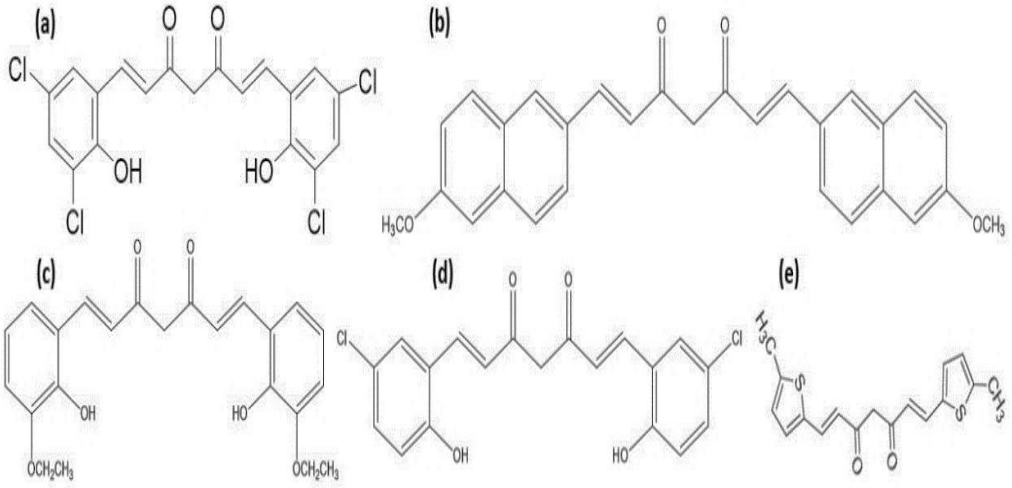

Fig.5.7 The best ligands demonstrated anti-inflammatory effects.

(a) NLD(1,7-bis(3,5-dichloro-2-hydroxyphenyl) hepta-1,6-diene-3,5-dione)
(b) NLE (1,7-bis (6-methoxynaphthalen-2-yl) hepta-1,6-diene-3,5-dione)
(c) NLF(1,7-bis(3-ethoxy-2-hydroxyphenyl) hepta-1,6-diene-3,5-dione)
(d) NLH(1,7-bis(5-chloro-2-hydroxyphenyl) hepta-1,6-diene-3,5-dione)
(e) NLK(1,7-bis(5-methylthiophen-2-yl) hepta-1,6-diene-3,5-dione)

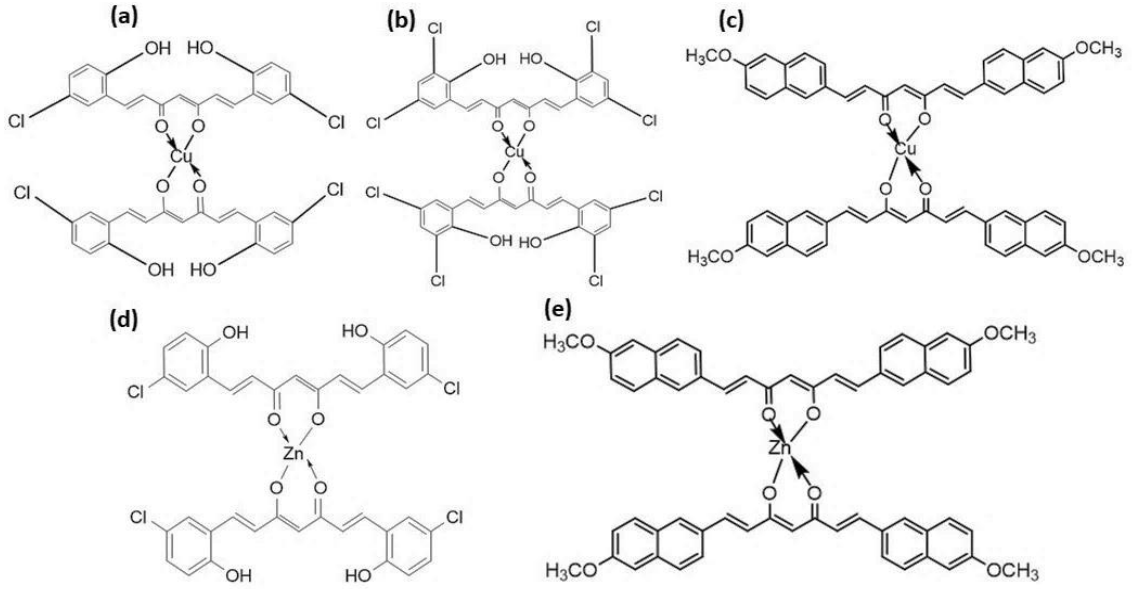

Fig.5.8 The best Cu(II) and Zn(II) complexes of curcumin analogues demonstrate anti-inflammatory effects.

(a) $Cu(NLH)_2$ (Cu(II) complex of 1,7-bis(5-chloro-2-hydroxy phenyl) hepta-1,6-diene-3,5-dione)
(b) $Cu(NLD)_2$ (Cu(II) complex of 1,7-bis(3,5-dichloro-2-hydroxyphenyl)hepta-1,6-diene-3,5-dione)
(c) $Cu(NLE)_2$ (Cu(II) complex of 1,7-bis(6-methoxy naphthalen-2-yl)hepta-1,6-diene-3,5-dione)
(d) $Zn(NLH)_2$ (Zn(II) complex of 1,7-bis(5-chloro-2-hydroxy phenyl) hepta-1,6-diene-3,5-dione)
(e) $Zn(NLE)_2$ (Zn(II) complex of 1,7-bis(6-methoxy naphthalen-2-yl)hepta-1,6-diene-3,5-dione)

5.4.2. Anti-diabetic effect of curcumin analogues and their metal complexes

5.4.2.1. *In silico* Studies

Two key proteins that harbour germline mutations influencing diabetes were chosen as molecular targets from RCSB. The proteins are:(PDB ID:1IR3) (TG3), (PDB ID:3DH4) (TG4)

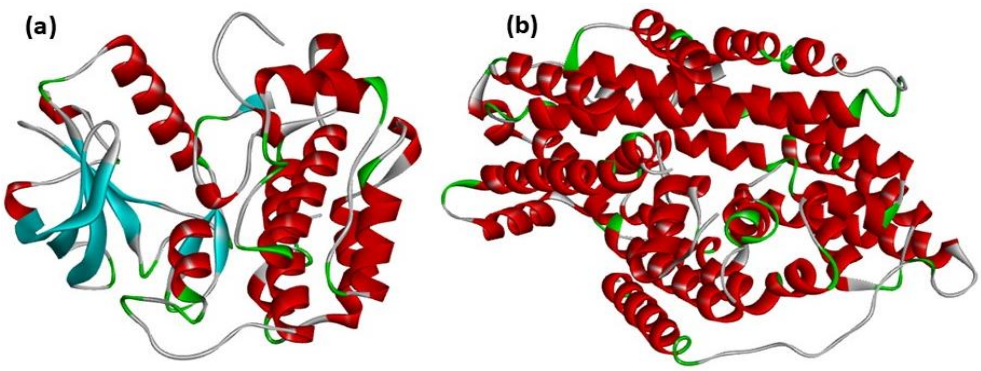

Fig.5.9 Proteins with germline mutations affect diabetes. (a) 1IR3 (b) 3DH4

5.4.2.1.1. Computational screening of designed molecules

The nine molecules—NLB, NLD, NLE, NLF, NLG, NLH, NLI, NLJ, and NLK—underwent virtual screening using pre-ADMET and Swiss ADME platforms. These molecules met both the CMC-like rule and the Rule of Five criteria. Further evaluations of drug-likeness, ADME properties, and toxicity confirmed their suitability, leading to their selection as lead compounds.

5.4.2.1.2. Molecular docking Studies of anti-diabetic effect of curcumin analogues

Table 5.5 presented molecular docking results for various ligands against two antidiabetic targets, 1IR3 and 3DH4. The ligands evaluated included Curcumin, Acarbose, NLB, NLD, NLE, NLF, NLG, NLH, NLI, NLJ, and NLK. Key parameters assessed were Binding Energy (BE), Ligand Efficiency (LE), Inhibition Constant (Ki), Intermolecular Energy, van der Waals, Hydrogen Bonding and Desolvation Energy (vdwhbdisolv energy), Electrostatic Energy, Total Internal Energy, Torsional Energy, and Unbound Energy.

Table 5.5 The predicted binding potentials of the nine synthesised curcumin analogues and the reference compounds (curcumin and Acarbose) to the prioritised inflammatory targets.

Active Target	1IR3											3DH4										
Ligands	Curcumin	Acarbose	NLB	NLD	NLE	NLF	NLG	NLH	NLI	NLJ	NLK	Curcumin	Acarbose	NLB	NLD	NLE	NLF	NLG	NLH	NLI	NLJ	NLK
Active Site and Run	3	4	4	3	4	4	7	6	4	8	3	4	8	1	10	9	10	10	10	7	10	7
BE(kcal /mol)	-5.5	-0.77	-8.16	-7.76	-8.1	-6.22	-7.87	-8.77	-7.2	-7.36	-7.53	-5.96	-1.24	-6.77	-8.51	-8.42	-6.52	-8.78	-8.13	-7	-7.74	-9.13
Ligand efficiency	-0.2	-0.02	-0.28	-0.29	-0.25	-0.21	-0.29	-0.35	-0.27	-0.27	-0.36	-0.22	-0.03	-0.23	-0.32	-0.26	-0.22	-0.33	-0.33	-0.26	-0.29	-0.43
Inhib constant (nM)	93.19	271.26	1.04	2.04	1.16	27.54	1.71	374.48	5.27	4.05	3	42.58	123.61	10.86	579.09	670.6	16.52	365.08	1.1	7.37	2.13	201.85
Intermolar energy	-9.08	-8.53	-11.15	-10.15	-10.48	-9.8	-10.25	-11.15	-10.18	10.34	-9.32	-9.54	-8.99	-9.76	-10.9	-10.81	-10.1	-11.17	-10.52	-9.98	10.72	-10.92

Active Target	1IR3											3DH4									
Ligands	Curcumin	Acarbose	NLB	NLD	NLE	NLF	NLG	NLH	NLI	NLJ	NLK	Curcumin	Acarbose	NLB	NLD	NLE	NLF	NLG	NLH	NLI	NLJ	NLK
vdwhb disolv energy	-8.56	-7.29	-10.87	-9.97	-10.13	-9.17	-9.69	-10.93	-10.17	-9.38	-9.27	-9.08	-8.32	-9.68	-10.72	-10.71	-10.05	-11.06	-10.36	-9.6	-10.54	-10.91
Electrostatic energy	0.52	-1.24	-0.28	-0.18	-0.36	-0.63	-0.56	-0.22	-0.02	-0.96	-0.06	-0.46	-0.68	-0.07	-0.17	-0.1	-0.05	-0.11	-0.16	-0.38	-0.18	-0.01
Total internal	-2.46	-13.78	-1.66	-1.34	-1.37	-2.52	-1.2	-1.31	-3.1	-0.99	-0.6	-2.41	-12.57	-1.89	-1.35	-1.35	-3.02	-1.05	-1.26	-1.81	-2.79	-0.71
Torsional energy	3.58	7.76	2.98	2.39	2.39	3.58	2.39	2.39	2.98	2.98	1.79	3.58	7.76	2.98	2.39	2.39	3.58	2.39	2.39	2.98	2.98	1.79
Unbound energy	-2.46	-13.78	-1.66	-1.34	-1.37	-2.52	-1.2	-1.31	-3.1	-0.99	-0.6	-2.41	-12.57	-1.89	-1.35	-1.35	-3.02	-1.05	-1.26	-1.81	-2.79	-0.71
clRMS	0	0	0	0	0	0	0	0	0	0	0	0	0	0	0	0	0	0	0	0	0	0
refRMS	37.08	52.74	28.51	30.14	46.43	34.53	41.45	40.98	48.61	35.39	30.89	90.76	87.5	80.41	74.52	83.13	78.2	63.83	74.28	74.23	63.88	71.1

In the case of 1IR3, NLB emerged as the top ligand due to its strong binding energy (-8.16 kcal/mol), the lowest inhibition constant (Ki: 1.04 nM), and moderate ligand efficiency (-0.28), indicating high potency. NLE followed closely with a binding energy of -8.1 kcal/mol and a very low inhibition constant (Ki: 1.16 nM), although its ligand efficiency (-0.25) was slightly lower. NLG, with a binding energy of -7.87 kcal/mol, a low inhibition constant (Ki: 1.71 nM), and a slightly higher ligand efficiency (-0.29) than NLE, ranked next. NLD, showing good binding energy (-7.76 kcal/mol), a low inhibition constant (Ki: 2.04 nM), and similar ligand efficiency (-0.29) to NLG, followed.

NLK exhibited strong binding energy (-7.53 kcal/mol), a low inhibition constant (Ki: 3 nM), and high ligand efficiency (-0.36), indicating good effectiveness relative to its size. NLJ and NLI, with binding energies of -7.36 kcal/mol and -7.2 kcal/mol respectively, had relatively low inhibition constants (Ki: 4.05 nM for NLJ and Ki: 5.27 nM for NLI) and comparable ligand efficiencies (-0.27). Despite having the lowest binding energy (-8.77 kcal/mol), NLH was less potent owing to its high inhibition constant (Ki: 374.48 nM), though its ligand efficiency (-0.35) was relatively high.

NLF, with a binding energy of -6.22 kcal/mol, a higher inhibition constant (Ki: 27.54 nM), and lower ligand efficiency (-0.21), was considered moderate. Curcumin showed lower binding energy (-5.5 kcal/mol), a higher inhibition constant (Ki: 93.19 nM), and lower ligand efficiency (-0.2), making it less effective. Acarbose, with the poorest binding energy (-0.77 kcal/mol), the highest inhibition constant (Ki: 271.26 nM), and very low ligand efficiency (-0.02), was deemed the least effective ligand.

In molecular docking studies of anti-diabetic effects, the interactions between curcumin analogues and amino acid residues of target proteins were crucial for understanding the binding affinity, stability, and efficacy of these compounds. Each type of interaction contributed uniquely to the overall binding profile. Collectively, these interactions determined the binding affinity, specificity, and stability of curcumin analogues with target proteins, aiding in the rational design and optimization of curcumin analogues as potential anti-diabetic agents by ensuring effective binding to the target proteins involved in diabetes management.

Figures 5.10 and **5.11**, along with **Tables 5.6** and **5.7**, represented the various ligand interactions with the amino acid residues of the targeted proteins 1IR3 and 3DH4.

1IR3 – CURCUMIN ANALOGUE COMPLEXES

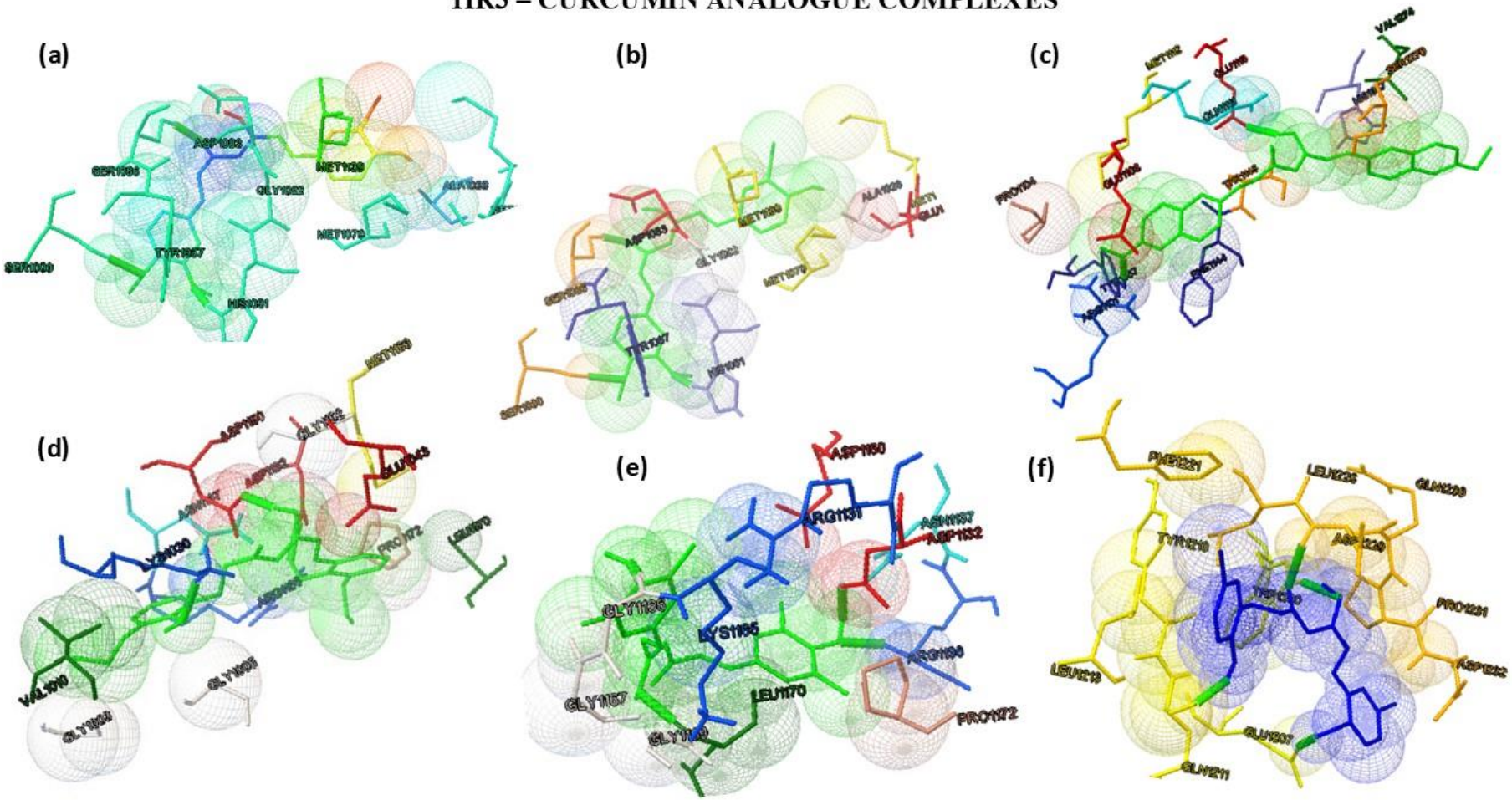

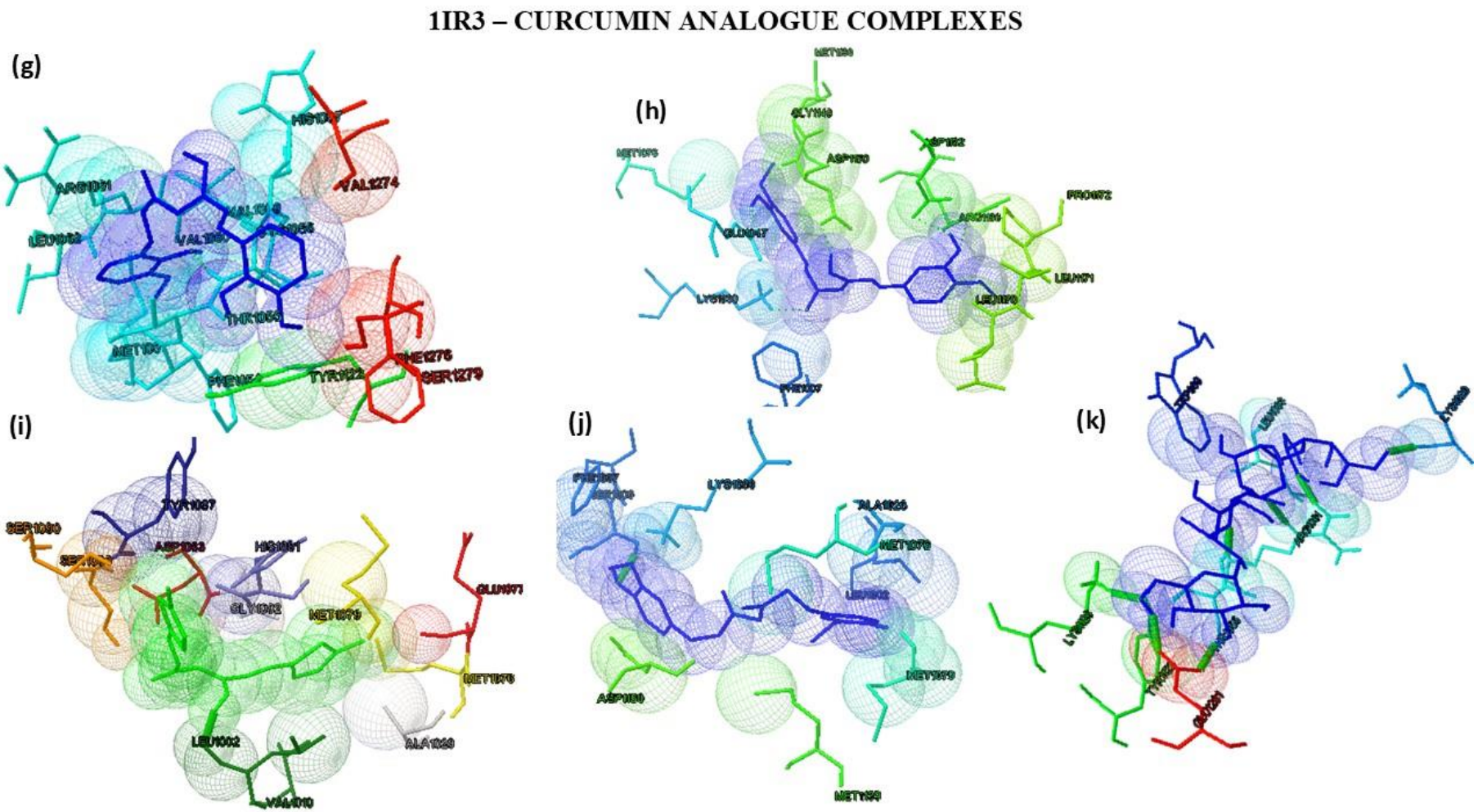

Fig.5.10 1IR3-Curcumin Analogue Complexes (a) 1IR3-NLB Complex (b) 1IR3-NLD Complex (c) 1IR3-NLE Complex (d) 1IR3-NLF Complex (e) 1IR3-NLG Complex (f) 1IR3-NLH Complex (g) 1IR3-NLI Complex (h) 1IR3-NLJ Complex (i) 1IR3-NLK Complex (j)1IR3-Curcumin Complex (k)1IR3-Acarbose Complex.

Table 5.6. The interactions of ligands with 1IR3 through various amino acid residues

Active Target	Compound		Types of Interactions												
			Van der Waals	Conventional Hydrogen Bond	Carbon Hydrogen Bond	Pi-Sigma	Pi-Alkyl	Pi-lone pair	Pi-Pi stacked	Alkyl	Pi-Anion	Pi-Pi T shaped	Unfavourable donor-donor	Pi-Cation	Pi-Sulfur
1IR3	NLB	No.of Interactions	9	3	2		4								
		Amino acid residues	JLYA:1003: META:1076; GLUA:1077; VAL A:1060; LEU A:1078; GLYA:1082; ASN A:1087; PRO A:1099; TYRA:1087	ERA:1086; HISA:1081; SER A:1090	GLUA:1077; ALA A:1080		META:1139; ALAA:1011; ALAA:1028; LEUA1002								
	NLD	No.of Interactions	5	2	2	1	3				1				
		Amino acid residues	MET A :1076;GLU A:1077,GLY A:1003;TYRA:1087;SER A:1090;ASN A:1097;TRO A: 1099	LYS A:1030; SER A:1000	GLU A:1043; GLU A:1047	LEU A:1002	VAL A:1010; ALAA:1028; MET A:1139				ASP A:1150				
	NLE	No.of Interactions	10	2	1	1	1		1		1	1	1	1	
		Amino acid residues	ARG A:1101; PROA:110LEUA:1091;THR A:1145;THEA:1271;HIA:1058;ASPA:1143; SERA :1270; HIS A:1268;GLUA:123	TYR A:1087; GLU A:1115	GLU A:1108	VAL A:1274	VAL A:1274		PHE A:1144		HIS A:1057	PHE A:1144	GLN A:1111	MET A:11112	
	NLF	No.of Interactions	5	5											
		Amino acid residues	LEU A:1063;ILEA:1018;ILE A:1019;TRP A:989;THR A:1055	ARGA:1061; LYSA:1020;GLU A:1281;TYRA:1122;LYS A:1126											

			Van der Waals	Conventional Hydrogen Bond	Carbon Hydrogen Bond	Pi-Sigma	Pi-Alkyl	Pi-lone pair	Pi-Pi stacked	Alkyl	Pi-Anion	Pi-Pi T shaped	Unfavourable donor-donor	Pi-Cation	Pi-Sulfur
	NLG	No.of Interactions	8	1			2			1			1	1	1
		Amino acid residues	ARG A:1131;ARGA:116;ASP A:1150;GLUA:103;ARG A:1039;GLYA:119;LYS A:1168; GLYA:117	ASP A:1132			LYSA:1165 ; PROA:1172			PRO A:1172			ASN A:1137	ARG A:1155	ET A:1153
	NLH	No.of Interactions	5	3		1	1			2	2				
		Amino acid residues	GLNA:1230; LEUA:1228; TYR A:1210;THR A:1203;SERA:1204	ASP A:1229; TRPA:1200; GLU A:1207		PHE A:1221	LEU A:1213			LEU A:1213; PROA: 1231	ASP A:1232; GLU A:1207				
	NLI	No.of Interactions	9	4	1		1	1							
		Amino acid residues	GLU A:1281; TYRA:112;PHEA:1276; SERA1279; SERA:1275; VALA:1274; TRP A:989; LEUA:1062; VAL A:1060	VAL A:1059; CYS A:1056; THR A:1055; HIS A:1057	MET A:1051		1ARG A:1061	PHE A:1054							
	NLJ	No.of Interactions	15	3			1								1
		Amino acid residues	GLUA:1043;GLYA:115 SERA:1006;GLYA1005; PHEA:1007;PHEA;GY A:1149;VALA:1060;MET A:1139;MET A:1076;VALA:1010;ASNA:1137;ASPA:1132;ARGA:1136; LEU A:1171	LYS A:1030; ASP A:1150; GLU A:1047			PRO A:1172								MET A:1153

			Van der Waals	Conventional Hydrogen Bond	Carbon Hydrogen Bond	Pi-Sigma	Pi-Alkyl	Pi-lone pair	Pi-Pi stacked	Alkyl	Pi-Anion	Pi-Pi T shaped	Unfavourable donor-donor	Pi-Cation	Pi-Sulfur
	NLK	No.of Interactions	16	3			1								1
		Amino acid residues	GLUA:1043;GLYA :1152;SER A:1006;GLY A:1005;PHEA:1007 ;PHE A:1151;GLY A:1149;VALA:1060 ;MET A:1139;MET A:1076;VALA:1010 ;ASN A:1137;ASP A:1132;ARGA:113 6;LEU A:1171;LEU A:1170	LYS A:1030;ASP A;1150;GL U A:1047			PRO A:1172								MET A:1153
	CURCUMIN	No.of Interactions	7	2	2	1	3				1				
		Amino acid residues	PHE A:1007; GLY A:1005; ASN A:1137; MET A:1076; ASV A:108 LEU A:1078; MET A:1079	LYS A:1030; SER A:1006	GLU A:1043; GLUA:10 47	LEU A:1002	VAL A:1010;M ETA:1139 ;ALA A:1028				ASP A:11 50				
	ACARBOSE	No.of Interactions	5	5											
		Amino acid residues	LEU A:1063; ILE A:1018; ILE A:1019; TRP A:989; THR A:1055	ARG A:1061 LYS A:1020; GLUA:1281 ;TYRA:1122 ;LYSA:1126											

Table 5.6 comprehensively analyses the types and quantities of interactions between various antidiabetic compounds and the active target 1IR3. Each compound exhibited a unique set of interactions, including Van der Waals forces, hydrogen bonds, carbon-hydrogen bonds, and various pi interactions, which were crucial for stabilising the compound within the active site.

NLB engaged in nine Van der Waals interactions with residues such as JLY A:1003: MET A:1076; GLU A:1077; VAL A:1060; LEU A:1078; GLY A:1082; ASN A:1087; PRO A:1099 and TYR A:1087, three conventional hydrogen bonds with SER A:1086 and HIS A:1081, SER A:1090, two carbon-hydrogen bonds with GLU A:1077 and ALA A:1080, and four pi-alkyl interactions with MET A:1139; ALA A:1011; ALA A:1028; LEU A1002.

NLD showed five Van der Waals interactions, two conventional hydrogen bonds with LYS A:1030 and SER A:1000, two carbon-hydrogen bonds with GLU A:1043 and GLU A:1047, one pi-sigma interaction with LEU A:1002, three pi-alkyl interactions with VAL A:1010 and ALA A:1028, MET A:1139 and one pi-anion interaction with ASP A:1150.

NLE demonstrated ten Van der Waals interactions, two conventional hydrogen bonds with TYR A:1087 and GLU A:1115, and various pi interactions such as pi-sigma, pi-alkyl with VAL A:1274, Pi-Pi stacked, Pi-Anion, Pi-Pi T- shaped, and Pi-Cation. It also had an unfavourable donor-donor interaction with GLN A:1111.

NLF engaged in five Van der Waals interactions and five conventional hydrogen bonds with ARG A:1061, LYS A:1020, GLU A: 1281, TYR A:1122, LYS A:1126.

NLG produced eight Van der Waals interactions, one conventional hydrogen bond with ASP A:1132, and several pi interactions.

NLH involved five Van der Waals interactions, three conventional hydrogen bonds with ASP A:1229, TRP A:1200, GLU A:1207 and pi interactions including pi-alkyl with LEU A:1213.

NLI exhibited nine Van der Waals interactions, four conventional hydrogen bonds with VAL A:1059, CYS A:1056, THR A:1055 and HIS A:1057 and other pi interactions.

NLJ had fifteen Van der Waals interactions, three conventional hydrogen bonds with LYS A:1030, ASP A:1150 and GLU A:1047, one pi-alkyl interaction and one pi-sulfur interaction with MET A:1153.

NLK depicted sixteen Van der Waals interactions, three conventional hydrogen bonds with LYS A:1030, ASP A:1150, GLU A:1047 and two pi interactions.

Curcumin displayed seven Van der Waals interactions, two conventional hydrogen bonds with LYS A:1030 and SER A:1006, and several pi interactions.

Acarbose engaged in five Van der Waals interactions and five conventional hydrogen bonds. This detailed breakdown helped in understanding the binding affinities and potential efficacy of these compounds as antidiabetic agents.

3DH4 – CURCUMIN ANALOGUE COMPLEXES

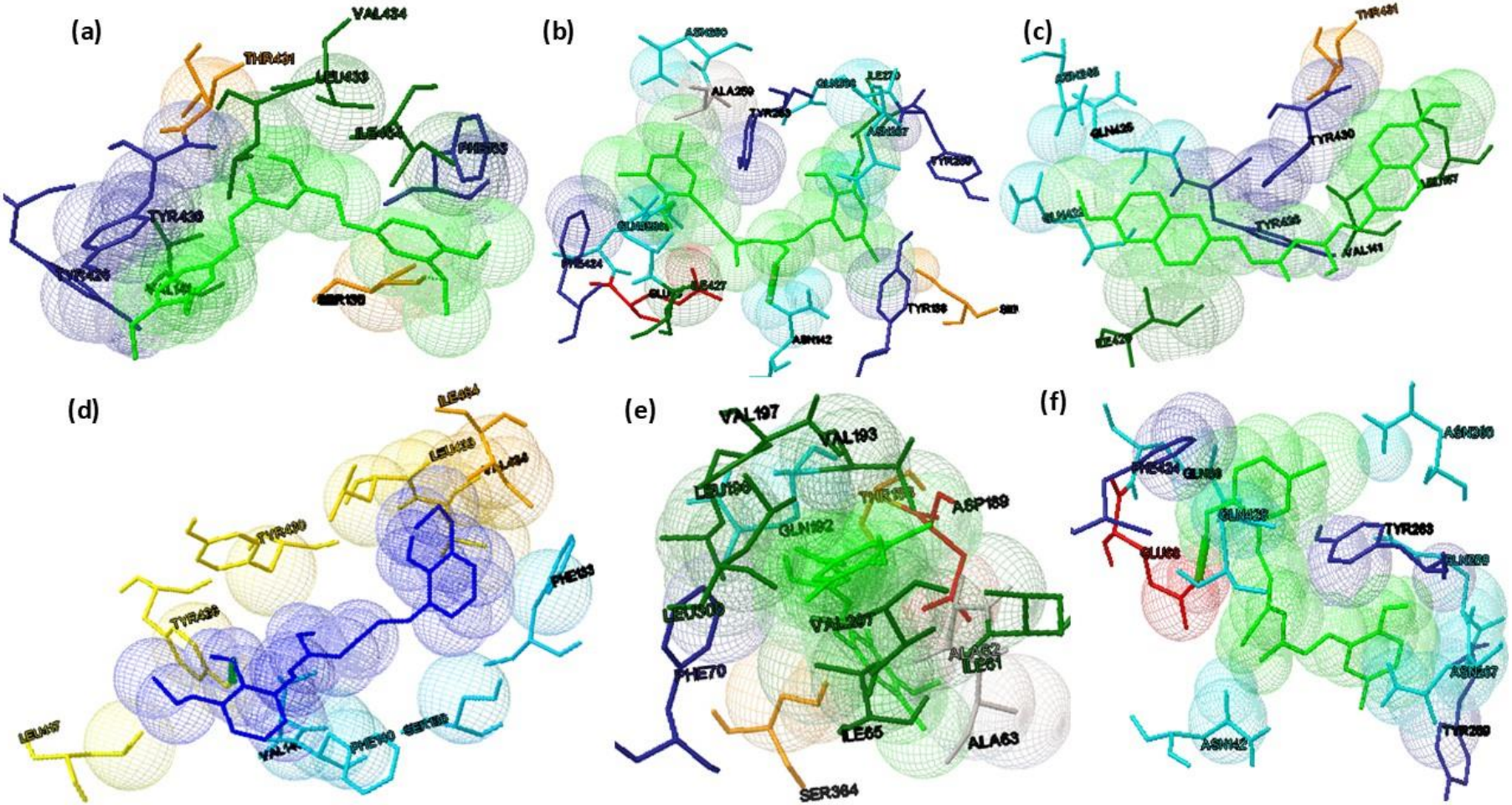

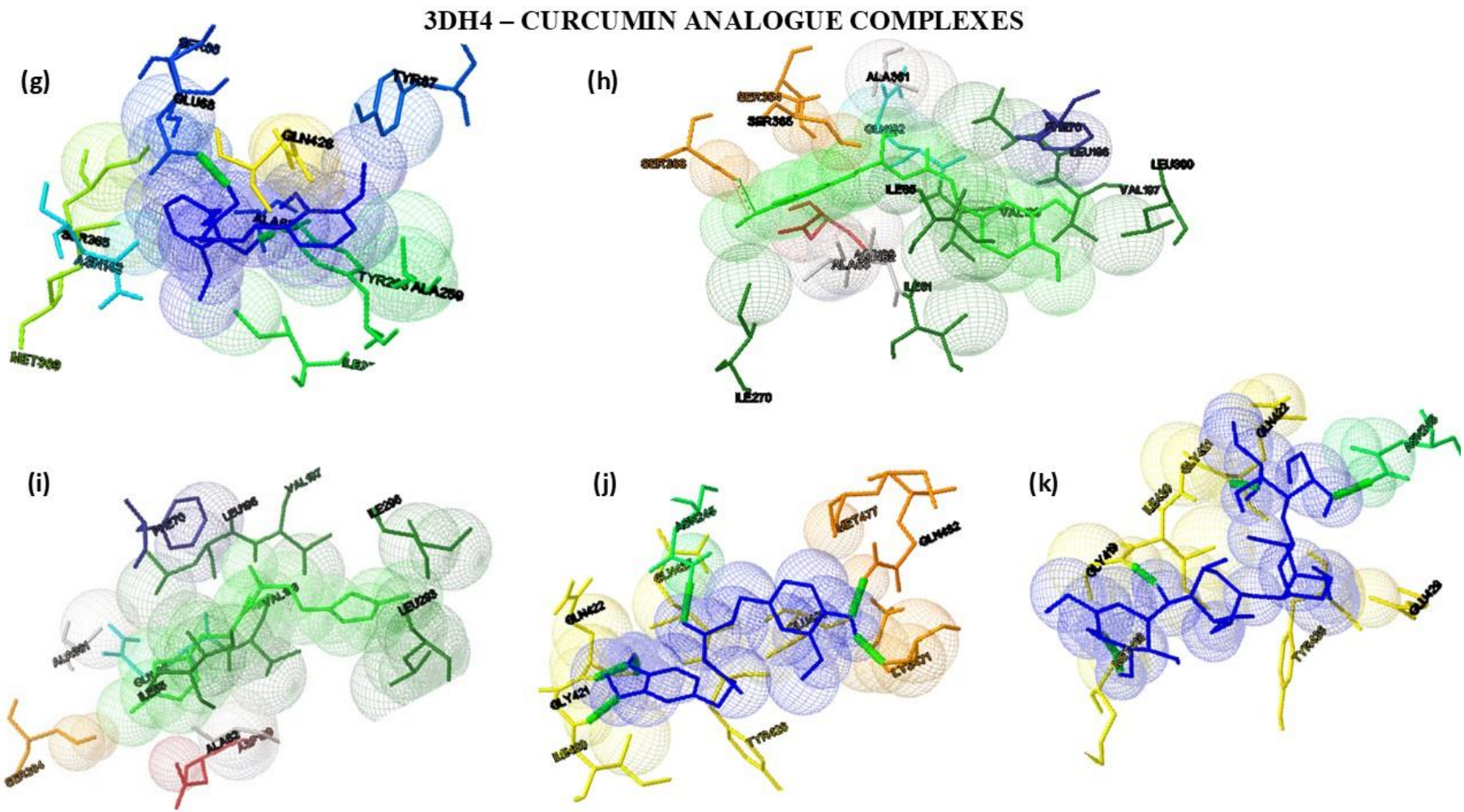

Fig. 5.11 3DH4-Curcumin Analogue Complexes (a) 3DH4-NLB Complex (b) 3DH4-NLD Complex (c) 3DH4-NLE Complex (d) 3DH4-NLF Complex (e) 3DH4-NLG Complex (f) 3DH4-NLH Complex (g) 3DH4-NLI Complex (h) 3DH4-NLJ Complex (i) 3DH4-NLK Complex (j)3DH4-Curcumin Complex (k)3DH4-Acarbose Complex

Table 5.7 The interactions of ligands with 3DH4 through various amino acid residues

Active Target	Compound		Types of Interactions								
			Van der Waals	Conventional Hydrogen Bond	Carbon Hydrogen Bond	Unfavourable Acceptor-Acceptor	Pi-Sigma	Pi-Alkyl	Pi-lone pair	Pi-Pi stacked	Alkyl
3DH4	NLB	No. of Interactions	8	2				1		1	
		Amino acid residues	LEU A:137; THR A;431; VAL A:434; LEU A:433; VAL A:132; PHE A:472; TYR A:426; VAL A:141	TYR A:430; SER A:136				ILE A:464		PHE A:133	
	NLD	No. of Interactions	8	4		1					11
		Amino acid residues	SER A:372; ASN A:260; GLN A:268; LEU A:137; THR A:431; ILE A:427; GLN A:428; GLU A:88	ASNA:267; ASNA:142; GLUA:68; GLUA A:69		ASN A:142					MET A:73; PHE A:424; ALA A:259; TYR A:138; MET A:369; ILE A:270; TYR A:269; TYR A:87; TYR A:263; MET A:7; THE A:424
	NLE	No. of Interactions	9	1	2		1	2			
		Amino acid residues	LEU A:433; TYR A:430; GLY A;421; GLN A:425; GLU A:429; TYR A:426; PHE A:140; VAL A:434; THR A:431	GLN A:422	ASN A:245; PHE A:133		VAL A:141	LEU A:137;VAL A:141			
	NLF	No. of Interactions	8	1	2		2	2			
		Amino acid residues	LEU A:433; GLY A:421; GLN A:425; GLU A:429; TYR A:426; PHE A:140; VAL A:434;THR A:431	GLN A:422	ASN A:245; PHE A:133		ILE A:420;VAL A:141	LEU A:137;VAL A:141			
	NLG	No. of Interactions	8	1			1	3	1		7
		Amino acid residues	ALA A:361; LEUA:196; VAL A:193; ILE A:296;ALA A:62;TYR A:176;THR A:188;SER A:365	ASP A:189			VAL A:197	VAL A:297;AL A:197;ILE A:65	SER A:364		ILE A:61; LEU A:293;VAL A:297;LEU A:300;VAL A:301;PHE A:70;ALA A;63

			Van der Waals	Conventional Hydrogen Bond	Carbon Hydrogen Bond	Unfavourable Acceptor-Acceptor	Pi-Sigma	Pi-Alkyl	Pi-lone pair	Pi-Pi stacked	Alkyl
	NLH	No. of Interactions	12	3							3
		Amino acid residues	THR A:431;MET A:369;SER A:372;GLN A:268;ASN A:267;SER A:91;GLN A:428;TRP A:264;ASN A:260;PHE A:424;GLN A:69;ILE A:427	ASN A:142TYR A:263; GLU A:68				TYR A:263			TYR A:269; ILE A:270; TYR A:87
	NLI	No. of Interactions	14	2			1	1	1	1	
		Amino acid residues	ALA A:63; ILE A:270; PHE A:424; TYR A:87; SER A:91;ASN A:260;TRP A:264;THR A:431;ILE A:427;ASN A:142;GLN A:69;ASN A:64;SER A:66;SER A:365	TYR A:263, GLU A:68			MET A:369	ALA A;259	GLN A:428	TYR A:263	
	NLJ	No. of Interactions	14	1			1	1	1	1	
		Amino acid residues	ALA A:63; ILE A:270; PHE A:424; TYR A:87; SER A:91; ASN A:260; TRP A:264; THRA:431; ILE A:427; ASN A:142: GLN A:69; ASN A:64; SER A:66;SER A:365	TYR A:263			MET A:369;	Al a a:259	GLN A:428	TYR A:263	
	NLK	No.of Interactions	9	1			1	3			3
		Amino acid residues	LEU A:300; PHE A:70; ILE A:65; GLN A:192; AP A:189; SER A:364; PHE A:194; ILE A:61; VAL A:297	VAL A:193			VAL A:197	ALA A:62;LEUA:196;ALAA:361			ILE A:296, LEU A:293; ALA A:361
	Curcumin	No. of Interactions	11	3			1	1			
		Amino acid residues	TYR A:426; TYR A:430; GLU A:429; GLN A:482; LEU A:470; MET A:477; PRO A:478; PHE A:479; MET A:244; GLN A:425; ALA A:423	LYS A:471; GLY A:421; GLN A:422			ILE A:420	LYS A:471			
	Acarbose	No. of Interactions	7	2	1						
		Amino acid residues	GLY A:418; LEU A:417; GLN A:242; GLN A:422; GLN A:425; TYR A:426; ILE A:420	GLU A:429; GLY A:421	ILE A:420						

Table 5.7 outlines various interactions between different antidiabetic compounds and the active site residues of the target protein 3DH4. NLB exhibited 8 van der Waals interactions with residues LEU A:137, THR A:431, VAL A:434, LEU A:433, VAL A:132, PHE A:472, TYR A:426, and VAL A:141, along with 2 conventional hydrogen bonds with TYR A:430 and SER A:136. It also formed 1 pi-alkyl interaction with ILE A:464, and 1 pi-pi stacked interaction with PHE A:133.

NLD sketched 8 van der Waals interactions with residues SER A:372, ASN A:260, GLN A:268, LEU A:137, THR A:431, ILE A:427, GLN A:428, and GLU A:88, 4 conventional hydrogen bonds with ASN A:267, ASN A:142, GLU A:68, and GLU A:69, 1 carbon hydrogen bond with ASN A:142, and 11 pi-alkyl interactions with MET A:73, PHE A:424, ALA A:259, TYR A:138, MET A:369, ILE A:270, TYR A:269, TYR A:87, TYR A:263, MET A:73, and THE A:424.

NLE witnessed 9 van der Waals interactions with residues LEU A:433, TYR A:430, GLY A:421, GLN A:425, GLU A:429, TYR A:426, PHE A:140, VAL A:434, and THR A:431, 1 conventional hydrogen bond with GLN A:422, 2 carbon hydrogen bonds with ASN A:245 and PHE A:133, 1 pi-sigma interaction with VAL A:141, 2 pi-alkyl interactions with LEU A:137 and VAL A:141.

NLF unveiled 8 van der Waals interactions with residues LEU A:433, GLY A:421, GLN A:425, GLU A:429, TYR A:426, PHE A:140, VAL A:434, and THR A:431, 1 conventional hydrogen bond with GLN A:422, 2 carbon-hydrogen bonds with ASN A:245 and PHE A:133, 2 pi-sigma interactions with ILE A:420 and VAL A:141, 2 pi-alkyl interactions with LEU A:137 and VAL A:141.

NLG interacted via 8 van der Waals forces with residues ALA A:361, LEU A:196, VAL A:193, ILE A:296, ALA A:62, TYR A:176, THR A:188, and SER A:365, 1 conventional hydrogen bond with ASP A:189, 1 pi-sigma interaction with VAL A:197, 3 pi-alkyl interactions with VAL A:297, VAL A:197, and ILE A:65, 1 pi-lone pair interaction with SER A:364, 7 pi-pi stacked interactions with ILE A:61, LEU A:293, VAL A:297, LEU A:300, VAL A:301, PHE A:70, and ALA A:63.

NLH showed 12 van der Waals interactions with residues THR A:431, MET A:369, SER A:372, GLN A:268, ASN A:267, SER A:91, GLN A:428, TRP A:264, ASN A:260, PHE A:424, GLN A:69, and ILE A:427, 3 conventional hydrogen bonds with ASN A:142, TYR A:263, and GLU A:68, 1 pi-alkyl interaction, 3 alkyl interactions.

NLI produced 14 van der Waals interactions with residues ALA A:63, ILE A:270, PHE A:424, TYR A:87, SER A:91, ASN A:260, TRP A:264, THR A:431, ILE A:427, ASN A:142, GLN A:69, ASN A:64, SER A:66, and SER A:365, 2 conventional hydrogen bonds with TYR A:263 and GLU A:68, 1 pi-sigma interaction with MET A:369, 1 pi-alkyl interaction with ALA A:259, 1 pi-lone pair interaction with GLN A:428, and 1 pi-pi stacked interaction with TYR A:263.

NLJ gave rise to 14 van der Waals interactions with residues ALA A:63, ILE A:270, PHE A:424, TYR A:87, SER A:91, ASN A:260, TRP A:264, THR A:431, ILE A:427, ASN A:142, GLN A:69, ASN A:64, SER A:66, and SER A:365, 1 conventional hydrogen bond with TYR A:263, 1 pi-sigma interaction with MET A:369, 1 pi-alkyl interaction with ALA A:259, 1 pi-lone pair interaction with GLN A:428, and 1 pi-pi stacked interaction with TYR A:263.

NLK germinated 9 van der Waals interactions with residues LEU A:300, PHE A:70, ILE A:65, GLN A:192, ASP A:189, SER A:364, PHE A:194, ILE A:61, and VAL A:297, 1 conventional hydrogen bond with VAL A:193, 1 pi-sigma interaction with VAL A:197, 3 pi-alkyl interactions with ALA A:62, LEU A:196, and ALA A:361, and 3 alkyl interactions with ILE A:296, LEU A:293, and ALA A:361.

Curcumin interacted via 11 van der Waals forces with residues TYR A:426, TYR A:430, GLU A:429, GLN A:482, LEU A:470, MET A:477, PRO A:478, PHE A:479, MET A:244, GLN A:425, and ALA A:423, 3 conventional hydrogen bonds with LYS A:471, GLY A:421, and GLN A:422, 1 pi-sigma interaction with ILE A:420, and 1 pi-alkyl interaction with LYS A:471.

Acarbose awakened 7 van der Waals interactions with residues GLY A:418, LEU A:417, GLN A:242, GLN A:422, GLN A:425, TYR A:426, and ILE A:420, 2 conventional hydrogen bonds with GLU A:429 and GLY A:421, 1 carbon-hydrogen bond with ILE A:420.

This detailed breakdown highlighted the diverse interactions each compound had with the active site residues of the target protein 3DH4, aiding in understanding their binding affinities and potential efficacy as antidiabetic agents.

The prioritisation of ligands against target 3DH4 is based on their docking scores especially their binding energy (BE), inhibition constant (Ki), and ligand efficiency (LE). NLH is the top ligand, exhibiting strong binding energy (-8.13 kcal/mol), the lowest inhibition constant (Ki: 1.1 nM), and solid ligand efficiency (-0.33), indicating high

potency and efficacy. NLJ ranks second, with good binding energy (-7.74 kcal/mol) and a low inhibition constant (Ki: 2.13 nM), supported by respectable ligand efficiency (-0.29). NLI follows, with moderate binding energy (-7 kcal/mol) and a relatively low inhibition constant (Ki: 7.37 nM), though its ligand efficiency (-0.26) is slightly lower than NLJ.

NLB is next, displaying moderate binding energy (-6.77 kcal/mol) and a higher inhibition constant (Ki: 10.86 nM) than the top ligands, with lower ligand efficiency (-0.23). NLF, with moderate binding energy (-6.52 kcal/mol) and a relatively low inhibition constant (Ki: 16.52 nM), is ranked after NLB, supported by lower ligand efficiency (-0.22).

Despite strong binding energy (-9.13 kcal/mol), NLK is ranked lower due to a high inhibition constant (Ki: 201.8 nM), indicating lower potency. However, its high ligand efficiency (-0.43) suggests good effectiveness relative to its size. NLG, with strong binding energy (-8.78 kcal/mol) but a very high inhibition constant (Ki: 365.08 nM), ranks below NLK due to its high Ki, despite solid ligand efficiency (-0.33). NLD, exhibiting strong binding energy (-8.51 kcal/mol) but an even higher inhibition constant (Ki: 579.09 nM), indicates lower potency, with comparable ligand efficiency (-0.32) to NLG. NLE, with strong binding energy (-8.42 kcal/mol) but the highest inhibition constant (Ki: 670.6 nM) among the top ligands, ranks lower due to its higher Ki and lower ligand efficiency (-0.26).

Curcumin, showing lower binding energy (-5.96 kcal/mol) and a higher inhibition constant (Ki: 42.58 nM) compared to other ligands, is less effective, supported by lower ligand efficiency (-0.22). Lastly, Acarbose, with the poorest binding energy (-1.24 kcal/mol) and the highest inhibition constant (Ki: 123.61 nM) among the ligands, has very low ligand efficiency (-0.03), making it the least effective.

This prioritisation emphasises ligands with the strongest binding energies and lowest inhibition constants, ensuring high efficacy while considering ligand efficiency for effectiveness relative to size. The ligands NLB and NLH rank highest for targets based on their strong binding energies, low inhibition constants, and solid ligand efficiencies, indicating high potency and efficacy for the anti-diabetic targets 1IR3 and 3DH4 respectively. Other ligands like NLE, NLG, and NLJ also show strong efficacy across both targets. In contrast, Acarbose and Curcumin rank lowest due to their poor binding energies, high inhibition constants, and low ligand efficiencies.

5.4.2.2. *In vitro* studies

The Alpha-amylase inhibition assay was analysed for finalising the percentage of inhibition and subsequently the IC_{50} values of the synthesised curcumin analogues and their Cu(II) and Zn(II) metal complexes for their antidiabetic effects.

5.4.2.2.1. Anti-diabetic effect of curcumin analogues

The IC_{50} values established the potency of various ligands, with lower values representing higher potency. Among the tested ligands, 1,7-bis(3,4-dimethoxy phenyl) hepta-1,6-diene-3,5-dione (NLB) (26.68 µg), 1,7-bis(5-chloro-2-hydroxy phenyl) hepta-1,6-diene-3,5-dione (NLH) (29.90 µg), and 1,7-bis(6-methoxy naphthalen-2-yl)hepta-1,6-diene-3,5-dione (NLE) (30.45 µg) emerged as the most potent inhibitors, demonstrating the lowest IC_{50} values. Moderately potent ligands included 1,7-bis(4-hydroxy-3,5 dimethyl phenyl) hepta-1,6-diene-3,5-dione (NLG) (44.06 µg), 1,7-bis(3,5-dichloro-2-hydroxyphenyl)hepta-1,6-diene-3,5-dione (NLD) (44.66 µg), 1,7-bis(5-methyl thiophen-2-yl) hepta-1,6-diene-3,5-dione (NLK) (47.64 µg), and 1,7-bis(3-hydroxy-4-methoxy phenyl) hepta-1,6-diene-3,5-dione) (NLJ) (48.09 µg). In contrast, 1,7-bis(3-ethoxy-2-hydroxy phenyl) hepta-1,6-diene-3,5-dione (NLF) (60.34 µg), 1,7-bis(2-hydroxy-3-methoxy phenyl)hepta-1,6-diene-3,5-dione (NLI) (74.39 µg), curcumin (74.39 µg), and acarbose (78.81 µg) were the least potent. These findings suggested that the synthetic ligands, particularly NLB, NLH, and NLE, were more effective inhibitors than the natural compounds curcumin and acarbose.

The observed differences in the antidiabetic effects of the tested compounds, as reflected by their IC_{50} values, were explained by the types and positions of functional groups that influenced their stability, binding affinity, and interactions with molecular targets involved in glucose metabolism and insulin regulation. In NLB, the dimethoxy groups at the 3,4-positions increased electron donation and stabilized the conjugated system, enhancing interactions with enzyme active sites and improving hydrophobicity for better cellular uptake. In NLH, the chloro and hydroxy groups at the 5 and 2 positions, respectively, facilitated a combination of hydrogen bonding and halogen-mediated interactions with target proteins such as α-amylase and α-glucosidase, thereby enhancing inhibitory activity. In NLE, the methoxy groups on naphthyl rings provided hydrophobic interactions and stabilized the interaction of the compounds with enzyme active sites due to increased conjugation and planarity. In NLG, the hydroxy and methyl groups at the 4, 3, and 5 positions enhanced hydrogen bonding but were less effective due to steric hindrance, reducing overall potency compared to the most potent ligands. In NLD, the

dichloro groups at the 3,5 positions increased electron withdrawal and stabilized binding, but excessive electron deficiency reduced affinity for some targets. In NLK, the thiophenyl groups provided π-π interactions and hydrophobicity, but the lack of additional hydrogen-bonding groups limited binding affinity. In NLJ, the hydroxy and methoxy groups, while offering moderate hydrogen bonding and electron donation, did not align optimally for high binding affinity. In NLF, the ethoxy and hydroxy groups increased hydrophilicity, which hindered interactions with hydrophobic enzyme pockets, thereby reducing potency. In NLI, the hydroxy and methoxy groups at the 2,3 positions, while providing stabilization, were less effective at maximizing interactions with active site residues due to their positioning. Curcumin, despite its conjugated structure, exhibited limited functional group diversity, which reduced its ability to form strong and specific interactions with targets. Acarbose, had a bulky structure and lacked optimal hydrophobic or hydrogen-bonding substituents, making it less effective than the synthetic ligands.

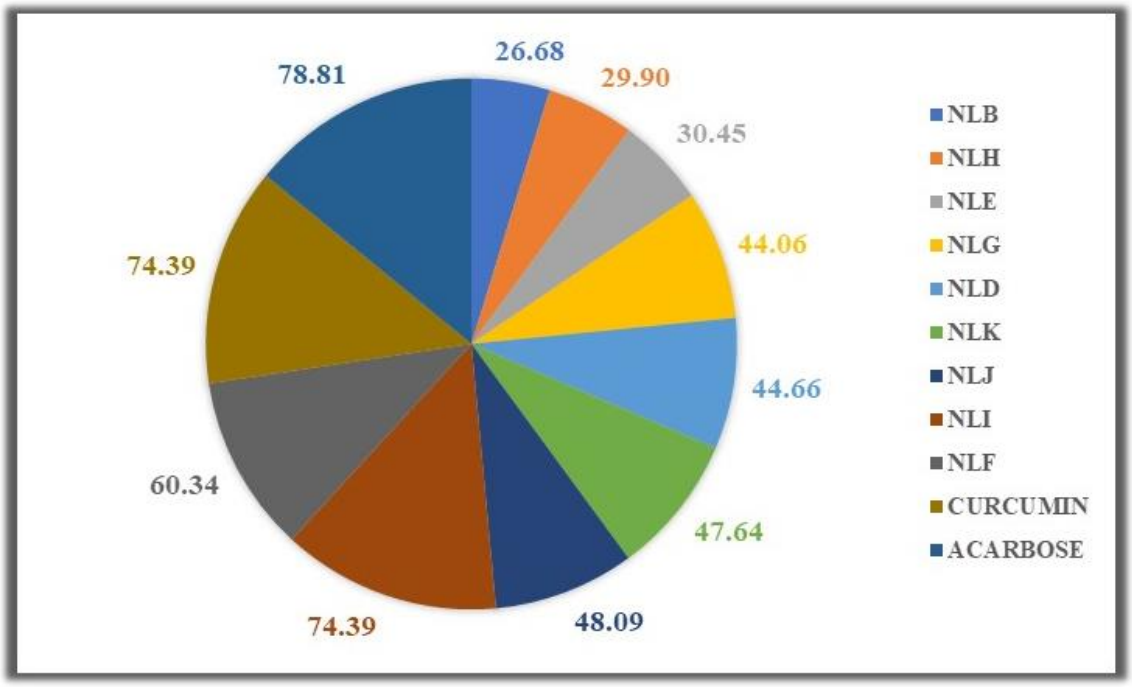

Fig.5.12 The IC_{50} values (in µg) of various curcumin analogues and reference compounds (Curcumin and Acarbose).

5.4.2.2.2. Anti-diabetic effect of Cu (II) metal complexes

The IC_{50} values of the Cu(II) complexes of curcumin analogues proved that $Cu(NLD)_2$ (25.43 µg), $Cu(NLB)_2$ (25.88 µg), and $Cu(NLE)_2$ (27.55 µg) were the most potent inhibitors. Moderately potent complexes included $Cu(NLF)_2$ (43.06 µg), $Cu(NLG)_2$ (42.86 µg), $Cu(NLH)_2$ (45.53 µg), and $Cu(NLI)_2$ (45.11 µg). The least potent

complexes were $Cu(NLJ)_2$ (66.31 µg), $Cu(NLK)_2$ (57.54 µg), natural curcumin (74.39 µg), and acarbose (78.81 µg). These results indicated that the synthesized Cu(II) complexes were more effective inhibitors for antidiabetic effects, with $Cu(NLD)_2$, $Cu(NLB)_2$, and $Cu(NLE)_2$ emerging as promising candidates for further development and testing in antidiabetic therapies. Conversely, the natural compounds curcumin and acarbose were less potent inhibitors compared to the synthesized Cu(II) complexes.

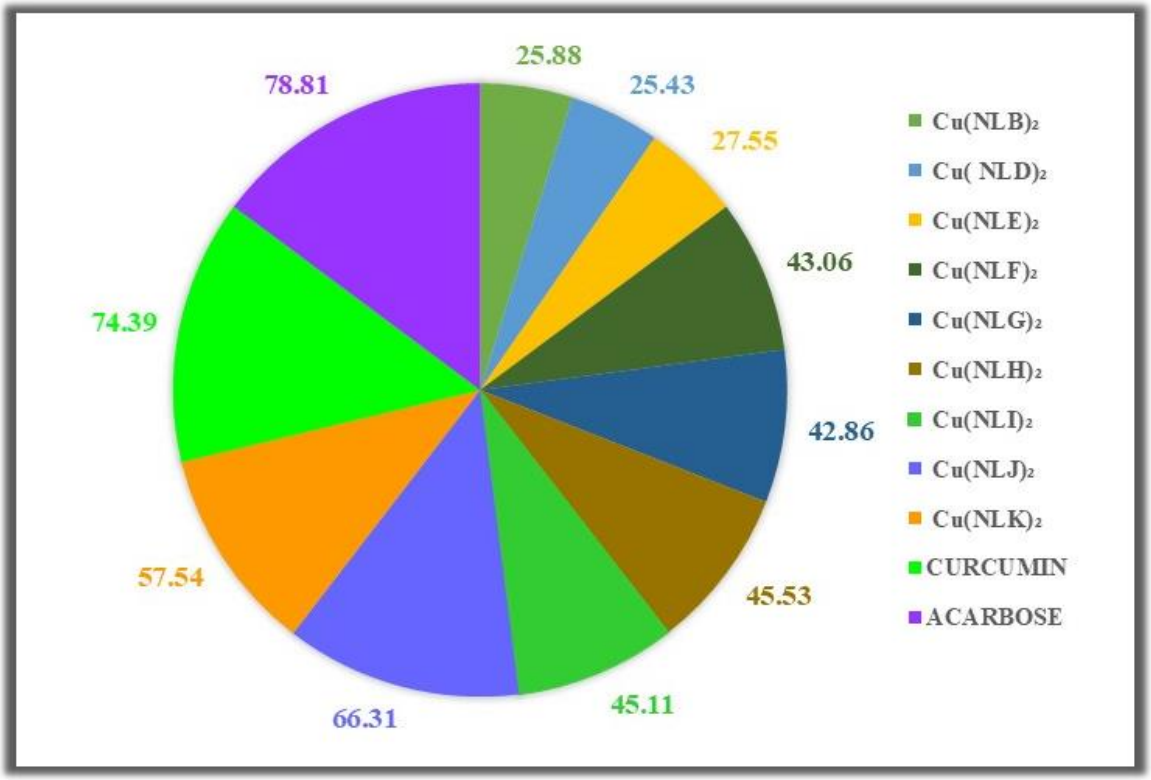

Fig.5.13 IC_{50} values (in µg) for Cu(II) complexes of various curcumin analogues and reference compounds curcumin and Acarbose.

5.4.2.2.3. Anti-diabetic effect of Zn (II) metal complexes

The Zn(II) complexes manifested a range of IC_{50} values, with $Zn(NLB)_2$ (22.18 µg) being the most potent, as evidenced by its lowest IC_{50} value, and $Zn(NLJ)_2$ (61.56 µg)being among the least potent. $Zn(NLD)_2$ (23.83 µg), $Zn(NLE)_2$ (25.55 µg) and $Zn(NLH)_2$ (32.33 µg)were also highly potent inhibitors. $Zn(NLF)_2$ (40.86 µg), $Zn(NLG)_2$ (41.46 µg), $Zn(NLI)_2$ (42.09 µg), and $Zn(NLK)_2$ (53.54 µg) were moderately potent inhibitors. This suggested that the specific ligand and the nature of its interaction with Zn(II) significantly impacted the biological activity. When compared with natural curcumin and Acarbose, which had higher IC_{50} values (74.39 µg and 78.81 µg,

respectively), it was evident that the Zn(II) complexes of the curcumin analogues were generally more effective in inhibiting the target.

The differences in IC_{50} values highlighted the potential of these complexes as more effective inhibitors and they necessitated further exploration of these Zn(II) complexes would lead to the development of more potent therapeutic agents. The observed structure-activity relationship also foretold that specific ligand modifications could significantly impact the effectiveness of the complexes.

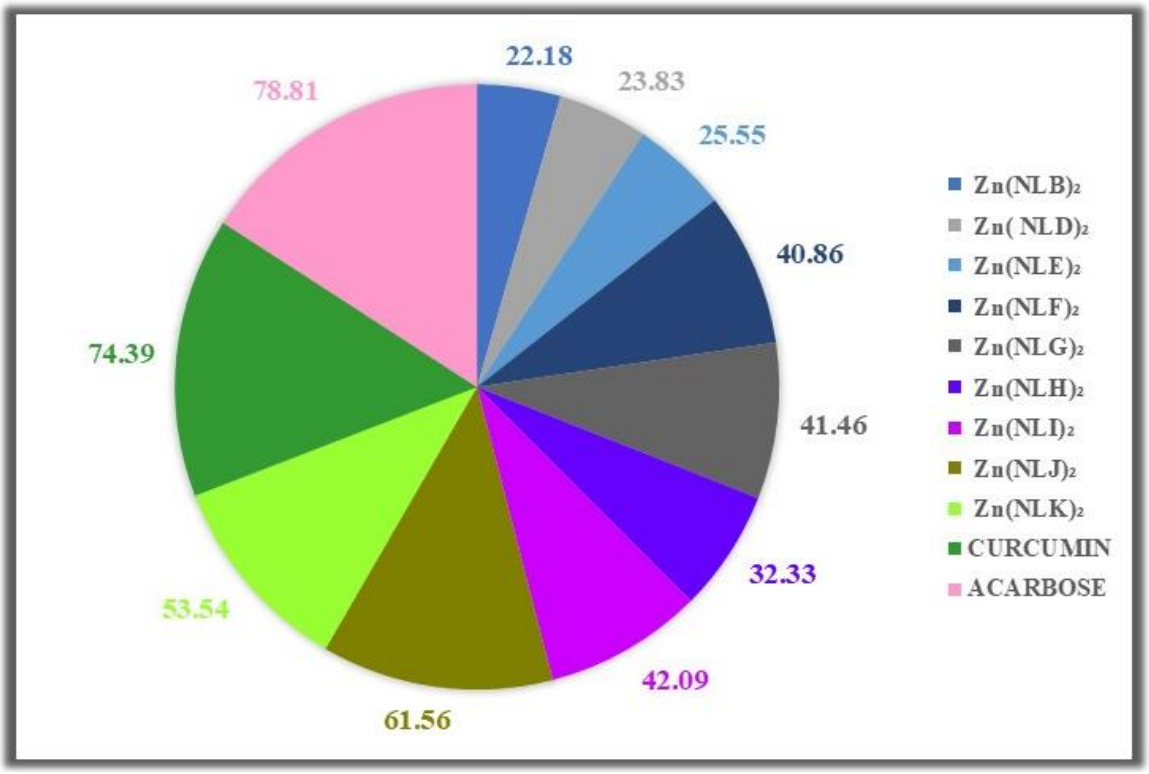

Fig.5.14 IC_{50} values for various Zn(II) complexes of curcumin analogues, natural curcumin, and a reference compound, Acarbose.

Comparative analysis of antidiabetic effects of curcumin analogues and their Cu(II) and Zn(II) complexes

The comparative study of anti-diabetic potency across curcumin analogues, their Cu(II) and Zn(II) complexes, and standard compounds revealed that both metal complexes and synthetic ligands exhibited notable improvements in activity compared to natural curcumin and Acarbose. Among the ligands, NLB, NLH, and NLE witnessed superior potency. The Cu(II) and Zn(II) complexes generally outperformed these ligands,

with $Cu(NLD)_2$, $Cu(NLB)_2$, $Cu(NLE)_2$, $Zn(NLB)_2$, $Zn(NLD)_2$, $Zn(NLE)_2$ and $Zn(NLH)_2$ demonstrating the highest anti-diabetic activity. This substantiated that metal complexation would significantly foster the inhibitory effects of curcumin analogues.

Zn(II) complexes of curcumin analogues were generally found to be more effective than Cu(II) complexes for antidiabetic effects due to several factors. Zinc stabilized insulin hexamers in pancreatic β-cells, aiding in insulin release and enhancing glucose uptake through insulin signalling. Its anti-inflammatory and antioxidant properties further protected pancreatic β-cells from oxidative stress. Zn(II) complexes offered better stability, bioavailability, and safety compared to Cu(II) complexes, which were less stable and could produce harmful reactive oxygen species. The lower toxicity of zinc, combined with its synergistic effects with the bioactive properties of curcumin, made Zn(II) complexes a promising option for diabetes management.

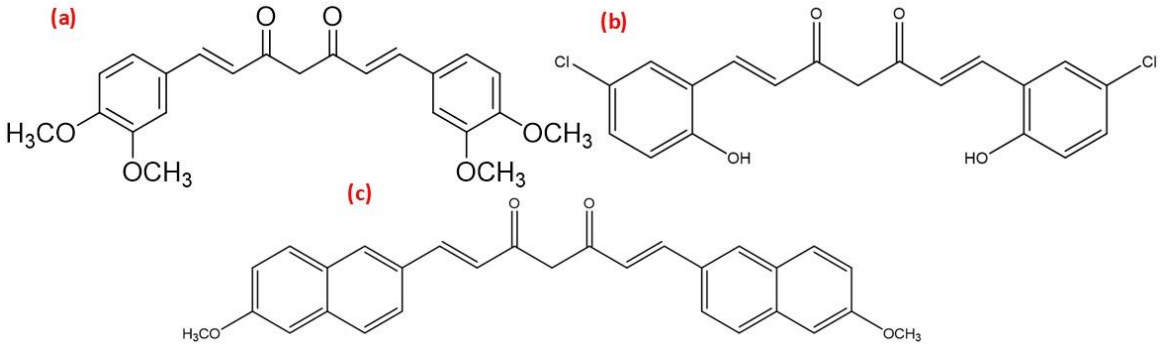

Fig.5.15 The best ligands demonstrating anti-diabetes effects.
(a) NLB(1,7-bis(3,4-dimethoxyphenyl)hepta-1,6-diene-3,5-dione)
(b) NLH(1,7-bis(5-chloro-2-hydroxyphenyl) hepta-1,6-diene-3,5-dione)
(c) NLE(1,7-bis (6-methoxynaphthalen-2-yl) hepta-1,6-diene-3,5-dione)

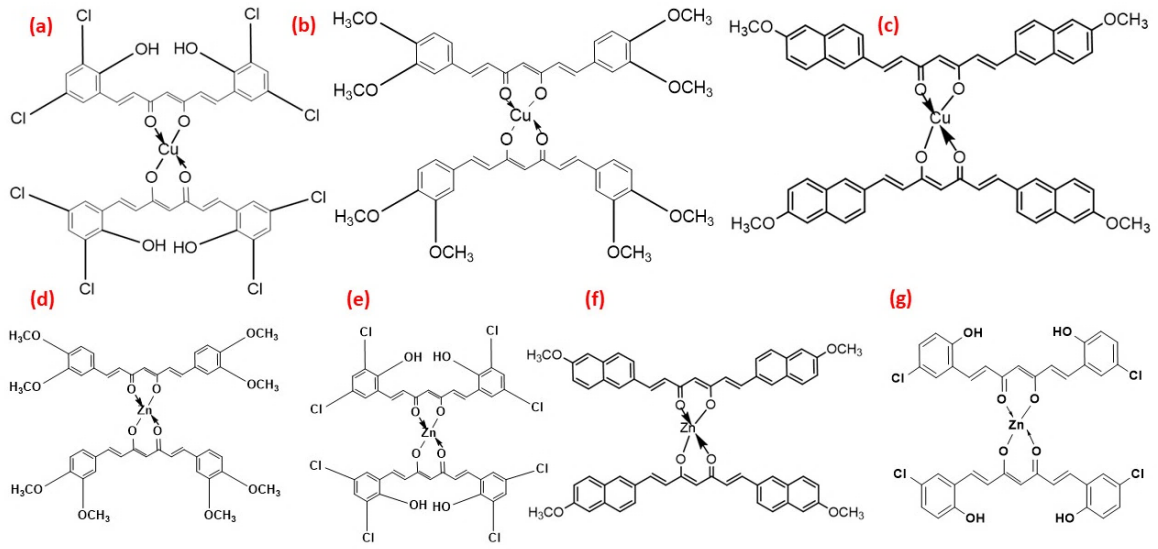

Fig.5.16 The best Cu(II) and Zn(II) complexes of curcumin analogues demonstrating antidiabetes effects.
(a) Cu(NLD) (Cu(II) complex of 1,7-bis(3,5-dichloro-2-hydroxyphenyl)hepta-1,6-diene-3,5-dione)
(b) Cu(NLB) (Cu(II) complex of 1,7-bis(3,4-dimethoxyphenyl)hepta-1,6-diene-3,5-dione)
(c) Cu(NLE) (Cu(II) complex of 1,7-bis(6-methoxy naphthalen-2-yl)hepta-1,6-diene-3,5-dione)
(d) Zn(NLB) (Zn(II) complex of 1,7-bis(3,4-dimethoxyphenyl)hepta-1,6-diene-3,5-dione)
(e) Zn(NLD) (Zn(II) complex of 1,7-bis(3,5-dichloro-2-hydroxyphenyl)hepta-1,6-diene-3,5-dione)
(f) Zn(NLE) (Zn(II) complex of 1,7-bis(6-methoxy naphthalen-2-yl)hepta-1,6-diene-3,5-dione)
(g) Zn(NLH) (Zn(II) complex of 1,7-bis(5-chloro-2-hydroxyphenyl) hepta-1,6-diene-3,5-dione)

5.4.3. Splenocytic Assay (Spleen Cell Lines)

Based on the studies of anti-inflammatory and antidiabetic activity, the most promising ligands and complexes were selected for splenocytic assays. These assays ought to predict the potential toxicity of these compounds to normal cells while evaluating their suitability as drug candidates for anti-inflammatory and antidiabetic therapies. The percentage of splenocytic death at various concentrations of each compound is shown in **Table 5.8** and **Fig.5.17**.

Table 5.8 The percentage of cell death at different concentrations for each compound in Spleen Cell Lines.

Concentration µg/mL		NLD	NLB	NLE	NLH	$Cu(NLH)_2$	$Cu(NLD)_2$	$Cu(NLE)_2$	$Cu(NLB)_2$	$Zn(NLH)_2$	$Zn(NLB)_2$	$Zn(NLD)_2$	$Zn(NLE)_2$
10	% of Spean Cell death	4.55	3.65	5.01	4.59	4.62	4.32	3.9	3.55	3.57	3.25	5.4	5.04
20		4.55	3.69	5.5	4.59	4.62	4.59	4.5	3.58	3.57	3.25	5.9	5.7
50		5.21	4.68	6.2	4.59	4.65	5.99	6.9	4.5	3.57	4.01	7.1	6.8
100		13	12.1	12.1	8.66	7.55	14	14.5	7.26	4.89	5.86	15.2	12.5
200		20	17.5	17.9	14.5	10.56	20.01	18.05	13.4	8.07	12.1	20.2	18.1

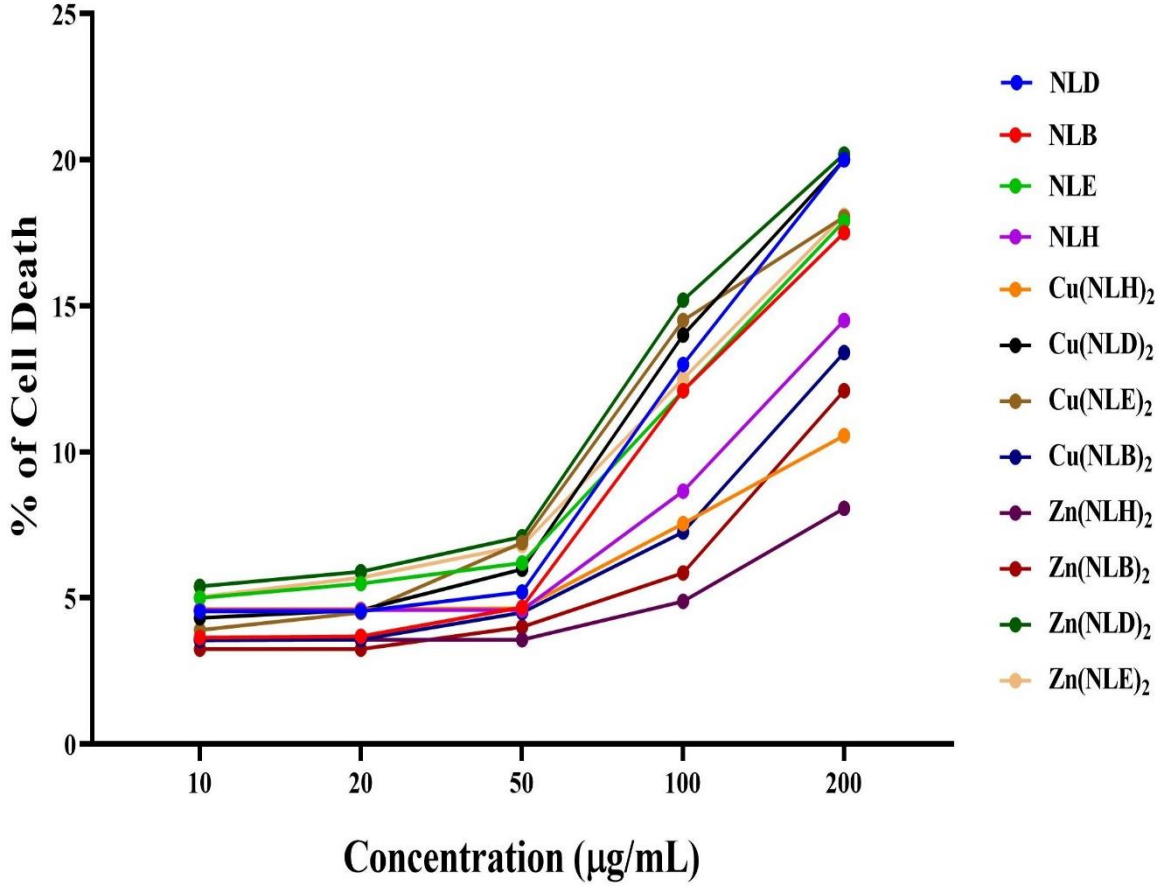

Fig.5.17 The percentage of cell death at different concentrations for each compound in Spleen Cell Lines. The data points are connected to illustrate the trend for each compound across the concentration range of 10 to 200 µg/mL.

For the individual ligands (NLD, NLB, NLE, NLH), cell death is generally augmented with concentration. NLD, NLE, and NLH showed comparable cell death percentages at lower concentrations (10-50 µg/mL), but at higher concentrations (100-200 µg/mL), NLD and NLE exhibited slightly higher toxicity compared to NLB and NLH.

Copper complexes ($Cu(NLH)_2$, $Cu(NLD)_2$, $Cu(NLE)_2$, $Cu(NLB)_2$) followed a similar trend where cell death increased with concentration. The copper complexes, particularly $Cu(NLH)_2$ and $Cu(NLB)_2$, generally showed decreasing cell death percentages compared to their corresponding ligands at higher concentrations (100-200 μM). This asserted a potential reduction in toxicity when the ligands were complexed with copper.

Zinc complexes ($Zn(NLH)_2$, $Zn(NLB)_2$, $Zn(NLD)_2$, $Zn(NLE)_2$) exhibited an increase in cell death with concentration, similar to the copper complexes. However, zinc complexes $Zn(NLH)_2$ and $Zn(NLB)_2$ consistently figured lower cell death percentages compared to their corresponding ligands, indicating a more pronounced reduction in toxicity with zinc complexation.

The reduced cell death observed in Zn(II) and Cu(II) complexes compared to their corresponding ligands was attributed to the stabilization of ligand structures upon metal complexation, which likely reduced the availability of free ligand molecules to interact with cellular components and mitigated toxicity by controlling the release and bioavailability of reactive species. Zn(II) complexes, being redox-inactive due to their full d10 electron configuration, minimized the generation of reactive oxygen species (ROS), whereas Cu(II) complexes, with their redox-active d9 configuration, catalyzed ROS production, potentially leading to oxidative stress and higher cell toxicity. Zinc, as an essential trace element, exhibited greater biological compatibility and minimal inherent toxicity compared to copper, which in excess could disrupt redox balance. Zn(II) also formed highly stable complexes due to its strong coordination properties, reducing the concentration of free ligands and ensuring controlled release, thereby lowering cytotoxic effects. Moreover, Zn(II) complexes engaged in less aggressive interactions with cellular components than Cu(II) complexes, as they were less prone to redox cycling or electron transfer reactions that could damage biomolecules.

These findings consolidated that Zn(II) complexes provided a safer therapeutic profile through reduced ROS generation, enhanced stability, and superior biocompatibility, making them less toxic than Cu(II) complexes.

5.5. CONCLUSION

This chapter evaluated nine synthesised curcumin analogues as inhibitors for inflammatory and diabetes receptors through molecular docking and *in vitro* experiments. It also compared their binding affinities with natural curcumin and FDA-approved drugs (Diclofenac and Acarbose). It included *in vitro* assessments of Cu(II) and Zn(II) complexes of curcumin analogues and splenocytic assays of top candidates.

Among curcumin analogues, 1,7-bis(3,5-dichloro-2-hydroxy phenyl)hepta-1,6-diene-3,5-dione (NLD), 1,7-bis (6-methoxynaphthalen-2-yl) hepta-1,6-diene-3,5-dione (NLE), and 1,7-bis (3-ethoxy-2-hydroxyphenyl) hepta-1,6-diene-3,5-dione (NLF) were identified as the most potent anti-inflammatory inhibitors, followed by 1,7-bis (5-chloro-2-hydroxyphenyl) hepta-1,6-diene-3,5-dione (NLH), 1,7-bis(5-methylthiophen-2-yl) hepta-1,6-diene-3,5-dione (NLK), and Diclofenac. Curcumin itself, along with 1,7-bis (3,4-dimethoxy phenyl) hepta-1,6-diene-3,5-dione (NLB),1,7-bis(4-hydroxy-3,5-dimethyl phenyl) hepta-1,6-diene-3,5-dione (NLG), 1,7-bis (2-hydroxy-3-methoxyphenyl) hepta-1,6-diene-3,5-dione (NLI), and 1,7-bis (3-hydroxy-4-methoxyphenyl) hepta-1,6-diene-3,5-dione (NLJ), showed lower potency, with NLI and NLJ being the least effective.

The differences in the anti-inflammatory potency of the mentioned curcumin analogues were attributed to the types and positions of their functional groups, which influenced stability, binding affinity, and interactions with molecular targets such as COX enzymes and inflammatory mediators. Compounds like NLD and NLH, with chloro groups, exhibited enhanced potency due to the electron-withdrawing nature of halogens, with dichloro substitution of NLD further increasing its efficacy. The methoxy groups of NLE and the ethoxy and hydroxy groups of NLF enhanced lipophilicity and hydrogen bonding, improving their binding stability and potency. In contrast, NLK, with methyl thiophenyl groups, showed moderate efficacy due to limited hydrogen bonding potential, while the dimethoxy groups of NLB reduced electrophilicity, weakening target interactions. NLI and NLJ exhibited the least potency due to the suboptimal positioning of their hydroxy and methoxy groups for strong interactions. Thus, the compounds like NLD, NLE, and NLF, which balanced hydrophilic (hydroxy) and hydrophobic (halogen, methoxy, ethoxy) substituents, demonstrated superior potency due to improved binding affinity and cellular uptake, while excessive hydrophilicity or hydrophobicity without functional diversity diminished efficacy, as seen in curcumin, NLI, and NLJ.

Cu(II) complexes exhibited superior potency over curcumin analogues, with $Cu(NLH)_2$, $Cu(NLD)_2$, and $Cu(NLE)_2$ demonstrating enhanced inhibitory activity. Similarly, Zn(II) complexes demonstrated better anti-inflammatory effects than curcumin, with $Zn(NLH)_2$ and $Zn(NLE)_2$ being particularly potent. Zn(II) complexes generally surpassed Cu(II) complexes in effectiveness. The enhanced anti-inflammatory efficacy of Zn(II) complexes in comparison to Cu(II) complexes was attributed to their superior stability, antioxidant properties, and compatibility with biological systems. The electron configuration of Zn(II), characterized by a d10 arrangement, facilitated the formation of stable complexes with curcumin analogues, thereby improving their bioavailability and persistence, whereas the d9 configuration of Cu(II), which was redox-active, contributed to the generation of reactive oxygen species (ROS) and induced oxidative stress. The non-redox nature of Zn(II) complexes, along with their essential role in biological processes, rendered them more efficacious for anti-inflammatory interventions.

For anti-diabetic activity, 1,7-bis (3,4-dimethoxy phenyl) hepta-1,6-diene-3,5-dione (NLB), 1,7-bis (5-chloro-2-hydroxyphenyl) hepta-1,6-diene-3,5-dione (NLH) (NLH), and 1,7-bis (6-methoxynaphthalen-2-yl) hepta-1,6-diene-3,5-dione (NLE) analogues portrayed superior potency. Cu(II) and Zn(II) complexes generally outperformed these ligands, with $Cu(NLD)_2$, $Cu(NLB)_2$, $Cu(NLE)_2$, $Zn(NLB)_2$, $Zn(NLD)_2$, $Zn(NLE)_2$, and $Zn(NLH)_2$ presenting the highest activity. Zn(II) complexes were more effective due to their role in stabilizing insulin hexamers, enhancing glucose uptake, and offering better stability, bioavailability, and safety compared to Cu(II) complexes. The lower toxicity and synergistic effects of Zn(II) complexes with the bioactive properties of curcumin made them promising for diabetes management. The splenocytic assay confirmed the efficacy of the most promising drug candidates.

5.6. REFERENCES

1. Bezzio, C., Della Corte, C., Vernero, M., Di Luna, I., Manes, G., &Saibeni, S. (2022). Inflammatory bowel disease and immune-mediated inflammatory diseases: looking at the less frequent associations. *Therapeutic Advances in Gastroenterology*, *15*, 17562848221115312.
2. Kunnumakkara, A. B., Sailo, B. L., Banik, K., Harsha, C., Prasad, S., Gupta, S. C., ... & Aggarwal, B. B. (2018). Chronic diseases, inflammation, and spices: how are they linked?.*Journal of translational medicine*, *16*, 1-25.
3. Oray, M., Abu Samra, K., Ebrahimiadib, N., Meese, H., & Foster, C. S. (2016). Long-term side effects of glucocorticoids. *Expert opinion on drug safety*, *15*(4), 457-465.
4. Pradeepa, R., & Mohan, V. (2021). Epidemiology of type 2 diabetes in India. *Indian journal of ophthalmology*, *69*(11), 2932-2938.
5. Balaji, R., Duraisamy, R., & Kumar, M. P. (2019). Complications of diabetes mellitus: A review. *Drug Invention Today*, *12*(1),1-98.
6. Hu, C., & Jia, W. (2021). Multi-omics profiling: the way toward precision medicine in metabolic diseases. *Journal of molecular cell biology*, *13*(8), 576-593.
7. Wishart, D. S. (2019). Metabolomics for investigating physiological and pathophysiological processes. *Physiological reviews*, *99*(4), 1819-1875.
8. Vishwakarma, R. K., & Negi, D. S. (2020). The development of COX-1 and COX-2 inhibitors: a review. *Int J Pharm Sci Res*, *11*(8), 3544-3558.
9. Rajakariar, R., Yaqoob, M. M., & Gilroy, D. W. (2006). COX-2 in inflammation and resolution. *Molecular interventions*, *6*(4), 199-218.
10. Gilbert, N. C., Newcomer, M. E., & Werz, O. (2021). Untangling the web of 5-lipoxygenase-derived products from a molecular and structural perspective: the battle between pro-and anti-inflammatory lipid mediators. *Biochemical pharmacology*, *193*, 114759-114785.
11. Giménez-Bastida, J. A., Gonzalez-Sarrias, A., Laparra-Llopis, J. M., Schneider, C., &Espín, J. C. (2021). Targeting mammalian 5-lipoxygenase by dietary phenolics as an anti-inflammatory mechanism: A systematic review. *International Journal of Molecular Sciences*, *22*(15), 7937-7954.
12. Salemi, S., Rethage, J., Wollina, U., Michel, B. A., Gay, R. E., Gay, S., & Sprott, H. (2003). Detection of interleukin 1beta (IL-1beta), IL-6, and tumor necrosis factor-alpha in skin of patients with fibromyalgia. *The Journal of rheumatology*, *30*(1), 146-150.
13. Möller, B., & Villiger, P. M. (2006, June). Inhibition of IL-1, IL-6, and TNF-α in immune-mediated inflammatory diseases. In *Springer seminars in immunopathology* (Vol. 27, pp. 391-408). Springer-Verlag.
14. Bąska, P., & Norbury, L. J. (2022). The role of nuclear factor kappa B (NF-κB) in the immune response against parasites. *Pathogens*, *11*(3), 310-342.
15. Malemud, C. J., & Pearlman, E. (2009). Targeting JAK/STAT signaling pathway in inflammatory diseases. *Current Signal Transduction Therapy*, *4*(3), 201-221.
16. Ravid, J. D., Leiva, O., & Chitalia, V. C. (2022). Janus kinase signaling pathway and its role in COVID-19 inflammatory, vascular, and thrombotic manifestations. *Cells*, *11*(2), 306-314.
17. Tibbo, A. J., & Baillie, G. S. (2020). Phosphodiesterase 4B: master regulator of brain signaling. *Cells*, *9*(5), 1254-1268.
18. Rajakariar, R., Yaqoob, M. M., & Gilroy, D. W. (2006). COX-2 in inflammation and resolution. *Molecular interventions*, *6*(4), 199-214.
19. Parente, L., & Perretti, M. (2003). Advances in the pathophysiology of constitutive and inducible cyclooxygenases: two enzymes in the spotlight. *Biochemical pharmacology*, *65*(2), 153-159.
20. Ferrer, M. D., Busquets-Cortés, C., Capó, X., Tejada, S., Tur, J. A., Pons, A., & Sureda, A. (2019). Cyclooxygenase-2 inhibitors as a therapeutic target in inflammatory diseases. *Current medicinal chemistry*, *26*(18), 3225-3241.
21. Yadav, D. K., Saloni, Sharma, P., Misra, S., Singh, H., Mancera, R. L., ... & Kumar, S. (2018). Studies of the benzopyran class of selective COX-2 inhibitors using 3D-QSAR and molecular docking. *Archives of pharmacal research*, *41*, 1178-1189.
22. Yang, M., Jin, Y., & Li-Ping, Y. (2018). Screening for cyclooxygenase 2 inhibitors from natural compounds of Radix Glycyrrhizae using computer simulation. *Traditional Medicine Research*, *3*(3), 115-124.
23. Nadia, L., Mouna, C., &Djadi, N. (2024). Exploring the Interactions of Natural Flavonoids with COX-2: Insights from Molecular Docking, DFT Analysis, and ADME Calculations. *Physical Chemistry Research*, *12*(3), 675-691.

24. Agus, A. S. R., Siswandono, M. E. T. B. B., Taufiqurrahman, M., Fernandes, A., & Maharani, R. (2024). Molecular Docking Of The Keruing's (Dipterocarpus) Genus, Secondary Metabolites Of The Dipterocarpaceae Family's As Anti-Inflammation Against Cyclooxygenase-2 (Cox-2). *Int J App Pharm*, *16*(2), 313-319.
25. Tutar, L., & Tutar, Y. (2010). Heat shock proteins; an overview. *Current Pharmaceutical Biotechnology*, *11*(2), 216-222.
26. Stetler, R. A., Gan, Y., Zhang, W., Liou, A. K., Gao, Y., Cao, G., & Chen, J. (2010). Heat shock proteins: cellular and molecular mechanisms in the central nervous system. *Progress in neurobiology*, *92*(2), 184-211.
27. Penke, B., Bogár, F., Crul, T., Sántha, M., Tóth, M. E., & Vígh, L. (2018). Heat shock proteins and autophagy pathways in neuroprotection: from molecular bases to pharmacological interventions. *International journal of molecular sciences*, *19*(1), 325-333.
28. Jiang, Y., Castro, J., Blomster, L. V., Agwa, A. J., Maddern, J., Schober, G., ... & King, G. F. (2021). Pharmacological inhibition of the voltage-gated sodium channel Nav1. 7 alleviates chronic visceral pain in a rodent model of irritable bowel syndrome. *ACS pharmacology & translational science*, *4*(4), 1362-1378.
29. Hoter, A., El-Sabban, M. E., & Naim, H. Y. (2018). The HSP90 family: structure, regulation, function, and implications in health and disease. *International journal of molecular sciences*, *19*(9), 2560-2574.
30. Hu, C., Yang, J., Qi, Z., Wu, H., Wang, B., Zou, F., ... & Liu, Q. (2022). Heat shock proteins: Biological functions, pathological roles, and therapeutic opportunities. *MedComm*, *3*(3), e161.
31. Tukaj, S., & Sitko, K. (2022). Heat shock protein 90 (Hsp90) and Hsp70 as potential therapeutic targets in autoimmune skin diseases. *Biomolecules*, *12*(8), 1153-1165.
32. Fan, X., Sun, L., Qin, Y., Liu, Y., Wu, S., & Du, L. (2024). The Role of HSP90 Molecular Chaperones in Depression: Potential Mechanisms. *Molecular Neurobiology*, 1-10.
33. Chainoglou, E., &Hadjipavlou-Litina, D. (2019). Curcumin analogues and derivatives with anti-proliferative and anti-inflammatory activity: Structural characteristics and molecular targets. *Expert opinion on drug discovery*, *14*(8), 821-842.
34. Wang, Z. S., Chen, L. Z., Zhou, H. P., Liu, X. H., & Chen, F. H. (2017). Diarylpentadienone derivatives (curcumin analogues): Synthesis and anti-inflammatory activity. *Bioorganic & Medicinal Chemistry Letters*, *27*(8), 1803-1807.
35. Prasad, S., DuBourdieu, D., Srivastava, A., Kumar, P., & Lall, R. (2021). Metal–curcumin complexes in therapeutics: an approach to enhance pharmacological effects of curcumin. *International journal of molecular sciences*, *22*(13), 7094-7109.
36. Shakeri, A., Panahi, Y., Johnston, T. P., &Sahebkar, A. (2019). Biological properties of metal complexes of curcumin. *BioFactors*, *45*(3), 304-317.
37. Prasad, S., & Lall, R. (2022). Zinc-curcumin based complexes in health and diseases: An approach in chemopreventive and therapeutic improvement. *Journal of Trace Elements in Medicine and Biology*, *73*, 127023-127035.
38. Banerjee, S., & Chakravarty, A. R. (2015). Metal complexes of curcumin for cellular imaging, targeting, and photoinduced anticancer activity. *Accounts of chemical research*, *48*(7), 2075-2083.
39. Wanninger, S., Lorenz, V., Subhan, A., & Edelmann, F. T. (2015). Metal complexes of curcumin–synthetic strategies, structures and medicinal applications. *Chemical Society Reviews*, *44*(15), 4986-5002.
40. Mittal, A., Nagpal, M., Vashistha, V. K., Arora, R., & Issar, U. (2024). Recent advances in the antioxidant activity of metal-curcumin complexes: a combined computational and experimental review. *Free Radical Research*, *58*(1), 11-26.
41. Tran, Q. H., & Doan, T. T. (2020). A novel study on curcumin metal complexes: solubility improvement, bioactivity, and trial burn wound treatment in rats. *New Journal of Chemistry*, *44*(30), 13036-13045.
42. Wanninger, S., Lorenz, V., Subhan, A., & Edelmann, F. T. (2015). Metal complexes of curcumin–synthetic strategies, structures and medicinal applications. *Chemical Society Reviews*, *44*(15), 4986-5002.
43. Wang, Q., Umar Imam, M., Yida, Z., & Wang, F. (2017). Peroxisome proliferator-activated receptor gamma (PPARγ) as a target for concurrent management of diabetes and obesity-related cancer. *Current Pharmaceutical Design*, *23*(25), 3677-3688.
44. Ahmed, S., Islam, N., Shahinozzaman, M., Fakayode, S. O., Afrin, N., & Halim, M. A. (2021). Virtual screening, molecular dynamics, density functional theory and quantitative structure activity relationship studies to design peroxisome proliferator-activated receptor-γ agonists as anti-diabetic drugs. *Journal of Biomolecular Structure and Dynamics*, *39*(2), 728-742.

45. Makrilakis, K. (2019). The role of DPP-4 inhibitors in the treatment algorithm of type 2 diabetes mellitus: when to select, what to expect. *International journal of environmental research and public health*, *16*(15), 2720-2735.
46. Chawla, G., Pradhan, T., & Gupta, O. (2024). An insight into the combat strategies for the treatment of type 2 diabetes mellitus. *Mini Reviews in Medicinal Chemistry*, *24*(4), 403-430.
47. Mulvihill, E. E., & Drucker, D. J. (2014). Pharmacology, physiology, and mechanisms of action of dipeptidyl peptidase-4 inhibitors. *Endocrine reviews*, *35*(6), 992-1019.
48. Madaan, T., Akhtar, M., & Najmi, A. K. (2016). Sodium glucose CoTransporter 2 (SGLT2) inhibitors: Current status and future perspective. *European Journal of Pharmaceutical Sciences*, *93*, 244-252.
49. Abdul-Ghani, M. A., Norton, L., & DeFronzo, R. A. (2011). Role of sodium-glucose cotransporter 2 (SGLT 2) inhibitors in the treatment of type 2 diabetes. *Endocrine reviews*, *32*(4), 515-531.
50. Fonseca-Correa, J. I., & Correa-Rotter, R. (2021). Sodium-glucose cotransporter 2 inhibitors mechanisms of action: a review. *Frontiers in Medicine*, *8*, 777861-777886.
51. Guyton, J., Jeon, M., & Brooks, A. (2019). Glucagon-like peptide 1 receptor agonists in type 1 diabetes mellitus. *American Journal of Health-System Pharmacy*, *76*(21), 1739-1748.
52. Lee, S., & Lee, D. Y. (2017). Glucagon-like peptide-1 and glucagon-like peptide-1 receptor agonists in the treatment of type 2 diabetes. *Annals of pediatric endocrinology & metabolism*, *22*(1), 15-26.
53. Samovski, D., Dhule, P., Pietka, T., Jacome-Sosa, M., Penrose, E., Son, N. H., ... &Abumrad, N. A. (2018). Regulation of insulin receptor pathway and glucose metabolism by CD36 signaling. *Diabetes*, *67*(7), 1272-1284.
54. Koren, S., & Fantus, I. G. (2007). Inhibition of the protein tyrosine phosphatase PTP1B: potential therapy for obesity, insulin resistance and type-2 diabetes mellitus. *Best practice & research Clinical endocrinology & metabolism*, *21*(4), 621-640.
55. Kołodziej-Sobczak, D., Sobczak, Ł., &Łączkowski, K. Z. (2024). Protein Tyrosine Phosphatase 1B (PTP1B): A Comprehensive Review of Its Role in Pathogenesis of Human Diseases. *International Journal of Molecular Sciences*, *25*(13), 7033-7045.
56. Elchebly, M., Cheng, A., & Tremblay, M. L. (2000). Modulation of insulin signaling by protein tyrosine phosphatases. *Journal of Molecular Medicine*, *78*, 473-482.
57. Le Sommer, S., Martina, P., Martin-Granados, C., &Delibegovic, M. (2015). Protein tyrosine phosphatase 1B (PTP1B) in the immune system. *Inflammation & Cell Signaling*.
58. Viollet, B., &Andreelli, F. (2011). AMP-activated protein kinase and metabolic control. *Diabetes-perspectives in drug therapy*, 303-330.
59. Grahame Hardie, D. (2014). AMP-activated protein kinase: a key regulator of energy balance with many roles in human disease. *Journal of internal medicine*, *276*(6), 543-559.
60. Brown, O. I., Bridge, K. I., & Kearney, M. T. (2021). Nicotinamide adenine dinucleotide phosphate oxidases in glucose homeostasis and diabetes-related endothelial cell dysfunction. *Cells*, *10*(9), 2315-2328.
61. Koju, N., Taleb, A., Zhou, J., Lv, G., Yang, J., Cao, X., ... & Ding, Q. (2019). Pharmacological strategies to lower crosstalk between nicotinamide adenine dinucleotide phosphate (NADPH) oxidase and mitochondria. *Biomedicine & Pharmacotherapy*, *111*, 1478-1498.
62. Laddha, A. P., & Kulkarni, Y. A. (2020). NADPH oxidase: A membrane-bound enzyme and its inhibitors in diabetic complications. *European journal of pharmacology*, *881*, 173206-173229.
63. Gupta, J. K. (2024). The role of aldose reductase in polyol pathway: An emerging pharmacological target in diabetic complications and associated morbidities. *Current Pharmaceutical Biotechnology*, *25*(9), 1073-1081.
64. Thakur, S., Gupta, S. K., Ali, V., Singh, P., & Verma, M. (2021). Aldose Reductase: A cause and a potential target for the treatment of diabetic complications. *Archives of Pharmacal Research*, *44*, 655-667.
65. Singh, M., Kapoor, A., & Bhatnagar, A. (2021). Physiological and pathological roles of aldose reductase. *Metabolites*, *11*(10), 655-685.
66. Kumar, P. A., & Reddy, G. B. (2007). Focus on molecules: aldose reductase. *Experimental eye research*, *85*(6), 739-740.
67. Dănilă, A. I., Ghenciu, L. A., Stoicescu, E. R., Bolintineanu, S. L., Iacob, R., Săndesc, M. A., & Faur, A. C. (2024). Aldose Reductase as a Key Target in the Prevention and Treatment of Diabetic Retinopathy: A Comprehensive Review. *Biomedicines*, *12*(4), 747-758.
68. Susilawati, Y., Indradi, R. B., Asnawi, A., &Febrina, E. (2024). Molecular docking and dynamics studies of 8, 9-dimethoxy ellagic acid contained in Peperomia pellucida (L.) Kunth against various diabetes mellitus receptors. *Journal of Pharmacy & Pharmacognosy Research*, *12*(5), 929-942.

69. Shanak, S., Bassalat, N., Barghash, A., Kadan, S., Ardah, M., & Zaid, H. (2022). Drug discovery of plausible lead natural compounds that target the insulin signaling pathway: Bioinformatics approaches. *Evidence-Based Complementary and Alternative Medicine*, *2022*(1), 2832889.
70. Thakur, S., Gupta, S. K., Ali, V., Singh, P., & Verma, M. (2021). Aldose Reductase: A cause and a potential target for the treatment of diabetic complications. *Archives of Pharmacal Research*, *44*, 655-667.
71. Singh Grewal, A., Bhardwaj, S., Pandita, D., Lather, V., & Singh Sekhon, B. (2016). Updates on aldose reductase inhibitors for management of diabetic complications and non-diabetic diseases. *Mini reviews in medicinal chemistry*, *16*(2), 120-162.
72. Deacon, C. F. (2019). Physiology and pharmacology of DPP-4 in glucose homeostasis and the treatment of type 2 diabetes. *Frontiers in endocrinology*, *10*, 80-95.
73. Ahrén, B. (2019). DPP-4 inhibition and the path to clinical proof. *Frontiers in endocrinology*, *10*, 376-384.
74. Röhrborn, D., Wronkowitz, N., & Eckel, J. (2015). DPP4 in diabetes. *Frontiers in immunology*, *6*, 386-395.
75. Deacon, C. F. (2020). Metabolism of GIP and the contribution of GIP to the glucose-lowering properties of DPP-4 inhibitors. *Peptides*, *125*, 170196-170226.
76. Lamos, E. M., Hedrington, M., & Davis, S. N. (2019). An update on the safety and efficacy of oral antidiabetic drugs: DPP-4 inhibitors and SGLT-2 inhibitors. *Expert opinion on drug safety*, *18*(8), 691-701.
77. Stoian, A. P., Sachinidis, A., Stoica, R. A., Nikolic, D., Patti, A. M., & Rizvi, A. A. (2020). The efficacy and safety of dipeptidyl peptidase-4 inhibitors compared to other oral glucose-lowering medications in the treatment of type 2 diabetes. *Metabolism*, *109*, 154295-154324.
78. Scheen, A. J. (2012). DPP-4 inhibitors in the management of type 2 diabetes: a critical review of head-to-head trials. *Diabetes & metabolism*, *38*(2), 89-101.
79. Sharma, P., Joshi, T., Mathpal, S., Chandra, S., &Tamta, S. (2022). In silico identification of antidiabetic target for phytochemicals of A. marmelos and mechanistic insights by molecular dynamics simulations. *Journal of Biomolecular Structure and Dynamics*, *40*(21), 10543-10560.
80. Deacon, C. F. (2020). Metabolism of GIP and the contribution of GIP to the glucose-lowering properties of DPP-4 inhibitors. *Peptides*, *125*, 170196-170209.
81. Deacon, C. F. (2020). Dipeptidyl peptidase 4 inhibitors in the treatment of type 2 diabetes mellitus. *Nature Reviews Endocrinology*, *16*(11), 642-653.
82. Makrilakis, K. (2019). The role of DPP-4 inhibitors in the treatment algorithm of type 2 diabetes mellitus: when to select, what to expect. *International journal of environmental research and public health*, *16*(15), 2720-2735.
83. Udrea, A. M., GradisteanuPircalabioru, G., Boboc, A. A., Mares, C., Dinache, A., Mernea, M., & Avram, S. (2021). Advanced bioinformatics tools in the pharmacokinetic profiles of natural and synthetic compounds with anti-diabetic activity. *Biomolecules*, *11*(11), 1692.
84. Hoda, M., Hemaiswarya, S., & Doble, M. (2019). Role of phenolic phytochemicals in diabetes management. *Role of phenolic phytochemicals in diabetes management*, 123-143.
85. Tshiyoyo, K. S. (2022). *In Silico Docking and ADMET Studies on Clinical Targets for Type 2 Diabetes Correlated to In Vitro Inhibition of α-Glucosidase and Pancreatic α-Amylase by Curcumin, 18α-Glycyrrhetinic Acid, Rosmarinic Acid, and Quercetin* (Master's thesis, University of Pretoria (South Africa)).31277431-31277458.
86. Momtaz, S., Salek-Maghsoudi, A., Abdolghaffari, A. H., Jasemi, E., Rezazadeh, S., Hassani, S., ... & Nabavi, S. M. (2019). Polyphenols targeting diabetes via the AMP-activated protein kinase pathway; future approach to drug discovery. *Critical Reviews in Clinical Laboratory Sciences*, *56*(7), 472-492.
87. Vijaykrishnaraj, M., & Wang, K. (2021). Dietary natural products as a potential inhibitor towards advanced glycation end products and hyperglycemic complications: A phytotherapy approaches. *Biomedicine & Pharmacotherapy*, *144*, 112336-112348.
88. Roman, B., Retajczyk, M., Sałaciński, Ł., &Pełech, R. (2020). Curcumin-properties, applications and modification of structure. *Mini-Reviews in Organic Chemistry*, *17*(5), 486-495.
89. Retnaningtyas, E., Setiawan, A., Susatia, B., Hariyanto, T., &Sudiwati, N. L. P. E. (2024). In silico studies of Ruellia tuberosa L. compounds as aldose reductase, dipeptidyl peptidase 4, and α-glucosidase inhibitors against type 2 diabetes mellitus. *Journal of Pharmacy & Pharmacognosy Research*, *12*(4), 735-747.
90. Holst, J. J. (2019). The incretin system in healthy humans: the role of GIP and GLP-1. *Metabolism*, *96*, 46-55.

91. Hubbard, S. R. (1997). Crystal structure of the activated insulin receptor tyrosine kinase in complex with peptide substrate and ATP analog. EMBO J. *(No Title)*, *16*, 6673-6697.
92. Faham, S., Watanabe, A., Besserer, G. M., Cascio, D., Specht, A., Hirayama, B. A., ... & Abramson, J. (2008). The crystal structure of a sodium galactose transporter reveals mechanistic insights into Na+/sugar symport. *Science*, *321*(5890), 810-814.
93. Sirvent, R., Pérez, J. M., Badia, R. M., & Labarta, J. (2006). Automatic grid workflow based on imperative programming languages. *Concurrency and Computation: Practice and experience*, *18*(10), 1169-1186.
94. Rizvi, S. M. D., Shakil, S., & Haneef, M. (2013). A simple click by click protocol to perform docking: AutoDock 4.2 made easy for non-bioinformaticians. *EXCLI journal*, *12*, 831-852.
95. Mizushima Y and Kobayashi M. Interaction of antiinflammatory drugs with serum proteins, especially with some biologically active proteins. Journal of Pharma Pharmacol. 1968; 20:169-173.
96. Sakat S, Juvekar AR, Gambhire MN. In vitro antioxidant and anti-inflammatory activity of methanol extract of Oxalis corniculata Linn. International Journal of Pharma and Pharmacological Sciences 2010; 2(1):146-155.
97. Kwon, Y.I.I., Vattem, D.A. and Shetty, K., 2006. Evaluation of clonal herbs of Lamiaceae species for management of diabetes and hypertension. Asia pacific journal of clinical nutrition, 15(1), pp.107-125.
98. Cao, Y., Sun, J., Qin, S., Zhou, Z., Xu, Y., & Liu, C. (2024). Advances and Challenges in Immune-Modulatory Biomaterials for Wound Healing Applications. *Pharmaceutics*, *16*(8), 990.
99. Lakshman, T. R., Deb, J., & Paine, T. K. (2016). Anti-inflammatory activity and enhanced COX-2 selectivity of nitric oxide-donating zinc (ii)–NSAID complexes. *Dalton Transactions*, *45*(36), 14053-14057.

CHAPTER 6

In silico and in vitro evaluation of antibacterial and antifungal potency of curcumin analogues and their metal complexes

CHAPTER 6

IN SILICO AND *IN VITRO* EVALUATION OF ANTIBACTERIAL AND ANTIFUNGAL POTENCY OF CURCUMIN ANALOGUES AND THEIR METAL COMPLEXES

6.1. INTRODUCTION

Antibacterial and antifungal studies are crucial in addressing significant public health threats and advancing medical and healthcare applications. The rise of antibiotic-resistant bacteria and antifungal-resistant fungi poses a severe global health risk, complicating the treatment of diseases that were once easily manageable, leading to longer illnesses, increased hospital stays, and higher mortality rates[1]. Emerging pathogens further complicate this landscape, making the development of new antibacterial and antifungal treatments essential. Healthcare-associated infections (HAIs), often caused by resistant bacteria and fungi, underscore the need for effective agents to prevent and treat infections, particularly in immunocompromised patients such as those undergoing chemotherapy or living with HIV/AIDS[2].

The implications of these studies extend beyond healthcare to encompass agriculture, the environment, and scientific progress. Within agriculture, the importance of antibacterial and antifungal agents cannot be overstated in safeguarding crops and livestock, thereby upholding food security and economic stability[3]. Environmental applications, such as bioremediation, stand to gain from a comprehensive grasp of resistance mechanisms to enhance the efficiency of cleanup procedures[4]. Scientific and technological progressions, encompassing drug discovery and breakthroughs in nanotechnology and biomaterials, derive from the continuous exploration within this domain. Tackling infections induced by resistant bacteria and fungi is imperative for managing healthcare expenses and sustaining workforce productivity. Consequently, the ongoing research on antibacterial and antifungal agents is indispensable for devising novel strategies and therapies to counteract the evolving challenges presented by these pathogens, ultimately safeguarding public health and nurturing innovation.

This chapter is primarily destined to screening potential curcumin analogue inhibitors for bacterial (both Gram-positive and Gram-negative) and fungal receptors. These analogues were created by modifying the functional groups on the aryl rings of natural curcumin. The screening process involved molecular docking studies, which were subsequently validated through in vitro experiments. A comparison was made between the binding affinities of curcumin analogues, natural curcumin, and FDA-approved antibacterial and antifungal drugs (Gentamycin and Fluconazole, respectively) towards the specified targets.

This chapter also included *in vitro* antibacterial and antifungal assays of Cu(II) and Zn(II) metal complexes derived from the nine curcumin analogues, excluding computational screening studies. The splenocytic assay of the most promising drug candidates was also conducted.

6.2. REVIEW OF LITERATURE

This section comprehensively analysed the existing research and developments concerning curcumin analogues and their antibacterial and antifungal properties. It began with an overview of *in silico* studies, highlighting their role in understanding mechanisms of action, predicting efficacy, and guiding compound design. The section delved into the antibacterial effects of curcumin analogues against Gram-positive and Gram-negative bacteria, emphasising mechanistic insights such as enzyme inactivation, membrane disruption, and oxidative stress induction. Key bacterial targets like *Staphylococcus aureus, Mycobacterium smegmatis, Pseudomonas aeruginosa,* and *Klebsiella pneumoniae* were discussed.

The review further explored *in vitro* studies, demonstrating enhanced antibacterial and antifungal activity of curcumin analogues and their metal complexes compared to natural curcumin. It highlighted their improved membrane permeability, ROS generation, and enzyme inhibition while noting challenges such as stability, toxicity, and the need for *in vivo* validation.

The survey covered the antifungal potential of curcumin analogues, mainly consisting of molecular docking studies, enzyme inhibition, and cell wall disruption, and identified Candida albicans as a model organism for understanding fungal infections. This comprehensive review underscored the need for novel antibacterial and antifungal agents, validated through rigorous experimental studies, to combat resistant pathogens

effectively. **Table 6.1** summarises relevant references and brief explanations of the key findings for each category.

Table 6.1 Key findings and references on the antibacterial and antifungal properties of the curcumin analogues and their metal complexes, highlighting mechanisms, targets, and challenges, emphasising novel agent development.

About	Insights and Limitations	Reference
In Silico Studies of the antibacterial effect of curcumin analogues against Gram-positive and Gram-negative bacteria	*In silico* studies were instrumental in elucidating mechanisms of action, predicting efficacy, and guiding the design of new compounds. Mechanistic insights revealed potential enzyme inactivation, bacterial membrane disruption, and oxidative stress induction by curcumin and its analogues, which enhanced their antibacterial activity. Structure-activity relationship studies highlighted specific features of curcumin derivatives that boosted efficacy, though these compounds often showed low efficacy against Gram-negative bacteria. Many studies focused on Gram-positive bacteria, indicating a need for broader evaluations. While *in silico* studies offered valuable insights, their findings required validation through *in vitro* and *in vivo* experiments to ensure safety and clinical applicability.	5-12
Gram-positive Bacteria 1.*Staphylococcus aureus* (A Grade Gram-Positive Bacteria)	*Staphylococcus aureus* was a significant human pathogen responsible for infections ranging from minor skin issues to severe diseases like sepsis, pneumonia, and endocarditis. It posed a major challenge in healthcare due to healthcare-acquired infections and the emergence of Methicillin-resistant *Staphylococcus aureus* (MRSA), which resisted many antibiotics. The need for new antibacterial agents was urgent. *S. aureus* secreted various virulence factors that enhanced its spread and pathogenicity, making them critical targets	13-16

2.*Mycobacterium smegmatis* (A Grade Gram-Positive Bacteria)	for effective therapies. *Mycobacterium smegmatis* served as an essential model for *Mycobacterium tuberculosis*, the TB-causing agent, due to its virulence and rapid growth. It aided TB research by sharing many genetic and biochemical pathways with *M.tuberculosis*. The study of *M. smegmatis*, with its complex cell envelope rich in mycolic acids, was crucial for understanding drug resistance mechanisms and developing new anti-tuberculosis drugs.	17-21
Gram-negative Bacteria 1.*Pseudomonas aeruginosa* (A Grade Gram-Negative Bacteria) 2.*Klebsiella pneumoniae* (B Grade Gram-Negative Bacteria)	*Pseudomonas aeruginosa*, a major cause of hospital-acquired infections such as pneumonia, UTIs, and sepsis, posed particular challenges for cystic fibrosis, burn, and immunocompromised patients. Known for its intrinsic antibiotic resistance and ability to acquire more, it formed multidrug-resistant (MDR) and extensively drug-resistant (XDR) strains. Its biofilm formation on medical devices and tissues further complicated treatment, demanding innovative therapeutic strategies. *Klebsiella pneumoniae* causes healthcare-associated infections like pneumonia, bloodstream infections, and meningitis, posing a significant threat to immunocompromised individuals, neonates, and the elderly. The emergence of carbapenem-resistant strains (CRKP) increased morbidity and mortality rates, highlighting the urgent need for new antibacterial agents. Its virulence factors, including capsules, siderophores, and adhesins, enabled immune evasion and infection, making it a prime target for the development of targeted therapies and vaccines.	22-27 28-32

Targets of Gram-positive Bacteria 4H8E	The 4H8E target corresponded to the dihydrofolate reductase (DHFR) enzyme found in Staphylococcus aureus. DHFR was a key player in folate metabolism, necessary for DNA synthesis and replication. Targeting DHFR in *Staphylococcus aureus* disrupted these critical processes, rendering it an important focus for antibiotic development aimed at combating bacterial growth and proliferation.	33-36
1UZN	Sortase A, linked to the 1UZN target, was an enzyme that played a vital role in anchoring surface proteins to the cell wall of Gram-positive bacteria like *Staphylococcus aureus*. This process was essential for the virulence of the bacterium. Inhibiting Sortase A reduced the ability of *Staphylococcus aureus* to cause infection, making it a crucial target for therapeutic strategies aimed at reducing bacterial pathogenicity.	37-41
2W9S	The 2W9S target was associated with the InhA enzyme, which played a crucial role in *Mycobacterium smegmatis*. InhA was an enoyl-ACP reductase involved in fatty acid synthesis, essential for the survival and cell wall biosynthesis of *Mycobacterium* species. Inhibiting this enzyme disrupted these vital processes, making it a significant target for therapeutic intervention against mycobacterial infections.	42-45
4Q8I	It represented the structure of a putative hexapeptide kinase from *Mycobacterium smegmatis*. KasA, the enzyme associated with the 4Q8I target, was pivotal in the biosynthesis of mycolic acids, crucial components of the mycobacterial cell wall. Inhibiting KasA compromised the integrity of the cell wall in Mycobacterium species, including *Mycobacterium*	

	smegmatis. This made KasA a valuable target for developing treatments that weakened and ultimately eradicated mycobacterial cells.	46-50
Targets of Gram-negative Bacteria 1NPB	The 1NPB structure referred to the crystal structure of the *Pseudomonas aeruginosa* FabF enzyme, which was a key enzyme in the fatty acid biosynthesis pathway (FAS-II pathway). 1NPB represented beta-lactamase, an enzyme that provided resistance to beta-lactam antibiotics by hydrolyzing the antibiotic's beta-lactam ring. This enzyme was particularly important because *Pseudomonas aeruginosa* and *Klebsiella pneumoniae* were notorious for their resistance to multiple antibiotics, largely due to the production of beta-lactamases. Targeting this enzyme with inhibitors could restore the efficacy of beta-lactam antibiotics, making it a crucial target for developing new antimicrobial therapies.	51-57
5O7N	The 5O7N structure referred to a crystal structure of the Pseudomonas aeruginosa AmpC beta-lactamase. 5O7N corresponded to DNA gyrase, an enzyme involved in the supercoiling and uncoiling of bacterial DNA, which was essential for DNA replication and transcription. DNA gyrase was vital for bacterial growth and replication, and it was a target for fluoroquinolone antibiotics. However, resistance to these antibiotics had emerged, underscoring the importance of continued study and development of gyrase inhibitors to combat resistant strains of *Pseudomonas aeruginosa*.	58-62

4JVD 6B8A	The 4JVD structure referred to the crystal structure of the *Klebsiella pneumoniae* NDM-1 (New Delhi metallo-beta-lactamase-1) enzyme. 4JVD was associated with LpxC, an enzyme involved in the biosynthesis of lipid A, a key component of the lipopolysaccharide (LPS) layer in the outer membrane of Gram-negative bacteria like *Klebsiella pneumoniae*. The LPS layer was crucial for the structural integrity and defense mechanisms of these bacteria. Inhibiting LpxC could disrupt the LPS layer, compromising the defence of bacteria and making them more susceptible to the host immune response and other antibiotics, highlighting its potential as an antibiotic target. The 6B8A structure represented the crystal structure of the Klebsiella pneumoniae SHV-1 beta-lactamase enzyme. 6B8A corresponded to penicillin-binding protein 3 (PBP3), which was involved in the final stages of synthesizing and maintaining the bacterial cell wall by cross-linking peptidoglycan chains. PBP3 was decisive for maintaining the structural integrity of the bacterial cell wall. This protein was also a target for beta-lactam antibiotics such as penicillins and cephalosporins. Inhibiting PBP3 disrupted cell wall synthesis, leading to bacterial cell death, making it a significant target for antibiotic development against *Klebsiella pneumoniae*.	63-66 67-70
In vitro Antibacterial effect of curcumin analogues and their Cu(II) and Zn(II) metal complexes	Curcumin analogues and their Cu(II) and Zn(II) metal complexes showed enhanced antibacterial activity compared to curcumin alone, effectively targeting both Gram-positive and Gram-negative bacteria through improved membrane permeability, ROS generation, and enzyme inhibition. Structural modifications in these	71-80

	complexes enhanced stability and bioavailability, while synergistic effects with curcumin potentially reduced dosage and side effects. However, variability in efficacy, stability issues, toxicity concerns, and the need for *in vivo* validation and broader-spectrum studies remained challenges for their development as effective antibacterial agents.	
In silico studies of antifungal effect of curcumin analogues.	*In silico* studies of curcumin analogues revealed insights into their antifungal potential by using molecular docking to assess binding affinity, exploring mechanisms like enzyme inhibition and cell wall disruption, and analyzing structure-activity relationships. However, limited experimental validation, complex fungal biology, and the need for integration with experimental data were major limitations.	81-88
Candida albicans (A Grade Fungi)	*Candida albicans*, a common fungal pathogen, caused a range of infections from superficial to systemic, especially in immunocompromised individuals. Its resistance to many antifungal drugs confirmed the need for new treatments. As a model organism, it assisted in understanding fungal biology and biofilm formation on medical devices, helping to develop targeted antifungal therapies with broader applicability.	89-97
Targets of Fungus 4LEB	4LEB, or Cytochrome P450 Lanosterol 14-alpha-demethylase, was essential in the ergosterol biosynthesis pathway, a critical component of fungal cell membranes. Targeting this enzyme disrupted the integrity and functionality of the fungal cell membrane, leading to the fungus's death. Since human cells did not have ergosterol in their membranes, antifungal drugs targeting this enzyme achieved high specificity, minimizing effects on human cells. 1IYL, or Dihydrofolate Reductase, played a key role in	98-104

1IYL	the folic acid pathway, which was crucial for DNA synthesis and cell division. Inhibiting this enzyme prevented the synthesis of nucleotides necessary for DNA replication, thereby inhibiting fungal growth. This high selectivity reduced the risk of side effects in human patients, as these fungal-specific enzymes were not present in human cells.	105-110
In vitro Antifungal effect of curcumin analogues and their Cu(II) and Zn(II) metal complexes	*In vitro* studies showed that curcumin analogues and their Cu(II) and Zn(II) metal complexes exhibited enhanced antifungal activity, disrupted fungal cell membranes, inhibited enzymes, and generated reactive oxygen species. They also had synergistic effects and could disrupt resistant biofilms. However, challenges included limited biological relevance, variable efficacy, stability issues, toxicity concerns, and the need for extensive experimental validation.	111-115

6.3. MATERIALS AND METHODS

6.3.1. *In silico* studies of antibacterial and antifungal effects of curcumin analogues

The *in silico* studies focused on the molecular docking of designed curcumin analogues that had already undergone pharmacokinetic prediction, comparing them with natural curcumin and FDA-approved antibacterial and antifungal drugs.

6.3.1.1. Molecular docking studies

6.3.1.1.1. Ligand preparation and pharmacokinetic prediction

Curcumin analogues, known for their antibacterial properties, were formulated using Chem Draw Ultra and structurally optimized with Gaussian 6.0's Berny algorithm. The energy-minimized molecules were saved in GPF format and converted to PDB using Open Babel. Pharmacokinetic predictions indicated good oral bioavailability and drug-like properties for all nine compounds (**Table 2.2**, **Table 2.3**). Following wet lab synthesis, the compounds underwent diverse characterization analyses, declining their suitability for further drug development as explained in Chapter 3.

6.3.1.1.2. Identification of molecular targets

6.3.1.1.2.1. Molecular targets of gram-positive and gram-negative bacteria

From the literature survey, it was understood that *Staphylococcus aureus* must be a major pathogen responsible for a range of infections, including severe hospital-acquired cases, with MRSA strains emphasizing the urgent need for new antibacterial agents. It used to virulence factors crucial for its infectivity. *Mycobacterium smegmatis* serves as a model for Mycobacterium tuberculosis, aiding TB research due to its non-pathogenic nature and faster growth. By targeting specific enzymes, researchers can develop therapeutics that effectively disrupt critical biological pathways in these Gram-positive bacteria, offering potent treatment options.

It was found that the 4H8E target corresponded to the dihydrofolate reductase (DHFR) enzyme found in *Staphylococcus aureus*. This enzyme was noted to be crucial for DNA synthesis and replication, making it vital for antibiotic development. Sortase A, linked to the 1UZN target, anchors surface proteins to the cell wall and is essential for *S. aureus* virulence. Inhibiting Sortase A reduced the infection capability of the bacterium. The 2W9S target corresponded to the InhA enzyme in *Mycobacterium smegmatis*, which was also key for fatty acid synthesis and cell wall biosynthesis, making it a significant therapeutic target. KasA ((β-Ketoacyl-ACP Synthase A)-the bacterium responsible for tuberculosis (TB)), associated with the 4Q8I target, was also very important for mycolic acid biosynthesis in mycobacteria, and its inhibition compromises cell wall integrity, presenting a target for mycobacterial treatments. Consequently, selecting the specific targets—4H8E(TG1) X-RAYDIFFRACTION, Resolution:1.30Å, R-ValueFree:0.194, R-Value Work:0.174, No. of chains:2[116]; 1UZN(TG2) X-Ray Diffraction, Resolution: 1.91 Å, R-Value Free: 0.227, R-Value Work: 0.185, No. of chains:1[117]; 2W9S(TG3)X-Ray Diffraction, Resolution: 2.45 Å, R-Value Free:0.272, R-Value Work: 0.225, No. of chains:1[118]; and 4Q8I(TG4) X-Ray Diffraction, Resolution: 1.90 Å Å, R-Value Free:0.225, R-Value Work: 0.161, No. of chains:1[119]—was strategic for conducting molecular docking studies.

Based on a literature survey, it was evident that *Klebsiella pneumoniae*, a Gram-negative bacterium, caused severe healthcare-associated infections and posed a significant

threat to immunocompromised individuals, neonates, and the elderly. The emergence of carbapenem-resistant strains (CRKP) highlighted the urgent need for new antibacterial agents. This bacterium produced virulence factors, such as capsules and adhesins, which helped it evade the immune system, making infections more difficult to treat and control. *Pseudomonas aeruginosa*, another Gram-negative pathogen, caused hospital-acquired infections and was particularly problematic for patients with cystic fibrosis and burn injuries. Its intrinsic and acquired antibiotic resistance, along with its ability to form biofilms, necessitated innovative therapeutic strategies to combat its multidrug-resistant strains.

1NPB (beta-lactamase) and 6B8A (PBP3) were vital for cell wall integrity and antibiotic resistance. 5O7N (DNA gyrase) was essential for DNA processes, while 4JVD (LpxC) was key for the LPS layer integrity. The selection of 1NPB (TG5), X-ray diffraction with a resolution of 2.50 Å, R-Value Free of 0.230, R-Value Work of 0.183, and 5120 chains; 5O7N (TG6), X-ray diffraction with a resolution of 1.50 Å, R-Value Free of 0.211, R-Value Work of 0.187, and 2121 chains; 4JVD (TG7), X-ray diffraction with a resolution of 2.95 Å, R-Value Free of 0.256, R-Value Work of 0.203, and 1122 chains; and 6B8A (TG8), X-ray diffraction with a resolution of 2.65 Å, R-Value Free of 0.251, R-Value Work of 0.216, and 2123 chains, as targets for *Pseudomonas aeruginosa* and *Klebsiella pneumoniae* was crucial due to their roles in antibiotic resistance and bacterial survival. Targeting these proteins enabled the development of novel inhibitors, enhanced existing antibiotics, and combat multidrug-resistant strains.

6.3.1.1.2.2. Molecular targets of fungus

According to the literature survey, choosing specific targets like 4LEB and 1IYL for antifungal studies, particularly for pathogens like *Candida albicans*, was found crucial due to their specificity and effectiveness. 4LEB disrupted fungal cell membranes by targeting the ergosterol biosynthesis pathway, while 1IYL inhibited DNA synthesis. These targets minimized side effects in humans and offered broad-spectrum efficacy against various fungal pathogens. Research on these enzymes improved existing therapies, making them more potent and overcoming resistance. Thus, 4LEB (TG9), X-ray diffraction with a resolution of 1.40 Å, R-Value Free of 0.178, R-Value Work of 0.178, and one chain, and 1IYL (TG10), X-ray diffraction with a resolution of 3.20 Å, R-Value

Free of 0.366, R-Value Work of 0.284, and 4 chains, were strategic targets for developing effective, safe, and broad-spectrum antifungal treatments.

6.3.1.1.3. Receptor priming

The 3D structures of each protein target were retrieved from the PDB and prepared by removing any water molecules, ions, or ligands irrelevant to the docking process. Missing atoms, such as hydrogen atoms, were added to ensure completeness, and the geometry was optimized by minimizing the receptor's energy to relax any strained bond angles or interactions. Appropriate charges were assigned to the receptor atoms, and the binding site were defined by identifying and preparing the specific region where the ligand would dock. The binding site of each target was assigned based on the coordinate files in the active site using the Auto Grid program[126], with the appropriate coordinate dimensions for X, Y, and Z. The target and ligand files were then saved in pdbqt format. These steps helped ensure that the receptor was in a biologically relevant and energetically favourable conformation, thereby increasing the accuracy and reliability of the docking results.

6.3.1.1.4. Molecular docking

The binding affinity of each curcumin analogue to the selected target proteins was computationally modelled using molecular docking via Auto Dock 4.2[127]. The binding centres of the target proteins were assigned by the Auto Grid program using the following X, Y, and Z coordinates: TG1 at 18.532,4.757 and 7.604; TG2 at 4.792,14.281 and 12.796; TG3 at 10.026,0.810 and 45.441; TG4 at 18.796,13.654 and 2.273; TG5 at 37.963,73.139 and-2.847; TG6 at 82.111,9.52 and 48.656; TG7at -33.664,65.098 and 10.095; TG8at 26.723,21.065 and 0.715; TG9at -2.982,-3.049 and -16.319 and TG10at 26.914,44.04 and 1.831.

The best-docked conformations were evaluated based on binding energy (kcal/mol), the number of hydrogen bonds, upper and lower bound root mean square deviation (RMSD), the number of interacting residues, and other weak forces stabilizing the receptor-ligand complex. The binding potential of the synthesized curcumin analogues to the selected proteins was compared to that of native curcumin and the selected targets, as well as to the FDA-approved antibacterial prescription medicine

Gentamicin (PubChem ID: 3467)[128] and Fluconazole (PubChem ID: 3365) which is an antifungal drug approved by FDA[129].

6.3.2. *In vitro* studies of antibacterial and antifungal effects of curcumin analogues and their metal complexes

6.3.2.1. Antibacterial Assay (Agar Well Diffusion Method)[130]

Procedure: The agar well diffusion method was employed to assess the antimicrobial activity of the test sample. Mueller-Hinton agar (15-20 mL) was poured onto glass Petri plates of the same size and allowed to solidify. A standardized inoculum of the test organism was evenly spread on the plate surface using a sterile cotton swab. Four wells with a diameter of 8 mm (20 mm apart from one another) were aseptically punched with a sterile cork borer in each plate.

The test sample (40 and 80 µL) was added into wells T1 and T2 from a 10 mg/mL stock. Gentamycin (40 µL from a 4 mg/mL stock) and the solvent used for sample dilution were added as positive and negative controls, respectively. The plates were then incubated for 24 hours at 36ºC ± 1ºC under aerobic conditions. Following incubation, the plates were observed, and the zone of bacterial growth inhibition around the wells was measured in millimetres.

Culture media Details: The Muller Hinton Agar medium (HIMEDIA- M173) was utilized to determine the susceptibility of microorganisms to antimicrobial agents. To prepare the medium, 38 grams were suspended in 1000 ml of distilled water. The mixture was heated until it boiled to ensure complete dissolution of the medium. Sterilization was achieved by autoclaving at 15 lbs pressure (121°C) for 15 minutes. After autoclaving, the medium was cooled to 45-50°C, mixed thoroughly, and then poured into sterile petri plates.

Inoculums details: Inoculums were procured from the Microbial Type Culture Collection (MTCC) in Chandigarh.

Table 6.2 Inoculums details of Bacterial cell lines

Name of organism	MTCC No	Incubation Condition
Staphylococcus aureus (Gram-positive)	87	37°C for 24 h
Mycobaterium smegmatis (Gram-positive)	6	37°C for 24 h
Pseudomonas aeruginosa (Gram-negative)	741	37°C for 24 h
Klebsiella pneumoniae (Gram -negative)	3384	37°C for 24 h

6.3.2.2. Antifungal Assay (Agar Well Diffusion Method)[130]

Procedure: The agar well diffusion method was employed to assess the antimicrobial activity of the test sample. A mixture of Mueller-Hinton agar and Potato Dextrose Agar (MH096 Himedia) in a 1:1 ratio was poured onto glass petri plates of the same size and allowed to solidify. A standardized inoculum of the test organism was evenly spread on the plate surface using a sterile cotton swab. Four wells with a diameter of 7 mm (20 mm apart from one another) were aseptically punched with a sterile cork borer in each plate.

The test sample (40 and 80 µL) was added into wells T_1 and T_2 from a 10 mg/mL stock. Clotrimazole (40 µL from a 300 mcg/ml stock) and the solvent used for sample dilution were added as positive and negative controls, respectively. The plates were then incubated for 24 hours at 27ºC ± 1ºC under aerobic conditions. After incubation, the plates were observed, and the zone of microbial growth inhibition around the wells was measured in millimetres

Culture medium details: To resolve the susceptibility of fungal strains to antifungal agents, a medium consisting of Mueller-Hinton agar and Potato Dextrose Agar MH096 Himedia in a 1:1 ratio was used. The preparation involved heating the medium until it boiled to ensure complete dissolution. Sterilization is achieved by autoclaving at 15 lbs pressure (121°C) for 15 minutes. After autoclaving, the medium is cooled to 45-50°C, mixed thoroughly, and then poured into sterile Petri plates for further use.

Inoculums details: Inoculums were procured from the Microbial Type Culture Collection and Gene Bank (MTCC) Chandigarh.

Table 6.3 Inoculums details of Fungal cell lines

Fungi	MTCC No.	Incubation time
Candida albicans	227	27°C for 48h

6.3.2.3. *Invitro* cytotoxic activity using splenocyte[131]

In order to examine the short-term in vitro cytotoxicity of the test substance, rat spleen cells were used. To obtain the spleen tissue, a rat (purchased from the Small Animal Breeding Station (SABS), Kerala Veterinary and Animal Sciences University,

Mannuthy, Thrissur, Kerala) was slaughtered under carbon dioxide anaesthesia. It was then broken down into a single-cell suspension in an antibiotic (Penicillin-streptomycin solution at a concentration of 50 I.U./mL)-containing Dulbecco's modified Eagle's medium (DMEM) before being filtered through mesh cloth. The obtained cells were washed three times, suspended in a predetermined amount of antibiotic-containing DMEM complete media, and counted using a haemocytometer. Into the tubes containing various concentrations of the test substance, a viable cell suspension (1 106 cells in 0.1 ml) was introduced, and the volume was boosted to 1 ml using DMEM medium. The cell suspension without any additives was present in the control tubes. At 37°C, these tubes were incubated for 3 hours. After incubation, 0.1 mL of 1% trypan blue was added to the cell suspension in the tubes, which was then maintained for 2–3 minutes before being placed into a haemocytometer. Trypan blue had a blue tint that only dead cells could absorb; healthy cells didnot. Separate counts were made of labelled cells.

$$Percentage\ of\ cytotoxicity = \frac{Number\ of\ dead\ cells}{Number\ of\ dead\ cells\ +\ Number\ of\ live\ cells} \times 100$$

6.4. RESULTS AND DISCUSSION

6.4.1 Antibacterial effects of curcumin analogues and their metal complexes

6.4.1.1. *In silico* studies

Eight key proteins that harbour germline mutations influencing both Gram-positive and Gram-negative bacterial infections were chosen as molecular targets from RCSB. The proteins are:(PDB ID:4H8E) (TG1), (PDB ID:1UZN) (TG2), (PDB ID:2W9S) (TG3), PDB ID:4Q8I) (TG4),(PDB ID: 1NPB) (TG5),(PDB ID:5O7N)(TG6),(PDB ID:4JVD)(TG7),(PDB ID:6B8A)(TG8). Among these the first four targets related to gram-positive (TG1, TG2, TG3, and TG4) and the latter four related to gram-negative bacteria (TG5, TG6, TG7, and TG8).

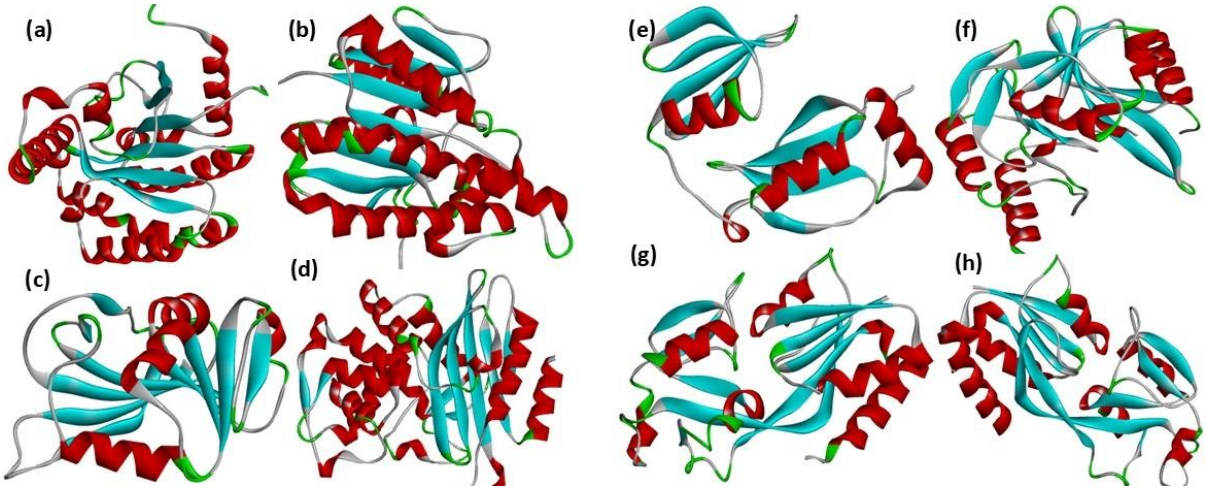

Fig.6.1 Proteins with germline mutations affect both Gram-positive and Gram-negative bacterial infections. (a) 4H8E (b) 1UZN(c) 2W9S(d) 4Q8I(e) 1NPB(f) 5O7N(g) 4JVD(h) 6B8A

6.4.1.1.1. Computational screening of designed molecules

The nine molecules—NLB, NLD, NLE, NLF, NLG, NLH, NLI, NLJ, and NLK—underwent virtual screening via Pre ADMET and Swiss ADME, meeting the CMC-like rule and Rule of Five criteria. Further drug-likeness, ADME, and toxicity evaluations confirmed their suitability, leading to their selection as lead compounds.

6.4.1.1.2. Molecular docking studies of antibacterial effect of curcumin analogues

Molecular docking was employed to predict the binding strength of the nine curcumin analogues to the selected eight molecular targets associated with bacterial infections. The process also analyzed the interaction patterns of curcumin and Gentamycin, used as reference compounds, with these targets. Key docking parameters included active site analysis, binding energy, ligand efficiency energy, inhibition constant, intermediate energy, Van der Waals dissociation energy, torsional energy, unbound energy, and reference RMS values. The resulting conformations were evaluated based on the above parameters. The best-docked complexes were evaluated based on several criteria: lower values were preferred to Binding Energy (BE), Inhibition Constant (Ki), Intermolar Energy, Van der Waals, hydrogen bond, desolvation energies, Total Internal Energy, Torsional Energy, Unbound Energy, clRMS (Cluster Root Mean Square Deviation), and refRMS (Reference Root Mean Square Deviation). The more negative values are better for Ligand Efficiency (LE) and Electrostatic Energy. The binding potentials of these molecules are summarized in **Tables 6.4**, **6.5**,**6.6** and **6.7**.

6.4.1.1.2.1. Molecular docking studies of gram-positive antibacterial effect of curcumin analogues

The specific targets of gram-positive bacteria, *Staphylococcus aureus* and *Mycobacterium smegmatis*, namely 4H8E, 1UZN, 2W9S, and 4Q8I, were employed for the molecular docking studies. The predicted binding potentials of the nine synthesised curcumin analogues and reference compounds (curcumin and Gentamycin) to the prioritized Gram-positive bacterial targets are shown in **Table 6.4** and **Table 6.5**.

It was found that for *Staphylococcus aureus* (4H8E), the ligand NLE demonstrated the highest binding energy (BE) of -12.63 kcal/mol, with a ligand efficiency (LE) of -0.38 and an inhibition constant (Ki) of 548.63 nM. NLD, NLH, and NLK also showed promising results, with BEs of-9.65 kcal/mol, -9.58 kcal/mol and -9.43 kcal/mol, LEs of -0.36,-0.38, and -0.45, inhibition constants of 84.29 nM, 94.5 nM and 122.77 nM, respectively. For *Staphylococcus aureus* (1UZN), NLE again exhibited the best binding energy at -10.34 kcal/mol, LE of -0.31, and Ki of 26.2 nM. NLH and NLG followed with BEs of -9.08 kcal/mol and -8.81 kcal/mol, LEs of -0.36 and -0.33, and inhibition constants of 220.78 nM and 349.5 nM, respectively (**Table 6.4**).

In the case of *Mycobacterium smegmatis* (4Q8I), NLE showed a binding energy of -10.07 kcal/mol, LE of -0.31, and a Ki of 41.87 nM. NLH and NLG were also effective, with BEs of -8.08 kcal/mol and -8.04 kcal/mol, LEs of -0.32 and -0.30, and inhibition constants of 1.19 nM and 1.28 nM, respectively. For *Mycobacterium smegmatis* (2W9S), NLE had the highest binding energy at -11.72 kcal/mol, LE of -0.36, and Ki of 2.55 nM. NLB and NLD also figured good results, with BEs of -9.44 kcal/mol and -9.38 kcal/mol, LEs of -0.33 and -0.35, and ICs of 120.3 nM and 133.1 nM, respectively (**Table 6.5**).

Figures 6.2 to **6.5** detail the interactions of each ligand with the corresponding target molecules of Gram-positive bacteria through the various amino acid residues.

Table 6.4 The predicted binding potentials of the nine synthesised curcumin analogues and reference compounds (curcumin and Gentamycin) to the prioritized gram-positive *Staphylococcus aureus* bacterial targets.

Active Target	**4H8E**											**1UZN**										
Ligands	**Curcumin**	**Gentamycin**	**NLB**	**NLD**	**NLE**	**NLF**	**NLG**	**NLH**	**NLI**	**NLJ**	**NLK**	**Curcumin**	**Gentamycin**	**NLB**	**NLD**	**NLE**	**NLF**	**NLG**	**NLH**	**NLI**	**NLJ**	**NLK**
Active Site and Run	7	3	6	3	6	2	6	7	10	5	8	7	3	10	9	1	2	7	8	7	1	2
BE(kcal/ mol)	-5.52	-9.35	-8.4	-9.65	-12.63	-9.33	-9.33	-9.58	-8.65	-8.86	-9.43	-7.01	-8.27	-8.52	-8.75	-10.34	-7.36	-8.81	-9.08	-7.76	-7.96	-7.31
Ligand efficiency	-0.2	-0.28	-0.29	-0.36	-0.38	-0.32	-0.35	-0.38	-0.32	-0.33	-0.45	-0.26	-0.25	-0.29	-0.32	-0.31	-0.25	-0.33	-0.36	-0.29	-0.29	-0.35
Inhib constant (nM)	90.61	140.44	692.3	84.29	548.63	144.07	144.89	94.5	454.87	320.64	122.77	7.31	868.9	567.8	385.3	26.2	4.02	349.5	220.78	2.05	1.47	4.36
Intermolar energy	-9.09	-13.23	-11.39	-12.04	-15.02	-12.91	-11.72	-11.97	-11.64	-11.84	-11.22	-10.59	-12.15	-11.5	-11.14	-12.73	-10.94	-11.19	-11.47	-10.74	-10.94	-9.1
vdw hb disolv energy	-8.69	-7.88	-11.35	-11.74	-14.97	-12.9	-11.65	-11.79	-10.93	-11.68	-1.21	-10.34	-5.5	-11.2	-10.94	-12.7	-10.57	-11.06	-11.04	-10.56	-10.75	-9.04
Electrostatic energy	-0.4	-5.34	-0.04	-0.3	-0.05	-0.01	-0.07	-0.18	-0.7	-0.16	0	-0.25	-6.65	-0.29	-0.2	-0.03	-0.37	-0.13	-0.43	-0.18	-0.19	-0.06
Total internal	-1.98	-5.68	-1.72	-0.92	-1.5	-2.99	-0.76	-1.73	-2.14	-2.32	-1.25	-3.51	-6.3	-1.85	-1.4	-1.29	-2.7	-0.71	-1.23	-2.06	-2.22	-1.26
Torsional energy	3.58	3.88	2.98	2.39	2.39	3.58	2.39	2.39	2.98	2.98	1.79	3.58	3.88	2.98	2.39	2.39	3.58	2.39	2.39	2.98	2.98	1.79
Unbound energy	-1.98	-5.68	-1.72	-0.92	-1.5	-2.99	-0.76	-1.73	-2.14	-2.32	-1.25	-3.51	-6.3	-1.85	-1.4	-1.29	-2.7	-0.71	-1.23	-2.06	-2.22	-1.26

Table 6.5 The predicted binding potentials of the nine synthesised curcumin analogues and reference compounds (curcumin and Gentamycin) to the prioritized gram-positive *Mycobacterium Smegmatis* bacterial targets.

Active Target	4Q8I											2W9S										
Ligands	Curcumin	Gentamycin	NLB	NLD	NLE	NLF	NLG	NLH	NLI	NLJ	NLK	Curcumin	Gentamycin	NLB	NLD	NLE	NLF	NLG	NLH	NLI	NLJ	NLK
Active Site and Run	6	9	4	9	2	10	5	4	6	3	1	4	8	1	2	4	7	9	1	4	6	7
BE(kcal/ mol)	-5.25	-8.66	-7.29	-8.26	-10.07	-5.66	-8.04	-8.08	-6.04	-7.29	-7.48	-7.38	-7.05	-9.44	-9.38	-11.72	-8.93	-9.27	-9.4	-8.48	-9.17	-8.98
Ligand efficiency	-0.19	-0.26	-0.25	-0.31	-0.31	-0.2	-0.30	-0.32	-0.22	-0.27	-0.36	-0.27	-0.21	-0.33	-0.35	-0.36	-0.31	-0.34	-0.38	-0.31	-0.34	-0.43
Inhib constant (nM)	141.3	452.4	4.53	883.6	41.87	71.42	1.28	1.19	37.47	4.5	3.28	3.89	6.78	120.3	133.1	2.55	284.8	160.7	129.1	609.5	190.2	261.9
Intermolar energy	-8.83	-12.53	-10.27	-10.65	-12.45	-9.24	-10.43	-10.47	-9.02	-10.28	-9.27	-10.96	-10.93	-12.42	-11.77	-14.11	-12.51	-11.65	-11.78	-11.46	-12.55	-10.77
vdw hb disolv energy	-8.41	-6.83	-9.88	-10.23	-11.95	-8.79	-9.9	-9.91	-8.85	-9.78	-8.95	-10.8	-7.49	-12.35	-11.56	-14.1	-12.34	-11.38	-11.26	-11.36	-11.85	-10.68
Electrostatic energy	-0.42	-5.7	-0.39	-0.42	-0.5	-0.44	-0.53	-0.56	-0.17	-0.5	-0.32	-0.16	-3.44	-0.07	-0.2	-0.02	-0.17	-0.28	-0.53	-0.1	-0.3	-0.09
Total internal	-2.99	-5.68	-1.33	-1.09	-0.78	-2.91	-1.06	-1.28	-2.82	-1.92	-0.64	-2.22	-6.74	-1.23	-0.84	-0.96	-3.11	-1.05	-0.81	-2.98	-2.7	-0.6
Torsional energy	3.58	3.88	2.98	2.39	2.39	3.58	2.39	2.39	2.98	2.98	1.79	3.58	3.88	2.98	2.39	2.39	3.58	2.39	2.39	2.98	2.98	1.79
Unbound energy	-2.99	-5.68	-1.33	-1.09	-0.78	-2.91	-1.06	-1.28	-2.82	-1.92	-0.64	-2.22	-6.74	-1.23	-0.84	-0.96	-3.11	-1.05	-0.81	-2.98	-2.7	-0.6

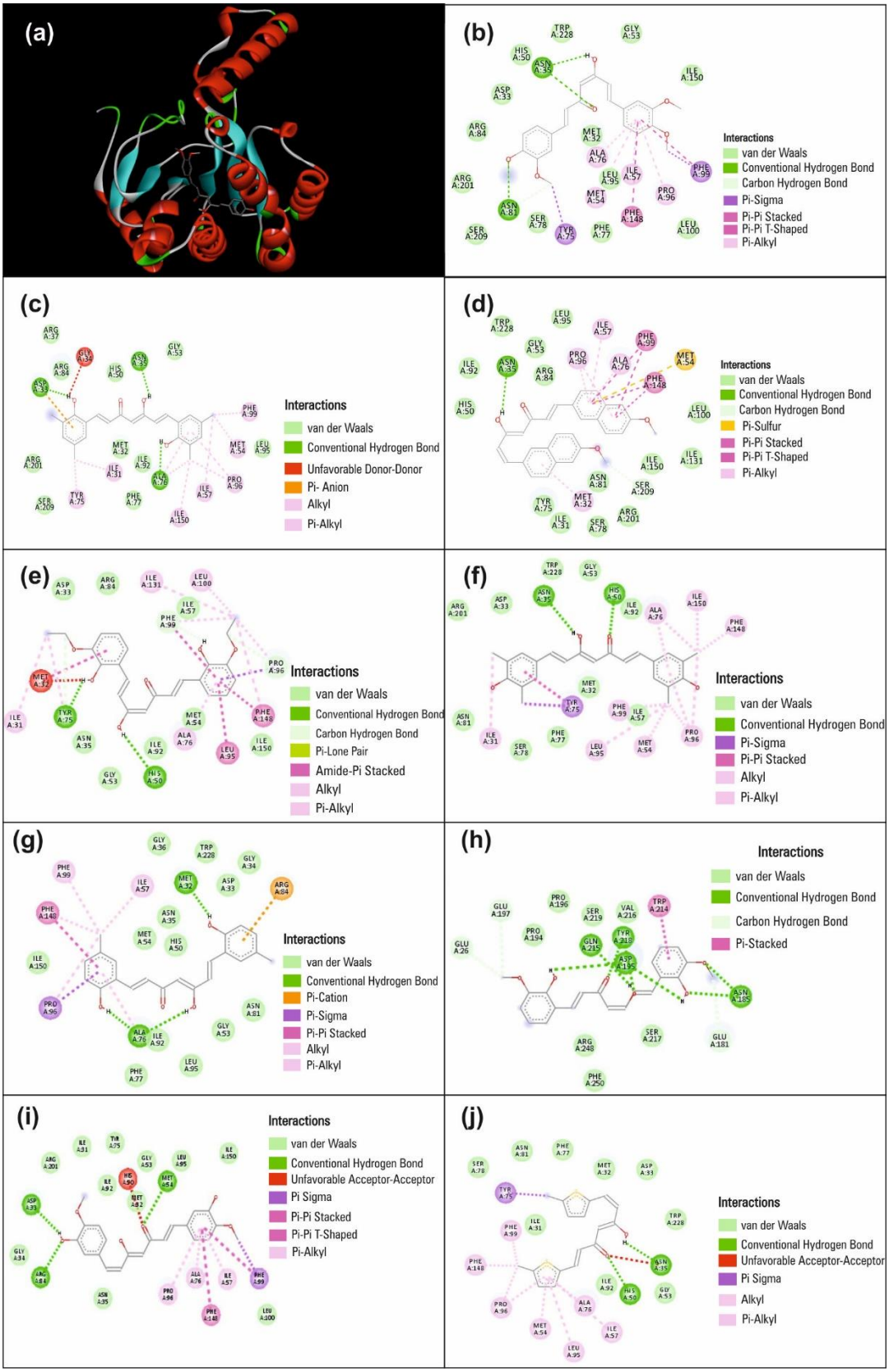

Fig.6.2 4H8E-Curcumin Analogue Complexes (a) 4H8E-NLB Complex(3D) (b) 4H8E-NLB Complex(2D) (c) 4H8E-NLD Complex(2D) (d) 4H8E-NLE Complex(2D) (e) 4H8E-NLF Complex(2D) (f) 4H8E-NLG Complex(2D) (g) 4H8E-NLH Complex(2D) (h) 4H8E-NLI Complex(2D) (i) 4H8E-NLJ Complex(2D) (j) 4H8E-NLK Complex

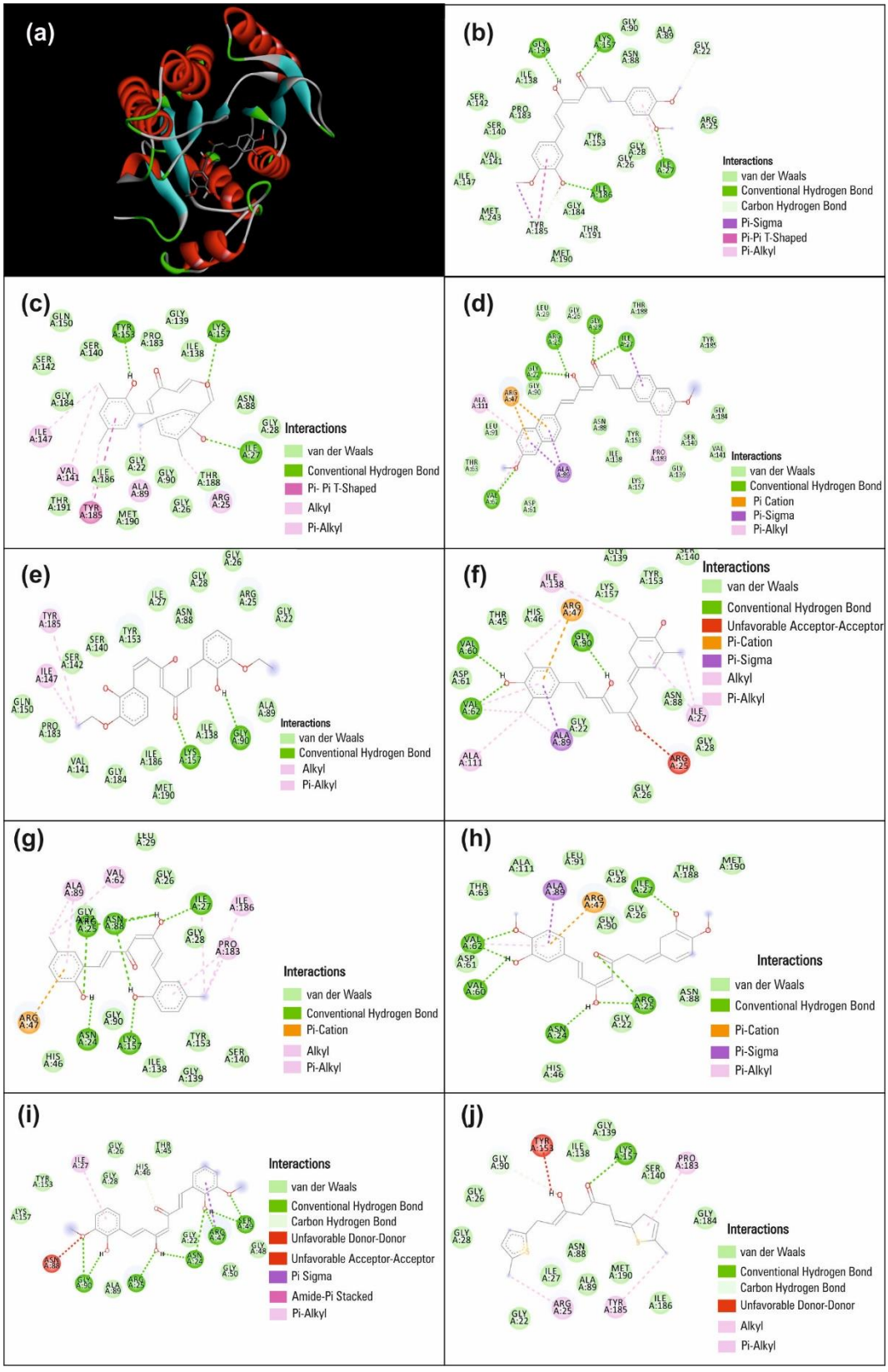

Fig.6.3 1UZN -Curcumin Analogue Complexes (a) 1UZN -NLB Complex(3D) (b) 1UZN -NLB Complex(2D) (c) 1UZN -NLD Complex(2D) (d) 1UZN -NLE Complex(2D) (e) 1UZN -NLF Complex(2D) (f) 1UZN -NLG Complex(2D) (g) 1UZN -NLH Complex(2D) (h) 1UZN -NLI Complex(2D) (i) 1UZN -NLJ Complex(2D) (j)1UZN -NLK Complex

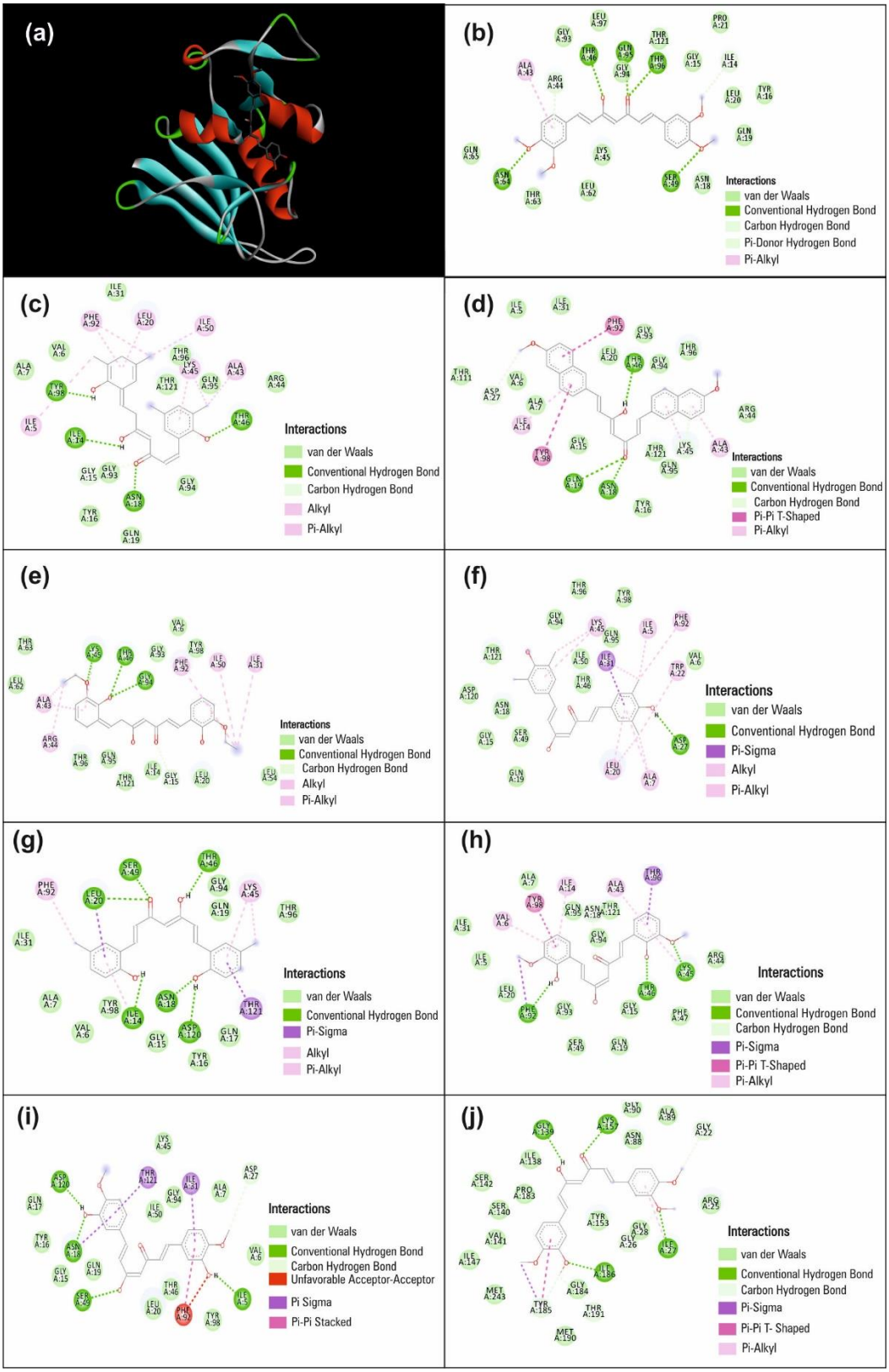

Fig.6.4 2W9S -Curcumin Analogue Complexes (a) 2W9S -NLB Complex(3D) (b) 2W9S -NLB Complex(2D) (c) 2W9S -NLD Complex(2D) (d) 2W9S -NLE Complex(2D) (e) 2W9S -NLF Complex(2D) (f) 2W9S -NLG Complex(2D) (g) 2W9S-NLH Complex(2D) (h) 2W9S -NLI Complex(2D) (i) 2W9S -NLJ Complex(2D) (j) 2W9S -NLK Complex

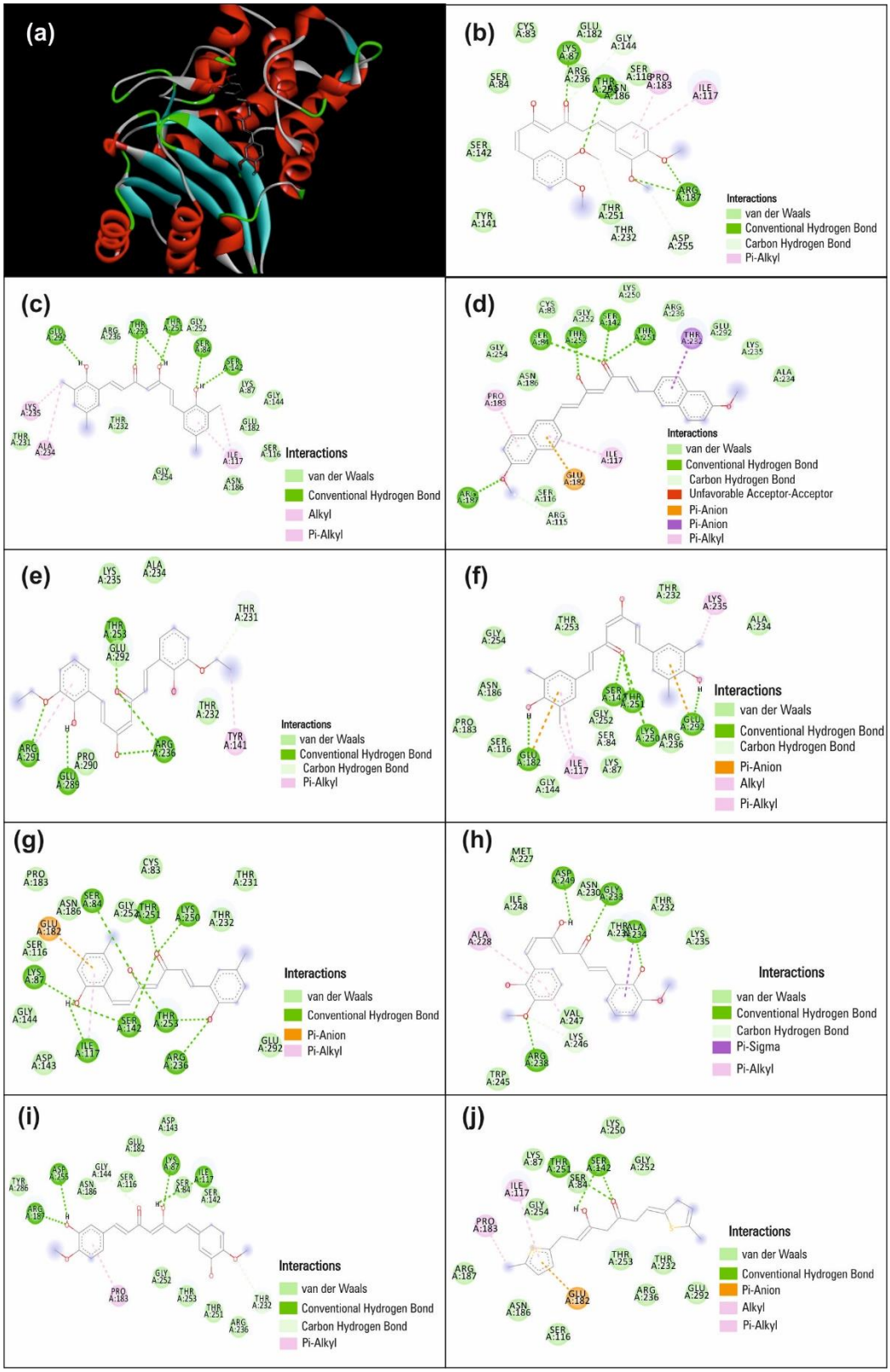

Fig.6.5 4Q8I -Curcumin Analogue Complexes (a) 4Q8I-NLB Complex(3D) (b) 4Q8I-NLB Complex(2D) (c) 4Q8I-NLD Complex(2D) (d) 4Q8I-NLE Complex(2D) (e) 4Q8I-NLF Complex(2D) (f) 4Q8I -NLG Complex(2D) (g) 4Q8I -NLH Complex(2D) (h) 4Q8I -NLI Complex(2D) (i) 4Q8I -NLJ Complex(2D) (j) 4Q8I -NLK Complex(2D)

The compounds engaged in various interactions with the target protein, with Van der Waals interactions being the most common, indicating significant surface contact. Traditional hydrogen bonds demonstrated robust, precise binding. The presence of a wide array of interaction types—such as Pi-Sigma, Pi-Alkyl, Pi-lone pair, Pi-Pi stacked, Alkyl, Pi-Anion, Pi-Pi T-shaped, unfavourable bump, Pi-Cation, Pi-Carbon, Pi-Sulfur, Attractive Charge, Amide-Pi stacked, Sulfur-X, and Pi-Donor interactions—contributed to the complexity and stability of the binding. The specific amino acid residues involved in these interactions highlighted crucial contact points and potential areas for further modifications to enhance binding affinity and specificity. This comprehensive interaction profile underscored the therapeutic potential of each compound, warranting further exploration and refinement.

The prioritization of ligands for antibacterial effects against Gram-positive bacteria, particularly *Staphylococcus aureus* and *Mycobacterium smegmatis*, was carefully evaluated based on docking parameters, functional group characteristics, and their interactions with target proteins. Binding energy (BE) was identified as a critical indicator, with lower values signifying stronger interactions between the ligand and the target protein. Ligand efficiency (LE) provided insights into the binding energy per heavy atom, reflecting how effectively each atom contributed to the interaction. The inhibition constant (Ki) highlighted the binding affinity, where lower Ki values suggested stronger binding capabilities. The functional group composition of the ligands significantly influenced their antibacterial activity. Groups such as hydroxy, chloro, methoxy, and ethoxy were noted for their roles in hydrogen bonding, hydrophobic interactions, and lipophilicity. These properties were essential for facilitating ligand penetration through bacterial membranes and ensuring effective binding with target proteins. The structural differences in bacterial cell walls were crucial in explaining the varying antibacterial activity. Gram-positive bacteria had a thick peptidoglycan layer that was relatively porous, allowing the curcumin analogues to penetrate and reach their targets more easily.

Among the ligands, NLE was ranked as the top priority due to its exceptional binding energy (-12.63 kcal/mol for 4H8E and -11.72 kcal/mol for 2W9S) and low Ki (2.55 nM for 2W9S). Its high ligand efficiency (-0.36) and structural features, including methoxy naphthyl groups, enhanced its binding through π-π stacking interactions with aromatic residues in the proteins. NLD and NLH followed closely in the ranking. NLD

exhibited a binding energy of -9.65 kcal/mol (4H8E) and dual functional groups (hydroxy and chloro) that supported strong hydrogen bonding and increased lipophilicity. Similarly, NLH demonstrated a binding energy of -9.58 kcal/mol (4H8E), with a combination of hydroxy and chloro groups contributing to effective protein interactions.

In the third tier, NLK and NLB were identified as moderate performers. NLK had a binding energy of -9.43 kcal/mol (4H8E) and benefited from methyl thiophene groups that enhanced lipophilicity, aiding membrane interactions. NLB, with a binding energy of -9.44 kcal/mol (2W9S), relied on methoxy groups for hydrophobic interactions, making it moderately effective in targeting bacterial membranes.

The ligands NLG, NLF, NLI, and NLJ exhibited moderate antibacterial activity. NLG and NLF both achieved a binding energy of -9.33 kcal/mol (4H8E). The hydroxy and methyl groups of NLG ensured a balanced approach to hydrophobic and hydrogen bonding properties, while the hydroxy and ethoxy groups of NLF offered a similar balance. NLI and NLJ, despite structural similarities to NLF, displayed slightly reduced interaction efficiency due to the presence of methoxy groups, which limited hydrogen bonding potential.

Gentamycin, while known for disrupting protein synthesis, had a binding energy of -9.35 kcal/mol (4H8E) and a lower ligand efficiency (-0.28), placing it below NLE. Curcumin, with a moderate binding energy of -7.38 kcal/mol (2W9S), was less effective due to its general hydrophobicity, which limited interaction specificity compared to optimized analogues such as NLE and NLH.

The final prioritization order for targeting Gram-positive bacteria was established as follows: NLE, NLD, NLH, NLK, NLB, NLG, NLF, gentamycin, NLI, NLJ, and curcumin. This ranking reflected a comprehensive integration of docking parameters and functional group characteristics, providing a clear rationale for ligand selection in antibacterial applications.

6.4.1.1.2.2. Molecular docking studies of gram-negative antibacterial effect of curcumin analogues

The molecular docking studies used the specific targets of gram-negative bacteria (Pseudomonas aeruginosa and Klebsiella pneumoniae), 1NPB, 5O7N, 4JVD, and 6B8A. **Tables 6.6 and 6.7** arrange the predicted binding potentials of the nine synthesized curcumin analogues and reference compounds (curcumin and gentamycin) to the prioritized gram-negative bacterial targets.

Considering the antibacterial activity against *Pseudomonas aeruginosa* (5O7N), NLE was identified as the top priority due to its superior combination of low binding energy (-10.21 kcal/mol), low inhibition constant (32.6 nM), and good ligand efficiency (-0.31). Gentamycin followed as the second-best ligand with strong binding energy (-9.6 kcal/mol) and low inhibition constant (91.5 nM), despite slightly lower ligand efficiency (-0.29). Curcumin offered a balanced profile with a binding energy of -9.25 kcal/mol, an inhibition constant of 164.5 nM, and the highest ligand efficiency (-0.34) among the top three. NLG showed a reasonable combination of binding energy (-8.99 kcal/mol), inhibition constant (258.8 nM), and ligand efficiency (-0.33), while NLD had similar binding energy (-8.64 kcal/mol) but higher inhibition constant (466.5 nM) and slightly lower ligand efficiency (-0.32).

For *Pseudomonas aeruginosa* (1NPB), NLB emerged as the leading candidate due to its very low inhibition constant (18.12 nM) and unusually high ligand efficiency (-0.22), despite having a higher binding energy (-6.47 kcal/mol). NLH exhibited strong binding energy (-7.75 kcal/mol), very low inhibition constant (2.07 nM), and good ligand efficiency (-0.31). NLJ presented a favourable combination of binding energy (-7.18 kcal/mol) and low inhibition constant (5.48 nM), with slightly lower ligand efficiency (-0.27). NLK witnessed a low inhibition constant (7.98 nM) but had higher binding energy (-6.95 kcal/mol) and ligand efficiency (-0.33). NLF and NLI, with higher binding energies (-6.75 and -6.67 kcal/mol, respectively) and inhibition constants (11.31 and 12.93 nM, respectively), demonstrated lower ligand efficiencies (-0.23 and -0.25, respectively).

It was found that antibacterial activity against *Klebsiella pneumoniae* (6B8A) prioritized NLK due to its strong binding energy (-9.58 kcal/mol), low inhibition constant (94.85 nM), and high ligand efficiency (-0.46). NLG, with similarly strong binding energy (-9.54 kcal/mol), low inhibition constant (102.48 nM), and high ligand efficiency (-0.35), was another top contender. NLE also showed promise with a good combination of binding energy (-9.63 kcal/mol), moderate inhibition constant (187.68 nM), and good ligand efficiency (-0.29).

For *Klebsiella pneumoniae* (4JVD), NLD emerged as the leading candidate, showing strong binding energy (-8.32 kcal/mol) and high ligand efficiency (-3.01) with inhibition constant (794.1nM). NLH followed closely, offering a good combination of binding energy (-9.01 kcal/mol), inhibition constant (249.5 nM), and high ligand efficiency (-0.36). NLI, despite its higher binding energy (-6.88 kcal/mol), exhibited an extremely low inhibition constant (9.03 nM) and good ligand efficiency (-0.25), making it highly effective. Gentamycin showed reasonable binding energy (-8.4kcal/mol), inhibition constant (690.9 nM), and ligand efficiency (-0.25), while NLB, despite higher binding energy (-7.82 kcal/mol), demonstrated a very low inhibition constant (1.84 nM) and reasonable ligand efficiency (-0.27).NLF exhibited good binding energy (-8.36 kcal/mol), higher inhibition constant (744.9 nM), and ligand efficiency (-0.29), while NLJ, with higher binding energy (-7.58 kcal/mol), low inhibition constant (2.77 nM), and reasonable ligand efficiency (-0.28), also showed effectiveness. Curcumin, despite its higher binding energy (-5.08 kcal/mol), demonstrated a low inhibition constant (189.8 nM) and good ligand efficiency (-0.19).

Comprehensive interactions between individual ligands and target molecules for Gram-negative bacteria were illustrated in **Figures 6.6 to 6.9**. The molecules exhibited multiple interactions with the target protein, primarily through Van der Waals forces, indicating significant surface contact. They formed strong, precise bonds, including traditional hydrogen bonds. Various interaction types—such as Pi-Sigma, Pi-Alkyl, Pi-lone pair, Pi-Pi stacked, Alkyl, Pi-Anion, Pi-Pi T-shaped, unfavourable bump, Pi-Cation, Pi-Carbon, Pi-Sulfur, Attractive Charge, Amide-Pi stacked, Sulfur-X, and Pi-Donor—contributed to the complex and stable binding process. Specific amino acid residues involved in these interactions were pivotal in identifying key contact points and areas with the potential for further optimization to enhance binding affinity and specificity. This detailed interaction profile emphasized the therapeutic potential of each compound, warranting additional investigation and refinement.

Table 6.6 The predicted binding potentials of the nine synthesised curcumin analogues and reference compounds (curcumin and Gentamycin) to the prioritized gram-negative *Pseudomonas aeruginosa* bacterial targets.

Active Target	**1NPB**											**5O7N**										
Ligands	**Curcumin**	**Gentamycin**	**NLB**	**NLD**	**NLE**	**NLE**	**NLG**	**NLH**	**NLI**	**NLJ**	**NLK**	**Curcumin**	**Gentamycin**	**NLB**	**NLD**	**NLE**	**NLF**	**NLG**	**NLH**	**NLI**	**NLJ**	**NLK**
Active Site and Run	**10**	**2**	**3**	**9**	**4**	**4**	**4**	**5**	**9**	**8**	**9**	**10**	**8**	**4**	**2**	**3**	**4**	**8**	**2**	**1**	**8**	**3**
BE (kcal/mol)	**-5.48**	**-7.74**	**-6.47**	**-7.38**	**-8.69**	**-6.75**	**-6.97**	**-7.75**	**-6.67**	**-7.18**	**-6.95**	**-9.25**	**-9.6**	**-7.77**	**-8.64**	**-10.21**	**-7.57**	**-8.99**	**-8.67**	**-6.8**	**-6.99**	**-8.51**
Ligand efficiency	**-0.2**	**-0.23**	**-0.22**	**-0.27**	**-0.26**	**-0.23**	**-0.26**	**-0.31**	**-0.25**	**-0.27**	**-0.33**	**-0.34**	**-0.29**	**-0.27**	**-0.32**	**-0.31**	**-0.26**	**-0.33**	**-0.35**	**-0.25**	**-0.26**	**-0.41**
Inhib constant (nM)	**96.11**	**2.14**	**18.12**	**3.89**	**424.9**	**11.31**	**7.84**	**2.07**	**12.93**	**5.48**	**7.98**	**164.5**	**91.5**	**2.01**	**466.5**	**32.6**	**2.84**	**258.8**	**441.8**	**10.28**	**7.48**	**576.5**
Intermolar energy	**-9.06**	**-11.61**	**-9.45**	**-9.77**	**-11.08**	**-10.33**	**-9.35**	**-10.14**	**-9.65**	**-10.16**	**-8.74**	**-12.83**	**-13.48**	**-10.75**	**-11.02**	**-12.6**	**-11.15**	**-11.37**	**-11.06**	**-9.79**	**-9.98**	**-10.3**
vdw hb disolv energy	**-9.03**	**-5.86**	**-9.39**	**-9.67**	**-11.03**	**-10.21**	**-8.96**	**-9.91**	**-9.48**	**-10.02**	**-8.74**	**-12.69**	**-5.32**	**-10.69**	**-10.64**	**-12.31**	**-10.85**	**-11.22**	**-10.72**	**-9.61**	**-9.76**	**-10.18**
Electrostatic energy	**-0.03**	**-5.75**	**-0.06**	**-0.1**	**-0.05**	**-0.11**	**-0.4**	**-0.23**	**-0.17**	**-0.14**	**-0.01**	**-0.14**	**-8.16**	**-0.06**	**-0.38**	**-0.29**	**-0.29**	**-0.15**	**-0.34**	**-0.18**	**-0.22**	**-0.12**

Active Target	1NPB											5O7N										
Ligands	Curcumin	Gentamycin	NLB	NLD	NLE	NLE	NLG	NLH	NLI	NLJ	NLK	Curcumin	Gentamycin	NLB	NLD	NLE	NLF	NLG	NLH	NLI	NLJ	NLK
Total internal	-2.44	-6.76	-1.79	-1.25	-1.48	-2.98	-0.74	-0.81	-2.28	-2.61	-1.32	-2.75	-5.82	-1.92	-0.81	-1.57	-2.66	-1.28	-1.26	-2.89	-2.64	0.31
Torsional energy	3.58	3.88	2.98	2.39	2.39	3.58	2.39	2.39	2.98	2.98	1.79	3.58	3.88	2.98	2.39	2.39	3.58	2.39	2.39	2.98	2.98	1.79
Unbound energy	-2.44	-6.76	-1.79	-1.25	-1.48	-2.98	-0.74	-0.81	-2.28	-2.61	-1.32	-2.75	-5.82	-1.92	-0.81	-1.57	-2.66	-1.28	-1.26	-2.89	-2.64	0.31
clRMS	0	0	0	0	0	0	0	0	0	0	0	0	0	0	0	0	0	0	0	0	0	0
refRMS	74.53	57.88	74.73	74.55	71.88	78.02	82.38	79.51	73.53	79.22	76.56	92.18	96.49	91.78	92.3	100.7	91.7	91.24	97.25	86.65	91.96	94.42

Table 6.7 The predicted binding potentials of the nine synthesised curcumin analogues and reference compounds (curcumin and Gentamycin) to the prioritized gram-negative *Klebsiella Pneumonia* bacterial targets.

Active Target	**4JVD**											**6B8A**										
Ligands	**Curcumin**	**Gentamycin**	**NLB**	**NLD**	**NLE**	**NLF**	**NLG**	**NLH**	**NLI**	**NLJ**	**NLK**	**Curcumin**	**Gentamycin**	**NLB**	**NLD**	**NLE**	**NLF**	**NLG**	**NLH**	**NLI**	**NLJ**	**NLK**
Active Site and Run	**9**	**9**	**3**	**8**	**6**	**8**	**4**	**9**	**5**	**6**	**2**	**5**	**5**	**2**	**10**	**10**	**10**	**7**	**10**	**5**	**10**	**7**
BE(kcal/mol)	**-5.08**	**-8.4**	**-7.82**	**-8.32**	**-9.35**	**-8.36**	**-8.64**	**-9.01**	**-6.88**	**-7.58**	**-8.55**	**-7.37**	**-8.7**	**-8.27**	**-9.27**	**-9.63**	**-8.29**	**-9.54**	**-8.92**	**-8.05**	**-7.49**	**-9.58**
Ligand efficiency	**-0.19**	**-0.25**	**-0.27**	**-0.31**	**-0.28**	**-0.29**	**-0.32**	**-0.36**	**-0.25**	**-0.28**	**-0.41**	**-0.27**	**-0.26**	**-0.29**	**-0.34**	**-0.29**	**-0.29**	**-0.35**	**-0.36**	**-0.3**	**-0.28**	**-0.46**
Inhib constant (nM)	**189.8**	**690.9**	**1.84**	**794.1**	**140.11**	**744.9**	**462.8**	**249.5**	**9.03**	**2.77**	**543.11**	**3.97**	**419.55**	**869.8**	**161.4**	**187.68**	**833.42**	**102.48**	**290.8**	**1.25**	**3.21**	**94.85**
Intermolar energy	**-8.66**	**-12.28**	**-10.81**	**-10.71**	**-11.74**	**-11.94**	**-11.03**	**-11.39**	**-9.86**	**-10.56**	**-10.34**	**-10.95**	**-12.58**	**-11.25**	**-11.65**	**-12.01**	**-11.87**	**-11.92**	**-11.3**	**-11.04**	**-10.48**	**-11.37**
vdw hb disolv energy	**-8.56**	**-6.55**	**-10.59**	**-10.39**	**-11.63**	**-11.79**	**-10.76**	**-11.14**	**-9.9**	**-10.44**	**-10.29**	**-10.7**	**-6.76**	**-11.19**	**-11.59**	**-12.05**	**-11.81**	**-11.88**	**-11.28**	**-10.99**	**-10.29**	**-11.37**
Electrostatic energy	**-0.1**	**-5.73**	**-0.22**	**-0.32**	**-0.1**	**-0.15**	**-0.27**	**-0.25**	**0.03**	**-0.12**	**-0.05**	**-0.25**	**-5.82**	**-0.06**	**-0.06**	**0.03**	**-0.07**	**-0.04**	**-0.02**	**-0.05**	**-0.19**	**0**

Active Target	4JVD											6B8A										
Ligands	Curcumin	Gentamycin	NLB	NLD	NLE	NLF	NLG	NLH	NLI	NLJ	NLK	Curcumin	Gentamycin	NLB	NLD	NLE	NLF	NLG	NLH	NLI	NLJ	NLK
Total internal	0	-5.5	-1.31	-1.42	-1.49	-1.59	-1.01	-1.35	-3	-2.78	-1.16	-1.55	-5.44	-1.72	-1.31	-1.38	-2.54	-1.26	-1.24	-2.08	-2.7	-1.56
Torsional energy	3.58	3.88	2.98	2.39	2.39	3.58	2.39	2.39	2.98	2.98	1.79	3.58	3.88	2.98	2.31	2.39	3.58	2.39	2.39	2.98	2.98	1.79
Unbound energy	0.1	-5.5	-1.31	-1.42	-1.49	-1.59	-1.01	-1.35	-3	-2.78	-1.16	-1.55	-5.44	-1.72	-1.31	-1.38	-2.54	-1.26	-1.24	-2.08	-2.7	-1.56
clRMS	0	0	0	0	0	0	0	0	0	0	0	0	0	0	0	0	0	0	0	0	0	0
refRMS	80.03	66.75	61.51	63.18	64.85	60.9	61.18	76.6	60.28	-60.22	76.86	20.69	32.33	28.74	20.6	34.18	26.17	27.85	31.44	31.59	19.05	35.87

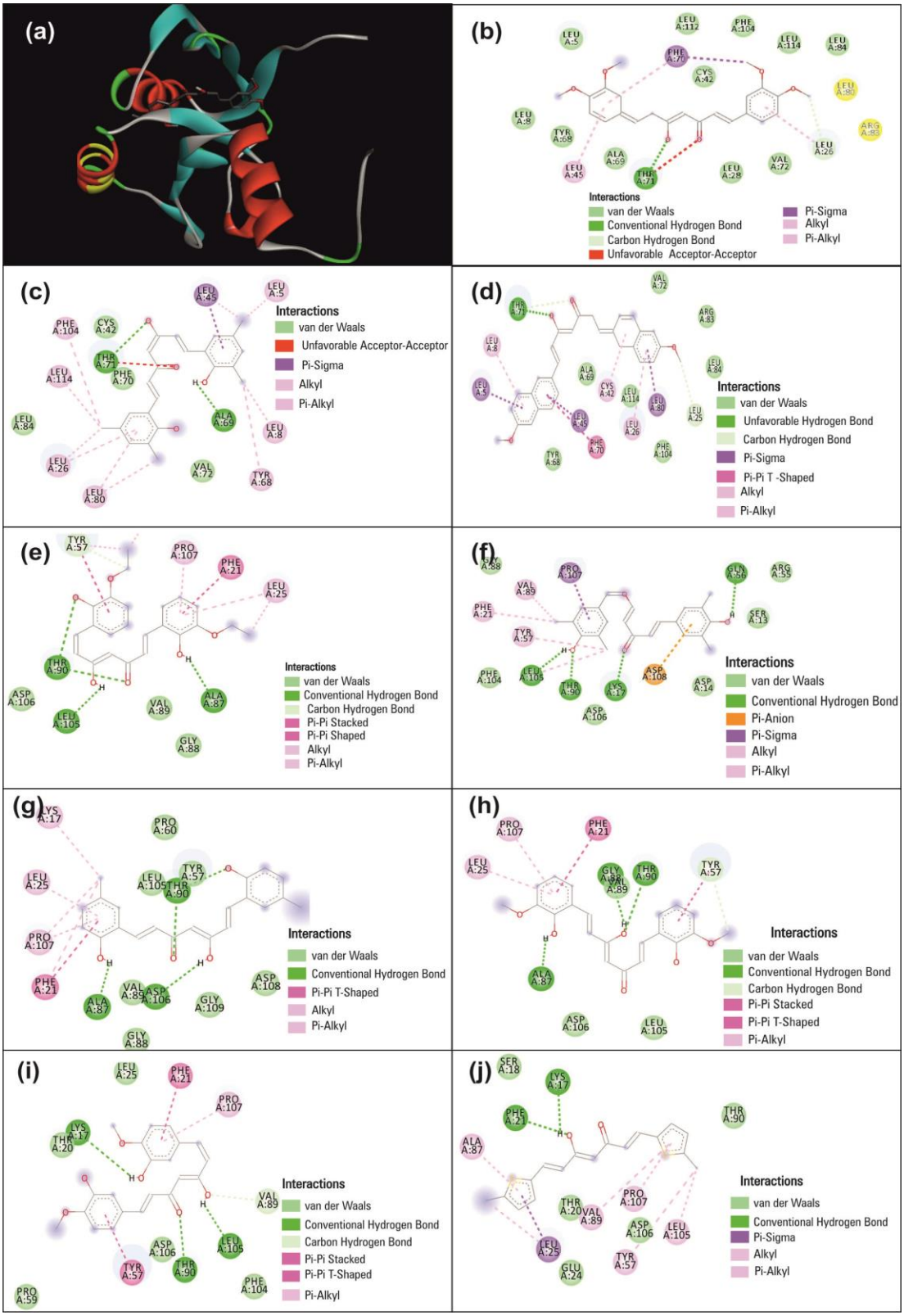

Fig.6.6 1NPB -Curcumin Analogue Complexes (a) 1NPB -NLB Complex(3D) (b) 1NPB -NLB Complex(2D) (c) 1NPB -NLD Complex(2D) (d) 1NPB -NLE Complex(2D) (e) 1NPB -NLF Complex(2D) (f) 1NPB -NLG Complex(2D) (g) 1NPB -NLH Complex(2D) (h) 1NPB -NLI Complex(2D) (i) 1NPB -NLJ Complex(2D) (j)1NPB-NLK Complex (2D)

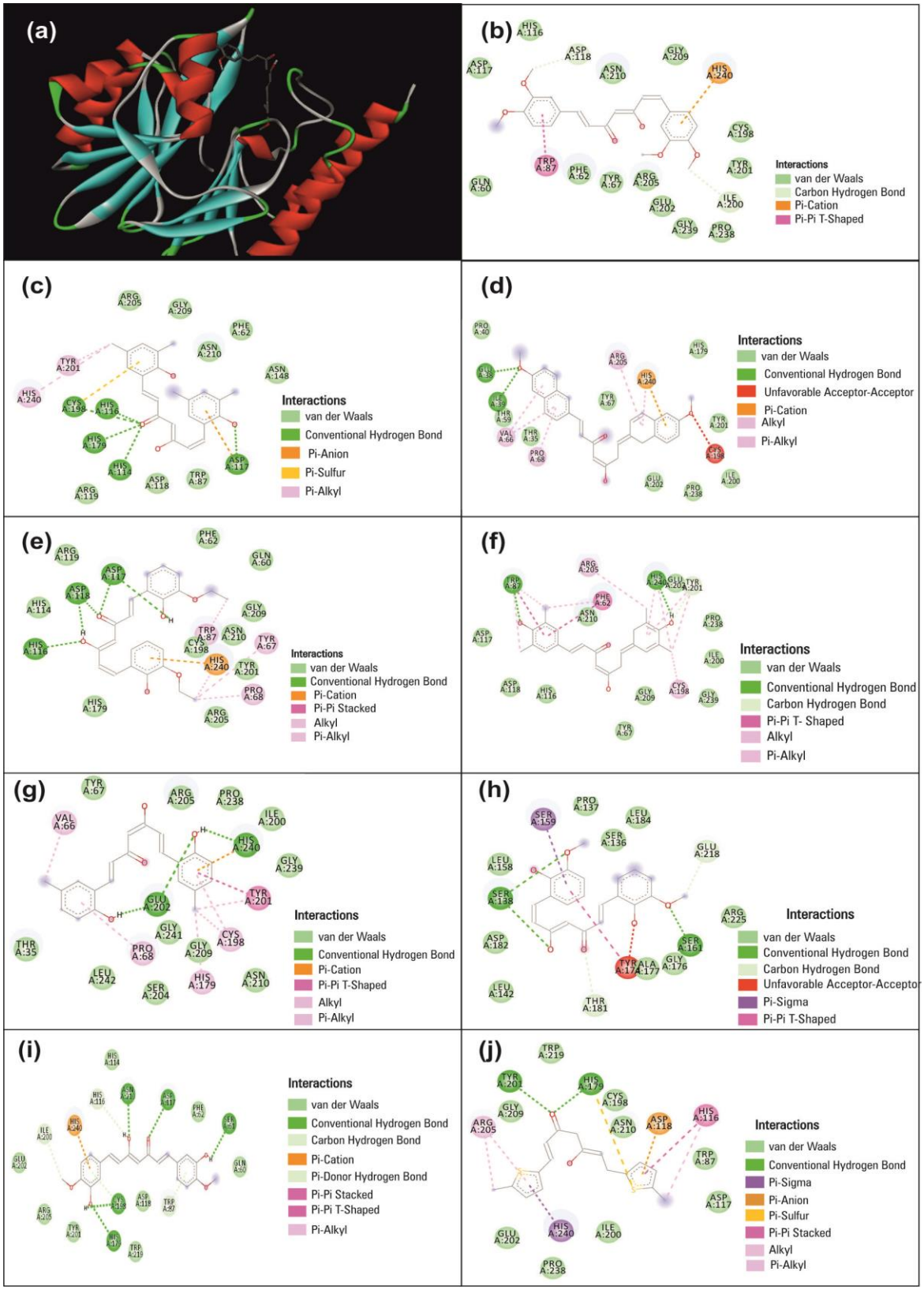

Fig.6.7 5O7N -Curcumin Analogue Complexes (a) 5O7N-NLB Complex(3D) (b) 5O7N-NLB Complex(2D) (c) 5O7N-NLD Complex(2D) (d) 5O7N-NLE Complex(2D) (e) 5O7N-NLF Complex(2D) (f) 5O7N-NLG Complex(2D) (g) 5O7N-NLH Complex(2D) (h) 5O7N-NLI Complex(2D) (i) 5O7N-NLJ Complex(2D) (j) 5O7N-NLK Complex(2D)

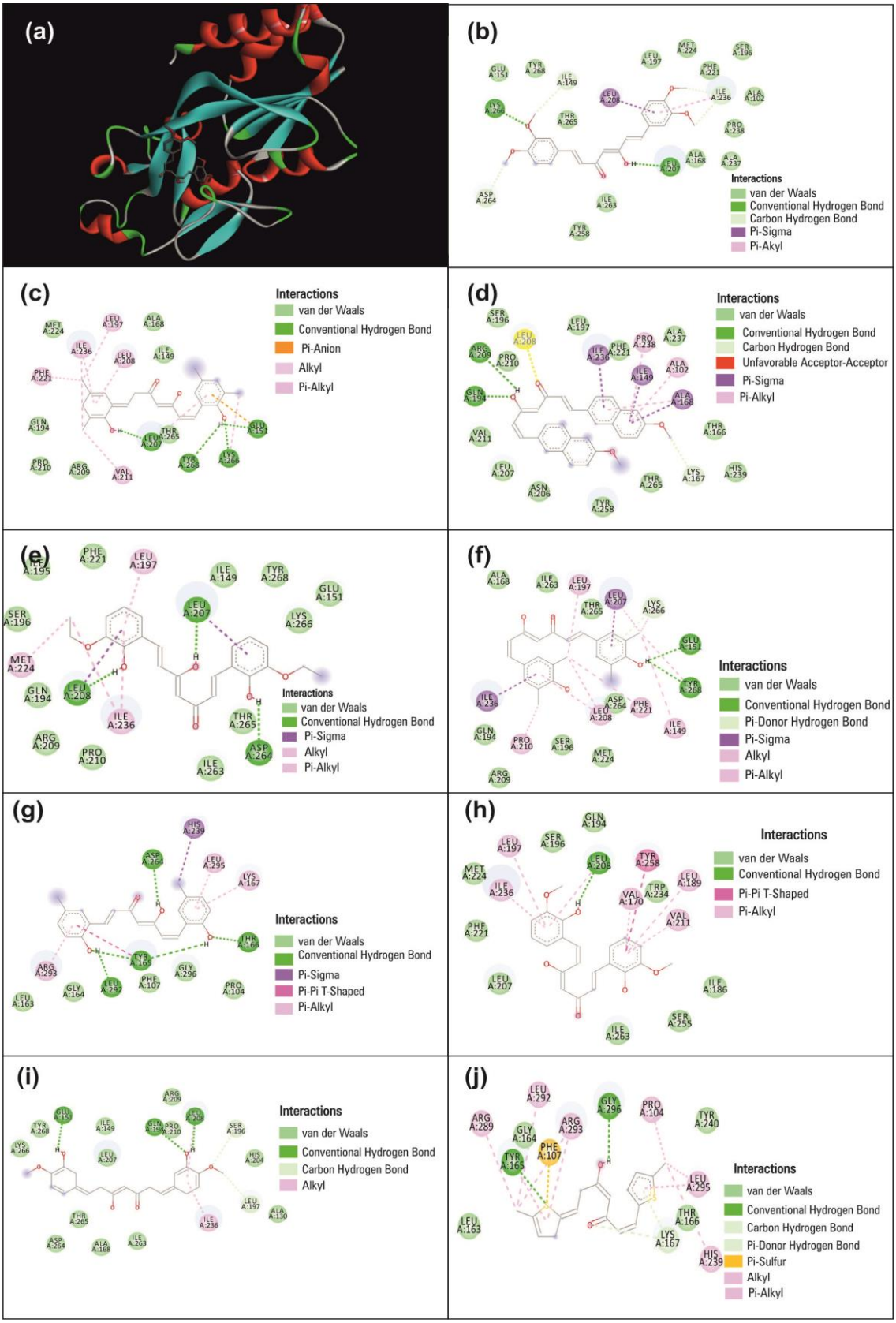

Fig.6.8 4JVD -Curcumin Analogue Complexes (a) 4JVD-NLB Complex(3D) (b) 4JVD-NLB Complex(2D) (c) 4JVD-NLD Complex(2D) (d) 4JVD-NLE Complex(2D) (e) 4JVD-NLF Complex(2D) (f) 4JVD-NLG Complex(2D) (g) 4JVD-NLH Complex(2D) (h) 4JVD-NLI Complex(2D) (i) 4JVD-NLJ Complex(2D) (j) 4JVD-NLK Complex(2D)

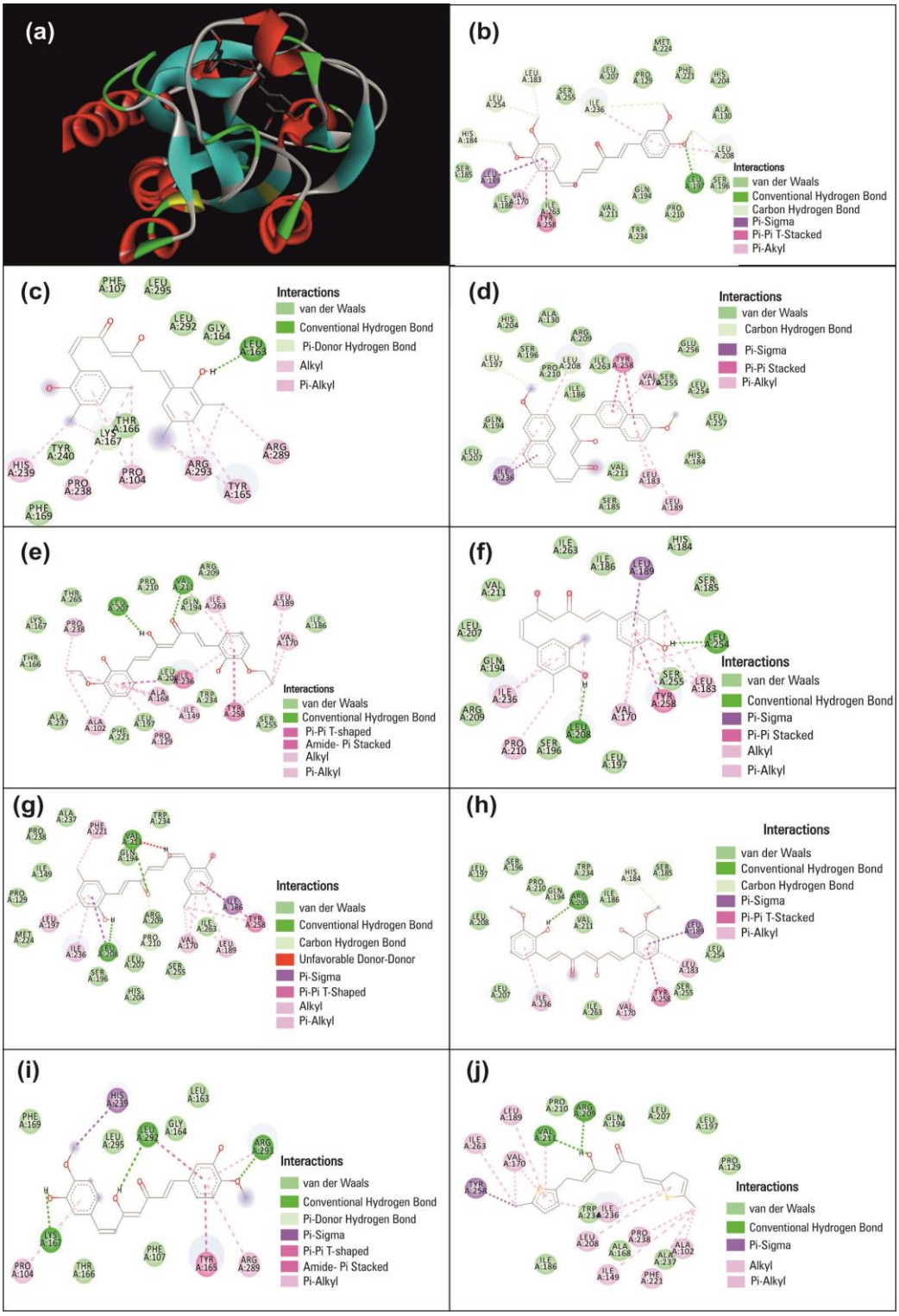

Fig.6.9 6B8A-Curcumin Analogue Complexes (a) 6B8A-NLB Complex(3D) (b) 6B8A-NLB Complex(2D) (c) 6B8A-NLD Complex(2D) (d) 6B8A-NLE Complex(2D) (e) 6B8A-NLF Complex(2D) (f) 6B8A-NLG Complex(2D) (g) 6B8A-NLH Complex(2D) (h) 6B8A-NLI Complex(2D) (i) 6B8A-NLJ Complex(2D) (j) 6B8A-NLK Complex(2D)

The evaluation of ligands concerning their antibacterial effectiveness against Gram-negative bacteria was contingent upon an extensive analysis of docking parameters, alongside their interactions with target proteins and the properties of functional groups. The structural disparities present in bacterial cell walls were imperative in elucidating the differential antibacterial activity observed. Gram-negative bacteria possessed an outer membrane rich in lipopolysaccharides, which functioned as a formidable barrier to hydrophobic and voluminous molecules. Furthermore, this membrane was equipped with efflux pumps that extruded foreign molecules, thereby rendering these bacteria intrinsically more resistant.

NLE (1,7-bis(6-methoxynaphthalen-2-yl)hepta-1,6-diene-3,5-dione) consistently demonstrated the best binding energy (-10.21 kcal/mol) and a low inhibition constant (32.6 nM) for 5O7N, along with high ligand efficiency (-0.31). For 6B8A, it maintained excellent binding energy (-9.63 kcal/mol) and a moderate inhibition constant (187.68 nM). Although its large, hydrophobic methoxy naphthyl groups limited penetration through the gram-negative outer membrane, its superior docking parameters compensated for this limitation.

Gentamycin was a highly effective antibiotic that actively penetrated the outer membrane and targeted the 30S ribosomal subunit, resulting in significant bactericidal activity. Its binding energy (-9.6 kcal/mol for 5O7N and -8.4 kcal/mol for 4JVD) and low inhibition constants (91.5 nM for 5O7N and 690.9 nM for 4JVD) were impressive. Despite its hydrophilic nature, active transport into bacterial cells allowed Gentamycin to rank among the top agents for combating Gram-negative bacteria.

NLH (1,7-bis(5-chloro-2-hydroxyphenyl)hepta-1,6-diene-3,5-dione) exhibited strong binding energy (-7.75 kcal/mol for 1NPB and -9.01 kcal/mol for 4JVD) and low inhibition constants (2.07 nM for 1NPB and 249.5 nM for 4JVD). Its ligand efficiency remained consistently high (-0.31 and -0.36). The presence of hydroxy and chloro groups enhanced its lipophilicity, enabling moderate interaction with the outer membrane, though penetration was more limited compared to Gentamycin.

NLK (1,7-bis(4-chloro-2-hydroxyphenyl)hepta-1,6-diene-3,5-dione) ranked highly due to its strong binding energy (-9.58 kcal/mol for 6B8A) and low inhibition constants (94.85 nM for 6B8A and 7.98 nM for 1NPB). Its ligand efficiency (-0.46) for

6B8A was among the highest observed for the ligands. The methyl thiophene groups contributed to its lipophilicity, enhancing interaction with the bacterial lipid bilayer, though full penetration was hindered by the outer membrane.

NLG(1,7-bis(4-hydroxy-3,5-dimethylphenyl)hepta-1,6-diene-3,5-dione) displayed a balanced profile, with strong binding energies (-8.99 kcal/mol for 5O7N and -9.54 kcal/mol for 6B8A), moderate inhibition constants (258.8 nM for 5O7N and 102.48 nM for 6B8A), and good ligand efficiency (-0.33 and -0.35). The hydroxy and methyl groups provided moderate hydrophobicity, improving interaction with lipid layers while slightly limiting penetration.

NLB (1,7-bis(3,4-dimethoxyphenyl)hepta-1,6-diene-3,5-dione) excelled in 1NPB with an extremely low inhibition constant (18.12 nM), though it exhibited relatively higher binding energy (-6.47 kcal/mol). For gram-negative bacteria overall, its activity was moderate due to the higher energy requirements for effective binding. The methoxy groups contributed to its hydrophobicity, enabling limited interaction with lipid bilayers but insufficient penetration through the outer membrane.

NLF (1,7-bis(3-ethoxy-2-hydroxyphenyl)hepta-1,6-diene-3,5-dione) performed well, exhibiting good binding energy (-8.36 kcal/mol for 5O7N) and moderate inhibition constants (11.31 nM for 1NPB). Its ligand efficiency was moderate (-0.29). The hydroxy and ethoxy groups imparted moderate hydrophobicity, aiding limited penetration through the outer membrane.

NLI (1,7-bis(2-hydroxy-3-methoxyphenyl)hepta-1,6-diene-3,5-dione) was highly effective for 1NPB, exhibiting a low inhibition constant (9.03 nM) and good ligand efficiency (-0.25). However, its performance against other Gram-negative bacteria was less impressive due to higher binding energy (-6.88 kcal/mol for 4JVD). The hydroxy and methoxy groups struck a balance between hydrophilicity and hydrophobicity, slightly improving its activity.

NLJ(1,7-bis(3-hydroxy-4-methoxyphenyl)hepta-1,6-diene-3,5-dione)demonstrated favourable binding energy (-7.18 kcal/mol for 1NPB) and low inhibition constants (5.48 nM for 1NPB and 2.77 nM for 4JVD), with reasonable ligand efficiency (-0.28).

Positional differences in its functional groups marginally affected its interaction with the outer membrane, limiting its overall efficacy.

NLD (1,7-bis(3,5-dichloro-2-hydroxyphenyl)hepta-1,6-diene-3,5-dione) showed a high inhibition constant for 4JVD (794.1 nM) and exhibited higher binding energy (-8.64 kcal/mol for 5O7N). Its limited lipophilicity reduced overall activity. While the hydroxy and chloro groups slightly enhanced lipophilicity, they were insufficient to effectively overcome the outer membrane barrier.

Curcumin, despite demonstrating strong ligand efficiency (-0.34 for 5O7N), exhibited poor binding energy (-5.08 kcal/mol for 4JVD) and higher inhibition constants (189.8 nM for 4JVD). Its hydrophobic properties reduced outer membrane penetration, making it less effective against gram-negative bacteria.

The detailed study of docking parameters and ligand interactions with amino acid residues of target molecules and the structural characteristics of the analogues resulted in the conclusion that NLE was the most promising ligand for antibacterial activity against gram-negative bacteria, followed by NLK and NLB. Gentamycin and curcumin also demonstrate significant potential with strong binding profiles. Additionally, ligands NLG, NLD, NLH, NLI, NLJ, and NLF exhibit strong binding affinities, low inhibition constants, high ligand efficiencies, and specific binding site interactions with amino acid residues, making them promising candidates for antibacterial agents. The selection of ligands should also consider the potential side effects for comprehensive drug development.

Fig.6.10 presented a comprehensive depiction of the interactions between natural curcumin and the specific target molecules of both gram-positive and gram-negative bacteria. Similarly, **Fig.6.11** provided a detailed representation of the interactions between Gentamycin and the target molecules in both gram-positive and gram-negative bacteria.

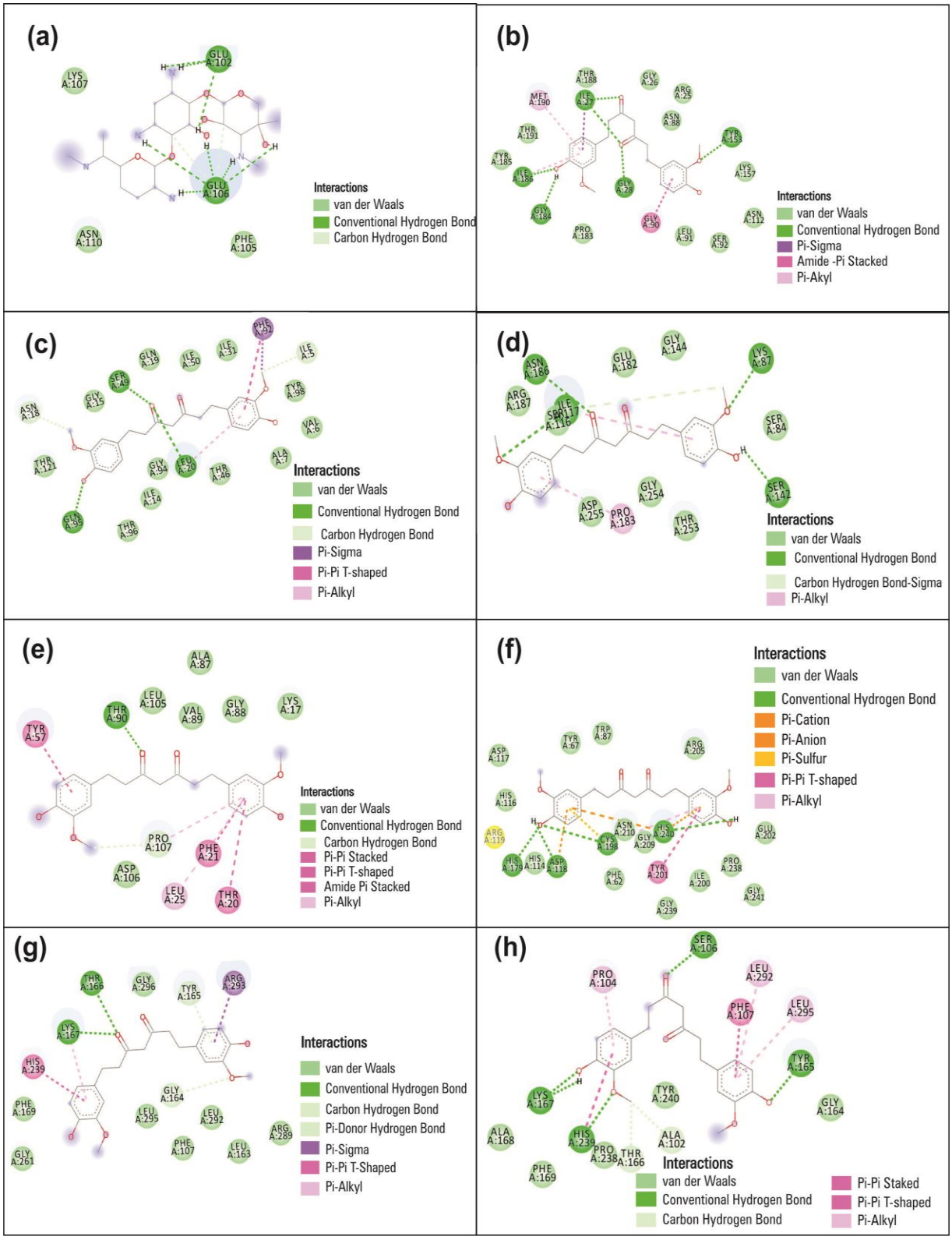

Fig.6.10 Interactions between natural curcumin and the specific target molecules of Gram-positive and Gram-negative bacteria (a) 4H8E - curcumin Complex(2D) (b) 1UZN - curcumin Complex(2D) (c) 2W9S- curcumin Complex(2D) (d) 4Q8I - curcumin Complex(2D) (e) 1NPB - curcumin Complex(2D) (f) 5O7N - curcumin Complex(2D) (g) 4JVD - curcumin Complex(2D) (h) 6B8A- curcumin Complex(2D)

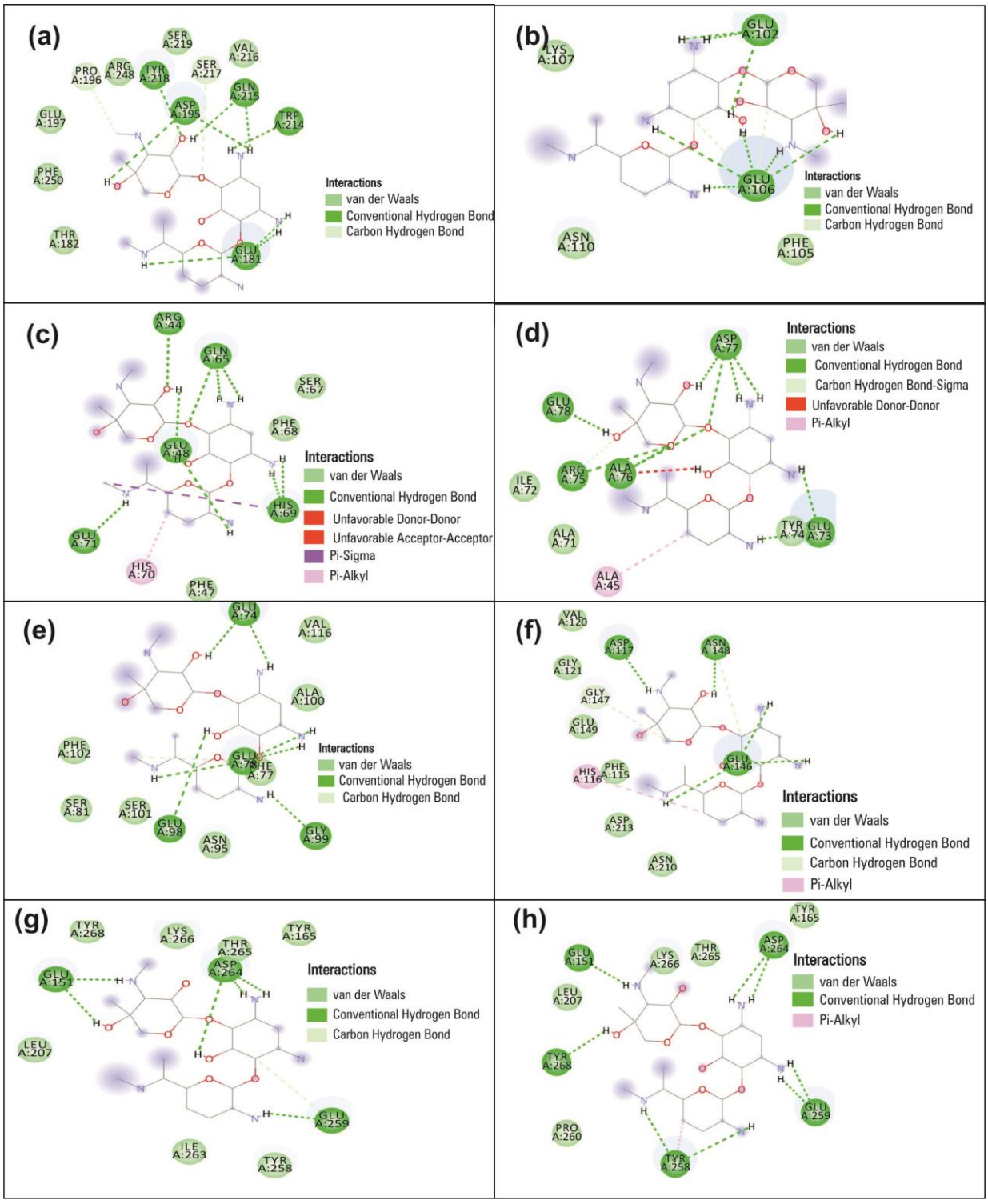

Fig.6.11 Interactions between Gentamycin and the specific target molecules of Gram-positive and Gram-negative bacteria (a) 4H8E -Gentamycin Complex(2D) (b) 1UZN -Gentamycin Complex(2D) (c) 2W9S -Gentamycin Complex(2D) (d) 4Q8I -Gentamycin Complex(2D) (e) 1NPB -Gentamycin Complex(2D) (f) 5O7N -Gentamycin Complex(2D) (g) 4JVD -Gentamycin Complex(2D) (h) 6B8A-Gentamycin Complex(2D)

6.4.1.2. *In vitro* studies

6.4.1.2.1. Antibacterial assay of curcumin analogues

The agar well diffusion method was employed to assess the antibacterial activity of the test samples. The FDA-approved drug Gentamycin was used as the standard, and a comparative study was also conducted using natural Curcumin.

The comparison of ligands revealed varied antibacterial effectiveness across different bacterial strains. NLB showed moderate effectiveness against *Mycobacterium smegmatis* but was generally less effective against other bacteria. NLD demonstrated high effectiveness against *Staphylococcus aureus* and *Mycobacterium smegmatis* but was less effective against gram-negative bacteria. NLE emerged as the most effective ligand across all bacterial strains. NLF was generally less effective compared to other ligands. NLG displayed moderate effectiveness, particularly against *Pseudomonas aeruginosa* and *Klebsiella pneumoniae*. NLH proved more effective against gram-positive bacteria but was less effective against *Pseudomonas aeruginosa*. NLI exhibited generally low antibacterial activity. NLJ showed moderate to low effectiveness across all bacteria. NLK demonstrated high effectiveness only against *Klebsiella pneumoniae*. Curcumin was effective against *Pseudomonas aeruginosa* but showed lower activity against other bacteria. Gentamycin was highly effective against *Staphylococcus aureus* and *Pseudomonas aeruginosa* but showed moderate to low activity against other bacteria.

NLE proved universally effective across all strains, while Gentamycin was highly effective, especially against gram-negative bacteria like *Pseudomonas aeruginosa*. Curcumin showed primary effectiveness against *Pseudomonas aeruginosa*. NLD was strong against gram-positive bacteria but less effective against gram-negative bacteria, and NLK was highly effective against *Klebsiella pneumoniae*. NLI and NLF were generally less effective, making them less ideal for antibacterial applications.

Curcumin was less effective than NLE, NLD, and NLH across the tested bacteria, particularly underperforming against *Staphylococcus aureus*. It also ascertained lower effectiveness than NLE, NLD, NLH, NLB, and NLG against *Mycobacterium smegmatis*. For *Klebsiella pneumoniae*, NLK, NLE, NLG, and NLD demonstrated better results compared to curcumin. However, curcumin performed relatively well against *Pseudomonas aeruginosa*.

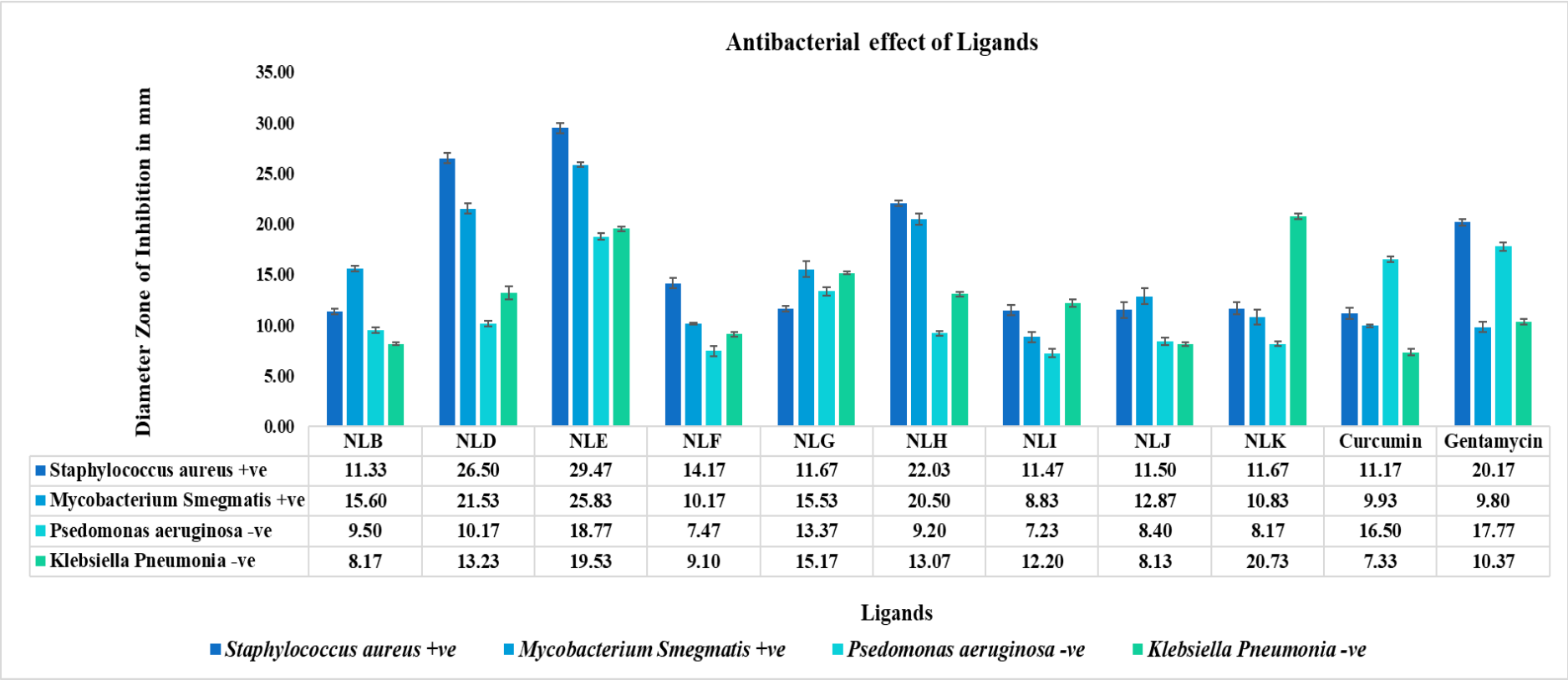

	NLB	NLD	NLE	NLF	NLG	NLH	NLI	NLJ	NLK	Curcumin	Gentamycin
Staphylococcus aureus +ve	11.33	26.50	29.47	14.17	11.67	22.03	11.47	11.50	11.67	11.17	20.17
Mycobacterium Smegmatis +ve	15.60	21.53	25.83	10.17	15.53	20.50	8.83	12.87	10.83	9.93	9.80
Psedomonas aeruginosa -ve	9.50	10.17	18.77	7.47	13.37	9.20	7.23	8.40	8.17	16.50	17.77
Klebsiella Pneumonia -ve	8.17	13.23	19.53	9.10	15.17	13.07	12.20	8.13	20.73	7.33	10.37

Fig.6.12 The antibacterial activity values, presumably inhibition zones in mm, for different ligands against four bacterial strains: *Staphylococcus aureus* (Gram-positive), *Mycobacterium smegmatis* (Gram-positive), *Pseudomonas aeruginosa* (Gram-negative), and *Klebsiella pneumoniae* (Gram-negative). Measured by inhibition zones in millimetres

On the basis of both *in silico* and *in vitro* studies, the synthesized curcumin analogues credited better antibacterial effects against gram-positive bacteria than gram-negative bacteria. By comparing these results, NLE was prioritized for further development due to its broad-spectrum effectiveness. Other ligands, such as NLH, NLK, NLD, NLG, and NLB, might also be considered for specific applications based on their unique effectiveness profiles.

6.4.1.2.2. Antibacterial assay of curcumin analogue metal complexes

6.4.1.2.2.1. Cu (II) metal complexes

The agar well diffusion technique was implemented to evaluate the antibacterial efficacy of the Cu(II) complexes derived from the synthesised analogues of curcumin. The standard agent employed was Gentamycin, which has been approved by the FDA, and an analysis comparing its effectiveness was carried out alongside natural Curcumin.

The graph provided a comprehensive analysis of the antibacterial activity of various copper (II) complexes (Cu-ligand) and two reference compounds, curcumin and gentamycin, against four bacterial strains: *Staphylococcus aureus* (positive), *Mycobacterium smegmatis* (positive), *Pseudomonas aeruginosa* (negative), and *Klebsiella pneumoniae* (negative). The values represented the inhibition zones in millimetres, indicating the effectiveness of each sample against these bacterial strains, with higher values suggesting greater antibacterial activity.

For *Staphylococcus aureus*, the highest activity was observed with $Cu(NLE)_2$, showing a zone of inhibition of 30.57 mm, followed by $Cu(NLD)_2$ at 27.30 mm, and $Cu(NLH)_2$ at 23.43 mm. Curcumin displayed the least activity with an inhibition zone of 11.17 mm. Against *Mycobacterium smegmatis*, $Cu(NLE)_2$ again brought to light the highest activity at 29.30 mm, with $Cu(NLD)_2$ and $Cu(NLH)_2$ following at 27.47 mm and 20.50 mm, respectively. Curcumin showed the least activity with an inhibition zone of 10.97 mm.

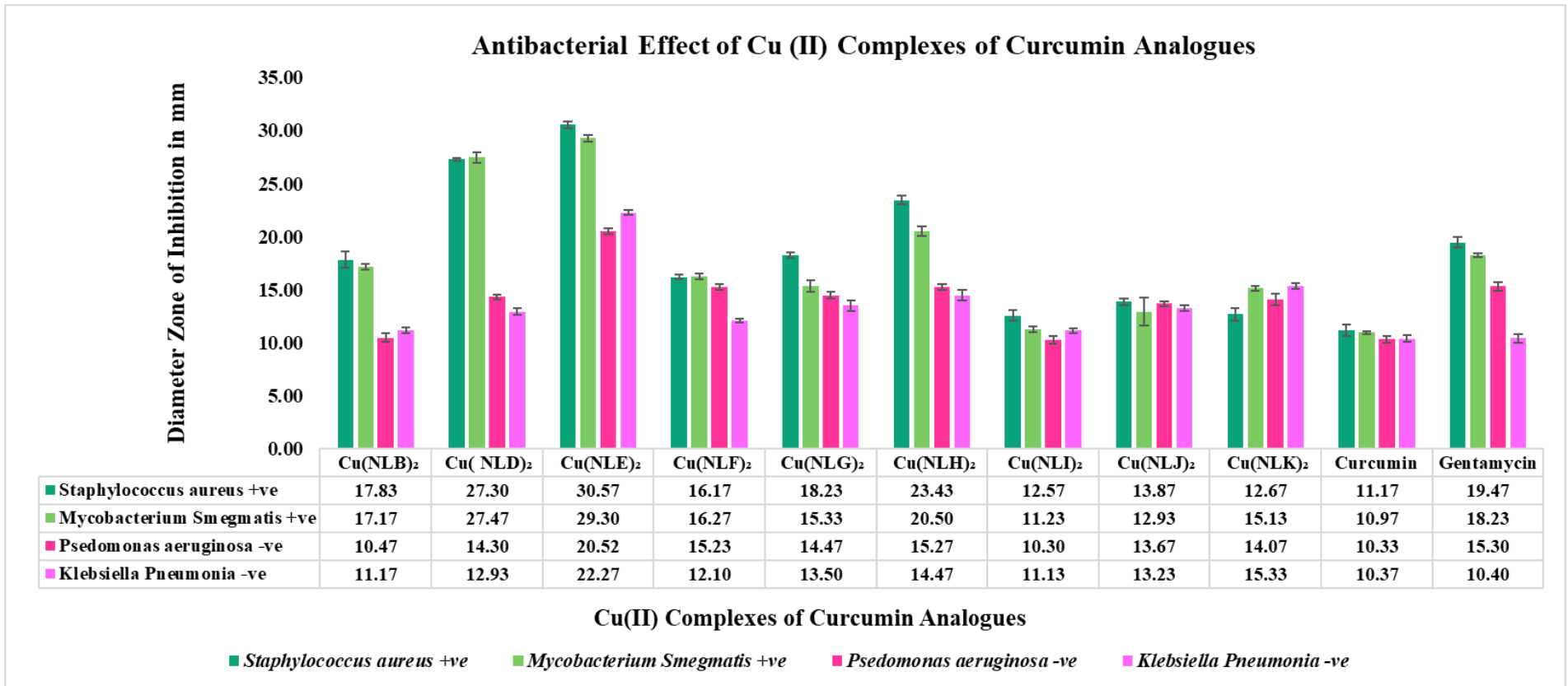

	Cu(NLB)₂	Cu(NLD)₂	Cu(NLE)₂	Cu(NLF)₂	Cu(NLG)₂	Cu(NLH)₂	Cu(NLI)₂	Cu(NLJ)₂	Cu(NLK)₂	Curcumin	Gentamycin
Staphylococcus aureus +ve	17.83	27.30	30.57	16.17	18.23	23.43	12.57	13.87	12.67	11.17	19.47
Mycobacterium Smegmatis +ve	17.17	27.47	29.30	16.27	15.33	20.50	11.23	12.93	15.13	10.97	18.23
Psedomonas aeruginosa -ve	10.47	14.30	20.52	15.23	14.47	15.27	10.30	13.67	14.07	10.33	15.30
Klebsiella Pneumonia -ve	11.17	12.93	22.27	12.10	13.50	14.47	11.13	13.23	15.33	10.37	10.40

Fig.6.13 The graph shows the antibacterial activity of copper (II) complexes, Curcumin, and Gentamycin against four bacterial strains: *Staphylococcus aureus* (Gram-positive), *Mycobacterium smegmatis* (Gram-positive), *Pseudomonas aeruginosa* (Gram-negative), and *Klebsiella pneumoniae* (Gram-negative). Measured by inhibition zones in millimetres.

In the case of *Pseudomonas aeruginosa*, $Cu(NLE)_2$ presented the highest activity, with a zone of inhibition of 20.52 mm, followed by $Cu(NLF)_2$ at 15.23 mm and gentamycin at 15.30 mm. Curcumin once more witnessed the least activity at 10.33 mm. For *Klebsiella pneumoniae*, $Cu(NLE)_2$ demonstrated the highest activity with a zone of inhibition of 22.27 mm, followed by $Cu(NLK)_2$ at 15.33 mm and $Cu(NLH)_2$ at 14.47 mm. Curcumin and gentamycin displayed similar low activities, with 10.37 mm and 10.40 mm inhibition zones, respectively.

In the sight of these observations, $Cu(NLE)_2$ emerged as the most effective antibacterial agent among the tested samples against all four bacterial strains. This finding aligned with the preference for NLE based on binding energy and other docking parameters. $Cu(NLD)_2$ and $Cu(NLH)_2$ also showed significant activity against most bacterial strains, making them strong candidates for antibacterial agents. In contrast, curcumin consistently was found to exercise the least activity against all strains, suggesting it was the least effective among the samples tested. Gentamycin demonstrated moderate activity but was less effective than the top-performing copper(II) complexes, particularly against *Klebsiella pneumoniae* and *Staphylococcus aureus*. These results supported further investigation and potential development of copper(II) complexes as antibacterial agents.

6.4.1.2.2.2. Zn (II) metal complexes

The agar well diffusion technique was utilized to evaluate the antibacterial efficacy of Zn(II) complexes derived from synthesized curcumin analogues. The FDA-approved agent Gentamycin was used as the standard, and its effectiveness was compared with that of natural Curcumin.

The graph analyzed the antibacterial activity of various zinc(II) complexes and two reference compounds, curcumin and gentamycin, against four bacterial strains: *Staphylococcus aureus* (Gram-positive), *Mycobacterium smegmatis* (Gram-positive), *Pseudomonas aeruginosa* (Gram-negative), and *Klebsiella pneumoniae* (Gram-negative). The values represented the inhibition zones in millimetres, indicating the effectiveness of each sample against the bacterial strains. Higher values pointed out greater antibacterial activity.

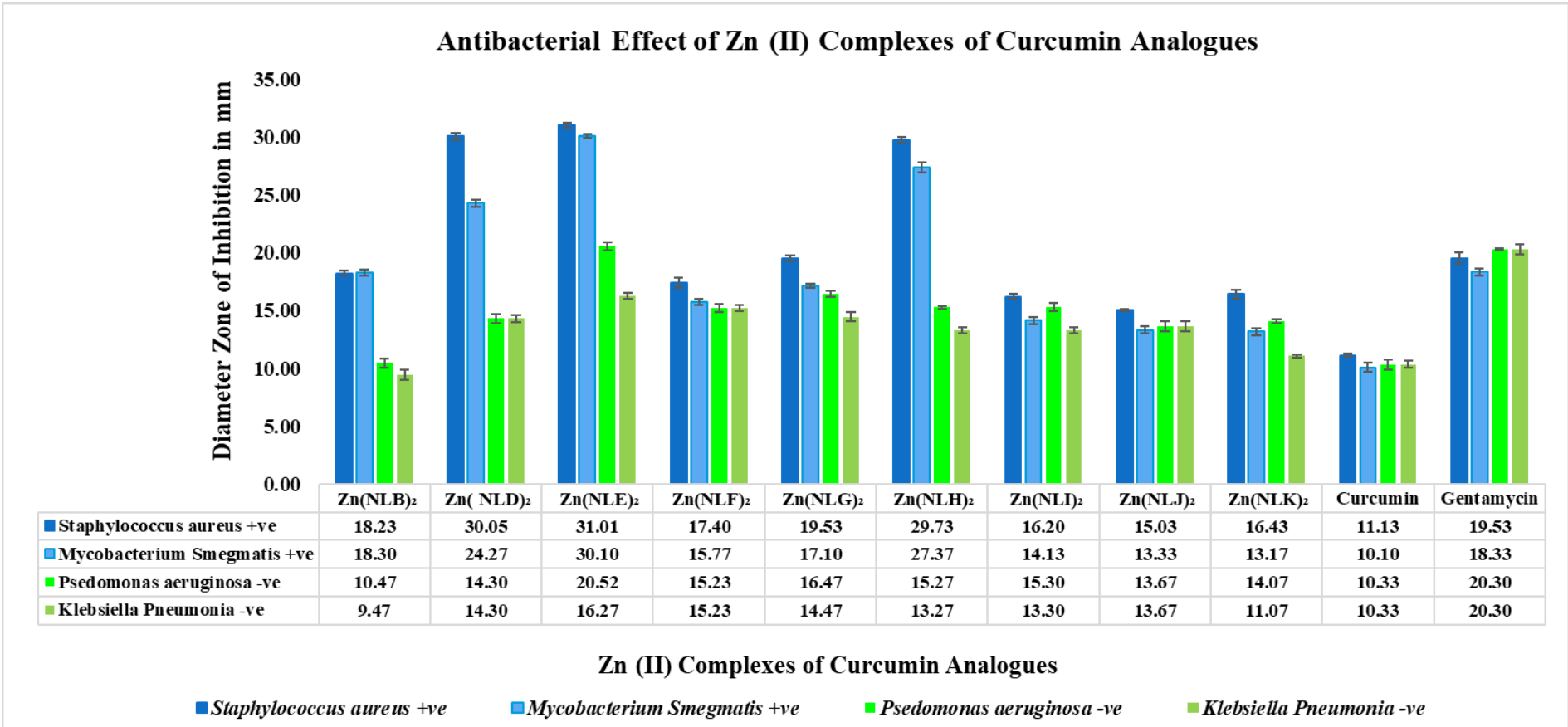

Fig.6.14 The antibacterial activity of Zinc (II) complexes, Curcumin, and Gentamycin against four bacterial strains: *Staphylococcus aureus* (Gram-positive), *Mycobacterium smegmatis* (Gram-positive), *Pseudomonas aeruginosa* (Gram-negative), and *Klebsiella pneumoniae* (Gram-negative). Measured by inhibition zones in millimetres.

For *Staphylococcus aureus*, the highest activity was observed with $Zn(NLE)_2$, showing a zone of inhibition of 31.01 mm, followed by $Zn(NLD)_2$ at 30.05 mm and $Zn(NLH)_2$ at 29.73 mm. Curcumin displayed the least activity, with an inhibition zone of 11.13 mm. Against *Mycobacterium smegmatis*, $Zn(NLE)_2$ again exhibited the highest activity at 30.10 mm, with $Zn(NLH)_2$ and $Zn(NLD)_2$ following at 27.37 mm and 24.27 mm, respectively, while curcumin showed the least activity at 10.10 mm.

For *Pseudomonas aeruginosa*, $Zn(NLE)_2$ demonstrated the highest activity with a zone of inhibition of 20.52 mm, followed closely by Gentamycin at 20.30 mm, and $Zn(NLG)_2$ at 16.47 mm. Curcumin showed the least activity with a zone of 10.33 mm. In the case of *Klebsiella pneumoniae*, gentamycin displayed the highest activity, with a zone of inhibition of 20.30 mm, followed by $Zn(NLE)_2$ at 16.27 mm and $Zn(NLF)_2$ at 15.23 mm, while $Zn(NLB)_2$ recorded the least activity at 9.47 mm.

These findings established that $Zn(NLE)_2$ emerged as the most potent antibacterial agent among the zinc complexes tested, showing significant efficacy against *Staphylococcus aureus*, *Mycobacterium smegmatis*, and *Pseudomonas aeruginosa*. Its performance synced with the preference for NLE based on binding energy and other docking parameters. $Zn(NLH)_2$ and $Zn(NLD)_2$ also demonstrated robust antibacterial efficacy, suggesting their potential as antibacterial agents. In contrast, curcumin consistently exhibited the lowest activity across all strains, indicating its comparatively lower effectiveness among the samples tested. Gentamycin showed strong antibacterial activity, particularly against *Pseudomonas aeruginosa* and *Klebsiella pneumoniae*, though it proved to be less potent than the top-performing zinc complexes against *Staphylococcus aureus* and *Mycobacterium smegmatis*.

Succinctly, zinc(II) complexes, particularly $Zn(NLE)_2$, exhibited promising antibacterial properties, outperforming both standard antibiotics and natural curcumin in this study. Gentamycin remained a strong antibacterial agent, particularly effective against *Klebsiella pneumoniae* and *Pseudomonas aeruginosa*. These results supported and powered the way for investigation and potential development of zinc(II) complexes as antibacterial agents.

Comparative analysis of antibacterial effects

The antibacterial effects of various ligands, copper(II) complexes, and zinc(II) complexes were evaluated against *Staphylococcus aureus*, *Mycobacterium smegmatis*, *Pseudomonas aeruginosa*, and *Klebsiella pneumoniae.* Among the ligands, NLE emerged as the most effective across all bacterial strains, while NLD was highly effective against gram-positive bacteria but less so against gram-negative bacteria. NLB, NLH, and NLG showed moderate effectiveness, with NLH being more potent against gram-positive bacteria. Conversely, NLI, NLJ and Curcumin exhibited poor antibacterial activity. Gentamycin proved highly effective against *Staphylococcus aureus* and *Pseudomonas aeruginosa,* though it showed moderate to low activity against other bacteria.

In terms of copper(II) complexes, $Cu(NLE)_2$ demonstrated the highest antibacterial activity across all strains, significantly outperforming both Curcumin and Gentamycin. $Cu(NLD)_2$ and $Cu(NLH)_2$ also showed notable activity, particularly against gram-positive bacteria. Other copper complexes, such as $Cu(NLF)_2$ and $Cu(NLK)_2$, displayed moderate activity against specific bacteria like *Pseudomonas aeruginosa* and *Klebsiella pneumoniae*, respectively. The zinc(II) complexes mirrored these trends, with $Zn(NLE)_2$ showing the highest effectiveness across most strains. $Zn(NLD)_2$ and $Zn(NLH)_2$ also performed well, particularly against gram-positive bacteria, while $Zn(NLG)_2$ and $Zn(NLF)_2$ demonstrated moderate activity against *Pseudomonas aeruginosa* and *Klebsiella pneumoniae*.

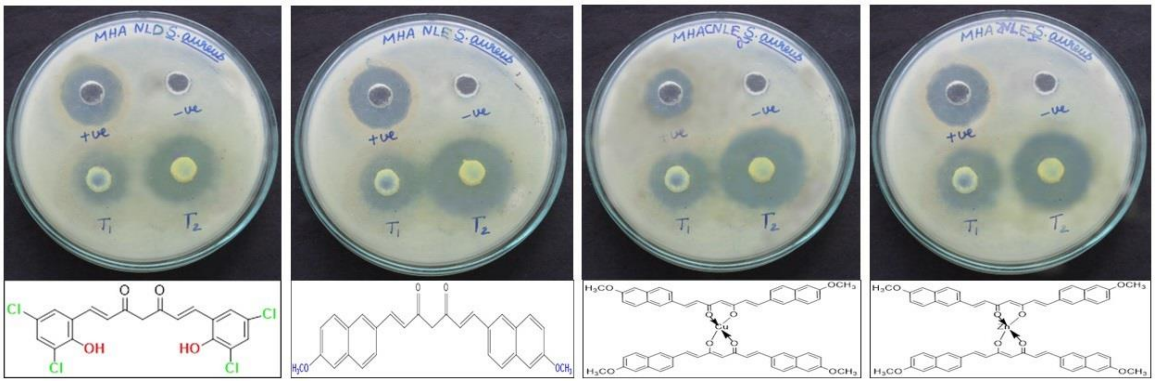

Fig.6.15 The best results of antibacterial assay and the structures of corresponding compounds. (a) antibacterial activity of NLD with its structure (b) antibacterial activity of NLE with its structure (c) antibacterial activity of $Cu(NLE)_2$ with its structure (d) antibacterial activity of $Zn(NLE)_2$ with its structure. Inhibition zones in mm. Positive control is gentamycin. T_1 and T_2 represent 40 and 80 µL of sample from 10mg/ml stock.

The observed results were attributed to several factors related to the chemical structures and properties of the ligands and their metal complexes.

The broad-spectrum effectiveness of NLE across all bacterial strains suggested that its chemical structure was particularly well-suited for binding to bacterial targets, likely enhancing its ability to disrupt essential bacterial processes. When NLE formed complexes with copper(II) or zinc(II), these metal ions appeared to further enhance antibacterial activity by stabilizing the ligand, improving its solubility, and potentially facilitating interactions with bacterial enzymes or cell walls.

The higher effectiveness of $Cu(NLE)_2$ and $Zn(NLE)_2$ compared to curcumin and gentamycin could be explained by the properties of the metal ions themselves. Copper and zinc were known to have antibacterial properties, as they interfere with bacterial cell membranes, generate reactive oxygen species (ROS), and inhibit essential bacterial enzymes. These effects, combined with the already potent NLE ligand, resulted in a synergistic effect that greatly enhanced antibacterial activity.

The differential effectiveness of NLD and NLH, particularly against Gram-positive bacteria, might have been owing to differences in cell wall structure between Gram-positive and Gram-negative bacteria. Gram-positive bacteria have been observed to have a thicker peptidoglycan layer, which might interact more effectively with certain ligands and their complexes. In contrast, the outer membrane of Gram-negative bacteria likely acted as a barrier, limiting the effectiveness of some compounds.

The relatively lower activity of curcumin, NLI and NLJ indicated that their chemical structures were less effective at penetrating bacterial cells or disrupting their functions. The effectiveness of curcumin against *Pseudomonas aeruginosa* but not other strains suggested specific interactions with this bacterium that did not extend to others. The moderate to high effectiveness of Gentamycin against specific strains reflected its known mechanism of inhibiting bacterial protein synthesis, although it lacked the additional enhancements observed with metal complexes.

The combination of structural suitability, metal ion properties, and specific interactions with bacterial cell structures contributed to the pre-noticed antibacterial effectiveness of the ligands and their complexes.

6.4.2. Antifungal effect of curcumin analogues and their metal complexes

6.4.2.1. *In silico* studies

Two key proteins with germline mutations that influence susceptibility to fungal infections, particularly from pathogens like *Candida albicans*, were selected as molecular targets from the RCSB database. These proteins were 4LEB(TG9) and 1IYL(TG10).

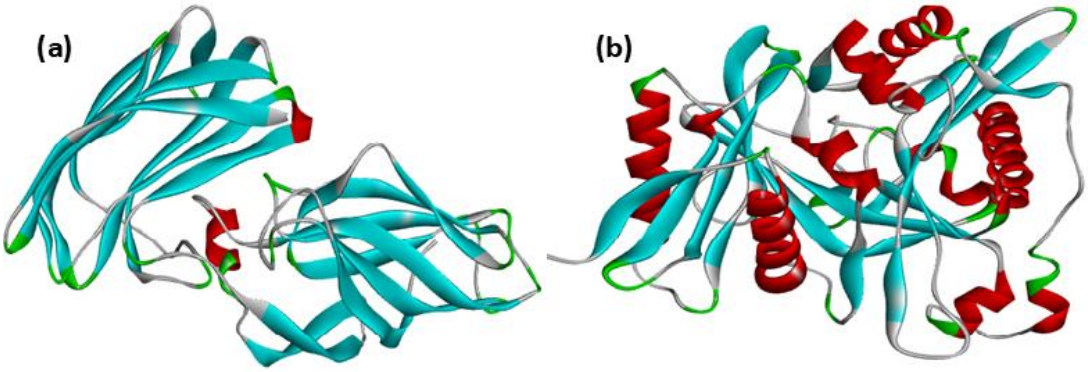

Fig.6.1 Proteins with germline mutations affect fungal infections. (a)4LEB (b)1IYL

6.4.2.1.1. Computational screening of designed molecules

The computational screening of the nine synthesized ligands has already been performed and is presented in **Table 2.2** and **Table 2.3**.

6.4.2.1.2. Molecular docking studies of antifungal effect of curcumin analogues

The specific targets of the fungus Candida albicans, 4LEB and 1IYL, were used for the molecular docking studies. The predicted binding potentials of the nine synthesized curcumin analogues and the reference compounds (curcumin and fluconazole) to the prioritized fungal targets are systemised in **Table 6.8**.

Table 6.8. The predicted binding potentials of the nine synthesised curcumin analogues and reference compounds (curcumin and Fluconazole) to the prioritized targets of *Candida Albicans*

Active Target	**4LEB**											**1IYL**										
Ligands	**Curcumin**	**Fluconazole**	**NLB**	**NLD**	**NLE**	**NLF**	**NLG**	**NLH**	**NLI**	**NLJ**	**NLK**	**Curcumin**	**Fluconazole**	**NLB**	**NLD**	**NLE**	**NLF**	**NLG**	**NLH**	**NLI**	**NLJ**	**NLK**
Active Site and Run	**7**	**8**	**4**	**8**	**8**	**3**	**8**	**5**	**4**	**2**	**8**	**8**	**5**	**10**	**5**	**8**	**6**	**5**	**6**	**5**	**5**	**1**
BE(kcal/mol)	**-6.52**	**-5.28**	**-7.29**	**-7.95**	**-9.85**	**-6.98**	**-8.95**	**-7.89**	**-7.01**	**-8.48**	**-8.08**	**-8.45**	**-6.21**	**-8.09**	**-11.79**	**-11.51**	**-8.94**	**-9.29**	**-9.94**	**-7.95**	**-8.9**	**-8.75**
Ligand efficiency	**-0.24**	**-0.24**	**-0.25**	**-0.29**	**-0.3**	**-0.24**	**-0.33**	**-0.32**	**-0.26**	**-0.31**	**-0.38**	**-0.31**	**-0.28**	**-0.28**	**-0.44**	**-0.35**	**-0.31**	**-0.34**	**-0.4**	**-0.29**	**-0.33**	**-0.42**
Inhib constant (nM)	**16.64**	**134.7**	**4.51**	**1.49**	**60.27**	**7.67**	**277.33**	**1.63**	**7.28**	**603.9**	**1.19**	**635.01**	**27.87**	**1.18**	**2.29**	**3.69**	**279.4**	**155.23**	**51.77**	**1.49**	**298.1**	**384.2**
Intermolar energy	**-10.1**	**-7.07**	**-10.28**	**-10.33**	**-12.24**	**-10.56**	**-11.33**	**-10.28**	**-9.99**	**-11.47**	**-9.87**	**-12.03**	**-8.0**	**-11.07**	**-14.17**	**-13.89**	**-12.52**	**-11.68**	**-12.33**	**-10.93**	**-11.89**	**-10.54**

vdw hb disolv energy	**-9.86**	**-7.03**	**-10.07**	**-9.95**	**-11.86**	**-10.42**	**-10.92**	**-9.96**	**-9.83**	**-10.99**	**-9.64**	**-11.7**	**-7.88**	**-10.9**	**-14.12**	**-13.77**	**-12.3**	**-11.42**	**-12.04**	**-10.84**	**-11.5**	**-10.52**
Electrostatic energy	**-0.23**	**-0.04**	**-0.2**	**-0.39**	**-0.38**	**-0.14**	**-0.74**	**-0.32**	**-0.16**	**-0.47**	**-0.23**	**-0.33**	**-0.13**	**-0.17**	**-0.05**	**-0.12**	**-0.22**	**-0.26**	**-0.28**	**-0.09**	**-0.38**	**-0.02**
Total internal	**-1.53**	**-1.81**	**-1.93**	**-0.92**	**-1.04**	**-2.8**	**2.39**	**-1.32**	**-2.89**	**-2.39**	**-1.19**	**-2.04**	**-1.6**	**-1.94**	**-0.14**	**-1.33**	**-2.35**	**-0.62**	**-0.71**	**-2.72**	**-2.64**	**-0.73**
Torsional energy	**3.58**	**1.79**	**2.98**	**2.39**	**2.39**	**3.58**	**-0.74**	**2.39**	**2.98**	**2.98**	**1.79**	**3.58**	**1.79**	**2.98**	**2.39**	**2.39**	**3.58**	**2.39**	**2.39**	**2.98**	**2.98**	**1.79**
Unbound energy	**-1.53**	**-1.81**	**-1.93**	**-0.92**	**-1.04**	**-2.8**	**2.39**	**-1.32**	**-2.89**	**-2.39**	**-1.19**	**-2.04**	**-1.6**	**-1.94**	**-0.14**	**-1.33**	**-2.35**	**-0.62**	**-0.71**	**-2.72**	**-2.64**	**-0.73**
clRMS	**0**	**0**	**0**	**0**	**0**	**0**	**0**	**0**	**0**	**0**	**0**	**0**	**0**	**0**	**0**	**0**	**0**	**0**	**0**	**0**	**0**	**0**
refRMS	**13.71**	**22.44**	**15.88**	**14.81**	**11.12**	**17.07**	**16.44**	**15.61**	**23.12**	**16.96**	**16.63**	**47.71**	**66.22**	**49.44**	**47.56**	**49.86**	**64.75**	**51.05**	**54.88**	**59.17**	**48.31**	**46.79**

Table 6.8 compared the docking results of various ligands against two active targets of *Candida albicans*, 4LEB and 1IYL, including Curcumin, Fluconazole, and nine curcumin analogues – NLB, NLD, NLE, NLF, NLG, NLH, NLI, NLJ and NLK. The parameters analyzed were binding energy (BE), ligand efficiency, inhibition constant (Ki), intermolecular energy, van der Waals (vdW) hydrogen bond (hb) desolvation energy, electrostatic energy, total internal energy, torsional energy, unbound energy, clRMS, and refRMS.

Lower BE values indicated stronger binding affinity, making ligands with lower BE values preferable. Similarly, lower Ki values suggested better inhibitory activity. Ligand efficiency, which balanced binding affinity and molecular size, was also a factor, with higher efficiency indicating better performance. Although other energies, such as intermolecular energy, vdW, hb, desolvation energy, and electrostatic energy were considered for a comprehensive analysis, the primary focus remained on BE and Ki.

A detailed portrayal of the interactions of each ligand with the corresponding target molecules of *Candida albicans* through various amino acid residues was presented in **Fig.6.17 and 6.18**. Similarly, the interactions of natural curcumin and Fluconazole with the specific target molecules of *Candida albicans* are shown in **Fig.6.19**.

The compounds engaged in diverse interactions with the target protein, specifically Van der Waals interactions. Conventional hydrogen bonds exhibited strong, accurate binding. The existence of a broad range of interaction categories—including Pi-Sigma, Pi-Alkyl, Pi-lone pair, Pi-Pi stacked, Alkyl, Pi-Anion, Pi-Pi T-shaped, unfavourable bump, Pi-Cation, Pi-Carbon, Pi-Sulfur, Attractive Charge, Amide-Pi stacked, Sulfur-X, and Pi-Donor interactions—played a role in the intricacy and strength of the binding. The particular amino acid residues participating in these interactions emphasized critical points of contact and potential regions for further adjustments to improve binding affinity and specificity. This thorough interaction profile emphasized the therapeutic promise of each compound, necessitating additional investigation and enhancement.

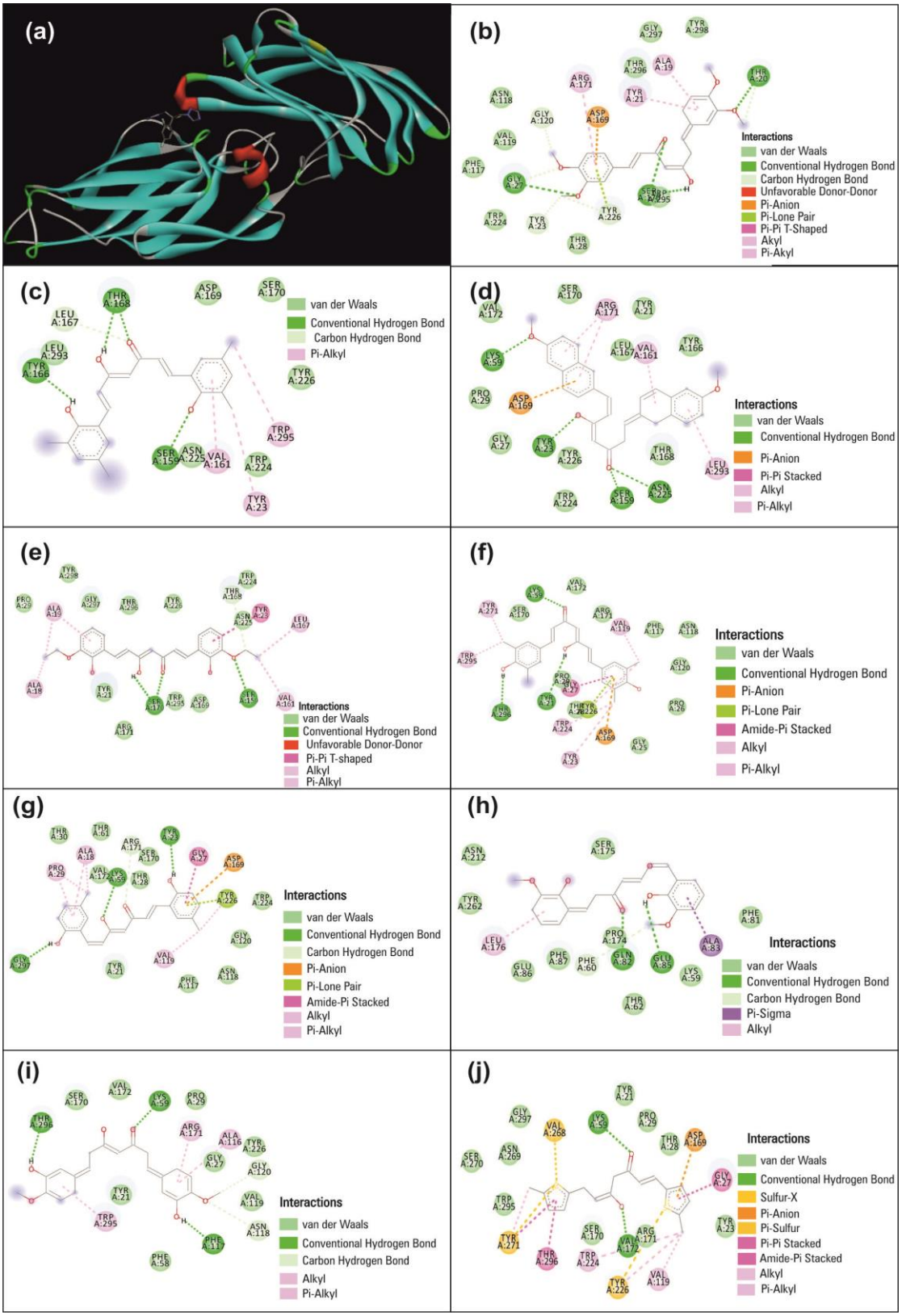

Fig.6.17 4LEB-Curcumin Analogue Complexes (a) 4LEB-NLB Complex(3D) (b) 4LEB-NLB Complex(2D) (c) 4LEB-NLD Complex(2D) (d) 4LEB-NLE Complex(2D) (e) 4LEB-NLF Complex(2D) (f) 4LEB-NLG Complex(2D) (g) 4LEB-NLH Complex(2D) (h) 4LEB-NLIComplex(2D) (i) 4LEB-NLJ Complex(2D) (j) 4LEB-NLK Complex(2D)

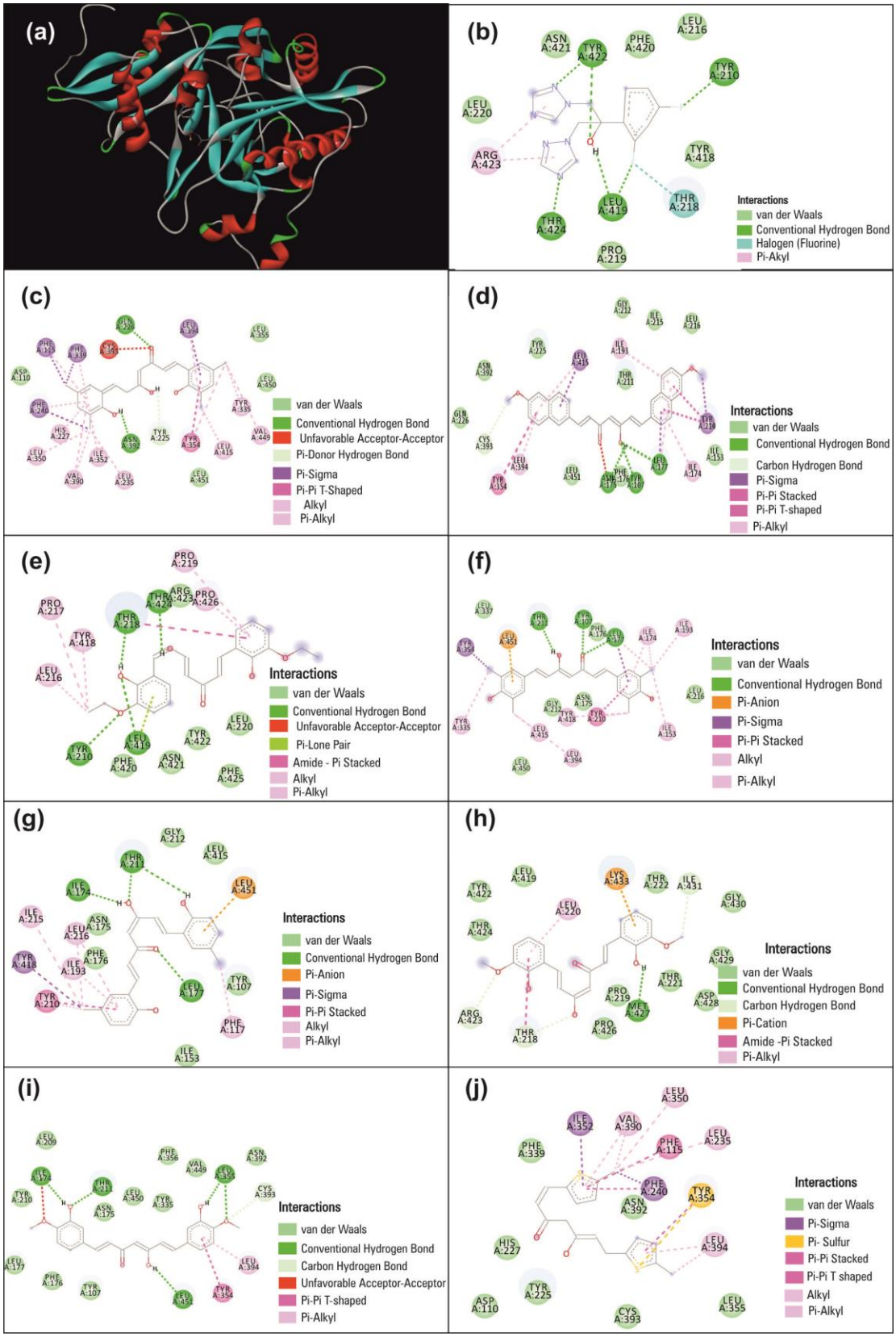

Fig.6.18 1IYL-Curcumin Analogue Complexes (a) 1IYL-NLB Complex(3D) (b) 1IYL-NLB Complex(2D) (c) 1IYL-NLD Complex(2D) (d) 1IYL-NLE Complex(2D) (e) 1IYL-NLF Complex(2D) (f)1IYL-NLG Complex(2D) (g) 1IYL-NLH Complex(2D) (h) 1IYL-NLI Complex(2D) (i) 1IYL-NLJ Complex(2D) (j) 1IYL-NLK Complex

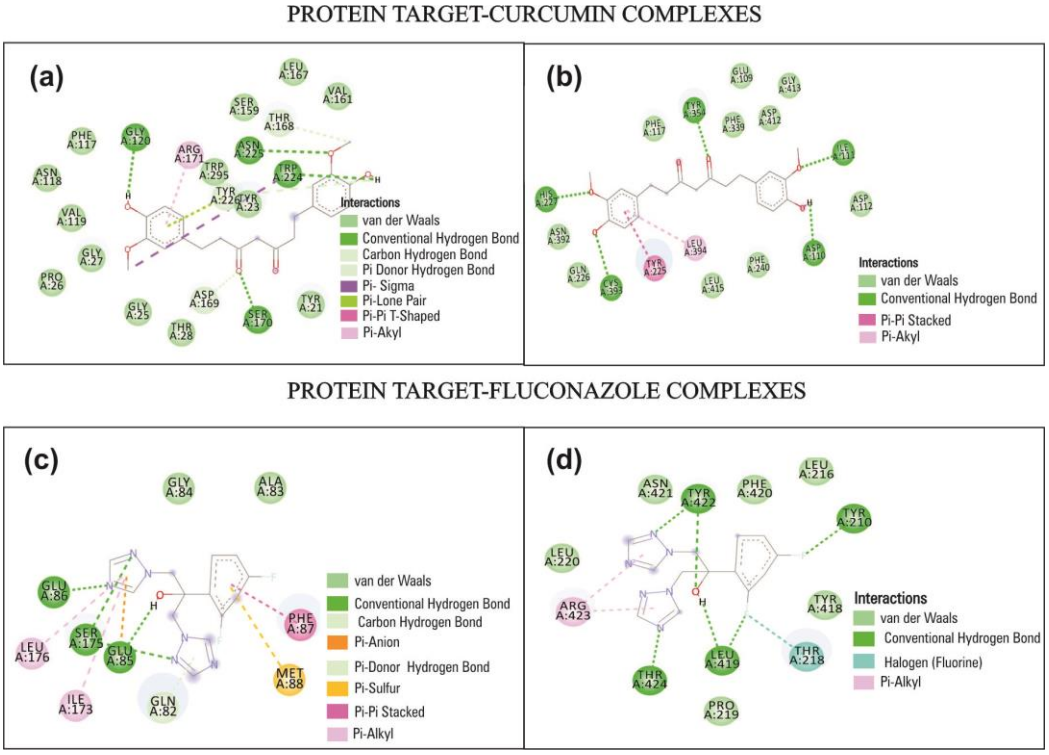

Fig.6.19 The interactions of natural curcumin and fluconazole with the specific target molecules of Candida albicans.

NLE (1,7-bis(6-methoxynaphthalen-2-yl)hepta-1,6-diene-3,5-dione) was identified as the top performer due to its lowest binding energy (-9.85 kcal/mol for 4LEB and -11.51 kcal/mol for 1IYL), high ligand efficiency (-0.3 for 4LEB and -0.44 for 1IYL) and strong inhibition constant values. Its unique structural features, including methoxy naphthalene rings, significantly enhanced π-π stacking, hydrophobic interactions, and lipophilicity, which contributed to its superior binding affinity.

NLD (1,7-bis(3,5-dichloro-2-hydroxy phenyl)hepta-1,6-diene-3,5-dione)excelled with exceptional binding energy (-11.79 kcal/mol for 1IYL) and inhibition constant (2.29 nM for 1IYL). Its hydroxyl groups facilitated efficient hydrogen bonding, while chlorine atoms provided strong electron-withdrawing effects. These synergistic electronic and steric effects enhanced its binding affinity for both targets, making it a close contender to NLE.

NLH(1,7-bis(5-chloro-2-hydroxyphenyl)hepta-1,6-diene-3,5-dione) demonstrated strong binding energy(-7.89 kcal/mol,-9.94 kcal/mol) and inhibition constant values(1.63

nM,51.77 nM) for both targets. Its hydroxyl and chlorine groups contributed to notable interactions, although their positioning was less optimal than in NLD. This slight limitation placed NLH below NLD in the priority order.

NLK (1,7-bis (5-methylthiophen-2-yl) hepta-1,6-diene-3,5-dione) was notable for its thiophene rings, which provided excellent π-π stacking and hydrophobic interactions. It showed strong performance for 4LEB, with a BE of -8.08 kcal/mol and an inhibition constant of 1.19 nM. However, its lack of hydroxyl groups reduced hydrogen bonding capacity, making it less effective than NLD and NLH.

NLG(1,7-bis (4-hydroxy-3,5-dimethylphenyl)hepta-1,6-diene-3,5-dione) exhibited moderate binding energy (-8.95 kcal/mol for 4LEB and -9.26 kcal/mol for 1IYL) and sufficient inhibition constant values. Its methyl and hydroxyl groups added to its binding potential, but the absence of halogens limited its potency compared to higher-ranked compounds.

NLJ(1,7-bis (3-hydroxy-4-methoxyphenyl) hepta-1,6-diene-3,5-dione) delivered competitive binding energy (-8.48 kcal/mol for 4LEB and -8.9 kcal/mol for 1IYL) and reasonable inhibition constants. The hydroxyl and methoxy groups supported its moderate efficiency; however, their suboptimal positioning prevented it from achieving higher ranks.

NLB(1,7-bis(3-hydroxy-4-methoxyphenyl) hepta-1,6-diene-3,5-dione) performed well in hydrophobic interactions due to its dimethoxy groups but lacked hydroxyl groups, resulting in weaker binding compared to other analogues. Its lower binding energy(-7.29 kcal/mol for 4LEB and -8.09 kcal/mol for 1IYL) and reduced hydrogen bonding potential placed it further down the list.

NLF(1,7-bis(3-ethoxy-2-hydroxyphenyl) hepta-1,6-diene-3,5-dione) demonstrated weaker binding energy (-6.98 kcal/mol for 4LEB and -8.94 kcal/mol for 1IYL) and higher inhibition constants(7.67nM for 4LEB and 279.4nMfor 1IYL) than top-ranked compounds. The bulky ethoxy groups diminished interaction efficiency, reducing its overall effectiveness.

NLI(1,7-bis (2-hydroxy-3-methoxyphenyl) hepta-1,6-diene-3,5-dione) showed suboptimal binding efficiency (-7.89kcal/mol for 4LEB and -7.95kcal/mol for 1IYL) compared to NLJ due to the less effective positioning of its hydroxyl and methoxy groups. This structural limitation impacted its performance, relegating it to a lower rank.

Curcumin served as a reference baseline, showing moderate binding energy(-6.52kcal/mol for 4LEB and -8.45kcal/mol for 1IYL) and inhibition constant values. Its lack of optimized substitutions limited its interactions with the targets, making it less effective than the curcumin analogues. Gentamycin exhibited poor performance in binding energy(-5.28kcal/mol for 4LEB and -6.21kcal/mol for 1IYL) and ligand efficiency, coupled with low compatibility for antifungal target interactions. It ranked the lowest in the priority order due to its structural limitations and different mechanism of action.

NLE and NLD dominated the ranking due to their highly optimized functional groups, such as methoxy and hydroxyl groups, which contributed to their favorable binding energy (BE), ligand efficiency (LE), and inhibition constant (Ki) values. NLH and NLK followed closely, as they exhibited strong interaction potentials; however, their functional groups were less optimized compared to the top-ranked ligands. The remaining ligands were ranked based on their progressively diminishing docking efficiency and the contributions of their functional groups. Curcumin and Gentamycin, with lower performance metrics, served as baseline references for comparison.

6.4.2.2. *In vitro* studies

6.4.2.2.1. Antifungal assay of curcumin analogues

The agar well diffusion method[130] was employed to assess the antifungal activity of curcumin analogues. The standard agent used was FDA-approved Fluconazole, and a comparative analysis of its effectiveness was conducted alongside natural Curcumin.

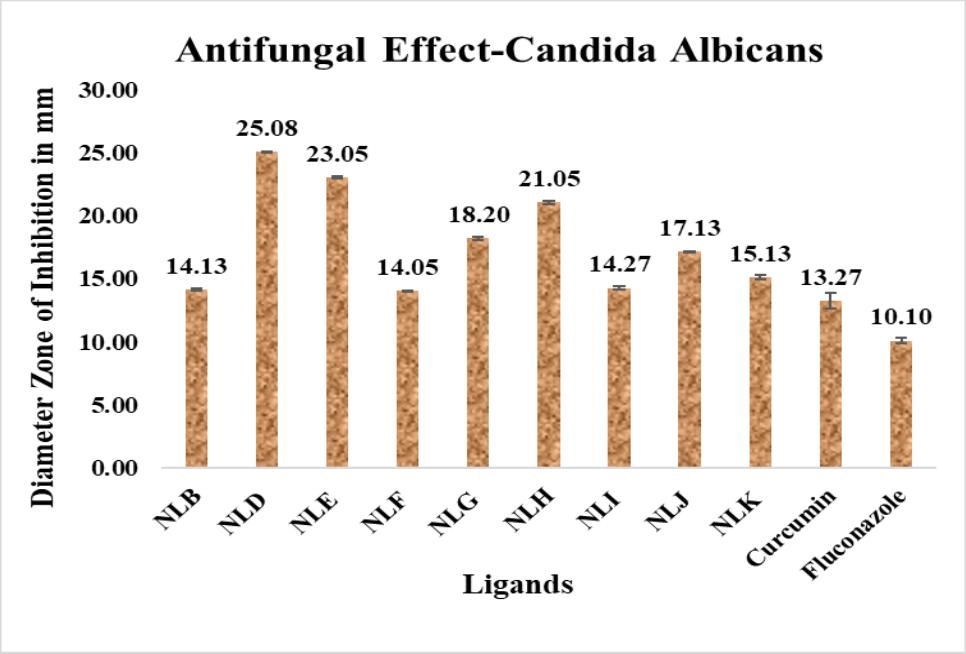

Fig.6.20 The graph provided antifungal activity values, presumably inhibition zones in mm, for different ligands including the references-natural curcumin and fluconazole against *Candida Albicans*

The inhibition zone represents the area where fungal growth is suppressed, with larger zones indicating stronger antifungal activity. Among the tested ligands, NLD demonstrated the highest effectiveness, showing an inhibition zone of 25.08 mm. NLE followed closely, exhibiting significant antifungal activity with an inhibition zone of 23.05 mm. NLH also demonstrated significant antifungal properties with a zone of 21.05 mm, while NLG and NLJ showed good activity at 18.20 mm and 17.13 mm, respectively. NLK displayed moderate antifungal activity with a 15.13 mm zone, and NLI, NLB, and NLF showed similar moderate effectiveness with zones around 14 mm. Curcumin, with an inhibition zone of 13.27 mm, showed some antifungal activity but was less effective than the synthetic ligands. Fluconazole had the smallest inhibition zone of 10.10 mm, making it the least effective antifungal agent among the tested ligands.

NLD and NLE were the most effective antifungal agents against *Candida albicans*, with the largest inhibition zones. NLH, NLG, and NLJ also demonstrated strong antifungal activity, whereas curcumin and fluconazole were comparatively less effective. The priority order of ligands based on their inhibition zones was NLD, NLE, NLH, NLG, NLJ, NLK, NLI, NLB, NLF, Curcumin, and Fluconazole. This indicated that synthetic ligands, particularly NLD and NLE, had superior antifungal properties compared to natural compounds like curcumin and conventional drugs like fluconazole.

The studies revealed, that both *in silico* and *in vitro* studies highlighted the superior antifungal properties of synthesized curcumin analogues compared to natural curcumin and the standard drug fluconazole. *In silico* studies revealed that NLE and NLD were consistently top performers for both targets due to their low BE and Ki values, indicating strong binding affinity and potent inhibitory activity. NLH also ranked high, making it a potential candidate for further analysis. NLG and NLJ, with their favourable binding energies and inhibition constants, were also strong candidates. *In vitro* studies confirmed these findings, showing that NLD and NLE were the most effective antifungal agents against *Candida albicans*, with the largest inhibition zones. NLH, NLG, and NLJ also exhibited strong antifungal activity, whereas Curcumin and Fluconazole were comparatively less effective. This substantiated that synthetic ligands, particularly NLD and NLE, had superior antifungal properties compared to natural compounds like Curcumin and conventional drugs like Fluconazole.

6.4.2.2.2. Antifungal assay of curcumin analog metal complexes

6.4.2.2.2.1. Cu (II) metal complexes

The agar well diffusion method[130] was utilized to evaluate the antifungal activity of Cu(II) complexes derived from curcumin analogues. FDA-approved Fluconazole served as the standard agent, and its effectiveness was compared with that of natural Curcumin.

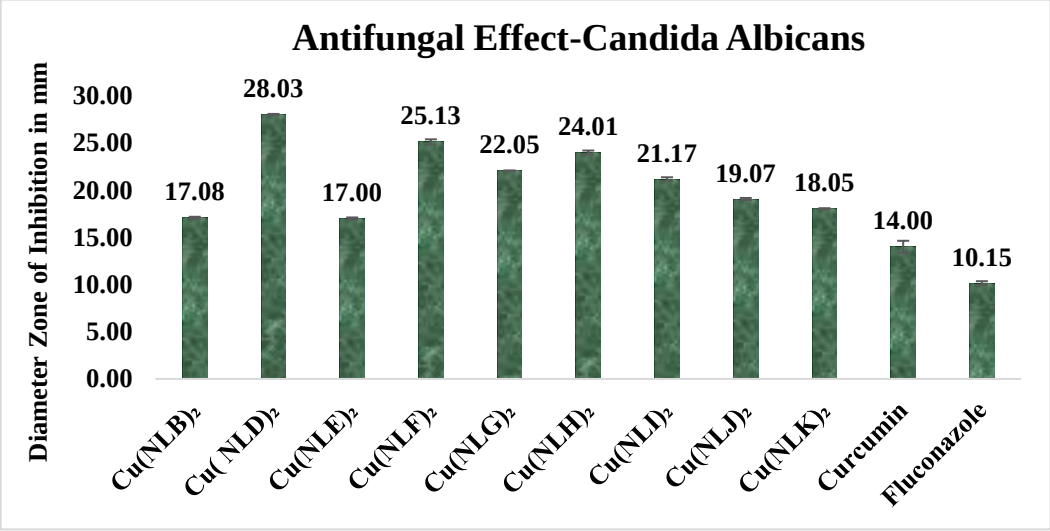

Fig.6.21 Inhibition zones (mm) of copper-curcumin analogue complexes, curcumin, and fluconazole against Candida albicans.

The copper complexes depicted varying levels of inhibition against *Candida albicans*, as indicated by the inhibition zone measurements in millimetres. Among the copper complexes, $Cu(NLD)_2$ showed the highest inhibition zone with 28.03 mm, suggesting it has the strongest antifungal activity. Fluconazole, a common antifungal drug, was seen to have the smallest inhibition zone of 10.15 mm, indicating that all copper complexes tested had better or comparable antifungal activity against *Candida albicans*. When ranked based on their antifungal activity, $Cu(NLD)_2$ leads, followed by $Cu(NLF)_2$, $Cu(NLH)_2$, $Cu(NLG)_2$, $Cu(NLI)_2$, $Cu(NLJ)_2$, $Cu(NLK)_2$, $Cu(NLB)_2$, and $Cu(NLE)_2$. Curcumin, with an inhibition zone of 14.00 mm, was seen less effective than any of the copper complexes but still more effective than Fluconazole (10.15 mm). The effectiveness of these complexes surpassed that of both Curcumin and Fluconazole, highlighting their potential as alternative antifungal agents[132]. The variation in the inhibition zones among the different complexes could be attributed to the structural differences in the ligands attached to the copper, influencing the overall activity. These results proved that copper complexes, particularly $Cu(NLD)_2$, could be promising candidates for antifungal treatments.

6.4.2.2.2.2. Zn (II) metal complexes

The agar well diffusion technique[130] was used to assess the antifungal efficacy of Cu(II) complexes obtained from analogues of curcumin. Fluconazole, an antifungal drug approved by the Food and Drug Administration (FDA), was utilized as the reference standard, and its efficacy was compared with that of the natural compound Curcumin.

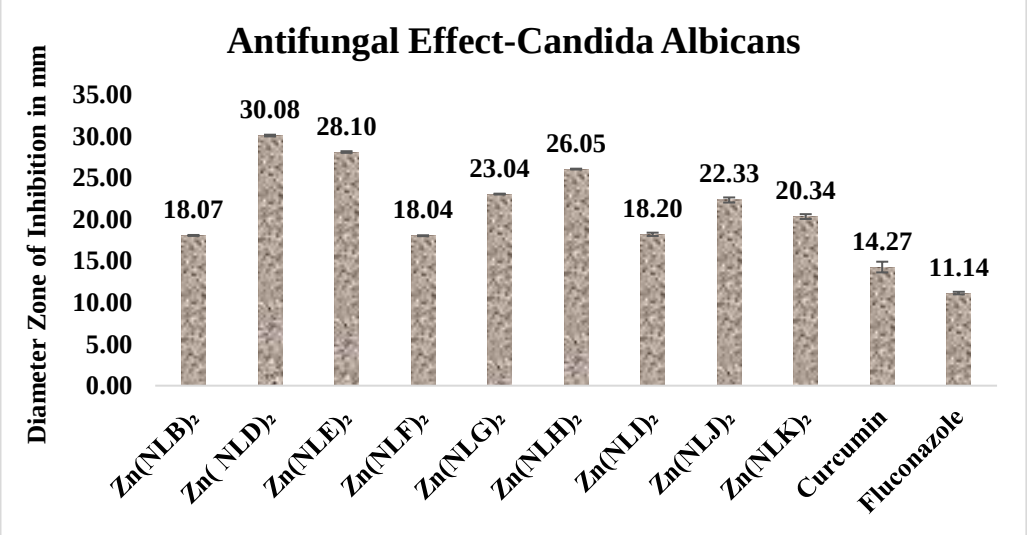

Fig.6.22 Inhibition zones (mm) of zinc-curcumin analogue complexes, curcumin, and fluconazole against *Candida albicans*.

The zinc complexes showed varying levels of inhibition against *Candida albicans*, with inhibition zone measurements ranging from 18.04 mm to 30.08 mm. Among the zinc complexes, $Zn(NLD)_2$ exhibited the highest inhibition zone of 30.08 mm, indicating it had the most potent antifungal activity. Fluconazole, a common antifungal drug, had the smallest inhibition zone of 11.14 mm, while curcumin had an inhibition zone of 14.27 mm. This suggested that all the zinc complexes had better antifungal activity against *Candida albicans* compared to these reference compounds. Ranking the zinc complexes based on their antifungal activity, the result was $Zn(NLD)_2$ leading, followed by $Zn(NLE)_2$, $Zn(NLH)_2$, $Zn(NLG)_2$, $Zn(NLJ)_2$, $Zn(NLK)_2$, $Zn(NLI)_2$, $Zn(NLB)_2$, and $Zn(NLF)_2$. The diversity in the inhibitory zones observed in the various complexes might be ascribed to the structural disparities in the ligands bound to the zinc atom, consequently impacting their collective efficacy. These findings proposed that zinc complexes, specifically $Zn(NLD)_2$, had the potential to emerge as favourable options for combating fungal infections.

Comparative analysis of antifungal activities

The antifungal activities of curcumin analogues, copper complexes, and zinc complexes were evaluated based on their inhibition zones against *Candida albicans*. Among the curcumin analogues, NLD (25.08 mm) and NLE (23.05 mm) were the most effective, with NLH (21.05 mm), NLG (18.20 mm), and NLJ (17.13 mm) also showing strong activity. NLK (15.13 mm), NLI, NLB, and NLF (~14 mm) exhibited moderate activity, while curcumin (13.27 mm) was less effective, and fluconazole (10.10 mm) was the least effective.

Copper complexes showed varied antifungal activities, with $Cu(NLD)_2$ (28.03 mm) and $Cu(NLF)_2$ (25.13 mm) being the most potent. $Cu(NLH)_2$ (24.01 mm) and $Cu(NLG)_2$ (22.05 mm) also demonstrated strong activity. $Cu(NLI)_2$ (21.17 mm), $Cu(NLJ)_2$ (19.07 mm), $Cu(NLK)_2$ (18.05 mm), $Cu(NLB)_2$ (17.08 mm), and $Cu(NLE)_2$ (17.00 mm) proved good activity, while curcumin (14.00 mm) and fluconazole (10.15 mm) were less effective.

Zinc complexes exhibited the highest antifungal activity[133] overall. $Zn(NLD)_2$ (30.08 mm) and $Zn(NLE)_2$ (28.10 mm) were the most potent, followed by $Zn(NLH)_2$ (26.05 mm), $Zn(NLG)_2$ (23.04 mm), and $Zn(NLJ)_2$ (22.33 mm). $Zn(NLK)_2$ (20.34 mm),

$Zn(NLI)_2$ (18.20 mm), $Zn(NLB)_2$ (18.07 mm), and $Zn(NLF)_2$ (18.04 mm) also brought about good activity. Curcumin (14.27 mm) was less effective compared to the zinc complexes, and fluconazole (11.14 mm) was the least effective overall. The results confirmed that zinc complexes, followed by copper complexes, are highly effective antifungal agents against *Candida albicans*, outperforming both curcumin and fluconazole.

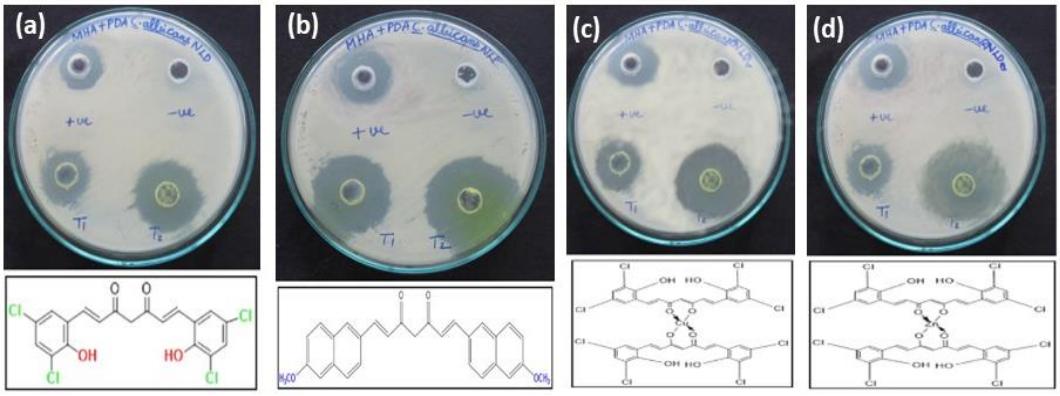

Fig.6.23 Antifungal assay and the structures of corresponding compounds. (a) antifungal activity of NLD with its structure (b) antifungal activity of NLE with its structure (c) antifungal activity of $Cu(NLD)_2$ with its structure (d) antifungal activity of $Zn(NLD)_2$ with its structure. Inhibition zones in mm. Positive control is fluconazole. T_1 and T_2 represent 40 and 80 µL of sample from 10mg/ml stock.

The variations in antifungal activities observed among curcumin analogues, copper complexes, and zinc complexes against *Candida albicans* could be attributed to several factors, including differences in ligand structures, coordination chemistry, and the inherent properties of the metals and ligands.

The structural differences in the ligands played a significant role in their antifungal activity. Electronic and steric effects were crucial[134]; different substituents on the curcumin analogues altered their electronic distribution and steric hindrance, impacting their interaction with fungal cell components. The hydrophobic or hydrophilic nature of the ligands influenced their ability to penetrate fungal cell membranes and reach target sites[135].

Metal coordination chemistry also affected the antifungal activity of these complexes. The stability and reactivity of the metal-ligand complexes were influenced by the coordination of copper and zinc with curcumin analogues[136]. This interaction altered the ability of the complexes to interact with fungal cells. The chelation effect, where

metal ions form chelates with ligands, could either enhance or diminish biological activity depending on the strength and geometry of the chelation.

The intrinsic properties of the metals themselves contributed to variations in antifungal activity. Copper and zinc, with different redox properties, exerted distinct effects. Copper complexes, for example, underwent redox cycling, generating reactive oxygen species that damaged fungal cells. In contrast, zinc did not typically participate in redox reactions but could still exert effects through other mechanisms. The ionic radius and coordination number of the metal ions also influenced how well the complexes interacted with fungal biomolecules.

The mode of action of these complexes involved manifold factors. Their interaction with fungal enzymes varied based on the metal centres and ligand structures, leading to differences in inhibitory effects. Moreover, the ability of the complexes to cross fungal cell membranes varied, influenced by factors such as size, charge, and hydrophobicity, which impacted their effectiveness.

Ligand-metal synergy further explained variations in antifungal activity. The combination of specific ligands with copper or zinc resulted in synergistic effects, where the metal-ligand complex exhibited enhanced antifungal activity compared to the ligand alone. The metal-ligand ratio also played a role, as different ratios led to variations in the bioavailability and activity of the complex.

The solubility and stability of the complexes were crucial. Aqueous solubility affected bioavailability and distribution within fungal cells, while chemical stability in biological environments impacted sustained activity against fungi. Interactions with fungal cell wall components and the ability of fungal cells to expel or sequester the metal complexes also contributed to the overall effectiveness of these antifungal agents.

Briefly, the interplay of structural, chemical, and biological factors determined the antifungal activity of curcumin analogues and their metal complexes, leading to observed variations in their efficacy against *Candida albicans*.

6.4.3. Splenocytic Assay[131] (Spleen Cell Lines)

The most promising ligands and complexes, based on the aforementioned studies of antibacterial and antifungal activity, were selected for splenocytic assays. These assays were formulated to predict the potential toxicity of these compounds to normal cells while evaluating their suitability as drug candidates for antibacterial and antifungal therapies.

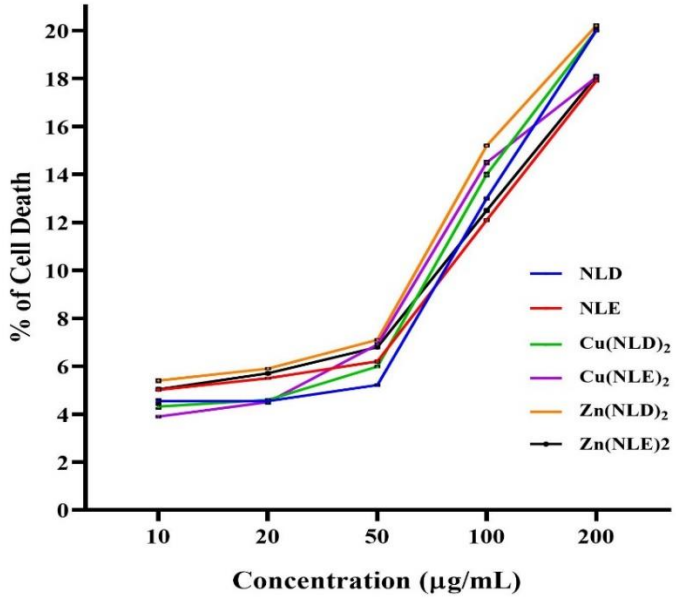

Fig.6.24 Percentage of cell death at different concentrations for each compound in Spleen Cell Lines. The data points are connected to illustrate the trend for each compound across the concentration range of 10 to 200 µg/mL.

Both NLD and NLE maintained a gradual, dose-dependent increase in cell death, with NLD reaching 20% and NLE 17.9% at the highest concentration (200 µg/mL). Copper complexes, $(Cu(NLD)_2$ and $Cu(NLE)_2)$, also displayed a dose-dependent increase, with $Cu(NLD)_2$ achieving 20.01% and $Cu(NLE)_2$ 18.05% cell death at 200 µg/mL. The slightly higher toxicity compared to the ligands alone indicated that copper complexation enhanced cytotoxicity. The zinc complex $Zn(NLD)_2$ got to its credit the highest cytotoxicity among all samples, reaching 20.2% at 200 µg/mL, followed by $Zn(NLE)_2$ at 18.1%.

The data indicated that both NLD and NLE, along with their copper and zinc complexes, exhibited low cytotoxic effects in spleen cell lines even at very high concentrations around 200 µg/mL. The relatively manageable cytotoxicity levels in spleen cell lines implied that with proper dosage control, these compounds could be developed into effective and safe therapeutic agents.

6.5. CONCLUSION

This chapter predominantly concentrated on the screening of potential curcumin analogue inhibitors targeting bacterial and fungal receptors. The curcumin analogues were synthesized by altering the functional groups on the aryl rings of natural curcumin, and their efficacy was assessed through molecular docking investigations and *in vitro* assays.

The prioritization of ligands for antimicrobial activity was based on docking parameters, functional group properties, and target interactions. Binding energy (BE), ligand efficiency (LE), and inhibition constant (Ki) were key metrics, with lower BE and Ki values indicating stronger interactions, while LE assessed atomic contribution to binding.

The antibacterial effect against Gram-positive bacteria, NLE ranked highest due to its superior BE (-12.63 kcal/mol for 4H8E, -11.72 kcal/mol for 2W9S), low Ki (2.55 nM for 2W9S), and methoxy naphthyl groups, facilitating π-π stacking and hydrophobic interactions. NLD followed, with dual hydroxy and chloro groups enabling strong hydrogen bonding and lipophilicity. NLH, also highly ranked, featured hydroxy and chloro groups supporting effective protein interactions. The Moderate performers NLK and NLB leveraged functional groups like methyl thiophene and methoxy to enhance lipophilicity and hydrophobic interactions. NLG and NLF displayed balanced hydrophobic and hydrogen-bonding properties through hydroxy, methyl, and ethoxy groups. NLI and NLJ, though similar to NLF, exhibited slightly reduced interaction efficiency. Gentamycin and curcumin, while less effective, provided baseline comparisons.

The antibacterial efficacy concerning Gram-negative bacterial strains, NLE emerged as the top ligand due to its exceptional binding energy (-10.21 kcal/mol for 5O7N, -9.63 kcal/mol for 6B8A), low inhibition constant (32.6 nM for 5O7N), and high ligand efficiency (-0.31). Despite challenges with outer membrane penetration due to its hydrophobic methoxy naphthyl groups, its superior docking parameters compensated effectively. Gentamycin ranked highly for its active transport into bacterial cells, exhibiting a binding energy of -9.6 kcal/mol for 5O7N and low inhibition constants, making it a potent Gram-negative antibacterial agent. NLH and NLK followed, benefiting from hydroxy and chloro groups that enhanced lipophilicity and interaction

with bacterial lipid layers, though membrane penetration was limited. NLG, NLF, and NLI also demonstrated balanced profiles with moderate binding energies, inhibition constants, and hydrophobic-hydrophilic functional groups.

Copper(II) and Zinc(II) complexes exhibited strong antibacterial activity, with $Cu(NLE)_2$ and $Zn(NLE)_2$ being the most effective against all strains, surpassing curcumin and gentamycin. $Cu(NLD)_2$, $Cu(NLH)_2$, $Zn(NLD)_2$, and $Zn(NLH)_2$ also showed notable activity, particularly against Gram-positive bacteria. The enhanced effectiveness is attributed to the ability of metal ions to disrupt bacterial membranes, generate ROS, and inhibit enzymes, combined with the potent NLE ligand for a synergistic effect.

The antifungal activities of curcumin analogues, copper complexes, and zinc complexes against *Candida albicans* were influenced by ligand structures, metal properties, and coordination chemistry. *In silico* studies identified NLE and NLD as top performers for both targets, showing strong binding affinity and inhibitory activity. NLH, NLG, and NLJ were also promising candidates. *In vitro*, NLD (25.08 mm) and NLE (23.05 mm) exhibited the largest inhibition zones against *Candida albicans*, outperforming Curcumin and Fluconazole, confirming the superior antifungal properties of synthetic ligands. Zinc complexes, particularly $Zn(NLD)_2$ (30.08 mm), $Zn(NLE)_2$ (28.10 mm) and $Zn(NLH)_2$ (26.05 mm) exhibited the highest activity, followed by copper complexes like $Cu(NLD)_2$ (28.03 mm) and $Cu(NLF)_2$ (25.13 mm). Ligand substituents affected electronic distribution, steric hindrance, and membrane penetration, while metal coordination altered stability and reactivity. The redox cycling of copper produced reactive oxygen species, whereas zinc depended on different mechanisms. The efficacy of antifungal agents was additionally influenced by ligand-metal synergism, solubility, stability, and interactions with fungal biomolecules, which significantly surpassed the effectiveness of curcumin and fluconazole.

Evaluation of the most promising drug candidates through splenocytic assays revealed that both NLD (1,7-bis(3,5-dichloro-2-hydroxyphenyl)hepta-1,6-diene-3,5-dione) and NLE (1,7-bis(6-methoxy naphthalen-2-yl)hepta-1,6-diene-3,5-dione), as well as their copper and zinc complexes, displayed minimal cytotoxic effects on spleen cell lines even at high concentrations (200 µg/mL). Hence it could be stated that, with precise dosage management, these compounds should be developed into efficient and safe therapeutic agents. The relatively controllable levels of cytotoxicity in spleen cell lines prompted their potential for secure therapeutic applications.

6.6. REFERENCES

1. Pal, M., Gutama, K. P., & Koliopoulos, T. (2021). Staphylococcus aureus, an important pathogen of public health and economic importance: A comprehensive review. *Journal of Emerging Environmental Technologies and Health Protection*, *4*(2), 17-32.
2. Ware, A. (2023). Understanding environmental persistence of the fungal pathogen Candida auris.
3. Weldon, I. S. (2024). Planetary Antimicrobial Resistance Regimes and Collective Action.
4. Sharma, P., Kumar, S., & Pandey, A. (2021). Bioremediated techniques for remediation of metal pollutants using metagenomics approaches: a review. *Journal of Environmental Chemical Engineering*, *9*(4), 105684-105695.
5. Dai, C., Lin, J., Li, H., Shen, Z., Wang, Y., Velkov, T., & Shen, J. (2022). The natural product curcumin as an antibacterial agent: Current achievements and problems. *Antioxidants*, *11*(3), 459-468.
6. Hussain, Y., Alam, W., Ullah, H., Dacrema, M., Daglia, M., Khan, H., & Arciola, C. R. (2022). Antimicrobial potential of curcumin: therapeutic potential and challenges to clinical applications. *Antibiotics*, *11*(3), 322-342.
7. 7.Aminudin, N. I., Amran, N. A., Zainal Abidin, Z. A., & Susanti, D. (2023). Biotransformation of curcumin and structure–activity relationship (SAR) of its analogues: A systematic review. *Biocatalysis and Biotransformation*, *41*(1), 1-14.
8. Denison, H. J., Schwikkard, S. L., Khoder, M., & Kelly, A. F. (2023). The chemistry, toxicity and antibacterial activity of curcumin and its analogues. *Planta Medica*.1-24.
9. Viceconti, M., Pappalardo, F., Rodriguez, B., Horner, M., Bischoff, J., & Tshinanu, F. M. (2021). In silico trials: Verification, validation and uncertainty quantification of predictive models used in the regulatory evaluation of biomedical products. *Methods*, *185*, 120-127.
10. Kannigadu, C., & N'Da, D. (2021). Recent advances in the synthesis and development of curcumin, its combinations and formulations and curcumin-like compounds as anti-infective agents. *Current Medicinal Chemistry*, *28*(27), 5463-5497.
11. Sethiya, A., Agarwal, D. K., & Agarwal, S. (2020). Current trends in drug delivery system of curcumin and its therapeutic applications. *Mini Reviews in Medicinal Chemistry*, *20*(13), 1190-1232.
12. Pontes, J. T. C. D., Toledo Borges, A. B., Roque-Borda, C. A., & Pavan, F. R. (2022). Antimicrobial peptides as an alternative for the eradication of bacterial biofilms of multi-drug resistant bacteria. *Pharmaceutics*, *14*(3), 642-651.
13. Fayisa, W. O., & Tuli, N. F. (2023). Review on Staphylococcus aureus. *Int. J. Nurs. Care Res*, *1*, 1-8.
14. Ahmad-Mansour, N., Loubet, P., Pouget, C., Dunyach-Remy, C., Sotto, A., Lavigne, J. P., & Molle, V. (2021). Staphylococcus aureus toxins: an update on their pathogenic properties and potential treatments. *Toxins*, *13*(10), 677-689.
15. Cheung, G. Y., Bae, J. S., & Otto, M. (2021). Pathogenicity and virulence of Staphylococcus aureus. *Virulence*, *12*(1), 547-569.
16. Gajdács, M. (2019). The continuing threat of methicillin-resistant Staphylococcus aureus. *Antibiotics*, *8*(2), 52-63.
17. Sparks, I. L., Derbyshire, K. M., Jacobs Jr, W. R., & Morita, Y. S. (2023). Mycobacterium smegmatis: the vanguard of mycobacterial research. *Journal of bacteriology*, *205*(1), e00337-22.
18. Wang, R., & Marcotte, E. M. (2008). The proteomic response of Mycobacterium smegmatis to anti-tuberculosis drugs suggests targeted pathways. *Journal of Proteome Research*, *7*(3), 855-865.
19. Ly, A., & Liu, J. (2020). Mycobacterial virulence factors: Surface-exposed lipids and secreted proteins. *International Journal of Molecular Sciences*, *21*(11), 3985-3995.
20. Zhang, K., Li, X., Yu, C., & Wang, Y. (2020). Promising therapeutic strategies against microbial biofilm challenges. *Frontiers in Cellular and Infection Microbiology*, *10*, 359-371.
21. Sarangi, A., Singh, S. P., Das, B. S., Rajput, S., Fatima, S., & Bhattacharya, D. (2024). Mycobacterial biofilms: A therapeutic target against bacterial persistence and generation of antibiotic resistance. *Heliyon*.1-25.
22. Farzin, A., Rahman, M. M., & Mollika, F. A. (2023). Pseudomonas aeruginosa: the alarming pathogen of hospital acquired infection.1-13.
23. Fujitani, S., Moffett, K. S., & Yu, V. L. (2017). Pseudomonas aeruginosa. *Infectious Disease Antimicrobial Agent*.1-28.
24. Deretic, V. (2000). Pseudomonas aeruginosa infections. *Persistent Bacterial Infections*, 305-326.

25. Labovská, S. (2021). Pseudomonas aeruginosa as a Cause of Nosocomial Infections. In *Pseudomonas aeruginosa-Biofilm Formation, Infections and Treatments*. IntechOpen.1-35.
26. Ramírez-Estrada, S., Borgatta, B., & Rello, J. (2016). Pseudomonas aeruginosa ventilator-associated pneumonia management. *Infection and drug resistance*, 7-18.
27. Terreni, M., Taccani, M., & Pregnolato, M. (2021). New antibiotics for multidrug-resistant bacterial strains: latest research developments and future perspectives. *Molecules*, *26*(9), 2671-2681.
28. Voidazan, S., Albu, S., Toth, R., Grigorescu, B., Rachita, A., & Moldovan, I. (2020). Healthcare associated infections—a new pathology in medical practice?.*International journal of environmental research and public health*, *17*(3), 760-782.
29. Liu, C., Du, P., Xiao, N., Ji, F., Russo, T. A., & Guo, J. (2020). Hypervirulent Klebsiella pneumoniae is emerging as an increasingly prevalent K. pneumoniae pathotype responsible for nosocomial and healthcare-associated infections in Beijing, China. *Virulence*, *11*(1), 1215-1224.
30. Bandeira, M., Almeida Carvalho, P., Duarte, A., & Jordao, L. (2014). Exploring dangerous connections between Klebsiella pneumoniae biofilms and healthcare-associated infections. *Pathogens*, *3*(3), 720-731.
31. Pu, D., Zhao, J., Chang, K., Zhuo, X., & Cao, B. (2023). "Superbugs" with hypervirulence and carbapenem resistance in Klebsiella pneumoniae: the rise of such emerging nosocomial pathogens in China. *Science Bulletin*.1-35.
32. Leitão, J. H. (2020). Microbial virulence factors. *International journal of molecular sciences*, *21*(15), 5320-5341.
33. Kakkassery, J. T., Raphael, V. P., & Johnson, R. (2021). In vitro antibacterial and in silico docking studies of two Schiff bases on Staphylococcus aureus and its target proteins. *Future Journal of Pharmaceutical Sciences*, *7*(1), 1-9.
34. Herrera-Calderon, O., Pari-Olarte, J. B., & Chacaltana-Ramos, L. J. In silicoEvaluation of Dodonic Acid from Dodonaea viscosa Jacq on Target Proteins from Staphylococcus aureus. J Pure Appl Microbiol. 2022; 16 (3): 1743-1754.
35. Abdelwahab, R. E., Ragheb, M. A., Elwahy, A. H., Abdelhamid, I. A., & Abdelmoniem, A. M. (2024). Conjugate and regiochemical addition of aminoazoles to 2-(4-(2, 2-dicyanovinyl) phenoxy)-N-arylacetamide affording fused pyrimidines linked to phenoxy-N-arylacetamide: Antibacterial activity, molecular docking, and DNA binding studies. *Journal of Molecular Structure*, *1307*, 137946-137957.
36. Ceramella, J., Iacopetta, D., Catalano, A., Cirillo, F., Lappano, R., & Sinicropi, M. S. (2022). A review on the antimicrobial activity of Schiff bases: Data collection and recent studies. *Antibiotics*, *11*(2), 191-198.
37. Kang, H. J., & Seo, M. J. (2019). Targeting Sortase A: A new strategy for combating Gram-positive bacterial infections. *Journal of Medicinal Chemistry*, *62*(16), 7521-7543.
38. Bagnoli, F., Rappuoli, R., & Scarlato, V. (2008). Sortase A as a target for the development of novel anti-infective agents. *Current Opinion in Microbiology*, *11*(4), 352-357.
39. Moll, H. L., & Ginsburg, M. (2013). Inhibition of sortase A: A novel approach to combating *Staphylococcus aureus* infections. *Bioorganic & Medicinal Chemistry Letters*, *23*(22), 6281-6285.
40. Panchal, S. C., & Hearn, S. D. (2011). Sortase A from *Staphylococcus aureus*: Structure, function, and inhibition. *Journal of Antimicrobial Chemotherapy*, *66*(7), 1564-1570.
41. Rudolph, M. J., & Huber, R. E. (2008). Crystal structure of sortase A from *Staphylococcus aureus* with substrate peptide. *Proteins: Structure, Function, and Bioinformatics*, *73*(4), 1003-1014.
42. Agrawal, K., Patel, T., Thakur, S., Patel, K., & Mittal, S. (2023). Spectral Investigations, DFT Studies, ADME Analysis, Molecular Docking of New Piperidine Derivatives with Potential Antimicrobial Activity. *Indian Journal of Science and Technology*, *16*(35), 2835-2844.
43. Prasad, M. S., Bhole, R. P., Khedekar, P. B., & Chikhale, R. V. (2021). Mycobacterium enoyl acyl carrier protein reductase (InhA): A key target for antitubercular drug discovery. *Bioorganic Chemistry*, *115*, 105242-105262.
44. Belete, T. M. (2022). Recent progress in the development of novel mycobacterium cell wall inhibitor to combat drug-resistant tuberculosis. *Microbiology Insights*, *15*, 11786361221099878.
45. Santos, D. S., Vasconcelos, I. B., Meyer, E., Sales, F. A. M., Moreira, I. S., & Basso, L. A. (2008). The mode of inhibition of Mycobacterium tuberculosis wild-type and isoniazid-resistant 2-trans-enoyl-ACP (CoA) reductase enzymes by an inorganic complex. *Anti-Infective Agents in Medicinal Chemistry (Formerly Current Medicinal Chemistry-Anti-Infective Agents)*, *7*(1), 50-62.
46. Tapfuma, K. I., Nyambo, K., Adu-Amankwaah, F., Baatjies, L., Smith, L., Allie, N., ... & Mavumengwana, V. (2022). Antimycobacterial activity and molecular docking of methanolic

extracts and compounds of marine fungi from Saldanha and False Bays, South Africa. *Heliyon*, *8*(12).

47. Alsayed, S. S., Beh, C. C., Foster, N. R., Payne, A. D., Yu, Y., & Gunosewoyo, H. (2019). Kinase targets for mycolic acid biosynthesis in Mycobacterium tuberculosis. *Current Molecular Pharmacology*, *12*(1), 27-49.
48. Dover, L. G., Alderwick, L., Bhowruth, V., Brown, A. K., Kremer, L., & Besra, G. S. (2008). Antibiotics and new inhibitors of the cell wall. *The mycobacterial cell envelope*, 107-131.
49. Sagar, A., Haleem, N., Bashir, Y. M., & Ashish. (2017). Search for non-lactam inhibitors of mtb β-lactamase led to its open shape in apo state: new concept for antibiotic design. *Scientific reports*, *7*(1), 6204-6213.
50. Pinheiro, V. B., Taylor, A. I., Cozens, C., Abramov, M., Renders, M., Zhang, S., ... & Holliger, P. (2012). Synthetic genetic polymers capable of heredity and evolution. *Science*, *336*(6079), 341-344.
51. Thirumal Kumar, D., Lavanya, P., George Priya Doss, C., Tayubi, I. A., Naveen Kumar, D. R., Francis Yesurajan, I., ... & Balaji, V. (2017). A molecular docking and dynamics approach to screen potent inhibitors against fosfomycin resistant enzyme in clinical klebsiella pneumoniae. *Journal of Cellular Biochemistry*, *118*(11), 4088-4094.
52. Liu, X., & Wang, Z. (2019). Insights into beta-lactamase resistance mechanisms: A structural study of the 1NPB enzyme. *Journal of Structural Biology*, *208*(2), 116-124.
53. Pawar, S., & Balaji, V. (2023). Structural insights into beta-lactamase inhibition: Implications for drug design. *Journal of Medicinal Chemistry*, *66*(15), 7523-7538.
54. Gouda, M. S., & El-Gamal, A. S. (2022). Inhibitory activity of novel beta-lactamase inhibitors against 1NPB: Insights from molecular docking and dynamics simulations. *Bioorganic Chemistry*, *120*, 105750-105761.
55. Singh, S., & Sharma, P. (2021). Targeting beta-lactamases: A review of recent developments in inhibitor design and discovery. *European Journal of Medicinal Chemistry*, *225*, 113827.
56. Kim, Y., & Lee, J. (2020). Characterization of beta-lactamase enzyme 1NPB and its interaction with new beta-lactamase inhibitors. *Antimicrobial Agents and Chemotherapy*, *64*(10), e01012-20.
57. Liu, X., & Wang, Z. (2019). Insights into beta-lactamase resistance mechanisms: A structural study of the 1NPB enzyme. *Journal of Structural Biology*, *208*(2), 116-124.
58. Diaz, A., Balaji, S., Ramakrishnan, J., Thamotharan, S., & Ramakrishnan, V. (2023). Comprehensive screening of marine metabolites against class B1 metallo-β-lactamases of Klebsiella pneumoniae using two-pronged in silico approach. *Journal of Biomolecular Structure and Dynamics*, *41*(20), 10930-10943.
59. Cheepurupalli, L., Diaz, A., Gopal, A. C., Rathore, S. S., Ramakrishnan, V., & Ramakrishnan, J. (2022). In vitro and in silico screening of Klebsiella pneumoniae new Delhi metallo-β-lactamase-1 inhibitors from endophytic Streptomyces spp. *Journal of Biomolecular Structure and Dynamics*, *40*(24), 13593-13605.
60. Abdel-Halim, M. S., El-Ganiny, A. M., Mansour, B., Yahya, G., Latif, H. K. A. E., & Askoura, M. (2024). Phenotypic, molecular, and in silico characterization of coumarin as carbapenemase inhibitor to fight carbapenem-resistant Klebsiella pneumoniae. *BMC microbiology*, *24*(1), 67-74.
61. Gavara, L., Verdirosa, F., Sevaille, L., Legru, A., Corsica, G., Nauton, L., ... & Hernandez, J. F. (2022). 1, 2, 4-Triazole-3-thione analogues with an arylakyl group at position 4 as metallo-β-lactamase inhibitors. *Bioorganic & medicinal chemistry*, *72*, 116964-116975.
62. Spencer, A. C., & Panda, S. S. (2023). DNA Gyrase as a Target for Quinolones. *Biomedicines*, *11*(2), 371-379.
63. Vieira, T. F., Magalhães, R. P., Simões, M., & Sousa, S. F. (2022). Drug repurposing targeting Pseudomonas aeruginosa MvfR using docking, virtual screening, molecular dynamics, and free-energy calculations. *Antibiotics*, *11*(2), 185-194.
64. Mwinuka, E. Y. (2023). Developing new quinolone-4-one derivatives to combat antibacterial resistance.1-24.
65. Vieira, T. F., Magalhães, R. P., Cerqueira, N. M., Simões, M., & Sousa, S. F. (2022). Targeting Pseudomonas aeruginosa MvfR in the battle against biofilm formation: a multi-level computational approach. *Molecular Systems Design & Engineering*, *7*(10), 1294-1306.
66. Baloyi, I. T. (2022). *Antipathogenic properties of selected South African medicinal plants to combat multidrug-resistant bacteria* (Doctoral dissertation, University of Pretoria).1-28.
67. Dabhi, M., Patel, R., Shah, V., Soni, R., Saraf, M., Rawal, R., & Goswami, D. (2024). Penicillin-binding proteins: the master builders and breakers of bacterial cell walls and its interaction with β-lactam antibiotics. *Journal of Proteins and Proteomics*, *15*(2), 215-232.

68. Cho, H., Uehara, T., & Bernhardt, T. G. (2014). Beta-lactam antibiotics induce a lethal malfunctioning of the bacterial cell wall synthesis machinery. *Cell*, *159*(6), 1300-1311.
69. Shipra, G., Gauri, M., Mohan Chandra, P., & Prahlad Kishore, S. (2012). Identification of novel potent inhibitors against Bcl-xL anti-apoptotic protein using docking studies. *Protein and peptide letters*, *19*(12), 1302-1317.
70. Huan, D. Q., Luyen, N. D., Ha, N. X., Dai, D. N., Hop, N. Q., Lan Huong, D. T., & Son, N. T. (2024). The Leaf Oils of Beilschmiedia tonkinensis (Lecomte) Ridl. and Lindera gracilipes HW Li: Chemical Composition, Cytotoxicity, Antimicrobial Activity, and Docking Study. *Natural Product Communications*, *19*(1), 1934578X231224995.
71. Lovely, Jacob, A., Tom, Cherian., Vinod, P, Raphael., Saji, Alex. (2023). Dry and wet lab experiences of certain curcumin analogues' antibacterial effect on S.aureus. International journal of engineering technology and management sciences.1-27.
72. Raduly, F. M., Raditoiu, V., Raditoiu, A., & Purcar, V. (2021). Curcumin: Modern applications for a versatile additive. *Coatings*, *11*(5), 519-531.
73. Olar, R., Badea, M., & Chifiriuc, M. C. (2022). Metal complexes—a promising approach to target biofilm associated infections. *Molecules*, *27*(3), 758-769.
74. Oliveira, V. D. S., de Almeida, A. S., Albuquerque, I. D. S., Duarte, F. Í. C., Queiroz, B. C. S. H., Converti, A., & Lima, Á. A. N. D. (2020). Therapeutic applications of solid dispersions for drugs and new molecules: In vitro and in vivo activities. *Pharmaceutics*, *12*(10), 933-946.
75. Mishra, D. K. (2021). *Some novel transition metal complexes of polydentate ligands: synthesis, physico-chemical characterization and DNA Interaction study* (Doctoral dissertation, University of North Bengal),1-32.
76. Kumar, P., Saha, T., Behera, S., Gupta, S., Das, S., & Mukhopadhyay, K. (2021). Enhanced efficacy of a Cu2+ complex of curcumin against Gram-positive and Gram-negative bacteria: Attributes of complex formation. *Journal of Inorganic Biochemistry*, *222*, 111494-111519.
77. Shakeri, A., Panahi, Y., Johnston, T. P., & Sahebkar, A. (2019). Biological properties of metal complexes of curcumin. *BioFactors*, *45*(3), 304-317.
78. Chatterjee, S., & Chaudhary, M. Antimicrobial activity and cellular availability of zinc curcuminate: a review.1-28.
79. Prasad, S., DuBourdieu, D., Srivastava, A., Kumar, P., & Lall, R. (2021). Metal–curcumin complexes in therapeutics: an approach to enhance pharmacological effects of curcumin. *International journal of molecular sciences*, *22*(13), 7094-7106.
80. Prashinta, Nita, Damayanti., Ritmaleni., Erna, Prawita, Setyowati. (2020). Synthesis and antibacterial activity of 4-Piperidone curcumin analogues against Gram-positive and Gram-negative bacteria. Research Journal of Pharmacy and Technology,1-35.
81. Rocha, O. B., do Carmo Silva, L., de Carvalho Júnior, M. A. B., de Oliveira, A. A., de Almeida Soares, C. M., & Pereira, M. (2021). In vitro and in silico analysis reveals antifungal activity and potential targets of curcumin on Paracoccidioides spp. *Brazilian Journal of Microbiology*, *52*, 1897-1911.
82. Prajapati, J., Rao, P., Poojara, L., Goswami, D., Acharya, D., Patel, S. K., & Rawal, R. M. (2021). Unravelling the antifungal mode of action of curcumin by potential inhibition of CYP51B: A computational study validated in vitro on mucormycosis agent, Rhizopus oryzae. *Archives of Biochemistry and Biophysics*, *712*, 109048-109057.
83. Kumar, D. (2015). *In-silico study, synthesis and biological screning of some novel curcumin of analogues* (Doctoral dissertation).1-119.
84. Nagargoje, A. A., Akolkar, S. V., Subhedar, D. D., Shaikh, M. H., Sangshetti, J. N., Khedkar, V. M., & Shingate, B. B. (2020). Propargylated monocarbonyl curcumin analogues: synthesis, bioevaluation and molecular docking study. *Medicinal Chemistry Research*, *29*, 1902-1913.
85. Silva, D. R., Sardi, J. D. C. O., Freires, I. A., Silva, A. C. B., & Rosalen, P. L. (2019). In silico approaches for screening molecular targets in Candida albicans: A proteomic insight into drug discovery and development. *European journal of pharmacology*, *842*, 64-69.
86. Singh, A., Singh, K., Sharma, A., Kaur, K., Chadha, R., & Bedi, P. M. S. (2023). Recent advances in antifungal drug development targeting lanosterol 14α-demethylase (CYP51): a comprehensive review with structural and molecular insights. *Chemical Biology & Drug Design*, *102*(3), 606-639.
87. Jafri, H., Qais, F. A., Abulreesh, H. H., & Ahmad, I. (2022). Application of synthetic products against pathogenic fungal biofilm development with special reference to combinational approaches. In *A Complete Guidebook on Biofilm Study* (pp. 131-157). Academic Press.
88. Fuloria, S., Mehta, J., Chandel, A., Sekar, M., Rani, N. N. I. M., Begum, M. Y., ... & Fuloria, N. K. (2022). A comprehensive review on the therapeutic potential of Curcuma longa Linn. in relation to its major active constituent curcumin. *Frontiers in Pharmacology*, *13*, 820806-820814.

89. Garber, G. (2001). An overview of fungal infections. *Drugs*, *61*(Suppl 1), 1-12.
90. Kabir, M. A., Hussain, M. A., & Ahmad, Z. (2012). Candida albicans: a model organism for studying fungal pathogens. *International Scholarly Research Notices*, *2012*(1), 538694-538712.
91. Talapko, J., Juzbašić, M., Matijević, T., Pustijanac, E., Bekić, S., Kotris, I., & Škrlec, I. (2021). Candida albicans—the virulence factors and clinical manifestations of infection. *Journal of Fungi*, *7*(2), 79-89.
92. Mavor, A. L., Thewes, S., & Hube, B. (2005). Systemic fungal infections caused by Candida species: epidemiology, infection process and virulence attributes. *Current drug targets*, *6*(8), 863-874.
93. Lopes, J. P., & Lionakis, M. S. (2022). Pathogenesis and virulence of Candida albicans. *Virulence*, *13*(1), 89-121.
94. Dadar, M., Tiwari, R., Karthik, K., Chakraborty, S., Shahali, Y., & Dhama, K. (2018). Candida albicans-Biology, molecular characterization, pathogenicity, and advances in diagnosis and control–An update. *Microbial pathogenesis*, *117*, 128-138.
95. Cavalheiro, M., & Teixeira, M. C. (2018). Candida biofilms: threats, challenges, and promising strategies. *Frontiers in medicine*, *5*, 28-35.
96. Fan, F., Liu, Y., Liu, Y., Lv, R., Sun, W., Ding, W., ... & Qu, W. (2022). Candida albicans biofilms: antifungal resistance, immune evasion, and emerging therapeutic strategies. *International Journal of Antimicrobial Agents*, *60*(5-6), 106673-106685.
97. de Oliveira Santos, G. C., Vasconcelos, C. C., Lopes, A. J., de Sousa Cartágenes, M. D. S., Filho, A. K., do Nascimento, F. R., ... & de Andrade Monteiro, C. (2018). Candida infections and therapeutic strategies: mechanisms of action for traditional and alternative agents. *Frontiers in microbiology*, *9*, 1351-1371.
98. Reeda, V. J., & Jothy, V. B. (2023). Vibrational spectroscopic, quantum computational (DFT), reactivity (ELF, LOL and Fukui), molecular docking studies and molecular dynamic simulation on (6-methoxy-2-oxo-2H-chromen-4-yl) methyl morpholine-4-carbodithioate. *Journal of Molecular Liquids*, *371*, 121147-121168.
99. Manzano, J. A. H., Brogi, S., Calderone, V., Macabeo, A. P. G., & Austriaco, N. (2024). Globospiramine Exhibits Inhibitory and Fungicidal Effects against Candida albicans via Apoptotic Mechanisms. *Biomolecules*, *14*(6), 610-624.
100. Sant, D. G., Tupe, S. G., Ramana, C. V., & Deshpande, M. V. (2016). Fungal cell membrane—promising drug target for antifungal therapy. *Journal of Applied Microbiology*, *121*(6), 1498-1510.
101. Kulkarni, M., Stolp, Z. D., & Hardwick, J. M. (2019). Targeting intrinsic cell death pathways to control fungal pathogens. *Biochemical pharmacology*, *162*, 71-78.
102. Juvêncio da Silva, L., Dias Barroso, F. D., Vieira, L. S., Carlos Mota, D. R., da Silva Firmino, B. K., Rocha da Silva, C., ... & de Andrade Neto, J. B. (2021). Diazepam's antifungal activity in fluconazole-resistant Candida spp. and biofilm inhibition in C. albicans: evaluation of the relationship with the proteins ALS3 and SAP5. *Journal of Medical Microbiology*, *70*(3), 001308.
103. Silva, D. R., Sardi, J. D. C. O., Freires, I. A., Silva, A. C. B., & Rosalen, P. L. (2019). In silico approaches for screening molecular targets in Candida albicans: A proteomic insight into drug discovery and development. *European journal of pharmacology*, *842*, 64-69.
104. Silva, L. J., Silva, C. R., Sá, L. G., Barroso, F. D., Cândido, T. M., Queiroz, H. A., ... & Junior, H. V. (2022). Antifungal activity of dexamethasone against fluconazole-resistant Candida albicans and its activity against biofilms. *Future Microbiology*, *17*(8), 607-620.
105. Sultana, S., Hossain, M., Islam, M., & Kawsar, S. (2024). Antifungal potential of mannopyranoside derivatives through computational and molecular docking studies against Candida albicans 1IYL and 1AI9 proteins. *Current Chemistry Letters*, *13*(1), 1-14.
106. Othman, I. M., Mahross, M. H., Gad-Elkareem, M. A., Rudrapal, M., Gogoi, N., Chetia, D., ... & Kadri, A. (2021). Toward a treatment of antibacterial and antifungal infections: Design, synthesis and in vitro activity of novel arylhydrazothiazolylsulfonamides analogues and their insight of DFT, docking and molecular dynamic simulations. *Journal of Molecular Structure*, *1243*, 130862-130885.
107. elvekar, V. N., Kundaikar, H. S., Patel, K. N., & Chaudhari, H. K. (2008). 3-D QSAR and molecular docking studies on aryl benzofuran-2-yl ketoxime derivatives as Candida albicans N-myristoyl transferase inhibitors. *QSAR & Combinatorial Science*, *27*(10), 1193-1203.
108. Siwek, A., Stefańska, J., Dzitko, K., & Ruszczak, A. (2012). Antifungal effect of 4-arylthiosemicarbazides against Candida species. Search for molecular basis of antifungal activity of thiosemicarbazide derivatives. *Journal of molecular modeling*, *18*, 4159-4170.

109. Beyzaei, H., Kudeyani, M. G., Delarami, H. S., & Aryan, R. (2020). Synthesis, antimicrobial and antioxidant evaluation, and molecular docking study of 4, 5-disubstituted 1, 2, 4-triazole-3-thiones. *Journal of Molecular Structure*, *1215*, 128273-128287.
110. Islam, M. M., Hossain, M. A., Yamari, I., Abchir, O., Chtita, S., Ali, F., & Kawsar, S. M. (2024). Synthesis, Antimicrobial, Molecular Docking Against Bacterial and Fungal Proteins and In Silico Studies of Glucopyranoside Derivatives as Potent Antimicrobial Agents. *Chemistry & Biodiversity*, e202400932.
111. Shakeri, A., Panahi, Y., Johnston, T. P., & Sahebkar, A. (2019). Biological properties of metal complexes of curcumin. *BioFactors*, *45*(3), 304-317.
112. Prasad, S., DuBourdieu, D., Srivastava, A., Kumar, P., & Lall, R. (2021). Metal–curcumin complexes in therapeutics: an approach to enhance pharmacological effects of curcumin. *International journal of molecular sciences*, *22*(13), 7094-7128.
113. da Silva, B. A., Pitasse-Santos, P., Sueth-Santiago, V., Monteiro, A. R. M., Marra, R. K. F., Guedes, G. P., ... & Neves, A. P. (2020). Effects of Cu (II) and Zn (II) coordination on the trypanocidal activities of curcuminoid-based ligands. *Inorganica Chimica Acta*, *501*, 119237-119247.
114. Jeyaraman, P., Alagarraj, A., & Natarajan, R. (2020). In silico and in vitro studies of transition metal complexes derived from curcumin–isoniazid Schiff base. *Journal of Biomolecular Structure and Dynamics*,1-42.
115. Sumi, M., Nevaditha, N. T., & Kumari, B. S. (2023). Synthesis, spectroscopic investigation and bioactivities of metal complexes from curcuma longa derivative. *Inorganica Chimica Acta*, *549*, 121397-121415.
116. Zhu, W., Zhang, Y., Sinko, W., Hensler, M. E., Olson, J., Molohon, K. J., ... & Oldfield, E. (2013). Antibacterial drug leads targeting isoprenoid biosynthesis. *Proceedings of the National Academy of Sciences*, *110*(1), 123-128.
117. Cohen-Gonsaud, M., Ducasse, S., Hoh, F., Zerbib, D., Labesse, G., & Quemard, A. (2002). Crystal structure of MabA from Mycobacterium tuberculosis, a reductase involved in long-chain fatty acid biosynthesis. *Journal of molecular biology*, *320*(2), 249-261.
118. Heaslet, H., Harris, M., Fahnoe, K., Sarver, R., Putz, H., Chang, J., ... & Miller, J. R. (2009). Structural comparison of chromosomal and exogenous dihydrofolate reductase from Staphylococcus aureus in complex with the potent inhibitor trimethoprim. *Proteins: Structure, Function, and Bioinformatics*, *76*(3), 706-717.
119. Hazra, S., Xu, H., & Blanchard, J. S. (2014). Tebipenem, a new carbapenem antibiotic, is a slow substrate that inhibits the β-lactamase from Mycobacterium tuberculosis. *Biochemistry*, *53*(22), 3671-3678.
120. Pakhomova, S., Rife, C. L., Armstrong, R. N., & Newcomer, M. E. (2004). Structure of fosfomycin resistance protein FosA from transposon Tn2921. *Protein science*, *13*(5), 1260-1265.
121. Büttner, D., Kramer, J. S., Klingler, F. M., Wittmann, S. K., Hartmann, M. R., Kurz, C. G., ... & Proschak, E. (2017). Challenges in the development of a thiol-based broad-spectrum inhibitor for metallo-β-lactamases. *ACS infectious diseases*, *4*(3), 360-372.
122. Ilangovan, A., Fletcher, M., Rampioni, G., Pustelny, C., Rumbaugh, K., Heeb, S., ... & Williams, P. (2013). Structural basis for native agonist and synthetic inhibitor recognition by the Pseudomonas aeruginosa quorum sensing regulator PqsR (MvfR). *PLoS pathogens*, *9*(7), e1003508.
123. Kitao, T., Lepine, F., Babloudi, S., Walte, F., Steinbacher, S., Maskos, K., ... & Rahme, L. G. (2018). Molecular insights into function and competitive inhibition of Pseudomonas aeruginosa multiple virulence factor regulator. *MBio*, *9*(1), 10-1128.
124. Lin, J., Oh, S. H., Jones, R., Garnett, J. A., Salgado, P. S., Rusnakova, S., ... & Cota, E. (2014). The peptide-binding cavity is essential for Als3-mediated adhesion of Candida albicans to human cells. *Journal of Biological Chemistry*, *289*(26), 18401-18412.
125. Sogabe, S., Masubuchi, M., Sakata, K., Fukami, T. A., Morikami, K., Shiratori, Y., ... & Ohtsuka, T. (2002). Crystal structures of Candida albicans N-myristoyltransferase with two distinct inhibitors. *Chemistry & Biology*, *9*(10), 1119-1128.
126. Sirvent, R., Pérez, J. M., Badia, R. M., & Labarta, J. (2006). Automatic grid workflow based on imperative programming languages. *Concurrency and Computation: Practice and experience*, *18*(10), 1169-1186.
127. Rizvi, S. M. D., Shakil, S., & Haneef, M. (2013). A simple click by click protocol to perform docking: AutoDock 4.2 made easy for non-bioinformaticians. *EXCLI journal*, *12*, 831-874.

128. Ayna, A., Khosnaw, L., Temel, Y., & Ciftci, M. (2021). Antibiotics as inhibitor of glutathione S-transferase: biological evaluation and molecular structure studies. *Current drug metabolism*, *22*(4), 308-314.
129. Liu, L., Jiang, T., Zhou, J., Mei, Y., Li, J., Tan, J., ... & Wang, H. (2022). Repurposing the FDA-approved anticancer agent ponatinib as a fluconazole potentiator by suppression of multidrug efflux and Pma1 expression in a broad spectrum of yeast species. *Microbial biotechnology*, *15*(2), 482-498.
130. S. Magaldi, S. Mata-Essayag, C. Hartung de Capriles, et al. Well diffusion for antifungal susceptibility testing Int. J. Infect. Dis., 8 (2004), pp. 39-45.
131. Liju, V. B., Jeena, K., & Kuttan, R. (2014). Article details cytotoxicity, antitumour and anticarcinogenic activity of Curcuma longa essential oil. *Indian drugs*, *51*, 28-34.
132. Călinescu, M., Fiastru, M., Bala, D., Mihailciuc, C., Negreanu-Pîrjol, T., & Jurcă, B. (2019). Synthesis, characterization, electrochemical behaviour and antioxidant activity of new copper (II) coordination compounds with curcumin derivatives. *Journal of Saudi Chemical Society*, *23*(7), 817-827.
133. Wilson, D. (2015). An evolutionary perspective on zinc uptake by human fungal pathogens. *Metallomics*, *7*(6), 979-985.
134. Jarrahpour, A., Sheikh, J., Mounsi, I. E., Juneja, H., & Hadda, T. B. (2013). Computational evaluation and experimental in vitro antibacterial, antifungal and antiviral activity of bis-Schiff bases of isatin and its derivatives. *Medicinal Chemistry Research*, *22*, 1203-1211.
135. Mehta, D., Saini, V., & Bajaj, A. (2023). Recent developments in membrane targeting antifungal agents to mitigate antifungal resistance. *RSC Medicinal Chemistry*, *14*(9), 1603-1628.
136. Stevanović, N. L., Aleksic, I., Kljun, J., Skaro Bogojevic, S., Veselinovic, A., Nikodinovic-Runic, J., ... & Glišić, B. Đ. (2020). Copper (II) and zinc (II) complexes with the clinically used fluconazole: comparison of antifungal activity and therapeutic potential. *Pharmaceuticals*, *14*(1), 24-36.

CHAPTER 7

Conclusions

CHAPTER 7
CONCLUSIONS

This thesis outlined a multidisciplinary approach to streamline drug discovery, integrating chemistry, pharmacology, and computational biology. The research focused on the design, synthesis, and evaluation of nine curcumin analogues and their copper (II) and zinc (II) metal complexes for potential anticancer, antidiabetic, anti-inflammatory, antibacterial, and antifungal activities. The curcumin analogues were modified with hydroxy, alkoxy, and chloro substituents to enhance bioactivity. Computational techniques, including molecular docking and dynamics simulations, were used to predict interactions with relevant protein targets and analyze stability. These findings were then validated through *in vitro* and *in vivo* studies.

Nine curcumin analogues with unique aryl ring alterations and eighteen related metal complexes of Cu(II) and Zn(II) were synthesized and their structural versatility was revealed through various spectral analyses such as IR,^{1}HNMR,^{13}CNMR and Mass Spectra. Employing computational and experimental approaches, the research highlighted the potential pharmacological applications, including anticancer, anti-inflammatory, antidiabetic, and antimicrobial activities of the compounds. Docking studies and molecular dynamics simulations provided insights into molecular interactions, while ADME-Tox and bioactivity predictions, alongside SAR analysis, informed pharmacokinetics and pharmacodynamics. Virtual screening, drug design, and lead optimization guided the development of novel therapeutic agents, supported by experimental validation. The findings demonstrated the promising potential of these compounds as candidates for diverse disease treatments, contributing significantly to medicinal chemistry and laying a robust foundation for future pharmaceutical innovation.

Nine curcumin analogues – NLB (1,7-bis (3,4-dimethoxy phenyl)hepta-1,6-diene-3,5-dione), NLD (1,7-bis(3,5-dichloro-2-hydroxyphenyl)hepta-1,6-diene-3,5-dione), NLE (1,7-bis (6-methoxy naphthalen-2-yl) hepta-1,6-diene-3,5-dione), NLF (1,7-bis(3-ethoxy-2-hydroxy phenyl)hepta-1,6-diene-3,5-dione), NLG (1,7-bis(4-hydroxy-3,5-dimethyl phenyl) hepta-1,6-diene-3,5-dione), NLH (1,7-bis (5-chloro-2-hydroxy phenyl)hepta-1,6-diene-3,5-dione), NLI (1,7-bis (2-hydroxy-3-methoxy phenyl)hepta-1,6-diene-3,5-dione), NLJ(1,7-bis (3-hydroxy-4-methoxyphenyl)hepta-1,6-diene-3,5-dione) and NLK(1,7-bis

(5-methyl thiophen-2-yl) hepta-1,6-diene-3,5-dione) were synthesized and evaluated for pharmacological potential. All adhered to the Rule of Five, CMC-like Rule, Lead-like Rule, and MDDR/WDI-like criteria, indicating strong oral bioavailability. Most compounds demonstrated high plasma protein binding, with NLB and NLI showing moderate binding. They exhibited good absorption, medium Caco-2 permeability, and favourable toxicity profiles, being non-carcinogenic, non-mutagenic, and posing medium ecotoxicity risk. Based on BBB penetration, compounds were identified for peripheral or central targets. Further steps involved scaling up synthesis and conducting *in-vitro* and *in-vivo* studies to explore their mechanisms of action against anticancer, anti-inflammatory, antidiabetic, antibacterial, and antifungal targets, supported by molecular docking for detailed interaction insights.

This study synthesized nine curcumin analogues by modifying aryl ring functional groups, utilizing Pabon's method based on the Claisen–Schmidt condensation mechanism. This method was selected for its simplicity, high yields, and minimal by-products, crucial for efficient β-diketone formation. Purified and characterized through analytical techniques, the analogues were confirmed to predominantly exist in the intramolecularly hydrogen-bonded enol tautomeric form. Cu(II) and Zn(II) complexes of these analogues were also synthesized, enhancing stability, solubility, and potential biomedical properties. These stable ML_2 chelates featured monobasic bidentate coordination through diketone oxygen atoms, forming six-membered rings. Analytical data indicated that other groups, like hydroxyl (-OH) and sulphur atoms in the thiophenyl ring, did not participate in metal coordination, underscoring the selectivity of the diketone groups.

The current work investigated the anticancer potential of curcumin analogues, focusing on 1,7-bis (5-chloro-2-hydroxy phenyl) hepta-1,6-diene-3,5-dione (NLH). Molecular docking analyses revealed a favourable binding energy of -8.3 kcal/mol for NLH with the BRCA1 homologous protein 1OQA (TG3), outperforming -3.8 kcal/mol binding energy of cyclophosphamide with its target Cyclophilin (TG7). Molecular dynamics and MM-GBSA simulations confirmed the stability of NLH-TG3 interactions.

In vitro studies demonstrated superior cytotoxicity of NLH against DLA and EAC cell lines, with minimal toxicity to spleen cells and lower inhibitory activity on Vero cells. NLH exhibited significant growth inhibition of breast cancer cells. Copper and zinc complexes of curcumin analogues, particularly $Cu(NLH)_2$ and $Zn(NLH)_2$, showed enhanced cytotoxicity due to increased bioavailability, cellular uptake, ROS generation, and stability.

In vivo experiments on Swiss albino mice revealed the strong anti-proliferative effect of NLH, significantly inhibiting DLA-induced solid tumours and surpassing cyclophosphamide in efficacy. The presence of chlorine in NLH enhanced hydrophobicity, membrane permeability, electrophilicity, and metabolic stability, strengthening interactions with nucleophilic targets like DNA and proteins while inducing oxidative stress.

Computational results aligned with experimental findings, highlighting the potential of NLH as a multi-target therapeutic candidate. Further research is essential to explore its structural features, anticancer mechanisms, and side effects. Rigorous *in vivo* studies and validation in animal models and humans are recommended to optimize its therapeutic application.

This research evaluated nine curcumin analogues as inhibitors for inflammatory and diabetic receptors through molecular docking and *in vitro* experiments, comparing their efficacy with curcumin, Diclofenac, and Acarbose. Among the analogues, 1,7-bis (3,5-dichloro-2-hydroxy phenyl) hepta-1,6-diene-3,5-dione (NLD), 1,7-bis (6-methoxy naphthalen-2-yl) hepta-1,6-diene-3,5-dione (NLE), and 1,7-bis (3-ethoxy-2-hydroxy phenyl) hepta-1,6-diene-3,5-dione (NLF) emerged as the most potent anti-inflammatory inhibitors (IC_{50} values of 57.07 µg, 59.69 µg and 64.85 µg respectively), with chloro, hydroxy, methoxy, and ethoxy functional groups enhancing binding affinity, stability, and cellular uptake. 1,7-bis (5-chloro-2-hydroxyphenyl) hepta-1,6-diene-3,5-dione (NLH) and 1,7-bis (5-methylthiophen-2-yl) hepta-1,6-diene-3,5-dione (NLK) showed moderate activity, while curcumin, 1,7-bis (3,4-dimethoxy phenyl) hepta-1,6-diene-3,5-dione (NLB),1,7-bis (2-hydroxy-3-methoxyphenyl) hepta-1,6-diene-3,5-dione (NLI), and 1,7-bis (3-hydroxy-4-methoxyphenyl) hepta-1,6-diene-3,5-dione (NLJ) exhibited lower potency due to suboptimal functional group positioning or reduced electrophilicity. Cu(II) and Zn(II) complexes exhibited superior anti-inflammatory activity, with Zn(II) complexes generally outperforming Cu(II). Zn(II) complexes offered better stability, antioxidant properties, and bioavailability due to their non-redox nature and d10 electron configuration. In contrast, Cu(II) complexes, being redox-active, generated reactive oxygen species, which led to tissue damage and reduced their effectiveness. Thus, Zn(II) complexes showed enhanced efficacy for anti-inflammatory interventions.

For anti-diabetic activity, NLB, NLH, and NLE demonstrated superior potency, with IC_{50} values of 26.68 µg, 29.90 µg, and 30.45 µg, respectively. Cu(II) and Zn(II) complexes showed enhanced activity compared to their parent ligands. Zn(II) complexes, such as $Zn(NLB)_2$ (22.18 µg), $Zn(NLD)_2$ (23.83 µg), and $Zn(NLE)_2$ (25.55 µg), were

particularly effective due to their improved stability, antioxidant properties, and compatibility with biological systems. These Zn(II) complexes also promoted glucose uptake and stabilized insulin hexamers, offering better bioavailability and safety than Cu(II) complexes. Cu(II) complexes, including $Cu(NLD)_2$ (25.43 µg), $Cu(NLE)_2$ (27.55 µg), and $Cu(NLB)_2$ (25.88 µg), exhibited strong activity but were less effective than Zn(II) complexes due to their redox-active nature, which generates reactive oxygen species (ROS). Both Cu(II) and Zn(II) complexes displayed improved efficacy through increased bioavailability, cellular uptake, and synergistic ligand-metal interactions. The differences in the antidiabetic effects of the compounds were attributed to the types and positions of their functional groups. In NLB, dimethoxy groups enhanced electron donation and stability, improving hydrophobicity and enzyme interactions. In NLH, chloro and hydroxy groups facilitated hydrogen bonding and halogen interactions. In NLE, methoxy groups stabilized enzyme interactions through increased conjugation and planarity.

The present study also focused on evaluating curcumin analogues for antimicrobial activity against bacterial and fungal pathogens, with insights from molecular docking and *in vitro* assays. Modifications to aryl rings of curcumin enhanced functional group diversity, influencing binding energy (BE), ligand efficiency (LE), and inhibition constants (Ki).

For Gram-positive bacteria, 1,7-bis (6-methoxynaphthalen-2-yl) hepta-1,6-diene-3,5-dione (NLE) demonstrated the highest efficacy due to its low BE (-12.63 kcal/mol for 4H8E), strong interactions via methoxy naphthyl groups, and superior hydrophobicity. 1,7-bis(3,5-dichloro-2-hydroxy phenyl)hepta-1,6-diene-3,5-dione (NLD), with hydroxy and chloro groups, followed, providing strong hydrogen bonding. 1,7-bis (5-chloro-2-hydroxyphenyl) hepta-1,6-diene-3,5-dione (NLH) also ranked highly, benefiting from its hydroxy and chloro substituents. Moderately effective ligands included 1,7-bis (5-methylthiophen-2-yl) hepta-1,6-diene-3,5-dione (NLK) and 1,7-bis (3,4-dimethoxy phenyl) hepta-1,6-diene-3,5-dione (NLB), leveraging hydrophobic functional groups like methyl thiophene. 1,7-bis (4-hydroxy-3,5-dimethyl phenyl) hepta-1,6-diene-3,5-dione (NLG) and 1,7-bis (3-ethoxy-2-hydroxyphenyl) hepta-1,6-diene-3,5-dione (NLF) balanced hydrophobic and hydrogen-bonding properties, while 1,7-bis (2-hydroxy-3-methoxyphenyl) hepta-1,6-diene-3,5-dione (NLI) and 1,7-bis (3-hydroxy-4-methoxyphenyl) hepta-1,6-diene-3,5-dione (NLJ) were less effective. Gentamycin and curcumin served as baseline comparisons.

Against Gram-negative bacteria, NLE emerged as the top ligand with exceptional BE (-10.21 kcal/mol for 5O7N) and low Ki (32.6 nM), despite challenges with outer membrane penetration. Gentamycin showed comparable efficacy due to its active transport mechanisms. NLH and NLK followed with moderate binding capabilities. Copper(II) and Zinc(II) complexes, especially $Cu(NLE)_2$ and $Zn(NLE)_2$, surpassed curcumin and gentamycin in potency, exhibiting strong activity across bacterial strains by disrupting membranes and generating reactive oxygen species.

In silico studies showed that NLD (25.08 mm) and NLE (23.05 mm) were the top performers against *Candida albicans*, with low binding energies (BE) and inhibition constants (Ki), indicating strong binding affinity and potent inhibitory activity. NLH, NLG, and NLJ were also promising candidates. *In vitro*, NLD (25.08 mm) and NLE (23.05 mm) exhibited the largest inhibition zones, outperforming Curcumin and Fluconazole. Zinc complexes, $Zn(NLD)_2$ (30.08 mm) and $Zn(NLE)_2$ (28.10 mm), showed superior antifungal activity compared to copper complexes, $Cu(NLD)_2$ (28.03 mm) and $Cu(NLF)_2$ (25.13 mm), due to better stability, reactivity, and enhanced ligand-metal synergy, improving solubility and biomolecular interactions.

Splenocytic assays further confirmed the efficacy and safety of the top-performing drug candidates, emphasizing their potential for therapeutic development. Precise dosage management could enable the development of these compounds into safe and effective antimicrobial agents.

The research successfully synthesized and characterized nine curcumin analogues and their Cu(II) and Zn(II) complexes, demonstrating their potential as multi-functional therapeutic agents. The research confirmed the therapeutic potential of curcumin analogues, especially 1,7-bis (5-chloro-2-hydroxyphenyl) hepta-1,6-diene-3,5-dione (NLH), 1,7-bis (6-methoxynaphthalen-2-yl) hepta-1,6-diene-3,5-dione (NLE), and 1,7-bis(3,5-dichloro-2-hydroxy phenyl)hepta-1,6-diene-3,5-dione (NLD), along with their copper and zinc complexes. The Zn(II) complexes were generally more effective and safer, making them more suitable for further drug development. The alignment of *in silico* findings with *in vitro* and *in vivo* data substantiated the promising bioactivity of these compounds. The study highlighted the potential of these compounds in the development of advanced multi-target drugs with minimized side effects.

CHAPTER 8

Recommendations for future studies

CHAPTER 8

RECOMMENDATIONS FOR FUTURE STUDIES

This research adopted a multidisciplinary approach to drug discovery, integrating synthetic chemistry, computational biology, and pharmacological evaluation. The study focused on synthesizing nine curcumin analogues and their copper(II) and zinc(II) complexes, evaluating their potential for anticancer, antidiabetic, anti-inflammatory, antibacterial, and antifungal activities. The analogues were modified with hydroxy, methoxy, ethoxy, and chloro substituents to enhance their bioactivity. The findings highlighted several avenues for future studies to optimize the therapeutic potential of curcumin analogues.

For enhancing bioactivity through functional group modifications, further studies can explore the effects of varying the position and types of functional groups on the aryl rings of curcumin analogues. Advanced molecular docking and dynamic simulations, such as quantum mechanical/molecular mechanical (QM/MM) docking, can be employed to predict the impact of these modifications with greater accuracy, particularly in active site interactions.

This study performed molecular docking studies on the ligands but not on the metal complexes. Extending this analysis to the copper(II) and zinc(II) complexes, as well as exploring the complexation with other metals, may provide valuable insights into their binding affinities and biological activities.

The most active anticancer compound in this study underwent molecular dynamic simulations. Future research should adopt all-atom molecular dynamics simulations to study the ligand-protein stability in biologically relevant environments over extended timescales. Free Energy Perturbation (FEP) or metadynamic simulations could also be applied to calculate binding free energy differences among ligands, offering a deeper understanding of binding pathways and mechanisms of ligand-protein interactions.

This study revealed that some compounds, such as NLD and NLH, possess multiple biological activities, including anticancer, anti-inflammatory, antidiabetic, and antibacterial properties. Future research should focus on multi-target optimization using docking and molecular dynamics simulations to refine these multifunctional molecules.

Further wet lab studies could include the design and synthesis of additional curcumin analogues and their metal complexes to improve binding efficiency and biological activity. Different biochemical assays, such as Cyclooxygenase (COX) assays for anti-inflammatory studies; α-Glucosidase inhibition assays for antidiabetic evaluations; Surface Plasmon Resonance (SPR) for quantifying binding kinetics and affinities; Isothermal Titration Calorimetry (ITC) to measure thermodynamic parameters (ΔH, ΔS) of ligand-protein interactions.

Extending the current findings to *in vivo* studies and clinical testing is essential to evaluate the therapeutic potential, safety profiles, and side effects of the synthesized curcumin analogues and their metal complexes. Testing these compounds in animal models will help assess their real-world efficacy.

Investigating the synergistic effects of these compounds in combination therapies could provide a pathway for developing multi-functional drugs with enhanced efficacy.

Future studies could incorporate nano-synthesis techniques to improve the stability, bioavailability, and targeted delivery of curcumin analogues. Nano-formulated compounds could then be evaluated for various biological applications, including their therapeutic potential in cancer and metabolic disorders.

This research laid a solid foundation for exploring curcumin analogues and their metal complexes for therapeutic applications. The proposed directions, combining computational, biochemical, biophysical, and *in vivo* studies, will further refine the understanding of these compounds, paving the way for innovative drug development.

PAPER PUBLICATIONS

AND

PRESENTATIONS

PUBLICATIONS:

1. **Jacob, L. A.**, & Cherian, T. (2020). A review on the relevance of curcuminoids in the corona pandemic situation. *International Research Journal of Ayurveda & Science and Humanity*, 2(8), Article 135. https://doi.org/10.47392/irjash.2020.135
2. **Jacob, L. A.**, Cherian, T., Jesy, E. J., Thomachan, S., & Varghese, D. (2022). Synthesis, characterization, and biochemical assessment of 1,7-diphenyl heptanoids. *International Advanced Research Journal in Science, Engineering and Technology*, 9(2), Article 9293. https://doi.org/10.17148/IARJSET.2022.9293
3. **Jacob, L. A**. (2022). Curcumin - A combatant against coronavirus: Some findings. In *Erudition* (pp. 45). Turn Books. ISBN: 978-93-87709-82-9
4. **Jacob, L. A.**, & Cherian, T. (2023). A review on antimicrobial effects of curcumin. In *Erudition* (pp. 84–95). Turn Books. ISBN: 978-93-87709-89-8
5. **Jacob, L. A.**, Cherian, T., Raphael, V. P., & Alex, S. (2023). Dry and wet lab experiences of certain curcumin analogues' antibacterial effect on *S. aureus*. *International Journal of Engineering Technology and Management Sciences*, 7(2). https://doi.org/10.46647/ijetms.2023.v07i02.003
6. **Aloor, L. J.**, Skariyachan, S., Raghavamenon, A. C., Kumar, K. M., Narayanappa, R., Uttarkar, A., Niranjan, V., & Cherian, T. (2023). BRCA1/TP53 tumor proteins inhibited by novel analogues of curcumin: Insight from computational modeling, dynamic simulation, and experimental validation. *International Journal of Biological Macromolecules*, 20, 126989. https://doi.org/10.1016/j.ijbiomac.2023.126989

PRESENTATIONS:

1. "A review on the relevance of curcuminoids in the corona Pandemic situation" at the First International Conference on advancement in Research and Development (ICARD- 2020) on 29th and 30th August 2020. Conducted by RSP Conference Hub.pg.49

2. "Characterization and biological assessment of newly synthesized curcuminoids and complexes" in the First International Conference on Advancement in Science, Management and Engineering (ICSME-2022 Online) organized by Nrupathunga

University, Bengaluru, Karnataka, India in collaboration with RSP Research Hub, Coimbatore, Tamil Nādu, India on 26th and 27th February 2022. pg.178

3. "*In vitro* and *In silico* studies of certain curcumin analogues antibacterial effect" in the National Conference on Interdisciplinary Academic Translational Research and Innovation 2023 (NCIATRI-2023)conducted on 7th and 8th February by MES Asmabi College, Kodungallur in association with Kerala State Higher Education council.pg.33

4. "Virtual Screening and biochemical studies of synthesized curcumin analogues" at the Fourth International Conference on Innovation in Engineering Sciences (ICIES) organized by Techno Engineering College, Banipur and Global Conference Hub, Coimbatore, India on 25th and 26th February 2023.pg. 82

5. "Antiproliferative and antitumor potential of a novel curcumin analogue against breast cancer: Insights from computational and experimental investigations" in the 9th International Conference (ICRAMC 2025) at SRMIST-KTR during 13th to 15th February 2025, Chennai, pg.227